Exploiting MS-based techniques to unveil elusive reaction intermediates of bioinorganic relevance

Thesis

in Partial Fulfillment of the Requirements

for the Degree of

Doctor of Philosophy in Pharmaceutical Sciences

XXXI cicle

Author

Davide Corinti

Supervisor

Prof. Simonetta Fornarini

Alle donne della mia vita

che mi hanno insegnato

la cultura, la dedizione e l'amore

Non quia difficilia sunt non audemus, sed quia non audemus difficilia sunt.

Lucius Annaeus Seneca

Table of contents

Abstract

The periodic table for a medicinal chemist or a biochemist is usually restricted to very few elements. More than 95% of the mass of living systems is indeed composed by carbon, hydrogen, nitrogen and oxygen. Besides, elements present only in trace amount can have irreplaceable roles in the chemistry of life. Even more surprisingly, transition metals completely unrelated to living systems have found their way in therapy and, nowadays, antineoplastic drugs containing for example platinum are widespread. However, many techniques routinely exploited for analyzing chemical reactions in solution fail to characterize the properties of metal complexes, in particular in their interaction with biological molecules. The aim of this thesis is to show how electrospray ionization (ESI) mass spectrometry (MS) may excel in capturing elusive species from solution. One can thus shed light on reaction mechanisms of biological relevance and gain insight about coordination sites of biomolecules in binding metals. This work is focusessed on platinum complexes moving from the Pt^{II}-containing anticancer drug cisplatin to novel Pt^{IV} complexes, which are promising candidates to be at the forefront of future platinum-based therapies. To obtain structural insights about the species of interest, several MS-based techniques have been exploited. IR multiple photon dissociation (IRMPD) spectroscopy was used to obtain the vibrational features of mass selected species. IRMPD spectroscopy combined with calculations at the DFT level, to interpret the experimental vibrational features, allowed us to tackle a variety of issues. Among them, we could unveil the nature of the encounter complex lying on the reaction coordinate of ligand exchange of cisplatin with model biological targets. IRMPD

spectroscopy was also employed to characterize the primary intermediates formed by cisplatin reacting with histidine and methionine, major platination targets in proteins. Eventually, IRMPD kinetics on isomer- and conformer-specific vibrational modes were also used to obtain semi-quantitative information about the conformational landscape of cisplatin derived complexes. Collision induced dissociation (CID) was instead the MS/MS technique of choice to gain information about the gas-phase reactivity of platinum(IV) complexes. Using high-resolution mass spectrometry a complete fragmentation pattern was achieved by assigning an unambiguous molecular formula and so characterizing exotic species generated by reduction of Pt^{IV}.

Introduction

1.1 Life and its connection with metal complexes, the role of bioinorganic chemistry

Thinking about the chemistry of life usually makes our mind wandering among hydrogen andcarbon containing molecules more or less derivatized by oxygen or nitrogen containing groups, with the participation of a few sulfur atoms. However, the so called "inorganic" elements, which comprehend among others alkaline and transition metals as well as halogens, are essential to many biological functions. Therefore, the understanding of their properties is needed to obtain a thorough description of living system. Indeed, stating the importance of metals like calcium, sodium and potassium, which are present in considerable quantities in the human body and are involved in neuron signaling and cell homeostasis, is trivial. The same, however, cannot be said about transition metals, which have found their placement in directing many biological functions, from participating to the structural folding of proteins to acting as cofactors in enzymatic processes.[1] The main transition metals involved in biological functions are, in order of decreasing abundance in the body: iron, zinc (which is not strictly a transition metal, but shares many biochemical properties with them), copper, molybdenum, cobalt, chromium, vanadium and nickel. Their importance is confirmed by the fact that their concentration in the human body greatly exceeds that in seawater, as reported in table 1.1.[2] Under these premises, it is not surprising that in the last 50 years the study of metals in life, discipline identified as "Bioinorganic chemistry", has risen as testified by the appearance in 1972 of the *Journal of Inorganic Biochemistry* and later in 1996 by the *Journal of Biological Inorganic Chemistry*, without mentioning the several books and manuals on the subject.

Table 1.1 Concentration of transition metals and zinc in sea water and human plasma. Data are collected from Ref. 2 and references therein.

Element	Sea water (M) * 10^8	Human plasma (M) * 10^8
Fe	0.005-0.002	2230
Zn	8.0	1720
Cu	1.0	1650
Mo	10.0	1000
Co	0.7	0.0025
Cr	0.4	5.5
V	4.0	17.7
Mn	0.7	10.9
Ni	0.5	4.4

Metals can be stored in several ways in the organism, for example iron is stored using ferritin, a highly conserved complicated protein composed by a protein coat that is important for its recognition by other cellular elements and helps to solubilize the Fe-containing inorganic core,[3,4] or employing proteins like metallothioneins that present clusters of cysteine residues whose SH groups can coordinate metals, in particular zinc and copper.[5,6] Indeed, the most common chemical tool used by living systems in order to make the stored metals available is complexation. Usually, metals are coordinated by the side chains of aminoacid residues like histidine, cysteine or tyrosine, however also small inorganic molecules may be involved as well as protein cofactors, e.g. porphyrins. Several examples can be gathered by the biochemistry of iron compounds which has been extensively studied being iron the metal with the highest abundance in all the living systems. In particular, the proteins of the transferrin family, which are implicated in the transfer of the iron ions, are a perfect example of how transition metals can be coordinated by the residues of a polypeptide. The iron ion in fact is coordinated in human transferrin by two phenoxide groups of tyrosine side chains, the imidazole nitrogen of a histidine residue and the carboxylate moiety of an aspartate. The octahedral coordination sphere is completed by the presence of a bidentate interaction with a bicarbonate ion. In figure 1.1 is reported a magnification of the

crystal structure of the N-lobe of a mutant human transferrin, which shows the wide range of interactions involved in the formation of the Fe-containing complex.[7]
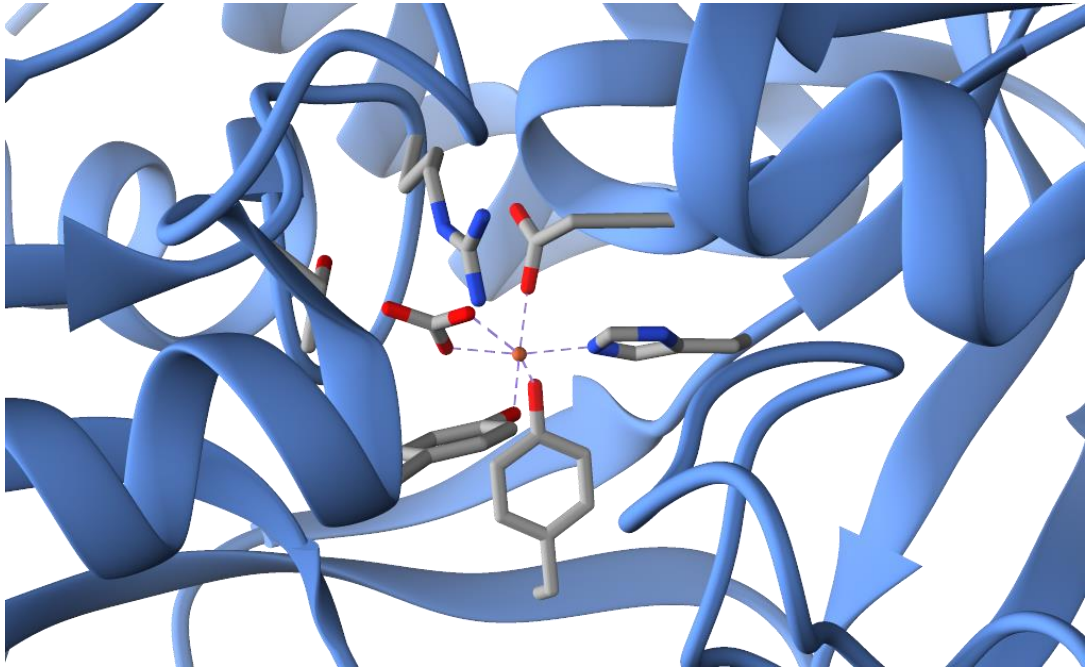
Figure 1.1 Crystal structure of a human transferrin N-lobe coordinating an iron atom (orange in the picture).

1.2 Cisplatin and other metal-containing drugs

Inorganic elements are not only essential for life, their use has crossed the frontier of medicine leading to the introduction in clinical therapy of several metal-based drugs for a broad range of applications, as summarized in Scheme 1.1.[8]

Therapeutic agents
•(Li, V, As, Ru, Ag, Pt, Au)

Chelation therapy
•Overload diseases (Fe, Cu, Pb)
•Removal of radionuclides

Contrast agents
•MRI (Gd, Mn, Fe)
•X-ray (I)

Medicinal Inorganic Chemistry

Radiopharmaceuticals
•Therapeutic (^{188}Re)
•Diagnostic (^{99m}Tc)

Protein/ enzyme regulators
•(metalloproteinases, O_2, CO, NO)

Mineral supplements
•Ca, Fe and Zn
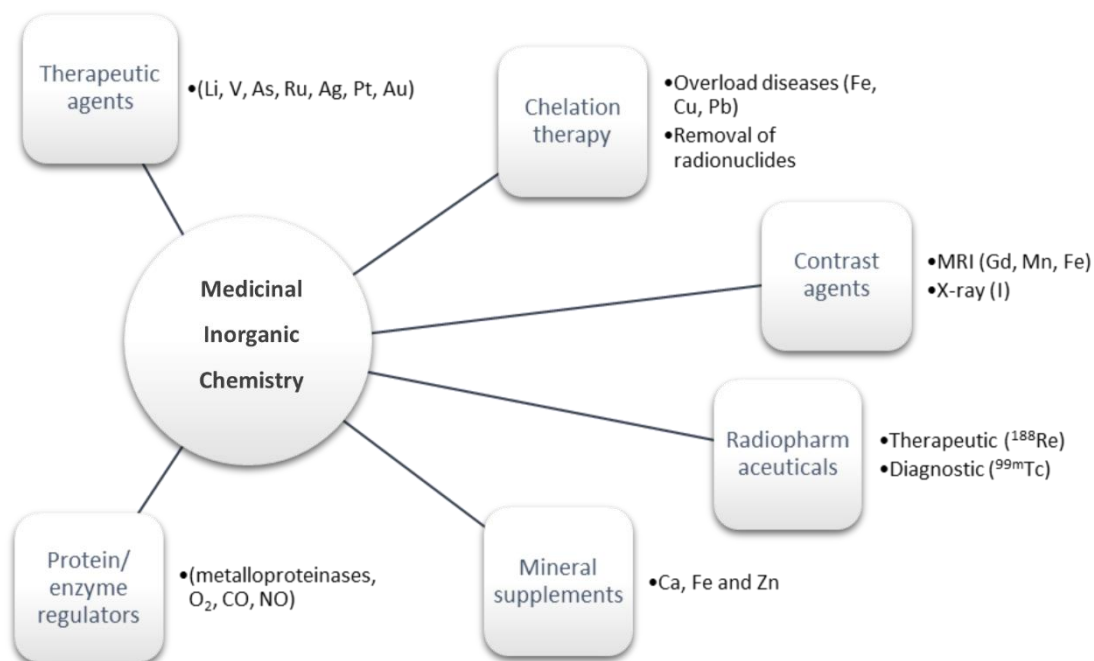
Scheme 1.1 Some of the key areas involving medicinal inorganic chemistry.

Besides the multitude of therapeutic and diagnostic areas where metals and inorganic elements in general are involved, there is still the need of a better comprehension of the molecular basis behind their activity. An interesting example regards aluminum, a metal used as adjuvant in human and veterinary vaccines due to its enhancing activity of the pharmacological effect. Despite its widespread implementation, there are no clear evidences on the chemical basis of this.[9] Moreover, as shown in section 1.1 metals in the biological media are mostly associated with ligands forming adducts that can show huge differences in their activity compared to the one of the element by itself. The dependence on both composition and environment on the behavior of metal complexes adds another complexity layer to the overall figure, thus explaining why it is so challenging to predict and control the behavior of inorganic pharmaceuticals.[8]

It is not surprising, though, that medicinal inorganic chemistry is a relatively young research area, stimulated by the progresses in analytical and spectroscopic techniques.[1,8] Also, the growing of this discipline is connected with the success of cisplatin, a Pt-based antineoplastic drug which is still widely used nowadays even if its discovery is dated back to the late '60s.[10,11] The activity of cisplatin (*cis*-[PtCl$_2$(NH$_3$)$_2$]) derives from its interaction with the nucleobases of DNA but a preliminary aquation step, which consists in the substitution of a chloride with a water molecule, is considered to be required for its activation.[12,13] The necessity of an *in vivo* transformation before reaching the target site is common among inorganic drugs. The possible transformations include a variety of reactions, from redox to substitution ones. Many efforts have been devoted to design more efficient and safer platinum drugs employing higher oxidation states of the metal, e.g. Pt^{IV}, unfortunately with scarce results. Nowadays, the FDA has approved only three Pt-containing drugs: cisplatin, carboplatin and oxaliplatin, reported in figure 1.2. These three pharmaceuticals contain a Pt^{II} atom and share a square planar geometry. However, several Pt^{IV} complexes have also been synthesized and are in clinical trial. A few examples are shown in figure 1.2. However, no Pt^{IV} containing complex has been currently approved for clinical use.
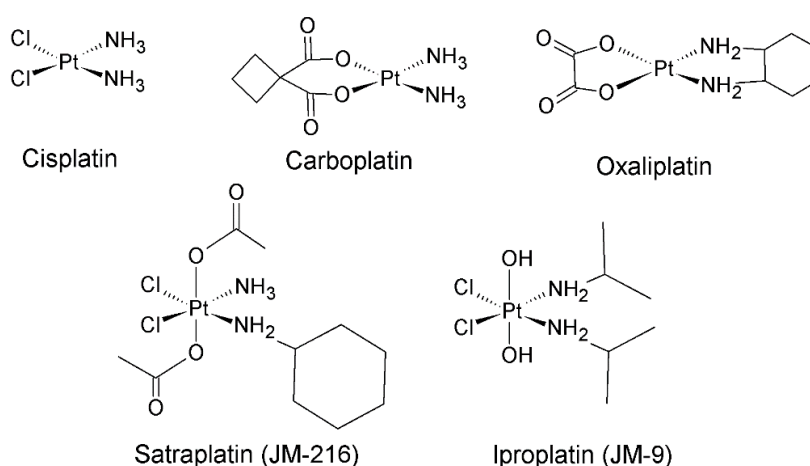
Figure 1.2. Cisplatin, carboplatin and oxaliplatin are square planar Pt^{II} complexes and have been approved by the FDA for clinical use. They are widely employed worldwide. Satraplatin and iproplatin are Pt^{IV} octahedral complexes still in clinical trial.

The development of novel platinum drugs has been stimulated by the fact that cisplatin produces severe side effects and its use is strongly limited by drug resistance.[14] However, many efforts devoted to prepare and screen new potential platinum antineoplastic drugs have met with little success till now.[15] In this regard, recent advances in spectrometric and spectroscopic techniques may be useful in obtaining a better understanding of platinum complexes interaction and reactivity with biological molecules and in general in the mainframe of the chemistry of living system, hoping to gain insight towards an appreciable improvement in efficacy and safety for platinum-based chemotherapy.

1.3 Analytical tools for bioinorganic chemists

Exploring metal involvement in the chemistry of life has not been an easy task for decades. Most of the analytical methods developed for biochemistry were not meant to investigate the presence and the role of inorganic elements in biomolecules and, in addition, advanced spectroscopic techniques have to be developed to a state which makes it feasible to work with little amount of sample and limited stability. From the 80s, however, things have drastically changed and nowadays the bioinorganic chemist can choose among a vast number of techniques, which include electron paramagnetic resonance (EPR) and NMR (nuclear magnetic resonance) spectroscopy, IR (infrared) and Raman spectroscopy, X-ray-based techniques and mass spectrometry in all its developments.

Starting from the low energy end of the spectroscopic techniques, NMR is now widely used in the field of protein characterization, in particular after improvement in multiple dimensional methods and the use of isotopes with nuclear spin different from that of the naturally occurring elements (^{2}H, ^{13}C, ^{15}N, ^{17}O and ^{57}Fe). NMR spectroscopy has also been involved in several studies regarding platinum complexes and their interaction with biological targets. In 1985 Saudek was already studying the complexes of cisplatin with nitrogen containing ligands using NMR. In fact, platinum complexation on a nucleophilic N atom gives rise to two satellites and produces a characteristic chemical shift on the ^{1}H NMR signals of the organic ligand.[16] Moreover, in the '90s many progresses were made in understanding donor atom preferences of platinum complexes using ^{195}Pt NMR, which shows characteristic coupling constants for nucleophiles containing atoms such as the ^{15}N isotope.[17] Moving on to the millimeter range, EPR was a decisive tool to determine the aspect and function of copper proteins and it played an important role in the discovery of Fe-S proteins and in the exploration of their electronic structure.[1,18] However, the pioneering work of Beinert on Fe-S clusters in proteins gained a new dimension using X-ray absorption spectroscopy (XAS) and in particular extended X-ray absorption fine structure (EXAFS) which allowed to discover and determine the structure of 3Fe clusters,[19] showing the potential of high energy photons

spectroscopy in the study of metal clusters. Furthermore the analysis of the X-ray absorption near edge structure (XANES) has also demonstrated its importance, focusing on the pre-edge features that, used to determine the degree of covalency of metal-to-organic ligand bonding, provided new insights about the electronic structure of Fe-S proteins.[20,21] XAS regions are schematized in figure 1.3
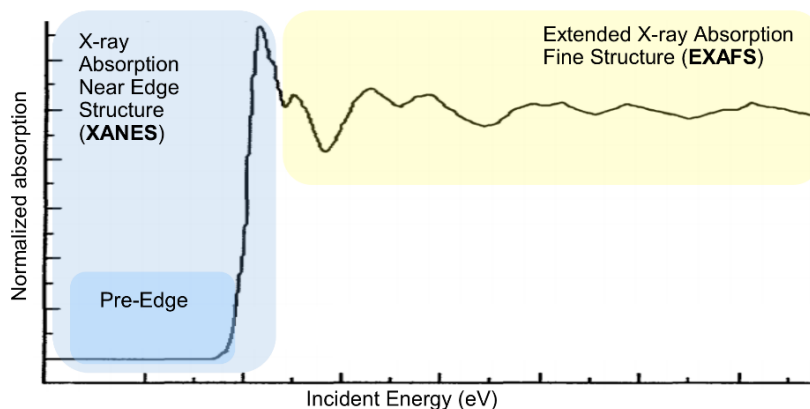
Figure 1.3 Schematic representation of an exemplary X-ray absorption spectrum. XANES and EXAFS region are pointed out.

Vibrational spectroscopy had also its important role in bioinorganic chemistry. Resonance Raman (RR) spectroscopy for example, which is based on the enhancement of ordinary Raman lines by the presence in the molecule of a transition metal, is largely employed to have information about the position of the ligands near the metal center. Not to mention infrared spectroscopy that showed its analytical power when it helped to discover the presence of CO and CN ligands bound to the 2Fe clusters in hydrogenases.[22] More recently, action IR spectroscopy performed on mass-isolated bare ions has started to yield a fine characterization of the vibrational features of transition metal complexes with organic ligands.[23,24]

1.3.1 Mass spectrometry and MS-based techniques

Mass spectrometry can probably be seen as one of the most versatile tool in the hand of scientists from any field. Based on the implementation of different ion sources and/or analyzers, its function has shifted from a tool to detect cathode rays in the late 19th century to one of the forefront techniques for proteomic.[25] The use of MS in inorganic chemistry dates back to the first decades of the 20th century where physicists like Aston and Nier used MS to discover new isotopes and determine their abundances and accurate masses.[26] However, mass spectrometry

was relegated to volatile compounds, therefore with little applications in the biological field. Things drastically changed with the development of new ionization methods, in particular fast atom bombardment (FAB) in 1981, matrix-assisted laser desorption/ionization (MALDI) in 1988 and electrospray ionization (ESI) in the second part of the eighties. The last two methods have been particularly relevant for the analysis of macro biomolecules because they allow to analyze species up to and also above 100 kilodaltons, mass range that comprehends many of the proteins and other biological macromolecules. This was essentially the beginning of contemporary proteomics, which extensively exploits mass spectrometry in order to obtain information about the aminoacid sequence in a protein or the position of post-translational modifications. Two main methodologies are used: the bottom up approach that is based on the analysis of a proteolytic digestion;[27] or the top-down approach in which an intact protein is brought to the gas-phase and then activated and dissociated using several possible methods (e.g. CID, IR multiple photon dissociation or UV photodissociation) in order to obtain sequence coverage.[28] In addition, mass spectrometrists are now dealing with the study in the gas-phase of native species. Using soft conditions in the ionization source, it is possible to retain a protein conformation that can be attributed to the native form of the macromolecule.[29] In this field, the developing of ion-mobility devices, which can be used to separate isobaric ions based on their morphology or collisional cross-section (CCS), provides the perfect allied for seeking native molecular characterization.[30] Now, what about bioinorganic chemistry? Mass spectrometry has been used in particular with inductively coupled plasma (ICP) sources to quantify and identify the presence of metals in biological samples due to its high sensitivity.[31] However, ICP-MS completely destroys the organic structure preventing to obtain structural information. Therefore soft sources like the above mentioned MALDI and ESI have been extensively exploited to understand the interaction of metals with biological molecules. The bottom-up approach on a protein such as calmoduline incubated with cisplatin allowed to obtain insights about the coordination sites of platinum within the protein and to have experimental evidences of its cross-linker character.[32] In recent years, mass spectrometry has been coupled with IR

spectroscopy in order to obtain the vibrational features of mass isolated ions, removing thus the effect of solvent and other contaminant species on the absorptions and allowing to have a direct correlation of the obtained frequencies with calculated ones. This technique is based on the coupling of a tunable IR laser with mass spectrometers such as Paul ion traps and the ones based on Fourier-transform ion cyclotron resonance (FT-ICR). The number density of ions in the cell of this trapping instrument is too low to record the IR absorption. Therefore, the abundance of photofragments compared to the product ion is monitored. Fragmentation happens only when photons are resonant with the vibrations of the mass isolated molecules thus allowing to obtain an IRMPD spectrum plotting the fragmentation yield versus the photon frequency.[33,34] IRMPD spectroscopy was employed to characterize [Hemin]$^+$ adducts with CO, N$_2$, and O$_2$[35] and complexes of nucleobases with metal cations[36] as well as to assess the coordination sites of cisplatin on adenine and guanine[37], to cite just few examples among many successful applications. Thanks to the absence of any solvent effect and to the possibility to analyze a single species from a complex mixture, IRMPD spectroscopy constitutes one of the most powerful tools in the hand on a bioinorganic chemist.

1.3.2 Theoretical methods

Theoretical simulations give an invaluable help in interpreting spectroscopic and kinetic data, in particular when dealing with a complex system involving metals interacting with organic molecules. At the same time, in the presence of a transition metal calculations have to be carefully planned and considered since usually a number of simplifications have to be made in order to obtain a fast and still reliable result. Therefore, despite the advances in computing power and in data storage have allowed to exploit *ab initio* or density functional theory (DFT) methods for simulating structures and properties of increasingly bigger molecules, we are still far from reaching a simple, homogeneous and automated protocol for calculations in the bioinorganic field. However, a careful choice of the calculation method, moving from DFT hybrid functionals to dispersion corrected ones, or employing post Hartree-Fock methods, permits to obtain fair results.[38] In addition, when dealing with heavy inorganic elements like gold or platinum, the influence of relativistic

effects needs to be considered.[39] Usually, an effective core potential (ECP) is used that replaces the explicit quantum-mechanical treatment of the metal core electrons with an effective potential. The parameters of the ECP can be designed to mimic the relativistic effects therefore avoiding artifacts generated by the non-relativistic treatment of the Hamiltonian energy, but keeping low the computational cost of the calculations. Therefore, the selection of the right ECP is a critical factor in the simulation.[40]

Using these precautions and minding the limitations of each method, excellent results have been obtained for the simulation of structures, vibrational frequencies and reaction coordinates in the field of metal complexes.

1.4 ESI-MS to understand mechanisms of liquid-phase reactions: gas- and liquid-phase dichotomy

As anticipated in section 1.3 electro-spray ionization has opened mass spectrometry to biochemists and biologists. Moreover, ESI-MS has the unique possibility to analyze compounds that have been extracted with soft conditions from the solution to the gas-phase. An exemplary application is the exploration of native protein conformations, but the method can be also used to elucidate the mechanism of organic and inorganic reactions.[41] Indeed, mass spectrometry has been extensively exploited to study reactions happening in the gas-phase, allowing the ionic species of interest to interact with other molecules directly in the mass spectrometer. The novelty of the approach permitted by ESI is that a reaction can be studied as it occurs in solution, for example extracting an elusive ionic intermediate from the solution and assaying it in the gas-phase.[42] One of the main concerns in this matter is the possibility that the structure of the observed ion may be different from the one in solution, although there are studies showing superposition between the species investigated in gas-phase and the one studied by NMR in solution regarding the same reactions.[43] What makes MS attractive to study reaction intermediates is that they can be extremely stable in high-vacuum conditions even if they are short-lived in solution, thus allowing to assay their structure with spectroscopic techniques or CID and to probe their reactivity using ion/molecule reactions. In addition, ESI-MS permits to detect ions at very low concentration so it is ideal for the rapid screening of micro-scale reactions.

Finally, ESI-MS has allowed to address the reactivity of microsolvated cluster ions with the aim to understand solution chemistry from gas-phase behavior.[44] From a bioinorganic chemist point of view, this is one of the most appealing features of ESI-MS that can be exploited to reveal with the definition and precision of gas-phase measurement, reaction mechanisms as they happen in the liquid environment of the biological media.

References

[1] Beinert, H. **Bioinorganic chemistry: A new field or discipline? Words, meanings, and reality** *J. Biol. Chem.* 277 (2002) 37967-37972.

[2] Bertini, I., Gray, H.B., Lippard, S.J., Valentine, J.S. *Bioinorganic Chemistry* University Science Books 20 Edgehill Rd., MIll Valley, CA, 1994.

[3] Theil, E.C. **Ferritin: structure, function, and regulation** *Adv. Inorg. Biochem.* 5 (1983) 1-38.

[4] Crichton, R.R., Charloteaux-Wauters, M. **Iron transport and storage** *Eur. J. Biochem.* 164 (1987) 485-506.

[5] Palmiter, R.D. **The elusive function of metallothioneins** *Proc. Nat. Acad. Sci. U.S.A.* 95 (1998) 8428-8430.

[6] Coyle, P., Philcox, J.C., Carey, L.C., Rofe, A.M. **Metallothionein: The multipurpose protein** *Cell. Mol. Life Sci.* 59 (2002) 627-647.

[7] Yang, A.H.-W., Macgillivray, R.T.A., Chen, J., Luo, Y., Wang, Y., Brayer, G.D., Mason, A.B., Woodworth, R.C., Murphy, M.E.P. **Crystal structures of two mutants (K206Q, H207E) of the N-lobe of human transferrin with increased affinity for iron** *Protein Sci.* 9 (2000) 49-52.

[8] Alessio, E. *Bioinorganic Medicinal Chemistry*, Wiley-VCH Verlag GmbH, Weinheim (2011).

[9] Gupta, R. K. **Aluminum compounds as vaccine adjuvants** *Adv. Drug. Deliv. Rev.* 32 (1998) 155-172.

[10] Rosenberg, B., Van Camp, L., Krigas, T. **Inhibition of cell division in Escherichia coli by electrolysis products from a platinum electrode** *Nature* 205 (1965) 698–699

[11] Rosenberg, B., Van Camp, L., Trosko, J.E., Mansour, V.H. **Platinum compounds: A new class of potent antitumour agents** *Nature* 222 (1969) 385–386.

[12] Berners-Price, S. J.; Appleton, T. G. **The Chemistry of Cisplatin in Aqueous Solution. In Platinum-Based Drugs in Cancer Therapy** in Platinum-Based Drugs in Cancer Therapy, Kelland, L. R., Farrell, N., Eds.; Humana Press: Totowa, NJ, (2000) 3-35.

[13] Davies, M. S.; Berners-Price, S. J.; Hambley, T. W. **Slowing of Cisplatin Aquation in the Presence of DNA but not in the Presence of Phosphate: Improved Understanding of Sequence Selectivity and the Roles of Monoaquated and Diaquated Species in the Binding of Cisplatin to DNA**. *Inorg. Chem.* 39 (2000) 5603–5613.

[14] Rabik, C.A., Dolan, M.E., **Molecular mechanisms of resistance and toxicity associated with platinating agents** *Cancer Treat. Rev* 33 (2007) 9-23.

[15] Xin Zhang, C., Lippard, S.J. **New metal complexes as potential therapeutics** *Curr. Opin. Chem. Biol.* 7 (2003) 481-489.

[16] Saudek, V., Pivcova, H., Noskova, D., Drobnik, J. **The reaction of Pt-antitumor Drugs with selected nucleophiles. II. Preparation and Characterization of Coordination Compounds of Pt(II) and L-Histidine** *J. Inorg. Biochem.* 23 (1985) 55-72.

[17] Appleton T.G. **Donor atom preferences in complexes of platinum and palladium with amino acids and related molecules** *Coord. Chem. Rev.* 166 (1997) 313-359.

[18] Beinert, H. **Spectroscopy of succinate dehydrogenases, a historical *perspective*** *Biochim. Biophys. Acta, Bioenerg.* 1553 (2002) 7-22

[19] Beinert, H., Emptage, M.H., Dreyer, J.L., Scott, R.A., Hahn, J.E., Hodgson, K.O., Thomson, A.J. **Iron-sulfur stoichiometry and structure of iron-sulfur clusters in three-iron proteins: evidence for [3Fe-4S] clusters** *Proc. Nat. Acad. Sci. U.S.A.* 80 (1983) 393-396.

[20] Anxolabéhère-Mallart, E., Glaser, T., Frank, P., Aliverti, A., Zanetti, G., Hedman, B., Hodgson, K.O., Solomon, E.I. **Sulfur K-edge X-ray absorption spectroscopy of 2Fe-2S ferredoxin: Covalency of the oxidized and reduced 2Fe forms and comparison to model complexes** *J. Am. Chem. Soc.* 123 (2001) 5444-5452.

[21] Glaser, T., Rose, K., Shadle, S.E., Hedman, B., Hodgson, K.O., Solomon, E.I. **S K-edge X-ray absorption studies of tetranuclear iron-sulfur clusters: µ-sulfide bonding and its contribution to electron delocalization** *J. Am. Chem. Soc.* 123 (2001) 442-454.

[22] Pierik, A.J., Roseboom, W., Happe, R.P., Bagley, K.A., Albracht, S.P.J., Lacey, D. **Carbon Monoxide and Cyanide as Intrinsic Ligands to Iron in the Active Site of [NiFe] -Hydrogenases** *J. Biol. Chem.* 274 (1999) 3331-3337.

[23] MacAleese, L., Maitre, P. **Infrared spectroscopy of organometallic ions in the gas phase: from model to real world complexes** *Mass Spectrom. Rev.* 26 (2007) 583-605.

[24] Duncan, M. A. **Structures, energetics and spectroscopy of gas phase transition metal ion-benzene complexes** *Int. J. Mass Spectrom.* 272 (2008) 99-118.

[25] Dass, C. *Fundamentals of Contemporary Mass Spectrometry* eds. John Wiley & Sons, Inc (2007).

[26] Vestal, M.L., **Methods of ion generation** *Chem. Rev.* 101 (2001) 361-375.

[27] Aebersold, R., Mann, M. **Mass spectrometry-based proteomics** *Nature* 422 (2003) 198-207.

[28] Sze, S.K., Ge, Y., Oh, H., McLafferty, F.W. **Top-down mass spectrometry of a 29-kDa protein for characterization of any posttranslational modification to within one residue** *Proc. Natl. Acad. Sci. U.S.A.* 99 (2002) 1774-1779.

[29] Heck, A.J.R. **Native mass spectrometry: A bridge between interactomics and structural biology** *Nat. Methods* 5 (2008) 927-933.

[30] Lanucara, F., Holman, S.W., Gray, C.J., Eyers, C.E. **The power of ion mobility-mass spectrometry for structural characterization and the study of conformational dynamics** *Nat. Chem.* 6 (2014) 281-294.

[31] Łobiński, R., Schaumlöffel, D., Szpunar, J. **Mass spectrometry in bioinorganic analytical chemistry** *Mass Spectrom. Rev.* 25 (2006) 255-289.

[32] Li, H., Zhao, Y., Phillips, H.I., Qi, Y., Lin, T.Y., Sadler, P.J., O'Connor, P.B. **Mass spectrometry evidence for cisplatin as a protein cross-linking reagent** *Anal. Chem.* 83 (2011) 5369-5376.

[33] Polfer, N.C., Oomens, J. **Vibrational spectroscopy of bare and solvated ionic complexes of biological relevance** *Mass Spectrom. Rev.* 28 (2009) 468-494.

[34] Eyler, J.R. **Infrared multiple photon dissociation spectroscopy of ions in Penning traps** *Mass Spectrom. Rev.* 28 (2009) 448-467.

[35] Dillinger, S., Lang, J., Niedner-Schatteburg, G. **Cryo IR spectroscopy of [Hemin](+) complexes in isolation** *J. Phys. Chem. A* 28 (2017) 7191-7196.

[36] Salpin, J.-Y., Macaleese, L., Chirot, F., Dugourd, P. **Structure of the Pb^{2+}-deprotonated dGMP complex in the gas phase: A combined MS-MS/IRMPD spectroscopy/ion mobility study** *Phys. Chem. Chem. Phys.* 16 (2014) 14127-14138.

[37] Chiavarino, B., Crestoni, M.E., Fornarini, S., Scuderi, D., Salpin, J.Y. **Interaction of cisplatin with adenine and guanine: A combined IRMPD, MS/MS, and theoretical study** *J. Am. Chem. Soc.* 135 (2013) 1445-1455.

[38] Ghosh, A. **Ab initio wavefunctions in bioinorganic chemistry: More than a succès d'estime?** *J. Biol. Inorg. Chem.* 16 (2011) 819-820.

[39] Schwarz, H. **Relativistic effects in gas-phase ion chemistry: An experimentalist's view** *Angew. Chemie – Int. Ed.* 42 (2003) 4442-4454.

[40] Schwerdtfeger, P. **The pseudopotential approximation in electronic structure theory** *ChemPhysChem* 12 (2011) 3143-3155.

[41] Leonardo S. Santos, *Reactive intermediates: MS Investigations in Solution*. Ed. Leonardo S. Santos (2010) WILEY-VCH Verlag GmbH & Co. KGaA, Weinheim.

[42] Aliprantis, A.O., Canary, J.W. **Observation of Catalytic Intermediates in the Suzuki Reaction by Electrospray Mass Spectrometry** *J. Am. Chem. Soc.* 116 (1994) 6985-6986.

[43] Colton, R., D'Agostino, A., Traeger, J.C. **Electrospray mass spectrometry applied to inorganic and organometallic chemistry** *Mass Spectrom. Rev.* 14 (1995) 79-106.

[44] Takashima, K., Riveros, J.M. **Gas-phase solvated negative ions** *Mass Spectrom Rev.* 17 (1998) 409-430.

Methods

2.1 Mass Spectrometry

Mass spectrometry (MS) is an analytical technique that permits to measure the mass of molecules after they are ionized and volatilized. More precisely, it records the *m/z* ratio of an ion where m is the mass in Da and z is the charge of the ion. MS presents unique features that have favored its use in several fields of scientific research[1]:

- It has unmatched molecular specificity due to its ability to measure accurate molecular masses. Also using tandem MS or other hyphenated techniques, MS can provide useful structural information.

- The detection sensitivity of mass spectrometry is extremely high allowing to identify molecules in attomole and zeptomole amounts.

- Using different kinds of ionization sources, MS is applicable virtually to all kind of samples.

- In addition mass spectrometry permits to study gas-phase reactivity of ions and to obtain data on physical properties such as ionization energy, enthalpy of reaction, proton affinities and so on.

The only major limit of mass spectrometry is that it can only measure the *m/z* ratio of charged species. Therefore, the experimental apparatus can be subdivided in different sections which are schematized in scheme 2.1.
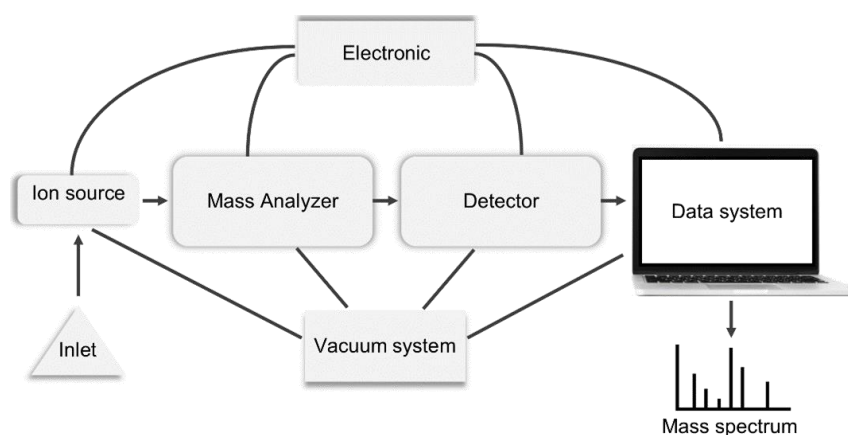
Scheme 2.1 Basic components of a mass spectrometer.

Several ion sources and analyzers have been developed along the years allowing the application of mass spectrometry in different fields of science, from the analysis of petroleum products to proteomics. For the aim of this thesis, we have employed electrospray ionization (ESI) as ion source and three different analyzers: triple quadrupole, a Paul ion trap and a Fourier-transform ion cyclotron resonance (FT-ICR) cell.

2.1.1 ESI source

Electrospray ionization has been a groundbreaking development for mass spectrometry and in general in the field of analytical chemistry, as testified by the 2002 Nobel Prize in chemistry awarded to the developer of ESI, John Fenn.[2,3] ESI is an atmospheric pressure ionization (API) technique and it is applicable to a conspicuous range of liquid-phase samples. It has the characteristic to be a soft ionization source, thus leading to poor in source fragmentation and consistency between the gas-phase nature of the ion with the solution one. This is particularly true when the observed species is already ionized in the solvent, but this is not always the case. In fact, the ions can also be generated at the surface of the droplets that are implied in the spray process. The ionization process will therefore follow a gas-phase like regime and be regulated by gas-phase basicity.[4] ESI has allowed to successfully couple liquid chromatography with mass spectrometry.[5] One of its main features is the possibility to form multiply charged ions, which can be useful for observing large molecules beyond the *m/z* limit of the chosen analyzer, thus enabling the study of proteins and other biological macromolecules with MS.[6]

The overall electrospray ionization process can be rationalized in two independent phases: the electrostatic dispersion of the sample liquid into droplets containing both ions and neutral species; and the separation of the charged molecules from the neutrals and the solvent leading to bare ions.[7] The formation of the droplets is usually obtained applying an electrostatic potential between a narrow-bore injection capillary and an opposing counter-electrode, as depicted in figure 2.1 A. Often the evaporation of the charged droplets is assisted by a flow of hot nitrogen.

Applying a high electric field at the capillary tip generates a partial charge separation, thus in positive ion mode, cations are enriched at the surface of the liquid at the capillary tip. The combination of electrostatic repulsion of the ions and electric field pull eventually overcomes the surface tension of the solvent shaping the liquid at the tip as a cone, called Taylor cone. Finally, the tip of the cone elongates into a filament that afterward breaks forming charged droplets (figure 2.1 B).
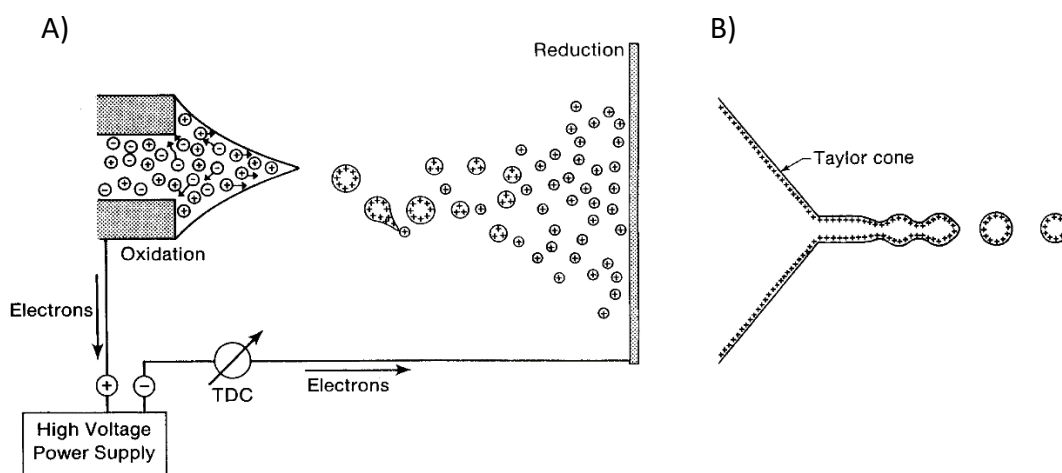
Figure 2.1 Representation of ESI process (A) and of the liquid cone at the tip of the capillary (B). The figure is adapted from ref. 7.

The electrospray formation process has been extensively studied and is now well understood.[8] The onset of the spray requires an electric field given by the equation 2.1:

$$E_0 = (\frac{2\gamma \cos 49°}{\varepsilon_0 r_c})^{1/2} \tag{2.1}$$

where γ is the surface tension of the liquid, cos49° is the half angle of the Taylor cone, ε_0 is the permittivity of vacuum and r_c is the capillary radius. From the equation it is clear that solvents with high surface tension, such as water, will require higher electric field for the electrospray formation. Thus, special arrangements could be needed when water is the sole solvent.

The evolution of the charged droplets to form the naked gas-phase ions is instead still a discussed theme. The process starts with progressive Coulomb fissions of the droplets. After formation, the heat supplied from the air, or the hot nitrogen,

produces solvent evaporation decreasing the droplet radius until it reaches the Rayleigh limit (equation 2.2) in which the surface tension is not enough to counterbalance the Coulombic repulsion of the charges inside the droplet:

$$q = 8\pi(\varepsilon_0 \gamma r^3)^{1/2} \qquad (2.2)$$

However, Coulombic fission has been observed only for big charged droplets, above 100 nm. Thus, two mechanisms have been proposed to explain the steps finally forming the bare ions: the ion evaporation model (IEM)[9,10] and the charge residue model (CRM)[11]. The CRM proposes that the droplets continue to shrink due to Coulombic fission until no further evaporation of the solvent is possible, while the IEM suggests a direct emission of ions M^+ from those droplets which present a size reduced to a radius comprised from 10 to 20 nm after solvent evaporation and Coulombic fissions. At present, there is no final word on which theory provides a better model for the ESI process despite the many efforts devoted to unambiguously prove the mechanism of the ions formation. In fact, it is probably a combination of the CRM and the IEM that is responsible for the high sensitivity and versatility of the ESI source. In particular, the ion evaporation process is considered to be involved in the formation of small ions, while CRM is invoked for clusters and big ions.[8] The overall ESI process clearly shows that the ions are formed in a gentle fashion due to the cooling provided by solvent evaporation, making possible to obtain molecular and pseudo-molecular ions, both protonated and metallated, which may retain isomeric and/or conformational fetures from the solution.

2.1.2 Time-of-flight mass spectrometers

Time-of-flight (TOF) mass analyzers are among the simplest devices to run mass analysis and are currently mainstream due to the potentially unlimited mass range, making TOF mass spectrometers preponderant in the analysis of biomolecules.[12] The developing of *reflectron* TOF instruments which have minimized the effect on mass resolution of initial spatial and energy spread,[13] helped to overcome the major limit of this technique, namely the low mass resolution at high masses, contributing to the popularity of the instrument.

Stephens presented the basics of TOF analysis in 1946.[14] Ions with defined kinetic energy present different velocities based on the inverse function of the square root of their *m/z* values. Therefore, when a packet of ions travels in a flight tube of length *L* the arrival time of the different species is given by:

$$t = \frac{L}{V} = L\sqrt{\frac{m}{2zV}} \qquad (2.3)$$

Measuring the arrival time provides a time-domain spectrum, which can be converted with an appropriate calibrating function to a mass spectrum. As previously mentioned, mass resolution in TOF instruments is highly dependent on having pulsed ions with defined and equal kinetic energy and without spatial spread, thus in standard instruments mass resolution was usually low and inadequate to analyze proteins and other biomolecules. *Reflectron* instruments allowed to overcome this issue, in particular the device permits to reduce the effect of spatial and energy spread using an electrostatic mirror at the end of the first field-free region (FFR or flight tube) of the instrument, as represented in figure 2.2.
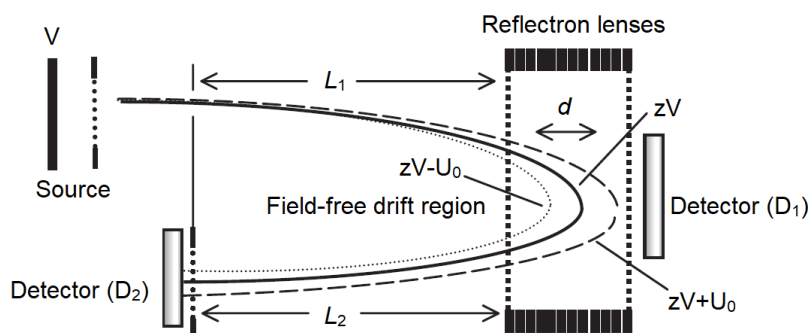
Figure 2.2 Reflectron time-of-flight mass spectrometer. Adapted from Ref. 1.

In principle an ion with excess energy $+U_0$ will arrive earlier at the *reflectron* but it will penetrate deeper in the field (*d*), thus slowing down and compensating for the excess of starting energy. *Reflectron* TOF opened the technique to proteomic and contributed to its success. To the scope of this thesis, a reflectron-TOF instrument coupled with an ion-mobility sector was employed for the mobility measurements.

2.1.3 Quadrupole analyzers

Quadrupole-based instruments are among the most common types of mass spectrometers mainly due to the low cost, mechanical simplicity and compactness of the device. The basic principles regarding the quadrupole mass filter can be dated back to the pioneering work of Paul and Steinwedel in the fifties.[15] Four metallic rods of ideally hyperbolic geometry are arranged symmetrically in a square array as shown in figure 2.3 and the mass separation is generated by the motion of ions into a high frequency oscillating electric field that is maintained by electrically connecting opposite pairs of rods.[16]
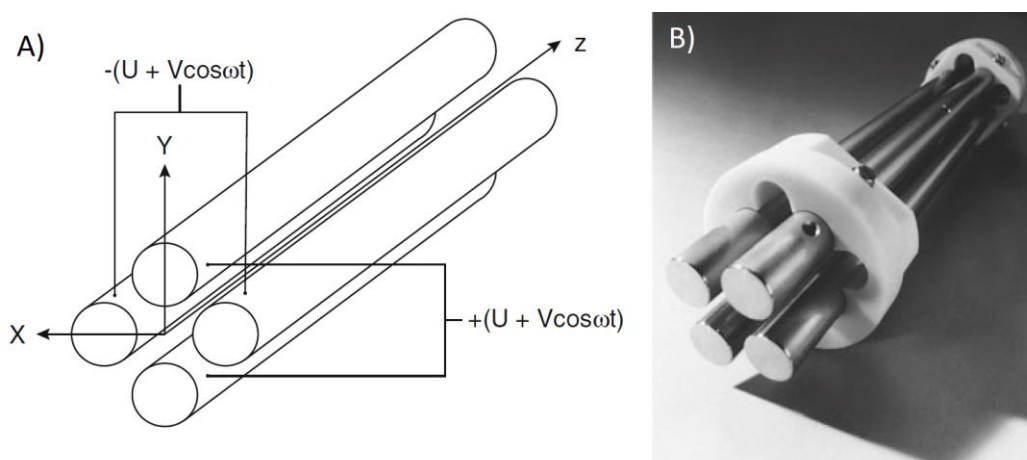
Figure 2.3 A) schematic and B) picture representation of a linear quadrupole mass filter. Figure adapted from Ref. 17.

One of the pair receives a superimposed dc potential U and a time-dependent rf potential $V \cos \omega t$, where ω is the angular frequency (in rad sec^{-1}), V is the amplitude and t the time, while the other pair presents a dc $-U$ and an rf potential equal in magnitude, but out of phase by 180°. The resulting oscillating field is given by:

$$\Phi_{(x,y)} = (U + V \cos \omega t) \frac{x^2 - y^2}{r_0} \tag{2.4}$$

where Φ is the applied potential, r_0 the inscribed radius so one-half the distance between the opposite electrodes), and x and y the distances from the center of the field. The ions are injected in the z direction and their motion is influenced by the applied potential based on their m/z ratio. Therefore, for given values of U, V and ω

only the ions presenting a certain *m/z* are able to sweep through the quadrupole and reach the detector or the other sectors of the mass spectrometer, while the others, presenting wrong trajectories, are discharged on the rods. To obtain the mass spectrum the quadrupole field is varied in order to force ions of consecutively *m/z* windows to break through the quadrupole. The advantages of a quadrupole analyzer comprise high scan speed, high transmission, good sensitivity and linear mass range, however quadrupoles present a practical upper mass limit of 4000 *m/z*, which can be limiting for applications on biomolecules, and the impossibility of obtaining perfect hyperbolic rods set a practical resolution limit to the unit.

Quadrupole ion-trap MS

Quadrupole ion-trap (QIT), also called Paul trap from the name of its inventor who introduced it in 1958,[18] and was awarded for this work of the Nobel Prize for Physics in 1989, are popular mass analyzers that work as three-dimensional analogs of quadrupole mass filters. QIT functions both as an ion store and as a mass analyzer. The trapping of the ions is generated by a potential well applied to the electrode of the ion trap, which can be visualized like a bowl of parabolic cross-section in which the ions are confined in horizontal layers based on their *m/z* ratio. The electrodes are arranged as shown in figure 2.4.
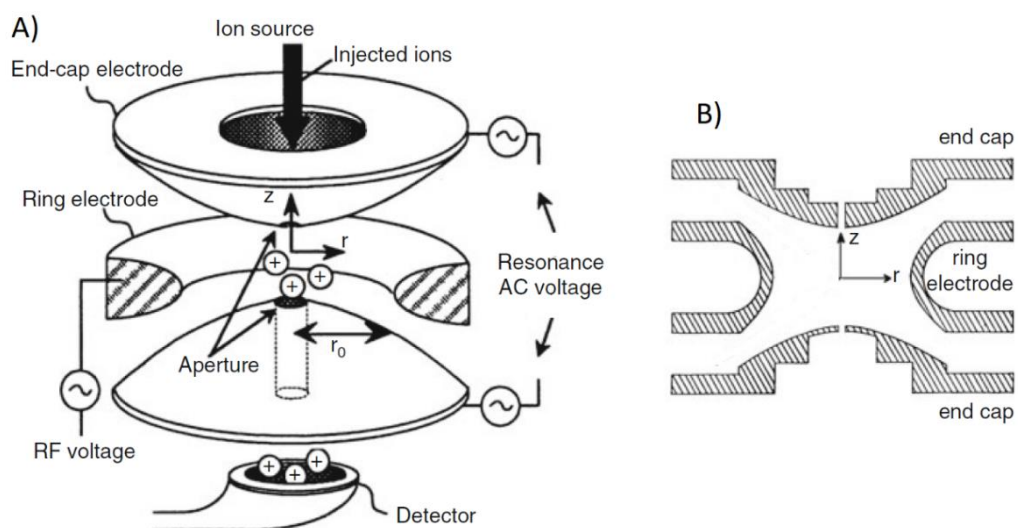
Figure 2.4 A) Schematic representation of a QIT. B) Section in the *rz*-plane of a QIT. Figure adapted from Ref. 17.

Two of the three electrodes, called end-caps, have a hyperboloidal geometry and are identical but for the number of holes in each of them. One end-cap electrode has a single small central aperture that permits the inlet of the ions, while the other can have more than one small aperture allowing the passage of the ions to the detector. The third electrode has a two sheets hyperboloidal geometry and is called the ring electrode. The potential well is created from the field generated when an rf potential is applied to the ring electrode, while the two end-cap electrodes are grounded. The overall geometry of the trap in this conditions produces an ideal quadrupole field which in turn generates a parabolic potential well for the confinement of the ions.[19] The ion trap acts as a mass spectrometer when the field is changed making the trajectories of ions of consecutive *m/z* ratio sequentially unstable, following a method developed by Stafford et al.[20] Therefore, the ions leave the trap based on their *m/z* ratio to a detector and, knowing the initial amplitude and ramping rate, it is possible to correlate a specific electronic signal to its *m/z* ratio. A prerequisite for the mass-selective axial ejection method is that the ions have to be collision constrained at the center of the ion trap, thus requiring a certain neutral gas background pressure, usually ca. 1 mTorr of Helium. The motion of the ions and therefore their stability regions is governed by the Mathieu's equation[21] and can be expressed in term of parametrized coordinates:

$$q_z = \frac{4zV}{m\omega^2 r_0^2} \qquad a_z = -\frac{8zU}{m\omega^2 r_0^2} \qquad \text{(2.5)}$$

where *V* is the rf peak voltage, *U* is the voltage applied to the ring electrode, r_0 its radius, ω is the angular frequency of the rf voltage and *m* and *z* are respectively the mass and charge of the ion.

2.1.4 FT-ICR analyzers

Fourier transform ion-cyclotron resonance mass spectrometry (FT-ICR MS) is one of the oldest ion trap techniques. The basic principle behind its functioning was firstly described in 1930 by Lawrence and Edlesen[22] and developed to mass spectrometry by Sommers et al.[23] in 1949, but its modern form is due to the work of Comisarow and Marshall[24]. The ions are trapped in a cell, also called Penning trap, laterally by a

strong static magnetic field and axially by a static electric field. There are lots of designs for Penning traps and the functioning of a cubic cell is schematized in figure 2.5 for its simplicity.However, nowadays the most widely used cells are cylindrically shaped.
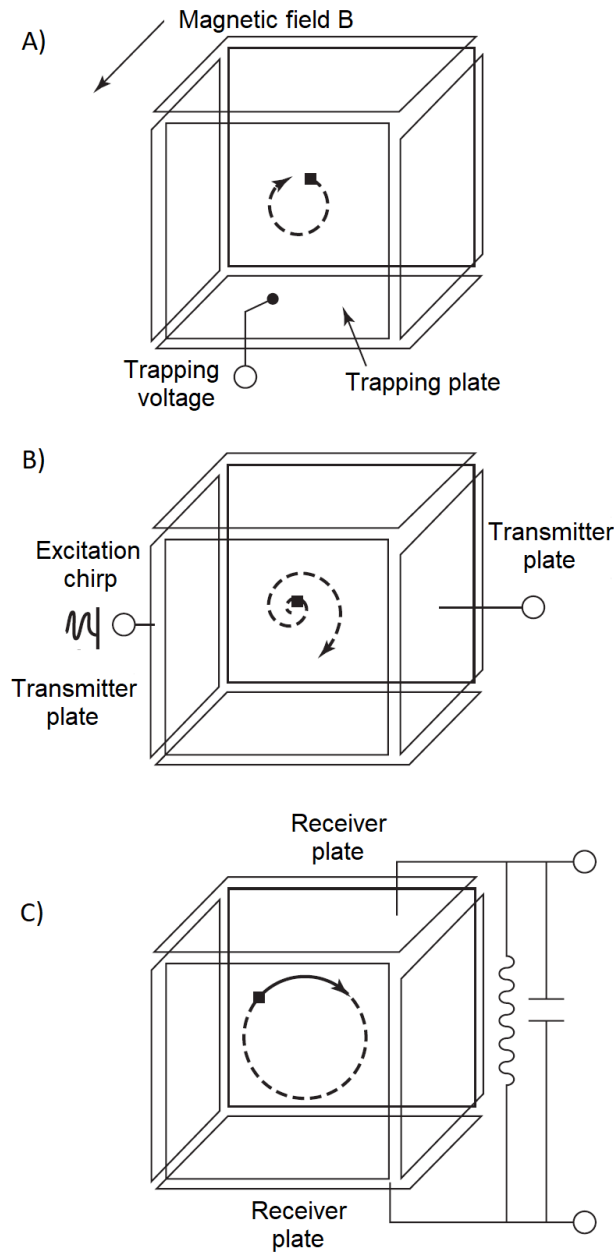
Figure 2.5 Schematic representation of FT-ICR MS operation. Mass analysis involves three main steps: A) ion formation and storage; B) excitation of the ions by a broad-frequency range pulse; C) detection by measuring their image current. Figure adapted from Ref. 1.

Two basic concepts are at the basis of mass analysis in ICR, in particular (i) an ion traveling in a magnetic field will precess at a frequency given depending on its *m/z*; (ii) energy can be absorbed by a precessing ion from an rf source only when the rf frequency coincides with the ion cyclotron one. The cyclotron frequency of the ion ω_c is defined as the number of revolution per second according to the equation:

$$\omega_c = \frac{qB}{2\pi m} \tag{2.6}$$

where *q* and *m* are respectively the charge and mass of the ion and *B* the strength of the magnetic field. The operation in ICR experiments is along four time-spread events: quenching, ion formation/injection, excitation and detection. These events happen inside the cell which is composed by three pairs of opposing plates devoted to a specific function: trapping, excitation or detection,[25] as shown in figure 2.5. To begin, a quench pulse is applied to empty the cell of any remaining ions, subsequently the ions to be analyzed are either formed in the cell or, which is more common nowadays, pulsed in the cell from an external source. At this point, a few volts are applied to the trapping electrodes (figure 2.5 A), in order to store the ions, and gas may be introduced in the cell to cool them. The next step is the application of an excitation pulse through the excitation electrodes (figure 2.5 B). This way, the ions whose precessional frequency is resonant with that of the excitation pulse absorb energy and get promoted to larger orbits. Finally, the ions, as they orbit the ICR cell, are detected by measuring the image current generated in the receiving plates (figure 2.5 C). The excitation pulse in the FT-ICR instruments is dispensed in the form of a chirp, a fast sweep of frequencies over a broadband. The ions, whose cyclotron frequencies fall in the range of frequencies applied, are promoted to larger orbital radii in phase coherent packets generating an image current containing the frequency components of all the excited ions. The time-domain transient signal obtained is finally converted to a frequency-domain signal that can be translated to a mass spectrum using a convenient calibration file.

2.2 Tandem mass spectrometry

Mass spectrometry when coupled with soft ionization sources such as ESI, while gaining the possibility to observe the molecular or pseudomolecular mass of the assayed ions, tends to lose structural information that was gathered from the dissociation paths generated with harsher ionization methods, such as electron ionization. Tandem MS or MS/MS is a tool that permits to recover the information about structures retaining the advantages of soft ionization sources. It is based on the coupling of two or more mass analysis steps either in time or space. Tandem MS was firstly used in the late sixties and nowadays there are several devices and instruments with different characteristics and fragmentation/assaying techniques that permit to gather structural information. We will focus on collision-induced dissociation (CID) and infrared multiple photon dissociation (IRMPD)

2.2.1 Collision induced dissociation

CID is the most common activation and dissociation tool and it is usually available in every commercial mass-spectrometer. This technique, which was firstly introduced in 1968,[26] is a two-step process: a preliminary collision activation followed by unimolecular dissociation. In the first step, the mass-selected ions are accelerated and excited to higher-energy states after collision with an inert gas (e.g. Ar, He or N_2). The kinetic energy is therefore transformed to internal energy based on the mass of the precursor ion and that of the neutral gas, following the equation:

$$E_{com} = \frac{N}{m_p+N} E_{lab} \tag{2.7}$$

where E_{com} is the center-of-mass kinetic energy of the ion, m_p and N are respectively the masses of the precursor ion and the neutral and E_{lab} is the ion's energy in the laboratory frame.[1] The unimolecular dissociation step has been fully theorized by the Rice–Ramsperger–Kassel–Marcus (RRKM) theory and quasiequilibrium theory (QET). A thorough introduction to the unimolecular dissociation theory can be found in Ref. 27.

Depending on the instrument, CID can be performed in either high- or low- energy regime. We will focus on the low-energy regime which is primarily used in triple quadrupole- and ion trap- (QIT, FT-ICR-MS) based tandem instruments. Low-energy CID,[28] has somewhat long activation time (milliseconds to seconds) and involves high vibrational states. Usually high pressure is present in the collisional cell to allow more ions to participate to the CID process, which can lead to a stepwise activation of the precursor.

2.2.2 IR multiple photon dissociation

IRMPD is a slow heating process usually performed in ion traps (FT-ICR or QIT). The trapped ions are bombarded with IR photons that, if resonant with the vibrational modes of the ions, are absorbed in a stepwise fashion until the dissociation threshold is reached and the ion eventually fragments. Usually, the lowest-energy decomposition pathways are sampled. The IRMPD technique is not dependent on the mass of the ion, thus it has acquired popularity in the –omics, in particular for top-down approaches.[29] The usual setup for this application requires a fixed frequency continuous-wave CO_2 laser coupled with FT-ICR-MS or Paul ion traps. Attention has to be devoted to obtaining a proper overlapping of the laser beam with the ion-cloud. Taking into account the differences regarding the ion clouds shapes and dimensions between the Penning trap and the quadrupole ion trap, two different coupling geometries are conveniently used, as showed in figure 2.6.
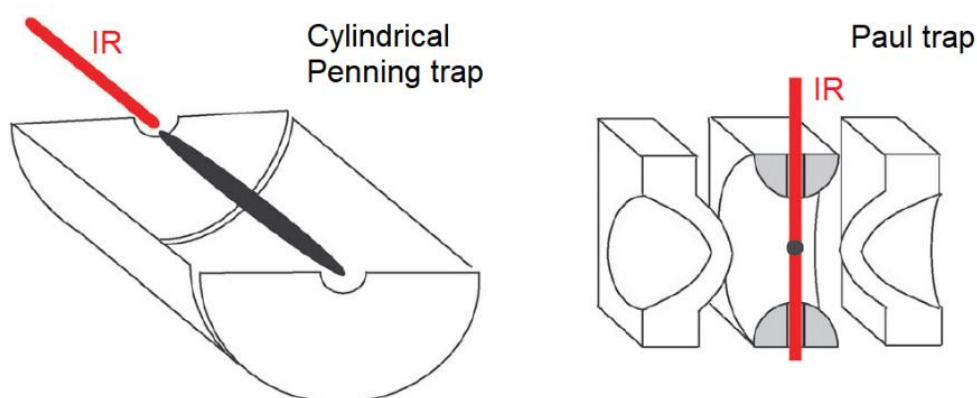
Figure 2.6 Section of Penning and Paul traps. The ion clouds are represented in black together with the optical access for the IR laser. Figure adapted from Ref. 30.

IRMPD spectroscopy

Ions in mass spectrometers are in extremely low density ($<10^8$ cm^{-3}) thus measuring the direct absorption of IR light is extremely challenging, *de facto* impeding to perform IR spectroscopy on mass selected ions in the gas-phase. The possibility to obtain dissociation upon IR absorption with IRMPD, however, showed a way to circumvent the need to measure light absorption in order to record the spectrum. In practice, a mass-selected ion is irradiated with a tunable laser beam at a particular frequency. If the laser frequency is resonant with one of the vibrational modes of the ion, the absorption may results in a dissociation, which can be recorded by the mass spectrometer. Finally, performing a scan with the tunable laser along the IR region of the electromagnetic spectrum, while monitoring the dissociation yield, permits to record an IRMPD spectrum related to the absorption one of the ion.[30] IRMPD spectroscopy is therefore an "action" spectroscopy that records a modification that happens when the absorption occurs, in this particular case the unimolecular dissociation of the starting ion. The measurement of the absorption consequence is more sensitive than directly monitoring the absorption, thus the method is well suited to study low-density samples such as the ions in a mass spectrometer. However, the advantages of this process are accompanied by an increased complexity of its mechanics, in particular due to the non-linear nature of IRMPD. In fact, the absorption of multiple photons is a *non-coherent* process where energy is quickly dissipated into the bath of vibrational degrees of freedom through intra-molecular vibrational redistribustion (IVR),[31,32] as illustrated in figure 2.7.
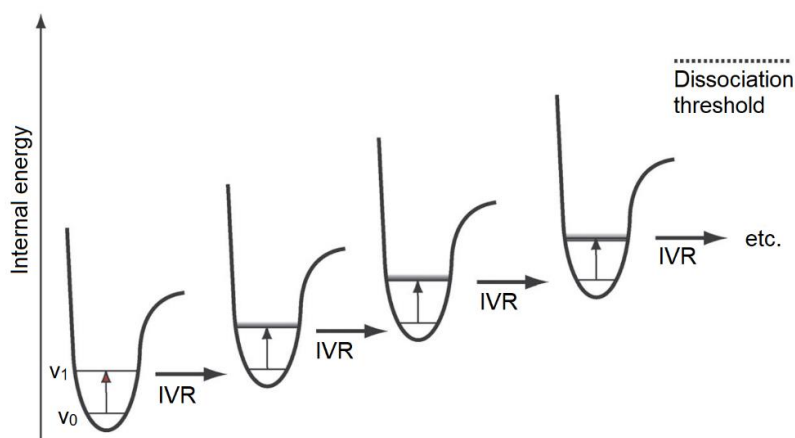
Figure 2.7 Schematic representation of the mechanism of IRMPD from Ref. 30.

The absorption of multiple photons leads to a progressive increase of the internal energy of the assayed ion until the dissociation threshold is reached and fragments can be observed. IVR is therefore avoiding the anharmonicity bottleneck that could happen for a "ladder-climbing" process, however since the normal modes of ions at higher internal energy are not orthogonal to the ground state ones, this process can shift the absorption frequency out of resonance with the laser. This effect is tempered by an increase of the density of states, which are functions of the internal energy, leading to a broadening of the absorption lines. Another factor to account when dealing with IRMPD is the presence of processes leading to loss of internal energy, in particular, stimulated emission, spontaneous emission and collision with background gas. Spontaneous emission among these can play an important role, while the others can be usually neglected in ultra-high vacuum condition. A collisionless environment has been estimated to exist at $<10^{-7}$ mbar,[33] which is a pressure well above the one in the Penning trap, but can be reached in Paul trap, thus adding another layer of complexity when coupling IRMPD with this kind of instruments.

2.3 Ion mobility mass spectrometry

Ion mobility (IM) is a technique that separates ions based on their mobility, or the ability to move through a medium, usually an inert gas, under the influence of a driving force. The basic principle of this technique can be traced back at the beginnings of the 20th century, however the first drift tube with characteristics similar to that of present IM instruments was developed by McDaniel in the fifties.[34] A gas-filled drift tube in which the ions move under the influence of a static electric field represents an ion mobility spectrometer in its basic form. In this kind of instruments the velocity of an ion (v) can be defined as the product of the electric field (E) and the mobility of the ion (K), and can be measured as the time required (t_d) to move through a drift cell of dimension d.[35]

$$v = KE = \frac{d}{t_d} \tag{2.8}$$

The mobility costant normalized for pressure and temperature (T) can also be described based on the characteristics of the ion and the parameters of the drift cell:

$$K_0 = \frac{3ze}{16N\omega} \frac{1}{\Omega} \left(\frac{2\pi}{\mu k_B T}\right)^{1/2} \tag{2.9}$$

where ze is the ion charge, Ω is the average collision cross section (CCS), N the number of density of the drift gas and μ is the reduced mass of the ion and buffer gas. Therefore, the velocity of an ion in a defined drift cell will depend on the mass, charge and collision cross section of the ion. If the IM sector (IMS) is coupled to a mass spectrometer, we can simultaneously obtain the m/z ratio, allowing the separation of isobaric ions through their CCS.

The first commercial IM-MS instrument was introduced by Waters in 2006 and consists in a reflectron-TOF analyzer preceded by a travelling wave (TW) ion-mobility device and a quadrupole sector which permits to mass-select ions (figure 2.8 A). [36] In the TWIMS (traveling wave ion-mobility sector), alternating phases of RF voltage are applied to a ring ion guide on which a traveling potential wave is superimposed, as shown in figure 2.8 B. A reverse gas flow is present in the IMS

that, antagonizing the movement of low mobility ions, eventually makes them to roll over the crest of the wave and exit the cell later. It has to be noted that the mobility of ions in TWIMS is not directly related to their CCS as in drift tube (DT) based IM-MS. Despite this, the use of carefully selected standards, whose CCS has been previously recorded using DT IM-MS, allowed to correlate the arrival time of an ion through a TWIMS with the corresponding collision cross section.[37]
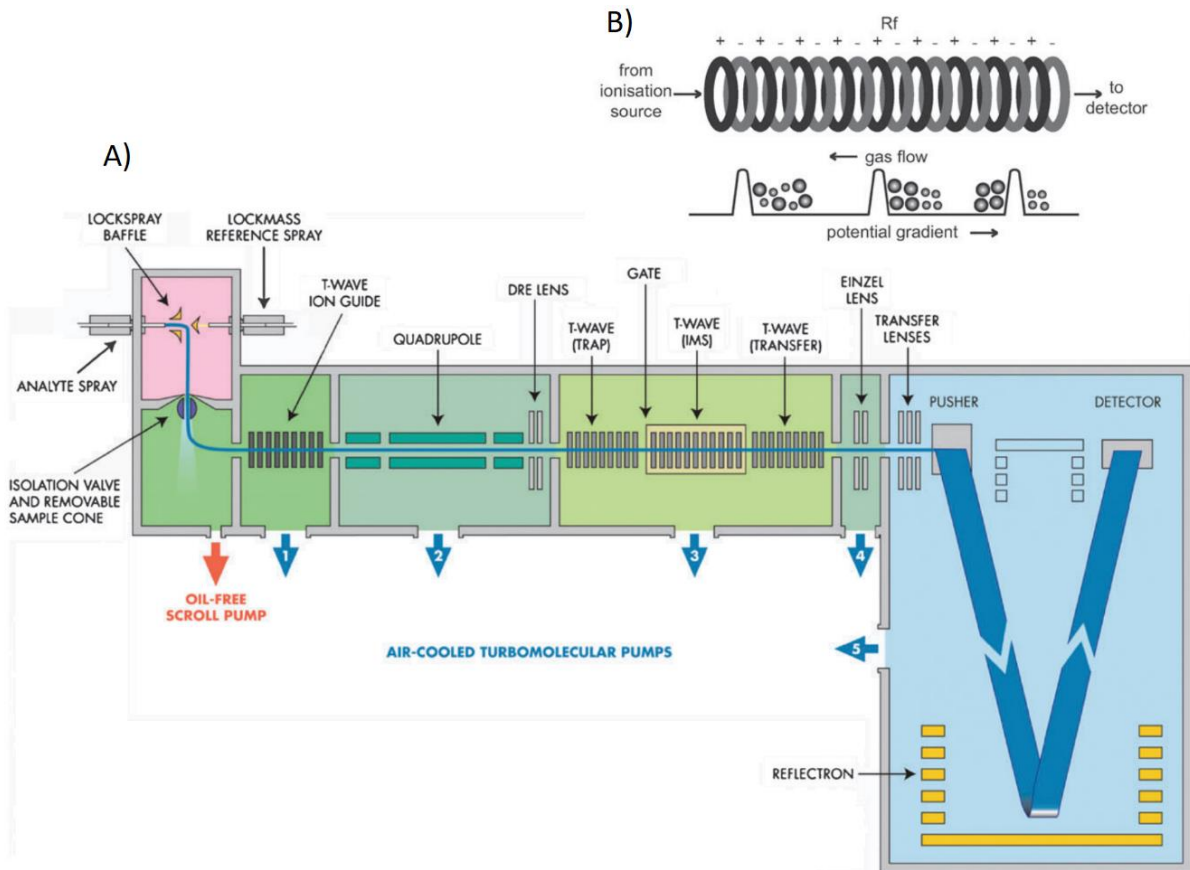
Figure 2.8 Schematic representations of B) the functioning of TWIMS and A) a commercial TWIMS instrument. Figure has been adapted from Ref. 35.

2.4 Computational methods

Computational chemistry is nowadays intertwined with all branches of experimental chemistry and accurate simulations of molecular features are required to obtain a proper description of observed phenomena. An impressive number of methods have been developed in order to employ calculations at all levels, starting from chemical physical problems on 2-atom systems to the screening of potential candidates to block the activity of an enzyme. This chapter will focus on specific problems related to the simulation of bioinorganic complexes by means of density-functional theory (DFT) calculations and post-Hartree Fock methods based on perturbation theory (MP2), in particular the implementation of dispersion energy in DFT and the use of relativistic pseudopotential to calculate the properties of species containing heavy atoms.

2.4.1 Basic principles of quantum chemistry applied to calculations

Quantum mechanics is based on postulates that have been experimentally tested in order to prove their validity. In particular, the first postulate states that to describe the state of a system exists a function Ψ of the particles coordinates called state function or wave function, which was firstly described by Schrödinger for a one-electron/one-dimension problem. The approach used to simulate a molecular system in *ab initio* computational chemistry is to resolve the wave function of that system. This is indeed not an easy task, in particular for polyatomic molecules, and appropriate mathematical tools as well as approximations have to be used.[38]

The wave function problem is nevertheless an eigenvalue problem, where to describe the energy of the system is necessary to find the eigenvalues E_i of the Hamiltonian operator $\hat{H}$ with respect to the eigenfunctions ψ that represent in our case the time-independent wave functions of our system:

$$\hat{H}\psi_i = E_i\psi_i \qquad (2.10)$$

For a polyatomic molecule, the Hamiltonian operator of equation 2.10 is of formidable appearance containing terms regarding the kinetic energies for the nuclei and the electrons and the potential energies for the repulsion and attraction

between nuclei and electrons with themselves and between them, respectively. However, Born and Oppenheimer helped in the first half of the 20th century to solve this problem stating that since nuclei are much heavier than electrons, the electrons move faster and as far as electrons are concerned we can approximate the position of the nuclei as fixed while the electrons carry out their motion. Thus, it is possible to omit the nuclear kinetic-energy term obtaining the pure electronic Hamiltonian $\hat{H}_{el}$:

$$\hat{H}_{el} = -\frac{\hbar^2}{2m_e}\sum_i \nabla_i^2 - \sum_\alpha \sum_i \frac{Z_\alpha e^2}{4\pi\varepsilon_0 r_{i\alpha}} + \sum_j \sum_{i>j} \frac{e^2}{4\pi\varepsilon_0 r_{ij}} \tag{2.11}$$

where α refers to nuclei position and i and j to the electrons. The first term of equation 2.11 is the kinetic energy of electrons, the second term is the potential energy of attraction between nuclei and electrons and the third is the repulsion between electrons. The potential energy of repulsion of the nuclei is considered a constant based on the distance between the nuclei and is calculated after resolving the Schrödinger equation.

2.4.2 The Hartree-Fock and post-Hartree-Fock methods

The exact wave function for the hydrogen atom is known and for helium and lithium it is possible to calculate very accurate wave functions. For atoms of higher atomic number as well as for polyatomic molecules it is required to use approximations. One method is using the Hartree-Fock procedure. A molecular Hartree-Fock wave function is written as the Slater determinant, so the antisymmetrized product, of spin-orbitals, which are the products of a spatial orbit φ_i and a spin function (either α or β). In order to find the lowest energy eigenvalue of the Hamiltonian of the exact wave function, the Hartree-Fock self-consistent-field (SCF) method is used. HF SCF is a variational method based on the theorem stating that given a system whose Hamiltonian operator is time-independent and the lowest-energy eigenvalue is E_1, if φ is a normalized well-behaved function of the coordinates of the system particles and satisfies the boundary condition of the problem then:

$$\frac{\int \Phi^* \hat{H} \Phi d\tau}{\int \Phi^* \Phi d\tau} \geq E_1 \tag{2.12}$$

Therefore the lowest solutions of the variational problem are approaching more and more the real solution. This allows to use iterative methods to determine the approximate lowest eigenvalue of the Hartree-Fock wave function based on the pure electronic nonrelativistic Hamiltonian.

Energies calculated by HF methods are usually in error by a 0.5% per light atom. For a chemist this error is however too big since energies in chemical bonds are usually in that order of magnitude. This issue rises from the way HF treats interactions between electrons. In fact, those interactions are seen only in an averaged way, while electrons repel each other and therefore instantaneous interactions should been taken into consideration. The energy difference between the exact nonrelativistic energy E_{nonrel} and the HF energy E_{HF} has been called correlation energy E_{corr} and is defined as:

$$E_{\text{corr}} = E_{\text{nonrel}} - E_{\text{HF}} \qquad (2.13)$$

Several so called post-Hartree-Fock methods have been developed to introduce in the resolution of the HF wave function the correlation energy. Configuration interaction (CI) and coupled-cluster (CC) are two of these methods, both rely on the use of more than one Slater determinant to write the wave function and can be used to do *ab initio* calculations with chemical accuracy. However, CI and CC have high computational cost and are time demanding, therefore they can be used only for small systems, usually far below in dimension with respect to the molecules relevant in living systems.

Another way to implement correlation energy in the HF calculations is to use perturbation-theory methods. The utilization of the Rayleigh-Schrödinger many-body perturbation theory (MBPT) to treat the unperturbed HF function was firstly proposed by Møller and Plesset in 1934. The present applications were however developed in the seventies.[39] Perturbation theory permits to correlate the unknown eigenvalues and eigenfunctions of a perturbed system to the known ones of an unperturbed one, applying gradually the perturbation through the insertion in the Hamiltonian of a parameter λ, which goes from 0 (unperturbed) to 1:

$$\hat{H} = \hat{H}^0 + \lambda\hat{H}'$$
(2.14)

where $\hat{H}$ is the perturbed Hamiltonian, thus the correlation correct one in the MP treatment, $\hat{H}^0$ is the unperturbed Hamiltonian and $\hat{H}'$ is the perturbation correction. The equation 2.14 can be expressed as a Taylor series in powers (k = 1, 2, 3, etc.) of λ. Therefore, the level of perturbation corrections will be indicated based on the cutting of the Taylor series as kth-order corrections. Second order correction (MP2) is usually sophisticated enough to simulate geometries and properties like vibrational frequencies of molecules, however higher order corrections are also employed, such as MP4 that has however a higher computational cost.[40] MP2 is widespread for its computational efficiency and the advantage to be size extensive, contrary to CI and CC methods, however the method is not variational so the energy found can be lower than the exact one. In addition, the MP methods cannot be used to simulate systems that are not in their ground state.

2.4.3 Density functional theory

Density functional theory derives from the Thomas-Fermi theorem that states that the properties of atoms can be derived from just its electronic density.[41,42] Subsequently in 1946, Hohenberg and Kohn proved that the ground-state molecular energy, wave function and other molecular properties are determined by the ground-state electron probability density $\rho_0(x, y, z)$.[43] In particular, it is possible to write that the electronic energy E_0 is a functional of ρ_0:

$$E_0 = E_0[\rho_0]$$
(2.15)

The square brackets in 2.15 denote a functional relation, which means that a rule exists that associate a number with each value of the variable x for which a function f is defined. This theory alone is not useful to calculate molecular properties since the exact functional is still unknown. However, following the intuition of Kohn-Sham and the Hohenberg-Kohn variational theorem it has been possible to obtain an analytical expression to approximate the exact energy. Hohenberg-Kohn proved that for every trial density function properly designed the true ground-state electron density minimizes their energy functional, putting the basis for using a

variational method to approach the exact DFT energy. The Kohn-Sham method instead provided the basis to design the exact functional $E_0[\rho_0]$. They proved that using a fictitious noninteracting reference system in which each electron experiences the same external potential-energy function $v(r)$ that make the ground state probability density of the reference system equal to the exact one of the real system, in theory it is possible to calculate the exact result of DFT as follow:

$$E_0 = E_v[\rho] = \int \rho(r)v(r)dr + \overline{T_s}[\rho] + \frac{1}{2} \int \int \frac{\rho(r_1)\rho(r_2)}{r_{1,2}} dr_1 r_2 + E_{xc}[\rho]$$

(2.16)

where $v(r)$ is the external potential of the fictitious system. It is possible to analytically resolve every term of equation 2.16, but the term $E_{xc}[\rho]$, that is called the exchange-correlation energy functional. This contribution, as little as it could be, has an unknown expression and most of the efforts in DFT are devoted to find the best approximation to $E_{xc}[\rho]$. Nowadays the local-spin-density approximation (LSDA) is used together with generalized-gradient approximation (GGA) to make gradient corrected functionals in which usually the exchange and correlations parts of E_{xc} are modeled separately. Hybrid exchange-correlation functionals are also widely used. They mix the exact exchange energy (E^{exact}) calculated with the Hartree-Fock theory, but using the Kohn-Sham orbitals, with E_x and E_c formulas from GGA. An example is the popular B3LYP functional proposed by Becke,[44] where 3 indicates that it is a three-parameter functional and LYP indicates the correlation formula approximation (from Lee-Yang-Parr who first proposed it):

$$E_{xc}^{B3LYP} = (1 - a_0 - a_x)E_x^{LSDA} + a_0 E_x^{exact} + a_x E_x^{B88} + (1 - a_c)E_c^{VWN} + a_c E_c^{LYP}$$

(2.17)

The dispersion problem in DFT

DFT is therefore a convenient method to simulate complex systems with high accuracy and can compete, using the latest functionals, even with MP2. It also describes electron correlation effects remarkably well. Indeed the absence of an exact functional to derive the energies from the electron distribution density implies that DFT does not account for the exact correlation, but reach a fair

agreement with it. However, there are particular kinds of interactions which are not well simulated by standard DFT functionals, in particular the ones deriving from London dispersion forces.[45] Those interactions are particularly important for large molecules such as biomolecules and have also roles in the metal complexes chemistry, thus for bioinorganic applications of DFT their influence should be considered. The DFT bad interpretation of dispersion forces depends on the impossibility for local and semi-local functionals, such as LSDA and GGA, to describe their typical asymptotic r^{-6} decaying.[46] In figure 2.7 is showed the poor agreement of DFT methods with the reference data at the CCSD(T) level in the description of the formation of Kr_2 and of the benzene dimer.
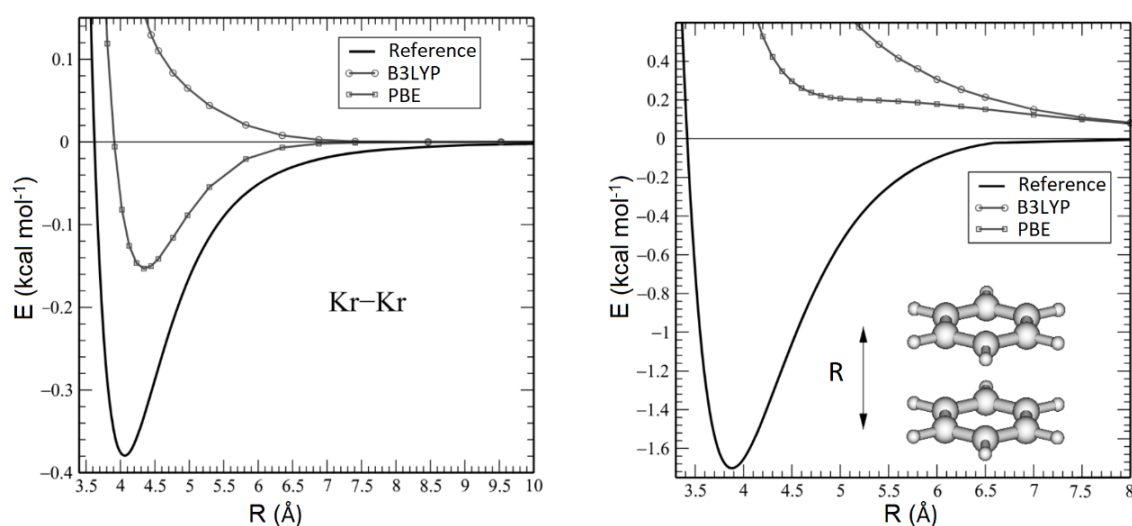
Figure 2.7. Potential energy curves for the Kr_2 (left) and the benzene dimer (right) calculated with two different density functionals (B3LYP and PBE) in comparison with accurate CCSD(T) reference data. Figure adapted from Ref. 47.

The most successful approach used nowadays to treat London forces is to add a dispersion correction term after the DFT energy calculation. This method is called DFT-D and in its simplest form the dispersion energy is defined as:

$$E_{disp} = -\sum_{AB}(C_{AB}/R_{AB})f(R_{AB}) \qquad (2.18)$$

where the sum goes over all pair of atoms A and B of the molecules, C is a constant, R is the distance between the atoms and f is a function that makes the energy to go to zero as R also tends to it. Nowadays the third version of this method DFT-D3 is

mostly employed.[48] It adds three empirical parameters to the E_{disp} calculation, whose values depend on the functional used.

Another approach is to use highly parametrized hybrid functionals that are specifically designed to take into account the dispersion forces. An example is the M06-2X functional.[49]

2.4.4 Basis functions and relativistic effective core potentials

Whatever molecular quantum-mechanical method we have chosen for our simulation, either DFT or post-Hartree-Fock, it is likely that it will be required to pick what is called a set of basis functions χ_r to start with. Basis functions are used to express the MOs or KS orbitals as $\varphi_i = \sum_i c_r \chi_{ri}$, where c are the parameters to be found in order to minimize the energy.

For polyatomic molecules basis functions are usually taken as atomic orbitals (AOs) centered on the corresponding atom. Initially, Slater-type orbitals (STOs) have been used, however due to their formulation, when in presence of a large number of atoms in a molecule a huge number of electron-repulsion integrals is generated, thus making calculations very time consuming. In the 1950 however Boys proposed the use of Gaussian-type functions (GTFs) which are nowadays widely used for all kind of calculations.[50] A Cartesian Gaussian centered on atom b is defined as:

$$g_{ijk} = N x_b^i y_b^j z_b^k e^{-\alpha r_b^2} \tag{2.19}$$

where α is a positive orbital exponent controlling the width of the GTO, i, j, and k are non-negative integers and x_b, y_b and z_b are Cartesian coordinates with origin at the nucleus b. When the sum of the indices i, j, and k is zero, one, or two, then the GTO is expressing an s-type, p-type, or d-type orbital, respectively. Gaussian integral evaluation takes less computer time than Slater integral one, however a Gaussian function does not have the correct cusp, which is present in STO when r tends to zero, therefore a linear combination of several Gaussian functions must be used as represented in figure 2.8 to approximate the electron behavior. Therefore to save computational time the current practice is to take each basis function as a linear combination of a few Gaussians centered on the same atom and with the same i, j

and *k* values, but with different orbital exponents. The resulting function is called contracted Gaussian-type orbital (CGTO).
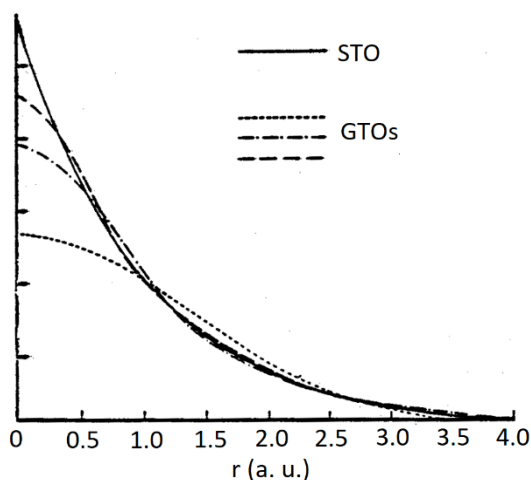
Figure 2.8 Comparison of the approximation obtained with the use of multiple GTOs with different α in approaching the behavior of a STO.

A minimal basis set will consist of one CGTO for each inner-shell and valence-shell, however this is usually not enough to simulate the behavior of polyatomic system therefore the single CGTO is substituted with two in a double-zeta (DZ) basis set and with three in a triple-zeta (TZ) one. The use of at least a DZ basis set is usually required to obtain a good description of a molecular system. Moreover, to have more orbital flexibility and reproduce the distorted shape and the shifted centers of charge of the AOs when they are connected in molecules, basis-functions with the *l* quantum number higher than the maximum one of the ground-state atom are used: the polarization sets. It could also be required, in particular for anions and compound with lone pairs or hydrogen bonds, to implement diffuse functions. These have very small orbital exponents, usually between 0.01 and 0.1, thus producing a Gaussian function with a large width that can improve the description of systems presenting significant electronic density at large distance from the nuclei.

The simulation of bioinorganic complexes presents an additional problem, in particular regarding the treatment of heavy atoms. As shown by equation (2.11) the electronic Hamiltonian does not comprehend corrections for the relativistic increase of mass with velocity. For a nonrelativistic hydrogen-like atom, the root-

mean-square speed of a $1s$ electron is $Zc/137$, where Z is the nuclear charge and c the speed of light. Therefore, the speed of inner-shell electrons in high-Z atoms is significantly close to c and the mass increase deriving from their relativistic movement shrinks the s orbitals and for a lesser extent the p ones. The contracted orbitals screen more efficiently the nucleus than in nonrelativistic atoms thus expanding the d and f orbitals.[38] It is of course possible to modify the Fock operator using the Dirac equation, which is the relativistic variant of the Schrødinger equation, in order to do relativistic Hartree-Fock calculations, however an all-electron Dirac-Fock calculation is very time-consuming. An approach to circumvent this issue is the use of effective core potentials (ECPs). The premises for the use of an ECP is that we have to partition the atom into a core and a valence electron system. The chemically inert core of the atom is considered to be frozen and removed from the explicit quantum treatment. Finally, its influence on the valence electrons is modeled by an effective Hamiltonian, which is the real ECP. Since in relativistic atoms only the core electrons are directly influenced by relativistic effects, a good approximation is to use the nonrelativistic Hamiltonian on valence electrons and implicitly account for the relativistic effects designing an opportunely parameterized ECP.[51] We can also choose to either maintain or simplify the nodal structure of the all-electron valence orbitals as in the model potential (MP) or pseudopotential (PP) approach, respectively. Indeed the PP approach saves computational time, but the parameterization implied are not always sufficient to compensate the influence of the absence of the radial nodes on the interactions between valence electrons.

References

[1] Dass, C. *Fundamentals of Contemporary Mass Spectrometry* eds. John Wiley & Sons, Inc (2007).

[2] Fenn, J.B., Mann, M., Meng, C.K., Wong, S.F., Whitehouse, C.M. **Electrospray ionization for mass spectrometry of large biomolecules** *Science* 246 (1989) 64–71.

[3] Fenn, J.B., Mann, M., Meng, C.K., Wong, S.F., Whitehouse, C.M. **Electrospray ionization: principles and practice** *Mass Spectrom. Rev.* 9 (1990) 37–70.

[4] Santos, L.S. *Reactive Intermediates: MS investigation in solution* (2010) Wiley-VCH Verlag GmbH &Co. KGaA, Weinheim.

[5] Dass, C. **Recent developments and applications of high-performance liquid chromatography– electrospray ionization mass spectrometry** *Curr. Org. Chem.* 3, 193– (1999) 209.

[6] Smith, R.D., Loo, J.A., Ogorzalek Loo, R. R., Busman, M., Udseth, H.R. **Principles and practice of electrospray ionization for mass spectrometry of large polypeptides and proteins** *Mass Spectrom. Rev.* 10 (1991) 359–451.

[7] Kebarle, P., Tang, L. **From ions in solution to ions in the gas phase** *Anal Chem.* 65 (1993) 972A-986A.

[8] Kebarle, P. **A brief overview of the present status of the mechanisms involved in electrospray mass spectrometry** *J. Mass Spectrom.* 35 (2000) 804-817.

[9] Iribarne, J.V., Thomson, B.A. **On the evaporation of small ions from charged droplets** *J. Chem. Phys.* 64 (1976) 2287-2294.

[10] Thomson, B.A., Iribarne, J.V. **Field induced ion evaporation from liquid surfaces at atmospheric pressure** *J. Chem. Phys.* 71 (1979) 4451-4463.

[11] Dole, M., Mack, L.L., Hines, R.L., Chemistry, D.O., Mobley, R.C., Ferguson, L.D., Alice, M.B. **Molecular beams of macroions** *J. Chem. Phys.* 49 (1968) 2240-2249.

[12] Cotter, R.J. **The new time-of-flight mass spectrometry** *Anal. Chem.* 71 (1999) 445A–451A.

[13] Mamyrin, B.A. **Laser assisted reflectron time-of-flight mass spectrometry** *Int. J. Mass Spectrom. Ion Proc.* 131 (1994) 1–19.

[14] Stephens, W.E. **A pulsed mass spectrometer with time dispersion** *Phys. Rev.* 69 (1946) 691.

[15] Paul, W., Steinwedel, H. **Ein neues Massenspektrometer ohne Magnetfeld** *Z. Naturforsch. A* 8 (1953) 448-450.

[16] Miller, P.E., Bonner Denton, M. **The quadrupole mass filter: basic operating concepts** *J. Chem. Educ.* 63 (1986) 617–622.

[17] Gross, J. *Mass Spectrometry: A Textbook*, Third edition (2017) Springer International Publishing AG, 6330 Cham, Switzerland.

[18] Paul, W., Reinhard, H.P., Zahn, O. **The electric mass filter as mass spectrometer and isotope separator** *Z. Phys.* 152 (1958) 143–182.

[19] March, R.E. **Introduction to quadrupole ion trap mass spectrometry** *J. Mass Spectrom.* 32 (1997) 351–369.

[20] Stafford, G.C., Kelley, P.E., Syka, J.E.P., Reynolds, W.E., Todd J.F.J. **Recent improvements in and analytical applications of advanced ion trap technology** *Int. J. Mass Spectrom. Ion Proc.* 60 (1984) 85–98.

[21] Mathieu, E. **Mémoire sur le mouvement vibratoire d'une membrane de forme elliptique** *J. Math Pures Appl.* 13 (1868) 137-203.

[22] Lawrence E.O., Edlefsen, N.E. **On the production of high speed protons** *Science* 72 (1930) 376-377.

[23] Sommer, H., Thomas, H.A., Hipple, J.A. **Measurement of e/m by cyclotron resonance** *Phys. Rev.* 82 (1951) 697–702.

[24] Comisarow, M.B., Marshall, A.G. **Fourier transform ion cyclotron resonance mass spectroscopy** *Chem. Phys. Lett.* 25 (1974) 282.

[25] Holland, J.H., Enke, C.G., Allison, J., Stults, J.T., Pinkston, J.D., Newcombe, B., Watson, J.T. **Mass spectrometry on the chromatographic time scale: realistic expectations** *Anal. Chem.* 55 (1983) 997A–1012A.

[26] Jennings, K.R. **Collision-induced decompositions of aromatic molecular ions** *Int. J. Mass Spectrom. Ion Phys.* 1 (1968) 227–235.

[27] Armentrout, P.B. in *The Encyclopedia of Mass Spectrometry*, 1st Edition, Volume 1: Theory and Ion Chemistry (2003) Elsevier.

[28] Yost, R.A., Enke, C.G., McGilvery, D.C., Smith, D., Morrison, J.D. **High efficiency collision-induced dissociation in an RF-only quadrupole** *Int. J. Mass Spectrom. Ion Proc.* 30 (1979) 127–136.

[29] Little, D.P., Speir, J.P., Senko, M.W., O'Connor, P.B., McLafferty, F.W. **Infrared Multiphoton Dissociation of Large Multiply Charged Ions for Biomolecule Sequencing** *Anal. Chem.* 66 (1994) 2809-2815.

[30] Polfer, N.C. **Infrared multiple photon dissociation spectroscopy of trapped ions** *Chem. Soc. Rev.* 40 (2011) 2211–2221.

[31] Fung, Y.M.E., Kjeldsen, F., Silivra, O.A., Chan T.W.D., Zubarev, R.A. **Facile Disulfide Bond Cleavage in Gaseous Peptide and Protein Cations by Ultraviolet Photodissociation at 157 nm** *Angew. Chem. - Int. Ed.* 44 (2005) 6399–6403.

[32] Grant, E.R., Schulz, P.A., Sudbo, A. S., Shen, Y. R., Lee, Y.T. **Is Multiphoton Dissociation of Molecules a Statistical Thermal Process?** *Phys. Rev. Lett.* 40 (1978) 115–118.

[33] Dunbar R.C., McMahon, T.B. **Activation of Unimolecular Reactions by Ambient Blackbody Radiation** *Science* 279 (1998) 194–197.

[34] McDaniel, E.W., Barnes, W.S., Martin, D.W. **Drift Tube-Mass Spectrometer for Studies of Low-Energy Ion-Molecule Reactions** *Rev. Sci. Instrum.* 33 (1962) 2-7.

[35] Uetrecht, C., Rose, R.J., Van Duijn, E., Lorenzen, K., Heck, A.J.R. **Ion mobility mass spectrometry of proteins and protein assemblies** *Chem. Soc. Rev.* 39 (2010) 1633–1655.

[36] Pringle, S.D., Giles, K., Wildgoose, J.L., Williams, J.P., Slade, S.E., Thalassinos, K., Bateman, R.H., Bowers, M.T., Scrivens, J.H. **An investigation of the mobility separation of some peptide and protein ions using a new hybrid quadrupole/travelling wave IMS/oa-ToF instrument** *Int. J. Mass Spectrom.* 261 (2007) 1-12.

[37] Jurneczko, E., Barran, P.E. **How useful is ion mobility mass spectrometry for structural biology? The relationship between protein crystal structures and their collision cross sections in the gas phase** *Analyst* 136 (2011) 20-28.

[38] Levine, I.N. *Quantum Chemistry*, 7th ed. (2014) Pearson Education Inc., NJ, U.S.A.

[39] Bartlett, R.J. **Many-body perturbation theory and coupled cluster rheoty for electron correlation in molecules** *Ann. Rev. Phys. Chem.* 32 (1981) 359-401.

[40] Krishnan, R., Pople, J.A. **Approximate fourth-order perturbation theory of the electron correlation energy** *Int. J. Quantum Chem.* 14 (1978) 91-100.

[41] Fermi, E. **Un metodo statistico per la determinazione di alcune proprietà dell'atomo** *Rend. Accad. Naz. Lincei* 6 (1927) 602–607.

[42] Thomas, L. H. **The calculation of atomic fields** *Proc. Camb. Phil. Soc.* 23 (1927) 542–548.

[43] Hohenberg, P., Kohn, W. **Inhomogeneous electron gas** *Phys. Rev.* 136 (1964) B864-.

[44] Becke, A.D. **Density-functional thermochemistry. III. The role of exact exchange** *J. Chem. Phys.* 98 (1993) 5648.

[45] Kristyán, S., Pulay, P. **Can (semi)local density functional theory account for the London dispersion forces?** *Chem. Phys. Lett.* 229 (1994) 175-180.

[46] Ehrlich, S., Moellmann, J., Grimme, S. **Dispersion-corrected density functional theory for aromatic interactions in complex systems** *Acc. Chem. Res.* 46 (2013) 916-926.

[47] Grimme, S. **Density functional theory with London dispersion corrections** *Wiley Interdiscip. Rev. Comput. Mol. Sci.* 1 (2011) 211-228.

[48] Grimme, S., Antony, J., Ehrlich, S., Krieg, H. **A consistent and accurate ab initio parametrization of density functional dispersion correction (DFT-D) for the 94 elements H-Pu** *J. Chem. Phys.* 132 (2010) 154104.

[49] Zhao, Y., Truhlar, D.G. **The M06 suite of density functionals for main group thermochemistry, thermochemical kinetics, noncovalent interactions, excited states, and transition elements: Two new functionals and systematic testing of four M06-class functionals and 12 other functionals** *Theor. Chem. Acc.* 120 (2008) 215-241.

[50] Boys, S.F. **Electronic wave functions. I. A general method of calculation for the stationary states of any molecular system** *Proc. R. Soc. Lond. A* 200 (1950) 542.

[51] Dolg, M. Chapter 14 **Relativistic Effective Core Potentials** in W. Liu (ed.), *Handbook of Relativistic Quantum Chemistry* (2017) Springer-Verlag Berlin Heidelberg.

Gas-phase kinetics and IRMPD spectroscopy to unveil elementary steps in the reaction of cisplatin with N- O- and S-containing nucleophiles

3.1 Introduction

Cisplatin (*cis*-diamminedichloroplatinum(II), *cis*-[Pt(NH$_3$)$_2$Cl$_2$]) and related platinum compounds are among the most widely prescribed anticancer drugs. The use of cisplatin in medicine traces its origin from the pioneering work of Rosenberg who envisaged the possibility of hindering cancer cell division by cisplatin ability to inhibit the division of bacterial cells.[1,2] Nowadays, it is well established that the binding of platinum to the N7-position of two adjacent guanosine bases causes unwinding of DNA and disrupts replication, leading to cell death.[3,4] It is also well documented that platinum complexes can react in the cell with several other biomolecules,[5,6] leading to altered biological activity. DNA bases do not replace the chloro ligand from platinum(II) directly but predominantly via a solvent assisted pathway. Cisplatin aquation (replacement of Cl$^-$ with H$_2$O) yields the aqua complex, *cis*-[PtCl(NH$_3$)$_2$(H$_2$O)]$^+$, and also the di-aqua complex *cis*-[Pt(NH$_3$)$_2$(H$_2$O)$_2$]$^{2+}$, species that are suggested to be important contributors to DNA platination.[7,8] The positive charge on the platinum complex can attract the negatively charged nuclear DNA, thus favoring the formation of DNA.[9-12] Interestingly, the charged aqua complexes are directly amenable to mass spectrometric investigation paving the way to an evaluation of their intrinsic properties and hopefully enlightening useful issues for Pt-drug design.[13] In this context the vibrational signatures of the isolated species *cis*-[PtCl(NH$_3$)$_2$(H$_2$O)]$^+$ have been assayed by infrared multiple photon dissociation (IRMPD) spectroscopy, in parallel with a characterization of the trans isomer, *trans*-[PtCl(NH$_3$)$_2$(H$_2$O)]$^+$.[14] The experimental vibrations have been interpreted with the aid of calculated IR spectra for the computed stable structures, as typically performed.[15-20] Using this approach, the binding motifs in the naked adducts from cisplatin with nucleobases (adenine and guanine) have been shown to involve the N7 position of guanine and N1/N3 positions of adenine, while the N7 attack to adenine is notably missing.[21] A simple glycine–linked cisplatin, [(Gly-H)PtCl$_2$]$^-$, has

provided a case study for IRMPD experiments combined with a survey of hybrid theoretical approaches for determining structures and IR spectra.[22]

Section 3.3 of this chapter reports on our investigation on the aqua-hydroxo *cis-* and *trans-*[Pt(OH)(NH$_3$)$_2$(H$_2$O)]$^+$ complexes with regard to both structure and reactivity, in relation to the aqua-chloro *cis-* and *trans-*[PtCl(NH$_3$)$_2$(H$_2$O)]$^+$ complexes whose features have already been reported.[14] In solution, considerable interest has been devoted to correlations of kinetic and thermodynamic parameters for the ligand substitution reaction of square planar platinum(II) complexes which led to define nucleophilic reactivity constants for various entering nucleophiles.[23-25] However, it is often difficult to discriminate among the various factors that may affect the reactivity of a metal complex in solution. In this regards, the gas-phase may represent the ultimate simplified environment.

Section 3.4 reports on the reactivity of cisplatin with pyridine, trimethylphosphate, 4(5)-methylimidazole, thioanisole, acetamide, dimethylacetamide, urea and thiourea models of biological targets, employing MS and IRMPD spectroscopy supported by DFT calculations. Ionic products obtained by addition and/or substitution by the selected ligands have been isolated in the gas phase and characterized by IRMPD spectroscopy. Based on the combined information coming from recognition of the charged species by ESI mass spectrometry, kinetic data by gas phase ion-molecule reactivity, structural characterization by IRMPD 'action' spectroscopy and thermodynamic and geometric features from density functional theory (DFT) calculations, reactive events accounting for cisplatin activity are elucidated at the molecular level in a controlled environment with unprecedented detail. The non-covalent cluster thus displays the nature of an Eigen-Wilkins encounter complex, lying on the reaction coordinate for the ligand substitution reaction (Eq. 3.1, see the {*cis-*[PtCl(NH$_3$)$_2$(H$_2$O)]$^+$ · L} encounter complex).

$$\textit{cis-}[PtCl(NH_3)_2(H_2O)]^+ + L \rightarrow \{\textit{cis-}[PtCl(NH_3)_2(H_2O)]^+ \cdot L\} \rightarrow \textit{cis-}[PtCl(NH_3)_2(L)]^+ + H_2O$$

$$(3.1)$$
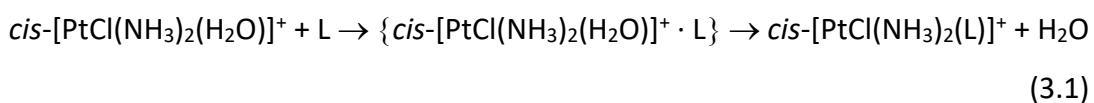
According to this recognized mechanistic model, ligand (L) exchange on a complex such as $[M(H_2O)_n]^{m+}$ occurs after rapid formation of an outer sphere encounter complex, $\{[M(H_2O)_n]^{m+}\cdot L\}$, bound by electrostatic interactions. The formation of this complex is diffusion controlled and the rate limiting event is typically the L/H_2O interchange between the first and the second coordination sphere within the encounter complex.[23,26,27] Evidence on the role of this complex in solution is mainly based on kinetics and thus the ESI formed ion provides an unprecedented opportunity to clarify its structure and mechanistic role.

3.2. Experimental details

3.2.1 Sample preparation

Cisplatin, *cis*-PtCl$_2$(NH$_3$)$_2$, transplatin, *trans*-PtCl$_2$(NH$_3$)$_2$, and selected reagents (pyridine, 4-methylimidazole, trimethylphosphate, thioanisole, dimethylsulfide, acetamide, dimethylacetamide, urea and thiourea) used in this work, were commercial products from Sigma-Aldrich and were used as received for solution preparation. Pyridine, trimethylphosphate and dimethylsulfide when used as pure substances for direct injection in the FT-ICR cell were purified by repeated evaporation/condensation cycles. All the compounds were dissolved in H$_2$O LC-MS grade at a concentration of 10^{-3} M and subsequently properly mixed and diluted in H$_2$O/MeOH 1:1 to obtain a final concentration of 10^{-5} M. In addition, the aqueous solutions of cisplatin and transplatin were allowed to rest for one night before the analysis. These end solutions contained an appreciable fraction of [PtCl(NH$_3$)$_2$(H$_2$O)]$^+$ ions. In order to favor the formation of hydrolyzed products, both cisplatin and transplatin dilute solutions were incubated two days longer leading to a conspicuous increase of the abundance of [Pt(OH)(NH$_3$)$_2$(H$_2$O)]$^+$ ions, at the expense of [PtCl(NH$_3$)$_2$(H$_2$O)]$^+$.

3.2.2 IRMPD spectroscopy

IRMPD spectroscopy has been performed in two ranges, 900-1900 and 2900-3700 cm^{-1}, encompassing the 'fingerprint' and the X-H (X = C,N,O) stretching region, using two different instrumental platforms. The 800-2000 cm^{-1} frequency range has been explored at the free-electron laser (FEL) beamline of the Centre Laser Infrarouge d'Orsay (CLIO) European facility. The FEL electron energy was set at 42 and 44 MeV, to optimize the laser power in the IR range of interest. The FEL beamline is coupled with a hybrid FT-ICR tandem mass spectrometer (APEX-Qe Bruker Daltonics),[28,29] equipped with a 7.0 T actively shielded magnet and a quadrupole–hexapole interface, under the control of the commercial software APEX 1.0. The ions studied in this work were mass selected in the quadrupole and accumulated in the hexapole, containing argon buffer gas, for 1.0 s in order to cool them prior to their

transfer into the ICR cell. The ions were then isolated and irradiated for 250 ms to 1 s with the IR FEL light and the products of IRMPD were mass analyzed.

IR spectroscopy in the 2800-3800 cm^{-1} wavenumber range was performed using an optical parametric oscillator/amplifier (OPO/OPA) (LaserVision) laser system pumped by a 10 Hz Nd:YAG laser coupled to a Paul ion trap mass spectrometer (Esquire 6000+, Bruker Daltonics), as previously described.[30,31] The ions were mass selected, trapped for 5 ms to 10 ms, and irradiated for 500 ms to 2 s. The typical output energy from the OPO/OPA laser was ca. 25 mJ pulse^{-1} with a spectral width of 5 cm^{-1}.

The IRMPD spectra are obtained by plotting the photofragmentation yield $R = -\log(I_p/(I_p + \Sigma I_f))$, where I_p and ΣI_f are the parent and sum of the fragment ion intensity, respectively, as a function of the radiation wavenumber.[32]

3.2.3 Ion-molecule reactions in FT-ICR mass spectrometry

Kinetic data on the ligand substitution reactions of *cis*- and *trans*-[PtX(NH$_3$)$_2$(H$_2$O)]$^+$ (X = Cl, OH) were obtained as described in detail elsewhere,[33] using a Fourier transform - ion cyclotron resonance (FT-ICR) mass spectrometer (Bruker BioApex) equipped with an Apollo I ESI source and a 4.7 T magnet, at the nominal cell temperature of 298K. The pseudo first order rate constants, obtained from the semilog plot of the parent ion decay with increasing reaction time, were divided by the neutral concentration to give the second order rate constant (k_{exp}). The reaction efficiency (Eff = $k_{exp}/k_{coll} \times 100$, where k_{coll} is the collisional rate constant) expresses the percentage of reactive collisions.[34]

3.2.4 Density functional theory calculations

Quantum mechanics calculations have been employed to aid in interpreting the experimental data using density functional (DFT) methods as implemented in the Gaussian 09 Rev D.01 package.[35] The hybrid functional B3LYP has been used in combination with either the 6-311+G(d,p) or aug-cc-pVTZ basis set for the light atoms. Relativistic effects affecting Pt were taken into account employing the pseudopotentials LanL2TZ in the case of the Pople basis set for light atoms or aug-cc-pVTZ-PP when using the correlation consistent one. The optimized structures

were submitted to harmonic vibrational frequency analysis at the same level of theory in order to characterize the obtained structures as local minima or transition states and to obtain thermodynamic corrections to the electronic energies and IR spectra. The harmonic frequencies were scaled by a factor of 0.957 and 0.974 for the XH (X = C, N, O) stretching and fingerprint regions, respectively, as used in previous studies.[30,36] However, no corrections were adopted for the frequencies of modes involving PO stretches of any kind. This approach was chosen because these scaling factors happen to be systematically too low for stretching modes associated to P−OC, P−OH, and P=O bonds. This effect was noticed in the study of molecular ions like phosphorylated nucleotides,[37-39] amino acids,[40,41] and peptides[42] and the same criterion was already applied for the interpretation of vibrations comprising PO bonds.[39,43] Calculated linear IR spectra are convoluted using a Lorentzian line shape with a width (fwhm) of 5 cm^{-1} and 20 cm^{-1} for the XH (X = C, N, O) stretching and fingerprint regions, respectively for convenient comparison with the experimental spectra in the inspected IR region.

Structures and energies pertaining the potential energy surface (PES) for the reaction of *cis-* and *trans-*[PtCl(NH$_3$)$_2$(H$_2$O)]$^+$ with thioanisole and *cis-*[PtCl(NH$_3$)$_2$(H$_2$O)]$^+$ with also pyridine, 2-methylimidazole and thioanisole were calculated at the ω-B97XD/6-311+G(d,p) level[44] with the LanL2TZ pseudopotential for the platinum atom in order to evaluate the role of dispersion energy and long range interactions. The ω-B97XD functional has in fact proven to be a proper tool to study compounds containing transition metals.[45] It consists a long-range corrected hybrid density functional modified to include the dispersion correction following Grimme's work with a modified damping function. Harmonic vibrational frequency were also calculated at ωB97X-D/6-311+G(d,p) in order to obtain the thermodynamic corrections.

3.3 Structure and reactivity of the aquacomplexes of cis- and transplatin in a solvent free-environment

The work reported in the following section has been adapted from the paper published in RSC Advances:

My personal contribution to the manuscript regarded performing the mass spectrometry and IRMPD spectroscopy experiments as well as preparing and submitting the calculations involved in both vibrational features and reaction mechanism interpretation. I have also prepared the first draft which was revised by Prof. Simonetta Fornarini.

3.3.1 Vibrational features and optimized structures of cis- and trans-[Pt(OH)(NH$_3$)$_2$(H$_2$O)]$^+$ ions

The complexes obtained by stepwise hydrolysis of cisplatin and transplatin in aqueous solution (cis-[Pt(OH)(NH$_3$)$_2$(H$_2$O)]$^+$ and trans-[Pt(OH)(NH$_3$)$_2$(H$_2$O)]$^+$), have been assayed by IRMPD spectroscopy in order to unveil vibrational features of the bare mass selected ions. The mass spectrum of trans-[Pt(OH)(NH$_3$)$_2$(H$_2$O)]$^+$ ions isolated in the ion trap mass spectrometer is shown in Figure 3.1a. The isotopic pattern is distinctive of a species containing a platinum atom, excluding the contribution of formally isobaric peaks of [PtCl(NH$_3$)$_2$]$^+$ composition, thus assessing the elemental composition of the ions.
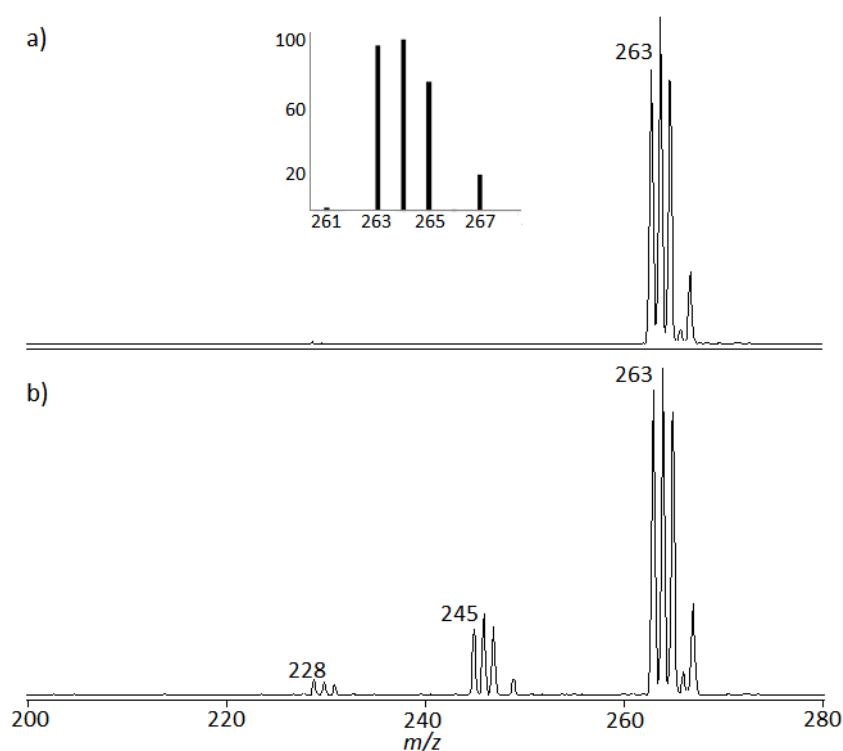
Figure 3.1 Mass spectrum showing isolated trans-[Pt(OH)(NH$_3$)$_2$(H$_2$O)]$^+$ ions at m/z 263 prior to (a) and after (b) irradiation by IR photons at 3600 cm^{-1} (Esquire 6000). The inset shows the calculated isotope pattern for the given atom composition.

Further confirmation of the ion composition is obtained by FT-ICR mass spectrometry operated in high resolution mode. As shown in Figure 3.2, the observed m/z values for the isotopic peaks are within ± 2 ppm of the theoretical m/z value. The mass spectrum of cis-[Pt(OH)(NH$_3$)$_2$(H$_2$O)]$^+$ is in everything similar.
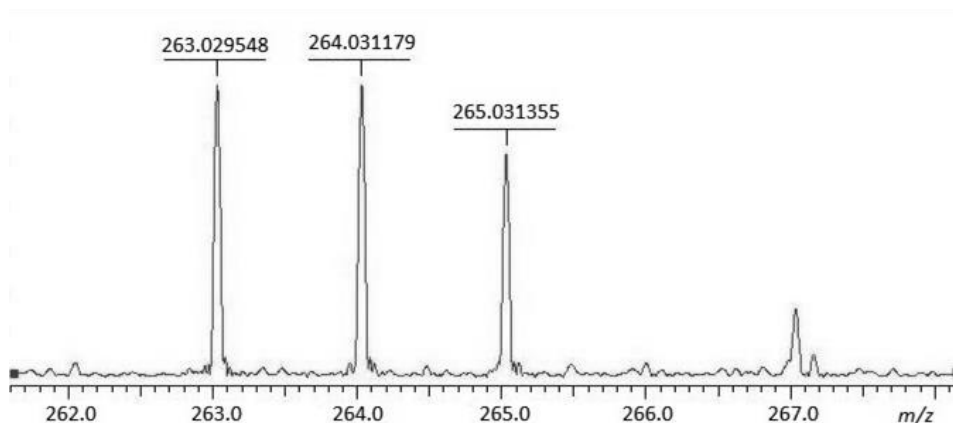
Figure 3.2 High resolution mass spectrum of *cis*-[Pt(OH)(NH$_3$)$_2$(H$_2$O)]$^+$. Calculated m/z values are: 263.029082 Da (^{194}Pt^{14}N$_2$^{1}H$_9$^{16}O$_2$); 264.031194 Da (^{195}Pt^{14}N$_2$^{1}H$_9$^{16}O$_2$); 265.031354 Da (^{196}Pt^{14}N$_2$^{1}H$_9$^{16}O$_2$). The deviation between experimental and calculated values is always within 2 ppm.

For the sake of simplicity, henceforth isotopic cluster ions are named by the mass of the ^{194}Pt isotope containing species. The collision induced dissociation (CID) behavior is quite comparable and leads to the formation of the ions *m/z* 245 and *m/z* 227 generated by two consecutive water losses, thus impeding any structural discrimination (see CID mass spectra reported in figure S3.1 in the Supporting Material). IR spectroscopy was therefore turned to as potential structural probe. Both *cis*- and *trans*-[Pt(OH)(NH$_3$)$_2$(H$_2$O)]$^+$, when submitted to irradiation by IR photons in resonance with an active vibrational mode, undergo water loss yielding ions at *m/z* 245 (Figure 3.1b). Additional NH$_3$ loss is also observed, albeit to a minor extent (*m/z* 228).

The experimental spectra are shown in blue in Figure 3.3a-b and are considerably different for the two isomers. To begin with, the differences in the photofragmentation yield suggest the process being more efficient in the case of the trans isomer relative to the cis. This behavior is traced to the diverse energy threshold for the loss of water which were proven by DFT calculations. In scheme 3.1 and table S3.1 and S3.2 in the SM are presented the optimized geometries and relative free energies and enthalpies for the dissociation processes of water from both *cis*- and *trans*-[Pt(OH)(NH$_3$)$_2$(H$_2$O)]$^+$ showing that the process is uphill by 149 and 119 kJ mol^{-1} (ΔH at 298 K) for the cis and trans isomer, respectively.
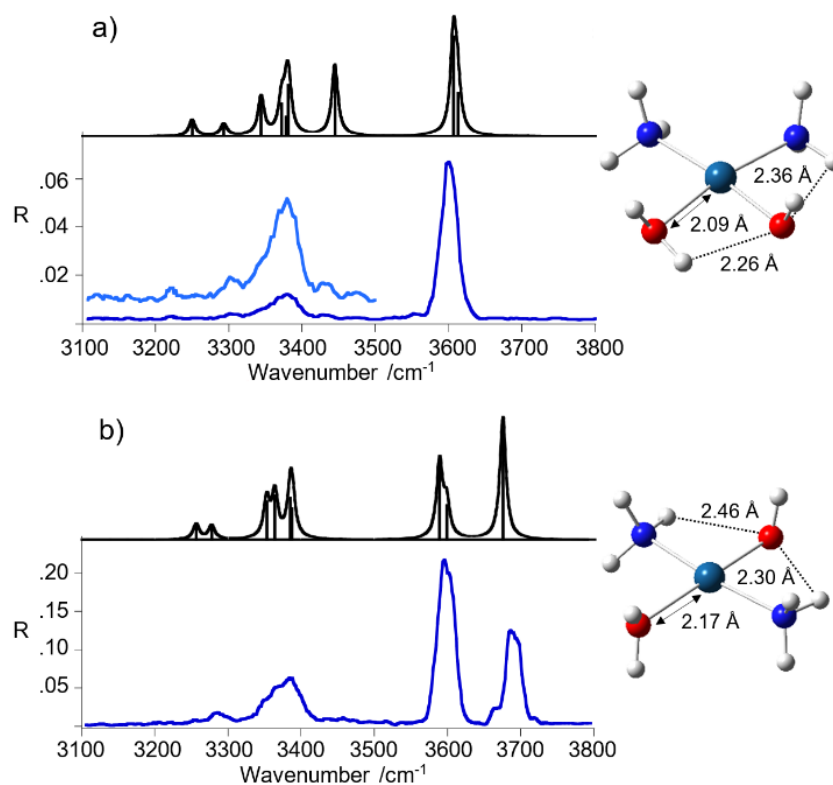
Figure 3.3 IRMPD spectra of *cis*-[Pt(OH)(NH₃)₂(H₂O)]⁺ (a) and *trans*-[Pt(OH)(NH₃)₂(H₂O)]⁺ (b)(blue profiles) compared with the calculated linear IR spectra (black profiles). Optimized geometries are shown.
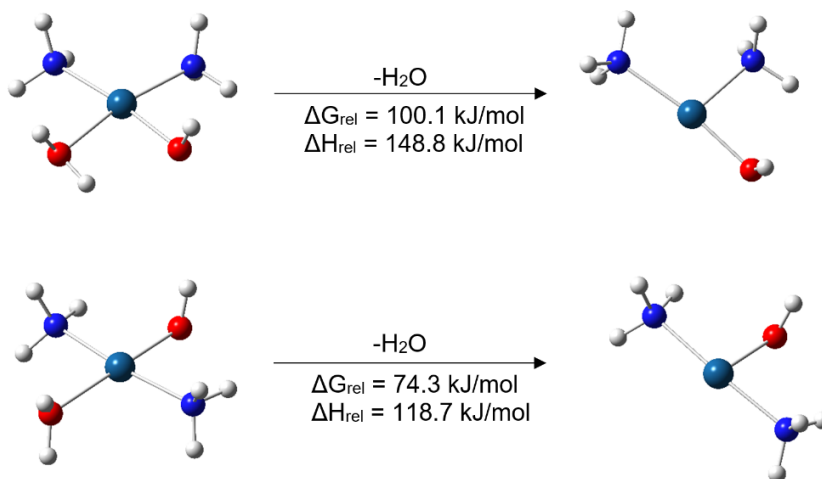
Scheme 3.1 Optimized geometries and relative energies at 298K calculated at the B3LYP/aug-cc-pVTZ level for the dissociation reaction of water from *cis* and *trans*-[Pt(OH)(NH₃)₂(H₂O)]⁺.

The spectrum of the cis isomer (Figure 3.3a) presents a strong signal at 3600 cm⁻¹ and less pronounced broad peaks from 3200 to 3450 cm⁻¹, in the range expected for

the asymmetric and symmetric N-H stretches of the ammonia ligands. A similar pattern appears in the spectrum of *trans*-[Pt(OH)(NH$_3$)$_2$(H$_2$O)]$^+$, where the band at 3600 cm^{-1} is however accompanied by another one at 3683 cm^{-1} of comparable intensity. In order to gain insight into the observed spectral features, the geometries of *cis*- and *trans*-[Pt(OH)(NH$_3$)$_2$(H$_2$O)]$^+$ have been optimized at B3LYP/aug-cc-pVTZ level using the aug-cc-pVTZ-PP pseudopotential for Pt. The structures are also reported in figure 3.3 while thermodynamic data are presented in table S3.1. Harmonic frequency calculations were performed at the same level of theory and the computed spectra are compared to the experimental ones in Figure 3.3, while vibrational frequencies and IR intensities are reported in Table 3.1.

Table 3.1 Vibrational frequencies for *cis*- and *trans*-[Pt(OH)(NH$_3$)$_2$(H$_2$O)]$^+$ complexes.

Vibrational mode[a]		Exp[b]	Theor[b,c]
cis-[Pt(OH)(NH$_3$)$_2$(H$_2$O)]$^+$			
ν	OH	3600	3612 (61)
ν_{as}	H$_2$O		3606 (142)
ν_s	H$_2$O	3442	3444 (101)
ν_{as}	NH$_3$	3379	3381 (72)
ν_{as}	NH$_3$		3378 (27)
ν_{as}	NH$_3$		3372 (46)
ν_{as}	NH$_3$		3344 (55)
ν_s	NH$_3$	3300	3293 (17)
ν_s	NH$_3$	3222	3250 (22)
trans-[Pt(OH)(NH$_3$)$_2$(H$_2$O)]$^+$			
ν_{as}	H$_2$O	3683	3674 (166)
ν	OH	3600	3598 (46)
ν_s	H$_2$O		3588 (103)
ν_{as}	NH$_3$	3384	3387 (42)
ν_{as}	NH$_3$		3385 (57)
ν_{as}	NH$_3$		3363 (60)
ν_{as}	NH$_3$		3352 (52)
ν_s	NH$_3$	3284	3277 (19)
ν_s	NH$_3$		3256 (21)

[a]ν_s and ν_{as} stand for symmetric and asymmetric stretching modes, respectively. [b]In cm^{-1}. [c]Computed harmonic intensities (km mol^{-1}) are reported in brackets.

The calculated linear IR spectra account well for the major signatures observed in the IRMPD spectra of both *cis*- and *trans*-[Pt(OH)(NH$_3$)$_2$(H$_2$O)]$^+$ isomers. The

matching is underlined in the data summarized in Table 3.1. Few structural and vibrational features may be highlighted. A notable difference between the two geometries is in the length of the Pt-OH$_2$ bond. The shorter distance in the cis isomer may be related to the presence of a H-bond interaction between the hydrogen of the water ligand lying on the molecular plane and the adjacent hydroxyl oxygen. This feature bears consequence in the vibrational spectrum.

The IRMPD spectrum of the *trans*-[Pt(OH)(NH$_3$)$_2$(H$_2$O)]$^+$ isomer shows two bands in the OH stretching region at 3683 and 3600 cm^{-1} corresponding to the H$_2$O asymmetric stretching and a combination of the OH and H$_2$O symmetric stretching modes, respectively.

Interestingly, the O-H stretching modes in the spectrum of *trans*-[Pt(OH)(NH$_3$)$_2$(H$_2$O)]$^+$ well reproduce the situation observed in the IRMPD spectrum of *trans*-[PtCl(NH$_3$)$_2$(H$_2$O)]$^+$, where absorbances at 3683 and 3596 cm^{-1} have been reported.[14] This finding highlights the comparable effect of either chloro or hydroxo substituents on the vibrational modes of the trans water ligand. A difference in relative intensity, enhancing the band at 3600 cm^{-1} compared to the one at 3683 cm^{-1} in *trans*-[Pt(OH)(NH$_3$)$_2$(H$_2$O)]$^+$, is proportional to the additive contribution in the former by the OH stretching and H$_2$O symmetric stretching oscillators.

In the *cis* isomer, one hydrogen atom of the water ligand on the molecular plane is oriented towards the adjacent hydroxyl oxygen, as aldready noticed. This interaction causes an important red shift of the water stretching modes. In particular, the asymmetric stretching shifts to 3606 cm^{-1}, coalescing with the OH stretching calculated at 3612 cm^{-1}, accounting for the band observed at 3600 cm^{-1}. The symmetric H$_2$O stretching is calculated at 3444 cm^{-1} and barely emerges at 3442 cm^{-1} in the IRMPD spectrum. However, it is not unusual to find an unexpectedly low intensity associated to stretching modes involved in hydrogen bonding. Possible reasons for this behavior include anharmonicity effects as well as effects related to the stepwise excitation in the IRMPD process, disrupting the hydrogen bond and removing the affected mode from resonance.[36,46-48]

Stretching modes of the ammonia ligands appear below 3400 cm^{-1}. These modes are not particularly influenced by the relative position of the other ligands. Indeed,

only few differences emerge from the analysis of the NH$_3$ stretching vibrations. The asymmetric stretching modes give rise to a broad feature with maximum at ca. 3380 cm^{-1} in the spectra of both isomers. The presence of multiple absorptions close in frequency is compatible with the broad signal, well interpreted by the calculations. The symmetric stretching modes, instead, are poorly active and are observed at lower frequencies. It is interesting to note that in the IRMPD spectrum of *cis*-[Pt(OH)(NH$_3$)$_2$(H$_2$O)]$^+$ the small band at 3300 cm^{-1} matches the NH$_3$ symmetric stretching calculated at 3293 cm^{-1}, while in the spectrum of the *trans* isomer the corresponding band is found at 3284 cm^{-1} (calculated value 3277 cm^{-1}). This slightly lower frequency is likely due to the interaction of both NH$_3$ ligands with the hydroxyl oxygen, a stronger binding motif that the one with water. In the *cis* isomer only one ammonia molecule is allowed to interact with the OH group while the second one may interact only with H$_2$O, yielding resonances calculated at 3250 cm^{-1} and 3293 cm^{-1}, respectively.

3.3.2 Reactivity of [PtX(NH$_3$)$_2$(H$_2$O)]$^+$ (X = Cl, OH) complexes in ligand substitution reactions

Cis- and *trans*-[PtX(NH$_3$)$_2$(H$_2$O)]$^+$ (X = Cl, OH) complexes, formed in solution by stepwise hydrolysis of the respective precursors, cisplatin and transplatin have been allowed to react with selected ligands of appropriate volatility introduced at stationary concentration in the cell of an FT-ICR mass spectrometer, in particular pyridine, trimethylphosphate, thioanisole and dimethylsulfide. The ligands are endowed with functional groups that are well established biomolecular platination sites: the pyridine ring comprises an aza group, functional group present in nucleobases such as adenine and guanine and favored site of cisplatin binding;[21,43] dimethylsulfide and thioanisole show sulfur-containing nucleophilic functions, in particular thioanisole incorporates the thiomethyl ether group of methionine which side chain is a well established binding sites of cisplatin in proteins;[6,49-51] trimethylphosphate is chosen to represent the ubiquitous biological phosphates that are also integral part of DNA. Phosphate groups do show affinity for Pt(II) as evidenced both in solution and in gas phase studies.[43,52-54] The phosphate groups are ionized at physiological pH while trimethylphosphate is neutral but this feature

allows it to be used as a reactant in the gas phase. At the same time, it represents an example of 'hard' ligand.

The reaction common to all complexes $[PtX(NH_3)_2(H_2O)]^+$ is ligand exchange whereby a water molecule is replaced by the incoming L, with L equal to trimethylphosphate (TMP), pyridine (Py), thioanisole (TA), and dimethylsulfide (DMS) (reaction 3.2).

$$cis/trans\text{-}[PtX(NH_3)_2(H_2O)]^+ \ + \ L \ \rightarrow \ cis/trans\text{-}[PtX(NH_3)_2(L)]^+ \ + H_2O \qquad (3.2)$$

Figure 3.4 shows an example of kinetic plot for the reaction of $cis\text{-}[PtCl(NH_3)_2(H_2O)]^+$ with DMS.
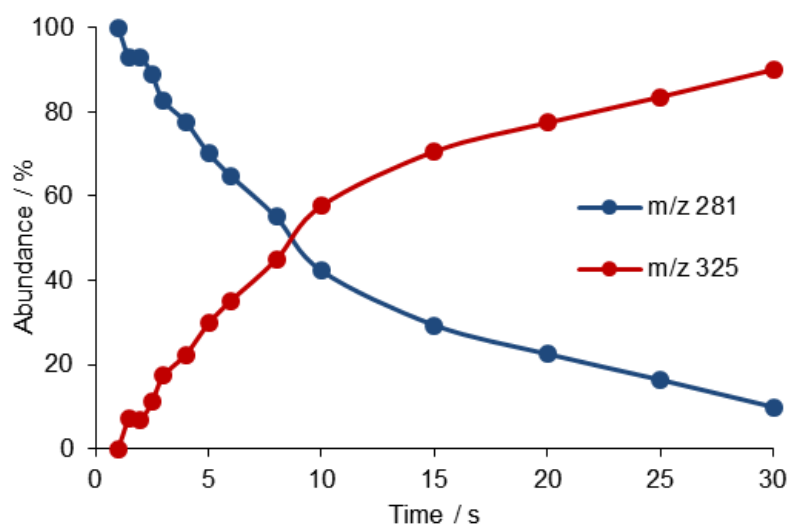
Figure 3.4 Time dependence of ion abundancies for the reaction of $cis\text{-}[PtCl(NH_3)_2(H_2O)]^+$ (m/z 281) with DMS forming $[PtCl(NH_3)_2(DMS)]^+$ at m/z 325 in the FT-ICR cell at the DMS pressure of 1.5×10^{-7} mbar.

Table 3.2 summarizes the second order rate constants and corresponding efficiencies, representing the fraction of reactive collisions. Pyridine, the most basic among the selected ligands, displays also proton transfer reactivity and ligand addition to some extent. All reactions show rather low efficiencies. This finding is in line with the behavior of platinum(II) complexes, characterized by typically slow ligand exchange kinetics.[23]

Table 3.2 Reactivity of $[PtX(NH_3)_2(H_2O)]^+$ (X = Cl, OH; *cis* and *trans* isomers) with simple molecules in the gas-phase.

Reagent Ion	Neutral	k_{exp}[a]	Eff (%)[b]
cis-$[PtCl(NH_3)_2(H_2O)]^+$	TMP	3.7	2.5
	pyridine	0.6	0.41[b]
	thioanisole	1.4	1.1
	dimethylsulfide	0.034	0.026
trans-$[PtCl(NH_3)_2(H_2O)]^+$	TMP	3.3	2.3
	pyridine	1.4	0.93[c]
	thioanisole	7.7	6.3
	dimethylsulfide	2.4	1.7
cis-$[Pt(OH)(NH_3)_2(H_2O)]^+$	TMP	0.96	0.66
	pyridine	0.46	0.31[d]
	thioanisole	0.1	0.08
	dimethylsulfide	n.r.[e]	
trans-$[Pt(OH)(NH_3)_2(H_2O)]^+$	TMP	1.1	0.78
	pyridine	0.05	0.03[f]
	thioanisole	0.46	0.37
	dimethylsulfide	n. r.[e]	

[a] Second order rate constant in units of 10^{-11} cm^3s^{-1} at 298 K, estimated error ±30%. Other sampled compounds proved to be unreactive: $H_2^{18}O$, H_2S. [b] The ligand substitution reaction is accompanied by ligand addition yielding $[PtCl(NH_3)_2(Py)(H_2O)]^+$ (Eff = 0.13 %) and by proton transfer to pyridine yielding $[PyridineH]^+$ (Eff = 1.6 %). [c] The ligand substitution reaction is accompanied by proton transfer to pyridine yielding $[PyridineH]^+$ (Eff = 12 %). [d] The ligand substitution reaction is accompanied by ligand addition (Eff = 0.10 %) and by proton transfer (Eff = 0.29 %). [e] n. r. stands for non-reactive. Other tested and found to be unreactive compounds are $H_2^{18}O$ and H_2S. [f] The ligand substitution reaction is accompanied by by proton transfer (Eff = 0.64 %).

The most notable feature emerging from the kinetic data in Table 3.2 is the consistently higher reactivity of $[PtCl(NH_3)_2(H_2O)]^+$ complexes with respect to the hydroxo counterparts $[Pt(OH)(NH_3)_2(H_2O)]^+$. For example, reaction efficiency ratios for the reaction of TA with *cis*-$[PtX(NH_3)_2(H_2O)]^+$ and *trans*-$[PtX(NH_3)_2(H_2O)]^+$ are 14 and 17, respectively. TA is a soft ligand expected to show high efficiency toward the

soft platinum center.[6,23-25,50,51,55-57] Surprisingly, TMP, an O-donor nucleophile, shows relatively high reactivity. It should be noticed, though, that the ligand exchange reaction outlined in equation 3.2 is in fact a stepwise process in the gas-phase involving: (i) formation of a reactant collision complex (RC); (ii) ligand substitution yielding the product complex (PC) and (iii) separation of the product pair, as depicted in equation 3.3.

$$[PtX(NH_3)_2(H_2O)]^+ + L \rightleftharpoons \underset{RC}{[PtX(NH_3)_2(H_2O)]^+ \cdot L} \overset{TS}{\rightleftharpoons} \underset{PC}{[PtX(NH_3)_2(L)]^+ \cdot H_2O} \longrightarrow [PtX(NH_3)_2(L)]^+ + H_2O$$

(3.3)
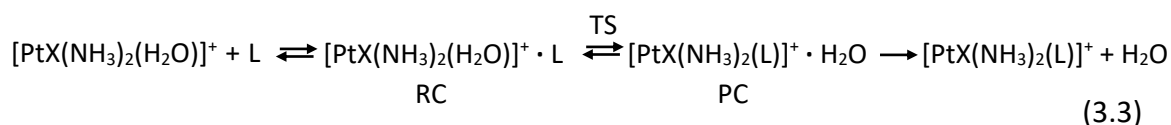
The efficiency of the overall process is determined by the branching of RC which may either proceed to the ligand substitution product (PC) or revert to separated reactants.[58,59] The kinetic data are well interpreted by the computed profile of the potential energy surface (PES). A detailed discussion of the reaction mechanism of substitution in platinum(II) complexes will be presented in the forthcoming section 3.4.

S-donor nucleophiles like TA and DMS do not engage in strong hydrogen bonding interactions and the binding energy of RC is not sizeable. Ligand exchange is kinetically highly favored in the *trans-* with respect to the *cis*-isomers for the chloro complexes with a 5.7 times higher efficiency for TA and a 65 fold higher efficiency for DMS. This finding may be ascribed to the trans effect operated by a resident ligand on the rate of substitution of the ligand trans to it.[23-25] In the present case, the water leaving group is displaced by S-nucleophiles more easily when the trans-site is occupied by a chloro ligand than by NH_3, in agreement with the qualitative trans-directing sequence $Cl^- > NH_3$. However, this effect is not apparently clear in other instances.

To shed light on this point, the potential energy surface for reaction 3.3 involving the substitution of water in both *cis* and *trans*-$[PtCl(NH_3)_2(H_2O)]^+$ with TA was explored and is reported in Figure 3.5 while thermodynamic data for the partaking species are reported in table S3.2 in the SM. The square planar Pt complexes conform to a substitution mechanism of prevailing associative character and this is clearly verified in the gas-phase reaction. The substitution process typically occurs

with stereoretention by way of a trigonal bipyramidal transition state where the formerly trans ligand and the entering and leaving ligands are placed on the equatorial plane.[23] The energy released in the formation of the RC complexes is comparable in the two species, 115 and 105 kJ mol^{-1} for *cis*-RC and *trans*-RC respectively. Both RC complexes present interactions between the π-system of the aryl group and the NH$_3$ ligands.
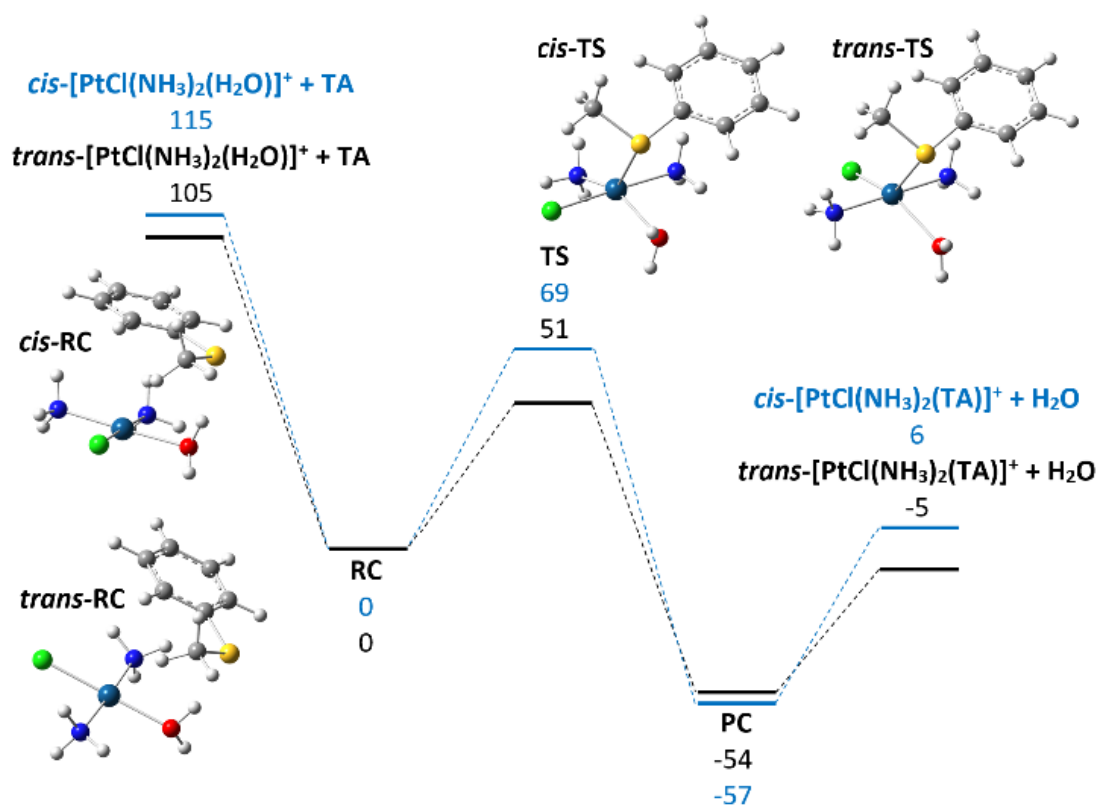
Figure 3.5 Computed profile for the reaction of *cis*- and *trans*-[PtCl(NH$_3$)$_2$(H$_2$O)]$^+$ with TA. Optimized geometries of the reactant collision complexes (*cis*- and *trans*-[PtCl(NH$_3$)$_2$(H$_2$O)]$^+ \cdot$ TA) and of the transition states TS are shown. Relative enthalpies at 298K (kJ mol^{-1}) are reported.

The observed difference in energy of ca. 10 kJ mol^{-1} is ascribable to the possibility for the *cis*-isomer to entangle interactions with both ammonia molecules due to their favorable arrangement. In contrast, the activation barrier involved to reach the TS for ligand exchange has a more pronounced variation. The two calculated TS structures are very similar, making the interpretation of the observed difference a difficult task. Two points should be highlighted: the presence of the chlorine atom in *trans* to the exchanging ligands leads to slightly longer bonds by ca. 0.07 Å

suggesting the effect of the *trans* ligand not to be negligible. Both transition states present multiple interactions between the two ligands engaged in the substitution and the ligands in the *cis*-sites that can be implicated in the calculated difference. The listed elements probably contribute to give the final results that are anyway in fair agreement with the experiments. The reaction efficiency of the *trans*-isomer being 5.7 times higher with respect to the *cis*- one (6.3 versus 1.1, see Table 3.2) is, in fact, well interpreted by the higher energy difference between the separated reactants and the transition state for the *trans* with respect to the *cis* configuration (54 and 46 kJ mol^{-1}, respectively). The trans isomer is thus more prone to undergo ligand substitution in view of the relatively more energy demanding back dissociation to reactants. The latter process remains, however, entropically favored which accounts for the low values of reaction efficiency, well below collision control.

Few other tested ligands proved to be unreactive, including $H_2^{18}O$, which suggests a sizeable activation barrier for the water exchange process. Figure 3.6 shows the symmetrical profile for reaction (3.3) with *cis*-[Pt(OH)(NH$_3$)$_2$(H$_2$O)]$^+$ as reactant and product ion (thermodynamic data of all species are given in table S3.1). Here the collision complexes RC and PC are symmetrical, apart from the ^{18}O-isotope distribution. Their geometry is characterized by two hydrogen bonds linking a hydrogen atom of ligated water with an O atom of the external water and a H atom of the external H_2O with the hydroxyl oxygen. In forming the RC complex, however, the hydrogen bond interaction between the in plane water hydrogen and the hydroxyl oxygen in *cis*-[Pt(OH)(NH$_3$)$_2$(H$_2$O)]$^+$ is impaired, which may account for the relatively small binding energy of 72 kJ mol^{-1}. The activation barrier for the ligand exchange (RC $\rightarrow$ TS) is 91 kJ mol^{-1}, protruding above the energy level of the isolated reactant pair. This feature implies that, in the single collision regime prevailing in the FT-ICR cell, the reaction will not occur, as experimentally observed. The RC complex would require an additional source of $\Delta E = 91\text{-}72 = 19$ kJ mol^{-1} for the reaction to proceed in the isolated, low pressure environment.
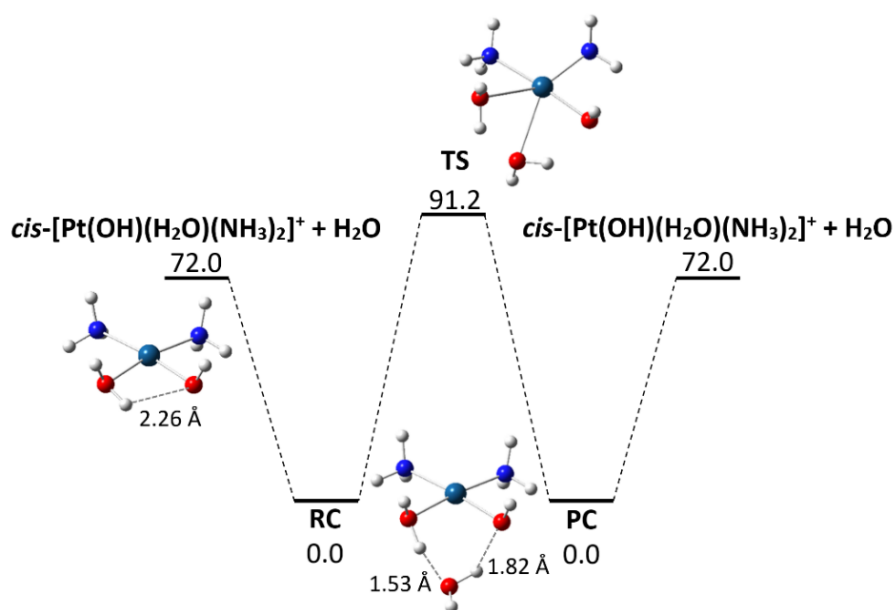
Figure 3.6 Computed profile for the degenerate reaction of *cis*-[Pt(OH)(NH$_3$)$_2$(H$_2$O)]$^+$ with H$_2$O. Optimized geometries of *cis*-[Pt(OH)(NH$_3$)$_2$(H$_2$O)]$^+$, of the collision complex RC/PC (*cis*-[Pt(OH)(NH$_3$)$_2$(H$_2$O)]$^+$ · H$_2$O) and of the transition state TS are shown. Relative enthalpies at 298K (kJ mol^{-1}) are reported.

The whole set of calculations performed is thus consistent in interpreting the experimental results as a function of multiple factors. The reactivity of square planar complexes is often related to the presence of certain ligated atoms in *trans* position. The evidence presently obtained points in a different direction showing a remarkable importance of the *cis*-sites in entangling interactions with the reacting ligands all along the entire reaction. Significantly, groups possessing multiple binding sites, e.g. TMP, present the worst agreement with the qualitative indications suggested by the trans effect.
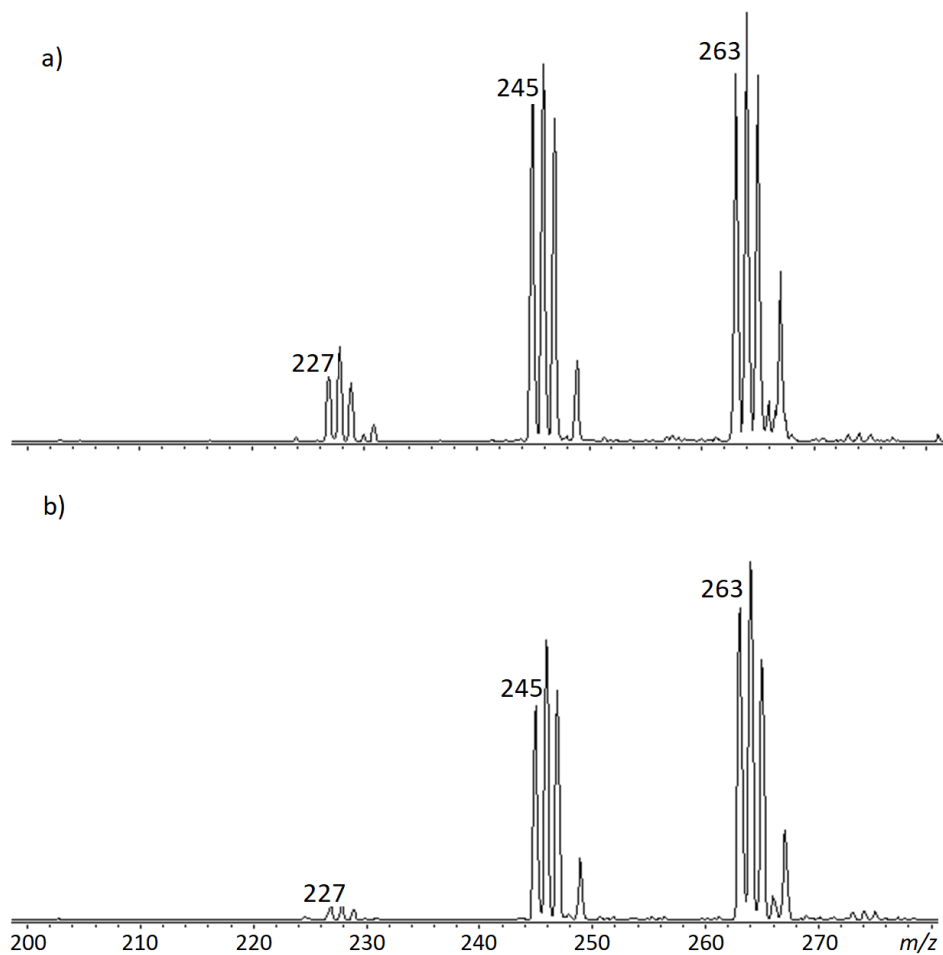
Figure S3.1 CID mass spectra of a) *cis*-[Pt(OH)(NH$_3$)$_2$(H$_2$O)]$^+$ and b) *trans*-[Pt(OH)(NH$_3$)$_2$(H$_2$O)]$^+$, recorded in a Paul ion trap (Esquire 6000+, Bruker Daltonics) upon mass selection of the isotopic cluster and activation with a radio frequency amplitude of 0.6.

Table S3.1 Theoretically calculated thermodynamic parameters for the most stable structures of sampled Pt(II) complexes. Calculation performed at B3LYP/aug-cc-pVTZ(-PP) level.

	B3LYP/aug-cc-pVTZ(-PP)				
Species	Energy[a]	Relative Energy[b]	Zero-point Energy[b]	Relative Enthalpy[b] (298K)	Relative Free Energy[b] (298K)
H_2O	-76.466197	0.0	55.76	0.00	0.00
$H_2{}^{18}O$	-76.466197	0.0	55.58	0.18	0.60
cis-[Pt(OH)(NH$_3$)$_2$(H$_2$O)]$^+$	-384.855559	5.5	313.05	6.60	7.56
cis-[Pt(OH)(NH$_3$)$_2$ (H$_2{}^{18}$O)]$^+$	-384.855559	0.0	312.64	6.26	6.89
$trans$-[Pt(OH)(NH$_3$)$_2$(H$_2$O)]$^+$	-384.857664	0.0	311.09	0.00	0.00
cis-[Pt(OH)(NH$_3$)$_2$(H$_2$O)]$^+$·H$_2$O	-461.351465	0.0	380.00	0.00	0.00
cis-[Pt(OH)(NH$_3$)$_2$(H$_2$O)]$^+$·H$_2{}^{18}$O	-461.351465	0.0	379.55	-0.34	-0.67
cis-[Pt(OH)(NH$_3$)$_2$(H$_2{}^{18}$O)]$^+$·H$_2$O	-461.351465	0.0	379.68	-0.25	-0.63
TS	-461.314935	95.9	375.68	92.59	91.19
TS-H$_2{}^{18}$O	-461.314935	95.9	375.36	92.35	90.61
cis-[Pt(OH)(NH$_3$)$_2$]$^+$	-308.329253	37.03	243.60	36.75	33.27
$trans$-[Pt(OH)(NH$_3$)$_2$]$^+$	-308.343356	0.00	244.49	0.00	0.00

[a] Electronic energy at 0K. In Hartree particle^{-1}. [b] In kJ mol^{-1}. [c] In J mol^{-1}K^{-1}.

Table S3.2 Theoretically calculated thermodynamic parameters for the structures of sampled Pt(II) complexes partaking the profile for the reaction of of *cis-* and *trans-*[PtCl(NH$_3$)$_2$(H$_2$O)]$^+$ with TA. Calculation performed at ωB97X-D/6-311++G** level employing the LanL2TZ PP for the platinum atom.

	ωB97X-D/6-311++G**				
Species	**Energy[a]**	**Relative Energy[b]**	**Zero-point Energy[b]**	**Relative Enthalpy[b] (298K)**	**Relative Free Energy[b] (298K)**
H$_2$O	-76.432249	-	56.91	-	-
TA	-669.726987	-	341.08	-	-
cis-[PtCl(NH$_3$)$_2$(H$_2$O)]$^+$	-768.790763	5.24	284.99	6.40	9.22
trans-[PtCl(NH$_3$)$_2$(H$_2$O)]$^+$	-768.792760	0.00	282.97	0.00	0.00
cis-[PtCl(NH$_3$)$_2$(H$_2$O)]$^+$·TA	-1438.563406	56.95	632.30	57.43	65.49
trans-[PtCl(NH$_3$)$_2$(H$_2$O)]$^+$·TA	-1438.562430	59.51	633.63	60.89	68.51
cis-TS	-1438.535468	130.30	625.50	126.12	127.31
trans-TS	-1438.540908	116.02	625.66	112.24	111.69
cis-[PtCl(NH$_3$)$_2$(TA)]$^+$·H$_2$O	-1438.585098	0.00	629.25	0.00	0.00
trans-[PtCl(NH$_3$)$_2$(TA)]$^+$·H$_2$O	-1438.582417	7.04	629.03	3.27	4.33
cis-[PtCl(NH$_3$)$_2$(TA)]$^+$	-1362.125910	8.37	562.50	7.30	2.48
trans-[PtCl(NH$_3$)$_2$(TA)]$^+$	-1362.129098	0.00	564.62	0.00	0.00

[a] Electronic energy at 0K. In Hartree particle^{-1}.   [b] In kJ mol^{-1}.   [c] In J mol^{-1}K^{-1}.

3.4 Probing the missing step in the understanding of metal complexes substitution reaction: the encounter complex of cisplatin with model ligands isolated and characterized by MS and IRMPD spectroscopy

The work reported in the following section has been partly published in the following papers:

D. Corinti, C. Coletti, N. Re, B. Chiavarino, M.E. Crestoni, S. Fornarini

Cisplatin Binding to Biological Ligands Revealed at the Encounter Complex Level by IR Action Spectroscopy

Chem. - A Eur. J. 22 (2016) 3794–3803

doi:10.1002/chem.201504521.

D. Corinti, C. Coletti, N. Re, R. Paciotti, P. Maître, B. Chiavarino, M. E. Crestoni, S. Fornarini

Short-lived intermediates (encounter complexes) in cisplatin ligand exchange elucidated by infrared ion spectroscopy

Int. J. Mass Spectrom. 435 (2019) 7-17

doi:10.1016/j.ijms.2018.10.012.

The contributions of myself to the work consisted in executing the CID and IRMPD spectroscopy experiments as well as performing the calculations involved in both vibrational features and reaction mechanism interpretation. The first draft of the the paper published in Int. J. Mass Spectrom. was prepared by myself and revised by Prof. Simonetta Fornarini.

3.4.1 Cisplatin complexes with model ligands: formation of cis-[PtCl(NH3)2(L)]+ in solution

When an incubated aqueous solution of cisplatin is sampled by ESI-MS, the formation of aqua complexes is directly observed (Figure 3.7 panel A). Upon mixing with a ligand (L) solution, the *cis*-[PtCl(NH$_3$)$_2$(H$_2$O)]$^+$ aqua complex has largely disappeared while *cis*-[PtCl(NH$_3$)$_2$(L)]$^+$ is formed, by substitution of the labile coordinated water molecule. As an example, in panel B of Figure 3.7 is reported the mass spectrum generated when cisplatin is allowed to react with pyridine (Py).
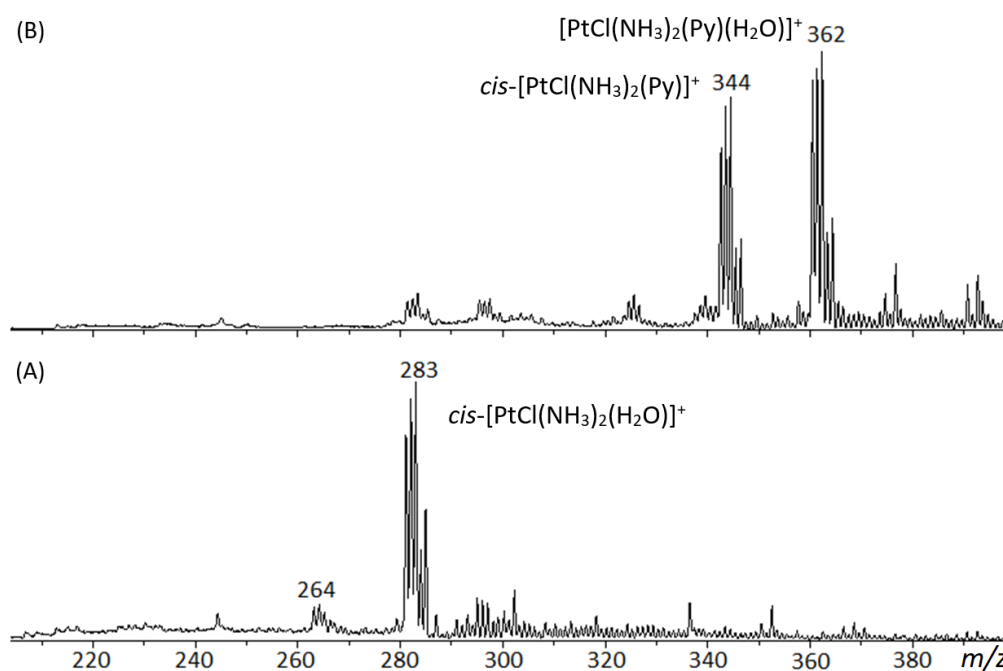
Figure 3.7 Panel A: ESI mass spectrum of a cisplatin solution showing the cluster with major peaks at m/z 281-283, assigned to the aqua complex *cis*-[PtCl(NH$_3$)$_2$(H$_2$O)]$^+$. Panel B: ESI mass spectrum of the solution obtained by mixing solution A with a solution of pyridine to attain a cisplatin/pyridine molar ratio of 1:1. The isotopic cluster centered at m/z 342-344 is assigned to *cis*-[PtCl(NH$_3$)$_2$(Py)]$^+$ and the cluster at m/z 360-362 to [PtCl(NH$_3$)$_2$(Py)(H$_2$O)]$^+$.

The ESI mass spectrum in panel B of figure 3.7 shows the presence of two prominent species, a cluster centered at m/z 342-344 consistent with the formation of *cis*-[PtCl(NH$_3$)$_2$(Py)]$^+$ and a second major species at m/z 360-362 assigned to an adduct corresponding to a [PtCl(NH$_3$)$_2$(Py)(H$_2$O)]$^+$ complex. The isotopic pattern of the two clusters indicates the presence of both one platinum and one chlorine atom, thus confirming the attribution of the observed ions. The formation of the *cis*-

[PtCl(NH$_3$)$_2$(L)]$^+$ complex is observed also with other tested ligands including trimethylphosphate (TMP), 4(5)-methylimidazole (MeIm), thioanisole (TA), acetamide (ACM), dimethylacetamide (DMA), urea (U) and thiourea (SU). It is worth noting that the [PtCl(NH$_3$)$_2$(L)(H$_2$O)]$^+$ cluster, owning formally five ligands, is also present for the whole set of ligands but when L is equal to TA or SU.

3.4.2 Vibrational and structural features of cis-[PtCl(NH$_3$)$_2$(L)]$^+$ complexes

The complexes obtained by ligand substitution from cis-[PtCl(NH$_3$)$_2$(H$_2$O)]$^+$ have been examined by IRMPD spectroscopy in the mid-IR region.[28,29,37] The discussion of the results will focus be divided in a first part about the species where L is either Py or TMP, followed by a detailed comparison of platinum binding with ACM, DMA, U and SU. Regarding 4(5)-Methylimidazole, which has been chosen to model the heterocyclic substituent of histidine, the substitution complex with cisplatin is poorly IRMPD active, presenting just one vibrational feature at 1294 cm^{-1} (the IRMPD spectrum is reported in figure S3.2 in the Supporting Materialand the vibrational frequencies in table S3.3). 4(5)-Methylimidazole exists in a rapidly equilibrating tautomeric mixture of 4-methyl-1H-imidazole and 5-methyl-1H-imidazole (scheme 3.2) so there are two possible binding sites for the metal. However, both potential isomers account for the experimental IR signal thus impeding to discriminate between them.
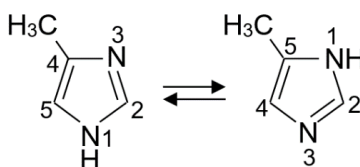
Scheme 3.2 4(5)-methylimidazole

Structural characterization of cis-[PtCl(NH$_3$)$_2$(Py)]$^+$

When probed by IR multiple photon absorption in resonance with an active vibrational mode, the cis-[PtCl(NH$_3$)$_2$(Py)]$^+$ complex exhibits sequential losses of NH$_3$ and HCl. The IRMPD spectrum in the 800-1800 cm^{-1} wavenumber range is plotted in Figure 3.8. The experimental spectrum is shown together with the computed IR spectrum for the sampled species. The optimized geometry of cis-[PtCl(NH$_3$)$_2$(Py)]$^+$, also shown in Figure 3.8 (**Py1**), is characterized by a pyridine plane approximately

perpendicular with respect to the square planar coordination at platinum, an eclipsed configuration of the NH_3 ligands and an interaction between chlorine and a hydrogen atom of the adjacent ammonia (Cl···H distance of 2.54 Å). The calculated IR spectrum (upper panel in Figure 3.8) provides good agreement with the experimental IRMPD spectrum, dominated by a band at 1288 cm^{-1}. This feature comprises the umbrella modes of the two NH_3 ligands expected at 1290 and 1304 cm^{-1}. Weaker bands at 1455 and 1602 cm^{-1} are assigned to CC stretching and asymmetric NH_3 bending modes.
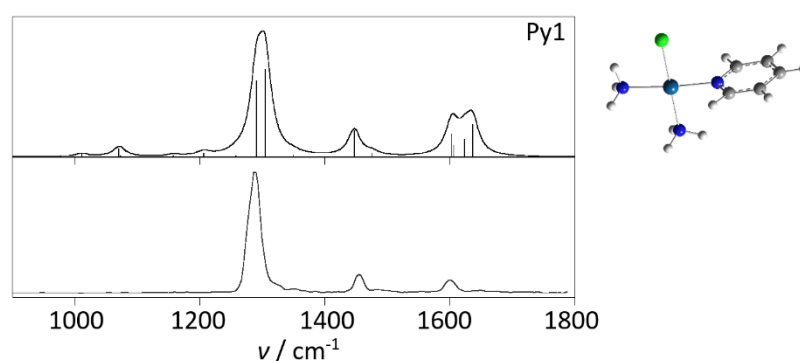
Figure 3.8 IRMPD spectrum (lower panel) compared with the IR spectrum of *cis*-[PtCl(NH₃)₂(Py)]⁺ calculated at B3LYP/6-311+G(d,p) level.

Structural characterization of *cis*-[PtCl(NH₃)₂(TMP)]⁺

The TMP complex, *cis*-[PtCl(NH₃)₂(TMP)]⁺, examined by IRMPD spectroscopy in the mid-IR range, presents major photofragmentation channels involving loss of NH_3 and/or HCl. Also from this complex, photofragmentation of the intact L ligand is never observed as shown in figure S3.3 in the SM. At variance with the pyridine ligand, TMP presents two potential sites for platinum binding and calculations have been performed taking into account the possible formation of two distinct isomers. In the first one (**TMP1**) shown in Figure 3.9, Pt is coordinated to the phosphoryl oxygen while in the second one (**TMP2**) Pt is bound to a methoxyl oxygen. Vibrational analysis of the optimized structures **TMP1** and **TMP2** yields the calculated IR spectra plotted in the upper panels of Figure 3.9. The first isomer **TMP1** is more stable by 43 kJ mol^{-1} and the calculated IR spectrum of **TMP1** is consistent with the observed IRMPD features, showing the phosphoryl group to be the coordination site.
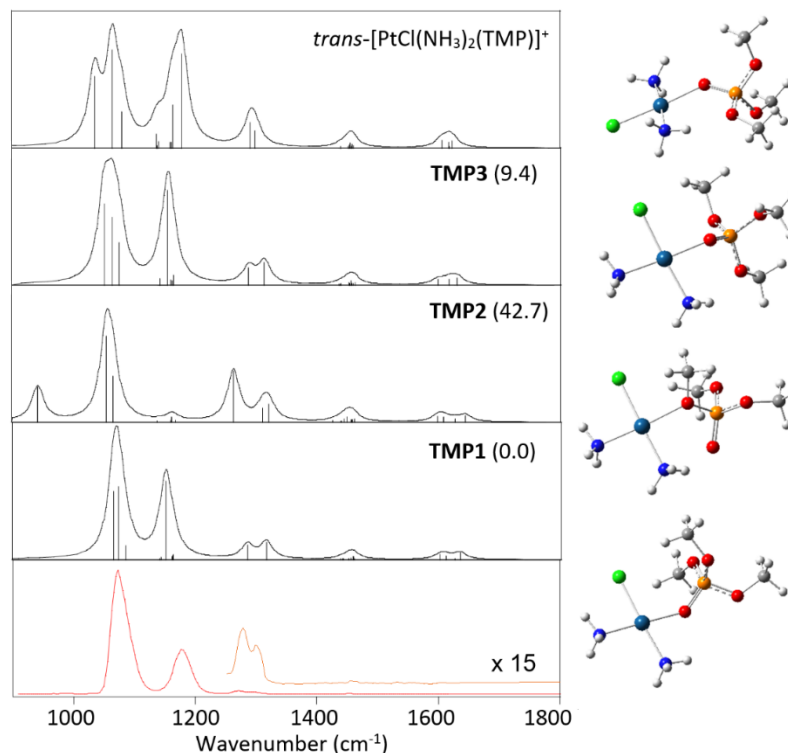
Figure 3.8 IRMPD spectrum (red line) compared with the calculated IR spectra (black line) of *cis*-[PtCl(NH₃)₂(TMP)]⁺ (isomers **TMP1**, **TMP2**, **TMP3**) and *trans*-[PtCl(NH₃)₂(TMP)]⁺. Relative energies at the ωB97X-D level (298K) of optimized structures are in kJ mol⁻¹.

The IRMPD spectrum of *cis*-[PtCl(NH₃)₂(TMP)]⁺ is characterized by two prominent bands at 1071 and 1178 cm⁻¹, assigned to P-OCH₃ and P-OPt stretching modes, respectively (figure 3.8). One may compare the free phosphoryl stretching mode of **TMP2** at 1280 cm⁻¹ with the P-OPt stretching in **TMP1** calculated at 1152 cm⁻¹. The observed decrease in the calculated frequencies goes in parallel with the lengthening of the P-O bond from 1.480 Å in **TMP2** to 1.520 Å in **TMP1**, an effect of the coordination with platinum, reducing the P=O bond strength. The broad IRMPD band at 1071 cm⁻¹ is assigned to a convolution of three P-OCH₃ stretches with similar frequencies, at 1066, 1074 and 1086 cm⁻¹. In contrast, a distinct IR signature of **TMP2** at 943 cm⁻¹, associated to the P-O stretch involving the methoxyl group coordinated to platinum, is missing in the experimental spectrum. The umbrella modes of the two NH₃ ligands calculated at 1286 and 1317 cm⁻¹ for **TMP1** account for the weak experimental signatures at 1271 and 1295 cm⁻¹. Other tested isomers

have included **TMP3**, a conformer of **TMP1** displaying a methoxyl group oriented towards the neighbouring ammonia to allow a NH···OCH$_3$ hydrogen bond interaction. This species, lying at 9.4 kJ mol^{-1} relative to **TMP1**, shows an IR spectrum in poor agreement with the experiment (figure 3.8), in particular owing to a red-shifted P-OCH$_3$ stretching frequency of the group involved in hydrogen bonding with ammonia (at 1051 cm^{-1}). Also depicted in Figure 3.8 is the optimized structure and calculated IR spectrum of the *trans*-[PtCl(NH$_3$)$_2$(TMP)]$^+$ isomer, rather disproving its presence in the sampled ion population.

Structural characterization of *cis*-[PtCl(NH$_3$)$_2$(L)]$^+$ (L=ACM, DMA, U and SU)

We have assayed using IRMPD spectroscopy in the mid-IR region the cisplatin derived complexes with ACM, DMA, U and SU. The selected ligands present two competing binding sites for platination, namely the amino nitrogen and the carbonyl group (thiocarbonyl in the case of SU). A preliminary computational survey permitted to identify the minima structures of the two possible isomers for the four inspected complexes. Geometries and free energies of the optimized structures calculated using both B3LYP and ωB97X-D are reported in figure 3.9. For the whole set of ligands, the N-bound isomers (**ACM_2**, **DMA_2**, **U_2** and **SU_2**) are higher in energy than their counterparts, either O-bound (**ACM_1**, **DMA_1** and **U_1**) or S-bound (**SU_1**). In addition, the geometries are fairly similar among the series of ligands showing for the (S-)O-bound isomers a preferential interaction of the chloride for the hydrogens of the amino group and, regarding the N-bound ones, the formation of an H-bond between the ammonia molecule in *cis* to the organic ligand and the (thio)carbonyl moiety. The energy gap between the two families of isomers, reported in figure 3.9, is notably different moving from ACM to SU revealing how relevant small modifications can be in influencing the preference of platinum to generate different kinds of adducts. For example, **DMA_2** is 49.7 kJ mol^{-1} higher in free energy relative to **DMA_1**, while **ACM_1** is only 36.6 kJ mol^{-1} lower than **ACM_2**. This difference in relative energy suggests that the electron donating property of the two methyl groups in DMA affords a more pronounced stabilizing effect when the carbonyl group is the ligation site rather than in the N-bound complex. However, some influence of steric encumbrance, due to the presence of

71

the methyl groups on the Pt-bound nitrogen atom in **DMA_2** cannot be discarded. One may also notice an important effect when sulfur in SU replaces oxygen in the U ligand. In fact, while the difference in energy between **U_1** and **U_2** is 22.4 kJ mol^{-1}, which is the smallest in the reported series of complexes, the presence of the thiocarbonyl group increases the relative energy of **SU_2** to 80.8 kJ mol^{-1} with respect to **SU_1**. This finding is in line with the well known affinity of "soft" platinum(II) for sulfur donor ligands.[55] However, mere consideration of thermodynamic data may not be adequate to interpret an ion population generated by ESI. It is in fact not unusual to find that high lying isomers, preferentially formed in solution, may be kinetically trapped in the gas-phase.[60,61]
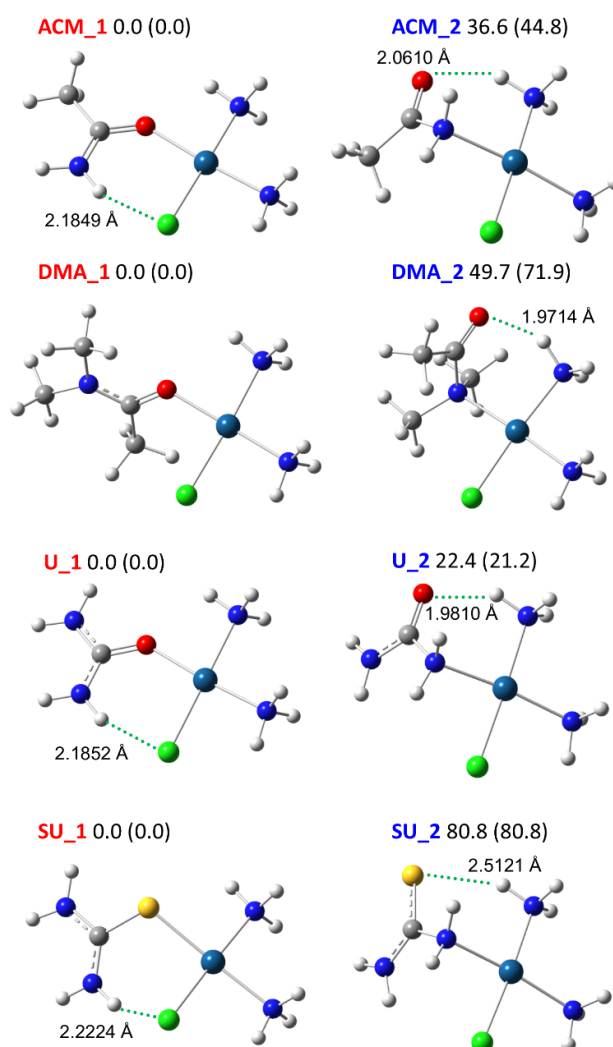
Figure 3.9 Structures of the *cis*-[PtCl(NH$_3$)$_2$(L)]$^+$ complexes optimized at the B3LYP/6-311+G** (LanL2TZ for Pt) level of theory. Relative free energies at 298 K are in kJ mol^{-1}, as calculated at the ωB97X-D and B3LYP (in brackets) level.

The vibrational frequency calculated from the geometries reported in figure 3.9 have, subsequently, been compared to the IRMPD spectra of the cis-[PtCl(NH$_3$)$_2$(L)]$^+$ ion in figure 3.10 and table S3.4 in the SM in order to obtain a fine characterization of the ions structural motifs. When submitted to resonant IR photons the easiest dissociation channel is the ammonia-loss, followed by HCl loss. Only a small percentage of L loss (comprised between the 3% and 6% of the total product ion abundance) is observed in the case of ACM, DMA and U complexes, while no [PtCl(NH$_3$)$_2$]$^+$ fragment is ever generated from the cis-[PtCl(NH$_3$)$_2$(SU)]$^+$ complex, in agreement with the expected stronger binding of platinum to the thiocarbonyl group when compared to carbonyl, IRMPD mass spectra are reported in figure S3.4 in the SM. The comparison of theoretical and experimental spectra reported in figure 3.10 supports platination to the carbonyl (or thiocarbonyl) group rather than to the amino nitrogen, as also suggested by thermodynamic data. In this regard, the lack any band in agreement with a free CO stretching in the IRMPD spectra of the ACM, DMA and U complexes, calculated at 1781, 1745 and 1772 cm^{-1} for **ACM_2**, **DMA_2** and **U_2**, respectively, indicates the absence of the N-bound isomers in the sampled population. In addition, a few vibrational features deserve to be highlighted. Three main features are present in the experimental spectrum of cis-[PtCl(NH$_3$)$_2$(ACM)]$^+$. All of them are well accounted for by the **ACM_1** calculated frequencies confirming the O-bound isomers to form the major part of the gas-phase population. The band at 1646 cm^{-1} can be interpreted as the scissor-like bending of NH$_2$ which was calculated for **ACM_1** at 1650 cm^{-1}, while the following signals at 1559 cm^{-1} is in agreement with a complex vibrational mode of **ACM_1** (1548 cm^{-1}) wherein the scissoring mode of the amino group is associated with the CO stretching. The pronounced signal at 1281 cm^{-1} is in agreement with a convoluted band consisting of the two umbrella modes of the ammonia molecules in the coordination sphere of platinum, calculated at 1289 and 1318 cm^{-1}. Finally, the barely visible signal at 1475 cm^{-1} is well accounted by the CH$_3$ umbrella mode of **ACM_1** simulated at 1465 cm^{-1}.

Moving to cis-[PtCl(NH$_3$)$_2$(DMA)]$^+$, the calculated spectrum of the O-bound isomer **DMA_1** is in perfect agreement with the experimental vibrational features. Indeed,

the IRMDP spectrum of the DMA adduct presents lots of similarities with the one of *cis*-[PtCl(NH$_3$)$_2$(Ac)]$^+$, although some bands just casually coincide and have a different interpretation. For example, the band at 1596 cm^{-1} consistent with the CN stretching of **DMA_1** (1588 cm^{-1}) fall in the same region of the NH$_2$ scissoring modes. The cluster of signals in the region 1400-1500 cm^{-1} of the IRMPD spectrum is well reproduced by the calculated umbrella modes of the methyl groups of DMA at 1402 and 1425 cm^{-1} and by the CO stretching coupled with CH$_3$ asymmetric bendings at 1488 cm^{-1} of **DMA_1**, while the asymmetric bending mode of the CH$_3$ (1014 cm^{-1}) accounts for the IRMPD signal at 1020 cm^{-1}. At 1280 cm^{-1} the second highest experimental band is consistent with a convolution of the two umbrella modes of the ammonia, as already reported for *cis*-[PtCl(NH$_3$)$_2$(ACM)]$^+$, which are simulated for **DMA_1** at 1283 and 1311 cm^{-1}.
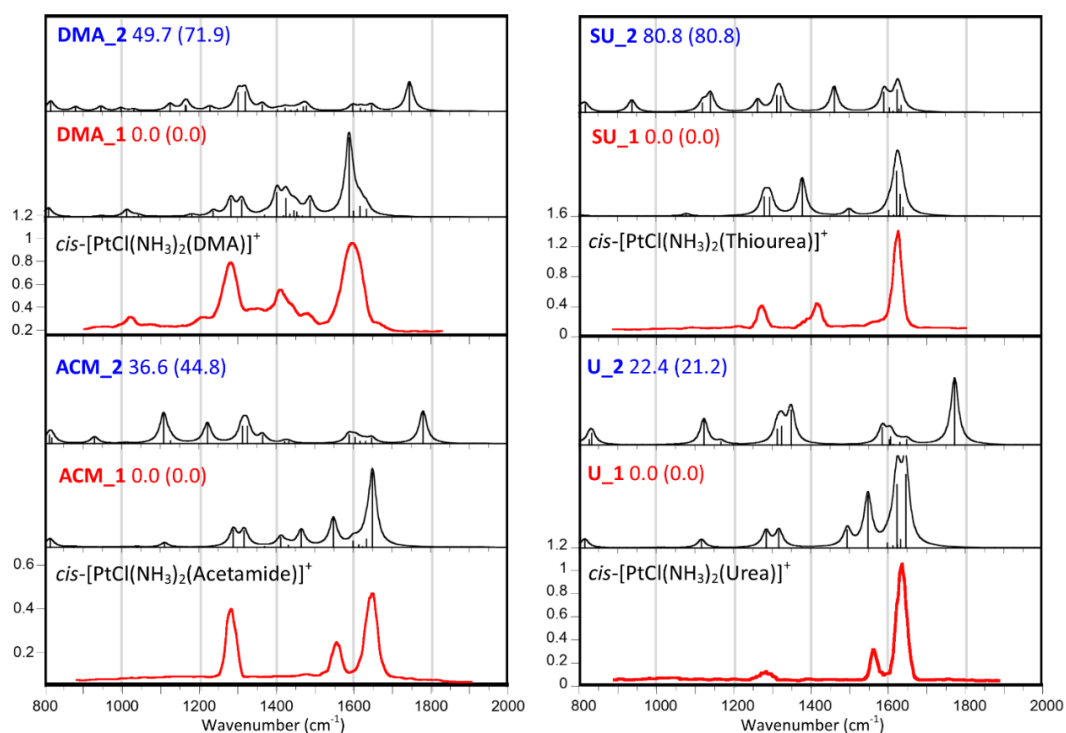
Figure 3.10 IRMPD spectra (red profiles) of *cis*-[PtCl(NH$_3$)$_2$(L)]$^+$ (L = ACM, DMA, U, TU) compared with the IR spectra (black profiles) calculated at B3LYP/6-311+G(d,p) level for the isomers reported in Fig. 3. Relative free energies at 298 K are in kJ mol^{-1}, as calculated at the ωB97X-D and B3LYP (in brackets) level.

The last species presenting a carbonyl moiety, *cis*-[PtCl(NH$_3$)$_2$(Urea)]$^+$, tells a similar story as the one of the acetamide complex. The only difference obviously pertains

to the presence of two NH_2 groups, which are spectroscopically different due to the interaction with the chloride, (geometries are depicted in figure 3.9). Therefore, two slightly different scissoring modes are calculated for the most stable isomer **U_1** at 1624 and 1646 cm^{-1} in fair agreement with the experimental band at 1625 cm^{-1}. Indeed the other IRMPD bands are perfectly reproduced by the IR calculated spectrum of the O-bound isomer **cPtU_1** which accounts for the experimental signals at 1560 and 1280 cm^{-1} by the CO stretching mode associated at the NH_2 scissoring at 1548 cm^{-1} and the umbrella modes of the ammonia at 1285 and 1318 cm^{-1}, respectively. The comparison of the vibrational features of *cis*-$[PtCl(NH_3)_2(SU)]^+$ with the calculated IR spectra of the S-bound isomer **SU_1** and the N-bound one **SU_2** is instead less straightforward. While the calculated modes of **SU_1** well interpret the experimental signatures, there are no evident spectroscopic indications allowing to discard the presence of the **SU_2** isomer, as was the case of the diagnostic C=O stretching that was missing in the spectra of the previous complexes. However, the sharpness of the band at 1627 cm^{-1} is better simulated by the NH_2 scissoring modes of **SU_1** which are calculated at 1623 and 1632 cm^{-1} than by the more widely parted ones of **SU_2** at 1625 and 1590 cm^{-1}. In the calculated normal modes of **SU_2**, in fact, one of the bending mode is fairly red-shifted due to the binding of the corresponding amino group to platinum. In addition, the bands at 1417 and 1280 cm^{-1} are in agreement with the CS stretching coupled with the NH_2 scissoring at 1378 cm^{-1} and the umbrella modes of the ammonia at 1280 and 1294 cm^{-1}, respectively, of **SU_1**.

3.4.3 Structural features of cis-$[PtCl(NH_3)_2(H_2O)(L)]^+$ complexes

Complexes of platinum(II) presenting a total of five potential ligands, $[PtCl(NH_3)_2(L)(H_2O)]^+$, are obtained by ESI as abundant ionic species when L is equal to Py, MeIm, TMP, ACM, DMA and U. Any structural assignment should account for their fragmentation behavior when sampled by CID, involving loss of either L or H_2O. As an example, The CID spectrum of *cis*-$[PtCl(NH_3)_2(H_2O)(ACM)]^+$ is reported in figure 3.11.

In order to elucidate this conduct, different hypotheses about the structure of the isolated ions can be conceived and several possible isomers of $[PtCl(NH_3)_2(L)(H_2O)]^+$

ions have been investigated by DFT using either the B3LYP hybrid functional, that is known to perform well in yielding IR spectra and is uniformly adopted to provide comparison with IRMPD spectra, or ωB97X-D, which includes empirical dispersion and is referred to for relative energy considerations. Five-coordinate platinum(II) complexes are not commonly observed in the gas phase by mass spectrometry though evidence has been reported from x-ray structural analysis.[62-64] More likely, the structure of the cis-[PtCl(NH$_3$)$_2$(L)(H$_2$O)]$^+$ complex is accounted for by a square planar, four-coordinate platinum(II) complex interacting with an additional molecule, either L or H$_2$O, weakly bound in an 'external' coordination level. Indeed, in the association of hydrogen bond donors, such as H$_2$O, with platinum(II) complexes, a role has been ascribed to both HO-H···Pt and H$_2$O···Pt interactions[65-70] and experimental evidence for Pt···H hydrogen bonding interactions both in solution and in the solid state have been reported.[69]
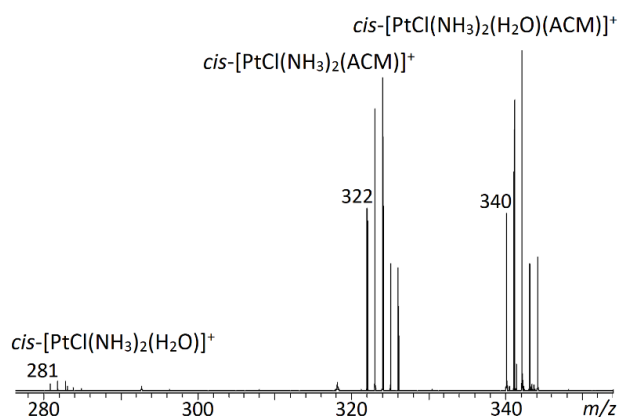
Figure 3.11 ESI-MS^2 obtained upon CID of cis-[PtCl(NH$_3$)$_2$(H$_2$O)(ACM)]$^+$ at m/z 340. The two observed fragmentation channels correspond to water loss (m/z 322) and ACM loss (m/z 281).

Accordingly, a computational survey of potential structures for cis-[PtCl(NH$_3$)$_2$(L)(H$_2$O)]$^+$ complexes has included various starting geometries with an axial approach of a water molecule to a square planar cis-[PtCl(NH$_3$)$_2$(L)]$^+$ complex. However, on geometry optimization of all sampled complexes (L = Py, MeIm, TMP, ACM, DMA and U) the water molecule ended in an 'external' solvating interaction with the square planar cis-[PtCl(NH$_3$)$_2$(L)]$^+$ complex . Evidence on the structure of the sampled complexes can be obtained by IRMPD spectroscopy. The IRMPD process of selected cis-[PtCl(NH$_3$)$_2$(L)(H$_2$O)]$^+$ complexes (L = Py, MeIm, TMP, ACM,

DMA and U) leads to two products, either cis-$[PtCl(NH_3)_2(H_2O)]^+$ or cis-$[PtCl(NH_3)_2(L)]^+$, namely the same products of ligand and water loss that were observed upon CID. Also the branching ratio for L/H_2O loss is similar, corresponding to 86/14, 19/81, and 2/98 in the case of L equal to Py, MeIm, and TMP, respectively, while the sampled species (cis-$[PtCl(NH_3)_2(H_2O)(L)]^+$, L = ACM, DMA, U) showed largely predominant water loss, the dehydration channel representing 94 ± 2 % of the total fragment ion abundance. Incidentally, the cis geometry was identified in the cis-$[PtCl(NH_3)_2(H_2O)]^+$ fragment obtained by CID of $[PtCl(NH_3)_2(Py)(H_2O)]^+$. The ion, assayed by IRMPD spectroscopy, displays an absorption pattern (figure S3.5 in the SM) consistent with the cis-aqua complex described previously.[14] In view of the computational survey, the cis-$[PtCl(NH_3)_2(L)(H_2O)]^+$ cluster is expected to conform to a four-coordinate platinum(II) complex solvated by either L or H_2O. The appearance of two dissociation routes may suggest the presence of two distinct families of cluster ions, namely cis-$[PtCl(NH_3)_2(L)](H_2O)^+$ and cis-$[PtCl(NH_3)_2(H_2O)](L)^+$, with a solvating water or ligand molecule, respectively. However, the comparable profile for L and H_2O loss channels in the IRMPD spectra of cis-$[PtCl(NH_3)_2(L)(H_2O)]^+$ ions speaks against this notion, supporting rather a single species undergoing competing fragmentation paths (figure 3.12 and figure S3.6). Therefore, an analysis of the IRMPD vibrational signatures is fundamental for an understanding of the structure of the clusters.
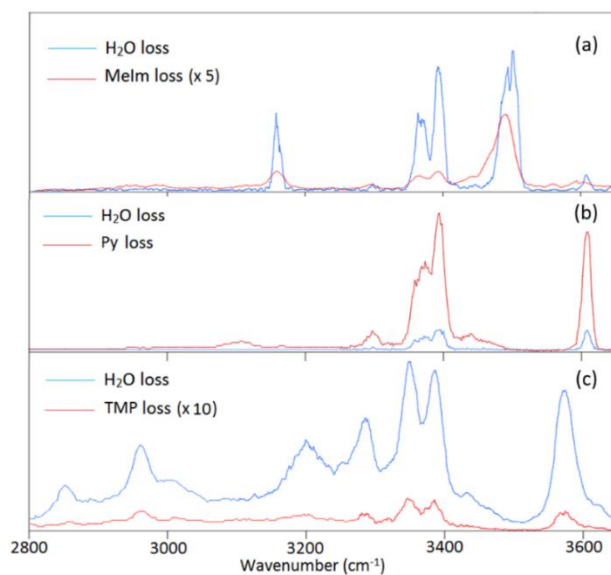
Figure 3.12 IRMPD profile of the two fragmentation channels of L (red) and H_2O (blue) loss from $[PtCl(NH_3)_2(L)(H_2O)]^+$ (L = MeIm (a), Py (b), TMP (c)).

Structural characterization of *cis*-[PtCl(NH₃)₂(Py)(H₂O)]⁺

The results of the computational survey regarding *cis*-[PtCl(NH₃)₂(H₂O)(Py)]⁺ and the comparison of the experimental spectrum with the calculated ones are shown in figure 3.13 and figure S3.7 in the SM, thermodunamic data are reported in table S3.5. The solvating water molecule may either interact with the positively polarized hydrogen atoms of the two NH₃ ligands (isomer **Py-H2O_1**) or establish a bridging interaction with an ammonia proton on one side and the chlorine atom on the other (isomer **Py-H2O_2**), the former isomer being energetically favored by 10 kJ mol⁻¹. However, a third isomer may be envisioned for *cis*-[PtCl(NH₃)₂(L)(H₂O)]⁺, involving the added ligand L 'externally' bound to the aqua complex (isomer **H2O-Py_1**). The ensuing species corresponds to the encounter complex of the incoming ligand with the reactant *cis*-[PtCl(NH₃)₂(H₂O)]⁺. The two families of possible isomers, either {[PtCl(NH₃)₂L]⁺ · H₂O} (indicated by the L-H2O notation) or {([PtCl(NH₃)₂(H₂O)]⁺ · L} (indicated by the H2O-L notation) are gathered by colors, either orange or blue, respectively.
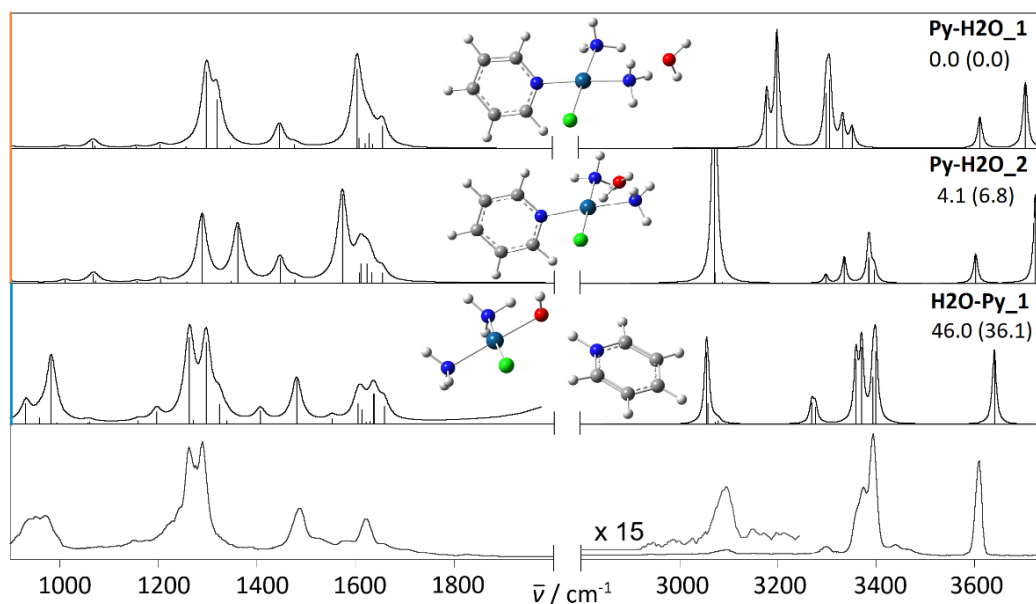
Figure 3.13 IRMPD spectrum of *cis*-[PtCl(NH₃)₂ (H₂O)(ACM)]⁺ (bottom panel) compared with calculated IR spectra of **Py-H2O_1**, **Py-H2O_2** and **H2O-Py_1**. Optimized geometries at B3LYP/6-311+G(d,p) are reported together with relative free energies at 298 K in kJ mol⁻¹, as calculated at the ωB97X-D and B3LYP (in brackets) level.

The aza group of pyridine is basic enough that in interacting with the polarized hydrogen of the aqua ligand a proton transfer event is occurring. The presence of **H2O-Py_1** is suggested by the prevailing loss of Py from cis-[PtCl(NH$_3$)$_2$(L)(H$_2$O)]$^+$ upon CID activation.

The IR spectrum of **H2O-Py_1** is clearly the one matching the experiment while the IR spectrum of **Py-H2O_1** and also the one of **Py-H2O_2** present considerable discrepancy. The experimental bands and the assigned vibrational modes of **H2O-Py_1** are listed in table S3.6 in the SM. Few significant features may be mentioned. The broad IRMPD absorbance at 955 cm^{-1} is associated with the IR modes at 932-983 cm^{-1} due to OH bends of the aqua ligand. The two strong IRMPD signals at 1259 and 1292 cm^{-1} are related to the NH$_3$ umbrella modes that are conserved in all structures, though their separation is well matched only in the IR spectrum of **H2O-Py_1** (35 cm^{-1}). In the OH stretch range, the symmetric and asymmetric stretching modes of the solvating water at 3625 and 3708 cm^{-1} in the IR spectrum of **Py-H2O_1** are missing in the IRMPD spectrum whereas the OH stretch of the hydroxo ligand of **H2O-Py_1** at 3640 cm^{-1} accounts for the only one experimental feature in this range, at 3610 cm^{-1}.

A weak signature at 3094 cm^{-1} in the IRMPD spectrum has a counterpart in the IR spectrum of **H2O-Py_1** at 3054-3058 cm^{-1}. This feature, characteristic of **H2O-Py_1**, is associated to the CH stretch of the bond directed towards the chlorine atom. The assignment has been probed using perdeuterated pyridine as ligand. In the ensuing IRMPD spectrum the band at 3094 cm^{-1} has vanished (the expected red shift at 2264 cm^{-1} moves this absorption outside the experimental range) while the signal at 3296 cm^{-1}, due to symmetric stretches of NH$_3$, has remained approximately unchanged, as shown in figure 3.14. Therefore the IRMPD assay of cis-[PtCl(NH$_3$)$_2$(Py)(H$_2$O)]$^+$ is consistent with an addition complex of pyridine with the primary hydrolytic product of cisplatin. This finding explains the loss of pyridine from the complex but at the same time it implies that a rearrangement is occurring to allow the competing loss of water and formation of the substitution complex.
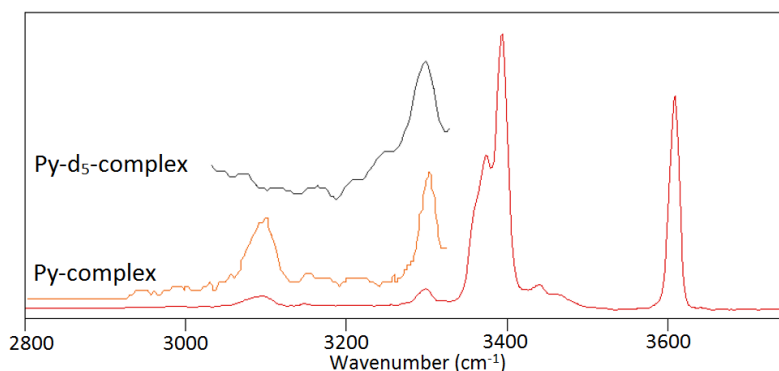
Figure 3.14 IRMPD spectrum of $[PtCl(NH_3)_2(Py)(H_2O)]^+$ (in red/orange, lower profiles) and of $[PtCl(NH_3)_2(Py\text{-}d_5)(H_2O)]^+$ (in gray, upper trace).

Structural characterization of *cis*-$[PtCl(NH_3)_2(MeIm)(H_2O)]^+$

cis-$[PtCl(NH_3)_2(MeIm)(H_2O)]^+$ complexes sampled by IRMPD spectroscopy present similar features as discerned for *cis*-$[PtCl(NH_3)_2(Py)(H_2O)]^+$ ions (figure 3.15). In the most informative region, 2900-3800 cm^{-1}, the IRMPD spectrum is remarkably well fitted by the IR spectrum pertaining to an isomer such as **H2O-4MI_1**, holding an externally bound MeIm (see table S3.7 in the SM). Once again, the pattern of the symmetric and asymmetric H$_2$O stretches, that characterizes a solvating water molecule as in **4MI-H2O_1**, is not observed experimentally. In this case, the fingerprint region is less diagnostic, although the prominent maxima at 1259 and 1289 cm^{-1} are well accounted for by the NH$_3$ umbrella modes calculated at 1262 and 1294 cm^{-1} in the IR spectrum of **H2O-4MI_1**. The resonance at 1206 cm^{-1} ascribed to an in plane CH bend of imidazole in **H2O-4MI_1** also explains the shoulder on the red side of this prominent band. The unresolved signature with maxima at 1083 and 1133 cm^{-1} is not explained by the IR spectrum of isomer **H2O-4MI_1** alone but is consistent with a contribution of isomer **H2O-5MI_1**. Cluster isomers differing for the position of the methyl group, as in the **4MI_n** and **5MI_n** series (figure S3.7 and table S3.5 in the SM), are very close in energy and also the IR spectra are quite similar, only differing for minor features as shown in figure 3.15 and reported in table S3.7.
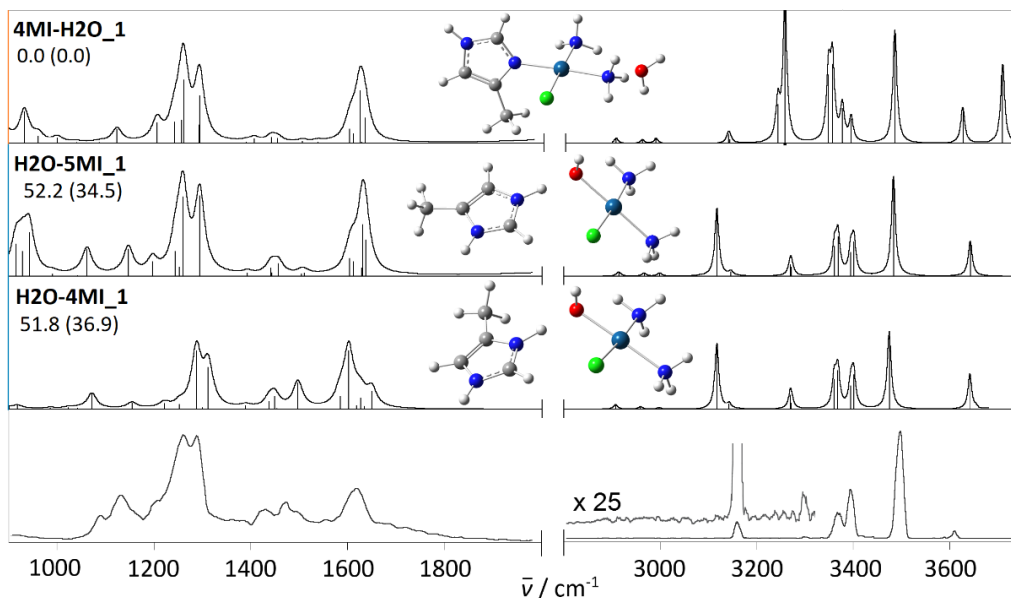
Figure 3.15 IRMPD spectrum (bottom panel) of [PtCl(NH₃)₂(MeIm)(H₂O)]⁺ and calculated IR spectra of **H2O-4MI_1**, **H2O-5MI_1** and **4MI-H2O_1**. Optimized geometries at B3LYP/6-311+G(d,p) are reported together with relative free energies at 298 K in kJ mol⁻¹, as calculated at the ωB97X-D and B3LYP (in brackets) level.

In the higher frequency range, a band at 3160 cm⁻¹ is consistent with the CH stretch of the imidazole hydrogen oriented towards chlorine. This signal has a counterpart in the one at 3094 cm⁻¹ reported in the IRMPD spectrum of [PtCl(NH₃)₂(Py)(H₂O)]⁺. The weak band at 3294 cm⁻¹ is ascribed to the NH₃ symmetric stretch, while the two bands at 3359 and 3393 cm⁻¹ are associated to the NH₃ asymmetric stretch. The most important absorption of this region is the NH stretch of imidazole at 3497 cm⁻¹ that is conserved in all computed spectra except the ones of clusters characterized by a solvating water bound to the imidazole NH. In this latter case, the NH stretch presents a significant red shift.

Structural characterization of cis-[PtCl(NH₃)₂(TMP)(H₂O)]⁺

The IRMPD assay of cis-[PtCl(NH₃)₂(TMP)(H₂O)]⁺ clusters, which structures and thermodynamic data are reported in figure S3.7 and table S3.5, reveals that also in this case the sampled species conforms to a four coordinate cis-[PtCl(NH₃)₂(H₂O)]⁺ aqua complex solvated by the added ligand. This finding is clearly shown in figure 3.16 and table S3.8 in the SM where the IRMPD spectrum is compared with the IR

spectra of **TMP-H2O_1** and **H2O-TMP_1**, exemplifying isomers with solvating water and solvating TMP, respectively.
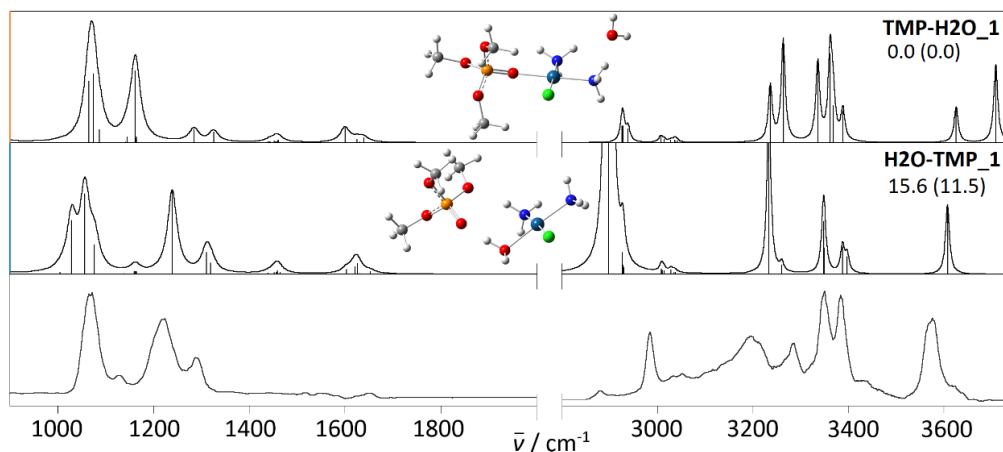
Figure 3.16 IRMPD spectrum (in red) of *cis*-[PtCl(NH$_3$)$_2$(TMP)(H$_2$O)]$^+$ and calculated IR spectra of **TMP_1-4** and **TMP_3-1**. Optimized geometries at B3LYP/6-311+G(d,p) are reported together with relative free energies at 298 K in kJ mol^{-1}, as calculated at the ωB97X-D and B3LYP (in brackets) level.

With respect to Py and MeIm ligands, TMP is endowed with greater conformational freedom so that the number of conformers to be taken into account within each class of isomers is considerably large. This fact explains the large bandwidth of several features in the IRMPD spectrum, testifying the presence of multiple species of similar energy. In the following discussion the focus is on the prototypical isomers **TMP-H2O_1** and **H2O-TMP_1**. Inspecting figure 3.16, direct coordination of TMP to Pt^{II} may be discarded in view of the missing feature at 1162 cm^{-1}, highly active in the IR spectrum of isomer **TMP-H2O_1**. The associated vibrational mode, the P-O stretch of the formerly phosphoryl double bond, is remarkably red-shifted as a consequence of coordination to the metal. The frequency is in fact 1239 cm^{-1} in the spectrum of **H2O-TMP_1**, accounting for the prominent IRMPD band 1220 cm^{-1}. This motif appears then to discriminate between alternative molecular structures. In contrast, the P-OCH$_3$ stretches, responsible for the band at 1068 cm^{-1}, are conserved in all isomers. The band at 1286 cm^{-1} is due to symmetric NH$_3$ bending (umbrella) modes. The band at highest frequency is the OH stretch at 3573 cm^{-1}. The rather large width and the presence of a shoulder on the blue side are evidence for the contribution of multiple conformers (e.g. **H2O-TMP_2** and **H2O-**

TMP_3, see figure S3.8 in the SM). As in the case of the Py and MeIm complexes, the absence of the asymmetric OH stretch of water at ca. 3700 cm^{-1} allows to discard any contribution of a water solvated cluster such as **TMP-H2O_1**. The two bands at 3346 and 3380 cm^{-1}, the asymmetric NH stretches of NH$_3$ ligands, are a common pattern in the IRMPD spectra of all sampled *cis*-[PtCl(NH$_3$)$_2$(TMP)(H$_2$O)]$^+$ clusters. The absorption at 3280 cm^{-1} is assigned to the symmetric stretches of ammonia while the broad signal at 3200 cm^{-1} is consistent with the stretching mode of the NH bond involved in hydrogen bonding with a TMP methoxyl group.

Structural characterization of *cis*-[PtCl(NH$_3$)$_2$(ACM)(H$_2$O)]$^+$

Figure 3.17 presents the IRMPD spectrum of *cis*-[PtCl(NH$_3$)$_2$ (H$_2$O)(ACM)]$^+$ (red profile) compared with the theoretical IR spectra of the lowest lying conformers pertaining to the two families of possible isomers, either {[PtCl(NH$_3$)$_2$L]$^+$ · H$_2$O} or {([PtCl(NH$_3$)$_2$(H$_2$O)]$^+$ · L}. Complete thermodynamic data are reported in table S3.9, while further calculated isomers are shown in figure S3.9 in the SM.

The global minimum is **ACM-H2O_1**. In this conformer the water molecule interacts by hydrogen bonds with the two ammonia ligands and the platinum complex presents a structure resembling closely **ACM_1** (figure 3.10). Other species in this family of isomers are higher in free energy. **ACM-H2O_2** at 6.9 kJ mol^{-1} holds the external water between chloro and ammonia ligands while **ACM-H2O_3** at 11.2 kJ mol^{-1} loses the stabilizing interaction between the amido NH$_2$ and Cl because the methyl group is now oriented towards the chloro ligand.

The lowest lying species in the family of complexes holding ACM in external position to the cisplatin complex is **H2O-ACM_1**, lying at 24.7 kJ mol^{-1} relative to **ACM-H2O_1**. In this geometry the carbonyl group of ACM acts as hydrogen bond acceptor for the inner sphere aqua ligand and a hydrogen bond interaction also binds the amido NH$_2$ to the chloro ligand. This latter bonding is instead lost in **H2O-ACM_2**, because the amido group is oriented far away from Cl and the free energy of this complex is 28.4 kJ mol^{-1} relative to the global minimum. Conformer **H2O-ACM_3**, lying at 28.5 kJ mol^{-1}, shows instead a bisected interaction of the carbonyl oxygen with both water and ammonia ligands of platinum.
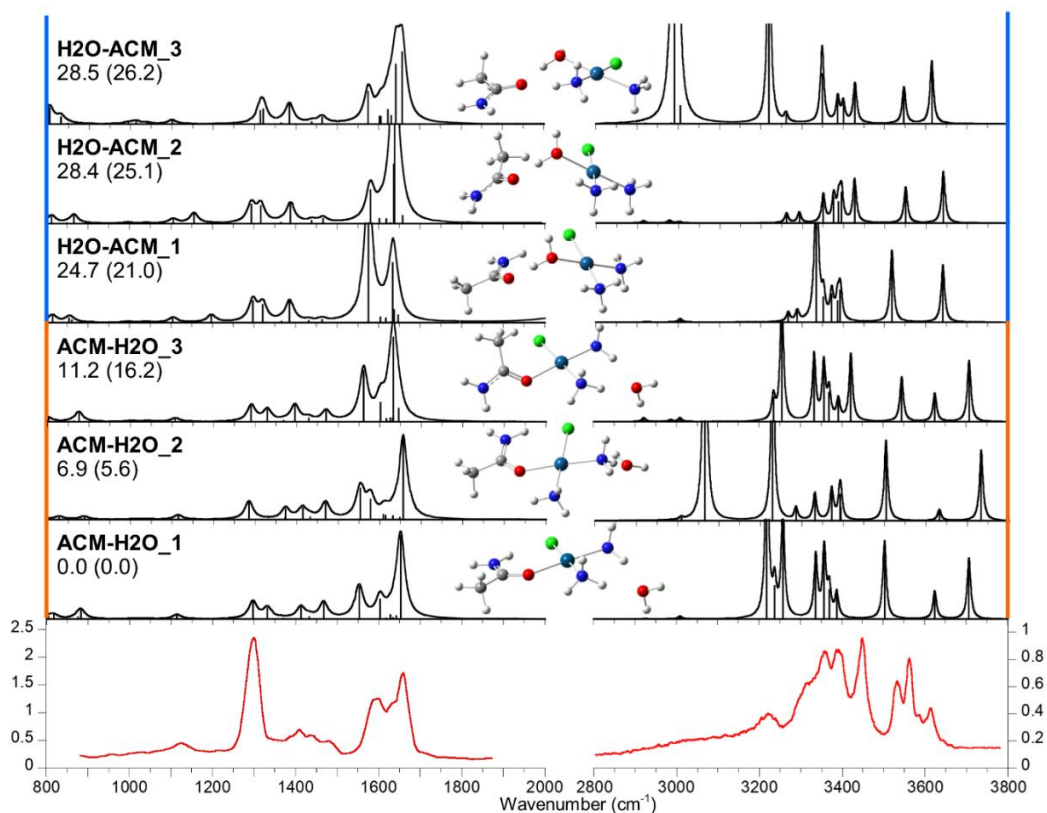
Figure 3.17 IRMPD spectrum of *cis*-[PtCl(NH$_3$)$_2$ (H$_2$O)(ACM)]$^+$ (red profile) compared with the theoretical IR spectra of **ACM-H2O_1**, **ACM-H2O_2**, **ACM-H2O_3**, **H2O-ACM_1**, **H2O-ACM_2** and **H2O-ACM_3**. Optimized geometries at the B3LYP/6-311+G(d,p) level are reported together with relative free energies at the ωB97X-D and B3LYP (in bracket) levels at 298 K in kJ mol^{-1}.

Structural information is gained from the IRMPD spectrum presented in figure 3.17 displaying several features in both the fingerprint and XH stretching regions, in high photofragmentation yield. However, most of the signals are shared by species pertaining to both families of isomers (either {[PtCl(NH$_3$)$_2$L]$^+$ · H$_2$O} or {([PtCl(NH$_3$)$_2$(H$_2$O)]$^+$ · L}). Notably, the absence of a band in the 3650-3750 cm^{-1} region of the experimental spectrum allows to assign the major part of the sampled population to {([PtCl(NH$_3$)$_2$(H$_2$O)]$^+$ · L} isomers, which therefore will be solely considered in the forthcoming interpretation of the experimental spectrum. The IRMPD spectrum of *cis*-[PtCl(NH$_3$)$_2$(ACM)(H$_2$O)]$^+$ shows a number of signals in the NH and OH stretching region, suggesting the presence of multiple structural arrangements (see figure 3.17 and table S3.10). Thus, in the 3500-3650 cm^{-1} region,

the band at 3613 cm^{-1} can be assigned to the OH stretching of the water ligand calculated at 3641 cm^{-1} for both **H2O-ACM_1** and **H2O-ACM_2**. A shoulder is also present at 3585 cm^{-1} compatible with the OH stretching of water for **H2O-ACM_3**, calculated at 3614 cm^{-1}. Further on, two intense signals at 3561 and 3532 cm^{-1} are in agreement with the NH$_2$ asymmetric stretch calculated at 3550/3547 and 3517 cm^{-1} for **H2O-ACM_2/H2O-ACM_3** and **H2O-ACM_1**, respectively, thus confirming the presence of at least the three species contributing to the sampled ions population.

At 3441 cm^{-1} the spectrum presents an important feature ascribed to the symmetric stretching of the amido NH$_2$, calculated at 3426 and 3428 cm^{-1} for **H2O-ACM_2** and **H2O-ACM_3**, respectively. Regarding **H2O-ACM_1**, this mode is red-shifted to 3335 cm^{-1} due to interaction between the amido NH$_2$ and the chloro ligand, thus falling in a rather congested region of the IRMPD spectrum and likely responsible for the shoulder at ca. 3322 cm^{-1} of a broad absorption with main signals at 3389 and 3354 cm^{-1} due to asymmetric stretching of the ammonia molecules. In the 2800-3300 cm^{-1} region of the experimental spectrum there appears broad, smeared IRMPD activity, in particular a wide feature at 3228 cm^{-1} is consistent with the NH stretching of the ammonia interacting with the carbonyl group of ACM within **H2O-ACM_3** (calculated 3219 cm^{-1}).

In the fingerprint region, the IRMPD spectrum shows several bands assigned to the combined contribution of **H2O-ACM_1**, **H2O-ACM_2**, and **H2O-ACM_3**. The major bands are mentioned here. An important feature at 1660 cm^{-1} followed by a shoulder at 1637 cm^{-1} can be attributed to the CO stretching coupled with H$_2$O bending of **H2O-ACM_3** (1657 cm^{-1}) and with NH$_2$ "scissor-like" bendings, calculated at 1633, 1637 and 1641 cm^{-1} for **H2O-ACM_1**, **H2O-ACM_2** and **H2O-ACM_3**, respectively. The maximum at 1587 cm^{-1} is in good agreement with the amide C=O stretching red-shifted by the interaction with the water molecule coordinated to platinum (calculated at 1575, 1579 and 1575 cm^{-1} for **H2O-ACM_1**, **H2O-ACM_2** and **H2O-ACM_3**, respectively). The symmetric bending of ammonia "umbrella" mode calculated around 1315 cm^{-1} for all three species, may account for the band at 1297 cm^{-1} of noticeably high intensity in the IRMPD spectrum.

Structural characterization of *cis*-[PtCl(NH$_3$)$_2$(DMA)(H$_2$O)]$^+$

The IRMPD spectrum of the *cis*-[PtCl(NH$_3$)$_2$(H$_2$O) (DMA)]$^+$ complex is presented in figure 3.18 together with the calculated IR spectra of the lowest lying species, conforming to either {[PtCl(NH$_3$)$_2$L]$^+$ · H$_2$O} (such as **DMA-H2O_1**) or {([PtCl(NH$_3$)$_2$(H$_2$O)]$^+$ · L}, such as **H2O-DMA_1** and **H2O-DMA_2**). Thermodynamic data and other assayed isomers are reported in table S3.9and figure S3.10 in the SM, respectively.
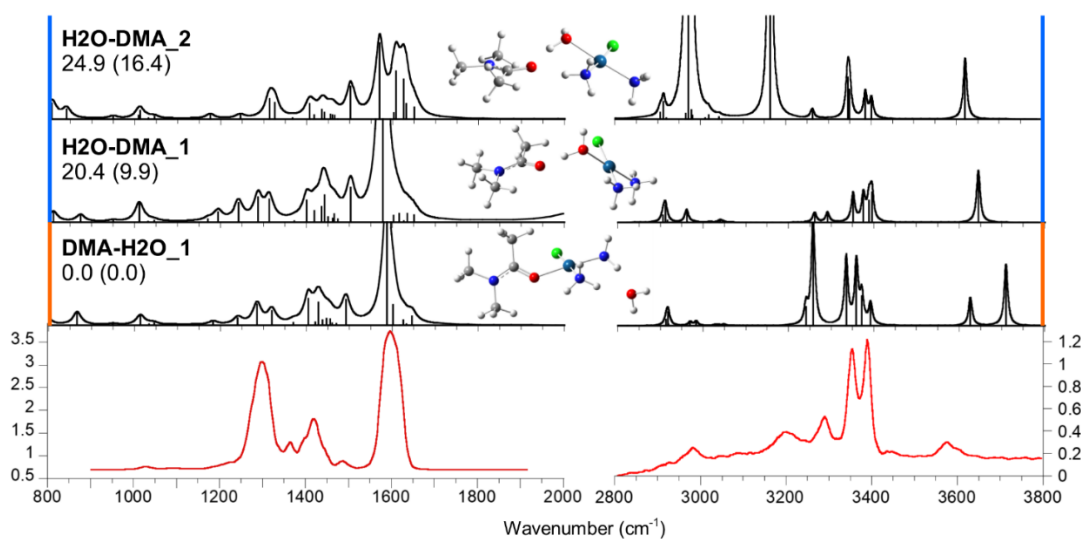
Figure 3.18 IRMPD spectrum of *cis*-[PtCl(NH$_3$)$_2$(H$_2$O)(DMA)]$^+$ (red profile) compared with the theoretical IR spectra of **DMA-H2O_1**, **H2O-DMA_1** and **H2O-DMA_2**. Optimized geometries at B3LYP/6-311+G(d,p) are reported together with relative free energies at the ωB97X-D and B3LYP (in bracket) levels at 298 K in kJ mol^{-1}.

The XH (X = C, N, O) stretching region is once again critical to distinguish between the adducts with either DMA or water outside the coordination sphere of platinum. In particular, the IRMPD spectrum lacks a signal for the asymmetric stretching of free water, calculated at 3709 cm^{-1} for **DMA-H2O_1**. On the contrary, the experimental spectrum presents a feature at 3573 cm^{-1} with a slope around 3600 cm^{-1} consistent with the presence in the sampled population of the two lowest lying conformers generated by the interaction of the aqua complex of cisplatin with DMA (**H2O-DMA_1** and **H2O-DMA_2**). In fact, the OH stretching vibration calculated for the two species is slightly different, 3645 and 3620 cm^{-1} for **H2O-DMA_1** and **H2O-**

DMA_2, respectively, thus suggesting a contribution of both (see table S3.10 in the SM). At lower frequency in the 2800-3500 cm^{-1} region, asymmetric stretching modes of the ammonia molecule are calculated at 3395, 3388, 3375 and 3351 cm^{-1} for **H2O-DMA_1**, and at 3400, 3386, 3349 and 3345 cm^{-1} for **H2O-DMA_2**, accounting also for the major peaks observed at 3389 and 3352 cm^{-1}. Symmetric stretching modes of ammonia ligands which are not involved in hydrogen bonding are calculated at 3291 and 3260 cm^{-1} for **H2O-DMA_1**, and 3262 cm^{-1} for **H2O-DMA_2** in agreement with the experimental band at 3290 cm^{-1}. In the second conformer however, one ammonia molecule is engaged in hydrogen bonding with the carbonyl group of DMA, causing a red-shift to 3162 cm^{-1}, which is consistent with the broad experimental feature at 3200 cm^{-1}. Finally, a signal at 2978 cm^{-1} can be attributed to the OH stretching involved in the interaction with the carbonyl group in the **H2O-DMA_2** geometry (calculated 2972 cm^{-1}).

The fingerprint region of the IRMPD spectrum is dominated by a broad band centered at 1597 cm^{-1}, expression of the presence of multiple absorptions in this range. In particular, at 1577 cm^{-1} an intense CN stretching coupled with CO stretch is calculated for **H2O-DMA_1**, while **H2O-DMA_2** presents three vibrational modes related to H_2O scissoring coupled with NH_3 bend at 1624 cm^{-1}, CO stretching at 1607 cm^{-1} and CN stretching at 1569 cm^{-1}, respectively. A broad absorption at 1417 cm^{-1} can be attributed to a convolution of CH_3 umbrella modes calculated at 1441, 1418 and 1400 cm^{-1} for **H2O-DMA_1**, and 1434, 1416 and 1406 cm^{-1} for **H2O-DMA_2**, while the pronounced band at 1295 cm^{-1} is ascribed to umbrella modes of the ammonia calculated at 1312/1287 and 1324/1312 cm^{-1} for **H2O-DMA_1** and **H2O-DMA_2**, respectively.

Structural characterization of *cis*-[PtCl(NH$_3$)$_2$(ACM)(H$_2$O)]$^+$

The IRMPD spectrum *cis*-[PtCl(NH$_3$)$_2$(H$_2$O)(U)]$^+$ is reported in figure 3.19. The experiment is compared with the IR spectra of the lowest lying conformers from the two families of isomers already discussed, while other calculated isomers and conformers are reported in figure S3.11 and complete thermodynamic data are presented in table S3.9.
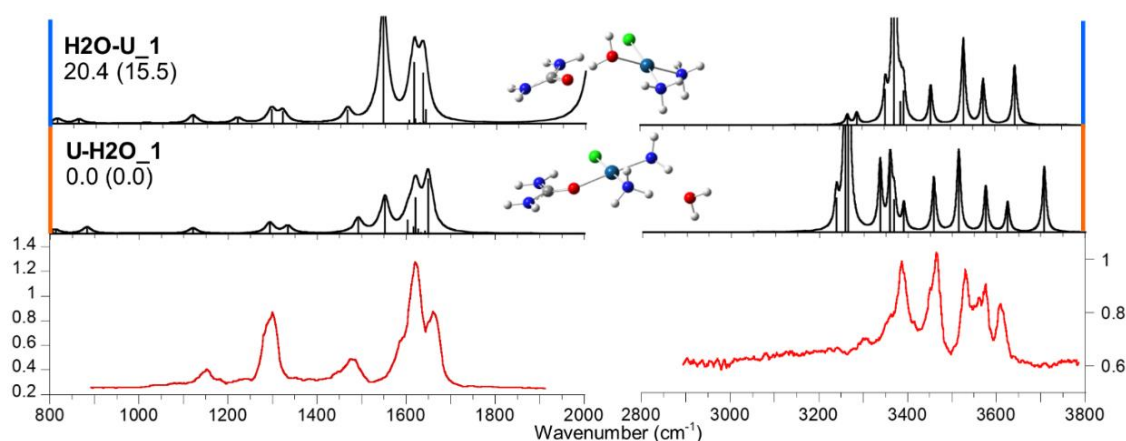
Figure 3.19 IRMPD spectrum of *cis*-[PtCl(NH$_3$)$_2$(H$_2$O)(U)]$^+$ (red profile) compared with the theoretical IR spectra of **U-H2O_1** and **H2O-U_1**. Optimized geometries at the B3LYP/6-311+G(d,p) level are reported together with relative free energies at the ωB97X-D and B3LYP (in bracket) levels at 298 K in kJ mol^{-1}.

H2O-U_1, presenting urea in an external hydrogen bond interaction with the inner water ligand, is 20.4 kJ mol^{-1} higher in energy relative to the **U-H2O_1** isomer where water is solvating the square-planar complex *cis*-[PtCl(NH$_3$)$_2$(U)]$^+$ complex. In spite of **U-H2O_1** being the global energetic minimum, as already observed in all the previous cases, the IRMPD spectrum rather supports the presence of an adduct between an aqua platinum(II) complex and an external U molecule. In this regards, particularly diagnostic is the absence of an absorption around 3708 cm^{-1}, the calculated asymmetric water stretching of **U-H2O_1**. Moreover, the calculated IR spectrum of the **H2O-U_1** isomer is in fair agreement with the experimental one as shown in figure 3.19 and table S3.10. In particular, the 2800-3800 cm^{-1} region of the IR spectrum is well interpreted although the experimental band at 3607 cm^{-1} is assigned to the OH stretching of water calculated at a somewhat higher frequency (3644 cm^{-1}). IRMPD bands at 3574 and 3526 cm^{-1} are consistent with the asymmetric stretching of free NH$_2$ at 3573 cm^{-1} and of NH$_2$ interacting with the chloro ligand at 3528 cm^{-1}, respectively. Two other important features in the higher frequency part of the IRMPD spectrum are at 3464 cm^{-1}, consistent with symmetric stretching of NH$_2$ remote from Cl calculated at 3454 cm^{-1}, and at 3384 cm^{-1}, which is interpreted by the NH$_2$ symmetric stretching red-shifted by the interaction with Cl

88

(3372 cm^{-1}). In the fingerprint region, a convoluted band comprises two peaks at 1663 and 1620 cm^{-1} and a shoulder at 1580 cm^{-1}. The former signals are consistent with NH$_2$ scissoring modes calculated at 1634 and 1613 cm^{-1}, while the shoulder can be attributed to the CO stretch of **H2O-U_1**, calculated at 1545 cm^{-1}. This carbonyl stretching mode is considerably red shifted with respect to typical absorbance ranges due to strong hydrogen bonding and coupling with OH stretching and NH$_2$ rocking motions and likely overestimated in activity by computation.

To summarize, all sampled cis-[PtCl(NH$_3$)$_2$(L)(H$_2$O)]$^+$ clusters assayed by IRMPD spectroscopy reveal the nature of cis-[PtCl(NH$_3$)$_2$(H$_2$O)]$^+$ complex solvated by the L molecule. The ligand is typically hydrogen bonded to the aqua ligand and, when L is basic enough as in the case of Py and MeIm, the proton may rather reside on the L partner within the complex.

3.4.4 Ligand substitution in the encounter complex of L and cis-[PtCl(NH$_3$)$_2$(H$_2$O)]$^+$

The combined information from the reactivity pattern, the computational survey and the IRMPD analysis of ESI formed [PtCl(NH$_3$)$_2$(L)(H$_2$O)]$^+$ ions has revealed the dynamics of a well characterized cluster corresponding to the encounter complex of a ligand with cis-[PtCl(NH$_3$)$_2$(H$_2$O)]$^+$, namely the primary hydrolytic product of cisplatin. The [PtCl(NH$_3$)$_2$(L)(H$_2$O)]$^+$ ions, holding Pt^{II} and five potential ligands, formed in an aqueous solution of cisplatin and ligand L, has in fact revealed the structure of a cluster of L combined with cis-[PtCl(NH$_3$)$_2$(H$_2$O)]$^+$. However, these species are higher in energy than their counterparts presenting water outside the first coordination sphere of platinum. Exploring the potential energy surface (PES) for the reaction between the aqua complex of cisplatin and the inspected ligands can shed light on the reasons beneath the bias between the experimental conformational sampling provided by IRMPD spectroscopy and the calculated energies of isomeric complexes. Moreover, when the cluster is imparted excess energy either by non-reactive collisions or by multiple IR photon absorption, thus activated to undergo dissociation, in a considerable fraction of events water is released. Loss of the 'external' ligand would be the expected, entropy driven dissociation path. Loss of water implies that in the activated cluster a net ligand

exchange process is taking place within the isolated reactant pair. When the process occurs under IRMPD conditions, it is reminiscent of the infrared induced reactivity of nitrogen oxides on rhodium clusters that has revealed elementary steps in a catalytic reaction[71,72] showing that IRMPD spectroscopy can provide information about the structure of the metal cluster, the state of the absorbed molecules and the degree of bond activation.

Mechanistic insight into the bimolecular, CID-activated and IR-induced reactivity behavior has been sought from a survey of the potential energy surface (PES) connecting the conceivable species. A schematic of the PESs regarding the reaction of cisplatin with Py, MeIm, TMP and TA is shown in figure 3.20, while in figure 3.21 is reported the PES for the formation of the substitution complexes *cis*-[PtCl(NH$_3$)$_2$(L)]$^+$, where L = ACM, DMA, U and SU.
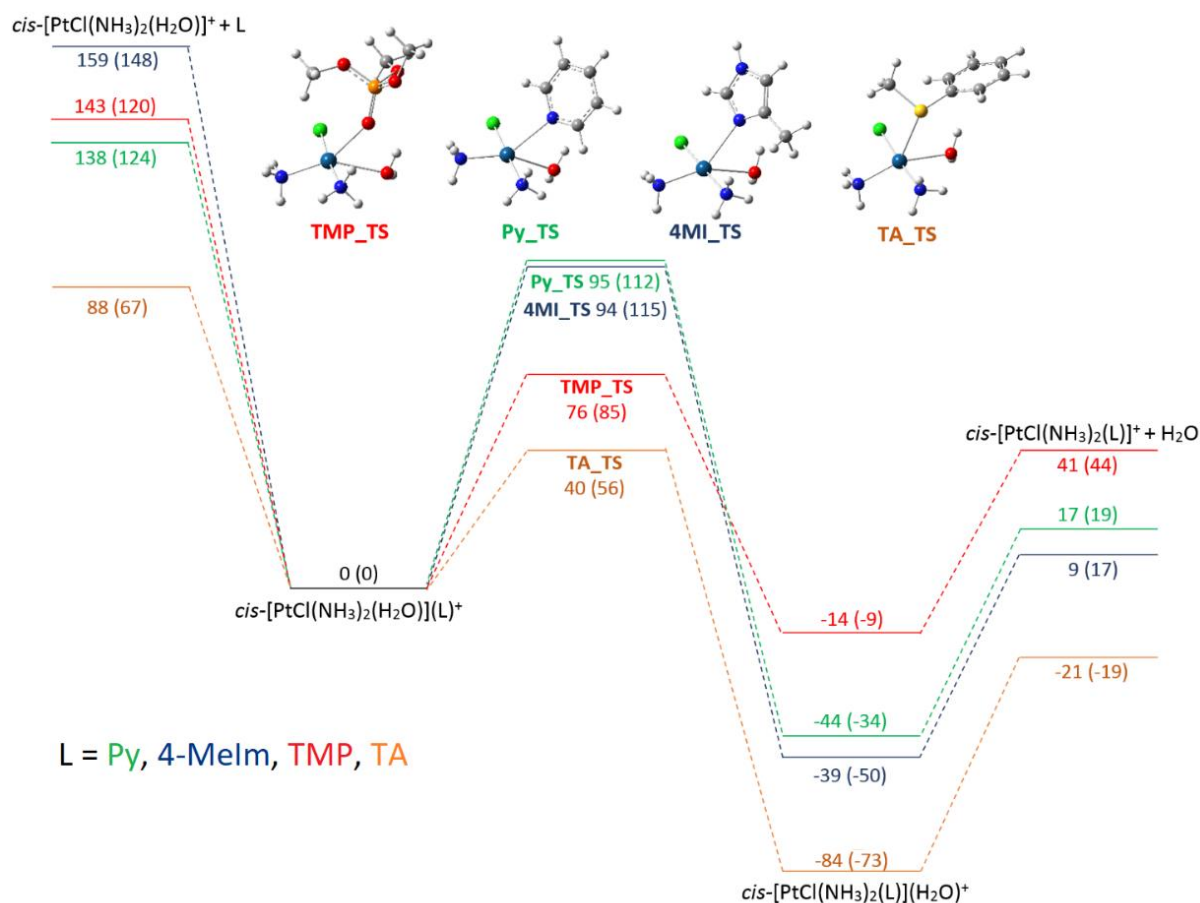
Figure 3.20 PES for the reaction of *cis*-[PtCl(NH$_3$)$_2$(H$_2$O)]$^+$ with L (L= Py, 4-MeIm, TMP, TA). Geometries of the transition states computed at B3LYP/6-311+G(d,p) level are shown. Relative enthalpies (kJ mol^{-1}) are reported as obtained at ωB97X-D/6-311+G(d,p) (values at B3LYP/6-311+G(d,p) level are in brackets).

90

Figure 3.21 PES for the reaction of *cis*-[PtCl(NH$_3$)$_2$(H$_2$O)]$^+$ with L (L= ACM, DMA, U, SU). Geometries of the transition states computed at B3LYP/6-311+G(d,p) level are shown. Relative enthalpies (kJ mol^{-1}) are reported as obtained at ωB97X-D/6-311+G(d,p) (values at B3LYP/6-311+G(d,p) level are in brackets).
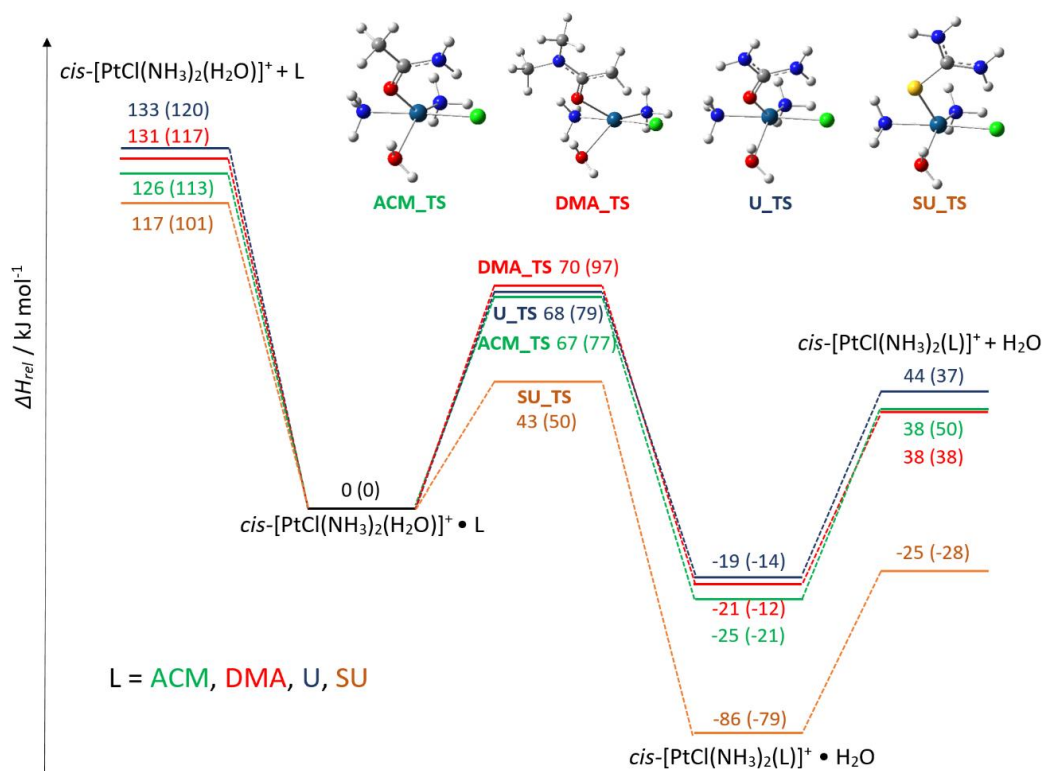
Relative enthalpies at 298K are reported at both B3LYP/6-311+G(d,p) and ωB97X-D/6-311+G(d,p) level of theory (LanL2TZ for Pt). The following discussion is based on ωB97X-D/6-311+G(d,p) data. Relative enthalpies are referred to the most stable isomer for the {*cis*-[PtCl(NH$_3$)$_2$(H$_2$O)]$^+$ · L} cluster with the 'external' ligand, namely **H2O-4MI_1** (L = 4-MeIm), **H2O-Py_1** (L = Py), **H2O-TMP_1** (L = TMP), **H2O-TA_1** (L = TA), **H2O-ACM_1** (L = ACM), **H2O-DMA_1** (L = DMA), **H2O-U_1** (L = U) and **H2O-SU_1** (L = SU). The PES shows a double well profile where the first minimum corresponds to the adduct with externally coordinated L, while the second one contains a species where water is solvating the substitution complex. The second well is lower in energy and therefore it should form the major part of the population if thermal equilibrium was achieved under sampling conditions. Instead, structural analysis by IRMPD spectroscopy showed a different landscape where {*cis*-[PtCl(NH$_3$)$_2$(H$_2$O)]$^+$ · L} is largely predominant, thus suggesting that the experimental

setup is able to extract from solution the earliest intermediate in the substitution reaction of the cisplatin aqua complex, the so called encounter complex.

The {cis-[PtCl(NH$_3$)$_2$(H$_2$O)]$^+$ · L} complex may rearrange to {cis-[PtCl(NH$_3$)$_2$(L)]$^+$ · H$_2$O } by way of a transition state involving pentacoordination at Pt^{II}. The structures of the transition states are depicted in figure 3.20 and figure 3.21 and complete thermodynamic data of the species partaking the PESs are reported in table S3.5 and S3.9 in the SM, respectively.. The energy needed to overcome the transition states and reach the global minima of the PES (95, 94, 76, 67, 70, 68 kJ mol^{-1} for the reaction with Py, 4-MeIm, TMP, ACM, DMA, and U, respectively) seems, thus, to be higher than the energy imparted to ions in the ESI process and transfer to the ion trap. In the case of thioanisole and thiourea, instead, the activation energy for ligand substitution is much lower (40 and 43 kJ mol^{-1}, respectively) which may be the reason preventing to observe a cis-[PtCl(NH$_3$)$_2$(H$_2$O)(L)]$^+$ (L=TA, SU) adduct in the mass spectrum.

Ligand exchange within the {cis-[PtCl(NH$_3$)$_2$(H$_2$O)]$^+$ · L} cluster is exothermic in all cases. The reaction of SU and TA are the most strongly favored (ΔH° = - 86 and - 84 kJ mol^{-1}, respectively) and is also characterized by the lowest activation barrier (43 and 40 kJ mol^{-1}, respectively). The binding of Pt^{II} with the sulfur ligand is so favored that even the dissociation into products, cis-[PtCl(NH$_3$)$_2$(TA)]$^+$ + H$_2$O, is still exothermic, again in line with the lack of any observed {cis-[PtCl(NH$_3$)$_2$(H$_2$O)]$^+$ · L} cluster, where L=TA or SU. The bimolecular reactivity of TA with cis-[PtCl(NH$_3$)$_2$(H$_2$O)]$^+$ is not the highest, though, as determined in the FT-ICR cell. Here, the single collision regime at the prevailing low pressure points to the difference between the back dissociation energy of the {cis-[PtCl(NH$_3$)$_2$(H$_2$O)]$^+$ · L} collision complex and the activation energy for ligand exchange as the key parameter determining relative efficiencies.[58,59,73] This difference is equal to 67, 48, and 43 kJ mol^{-1} in agreement with the % reaction efficiencies of 2.5, 1.1, and 0.41 (table 3.2) for the tested series of ligands, TMP, TA, and Py, respectively, in the bimolecular ligand substitution (equation 3.1). The PES outlined in figures 3.20 and 3.21 in fact conforms to Brauman's 'double well' potential energy surface model that explains the kinetic behavior of ion-molecule reactions at low pressure, in the absence of

collisions with a bath gas.[58,59,73] Even if the central barrier is lower than the energy of the separated reactants, it can be more likely for the collision complex ({*cis*-[PtCl(NH$_3$)$_2$(H$_2$O)]$^+$ · L}) to dissociate back to the free reactants because this process is entropically more favorable. As a consequence, the rate of the reaction may not reach the collision controlled limit and in the present case the observed reaction efficiencies are well below 100%. Taking into account the common entropic bias towards back dissociation, the difference in energy between separated (*cis*-[PtCl(NH$_3$)$_2$(H$_2$O)]$^+$ + L and the transition state for ligand exchange) will govern the branching into the two channels. The same energy difference is expected to govern the branching of isolated {*cis*-[PtCl(NH$_3$)$_2$(H$_2$O)]$^+$ · L} clusters when activated to fragment by L or H$_2$O loss (table 3.3).

Table 3.3 Branching ratio for loss of either L or H$_2$O from [PtCl(NH$_3$)$_2$(L)(H$_2$O)]$^+$ complexes in CID and IRMPD experiments

	CID		IRMPD	
Ligand	**% -H$_2$O**	**% -L**	**% -H$_2$O**	**% -L**
Py	5.1	94.9	14.3	85.7
MeIm	82.2	17.8	81.3	18.7
TMP	91.1	8.9	98.0	2.0
ACM	95.1	4.9	96.8	3.2
DMA	97.0	3.0	94.5	5.5
U	97.7	2.3	94.2	5.8

Indeed, the calculated energy differences of 67, 65, and 43 kJ mol^{-1} for TMP, MeIm, and Py clusters, respectively, is in line with the decreasing fraction of H$_2$O loss along the series, while a similar branching ratio is observed for the three encounter complexes where L = ACM, DMA and U, with a massive predominance of the water loss channel (ca. 96 %). The observed energy difference values of 59, 61, and 65 kJ mol^{-1} for ACM, DMA and U, respectively, are indeed consistent with the predominance of the water loss channel. Along the same reasoning, all {*cis*-[PtCl(NH$_3$)$_2$(H$_2$O)]$^+$ · L} clusters face competition between two channels both involving considerable energy barriers. Dissociation of 'externally' bound L is consistently more endothermic but is entropically favored. Ligand substitution to yield {*cis*-[PtCl(NH$_3$)$_2$(L)]$^+$ · H$_2$O} is a process proceeding by a tight transition state, highly organized and with relatively wide separation between internal energy levels.

So, statistically, there will be a smaller number of accessible states available at a given energy for the system to progress through the central barrier.[58,59,73] Thus, the calculated PES provides a congruent rationale for the observed reactivity pattern.
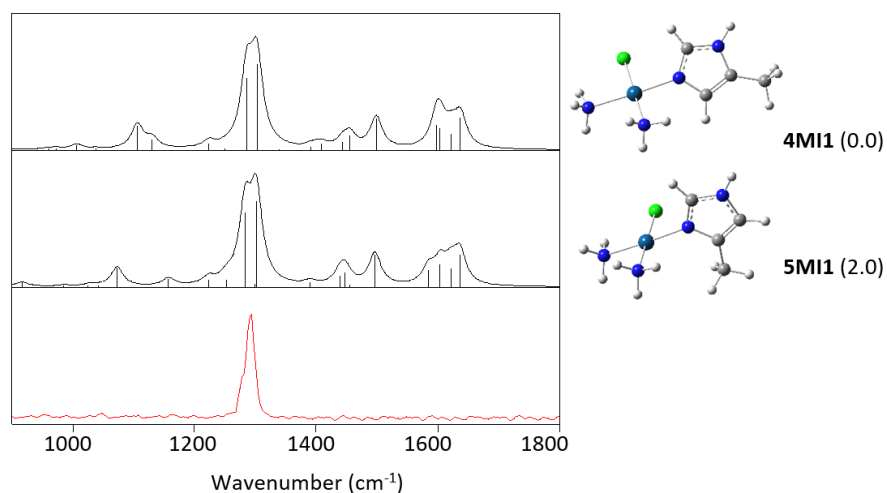
Figure S3.2 IRMPD spectrum (red line) compared with the calculated IR spectra (black line) of *cis*-[PtCl(NH$_3$)$_2$(MeIm)]$^+$ (isomers **5MI1**, **4MI1**). Relative energies (298K) of optimized structures are in kJ mol^{-1}.
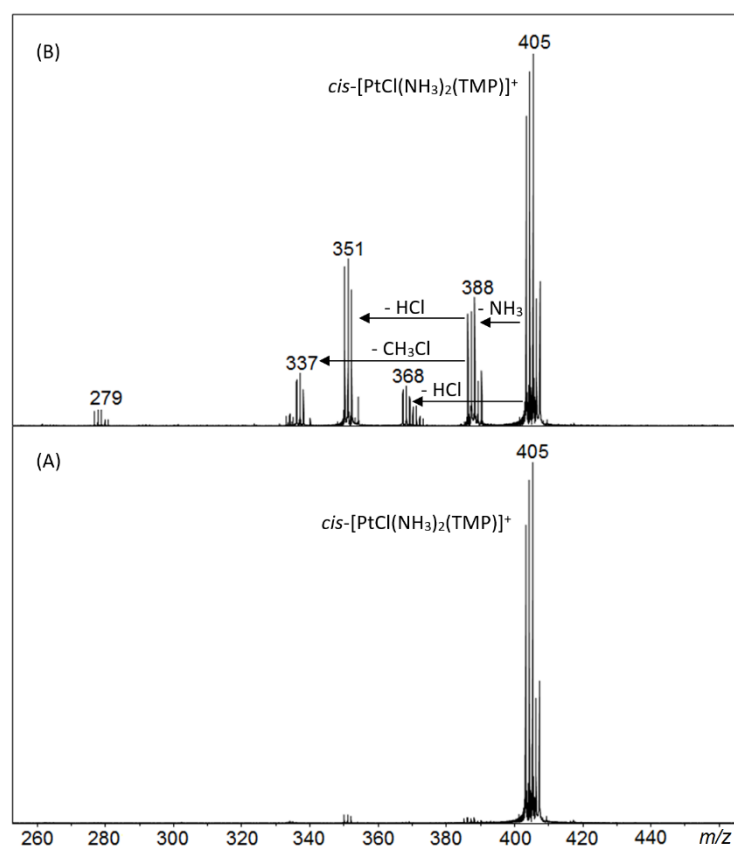
Figure S3.3 Panel A: Mass spectrum showing *cis*-[PtCl(NH$_3$)$_2$(TMP)]$^+$ ions formed by ESI and mass selected in the FT-ICR cell (isotopic cluster with major peaks at *m/z* 403-405). Panel B: Mass spectrum following mass selection of *cis*-[PtCl(NH$_3$)$_2$(TMP)]$^+$ ions and irradiation with IR photons at 1180 cm^{-1}.

95
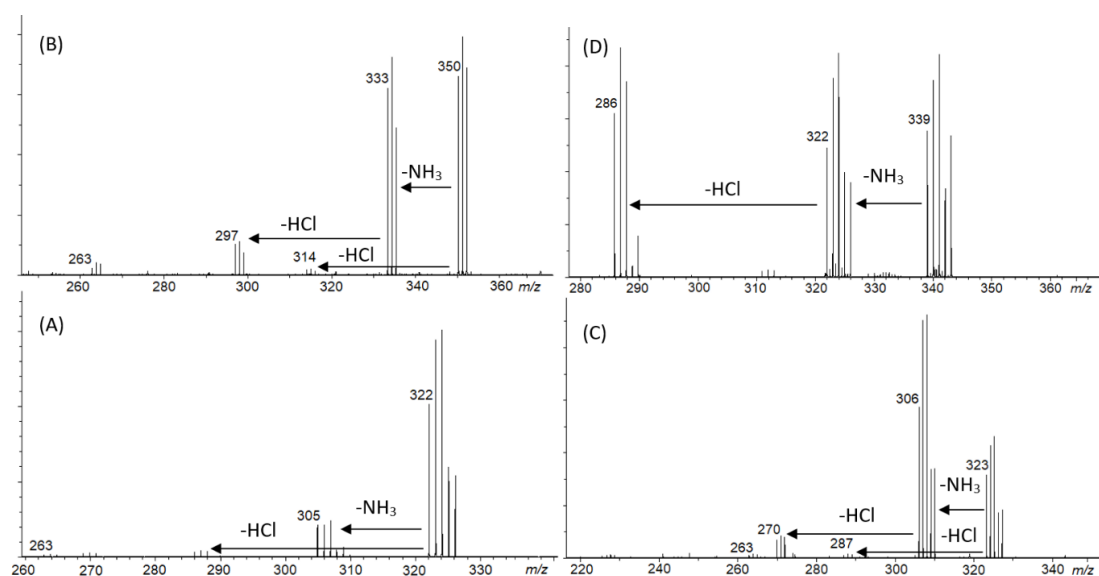
Figure S3.4 IRMPD mass spectra of *cis*-[PtCl(NH₃)₂(L)]⁺ (L = ACM (A), DMA (B), U (C) and SU (D)). Mass selection of the precursor ion comprises different *m/z* windows in the above reported spectra. For example, a narrower number of isotopic ions is isolated in the experiment reported in panel (B).
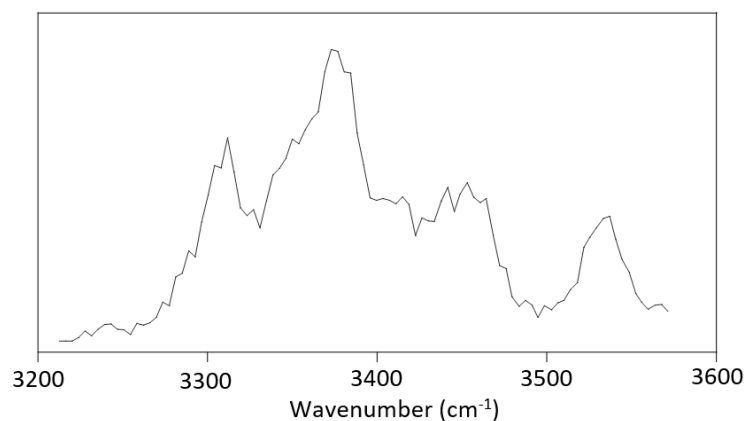
Figure S3.5 IRMPD spectrum of [PtCl(NH₃)₂(H₂O)]⁺ obtained by CID of ESI-formed [PtCl(NH₃)₂(Py)(H₂O)]⁺ ions. Spectral features are consistent with *cis*-[PtCl(NH₃)₂(H₂O)]⁺. See: De Petris, A.; Ciavardini, A.; Coletti, C.; Re, N.; Chiavarino, B.; Crestoni, M. E.; Fornarini, S. *J. Phys. Chem. Lett.* **2013**, *4*, 3631.
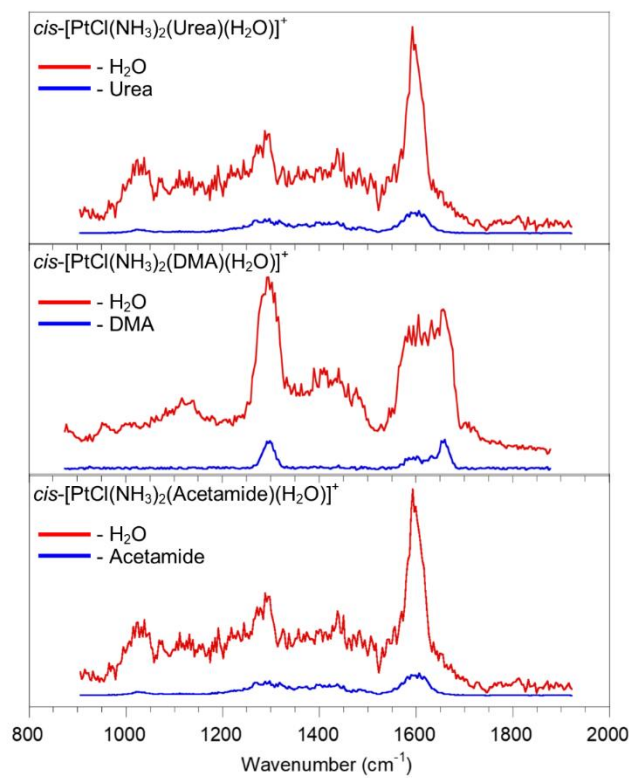
Figure S3.6 IRMPD profiles for the two fragmentation channels from [PtCl(NH₃)₂(H₂O)(L)]⁺ involving cleavage of either L (blue) or H₂O (red) (L = ACM, DMA, U).
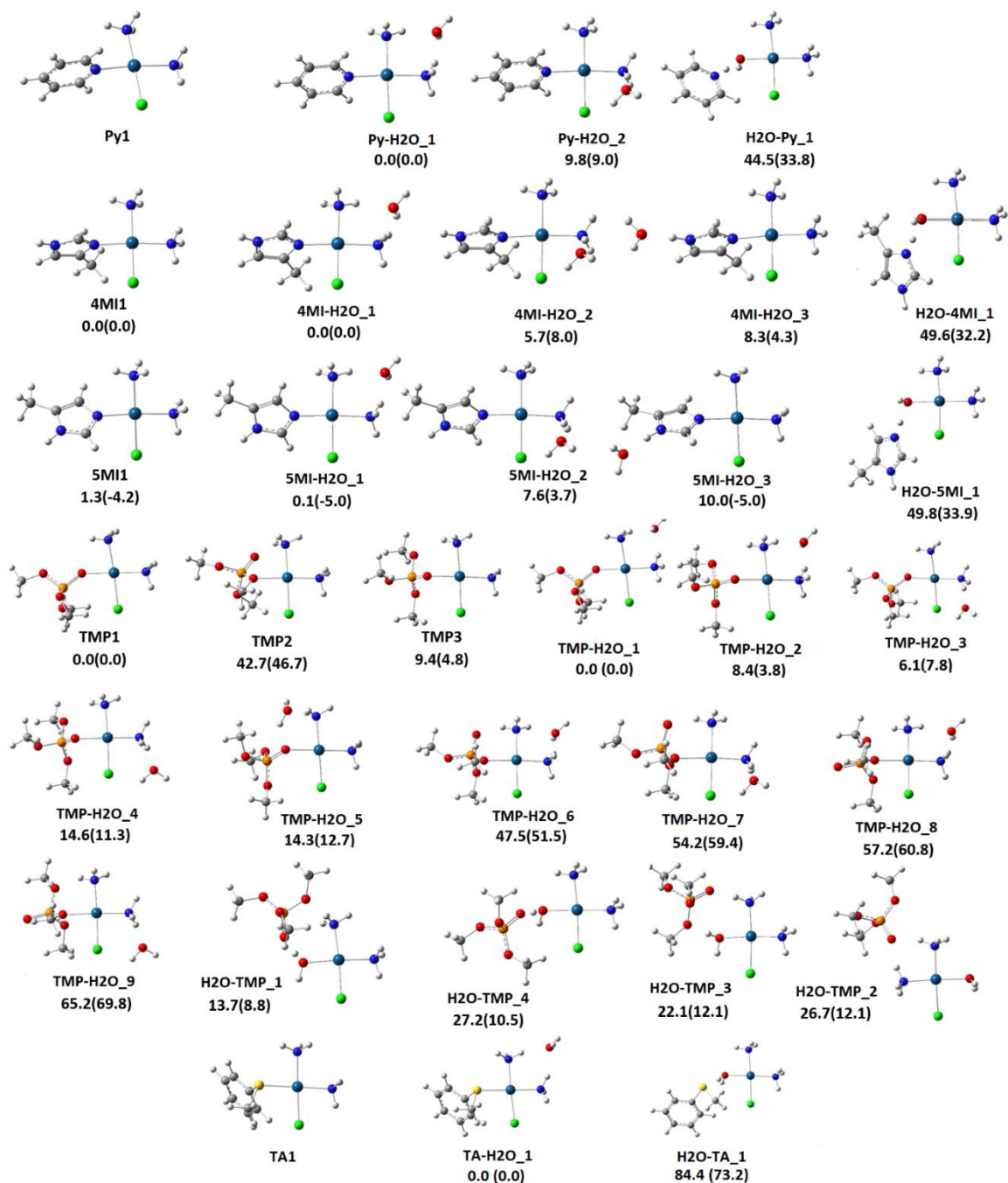
Figure S3.7 Optimized structures of the most stable isomers of sampled [PtCl(NH$_3$)$_2$(L)(H$_2$O)]$^+$ complexes, at B3LYP/6-311+G(d,p) level. Relative energies (standard enthalpy at 298K) at ωB97XD/6-311+G(d,p) level are reported in kJ mol^{-1} below each structure (in parentheses values obtained at B3LYP/6-311+G(d,p) level).
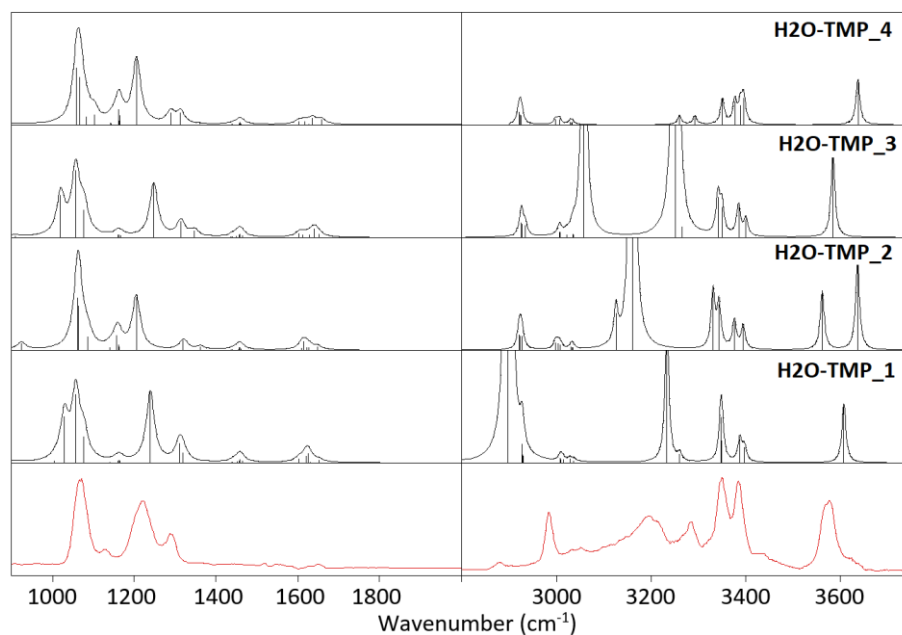
Figure S3.8 IRMPD spectrum (red line) compared with the calculated IR spectra (black line) of *cis*-[PtCl(NH$_3$)$_2$(H$_2$O)] (TMP)$^+$ (isomers **H2O-TMP_n**).
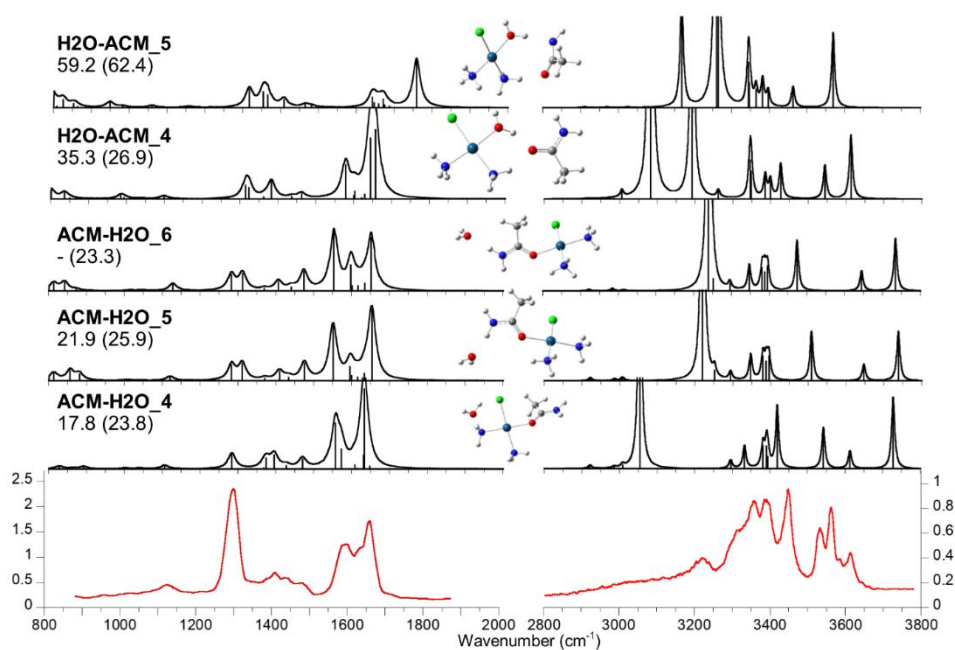
Figure S3.9 Geometries and calculated IR spectra of higher lying isomers and conformers of *cis*-[PtCl(NH$_3$)$_2$(ACM)(H$_2$O)]$^+$. Geometries are reported at B3LYP level. Relative (referred to **ACM-H2O_1**) free energies at 298 K (in kJ mol^{-1}) are obtained at the ωB97X-D and B3LYP (in brackets) level.
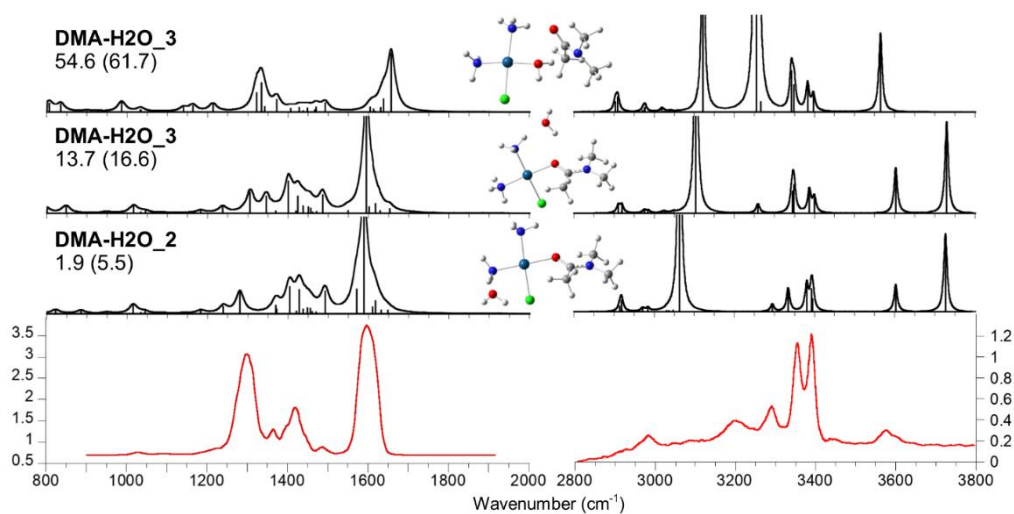
Figure S3.10 Geometries and calculated IR spectra of higher lying isomers and conformers of *cis*-[PtCl(NH₃)₂(DMA)(H₂O)]⁺. Geometries are reported at B3LYP level. Relative (referred to **DMA-H2O_1**) free energies at 298 K (in kJ mol⁻¹) are obtained at the ωB97X-D and B3LYP (in brackets) level.
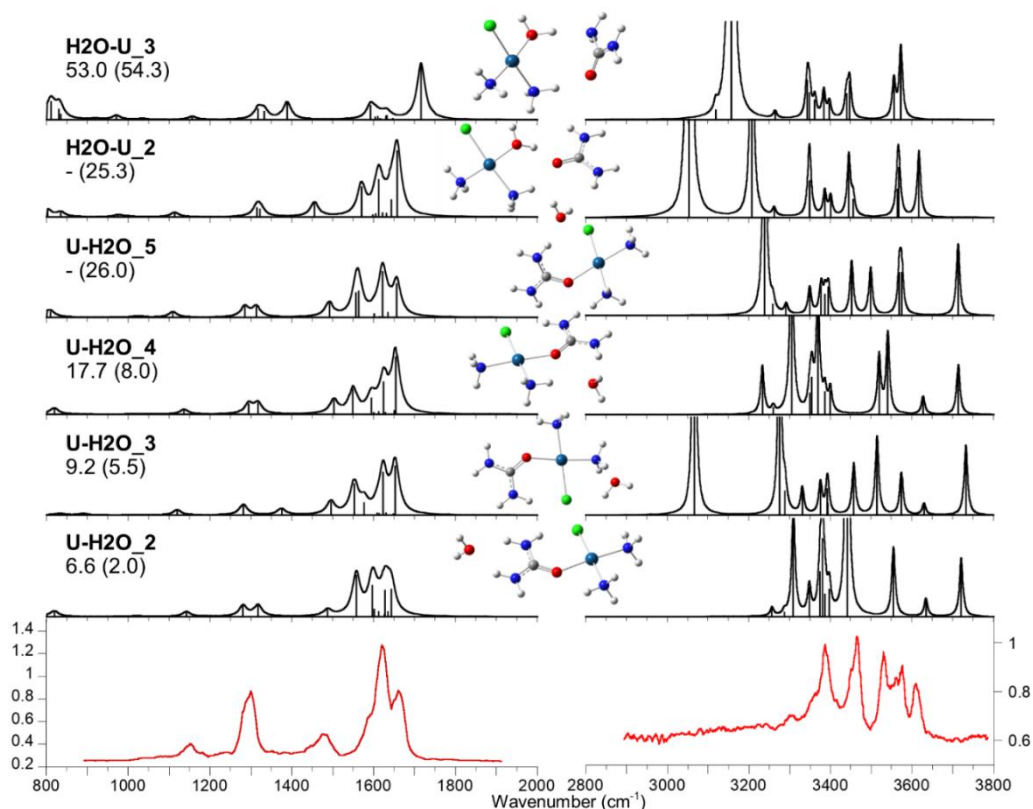
Figure S3.11 Geometries and calculated IR spectra of higher lying isomers and conformers of *cis*-[PtCl(NH₃)₂(U)(H₂O)]⁺. Geometries are reported at B3LYP level. Relative (referred to **U-H2O_1**) free energies at 298 K (in kJ mol⁻¹) are obtained at the ωB97X-D and B3LYP (in brackets) level.

Table S3.3 Observed IRMPD signatures and calculated vibrational frequencies for the most stable geometry of *cis*-[PtCl(NH$_3$)$_2$(L)]$^+$ (L = MeIm, Py, TMP).

cis[PtCl(NH$_3$)$_2$(MeIm)]$^+$

Experimental IRMPD[a]	Calculated IR[a,b] 4MeIm	Calculated IR[a,b] 5MeIm	Vibrational mode assignment
	1073 (28)	1106 (35)	in plane CH bend
		1130 (15)	in plane CH and NH bend
1294	1283 (109)	1286 (106)	symm NH$_3$ bend
	1301 (125)	1303 (126)	symm NH$_3$ bend
	1439 (16)	1443 (11)	asymm CH$_3$ bend
	1447 (21)	1494 (20)	asymm CH$_3$ bend
	1496 (47)	1499 (46)	Ring def
	1585 (24)	1598 (37)	CC ring stretch
	1604 (32)	1604 (31)	asymm NH$_3$ bend
	1621 (27)	1622 (22)	asymm NH$_3$ bend
	1680 (47)	1637 (50)	asymm NH$_3$ bend

cis[PtCl(NH$_3$)$_2$(Py)]$^+$

Experimental IRMPD[a]	Calculated IR[a,b] Py1	Vibrational mode assignament
	1070 (11)	in plane CH bend
1288	1290 (110)	symm NH$_3$ bend
	1304 (125)	symm NH$_3$ bend
1455	1447 (38)	Ring def
1602	1602 (33)	asymm NH$_3$ bend
	1606 (17)	CC ring stretch
	1623 (25)	asymm NH$_3$ bend
	1636 (47)	asymm NH$_3$ bend

cis[PtCl(NH$_3$)$_2$(TMP)]$^+$

Experimental IRMPD[a]	Calculated IR[a,b] TMP1	Vibrational mode assignament
1071	1066 (495)	P-OCH$_3$ stretch
	1074 (529)	P-OCH$_3$ stretch
	1086 (100)	P-OCH$_3$ stretch

1178	1152 (572	P=O stretch
	1163 (29)	symm CH$_3$ bend
1271	1286 (104)	symm NH$_3$ bend
1295	1317 (123)	symm NH$_3$ bend
	1459 (17)	asymm CH$_3$ bend
	1460 (18)	asymm NH$_3$ bend
	1612 (24)	asymm NH$_3$ bend
	1635 (49)	asymm NH$_3$ bend

[a] Frequencies in cm^{-1}. [b]Intensities (reported in parentheses) are in km mol^{-1}. Modes with intensity lower than 20 km mol^{-1} are omitted.

Table S3.4 Experimental IRMPD features and calculated vibrational frequencies at B3LYP/6-311+G** (LanL2TZ) level for the low-lying isomers of *cis*-[PtCl(NH$_3$)$_2$(L)]$^+$ (L = ACM, DMA, U and SU).

cis-[PtCl(NH$_3$)$_2$(ACM)]$^+$

Experimental IRMPD[a]	Calculated Ir[a,b]	Vibrational mode
1646	1650 (485)	NH$_2$ scissor + CN stretch
1559	1548 (184)	CO stretch + NH$_2$ scissor
1475	1465 (108)	CH$_3$ umbrella
1281	1318 (108)	NH$_3$ umbrella
	1289 (112)	NH$_3$ umbrella

cis-[PtCl(NH$_3$)$_2$(DMA)]$^+$

Experimental IRMPD[b]	Calculated Ir[a]	Vibrational mode
1596	1589 (513)	CN stretch
1480	1488 (110)	CO stretch + CH asymm bend
1433	1425 (119)	CH$_3$ umbrella
1410	1402 (160)	CH$_3$ umbrella
1280	1312 (109)	NH$_3$ umbrella
	1283 (114)	NH$_3$ umbrella
1020	1014 (46)	CH$_3$ asymm bend

cis-[PtCl(NH$_3$)$_2$(U)]$^+$

Experimental IRMPD[b]	Calculated Ir[a]	Vibrational mode
1625	1646 (478)	NH$_2$ scissor
	1624 (412)	NH$_2$ scissor
1560	1548 (340)	CO stretch + NH$_2$ scissor
	1535 (119)	NH$_2$ asymm bend
1280	1318 (111)	NH$_3$ umbrella
	1285 (108)	NH$_3$ umbrella

cis-[PtCl(NH$_3$)$_2$(SU)]$^+$

Experimental IRMPD[b]	Calculated Ir[a]	Vibrational mode
1627	1632 (141)	NH$_2$ scissor
	1623 (292)	NH$_2$ scissor
1417	1378 (244)	CS stretch + NH$_2$ bend
1280	1294 (123)	NH$_3$ umbrella
	1280 (125)	NH$_3$ umbrella

[a] In cm^{-1}. [b] Intensities are reported in parentheses (km mol^{-1}). Bands with an intensity lower than 50 km mol^{-1} are usually not included. Frequencies are scaled by a factor of 0.974.

Table S3.5 Theoretically calculated thermodynamic parameters for the most stable structures of sampled Pt(II) complexes. Calculation performed at B3LYP/6-311+G(d,p) and at ωB97X-D/6-311+G(d,p) level.

Species	Energy[a]	B3LYP/6-311+G(d,p) Relative Energy[b]	Zero-point Energy[b]	Relative Enthalpy [b](298K)	Relative Free Energy[b] (298K)
H$_2$O	-76.458463		55.8770		
cis-[PtCl(NH$_3$)$_2$(H$_2$O)]$^+$	-768.887878		281.3429		
cis-[PtCl(NH$_3$)$_2$(OH)]	-768.506945		246.4203		
Pyridine	-248.351217		232.0954		
Py1	-940.820256		451.7839		
Py-H2O_1	-1017.301804	0.00	517.7973	0.00	0.00
Py-H2O_2	-1017.297913	10.22	515.8680	8.99	6.79
H2O-Py_1	-1017.288056	36.10	517.4393	33.76	36.12
Py_TS	-1017.244559	150.30	514.27	145.88	149.22
4-Methyl-Imidazole	-265.613709	0.00	258.1876	0.00	0.00
5-Methyl-Imidazole	-265.612819	2.34	258.4503	2.59	2.63
4MI1	-958.090905	0.00	478.3061	0.00	0.00
5MI1	-958.092563	-4.35	478.4265	-4.18	-3.54
4MI-H2O_1	-1034.571617	0.00	544.0931	0.00	0.00
4MI-H2O_2	-1034.568211	8.94	542.7583	7.98	7.84
4MI-H2O_3	-1034.569510	5.53	540.4962	4.30	-4.48
H2O-4MI_1	-1034.557961	35.85	544.2989	33.89	36.92
5MI-H2O_1	-1034.573651	-5.34	544.4736	-5.00	-5.00
5MI-H2O_2	-1034.569807	4.75	542.2607	3.75	3.75
5MI-H2O_3	-1034.570852	2.01	540.8054	-5.00	-5.00
H2O-5MI_1	-1034.558499	34.44	543.8800	32.18	34.46
4MI_TS	-1034.513358	152.96	541.8131	149.07	154.19
5MI_TS	-1034.515969	146.10	541.0761	142.01	144.59
Trimethylphosphate	-762.207081		350.5231		
TMP1	-1454.665457	0.00	568.0651	0.00	0.00
TMP2	-1454.647698	46.63	569.9829	46.66	54.51
TMP3	-1454.663598	4.88	568.2591	4.84	97.73
TMP-H2O_1	-1531.144457	3.57	634.3553	3.77	3.98
TMP-H2O_2	-1531.141076	12.45	632.1551	11.29	8.31
TMP-H2O_3	-1531.140695	13.45	633.4357	12.69	14.23
TMP-H2O_4	-1531.145818	0.00	633.7417	0.00	0.00
TMP-H2O_5	-1531.142431	8.89	631.9905	7.85	5.83
TMP-H2O_6	-1531.122714	60.66	635.5551	51.46	51.46

TMP-H2O_7	-1531.118770	71.01	633.2526	59.39	59.39
TMP-H2O_8	-1531.126164	51.60	634.9822	60.83	67.98
TMP-H2O_9	-1531.122453	61.34	632.2896	69.76	74.08
H2O-TMP_1	-1531.142682	8.23	636.9332	8.83	11.51
H2O-TMP_2	-1531.141334	11.77	634.7257	10.50	10.60
H2O-TMP_3	-1531.141624	11.01	637.4508	12.10	15.16
H2O-TMP_4	-1531.141780	10.60	636.5739	12.15	9.13
TMP_TS	-1531.108147	98.90	630.8903	94.68	97.73
Thioanisole	-669.847536		337.3643		
TA1	-1362.308720		555.4424		
TA-H2O_1	-1438.790802	0.00	621.6222	0.00	0.00
H2O-TA_1	-1438.762375	74.63	621.0423	73.20	68.45
TA_TS	-1438.740302	132.59	618.8835	129.00	130.72

[a] Electronic energy at 0K. In Hartree particle[-1]. [b] In kJ mol^{-1}. [c] In J mol^{-1}K[-1].

ωB97XD/6-311+G(d,p)					
Species	Energy[a]	Relative Energy[b]	Zero-point Energy[b]	Relative Enthalpy[b] (298K)	Relative Free Energy[b] (298K)
H$_2$O	-76.432249		56.9070		
cis-[PtCl(NH$_3$)$_2$(H$_2$O)]$^+$	-768.790763		284.9900		
Pyridine	-248.255864		234.5591		
Py1	-940.659598		456.4786		
Py-H2O_1	-1017.118471	0.00	524.7178	0.00	0.00
Py-H2O_2	-1017.115254	8.45	522.4788	9.76	4.07
H2O-Py_1	-1017.100524	47.12	523.8065	44.55	45.98
Py_TS	-1017.063411	144.56	520.0942	139.68	139.74
4-Methyl-Imidazole	-265.519652	0.00	261.356	0.00	0.00
5-Methyl-Imidazole	-265.518985	1.75	261.6145	1.97	2.21
4MI1	-957.934781	0.00	484.4779	0.00	0.00
5MI1	-957.934237	1.43	484.4025	1.33	3.86
4MI-H2O_1	-1034.392523	0.00	552.1183	0.00	0.00
4MI-H2O_2	-1034.389819	7.10	549.9009	5.67	3.25
4MI-H2O_3	-1034.388891	9.54	548.8143	8.33	2.23
H2O-4MI_1	-1034.372716	52.01	551.6269	49.77	51.79
5MI-H2O_1	-1034.392543	-0.05	552.2359	0.10	0.49
5MI-H2O_2	-1034.389278	8.52	550.4413	7.61	6.35
5MI-H2O_3	-1034.388210	11.33	547.8478	10.00	0.51
H2O-5MI_1	-1034.372692	52.07	551.5340	49.62	52.22
4MI_TS	-1034.336230	147.80	550.2080	144.15	149.78
5MI_TS	-1034.336048	148.28	547.3596	143.45	142.32

Trimethylphosphate	-762.047520		355.0869		
TMP1	-1454.442758	0.00	575.7916	0.00	0.00
TMP2	-1454.426598	42.43	578.0014	42.67	50.67
TMP3	-1454.439078	9.66	575.2723	9.43	7.76
TMP-H2O_1	-1530.896988	9.19	642.2366	8.36	1.53
TMP-H2O_2	-1530.894269	16.32	641.1324	14.58	8.41
TMP-H2O_3	-1530.894445	15.86	642.2039	14.32	12.88
TMP-H2O_4	-1530.900486	0.00	644.3011	0.00	0.00
TMP-H2O_5	-1530.897622	7.52	641.9147	6.10	2.45
TMP-H2O_6	-1530.882202	48.01	644.2161	47.49	47.60
TMP-H2O_7	-1530.878816	56.90	640.8105	54.17	50.50
TMP-H2O_8	-1530.878408	57.97	643.9552	57.21	57.87
TMP-H2O_9	-1530.875026	66.84	642.564	65.18	65.39
H2O-TMP_1	-1530.895187	13.91	645.8209	13.66	15.63
H2O-TMP_2	-1530.889525	28.78	643.7041	27.18	22.82
H2O-TMP_3	-1530.892354	21.35	646.5682	22.14	21.09
H2O-TMP_4	-1530.890603	25.95	645.1160	26.74	19.10
TMP_TS	-1530.864362	94.84	639.8397	81.82	87.53
Thioanisole	-669.726987		341.0777		
TA1	-1362.125910		562.4989		
TA-H2O_1	-1438.585098	0.00	629.2484	0.00	0.00
H2O-TA_1	-1438.553020	84.22	630.7649	84.35	84.63
TA_TS	-1438.536430		627.2307	124.65	128.89

[a] Electronic energy at 0K.   [b] In Hartree particle[-1].   [c] In kJ mol^{-1}.   [d] In J mol^{-1}K[-1].

Table S3.6 Observed IRMPD signatures of $[PtCl(NH_3)_2(Py)(H_2O)]^+$ and calculated vibrational frequencies for the assigned isomer.

Experimental IRMPD[a]	Calculated IR[a,b] H2O-Py_1	Vibrational mode assignament
955	932 (29)	OH bend
	983 (97)	OH bend + ring def
1217	1197 (18)	CH bend in plane
1259	1262 (127)	symm NH_3 bend
1292	1297 (120)	symm NH_3 bend
	1324 (28)	OH-N bend out plane
	1407 (18)	CC ring stretch
1484	1480 (65)	CC ring stretch
1618	1605 (29)	asymm NH_3 bend
	1612 (20)	asymm NH_3 bend
	1636 (43)	asymm NH_3 bend
	1657 (26)	in plane O-HN bend
3094	3054 (53)	CH stretch
	3058 (16)	CH stretch
3296	3269 (16)	symm NH_3 stretch
	3276 (13)	symm NH_3 stretch
3368	3358 (48)	asymm NH_3 stretch
	3370 (57)	asymm NH_3 stretch
3397	3393 (35)	asymm NH_3 stretch
	3398 (53)	asymm NH_3 stretch
3610	3640 (55)	OH stretch

[a] Frequencies in cm^{-1}. [b]Intensities (reported in parentheses) are in km mol^{-1}. Modes with intensity lower than 20 km mol^{-1} are not included.

Table S3.7 Observed IRMPD signatures of [PtCl(NH$_3$)$_2$(MeIm)(H$_2$O)]$^+$ and calculated vibrational frequencies for the reference isomers.

Experimental IRMPD[a]	Calculated IR[a,b]		Vibrational mode assignment
	H2O-4MI_1	**H2O-5MI_1**	
		915 (48)	ring def
	932 (60)	942 (37)	OH bend
	961 (14)	942 (65)	asymm CH$_3$ bend + ring def
1083		1062 (40)	in plane CH - NH bend
1133	1123 (27)	1147 (40)	in plane CH - NH bend
1205	1206 (40)	1197 (21)	in plane CH bend
1259	1242 (40)		in plane CH bend
	1257 (45)	1244 (37)	OH bend
		1253 (13)	in plane CH bend
	1262 (119)	1260 (119)	symm NH$_3$ bend
1289	1294 (91)	1295 (120)	symm NH$_3$ bend
1427	1407 (10)		in plane NH bend
		1442 (12)	asymm CH$_3$ bend
1472	1442 (12)		asymm CH$_3$ bend
		1457 (18)	in plane NH bend
1618	1604 (28)	1604 (26)	asymm NH$_3$ bend
	1612 (19)	1612 (22)	asymm NH$_3$ bend
	1626 (99)	1631 (77)	CC stretch + O-HN
	1637 (49)	1637 (54)	asymm NH$_3$ bend
3160	3117 (99)	3116 (101)	CH stretch
3294	3270 (21)	3270 (18)	symm NH$_3$ stretch
	3270 (12)	3270 (13)	symm NH$_3$ stretch
3363	3359 (45)	3359 (44)	asymm NH$_3$ stretch
	3367 (58)	3367 (59)	asymm NH$_3$ stretch
3393	3394 (35)	3393 (35)	asymm NH$_3$ stretch
	3400 (52)	3400 (52)	asymm NH$_3$ stretch
3497	3474 (117)	3482 (148)	NH stretch
3604	3641 (54)	3641 (52)	OH stretch

[a]Frequencies in cm^{-1}. [b]Intensities (reported in parentheses) are in km mol^{-1}. Modes with intensity lower than 10 km mol^{-1} are not included.

Table S3.8 Observed IRMPD signatures of $[PtCl(NH_3)_2(TMP)(H_2O)]^+$ and calculated vibrational frequencies for the reference isomer.

Experimental IRMPD[a]	Calculated IR[a,b] H2O-TMP_1	Vibrational mode assignment
1068	1029 (328)	P-OCH$_3$ stretch
	1057 (488)	P-OCH$_3$ stretch
	1077 (182)	P-OCH$_3$ stretch
1129	1160 (18)	asymm CH$_3$ bend
	1163 (18)	asymm CH$_3$ bend
	1165 (13)	asymm CH$_3$ bend
1220	1239 (503)	P=O stretch
1286	1310 (135)	symm NH$_3$ bend
	1355 (70)	symm NH$_3$ bend
	1663 (47)	H$_2$O bend
	1669 (67)	H$_2$O bend
2876	2898 (2300)	OH stretch
2980	2926 (41)	symm CH$_3$ stretch
3200	3233 (311)	asymm NH$_3$ stretch
3280	3260 (18)	symm NH$_3$ stretch
3346	3347 (101)	asymm NH$_3$ stretch
3380	3387 (59)	asymm NH$_3$ stretch
	3397 (34)	asymm NH$_3$ stretch
3573	3607 (131)	OH stretch

[a]Frequencies in cm^{-1}. [b]Intensities (reported in parentheses) are in km mol^{-1}. Modes with intensity lower than 10 km mol^{-1} are not included

Table S3.9 Thermodynamic data calculated at the B3LYP and ωB97X-D levels for the conformers and isomers of *cis*-[PtCl(NH₃)₂(L)]⁺ and *cis*-[PtCl(NH₃)₂(H₂O)(L)]⁺ where L = ACM , DMA , U and SU, together with related species participating to the PES.

	B3LYP/6-311+G(d,p)				ωB97X-D/6-311+G(d,p)			
	EE (H)[b]	EE (G)[b]	H_{rel}[a,c]	G_{rel}[a,c]	EE (H)[b]	EE (G)[b]	H_{rel}[a,c]	G_{rel}[a,c]
H2O	-76.4334	-76.454823			-76.406794	-76.428203		
cis-[PtCl(NH₃)₂(H₂O)]⁺	-768.770124	-768.816539			-768.671696	-768.71799		
Acetamide	-209.209301	-209.243887			-209.135347	-209.169136		
ACM_1	-901.57648	-901.631653	0.0	0.0	-901.433763	-901.488464	0.0	0.0
ACM_2	-901.560966	-901.614593	40.7	44.8	-901.421305	-901.474506	32.7	36.6
DMA	-287.780261	-287.822643			-287.681223	-287.720874		
DMA_1	-980.146741	-980.209772	0.0	0.0	-979.981619	-980.04341	0.0	0.0
DMA_2	-980.124796	-980.182387	57.6	71.9	-979.967343	-980.024483	37.5	49.7
Urea	-225.280901	-225.312599			-225.203286	-225.234965		
U_1	-917.649353	-917.701563	0.0	0.0	-917.50215	-917.557168	0.0	0.0
U_2	-917.640884	-917.693491	22.2	21.2	-917.496451	-917.548633	15.0	22.4
Thiourea	-548.23556	-548.268792			-548.160979	-548.194274		
SU_1	-1240.621522	-1240.676645	0.0	0.0	-1240.479922	-1240.535037	0.0	0.0
SU_2	-1240.591769	-1240.645864	78.1	80.8	-1240.451322	-1240.504272	75.1	80.8
ACM-H2O_1	-978.030251	-978.091699	0.0	0.0	-977.864356	-977.924788	0.0	0.0
ACM-H2O_2	-978.026974	-978.089562	8.6	5.6	-977.86132	-977.922141	8.0	6.9
ACM-H2O_3	-978.023406	-978.085546	18.0	16.2	-977.859229	-977.920535	13.5	11.2
ACM-H2O_4	-978.020294	-978.082624	26.1	23.8	-977.856616	-977.918013	20.3	17.8
ACM-H2O_5	-978.017823	-978.081816	32.6	25.9	-977.851663	-977.916461	33.3	21.9
H2O-ACM_1	-978.022376	-978.083718	20.7	21.0	-977.854911	-977.915394	24.8	24.7
H2O-ACM_2	-978.019968	-978.082135	27.0	25.1	-977.85275	-977.913987	30.5	28.4
H2O-ACM_3	-978.019303	-978.081737	28.7	26.2	-977.85136	-977.913947	34.1	28.5
H2O-ACM_4	-978.018892	-978.081471	29.8	26.9	-977.850665	-977.911334	35.9	35.3
H2O-ACM_5	-978.005974	-978.067916	63.7	62.4	-977.842551	-977.902247	57.2	59.2
ACM-H2O_6[d]	-978.019861	-978.082839	27.3	23.3	-	-	-	-
H2O-ACM_TS	-977.993095	-978.053515	97.6	100.3	-977.829349	-977.888958	91.9	94.1
DMA-H2O_1	-1056.599441	-1056.66903	0.0	0.0	-1056.411048	-1056.478971	0.0	0.0
DMA-H2O_2	-1056.596802	-1056.666929	6.9	5.5	-1056.409157	-1056.478244	5.0	1.9
DMA-H2O_3	-1056.592849	-1056.662701	17.3	16.6	-1056.40606	-1056.473759	13.1	13.7
H2O-DMA_1	-1056.594817	-1056.665248	12.1	9.9	-1056.402985	-1056.471208	21.2	20.4
H2O-DMA_2	-1056.593483	-1056.662771	15.6	16.4	-1056.403028	-1056.469499	21.1	24.9
H2O-DMA_3	-1056.577539	-1056.645528	57.5	61.7	-1056.392993	-1056.458166	47.4	54.6

H2O-DMA_TS	-1056.562474	-1056.631525	97.1	98.5	-1056.376281	-1056.442355	91.3	96.1
U-H2O_1	-994.102064	-994.163945	0.0	0.0	-993.932664	-993.994091	0.0	0.0
U-H2O_2	-994.100574	-994.16317	3.9	2.0	-993.930004	-993.991585	7.0	6.6
U-H2O_3	-994.098821	-994.161846	8.5	5.5	-993.929552	-993.990596	8.2	9.2
U-H2O_4	-994.096318	-994.160879	15.1	8.0	-993.925996	-993.987352	17.5	17.7
H2O-U_1	-994.096742	-994.15805	14.0	15.5	-993.925552	-993.98634	18.7	20.4
H2O-U_2[e]	-994.092348	-994.154315	25.5	25.3	-993.925552	-993.98634	18.7	20.4
H2O-U_3	-994.083663	-994.14326	48.3	54.3	-993.914642	-993.973897	47.3	53.0
U-H2O_5[d]	-994.092726	-994.15404	24.5	26.0	-	-	-	-
H2O-U_TS	-994.066779	-994.126498	92.6	98.3	-993.899568	-993.959482	86.9	90.9
SU-H2O_1	-1317.074523	-1317.137093	0.0	0.0	-1316.90981	-1316.971001	0.0	0.0
H2O-SU_1	-1317.04425	-1317.107279	79.5	78.3	-1316.877211	-1316.938942	85.6	84.2
H2O-SU_TS	-1317.025146	-1317.086148	129.6	133.8	-1316.860869	-1316.921642	128.5	129.6

[a] in kJ mol^{-1}. [b] Enthalpy (H) and Gibbs free energy (G) corrected electronic energies (EE) at 298 K are reported in Hartree particle[-1]. [c] At 298 K [d] The optimization calculation starting from the correspondent geometry at the B3LYP level failed to converge. [d] The ωB97X-D optimization of the correspondent geometry at B3LYP leads to the **H2O-U_1** conformer.

Table S3.10 Experimental IRMPD signals and calculated vibrational frequencies at B3LYP/6-311+G(d,p) (LanL2TZ) level for selected isomers of $\{[PtCl(NH_3)_2(H_2O)]^+ \cdot L\}$ (L = ACM, DMA, U).

		***cis*-[PtCl(NH₃)₂(H₂O)(ACM)]⁺**		
		Calculated Ir[a,b]		
Experimental IRMPD[a]	H2O-ACM_1	H2O-ACM_2	H2O-ACM_3	Vibrational mode
3613	3641 (115)	3641 (104)		OH stretch
3585			3614 (126)	OH stretch
3561		3550 (72)	3547 (73)	NH₂ asymm stretch
3532	3517 (144)			NH₂ asymm stretch
3441		3426 (87)	3428 (80)	NH₂ symm stretch
3389	3392 (65)	3394 (61)	3399 (40)	NH₃ asymm stretch
	3372 (57)	3375 (53)	3386 (51)	NH₃ asymm stretch
3354	3351 (51)	3350 (57)	3348 (101)	NH₃ asymm stretch
3322	3335 (358)			NH₂ symm stretch
3228			3219 (453)	NH₃ symm stretch
3010 (broad)			2991 (1814)	OH stretching
	2187[c] (3216)	2443[c] (3236)		OH stretching
1660			1657 (434)	CO stretch + H₂O scissor
1637	1633 (360)	1637 (721)	1641 (360)	NH₂ scissor
		1636 (356)	1621 (85)	NH₃ asymm bend
1587	1575 (829)	1579 (204)	1575 (198)	CO stretch + NH₂ bend
1467	1463 (18)	1465 (31)	1463 (43)	CH₃ umbrella + NH₂ bend
1433	1430 (11)	1438 (18)	1438 (14)	CH₃ asymm bend
1407	1385 (127)	1387 (120)	1384 (120)	CH₃ umbrella + NH₂ bend
1297	1320 (109)	1315 (109)	1320 (88)	NH₃ umbrella
	1296 (130)	1327 (115)	1314 (80)	NH₃ umbrella
1120	1196 (46)	1154 (63)		OH bend
	1104 (31)	1134 (29)	1100 (25)	NH₂ rock

	***cis*-[PtCl(NH₃)₂(H₂O)(DMA)]⁺**		
Experimental IRMPD[a]	Calculated Ir[a,b]		Vibrational mode
	H2O-DMA_1	H2O-DMA_2	
3600	3645 (101)		OH stretch
3573		3620 (118)	OH stretch
3389	3395 (59)	3400 (39)	NH₃ asymm stretch
	3388 (43)	3386 (50)	NH₃ asymm stretch
	3375 (53)		NH₃ asymm stretch
3352	3351 (55)	3349 (58)	NH₃ asymm stretch
		3345 (81)	NH₃ asymm stretch
3290	3291 (19)	3262 (17)	NH₃ symm stretch
	3260 (19)		NH₃ symm stretch

3200		3162 (789)	NH₃ symm stretch
2978		2972 (1756)	OH stretch
	2961 (24)		CH₃ asymm stretch
	2910 (33)	2913 (34)	CH₃ symm stretch
	2170ᶜ (3910)		OH stretch
1597		1624 (193)	H₂O scissor + NH₃ bend
		1607 (232)	H₂O scissor +CO stretch
	1577 (1388)		CN stretch + CO stretch
		1569 (371)	H₂O scissor +CN stretch
1487	1501 (168)	1501 (158)	CO stretch
1417	1441 (131)	1434 (47)	CH₃ umbrella
	1418 (54)	1416 (21)	CH₃ umbrella
	1400 (106)	1406 (73)	CH₃ umbrella
1295	1312 (111)	1324 (79)	NH₃ umbrella
	1287 (121)	1312 (100)	NH₃ umbrella
	1241 (94)		OH bend + CN bend
	1010 (94)		CH₃ asymm bend
		1012 (42)	H₂O rock

cis-[PtCl(NH₃)₂(H₂O)(U)]⁺

Experimental IRMPD[a]	Calculated Ir[a,b]	Vibrational mode
	H2O-U_1	
3607	3644 (111)	OH stretch
3574	3573 (84)	NH₂ asymm stretch
3526	3528 (162)	NH₂ asymm stretch
3464	3454 (72)	NH₂ symm stretch
3384	3393 (64)	NH₃ asymm stretch
	3372 (426)	NH₂ symm stretch
	3352 (67)	NH₃ asymm stretch
3302	3288 (21)	NH₃ symm stretch
	2080ᶜ (2868)	OH stretch
1663	1634 (475)	NH₂ scissor
1620	1613 (569)	NH₂ scissor
1580 (shoulder)	1545 (1085)	CO stretch + OH stretch + NH₂ rock
1480	1464 (127)	CN stretch + CO bend
1297	1318 (108)	NH₃ umbrella
	1294 (132)	NH₃ umbrella
1143	1117 (78)	NH₂ rock

[a] In cm⁻¹. [b] Intensities are reported in parentheses (km mol⁻¹). Bands with an intensity lower than 50 km mol⁻¹ are usually not included. Frequencies are scaled by a factor of 0.974 in the 800-2000 cm⁻¹ range and 0.957 in the 2800-3800 cm⁻¹ one. ᶜThe reported frequencies are unscaled.

3.5 Summary

In section 3.3, the early hydrolysis products from cis and transplatin, *cis-* and *trans-*[PtX(NH$_3$)$_2$(H$_2$O)]$^+$ (X = Cl, OH), have been obtained by ESI and isolated in the gas-phase where their structure and reactivity properties have been comparatively examined. While an unambiguous characterization of these species is hard to achieve in solution where prototropic equilibria occur and the formation of hydroxo-bridged polynuclear complexes is an important competing process,[74] the gaseous environment permits to achieve this task.

IRMPD spectroscopy in the NH/OH stretching range has revealed the vibrational signatures of bare *cis-* and *trans-*[Pt(OH)(NH$_3$)$_2$(H$_2$O)]$^+$ ions. While the IR spectrum of *trans-*[Pt(OH)(NH$_3$)$_2$(H$_2$O)]$^+$ is very similar to the one of the chloro complex, *trans-*[PtCl(NH$_3$)$_2$(H$_2$O)]$^+$, the spectra of the cis complexes are rather different. The major variation in frequency affects the water OH stretching modes. Asymmetric and symmetric resonances are at 3624 and 3531 cm^{-1} in the chloro complex[14] and 3600 and 3442 cm^{-1} in the hydroxo complex, respectively. Hydrogen bonding interactions are responsible for the different behavior that is manifested in the orientation of the water ligand, establishing a bisected hydrogen bonding interaction with the adjacent Cl in *cis-*[PtCl(NH$_3$)$_2$(H$_2$O)]$^+$ while privileging a single H-bond between an in plane water hydrogen atom and the hydroxyl oxygen in *cis-*[Pt(OH)(NH$_3$)$_2$(H$_2$O)]$^+$.

Both hydrolyzed complexes, [PtCl(NH$_3$)$_2$(H$_2$O)]$^+$ and [Pt(OH)(NH$_3$)$_2$(H$_2$O)]$^+$, have been allowed to react in the gas-phase with model compounds of biological ligands. All reactions show rather low efficiencies, in line with the behavior of platinum(II) complexes, characterized by relatively slow ligand exchange kinetics.[23] This feature is critically related to antitumor activity because it allows cisplatin and related drugs to reach the cell intact and effectively bind to cellular DNA rather than to extracellular binding sites.[23]

The reactivity of the chloro complexes, [PtCl(NH$_3$)$_2$(H$_2$O)]$^+$, is consistently higher than for the hydroxo-ligated counterparts, [Pt(OH)(NH$_3$)$_2$(H$_2$O)]$^+$, the chloro substituent likely enhancing the electrophilicity of the metal. This finding may be

related to the observation that the majority of the binding of cisplatin to DNA occurs via the monoaquated species cis-[PtCl(NH$_3$)$_2$(OH$_2$)]$^+$.[7-12,75]

In the following section 3.4, the primary hydrolytic product of cisplatin, cis-[PtCl(NH$_3$)$_2$(H$_2$O)]$^+$, is exposed to react with several biological ligands and the ligand exchange process with representative functional groups has been investigated at the molecular level in an isolated environment. The encounter complex of the ligand L with cis-[PtCl(NH$_3$)$_2$(H$_2$O)]$^+$, formed in solution, evolves into the cis-[PtCl(NH$_3$)$_2$(L)]$^+$ substitution product, delivered into the gas phase and assayed by IRMPD spectroscopy. Structural features of cis-[PtCl(NH$_3$)$_2$(L)]$^+$ have thus been unveiled for Py, TMP, ACM, DMA, U, SU and, in lesser detail, MeIm. In addition ESI-MS showed the presence of a formally penta-coordinated complex, cis-[PtCl(NH$_3$)$_2$(L)(H$_2$O)]$^+$, which is found to conform to the aqua complex cis-[PtCl(NH$_3$)$_2$(H$_2$O)]$^+$ interacting with an externally bound L molecule, namely the encounter complex formed along the path of the ligand exchange process. Thus, the {cis-[PtCl(NH$_3$)$_2$(H$_2$O)]$^+$ · L} cluster is a prototypical example of the encounter complex in the Eigen-Wilkins reactant preassociation model of ligand interchange in metal complexes in aqueous solution. In this framework, the substitution by an incoming ligand into the first coordination sphere is always preceded by its entry into the second coordination sphere.

These adducts are assigned a key role in the initial steps involved in the substitution mechanisms of cisplatin[76,77] and related antitumoral molecules[78]. This inference from theoretical studies of cisplatin activation both in the gas phase and in solution is now supported by the experimental evidence presently obtained. The {(cis-[PtCl(NH$_3$)$_2$(H$_2$O)]$^+$ · L} cluster does in fact yield cis-[PtCl(NH$_3$)$_2$(L)]$^+$, by ligand substitution followed by loss of H$_2$O, when it is activated by energetic collisions or in the same IR multiple photon absorption process that is exploited to reveal the vibrational features in IRMPD 'action' spectroscopy. It is appropriate to underline once again that the product adduct, namely {(cis-[PtCl(NH$_3$)$_2$(L)]$^+$ · H$_2$O}, is not in fact observed in spite of the recognized presence of cis-[PtCl(NH$_3$)$_2$(L)]$^+$ in the solution sampled by ESI. Thus, the favorable circumstances allowing detection of

{*cis*-[PtCl(NH$_3$)$_2$(H$_2$O)]$^+$ · L} are (i) a relatively high barrier for back dissociation and (ii) a relatively high activation energy for the ligand substitution step. When the second condition is not met, e. g. in the TA and SU cases, no formal five-coordinate adduct is obtained by ESI in the experimental conditions adopted, in spite of efforts tending to optimize soft delivery of ionic species.

The branching of the {*cis*-[PtCl(NH$_3$)$_2$(H$_2$O)]$^+$ · L } cluster into dissociation by either L or H$_2$O loss is directed by the balance between the L dissociation energy and the activation barrier for water ligand substitution. The same energy difference is responsible for the bimolecular reactivity observed in the *cis*-[PtCl(NH$_3$)$_2$(H$_2$O)]$^+$ + L → *cis*-[PtCl(NH$_3$)$_2$(L)]$^+$ + H$_2$O ligand substitution reaction examined in FT-ICR mass spectrometry and reported in section 3.2. Interestingly, although the TMP reaction is the least exothermic (figure 3.20), it shows the relatively fastest kinetic, which may suggest a cisplatin 'carrier' role for this specimen of a functional group ubiquitous in the biological environment.[8]

It should be underlined that all reported data refer to charged species isolated in the gas phase, an environment very different from the biological medium where cisplatin-derived intermediates are acting. The gaseous environment is expected, however, to provide a reference condition allowing to better understand the role of other factors, such as the dielectric constant, on the reactivity and selectivity in the reactions of metal complexes with biomolecules.[79]

References

[1] Rosenberg, B., Van Camp, L., Krigas, T. **Inhibition of cell division in Escherichia coli by electrolysis products from a platinum electrode** *Nature* 205 (1965) 698–699.

[2] Rosenberg, B., Van Camp, L., Trosko, J.E., Mansour, V.H. **Platinum compounds: A new class of potent antitumour agents** *Nature* 222 (1969) 385–386.

[3] Cohen, S.M., Lippard, S.J. **Cisplatin: From DNA damage to cancer chemotherapy** *Prog. Nucleic Acid Res. Mol. Biol.* 67 (2001) 93-130.

[4] Reedijk, J. **The mechanism of action of platinum antitumor drugs** *Pure Appl. Chem.* 59 (1987) 181-192.

[5] Esposito, B.P., Najjar, R. **Interactions of antitumoral platinum-group metallodrugs with albumin** *Coord. Chem. Rev.* 232 (2002) 137-149.

[6] Casini, A., Reedijk, J. **Interactions of anticancer Pt compounds with proteins: an overlooked topic in medicinal inorganic chemistry?** *Chem. Sci.* 3 (2012) 3135-3144.

[7] Kozelka, J. **Molecular origin of the sequence-dependent kinetics of reactions between cisplatin derivatives and DNA** *Inorg. Chim. Acta* 362 (2009) 651-668.

[8] Davies, M. S.; Berners-Price, S. J.; Hambley, T. W. **Slowing of Cisplatin Aquation in the Presence of DNA but not in the Presence of Phosphate: Improved Understanding of Sequence Selectivity and the Roles of Monoaquated and Diaquated Species in the Binding of Cisplatin to DNA**. *Inorg. Chem.* 39 (2000) 5603–5613.

[9] Johnstone, T.C., Suntharalingam K., Lippard, S.J. **The next generation of platinum drugs: targeted Pt(II) agents, nanoparticle delivery, and Pt(IV) prodrugs** *Chem. Rev.* 116 (2016) 3436–3486.

[10] Harper, B.W., Krause-Heuer, A.M., Grant, M.P., Manohar, M., Garbutcheon-Singh K.B., Aldrich-Wright, J.R. **Advances in Platinum Chemotherapeutics** *Chem. Eur. J.* 16 (2010) 7064–7077.

[11] Wang, D., Lippard, S.J. **Cellular processing of platinum anticancer drugs** *Nat. Rev. Drug Discovery* 4 (2005) 307-320.

[12] Reedijk, J. **New clues for platinum antitumor chemistry: Kinetically controlled metal binding to DNA** *Proc. Nat. Acad. Sci. U.S.A.* 100 (2003) 3611- 3616.

[13] Springer, A., Bürgel, C., Böhrsch, V., Mitrić, R., Bonačić-Koutecký, V., Linscheid, M.W. **The gas-phase chemistry of cis-diammineplatinum(II) complexes: A joint experimental and theoretical study** *ChemPhysChem* 7 (2006) 1779-1785.

[14] De Petris, A., Ciavardini, A., Coletti, C., Re, N., Chiavarino, B., Crestoni, M.E., Fornarini, S. **Vibrational signatures of the naked aqua complexes from platinum(II) anticancer drugs** *J. Phys. Chem. Lett.* 4 (2013) 3631-3635.

[15] Oomens, J., Sartakov, B.G., Meijer, G., von Helden, G. **Gas-phase infrared multiple photon dissociation spectroscopy of mass-selected molecular ions** *Int. J. Mass Spectrom.* 254 (2006) 1–19.

[16] Polfer, N. C. **Infrared multiple photon dissociation spectros- copy of trapped ions** *Chem. Soc. Rev.* 40 (2011) 2211–2221.

[17] Roithova, J. **Characterization of reaction intermediates by ion spectroscopy** *Chem. Soc. Rev.* 41 (2012) 547–559.

[18] Fridgen, T.D. **Infrared consequence spectroscopy of gaseous protonated and metal ion cationized complexes** *Mass Spectrom. Rev.* 28 (2009) 586-607.

[19] Eyler, J. R. **Infrared multiple photon dissociation spectroscopy of ions in penning traps** *Mass Spectrom. Rev.* 28 (2009) 448–467.

[20] MacAleese, L., P. Maitre, P. **Infrared spectroscopy of organometallic ions in the gas phase: From model to real world complexes** *Mass Spectrom. Rev.* 26 (2007) 583-605.

[21] Chiavarino, B., Crestoni, M. E., Fornarini, S., Scuderi, D., Salpin, J. Y. **Interaction of Cisplatin with Adenine and Guanine: A Combined IRMPD, MS/MS, and Theoretical Study** *J. Am. Chem. Soc.* 135 (2013) 1445–1455.

[22] He, C.C., Kimutai, B., Bao, X., Hamlow, L., Zhu, Y., Strobehn, S.F., Gao, J., Berden, G., Oomens, J., Chow, C.S., Rodgers, M.T. **Evaluation of hybrid theoretical approaches for structural determination of a glycine-linked cisplatin derivative via infrared multiple photon dissociation (IRMPD) action spectroscopy** *J. Phys. Chem. A* 119 (2015) 10980-10987.

[23] Richens, T. **Ligand substitution reactions at inorganic centers** Chem. Rev., 2005, 105, 1961-2002

[24] Belluco, U., Cattalini, L., Basolo, F., Pearson, R.G., Turco, A. **Nucleophilic constants and substrate discrimination factors for substitution reactions of platinum(II) complexes** *J. Am. Chem. Soc.* 87 (1965) 241-246.

[25] Pitteri, B., Canovese, L., Chessa, G., Marangoni, G., Uguagliati, P. **Nucleophilic reactivity in substitution reactions at planar tetra-coordinate monocationic platinum(II) complexes. Kinetics of displacement of chloride from chloro[2,6-bis(methylthiomethyl)pyridine]platinum(II) cation** *Polyhedron* 11 (1992) 2363-2373.

[26] Dong, S., Shi, W., Zhang, J., Bi, S. **Theoretical studies of the formation mechanisms, thermodynamic stabilities, and water-exchange reactivities of aluminum-salicylate complexes in aqueous solution** *ACS Earth Space Chem.* 2 (2018) 422-431.

[27] Szabó, Z., Glaser, J., Grenthe, I. **Kinetics of ligand exchange reactions for uranyl(2+) fluoride complexes in aqueous solution** *Inorg. Chem.* 35 (1996) 2036-2044.

[28] Lemaire, J., Boissel, P., Heninger, M., Mauclaire, G., Bellec, G., Mestdagh, H., Simon, A., Le Caer, S., Ortega, J.M., Glotin, F., Maitre, P. **Gas phase infrared spectroscopy of selectively prepared ions** *Phys. Rev. Lett.* 89 (2002) 273002.

[29] Bakker, J.M., Besson, T., Lemaire, J., Scuderi, D., Maître, P. **Gas-phase structure of a -allyl-palladium complex: efficient infrared spectroscopy in a 7 T Fourier transform mass spectrometer** *J. Phys. Chem. A* 111 (2007) 13415-13424.

[30] Sinha, P., Boesch, S.E., Gu, C., Wheeler R.A., Wilson, A.K. **Harmonic vibrational frequencies: Scaling factors for HF, B3LYP, and MP2 methods in combination with correlation consistent basis sets** *J. Phys. Chem. A* 108 (2004) 9213-9217.

[31] Filippi, A., Fraschetti, C., Piccirillo, S., Rondino, F., Botta, B., D'Acquarica, I., Calcaterra, A., Speranza, M. **Chirality effects on the IRMPD spectra of basket resorcinarene/nucleoside complexes** *Chem. Eur. J.* 18 (2012) 8320-8328.

[32] Prell, J. S., O'Brien, J. T., Williams, E. R. **IRPD spectroscopy and ensemble measurements: Effects of different data acquisition and analysis methods** *J. Am. Soc. Mass Spectrom.* 21 (2010) 800–809.

[33] Angelelli, F., Chiavarino, B., Crestoni, M.E., Fornarini, S. **Binding of gaseous Fe(III)-heme cation to model biological molecules: Direct association and ligand transfer reactions** *J. Am. Soc. Mass Spectrom.* 16 (2005) 589-598.

[34] Su, T., Chesnavich, W.J. **Parametrization of the ion–polar molecule collision rate constant by trajectory calculations** *J. Chem. Phys.* 76 (1982) 5183-5185.

[35] Frisch, M. J.; Trucks, G. W.; Schlegel, H. B.; Scuseria, G. E.; Robb, M. A.; Cheeseman, J. R.; Montgomery, J. A., Jr.; Vreven, T.; Kudin, K. N.; Burant, J. C.; Millam, J. M.; Iyengar, S. S.; Tomasi, J.; Barone, V.; Mennucci, B.; Cossi, M.; Scalmani, G.; Rega, N.; Petersson, G. A.; Nakatsuji, H.; Hada, M.; Ehara, M.; Toyota, K.; Fukuda, R.; Hasegawa, J.; Ishida, M.; Nakajima, T.; Honda, Y.; Kitao, O.; Nakai, H.; Klene, M.; Li, X.; Knox, J. E.; Hratchian, H. P.; Cross, J. B.; Bakken, V.; Adamo, C.; Jaramillo, J.; Gomperts, R.; Stratmann, R. E.; Yazyev, O.; Austin, A. J.; Cammi, R.; Pomelli, C.; Ochterski, J. W.; Ayala, P. Y.; Morokuma, K.; Voth, G. A.; Salvador, P.; Dannenberg, J. J.; Zakrzewski, V. G.; Dapprich, S.; Daniels, A. D.; Strain, M. C.; Farkas, O.; Malick, D. K.; Rabuck, A. D.; Raghavachari, K.; Foresman, J. B.; Ortiz, J. V.; Cui, Q.; Baboul, A. G.; Clifford, S.; Cioslowski, J.; Stefanov, B. B.; Liu, G.; Liashenko, A.; Piskorz, P.; Komaromi, I.; Martin, R. L.; Fox, D. J.; Keith, T.; Al-Laham, M. A.; Peng, C. Y.; Nanayakkara, A.; Challacombe, M.; Gill, P. M. W.; Johnson, B.; Chen, W.; Wong, M. W.; Gonzalez, C.; Pople, J. A. *Gaussian 03, revision D.01* (2004) Gaussian, Inc.: Wallingford, CT.

[36] Bouchet, A., Schütz, M., Chiavarino, B., Crestoni, M.E., Fornarini, S., Dopfer, O. **IR spectrum of the protonated neurotransmitter 2-phenylethylamine: dispersion and anharmonicity of the NH 3 + –π interaction** *Phys. Chem. Chem. Phys.* 17 (2015) 25742-25754.

[37] Chiavarino, B., Crestoni, M.E., Fornarini, S., Lanucara, F., Lemaire, J., Maitre, P., Scuderi, D. **Direct probe of NO vibration in the naked ferric heme nitrosyl complex** *ChemPhysChem* 9 (2008) 826-828.

[38] Lanucara, F., Crestoni, M.E., Chiavarino, B., Fornarini, S., Hernandez, O., Scuderi, D., Maitre, P**. Infrared spectroscopy of nucleotides in the gas phase 2. The protonated cyclic 3',5'-adenosine monophosphate** *RSC Adv.* 3 (2013) 12711-12720

[39] Nei, Y.W., Hallowita, N., Steill, J.D., Oomens, J., Rodgers, M.T. **Infrared multiple photon dissociation action spectroscopy of deprotonated DNA mononucleotides: gas-phase conformations and energetics** *J. Phys. Chem. A* 117 (2013) 1319-1335.

[40] Correia, C.F., Balaj, P.O., Scuderi, D., Maitre, P., Ohanessian, G. **Vibrational signatures of protonated, phosphorylated amino acids in the gas phase** *J. Am. Chem. Soc.* 130 (2008) 3359-3370.

[41] Scuderi, D., Correia, C.F., Balaj, O.P., Ohanessian, G., Lemaire, J., Maitre, P. **Structural characterization by irmpd spectroscopy and DFT calculations of deprotonated phosphorylated amino acids in the gas phase** *ChemPhysChem* 10 (2009) 1630-1641.

[42] Correia, C.F., Clavaguera, C., Erlekam, U., Scuderi, D., Ohanessian, G. **IRMPD spectroscopy of a protonated, phosphorylated dipeptide** *ChemPhysChem* 9 (2008) 2564-2573

[43] Chiavarino, B., Crestoni, M.E., Fornarini, S., Scuderi, D., Salpin, J.-Y. **Interaction of cisplatin with 5'-dGMP: a combined IRMPD and theoretical study** *Inorg. Chem.* 54 (2015) 3513-3522.

[44] Chai, J.-D., Head-Gordon, M. **Long-range corrected hybrid density functionals with damped atom–atom dispersion corrections** *Phys. Chem. Chem. Phys.* 10 (2008) 6615-6620.

[45] Minenkov, Y., Singstad, A., Occhipinti, G., Jensen, V.R. **The accuracy of DFT-optimized geometries of functional transition metal compounds: a validation study of catalysts for olefin metathesis and other reactions in the homogeneous phase** *Dalton Trans.* 41 (2012) 5526-5541.

[46] Turecek, F., Moss, C.L., Pikalov, I., Pepin, R., Gulyuz, K., Polfer, N.C., Bush, M.F., Brown, J., Williams, J., Richardson, K. **Gas-phase structures of phosphopeptide ions: A difficult case** *Int. J. Mass Spectrom.* 354 (2013) 249-256.

[47] Chiavarino, B., Crestoni, M.E., Schütz, M., Bouchet, A., Piccirillo, S., Steinmetz, V., Dopfer, O., Fornarini, S. **Cation-π interactions in protonated phenylalkylamines** *J. Phys. Chem. A* 118 (2014) 7130–7138.

[48] Heine, N., Yacovitch, T.I., Schubert, F., Brieger, C., Neumark D.M., Asmis, K.R. **Infrared photodissociation spectroscopy of microhydrated nitrate–nitric acid clusters NO_3^- $(HNO_3)_m(H_2O)_n$** *J. Phys. Chem. A* 118 (2014) 7613-7622.

[49] Appleton, T.G. **Donor atom preferences in complexes of platinum and palladium with amino acids and related molecules** *Coord. Chem. Rev.* 166 (1997) 313–359.

[50] Ferraro, G., Messori, L., Merlino, A. **The X-ray structure of the primary adducts formed in the reaction between cisplatin and cytochrome c** *Chem. Commun.* 51 (2015) 2559-2561.

[51] Li, H., Zhao, Y., Phillips, H.I., Qi, Y., Lin, T.Y., Sadler, P.J., O'Connor, P.B. **Mass spectrometry evidence for cisplatin as a protein cross-linking reagent** *Anal. Chem.* 83 (2011) 5369-5376.

[52] Battle, A.R., Platts, J.A., Hambley, T.W., Deacon, G.B. **Synthesis, spectroscopy, and theoretical studies of platinum(II) phosphate complexes** *J. Chem. Soc. Dalton Trans.* 9 (2002) 1898-1902.

[53] Appleton, T.G., Berry, R.D., Davis, C.A., Hall, J.R., Kimlin, H.A. **Reactions of platinum(II) aqua complexes. 1. Multinuclear (^{195}Pt, ^{15}N, and ^{31}P) NMR study of reactions between**

the cis-diamminediaquaplatinum(ii) cation and the oxygen-donor ligands hydroxide, perchlorate, nitrate, sulfate, phosphate, and acetate *Inorg. Chem.* 23 (1984) 3514-3521.

[54] Bose, R.N., Moghaddas, S., Goswami, N. **Phosphato complexes of platinum(II): phosphorus-31 nmr and kinetics of formation and isomerization studies** *Inorg. Chem.* 29 (1990) 3461-3467.

[55] Bugarcic, Z.D., Bogojeski, J., Petrovic, B., Hochreuther, S., van Eldik, R. **Mechanistic studies on the reactions of platinum(II) complexes with nitrogen and sulfur-donor biomolecules** *Dalton Trans.* 41 (2012) 12329–12345.

[56] Vinje, J., Sletten, E., Kozelka, J. **Influence of dT$_{20}$ and [d(AT)$_{10}$]$_2$ on cisplatin hydrolysis studied by two-dimensional [^{1}H,^{15}N] HMQC NMR spectroscopy** *Chem. Eur. J.* 11 (2005) 3863-3871.

[57] Pinato, O., Musetti, C., Farrell, N.P., Sissi, C. **Platinum-based drugs and proteins: Reactivity and relevance to DNA adduct formation** *J. Inorg. Biochem.* 2013, 122, 27-37.

[58] Chabinyc, M.L., Craig, S.L., Regan, C.K., Brauman, J.I. **Gas-phase ionic reactions: Dynamics and mechanism of nucleophilic displacements** *Science* 279 (1998) 1882-1886.

[59] Gronert, S. **Mass spectrometric studies of organic ion/molecule reactions** *Chem. Rev.* 101 (2001) 329-360.

[60] Zehnacker, A. **Chirality effects in gas-phase spectroscopy and photophysics of molecular and ionic complexes: contribution of low and room temperature studies** *Int. Rev. Phys. Chem.* 33 (2014) 151-207.

[61] Voronina, L., Rizzo, T.R. **Spectroscopic studies of kinetically trapped conformations in the gas phase: the case of triply protonated bradykinin** *Phys. Chem. Chem. Phys.* 17 (2015) 25828-25836.

[62] Wee, S., O'Hair, R.A.J., McFadyen, W.D. **Gas-phase ligand loss and ligand substitution reactions of platinum(II) complexes of tridentate nitrogen donor ligands** *Rapid Comm. Mass Spectrom.* 18 (2004) 1221-1226.

[63] Lo, W.K.C., Cavigliasso, G., Stranger, R., Crowley, J.D., Blackman, A.G. **Five-coordinate [Pt^{II}(bipyridine)$_2$(phosphine)] $^{n+}$ complexes: Long-lived intermediates in ligand substitution reactions of [Pt(bipyridine)$_2$]$^{2+}$ with phosphine ligands** *Inorg. Chem.* 53 (2014) 3595-3605.

[64] Cross, R.J. **Ligand substitution reactions of square-planar molecules** *Chem. Soc. Rev.* 14 (1985) 197-223.

[65] Bergès, J., Fourré, I., Pilmé, J., Kozelka, J. **Quantum chemical topology study of the water-platinum(II) interaction** *Inorg. Chem.* 52, (2013) 1217-1227.

[66] Jalilehvand, F., Laffin, L.J. **Structure of the hydrated platinum(II) ion and the cis-diammineplatinum(II) complex in acidic aqueous solution: an EXAFS study** *Inorg. Chem.* 47 (2008) 3248-3254.

[67] Kocsis, L., Mink, J., Jalilehvand, F., Laffin, L.J., Berkesi, O., Hajba, L. **Vibrational spectroscopic study of the hydrated platinum(II), palladium(II) and cis-diammineplatinum(II) ions in acidic aqueous solutions** *J. Raman Spectr.* 40 (2009) 481-490.

[68] Sanchez-de-Armas, R., Ahlquist, M.S.G. **On the nature of hydrogen bonds to platinum(II) – which interaction can predict their strength?** *Phys. Chem. Chem. Phys.* 17 (2015) 812.

[69] Baya, M., Belío, U., Martín, A. **Synthesis, characterization, and computational study of complexes containing Pt···H hydrogen bonding interactions** *Inorg. Chem.* 53 (2014) 189-200.

[70] Kozelka, J., Berges, J., Attias, R., Fraitag, J. **O-H···Pt(II): Hydrogen bond with a strong dispersion component** *Angew. Chem. Int. Ed.* 39 (2000) 198-201.

[71] Hamilton, S.M., Hopkins, W.S., Harding, D.J., Walsh, T.R., Haertelt, M., Kerpal, C., Gruene, P., Meijer, G., Fielicke, A., MacKenzie, S.R. **Infrared-induced reactivity of N2O on small gas-phase rhodium clusters** *J. Phys. Chem. A* 115 (2011) 2489-2497.

[72] Harding, D.J., Fielicke, A. **Platinum group metal clusters: From gas-phase structures and reactivities towards model catalysts** *Chem. Eur. J.* 20 (2014) 3258-3267.

[73] Olmstead, W.N., Brauman, J.I. **Gas-phase nucleophilic displacement reactions** *J. Am. Chem. Soc.* 99 (1977) 4219-4228.

[74] Berners-Price, S. J.; Appleton, T. G. **The Chemistry of Cisplatin in Aqueous Solution. In Platinum-Based Drugs in Cancer Therapy** in Platinum-Based Drugs in Cancer Therapy, Kelland, L. R., Farrell, N., Eds.; Humana Press: Totowa, NJ, (2000) 3-35.

[75] White, J.D., Haley, M.M. DeRose, V.J. **Multifunctional Pt(II) Reagents: Covalent Modifications of Pt Complexes Enable Diverse Structural Variation and In-Cell Detection** *Acc. Chem. Res.* 49 (2016) 56–66.

[76] Lau, J.K.-C., Deubel, D.V. **Hydrolysis of the anticancer drug cisplatin: Pitfalls in the interpretation of quantum chemical calculations** *J. Chem. Theory Comput.* 2 (2006) 103-106.

[77] Zhang, Y., Guo, Z., You, X.-Z. **Hydrolysis theory for cisplatin and its analogues based on density functional studies** *J. Am. Chem. Soc.* 123 (2001) 9378-9387.

[78] Ciancetta, A., Coletti, C., Marrone, A., Re, N. **Activation of carboplatin by carbonate: a theoretical investigation** *Dalton Trans.* 41 (2012) 12960–12969.

[79] Deubel, D.V. **Factors governing the kinetic competition of nitrogen and sulfur ligands in cisplatin binding to biological targets** *J. Am. Chem. Soc.* 126 (2004) 5999-6004.

Elusive primary complexes of cisplatin with aminoacids: exploiting IRMPD kinetics to assay isomer composition

4.1 Introduction

The cisplatin mechanism of action nowadays is well understood, as explained in sections 1.2 and 3.1. In particular, cisplatin interaction with DNA to form 1,2-intrastrand cross links leading to distortion of the DNA helix and eventually causing apoptosis of the cancer cell has been extensively studied.[1-6] Fewer details are available on the interaction of cisplatin with other molecules in the biological medium. Indeed, cisplatin has been found to bind to a variety of biological targets,[7] notably amino acid residues in peptides and proteins.[8,9] Some data indicate that cisplatin interaction with proteins, held responsible for toxic side effects, may also account for antitumor activity.[8] In this scenario, we have exploited ESI-MS to extract to the gas-phase the primary ionic intermediates for the reaction of cisplatin with histidine (section 4.3) and of both cisplatin and its isomer transplatin with methionine (section 4.4) as they are formed in aqueous solution. In fact, residues of L-histidine (His) and L-methionine (Met) are among the most important binding sites of cisplatin in proteins.[10-12]

Studies in solution have highlighted the interaction of cisplatin with His to yield a variety of compounds in which His is coordinated to the metal via an imino N or amino N atom.[13] The His donor atom for diammine Pt^{II} complexes may also include a carboxylate oxygen and the coordination pattern tends to evolve forming stable chelate complexes.[14] However, the early complex cis-$[PtCl(NH_3)_2(His)]^+$ from the first substitution event, either directly on cisplatin or on the intermediate aqua complex cis-$[PtCl(NH_3)_2(H_2O)]^+$, has never been observed.

The cisplatin reaction with methionine also yields both monodentate and bidentate complexes, the latter ones formed by subsequent ligand exchange steps.[15,16] However, the monofunctional *cis*-$[PtCl(NH_3)_2Met]^+$ complex, namely the key intermediate primarily formed in aqueous solution, has been postulated or observed only as a minor component in reaction mixtures.[17,18] The interaction of hydrated cisplatin complexes, *cis*-$[PtCl(NH_3)_2(H_2O)]^+$ and cis-$[Pt(OH)(NH_3)_2(H_2O)]^+$,

with methionine has been examined with the polarizable continuum model suggesting a two-step reaction mechanism.[19-21] In the first one the aqua ligand is replaced by one of the three active amino acid sites (N, O, or S), and, in the second one, dissociation occurs to form a chelate complex releasing water or chloride anion. The thermodynamics of the reaction with methionine are reported to depend on the cisplatin hydration state. The formation of κ(S) monodentate complexes is favored in the hydroxo complex while κ(N) coordination is preferable in the monohydrated chloro complex. A similar (but less pronounced) selectivity was observed also in computations referring to the gas phase.[22]

4.2 Experimental details

4.2.1 Sample preparation

Cisplatin, transplatin, L-histidine and L-methionine used in this work were research grade products from commercial sources (Sigma-Aldrich s.r.l. Milan, Italy) and were used without additional purification. In order to produce the complexes of interest, stock aqueous solutions of L-histidine ,L-methionine and of either of the two platinum compounds were prepared at 10^{-3}M concentration, appropriately mixed in 1:1 molar ratio and diluted with water and methanol to reach a final concentration of $5 \cdot 10^{-5}$ M and a methanol/water ratio of (1:1 v/v). Cis- and transplatin solutions have been allowed to stand 24h prior to use.

4.2.2 Mass spectrometric experiments

The solutions were submitted to electrospray ionization (ESI) by direct infusion using a syringe pump at a typical flow rate of 180 µL h^{-1}. Mass spectra and collision induced dissociation (CID) experiments have been recorded on a hybrid triple quadrupole linear ion trap mass spectrometer (2000 Q-TRAP Applied Biosystems.[23] In this instrument the ESI conditions employed were: curtain gas at 20.0 psi, ion source gas at 20.0 psi, declustering potential at 80 V and entrance potential at 8 V. Nitrogen was used as collision gas at a nominal pressure of 2.7 10^{-5} mbar. Moderate changes (by a factor of five) in the pressure of the collision gas do not significantly affect the fragmentation behavior, suggesting prevailing single collision conditions. High resolution mass analysis of the isotopic pattern of Pt and Cl corresponding to cis-[PtCl(NH$_3$)$_2$(His)]$^+$ ions was acquired using a 7T SolariX hybrid Fourier transform - ion cyclotron resonance (FT-ICR) mass spectrometer (Bruker Daltonics, Bremen, Germany) sited at the Laboratoire de Chimie Moléculaire, École Polytechnique, Palaiseau, France. Elemental compositions for all peaks were obtained using the instrument software DataAnalysis and characterized by a tolerance below 5 ppm.

4.2.3 IRMPD spectroscopy and ion mobility experiments

IRMPD experiments have been carried out using two instrumental setups, covering different wavenumber ranges. The first one comprises the IR fingerprint region (650-1900 cm^{-1}). IRMPD spectra were recorded using the beamline of the IR free

electron laser (FEL) of the Centre Laser Infrarouge d'Orsay (CLIO). For the present studies, the electron energy of the FEL was set at 38 and 44 MeV in two separate runs, in order to optimize the laser power in the frequency regions of interest. In the FEL-based experiments the IR beamline was coupled with two different instrument: a commercial ion trap mass spectrometer (Bruker Esquire 3000+)[24] for the cisplatin-methionine experiment; and a hybrid FT-ICR tandem mass spectrometer (APEX-Qe Bruker Daltonics),[25] equipped with a 7.0 T actively shielded magnet and a quadrupole–hexapole interface for mass-filtering and ion accumulation, under the control of the commercial software APEX 1.0 to analyze the cisplatin complex with histidine. In the ion trap, the charged complexes of interest are accumulated for 5 ms and mass selected prior to IR irradiation. The isolated cis-[PtCl(NH$_3$)$_2$(Met)]$^+$complexes were irradiated for 0.5 s with the IR FEL light, after which the resulting mass spectrum was recorded. Regarding cis-[PtCl(NH$_3$)$_2$(His)]$^+$, the complex was mass selected in the quadrupole and accumulated for 1.0 s in the hexapole, containing Argon as buffer gas, in order to cool it prior to its transfer into the ICR cell. The isolated ions were then irradiated for 250-500 ms with the IR FEL light and the products of the excitation were mass analyzed.

The second wavenumber range is pertinent to the vibrational modes associated with the X-H (X=C,N,O) bond stretches which have been investigated by recording IRMPD spectra in the 2900-3700 cm^{-1} region. This spectral range is of particular interest for probing the vibrational features associated with stretches involved in hydrogen bonding motifs. Tunable infrared radiation used in this range is generated by a KTP/KTA optical parametric oscillator/amplifier system (OPO/OPA, Laser Vision) pumped by a non seeded Nd:YAG laser (Continuum Surelite II). The laser system is coupled to an ion trap mass spectrometer (Esquire 6000+, Bruker Daltonics), as previously described.[26] The typical output energy from the OPO/OPA laser was 20-25 mJ/pulse in the investigated spectral range with 3-4 cm^{-1} bandwidth. In the trap, ions were mass-selected and accumulated for 15 ms prior to IR irradiation. The irradiation time used in the experiment is 2 s.

IRMPD spectra are obtained by plotting the photofragmentation yield R (R = -ln[I_{parent}/(I_{parent} + $\Sigma I_{fragment}$)]), where I_{parent} and $I_{fragment}$ are the integrated intensities of the mass peaks of the precursor and of the fragment ions, respectively) as a function of the frequency of the IR radiation.

Ion mobility (IM) experiments were conducted on a Waters Synapt G2-S mass spectrometer. Samples were ionized using a nanoESI source in positive mode with a capillary voltage of 1.4 kV and source temperature at 60° C. As the sampled complexes are very prone to fragmentation, soft tuning parameters were employed for the experiment. The sampling cone was fixed at 15V. Trap entrance DC and Trap Bias voltages were respectively set to 0V and 25V and the T-Wave amplitude was lowered to 29V in the TWIMS region. MassLynx v4.1 software (Waters Corporation, USA) was used for data analysis.

4.2.4 Computational details
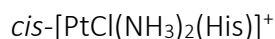
cis-[PtCl(NH$_3$)$_2$(His)]$^+$

An exploration of the conformer distribution for plausible isomers of *cis*-[PtCl(NH$_3$)$_2$(His)]$^+$ was made using a Monte Carlo search following a path that biases in favor of low energy conformers and employing the semi-empirical method PM6 .[27] The tool Conformer Distribution as implemented in the software suite Spartan'10 was used. The low energy conformers have been re-optimized using the Gaussian 09 Rev D.01 package at the B3LYP/6-311+G** level of theory.[28-30] In order to take into account relativistic effects the LanL2TZ effective core potential (ECP)), that contains the LANL2 relativistic ECP of Hay and Wadt and a flexible triple-zeta basis set, was used for the platinum atom in all the calculations.[31] Subsequently, the whole set of geometries was submitted to computations of the harmonic vibrational frequency, in order to obtain linear IR spectra and thermodynamic data. The analysis of the vibrational frequencies is used to characterize the optimized structures as local minima, if no imaginary frequencies are present, or as transition state (with one imaginary frequency corresponding to the motion along the reaction coordinate). Moreover, selected geometries were submitted to anharmonic vibrational analysis according to vibrational perturbation theory at the

second order, VPT2, as implemented in Gaussian09,[32] to account for anharmonicity effects that may affect in particular vibrational modes characteristic of H-bonded molecular groups. Calculated anharmonic frequencies are presented unscaled.

A Gaussian shape, having a fwhm of 20 cm^{-1} in the fingerprint range and of 5 cm^{-1} in the X-H stretching range, was adopted to simulate the experimental spectrum.

Low-lying conformers of the selected isomers have been re-optimized using the ωB97X-D and B3LYP-D3 functionals and the same basis set used above, in order to include the contribution of dispersion effects. In particular the ωB97X-D has proven to be a proper tool to calculate the energies and geometries of platinum complexes.[33] In order to obtain thermal corrections, harmonic vibrational frequencies of the newly optimized geometries have been calculated at the same level. Single point energy calculations were also performed on selected geometries at the MP2/cc-pVTZ level of theory using cc-pVTZ-PP as pseudopotential for the platinum atom in order to evaluate the importance of correlation energy with post-Hartree-Fock methods. MP2 thermodynamic parameters were obtained by using B3LYP-derived thermal corrections, thus yielding MP2/cc-pVTZ(-PP)//B3LYP/6-311+G(d,p) data.

cis-[PtCl(NH$_3$)$_2$(Met)]$^+$

For both isomers, *cis*-[PtCl(NH$_3$)$_2$Met]$^+$ and *trans*-[PtCl(NH$_3$)$_2$Met]$^+$, a conformational search was performed using the Multiple Minimum Monte Carlo (MMMC) method with AMBER FF, implemented in Macromodel 9.6.[34] For each isomer, similar conformations were grouped and their representative structures were minimized at B3LYP/6-311+G(d,p) level of theory, using the pseudopotential LANL2DZ for platinum. Then, a visual inspection was performed in order to devise additional conformers that may have escaped from the conformational search.

Thermodynamic properties (electronic energy values, zero point energy (ZPE) and thermal corrections, entropies and free energies) and harmonic frequencies were calculated at B3LYP level of theory using a combined basis set, hereafter indicated as BS1, consisting of the 6-311++G(3df) basis set for the sulfur atom and 6-311++G(2df,pd) for the remaining atoms, except platinum, for which the pseudopotential LANL2TZ-f was adopted. Anharmonic corrections to frequencies

128

were evaluated at the same level of theory, using second order perturbation theory, VPT2.[32] Only active modes falling in the range of the experimental spectra, namely 800-2000 cm^{-1} for the CLIO region and 2700-3800 cm^{-1} for the OPO/OPA region, were included in the latter calculation.

All the calculated spectra were obtained using anharmonic unscaled frequencies and harmonic intensities and convoluted assuming a Gaussian profile with associated width (FWHM) of 15 cm^{-1} in the 800-2000 cm^{-1} frequency range and 5 cm^{-1} in the 2700-3800 cm^{-1} interval.

All quantum chemical calculations were performed with the Gaussian09 package.[28]

4.3 Interaction of cisplatin with histidine: kinetically trapped isomers quantified by photofragmentation kinetics

The following discussion has been adapted from the paper published in ChemPhysChem:

I have personally contributed to the work performing the CID and IRMPD spectroscopy experiments, including photofragmentation kinetics. I have also prepared and evaluated the theoretical data. Ion mobility measurement were done by myself at The University of Manchester in the laboratories of Prof. Perdita Barran in the framework of a PhD mobility program by Sapienza Università di Roma.

4.3.1 Mass spectrometric characterization of *cis*-[PtCl(NH$_3$)$_2$(His)]$^+$

cis-[PtCl(NH$_3$)$_2$(His)]$^+$ complexes are directly revealed by ESI-MS as distinct ionic products from the reaction of cisplatin and His (mass spectrum shown in figure 4.1). The isotopic cluster at *m/z* 418 conforms to the calculated distribution as shown by the inset in figure 4.1.
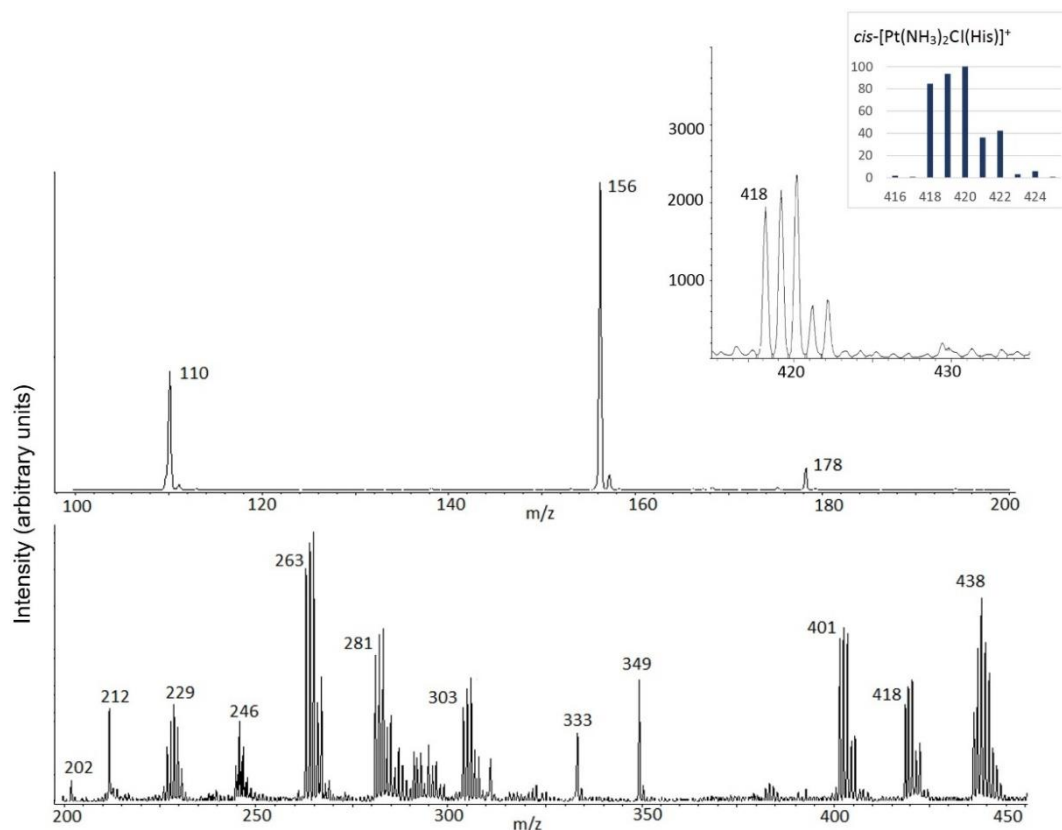
Figure 4.1 Mass spectrum of a solution of cisplatin and His (1:1) 5×10^{-5} M in methanol/water (50/50, v/v) recorded with an Esquire 6000 ion trap mass spectrometer. The species of interest, the *cis*-[PtCl(NH$_3$)$_2$His]$^+$ complex, corresponds to the cluster at *m/z* 418. The signals at *m/z* 110, 156, 178, 333 and 349 are related to His (e. g. *m/z* 156 is protonated His) while other signals belong to hydrolyzed cisplatin (e. g. *m/z* 281 is the *cis*-[PtCl(NH$_3$)$_2$(H$_2$O)]$^+$ complex) and other Pt complexes.

The assignment is further verified by high resolution mass analysis confirming the elemental composition of the sampled ion as illustrated in figure 4.2.
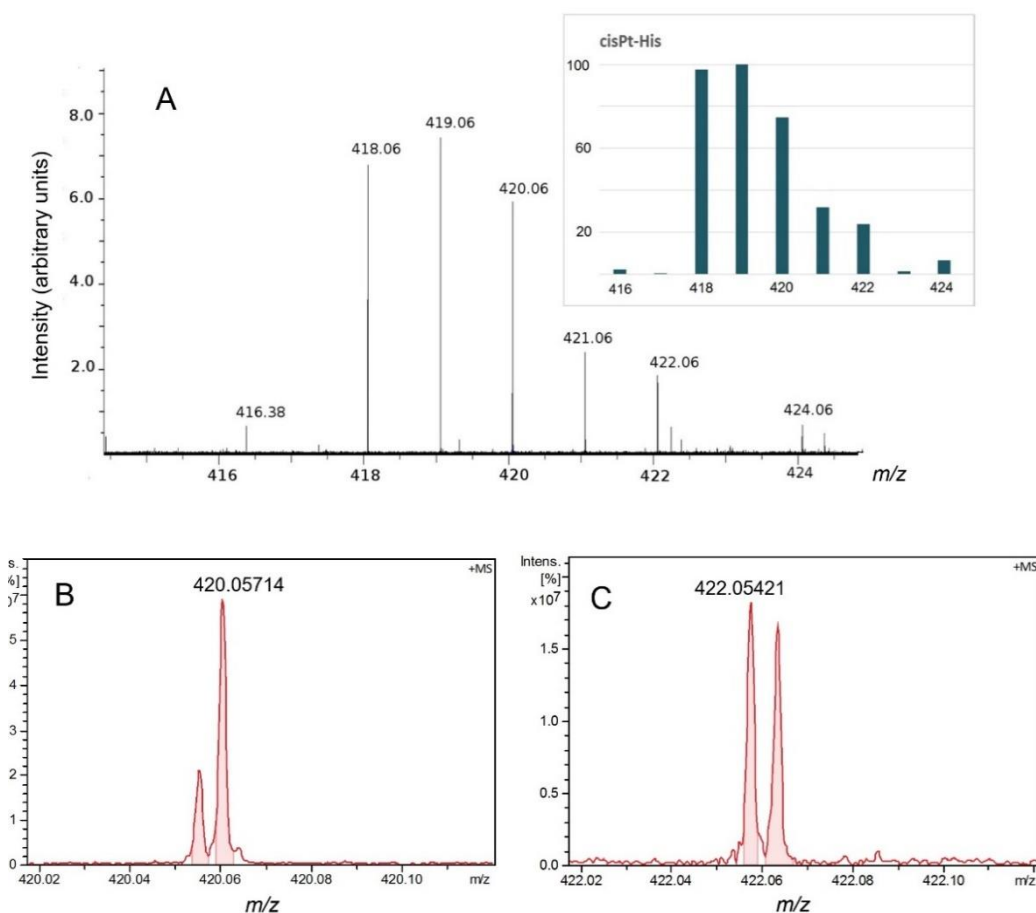
Figure 4.2 Excerpt of the mass spectrum of a solution of cisplatin and His recorded with a 7 T FT-ICR instrument showing the cluster at *m/z* 418 (panel A). The *cis*-[PtCl(NH$_3$)$_2$His]$^+$ complex yields an isotopic cluster at *m/z* 418 whose 'shape' is different from the same cluster recorded at lower resolution shown in the inset of figure 4.1. This effect, well accounted for in the calculated peak profile shown in the inset of panel A, is due to the baseline separation of formally isobaric ions, for example the ion at nominal *m/z* 420 is resolved into distinct peaks for [^{194}Pt^{37}Cl(NH$_3$)$_2$His]$^+$ and [^{196}Pt^{35}Cl(NH$_3$)$_2$His]$^+$ (B). The experimental mass of 420.05714 for [^{196}Pt^{35}Cl(NH$_3$)$_2$His]$^+$ is within 2 ppm of the calculated mass of 420.056375 Da for the ^{196}Pt^{35}Cl^{12}C$_6$H$_{15}$^{16}O$_2$^{14}N$_5$ chemical composition, thus confirming the assigned formula of the sampled ion. Another example is shown in the enlarged excerpt of panel C with baseline resolved peaks for the two isotopomers at *m/z* 422, namely [^{198}Pt^{35}Cl(NH$_3$)$_2$His]$^+$ and [^{196}Pt^{37}Cl(NH$_3$)$_2$His]$^+$.

In order to further ascertain the ion composition, collision induced dissociation experiments have been performed delivering variable energy to activate fragmentation in the intermediate collision sector of a triple quadrupole instrument. The prevailing dissociation channel involves loss of NH$_3$. Interestingly,

however, the sampled *cis*-[PtCl(NH$_3$)$_2$(His)]$^+$ ions display a dual behavior, as shown in figure 4.3. A fraction shows prompt fragmentation with NH$_3$ loss occurring already in the region preceding the collision quadrupole while a second component in the ion population is fairly resistant to dissociation.
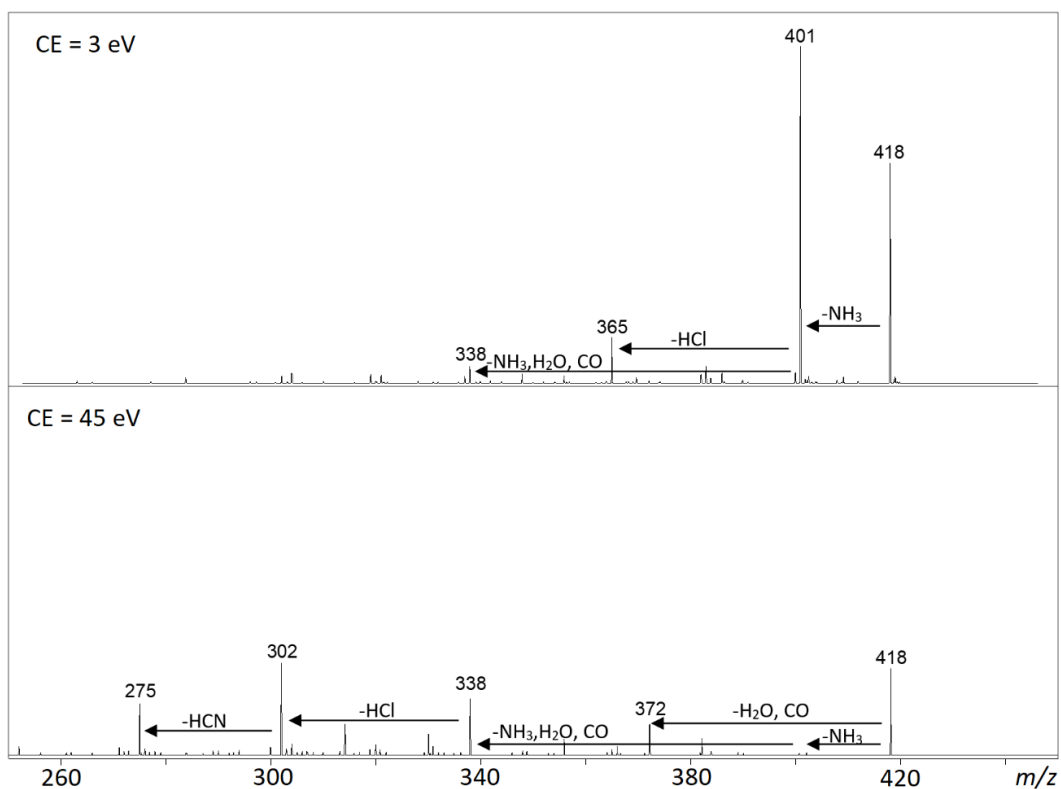
Figure 4.3 Collision induced dissociation mass spectra of selected *cis*-[PtCl(NH$_3$)$_2$His]$^+$ ions at m/z 418 obtained at a minimal collision lab energy (CE) of 3 eV (upper panel) and at the considerably higher value of 45 eV (lower panel) in a triple quadrupole mass spectrometer (QTrap API 2000).

As shown in figure 4.3, at minimal CE of 3eV (upper panel) a considerable fraction of *cis*-[PtCl(NH$_3$)$_2$His]$^+$ ions has undergone fragmentation by loss of NH$_3$. However, a sizeable portion of ions at m/z 418 is instead resistant to fragmentation even at collision energy as high as 45 eV (lower panel). This behavior could be indicative of a mixture of isomeric ions. Therefore, we performed ion-mobility measurement employing a Synapt G2-S mass spectrometer equipped with a TWIMS in order to evaluate the transport properties of the ions in a buffer gas, property related to their morphology.[35-37] In figure 4.4 is reported the mobility profile of the isotopic cluster *m/z* 418-422, identified as the ion *cis*-[PtCl(NH$_3$)$_2$(His)]$^+$. The experimental

data show the complex to have a dual behavior, in agreement with the presence of a mixture of at least two isomers in the sampled gas-phase population.
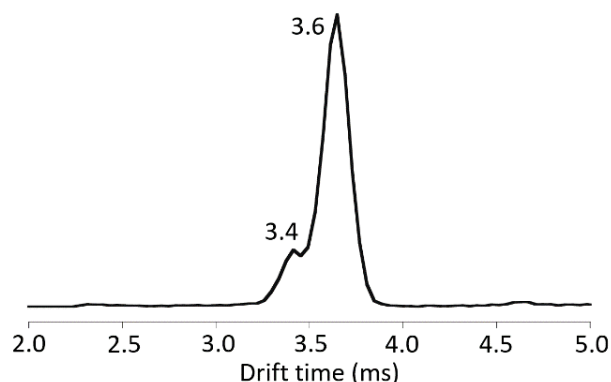
Figure 4.4 Mobility profile of *cis*-[PtCl(NH$_3$)$_2$(His)]$^+$. The arrival time in ms relative to the main peak (3.6) and the observed shoulder (3.4) is reported.

4.3.2 Vibrational features and structural characterization of *cis*-[PtCl(NH$_3$)$_2$(His)]$^+$

Structural characterization of what appears to be a mixture of isomers has been sought relying on the diagnostic power of IR spectroscopy of sampled gaseous ions as obtained by IRMPD spectroscopy supported by quantum chemical calculations.[38-40] Therefore, *cis*-[PtCl(NH$_3$)$_2$(His)]$^+$ ions are examined by IRMPD spectroscopy in two spectral ranges, namely 900-1900 cm^{-1} and 3000-3700 cm^{-1}, using the CLIO FEL and a tabletop OPO/OPA laser system as IR light sources, respectively.[41,42] The analysis of IRMPD spectra is aided by a comprehensive computational survey of the potential structures accounting for the sampled species and their respective calculated IR spectra. The results are illustrated in figure 4.5 where panel A shows the experimental IRMPD spectrum in the two spectral regions. It is worth mentioning that IRMPD recorded in correspondence with active bands in the 900-1900 cm^{-1} 'fingerprint' range grows with irradiation time till almost complete (>95%) depletion of the parent ion abundance, implying good overlap of the laser beam with the ion cloud and efficient IRMPD activity as ensured by the high fluence of the FEL. The situation is different in the OPO/OPA range as illustrated in following paragraphs. Sampling in the 'fingerprint' range then accounts for the overall ion population. The experimental spectrum presents vibrational signatures which find a counterpart in the anharmonic IR spectra calculated for *cis*-[PtCl(NH$_3$)$_2$(His)]$^+$

structures where the metal is coordinated to an imino imidazole nitrogen (figure 4.5 (B-E)).
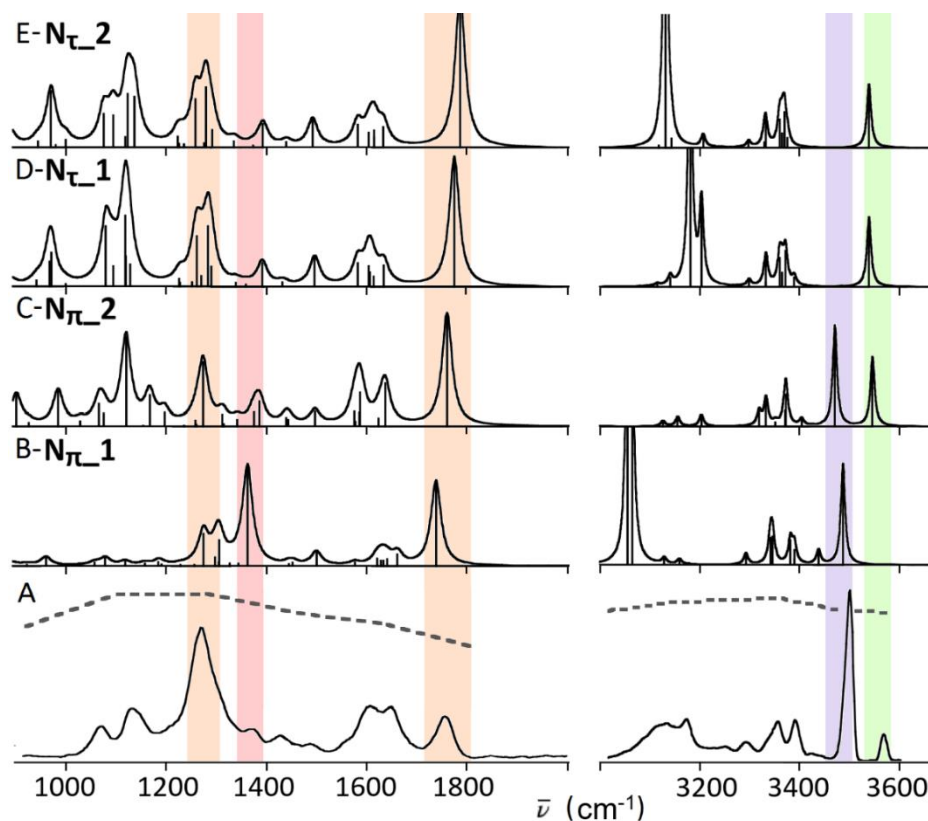
Figure 4.5 IRMPD spectrum of *cis*-[PtCl(NH$_3$)$_2$His]$^+$ (A) compared to the linear anharmonic IR spectra calculated at B3LYP/6-311+G** level of theory for the most stable conformers of N$_\pi$ and N$_\tau$ families of isomers (B-E). The laser power along the recorded IRMPD spectrum is reported as dashed line.

Figure 4.6 shows the optimized geometry of low energy conformers of two possible isomers arising from Pt binding to either one of the two N-atoms of the imidazole group. According to IUPAC recommendations,[43] they are named N$_\pi$ (pros, near) and N$_\tau$ (tele, far), referring to their position relative to the side chain. Quantum chemical calculations have been performed at B3LYP/6-311+G** and also at ωB97X-D/6-311+G** level in order to account for dispersion contributions[44] and results are presented in table 4.1 and table S4.1 in the supporting material (SM).
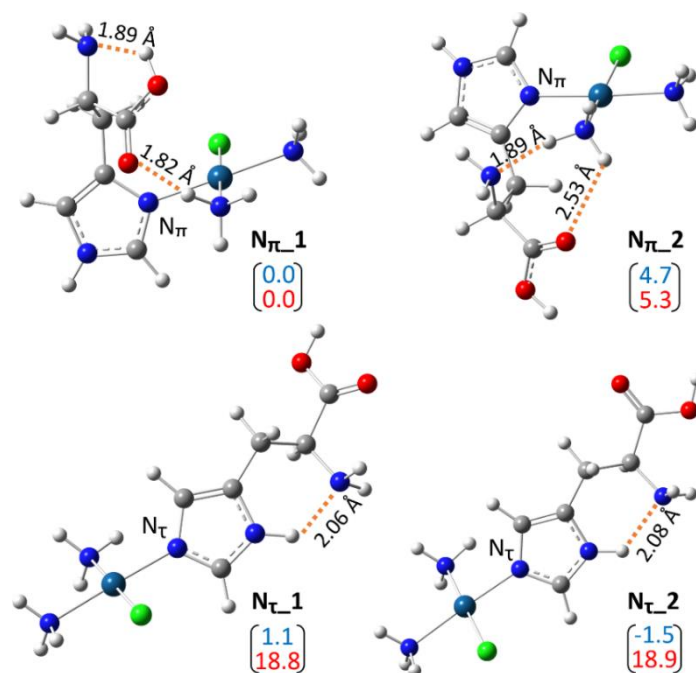
Figure 4.6 Calculated geometries of the most stable conformers of N_π and N_τ isomers of *cis*-[PtCl(NH₃)₂His]⁺. Relative free energies (kJ mol⁻¹) calculated at B3LYP/6-311+G** (blue) and ωB97X-D/6-311+G** (red) level are reported in parentheses.

While the ωB97X-D functional has proven good performances in the interpretation of the thermodynamic and geometrical features of Pt complexes,[33] calculations of vibrational modes employing this functional should be viewed with critical eyes. The harmonic IR spectra calculated at B3LYP/6-311+G** level have been compared with the corresponding ones obtained using the ωB97X-D hybrid functional. While no significant differences are observed (Figure S4.1), the frequency scaling factors (0.940 in the fingerprint range and 0.943 in the X-H stretching range) needed to provide adequate comparison of ωB97X-D calculated modes with the experimental absorptions suggest a poorer performance of the method in matching harmonic with experimental frequencies.

As shown by the data reported in figure 4.6 and table 4.1, the inclusion of dispersion effects tends to widen the relative energy of **N$_\pi$** and **N$_\tau$** isomers, favoring the more folded structures of **N$_\pi$_1** and **N$_\pi$_2**. Thermodynamic data for the lowest energy conformers are reported in table 4.1 while a complete summary for all optimized geometries illustrated in figure S4.2 can be found in table S4.1.

Table 4.1 Thermodynamic parameters for the most stable structures of N_π and N_τ conformers of *cis*-[PtCl(NH$_3$)$_2$(His)]$^+$ calculated at various levels of theory. Relative energies accounting for solvation effects are reported in brackets.

Species	Relative Energy (0K)[a]	Relative Enthalpy[a] (298K)	Relative Free Energy[a] (298K)
B3LYP/6-311+G**			
Nπ_1	0.0	0.0 (0.0)	0.0 (0.0)
Nπ_2	3.4	4.4 (11.6)	4.7 (11.9)
Nτ_1	11.7	11.7 (8.0)	1.1 (-2.5)
Nτ_2	7.9	7.8 (3.7)	-1.5 (-5.6)
ωB97XD/6-311+G**			
Nπ_1	0.0	0.0 (0.0)	0.0 (0.0)
Nπ_2	5.7	6.5 (14.0)	5.3 (12.7)
Nτ_1	33.1	32.1 (24.1)	18.8 (13.9)
Nτ_2	29.8	29.1 (27.6)	18.9 (14.3)
B3LYP-D3/6-311+G**			
Nπ_1	0.0	0.0	0.0
Nπ_2	7.5	8.4	6.5
Nτ_1	34.3	33.9	20.8
Nτ_2	30.6	30.3	18.3
MP2/cc-pVTZ(-PP)//B3LYP/6-311+G**[b]			
Nπ_1	0.0	0.0	0.0
Nπ_2	8.2	9.2	9.5
Nτ_1	29.6	29.5	20.2
Nτ_2	34.3	34.3	23.7

[a] In kJ mol^{-1}. [b] Zero-point energies and thermal corrections from B3LYP/6-311+G** calculations.

The significant effect on relative stability was confirmed employing the B3LYP-D3 functional and also performing single point energy calculations at the MP2/cc-pVTZ(-PP) level of theory on the geometries optimized with B3LYP/6-311+G**. The effect of solvation has also been considered and data accounting for it are given in parenthesis in table 4.1. The inclusion of solvation consistently favors the less folded N_τ isomers with respect to folded N_π species. This finding may could be related to the minor accessibility of N_π isomers to interactions with the solvent thus leading to less stabilization.

It is to be noted, though, that once delivered to the gas-phase by the ESI process, N_π and N_τ isomers are not expected to interconvert due to large isomerization barriers. In fact, an interconversion requires tautomerization of the imidazole unit, involving

migration of a hydrogen atom from one nitrogen to the other. The search for a transition state for a synchronous process has, not unexpectedly, failed. Alternative stepwise isomerization paths require the cleavage of the Pt-bond to the imidazole imino nitrogen atom. The breaking of this bond may be assisted by the amino group attacking the metal in a five-coordinate transition state. The ensuing intermediate then resembles an amino-ligated isomer **N_aH_a** (figure S4.3) which is calculated to lie at ca. 68 kJ mol-1 relative to **N_π_1** (see table S4.1). At this stage, the now freed imidazole group may undergo tautomerization in a process that, due to the absence of any solvent molecules, will require an intramolecular assistance. Thus, the N_π/N_τ isomerization is clearly a high energy process in the sampled isolated complexes. The underlying notion then is that the isomeric population characterized by IRMPD spectroscopy reflects the isomeric composition in solution.

Inspection of the IRMPD spectrum in figure 4.6 A indicates that multiple species need to be involved to account for the observed features. Table S4.2 in the SM lists the observed IRMPD bands together with both the harmonic and the anharmonic vibrational modes calculated for the low energy conformers **N_π_1**, **N_π_2**, **N_τ_1**, and **N_τ_2**, representative of the two families of N_π and N_τ isomers. In the quest for an appropriate matching between the computed and experimental bands we have employed the computationally demanding anharmonic calculations finding a significantly better agreement with the experiment in particular in the NH/OH stretches involved in hydrogen bonding interactions. In the IRMPD spectrum recorded in the fingerprint range, the C=O stretching band at 1755 cm^{-1} is better interpreted by the 1742-1763 cm^{-1} frequencies characteristic for species where the carbonyl group is involved in NH$^+$ ⋯ O=C hydrogen bonding, such as **N_π_1** and **N_π_2**, rather than by the 1778-1789 cm^{-1} values for the nearly unperturbed carboxylic group in **N_τ_1**, and **N_τ_2**. A contribution of the latter species in the tail of the observed band cannot be discarded though. On the basis of the calculated IR spectra one may assign the unresolved bands at 1645 and 1607 cm^{-1} to asymm NH$_3$ bendings, the tiny band at 1492 cm^{-1} to in plane CH bending, the band at 1433 cm^{-1} to imidazole NH in-plane bending, the bands at 1375 cm^{-1} mainly to OH bending of **N_π_1**, the band at 1270 cm^{-1} to NH$_3$ umbrella modes, the band at 1133 cm^{-1} to a

convolution of various modes including CH_2 twist and OH bend, and finally the band

at 1075 cm^{-1} combines CN stretch with imidazole ring deformation modes. It has to

be noted that the pronounced band at 1367 cm^{-1} in the calculated spectrum of

N_π_1, corresponding to the OH bending mode, hardly appears to contribute, at least

in terms of intensity, to the band observed at 1375 cm^{-1} in the IRMPD spectrum.

However, failure of computed spectra to properly describe an OH bending mode

involved in hydrogen bonding has already been noticed in previous works involving

deprotonated and modified aminoacids.[45,46] Possibly, the non-linear character of

the IRMPD process is responsible for this behavior which may arise from disruption

of the H bond, intervening early along the multiple photon absorption sequence

and hampering further resonant excitation. A note may be added about the broad

band at 3125 cm^{-1}. The large width is consistent with the assignment to OH and

asymmetric NH_3 stretching modes involved in hydrogen bonding. However, in this

case the anharmonic frequency calculations appear to overestimate the expected

red shift, an effect which is however documented for hydrogen-bonded OH and

NH.[47,48]
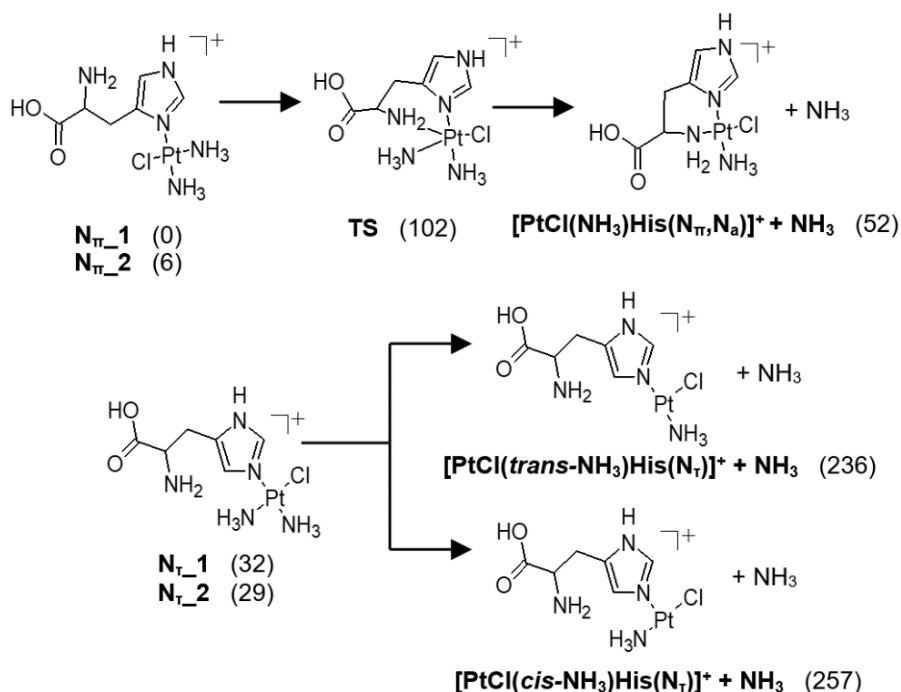
Scheme 4.1 Fragmentation paths for N_π and N_τ isomers. Relative enthalpies at
298 K in kJ mol^{-1} calculated at ωB97X-D/6-311+G** level are in parentheses.

Incidentally, the presence of both N_π and N_τ isomers is consistent with the fragmentation behavior upon CID if one recognizes that the N_π geometry may allow NH_3 loss leading to a chelate complex where the amino N atom (N_a) is the additional ligand ([PtCl(NH$_3$)His(N_π,N_a)]$^+$) while the N_τ geometry yields a three coordinate Pt complex in a considerably more energy demanding process (ca. 102 and 204 kJ mol^{-1}, respectively, see table S4.1 for complete thermodynamic data and Figure S4.4 for geometries of species partaking in scheme 4.1).

A comprehensive view of higher energy conformers, including species that are not expected to contribute significantly to the sampled population, for the two families of N_π and N_τ isomers is provided in figure S4.2, while figure S4.5 shows their IR harmonic spectra together with the experimental IRMPD spectrum. Table S4.1 summarizes the thermodynamic data for all tested species.

It is also conceivable that the histidine ligand in *cis*-[PtCl(NH$_3$)$_2$(His)]$^+$ ions may bind the metal by donor atoms other than N_π and N_τ belonging to the imidazole group. In this view a computational survey has examined a variety of plausible candidates whose structures are reported in figure S4.3. Thermodynamic data for the named species are collected in table S4.1 and the calculated IR spectra are reported in figure S4.5. None of these spectra compares well with the experimental IRMPD spectrum and a significant contribution of any of these species may thus be discarded. None of these isomers spectra compares well with the experimental IRMPD spectrum. In particular, it is worth noting that these isomers are characterized by C=O stretching frequencies appreciably lower than the experimental band at 1755 cm^{-1}. Thus, the finding that the ion population sampled at this resonance undergoes thorough photofragmentation speaks against a significant contribution of any of these alternative isomers.

4.3.3 Photofragmentation kinetics for isomer and conformer quantification

In the X-H stretching frequency range of the IRMPD spectrum a prominent band at 3497 cm^{-1} arises from the NH stretching mode of the imidazole group and is a distinct feature in the IR spectra of N_π isomers. The geometry of N_τ isomers allows the imidazole NH to be involved in a hydrogen bond, displacing the NH stretching to lower frequency. A second IRMPD band at 3565 cm^{-1} arises from the OH stretching

mode of a 'free' hydroxyl group as in **N$_\pi$_2**, **N$_\tau$_1** and **N$_\tau$_2** isomers. Because these frequencies are isomer/conformer specific, one can exploit IRMPD kinetics to probe the relative population of isomeric species and any possible mutual conversion process.[49-53] The ion cloud overlap with the OPO/OPA laser beam has been verified using protonated His (HisH$^+$) as model ion and testing the IRMPD kinetics. The gas-phase structure of protonated histidine has been examined by IRMPD spectroscopy in the fingerprint range.[54] Protonation occurs on the imidazole group and low-lying conformers are characterized by at least one H-bond involving N$_\pi$-H.[54,55] In contrast, the N$_\tau$-H bond is remote from the His chain and the calculated IR spectrum of the most stable conformer shows its frequency at 3466 cm^{-1} in fair agreement with the prominent IRMPD band at 3478 cm^{-1} (figure S4.6 in the SM). IRMPD kinetics performed at this frequency were based on recording the parent ion depletion (HisH$^+$ at *m/z* 156). The kinetics conform to a neat exponential decay (figure S4.7) with k = 0.13 s^{-1} to ca. 97% depletion of the parent ion abundance. The nearly complete depletion suggests that in our experimental setup there is good overlap of the IR beam with the ion cloud at the examined frequency. In the specific case of HisH$^+$ ions, the monoexponential decay indicates that either a single conformer is prevailing in the sampled mixture, or that distinct conformers display closely similar IRMPD activity or fast interconversion between different conformers is occurring. In the previously cited IRMPD study of HisH$^+$ ions in the fingerprint region it was shown that two distinct conformers are present, differing for the hydrogen bonding network at N$_\pi$-H, while both possessing a free N$_\tau$-H.[54]

In order to gain an insight into the isomeric population of *cis*-[PtCl(NH$_3$)$_2$(His)]$^+$ ions, IRMPD kinetics have been monitored at the two distinct frequencies of 3497 and 3565 cm^{-1} and plotted in figure 4.8. Both kinetics conform to a monoexponential decay with rate constants differing by less than a factor of 2 indicating that the photofragmentation process may involve the same or closely similar species. This behavior may be accounted for by a population of N$_\pi$ conformers (such as **N$_\pi$_1**, **N$_\pi$_2**), characterized by comparable oscillator strength in the 3497 and 3565 cm^{-1} resonances and similar fragmentation thresholds. The photofragmentation kinetics do not account for the overall ion population, though, ending with an unreactive

fraction of 25% and 70% at 3497 and 3565 cm^{-1}, respectively. In the IR spectra of

N_π_1 and N_π_2 shown in figure 4.5, one notes that N_π_1 is not IR active at 3565 cm^{-1}, in agreement with the reduced amplitude of the exponential decay at this frequency. The unreactive fraction at 3497 cm^{-1} may be related to the presence of the N_τ conformers that present a red-shifted imidazole NH stretching due to the presence of strong H-bonds with either CO or NH_2 groups.
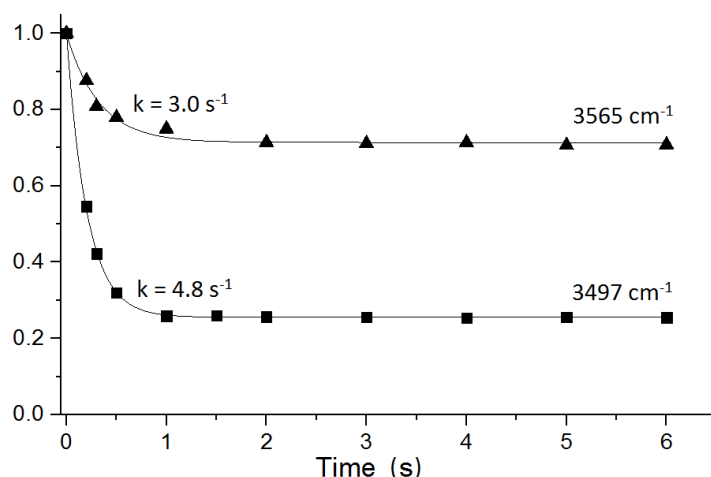
Figure 4.8 Decay of the parent ion *cis*-[PtCl(NH$_3$)$_2$His]$^+$ abundance plotted as a function of irradiation time. For each selected wavenumber the value of the kinetic constant is reported.

Furthermore, IRMPD kinetics were performed at 3350 and 3392 cm^{-1}, probing modes that are not isomer specific (see figure 4.5). In proximity with these frequencies, the ion cloud overlap has been verified on the IRMPD band at 3350 cm^{-1} of protonated dopamine, experiment that produced complete depletion of the parent ion (figure S4.7). The results (figure S4.8) confirm the presence of an unreactive fraction of ca. 25% of the parent ion suggesting the absence of IRMPD activity for the N_τ conformers in the whole XH (X = C, N, O) stretching region. Thus, the obtained evidence leads us to assign a contribution of 25% for N_τ isomers in the sampled *cis*-[PtCl(NH$_3$)$_2$His]$^+$ complexes. Hence, the analysis of the spectroscopic data in 3000-3700 cm^{-1} range supports the following outline: (i) N_τ isomers do not appear to contribute to IRMPD activity, likely due to a high fragmentation threshold and limited photon density in the range accessed by the OPO/OPA laser; (ii) N_π conformers (N_π_1, N_π_2) account for the IRMPD signatures as shown by the IR

spectra reported in figure 4.5; (iii) photodissociation kinetics provide a probe of isomer/conformer population showing that inactive N_τ isomers co-exist with N_π conformers characterized by a 'free' NH stretching at 3497 cm^{-1} of the imidazole group but differing for the presence of a 'free' OH stretching at 3565 cm^{-1} of the carboxylic functionality. Because only **N_π_2** possesses the 'free' OH stretching and is IR active at 3565 cm^{-1}, the percentage of photofragmenting ions at this frequency may be assigned to the contribution of **N_π_2** in the ion population, amounting to ca. 30 %. Because both **N_π_1** and **N_π_2** contribute to the 75 % depletion at 3497 cm^{-1}, the fraction of **N_π_1** may then be estimated to be ca. 45 %. Thus, a linear combination of calculated IR spectra can be derived, considering the contribution of all species in the fingerprint region while only **N_π_1** and **N_π_2** contribute to the observed IR spectrum in the XH stretching range. This experimentally weighted average of the IR spectra of the sampled N_π and N_τ isomeric population is depicted in the upper panel of figure 4.9, showing good agreement with the experimental IRMPD spectrum (lower panel), especially if one considers that IRMPD intensities reflect the efficiency of the photofragmentation process and are not a direct reflection of a linear IR spectrum, though frequently showing close correspondence.[38-40]
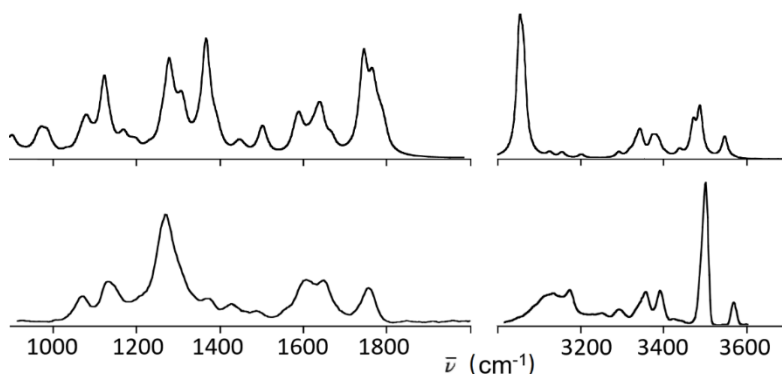
Figure 4.9 IRMPD spectrum of *cis*-[PtCl(NH$_3$)$_2$His]$^+$ (bottom panel) compared to the averaged linear anharmonic IR spectra (upper panel). The contribution of all species, **N_t_1/N_t_2** and **N_π_1/N_π_2**, is involved in the fingerprint region while only **N_π_1** and **N_π_2** contribute to the observed IR spectrum in the XH stretching range. No correction or scaling factors were used in the computed spectra.

Indeed, an accurate reproduction of IR intensities still represents a challenge for computations. It is also worth noting that no corrections or scaling factors have been used in the calculated anharmonic spectra.
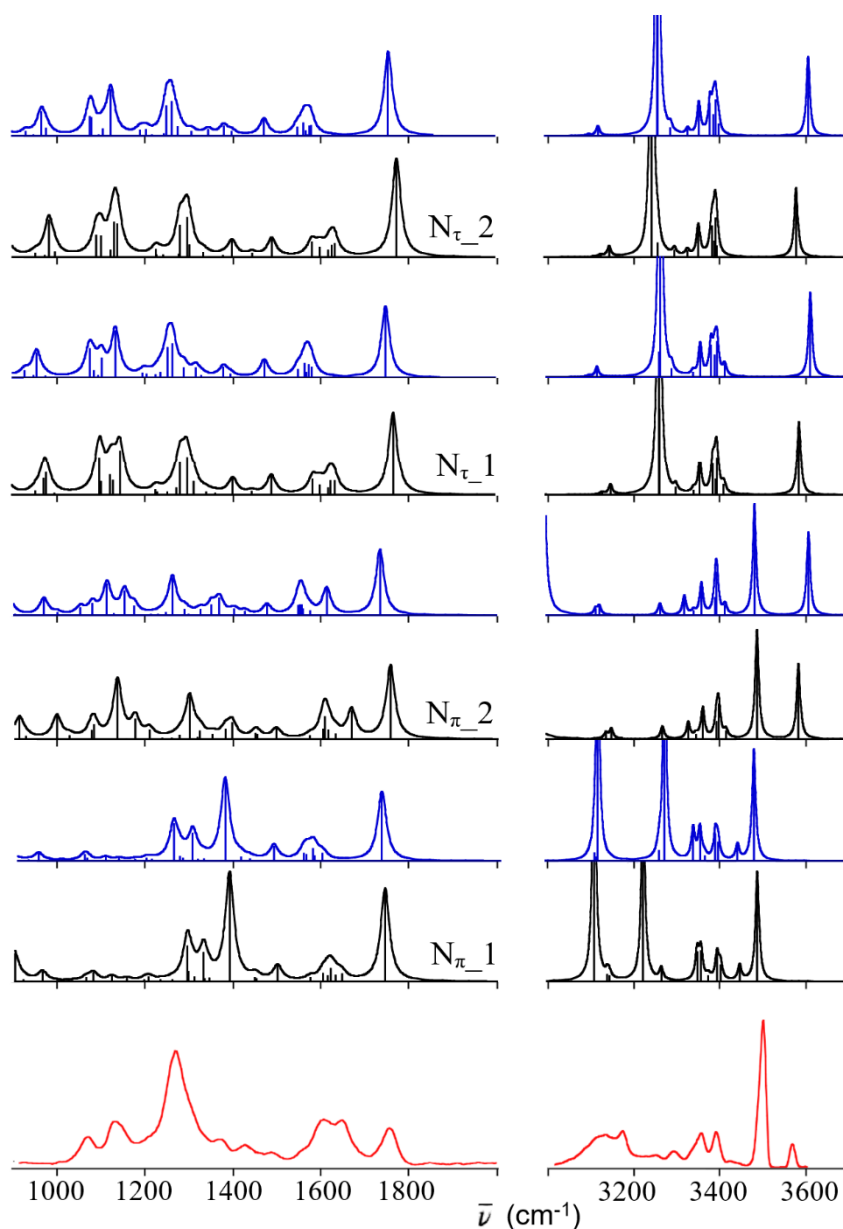
Figure S4.1 IR harmonic spectra of Nπ_1, Nπ_2 and Nτ_1, Nτ_2 obtained at the B3LYP/6-311+G** level of theory (black profile) and at the ωB97X-D/6-311+G** level (blue profile). The ωB97X-D calculated frequencies are scaled by a factor of 0.940 and 0.943 for the low frequency and high frequency region, respectively. Theoretical spectra are compared with the IRMPD spectrum of *cis*-[PtCl(NH$_3$)$_2$(His)]$^+$ (red profile).

N_π_1
(0.0   0.0)

N_π_2
(4.7   5.3)

N_π_3
(6.8   6.6)

N_π_4
(6.7   8.4)

N_π_5
(6.3   14.2)

N_π_6
(14.7   15.3)

N_π_7
(8.3   15.7)

N_π_8
(9.3   15.9)
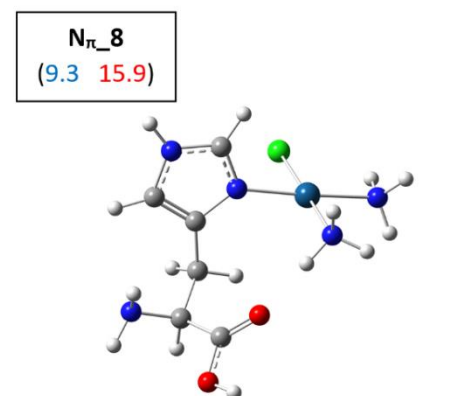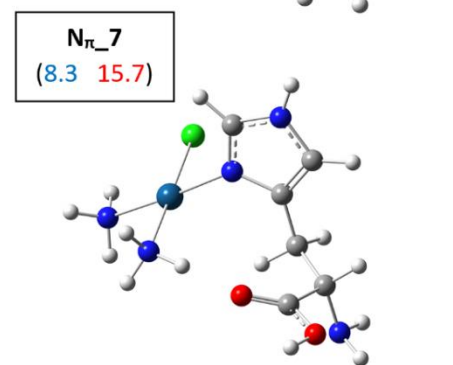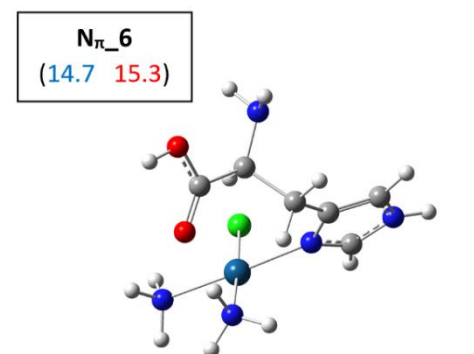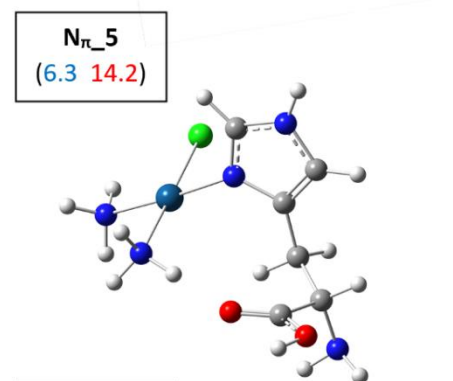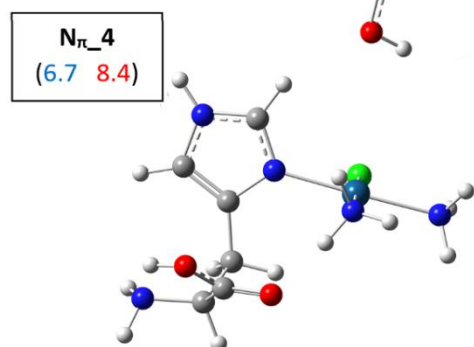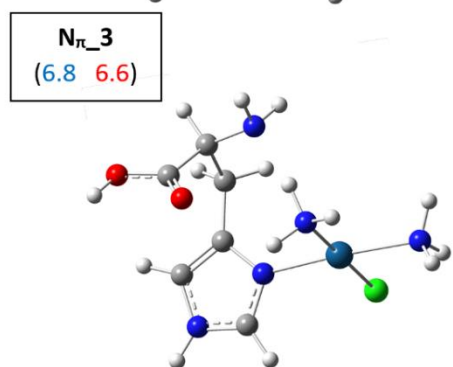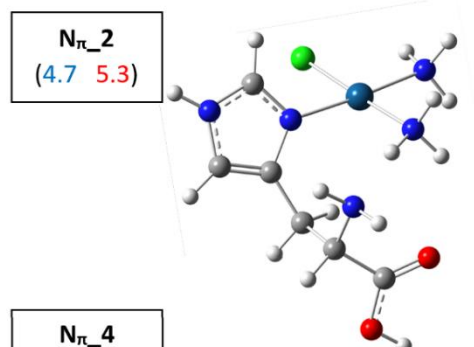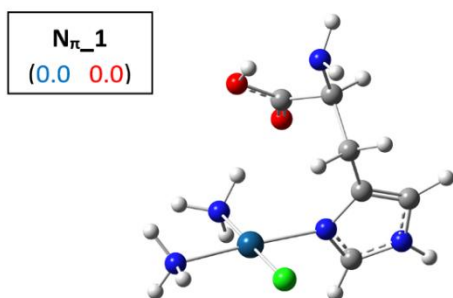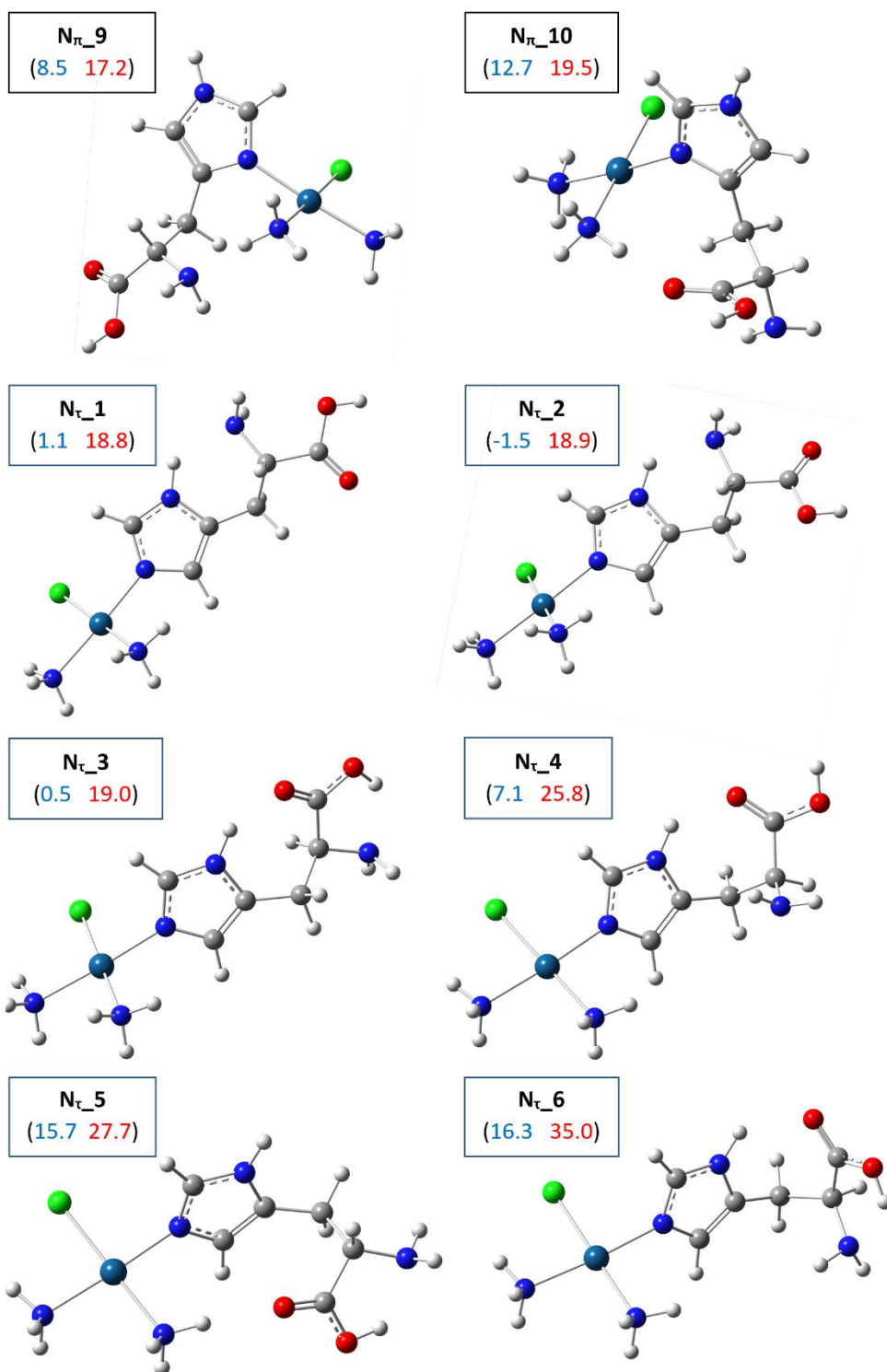
Figure S4.2 Structures of N_π and N_τ isomers. Optimized structures and relative free energies at 298K in kJ mol^{-1} calculated at B3LYP/6-311+G** (in blue) and ωB97X-D/6-311+G** (in red) levels of theory are reported for the most stable conformers of sampled *cis*-[PtCl(NH$_3$)$_2$(His)]$^+$ complexes coordinated via the imidazole nitrogen atoms.
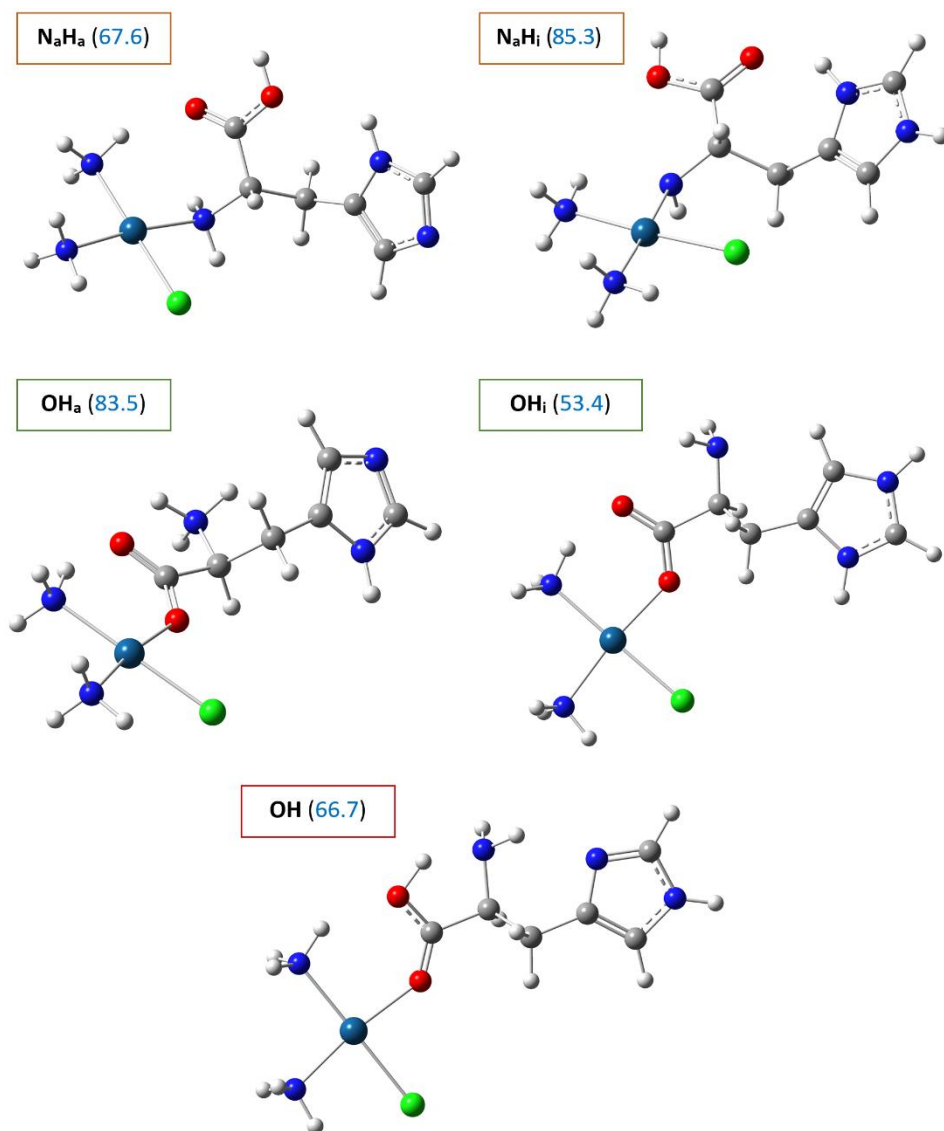
Figure S4.3 Optimized structures of the most stable isomers of *cis*-[PtCl(NH₃)₂(His)]⁺ complexes coordinated through the amino nitrogen or the carboxylic moiety. Relative free energies at 298K in kJ mol⁻¹ calculated at B3LYP/6-311+G** level of theory are reported.

[PtCl(NH₃)His(Nπ,Nₐ)]⁺

[PtCl(*cis*-NH₃)His(Nτ)]⁺
(0.0   0.0)

[PtCl(*trans*-NH₃)His(Nτ)]⁺
(24.0   22.2)

TS
(93.6   102.1)
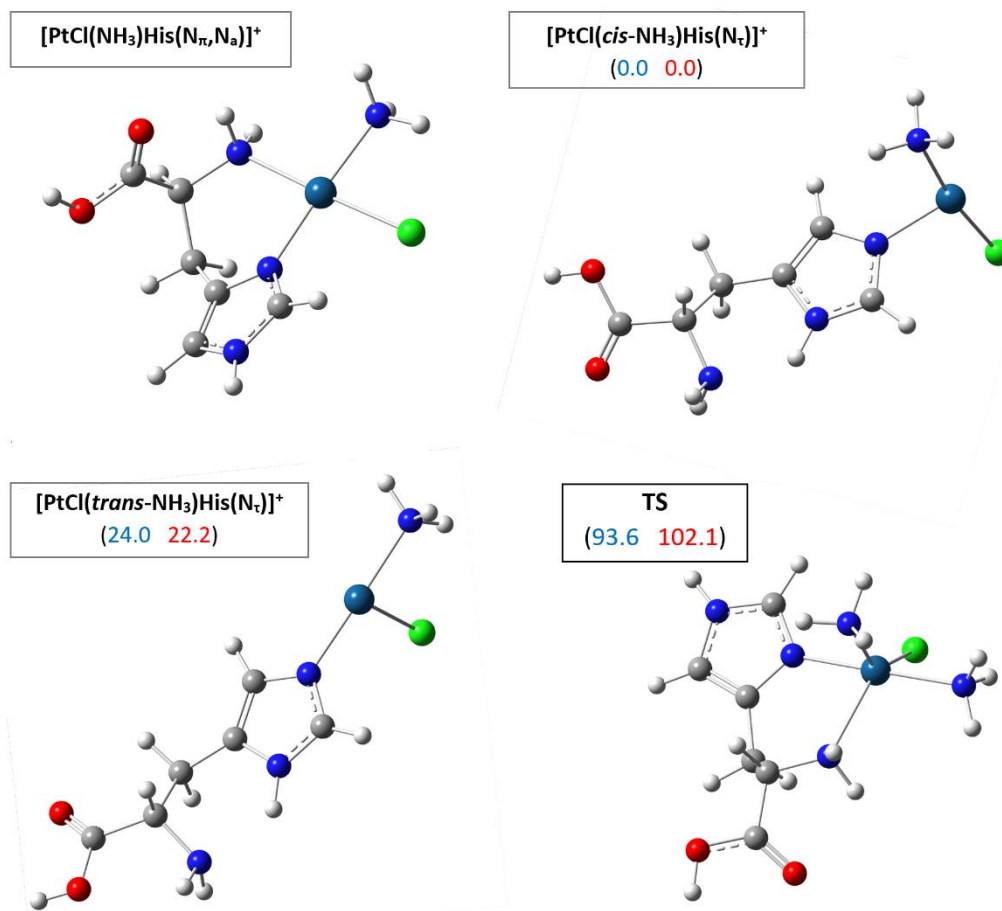
Figure S4.4 Geometries of the species partaking in Scheme 4.1. Optimized structures and relative free energies at 298K in kJ mol⁻¹ calculated at B3LYP/6-311+G** (in blue) and ωB97X-D/6-311+G** (in red) levels of theory are reported

N$_{\pi}$_9

N$_{\pi}$_8

N$_{\pi}$_7

N$_{\pi}$_6

N$_{\pi}$_5

N$_{\pi}$_4

N$_{\pi}$_3

N$_{\pi}$_2

N$_{\pi}$_1

1000   1200   1400   1600   1800   3200   3400   3600

$\bar{\nu}$ (cm^{-1})
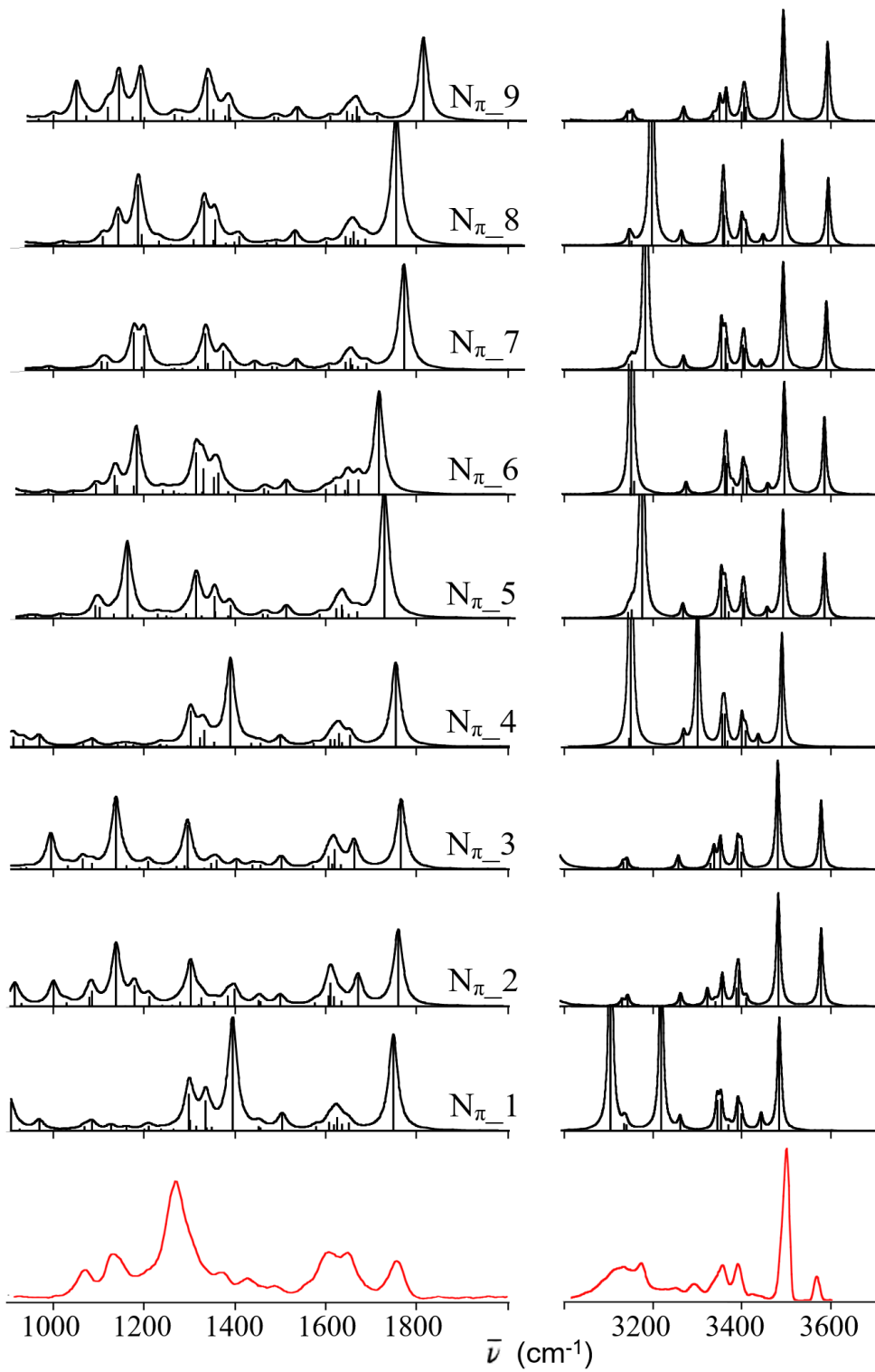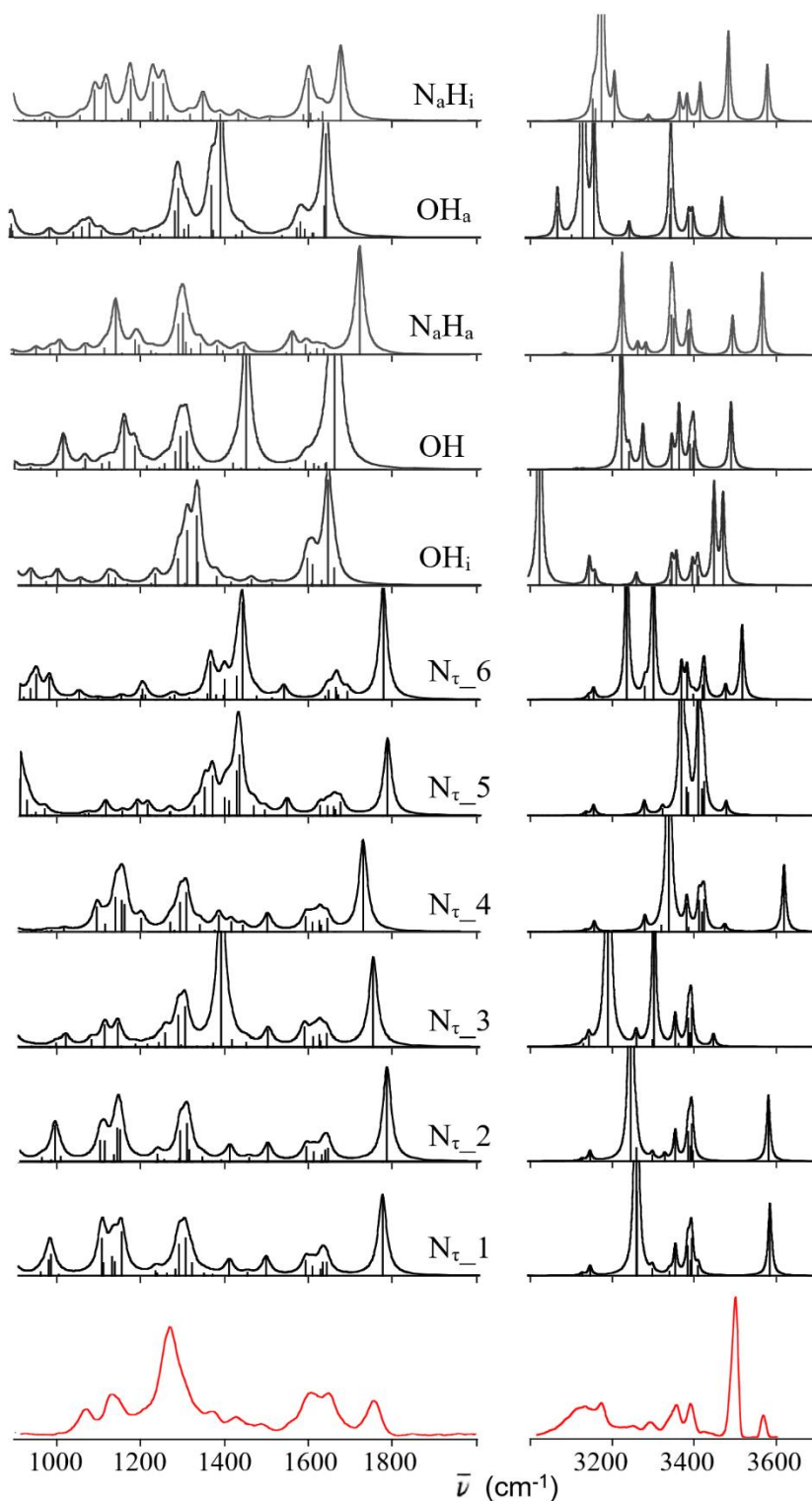
Figure S4.5 Harmonic IR spectra of *cis*-[PtCl(NH$_3$)$_2$(His)]$^+$ isomers obtained at the B3LYP/6-311+G** level of theory together with the experimental IRMPD spectrum (red profile).
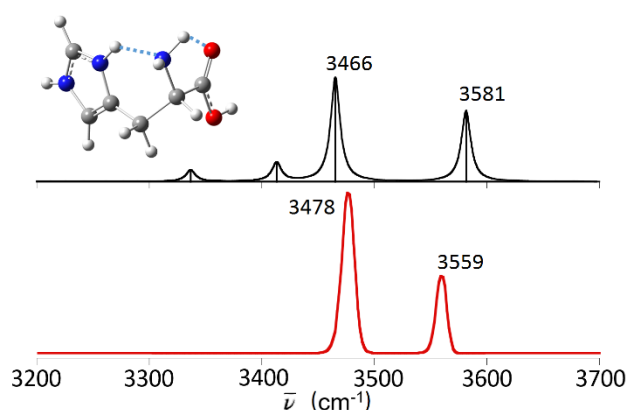
Figure S4.6 IRMPD spectrum of protonated histidine (red profile) compared to the linear IR spectrum of the optimized geometry depicted in figure (black profile). Calculations were performed at the B3LYP/6-311+G** level of theory.
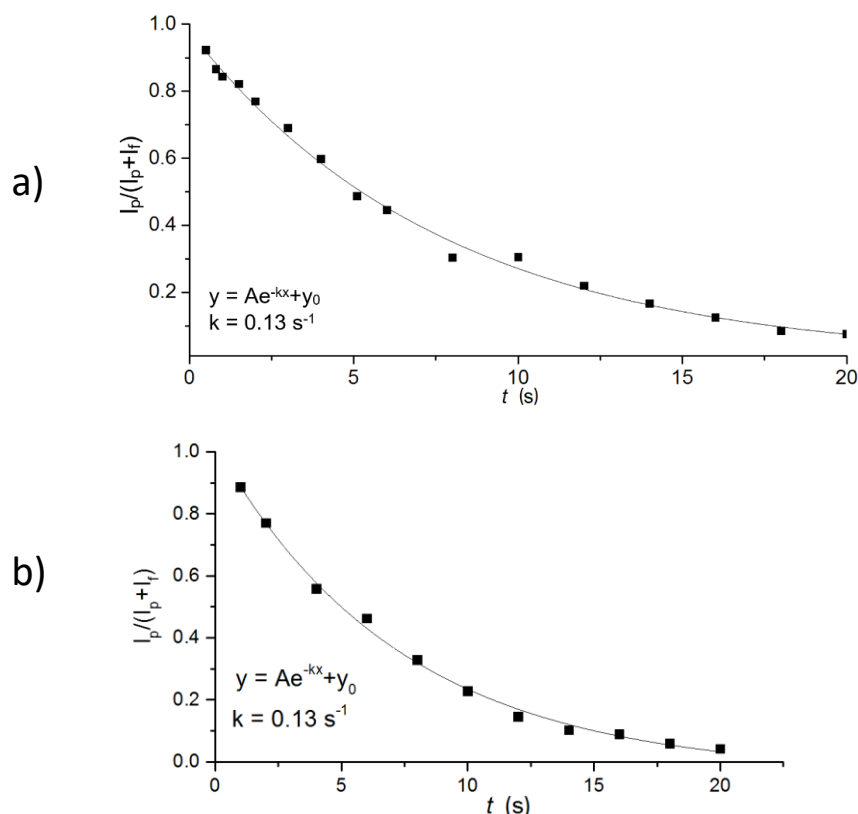
Figure S4.7 Decay of the parent ion abundance plotted as a function of the irradiation time: a) [HisH$^+$] at m/z 156 at 3478 cm^{-1} and b) [DopaH]$^+$ at 3350 cm^{-1}. Parameters of the mono-exponential fitting are reported in the figure. The experiment performed on protonated Dopa, [DopaH]$^+$, at 3350 cm^{-1}, was meant to inspect yet another frequency in the IR spectrum. This frequency is characterized by a small signal attributed to the NH$_2$ stretching mode of [DopaH]$^+$ (unpublished data). IRMPD kinetics performed at both frequencies shows a

nearly complete depletion in agreement with a good overlap of the IR beam with the ion cloud.
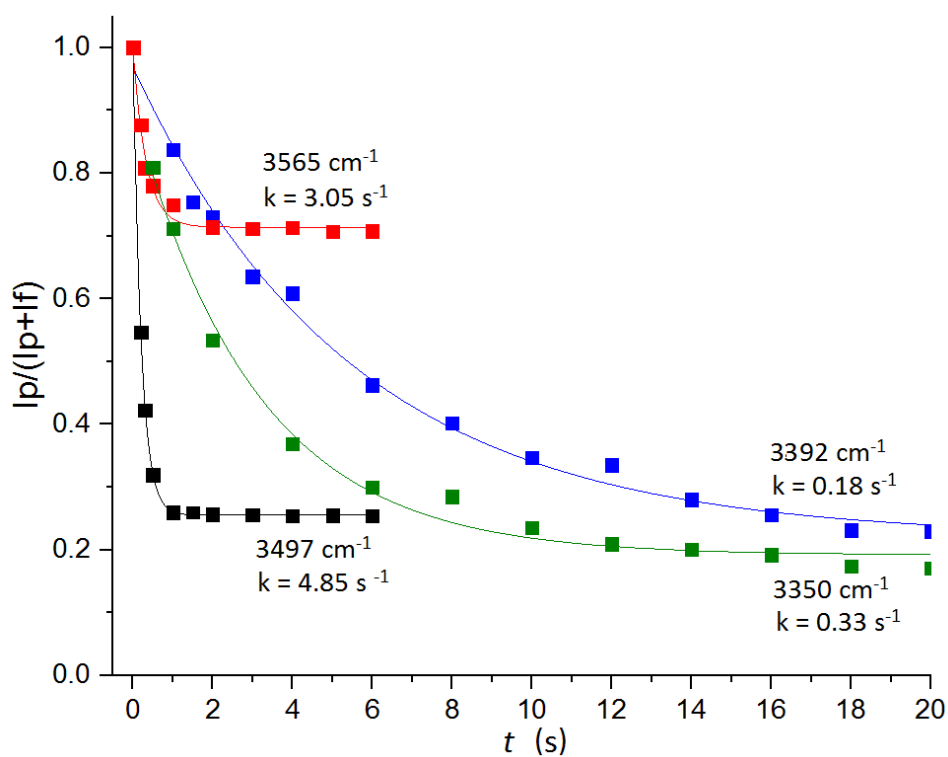
Figure S4.8 Decay of the parent ion *cis*-[PtCl(NH₃)₂His]⁺ abundance plotted as a function of the irradiation time. The selected wavenumbers are reported together with the values of the kinetic constant.

Table S4.1 Theoretically calculated thermodynamic parameters for the most stable structures of cis-[PtCl(NH$_3$)$_2$(His)]$^+$ complexes and related species.

	B3LYP/6-311+G(d,p)					
Species	**Energy[a]**	**Relative Energy[b]**	**Zero-point Energy[b]**	**Relative Enthalpy[b] (298K)**	**H-TS[b] (298K)**	**Relative Free Energy[b] (298K)**
NH$_3$	-56.582636	-	89.9	-	42.5	-
N$_\pi$_1[c]	-1241.426619	0.0	642.2	0.0	517.0	0.0
N$_\pi$_2[c]	-1241.425329	3.4	643.6	4.4	518.3	4.7
N$_\pi$_3[c]	-1241.424016	6.8	642.6	7.2	517.0	6.8
N$_\pi$_4[c]	-1241.424009	6.9	642.9	7.4	516.9	6.7
N$_\pi$_5[c]	-1241.423376	8.5	641.4	8.5	514.8	6.3
N$_\pi$_6[c]	-1241.421284	14.0	642.3	14.3	517.7	14.7
N$_\pi$_7[c]	-1241.422553	10.7	641.2	10.5	514.6	8.3
N$_\pi$_8[c]	-1241.422037	12.0	641.8	12.3	514.3	9.3
N$_\pi$_9[c]	-1241.421906	12.4	642.8	13.1	513.1	8.5
N$_\pi$_10[c]	-1241.420651	15.7	640.7	15.3	514.0	12.7
N$_\tau$_1[c]	-1241.422157	11.7	640.5	11.68	506.4	1.1
N$_\tau$_2[c]	-1241.423625	7.9	640.4	7.83	507.6	-1.5
N$_\tau$_3[c]	-1241.422754	10.1	641.0	9.91	507.4	0.5
N$_\tau$_4[c]	-1241.421248	14.1	640.7	14.27	510.0	7.1
N$_\tau$_5[c]	-1241.420137	17.0	642.2	17.38	515.7	15.7
N$_\tau$_6[c]	-1241.417923	22.8	641.4	23.03	510.5	16.3
OH$_a$[c]	-1241.391989	90.9	642.3	91.8	509.6	83.5
OH$_i$[c]	-1241.403150	61.6	641.4	61.8	508.8	53.4
OH[c]	-1241.397509	76.4	638.1	72.6	507.3	66.7
N$_a$H$_a$[c]	-1241.399258	71.8	643.2	73.4	512.8	67.6

	Energy	Relative Energy	Zero-point Energy	Relative Enthalpy (298K)	H-TS (298K)	Relative Free Energy (298K)
N$_a$H$_i$[c]	-1241.391637	91.8	639.5	89.3	510.4	85.3
TS[c]	-1241.387827	101.8	635.8	96.8	508.8	93.6
[PtCl(NH$_3$)His(N$_\pi$,N$_a$)]$^+$[d]	-1184.828349	0.0	542.9	0.0	427.2	0.0
[PtCl(*trans*-NH$_3$)His(N$_\tau$)]$^+$[d]	-1184.767191	160.6	535.7	156.4	407.4	140.8
[PtCl(*cis*-NH$_3$)His(N$_\tau$)]$^+$[d]	-1184.757813	185.2	534.5	180.3	406.8	164.8

ωB97X-D/6-311+G(d,p)

Species	Energy[a]	Relative Energy[b]	Zero-point Energy[b]	Relative Enthalpy[b] (298K)	H-TS[b] (298K)	Relative Free Energy[b] (298K)
NH$_3$	-56.560678	-	90.7	-	43.4	-
N$_\pi$_1[c]	-1241.192350	0.0	652.1	0.0	529.3	0.0
N$_\pi$_2[c]	-1241.190183	5.7	653.1	6.5	528.9	5.3
N$_\pi$_3[c]	-1241.189924	6.4	652.4	6.6	529.5	6.6
N$_\pi$_4[c]	-1241.190160	5.8	653.0	6.2	532.0	8.4
N$_\pi$_5[c]	-1241.185087	19.1	650.3	18.5	524.4	14.2
N$_\pi$_6[c]	-1241.186460	15.5	652.2	15.8	529.1	15.3
N$_\pi$_7[c]	-1241.184684	20.1	650.4	19.5	524.9	15.7
N$_\pi$_8[c]	-1241.184477	20.7	651.6	21.0	524.5	15.9
N$_\pi$_9[c]	-1241.184169	21.5	652.1	21.8	525.0	17.2
N$_\pi$_10[c]	-1241.182713	25.3	649.7	24.4	523.5	19.5
N$_\tau$_1[c]	-1241.179725	33.1	648.8	32.1	514.9	18.8
N$_\tau$_2[c]	-1241.181003	29.8	649.3	29.1	518.3	18.9
N$_\tau$_3[c]	-1241.180318	31.6	650.2	31.1	516.7	19.0
N$_\tau$_4[c]	-1241.179430	33.9	650.0	33.6	521.2	25.8
N$_\tau$_5[c]	-1241.180777	30.4	651.7	30.4	526.6	27.7
N$_\tau$_6[c]	-1241.176578	41.4	650.9	41.3	522.9	35.0
TS[c]	-1241.151311	107.7	645.0	102.1	517.9	96.4

Species	Energy[a]	Relative Energy[b]	Zero-point Energy[b]	Relative Enthalpy[b] (298K)	H-TS[b] (298K)	Relative Free Energy[b] (298K)
$[PtCl(NH_3)His(N_\pi,N_a)]^+$ [d]	-1184.608556	0.0	551.0	0.0	436.3	0.0
$[PtCl(trans\text{-}NH_3)His(N_\tau)]^+$ [d]	-1184.537247	187.2	543.7	183.0	418.0	168.9
$[PtCl(cis\text{-}NH_3)His(N_\tau)]^+$ [d]	-1184.529132	208.5	543.1	203.9	418.9	191.1

B3LYP-D3/6-311+G(d,p)

Species	Energy[a]	Relative Energy[b]	Zero-point Energy[b]	Relative Enthalpy[b] (298K)	H-TS[b] (298K)	Relative Free Energy[b] (298K)
$N\pi\_1$ [c]	-1241.468343	0.0	643.5	0.0	521.1	0.0
$N\pi\_2$ [c]	-1241.465467	7.5	644.4	8.4	520.0	6.5
$N\tau\_1$ [c]	-1241.455297	34.3	641.1	33.9	507.7	20.8
$N\tau\_2$ [c]	-1241.456684	30.6	640.9	30.3	508.9	18.3

MP2/cc-pVTZ//B3LYP/6-311+G** [e]**

Species	Energy[a]	Relative Energy[b]	Zero-point Energy[b]	Relative Enthalpy[b] (298K)	H-TS[b] (298K)	Relative Free Energy[b] (298K)
$N\pi\_1$ [c]	-1239.666669	0.0	642.2	0.0	517.0	0.0
$N\pi\_2$ [c]	-1239.663538	8.2	643.6	9.2	518.3	9.5
$N\tau\_1$ [c]	-1239.655410	29.6	640.5	29.5	506.4	20.2
$N\tau\_2$ [c]	-1239.653594	34.3	640.4	34.3	507.6	23.7

[a] Electronic energy at 0K in Hartree particle^{-1}. [b] In kJ mol^{-1}. [c] Relative energies, relative enthalpies and relative free energies are referred to N_π_1. [d] Relative energies, relative enthalpies and relative free energies are referred to $[PtCl(NH_3)His(N_\pi,N_a)]^+$. [e] Zero-point energies and thermal corrections from B3LYP/6-311+G** calculations.

Table S4.2 Observed IRMPD signatures and calculated vibrational frequencies for selected geometries of *cis*-[PtCl(NH₃)₂(His)]⁺.

cis-[PtCl(NH₃)₂His]⁺

Exp IRMPD[b]	Calculated Ir[a]								Vibrational mode assignment
	N_π_1		N_π_2		N_τ_1		N_τ_2		
	anh	har	anh	har	anh	har	anh	har	
	966	963 (31)							CH₂ rock
					972	972 (53)			ring def
			990	995 (75)	976	977 (73)	976	984 (122)	NH₂ bend symm
1075			1081	1074 (27)	1085	1098 (130)	1080	1091 (72)	CN stretch
	1084	1079 (28)	1071	1079 (48)					ring def
					1100	1102 (43)	1099	1103 (69)	CH imi bend in plane
							1123	1124 (22)	ring def
1133					1124	1123 (65)	1128	1132 (115)	CH imi + NH bend in plane
			1172	1173 (66)	1133	1131 (47)	1141	1140 (109)	CH₂ twist + NH₂ twist
			1125	1133 (193)	1124	1146 (153)			OH bend
			1201	1206 (30)					NH₂ twist
1270					1275	1274 (23)			CH₂ twist
	1279	1294 (117)	1278	1297 (139)	1265	1283 (108)	1263	1283 (104)	NH₃ umbrella
	1302	1296 (32)	1316	1322 (25)	1231	1227 (16)	1228	1227 (23)	CH bend
					1288	1299 (130)	1284	1299 (131)	NH₃ umbrella
					1295	1314 (44)	1296	1305 (39)	OH bend
1375	1310	1331 (95)	1379	1379 (31)					NH₃ umbrella
	1367	1390 (358)							OH bend
			1390	1394 (54)			1340	1336 (13)	CH bend
1433					1396	1403 (51)	1397	1402 (52)	NH bend in plane
			1443	1447 (18)					CH₂ scissor
1492	1504	1500 (49)	1500	1495 (33)	1500	1491 (63)	1496	1492 (60)	CH in plane bend

1607					1585	1586 (52)	1585	1584 (59)	CC imi stretch
	1624	1604 (27)	1579	1602 (33)	1609	1602 (32)	1607	1602 (32)	NH$_3$ bend asymm
			1590	1606 (74)	1607	1626 (42)	1618	1629 (37)	NH$_2$ bend symm
	1637	1614 (19)	1588	1615 (30)					NH$_3$ bend asymm
	1632	1632 (20)	1626	1631(16)	1617	1621 (22)	1618	1621 (21)	NH$_3$ bend asymm
1645	1645	1646 (25)	1640	1667 (94)	1637	1679 (45)	1637	1636 (45)	NH$_3$ bend asymm
	1666	1620 (43)							NH$_2$ bend symm
1755	1742	1745 (309)	1763	1756 (244)	1778	1769 (282)	1789	1777 (383)	CO stretch
			2904	2908 (35)					CH stretch
3125	3054	3109 (432)	2818	2955 (702)					NH$_3$ stretch asymm
			3153	3149 (17)	3150	3149 (17)	3153	3149 (17)	CH stretch
3175	3063	3221 (312)							OH stretch
					3190	3260 (615)	3141	3247 (616)	NH stretch
3290	3290	3263 (20)	3201	3265 (21)					NH$_3$ stretch symm
3350	3339	3345 (49)	3316	3325 (27)	3341	3354 (51)	3341	3354 (51)	NH$_3$ stretch asymm
	3343	3354 (51)	3330	3357 (50)	3369	3384 (52)	3369	3384 (52)	NH$_3$ stretch asymm
3392	3379	3391 (45)	3368	3389 (29)	3373	3391 (26)	3373	3391 (26)	NH$_3$ stretch asymm
	3387	3399 (27)			3380	3394 (65)	3378	3394 (64)	NH$_3$ stretch asymm
			3370	3394 (58)	3398	3410 (17)	3384	3397 (18)	NH$_2$ stretch asymm
3428	3435	3443 (26)							NH$_2$ stretch asymm
3497	3484	3484 (182)	3467	3482 (182)					NH stretch asymm
3565			3543	3576 (125)	3547	3582 (126)	3547	3578 (115)	OH stretch

[a] Frequencies in cm^{-1}. Intensities, reported in brackets, are in km mol^{-1}. Modes with intensity lower than 15 km mol^{-1} are omitted.

4.4 Binding differences of cisplatin and transplatin with methionine as assayed by IRMPD spectroscopy and kinetics

The following work has been published in Phys. Chem. Chem. Phys.:

My contributions to the work consist in performing the IRMPD kinetic data as well as collecting the IRMPD spectroscopy data. Ion mobility measurement were done by myself at The University of Manchester in the laboratories of Prof. Perdita Barran in the framework of a PhD mobility program by Sapienza Università di Roma. I have also participated in writing the first draft for the manuscript and in its revision.

4.4.1 ESI-MS/MS and IRMPD spectroscopy of methionine platinum(II) complexes

When an incubated aqueous solution of cisplatin is allowed to react with methionine, the formation of *cis*-[PtCl(NH$_3$)$_2$Met]$^+$ complexes is revealed by ESI-MS, as shown in the mass spectrum reported in figure 4.10 A.
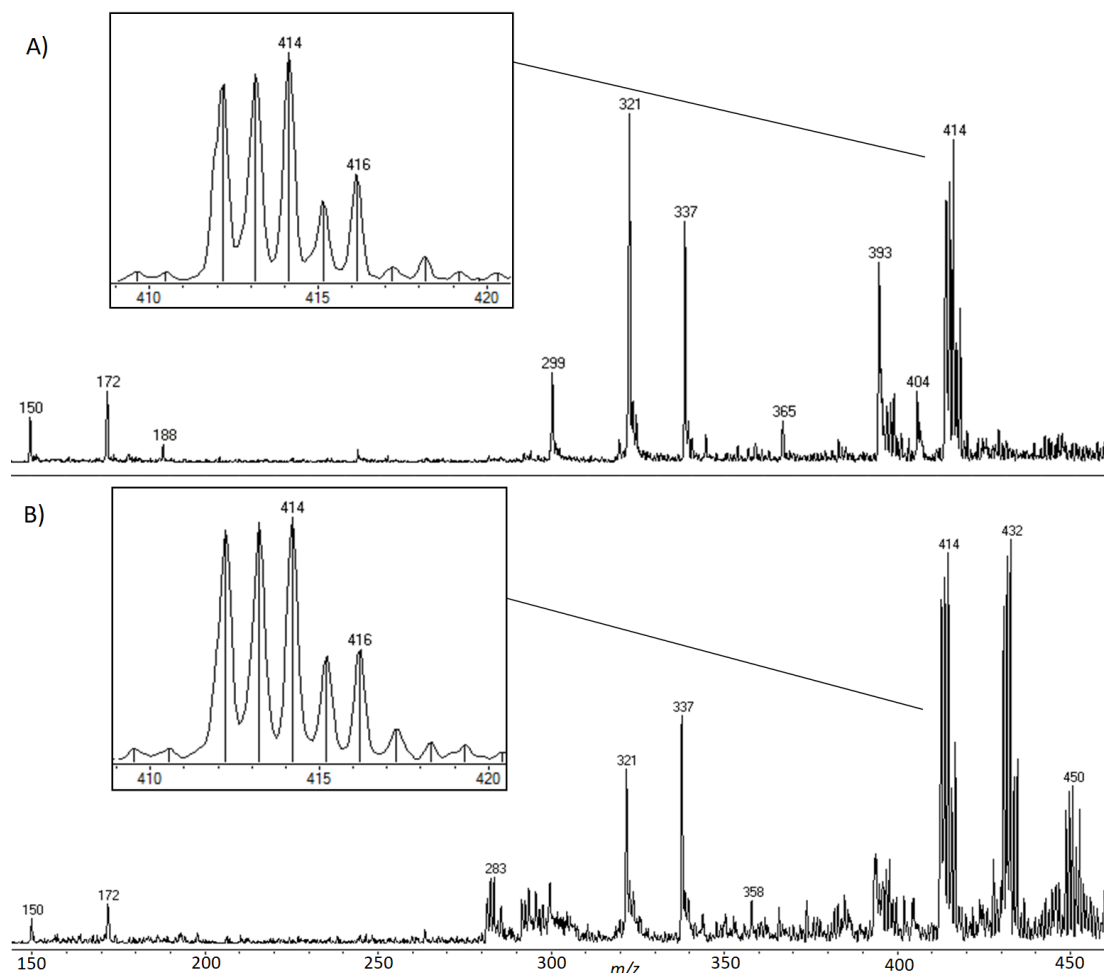
Figure 4.10 Mass spectrum of a solution of A) cisplatin and B) transplatin mixed with methionine (1:1) recorded with an Esquire 6000 ion trap mass spectrometer. The species of interest, the *cis*-[PtCl(NH$_3$)$_2$Met]$^+$ complex, corresponds to the cluster at *m/z* 412-416 and is highlighted in the inset. The signals at *m/z* 150, 172, 321, 337 are related to Met (e. g. *m/z* 150 is protonated Met) while other signals belong to hydrolyzed cisplatin (e. g. *m/z* 281-285 is the *cis*-[PtCl(NH$_3$)$_2$(H$_2$O)]$^+$ complex) and other Pt complexes. The ion at *m/z* 430-434 formally corresponds to a five-coordinate complex, namely [PtCl(NH$_3$)$_2$Met(H$_2$O)]$^+$.

The formal composition of the ions is consistent with the isotopic pattern of the cluster, comprising the major peaks at *m/z* 412-416. Ionic species sharing the same

peak pattern and *m/z* range are also observed when the reactant is the transplatin isomer (figure 4.10 B). The dilute solution and the prompt sampling by ESI likely contribute to minimize further ligand exchange at the metal and allow to isolate the primary complex formed from cis-/transplatin by substitution of a chloro ligand (possibly via the aqua intermediate, $[PtCl(NH_3)_2(H_2O)]^+$) with a methionine molecule. Henceforth, the isotopic cluster of the platinum(II) complex will be referred to by citing the *m/z* value of the lightest mass peak of major abundance. Thus, the $[PtCl(NH_3)_2Met]^+$ complex is referred to by the *m/z* value of 412, namely the isotopic peak containing ^{194}Pt and ^{35}Cl. Interestingly, only in the cisplatin reaction mixture, also a pronounced cluster at *m/z* 430-434 is observed, consistent with a five-coordinate complex of $[PtCl(NH_3)_2Met(H_2O)]^+$ composition. The nature of formal five coordinate complexes *cis*-$[PtCl(NH_3)_2L(H_2O)]^+$, obtained by ESI from an aqueous solution of cisplatin allowed to react with various ligands has been thoroughly elucidated by IRMPD spectroscopy, which allowed to assign it the character of an encounter complex of *cis*-$[PtCl(NH_3)_2(H_2O)]^+$ with L, where the platinum(II) complex is solvated by L in the external coordination sphere, as showed in section 3.4. Though not of direct interest in the present context, it is likely that also in the $[PtCl(NH_3)_2Met(H_2O)]^+$ complex presently observed, the Met molecule is interacting in the outer coordination sphere with the intermediate aqua complex.

The ion chemistry of $[PtCl(NH_3)_2Met]^+$ complexes has been preliminarily inspected by submitting the ions to collision induced dissociation (CID), also to test whether this tool, commonly adopted to gain structural information about ionized analytes, would be able to discriminate between isomers obtained from cis- and transplatin. To this end, ions at *m/z* 412 have been selected and submitted to CID in a triple quadrupole mass spectrometer. The isolated $[PtCl(NH_3)_2Met]^+$ complexes display a remarkable lability with respect to loss of ammonia. The process in fact occurs to a large extent already in the region preceding the collision quadrupole. The so formed ion at *m/z* 395 is instead highly resistant to further fragmentation, suggesting a chelate coordination of methionine onto the metal, as observed in solution. The overall fragmentation pattern is shown in scheme 4.2, leading ultimately to [Pt(Met-

H)]$^+$ along a dissociation path involving a proton transfer reaction among the metal ligands, a recognized process characterizing gaseous platinum(II) complexes.[56]
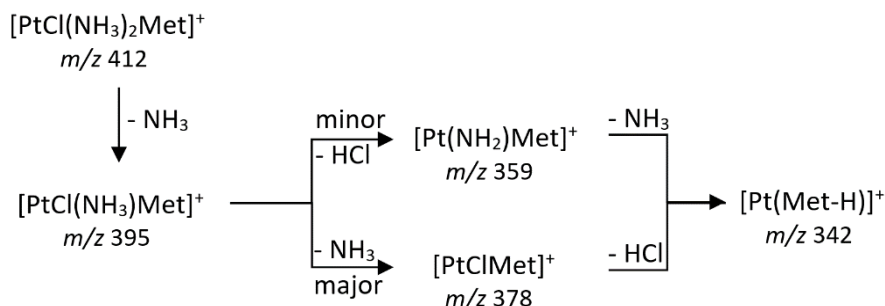
Scheme 4.2 Fragmentation paths of mass selected [PtCl(NH$_3$)$_2$Met]$^+$ complexes.

However, both [PtCl(NH$_3$)$_2$Met]$^+$ complexes deriving from either cis- or transplatin show comparable behavior upon CID, which does not seem to be a suitable probe for structural discrimination among these species. In another approach, *cis*- and *trans*-[PtCl(NH$_3$)$_2$Met]$^+$ complexes have been assayed by ion mobility mass spectrometry (IM-MS). IM-MS allows to unveil the transport properties of an ion moving in a buffer gas and has become a powerful analytical tool, separating ions on the basis of their *m/z* ratio as well as their interactions with the bath gas.[35-37] IM data for *cis*- and *trans*-[PtCl(NH$_3$)$_2$(Met)]$^+$ were acquired in two separate experiments using the same experimental conditions. Figure 4.11 displays the mobility profiles and the arrival times of both the *trans*- and *cis*-isomers obtained selecting the first peak of the [PtCl(NH$_3$)$_2$(Met)]$^+$ isotopic cluster (*m/z* 412) from the full mass spectrum.
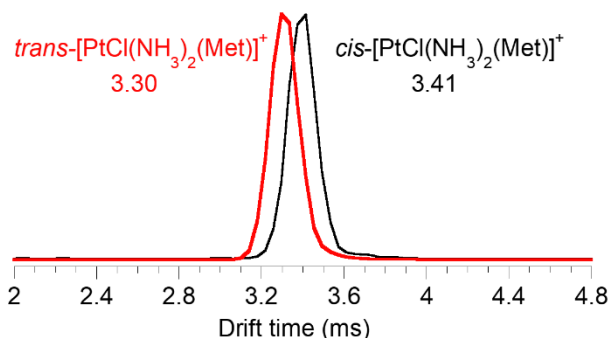
Figure 4.11 Mobility profile of *cis*- (black profile) and *trans*- (red profile) [PtCl(NH$_3$)$_2$(Met)]$^+$. The arrival time of the two species is reported in the figure.

Despite the expected highly similar geometry of the two isomers, it is possible to observe a slightly faster drift time for the *trans* isomer (3.30 ms and 3.41 ms for the *trans* and *cis* isomer, respectively). This finding suggests a somewhat tighter structure for *trans*-$[PtCl(NH_3)_2(Met)]^+$. The difference in arrival times is however too little to provide meaningful distinction. IRMPD spectroscopy has therefore been taken advantage of for an assay of diagnostic vibrational features both in the 'fingerprint' and in the X-H (X = C, N, O) stretching range.
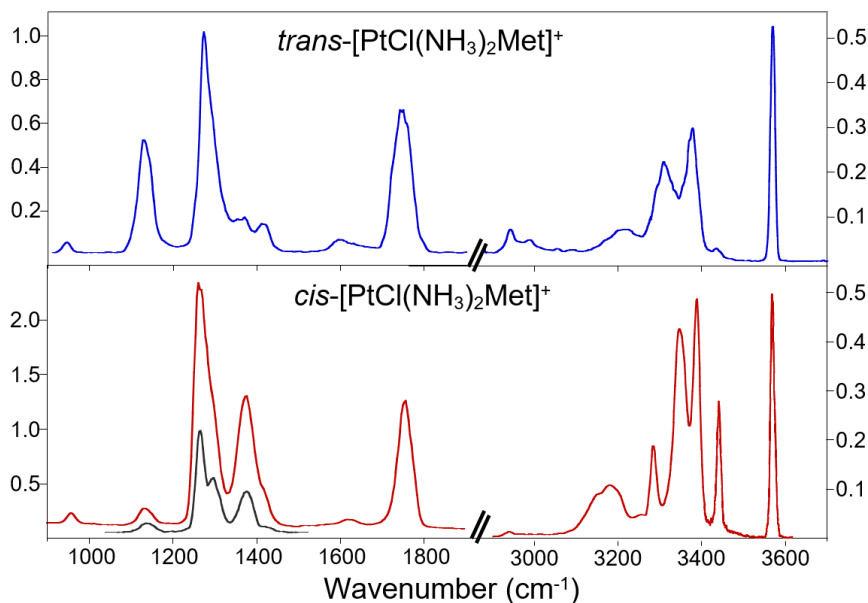
Figure 4.12 IRMPD spectra of *cis*-$[PtCl(NH_3)_2Met]^+$ (red, lower panel) and *trans*-$[PtCl(NH_3)_2Met]^+$ (blue, upper panel) complexes deriving from cis- and transplatin reaction with Met. The black trace in the spectrum of *cis*-$[PtCl(NH_3)_2Met]^+$ is recorded with an attenuated beam.

The spectra shown in figure 4.12 are clearly distinct for the two isomers. In fact, though several bands appear at similar frequency in the two panels pertaining to the *cis*-$[PtCl(NH_3)_2Met]^+$ and *trans*-$[PtCl(NH_3)_2Met]^+$ complexes, their intensity is in some cases largely different. For example, a highly active band at 1130 cm^{-1} in the spectrum of the trans isomer has a counterpart in a weak feature at about the same wavenumber in the spectrum of the cis species. Also, the intensity of the second most intense band at 1376 cm^{-1} in the fingerprint region of the cis complex is by no means comparable to the weak one found for the trans at ca. 1367 cm^{-1}. The wavenumbers of the IRMPD features in the spectra reported in figure 4.12 are listed

in tables S4.3 and S4.4 in the SM. The photofragmentation process on which the IRMPD 'action' spectroscopy is based involves the cleavage of an NH_3 ligand from both *cis*- and *trans*-[PtCl(NH$_3$)$_2$Met]$^+$ complexes, in compliance with the earliest dissociation observed under CID. Figure 4.13 reports as an example the mass spectra of the *cis*-[PtCl(NH$_3$)$_2$(Met)]$^+$ complex recorded A) after isolating the isotopic cluster of the complex to be assayed and B) when the complex has been irradiated at the IR active frequency of 3570 cm^{-1}.
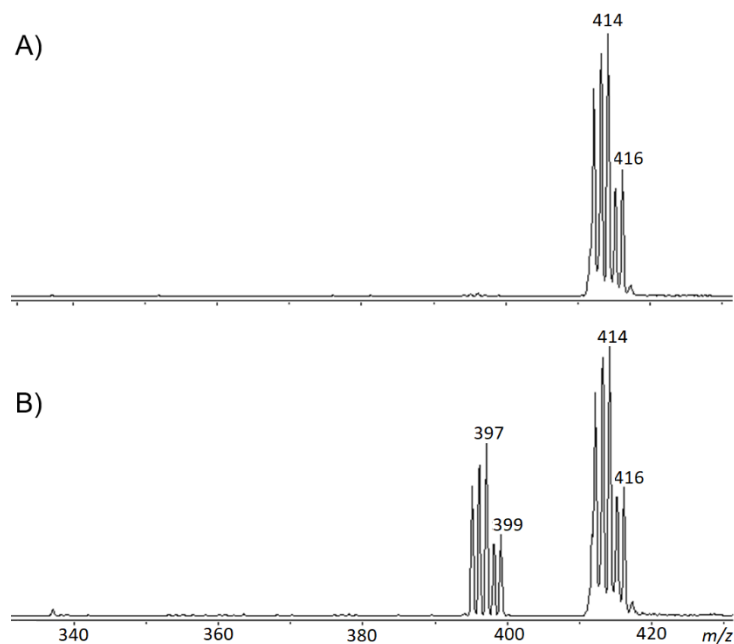
Figure 4.13 Mass spectra recorded upon selection of *cis*-[PtCl(NH$_3$)$_2$(Met)]$^+$ (*m/z* 412-416 before A) and after B) irradiation at 3570 cm^{-1}. The photofragmentation product by loss of NH_3 is observed at *m/z* 395-399.

As observed in CID, also under IR photon activated conditions the loss of ammonia is a facile process, which imposed the use of an attenuated beam to avoid saturation effects in some instance. The prompt fragmentation process hints to the formation of a significantly stable product, such as a chelate complex where platinum(II) maintains four-coordination. Bidentate coordination by methionine was in fact observed in the reaction reported in solution. However, the gas phase reaction displays loss of NH_3 while in solution the chloro ligand is typically the preferred leaving group in the reaction of cisplatin-derived complexes.

The IRMPD spectra, reported in figure 4.12, of the monofunctional *cis*- and *trans*-[PtCl(NH$_3$)$_2$Met]$^+$ complexes display characteristic vibrational features such as the

major band at 1754 and 1745 cm^{-1}, respectively, which may be associated to the C=O stretching mode of a 'free' carboxylic group, implying that this group is not coordinated to the metal. Furthermore, the sharp band at ca. 3570 cm^{-1} in the spectra of both species is indicative of an O-H stretching mode of a hydroxylic group that is not involved in hydrogen bonding. However, more detailed structural insight is obtained from a computational survey of potential isomers, based on the relationship between the calculated IR spectra for the optimized geometries and the recorded IRMPD spectra, as outlined in the following paragraphs.

4.4.2 Computational survey of *cis*-[PtCl(NH$_3$)$_2$Met]$^+$ and *trans*-[PtCl(NH$_3$)$_2$Met]$^+$ complexes

An extensive array of different structures, corresponding to the most stable conformers within each family of isomers, has been submitted to geometry optimization and vibrational analysis. Both the thioether sulfur and the amino nitrogen have been considered as potential binding sites and all computed structures are displayed in Figure S6. Because methionine is asymmetric, in S-platinated complexes an additional chiral center is introduced, beside the Cα in methionine, thus leading to couples of epimers of (S,S) and (S,R) configuration, which might have different physical chemical properties and different IR spectra. For this reason a preliminary survey was performed on the different conformers of such couples, resulting in comparable energies and very similar calculated IR spectra. Figure 4.14 shows selected examples among the most stable conformers of *cis*-[PtCl(NH$_3$)$_2$Met]$^+$.

cS1 (0.0, *0.0*)   **cS2**(3.8,*5.9*)   **cN1**(17.7, *24.8*)

Figure 4.14 Optimized geometries for selected isomers of *cis*-[PtCl(NH$_3$)$_2$Met]$^+$. Numbers in brackets report relative free energies and relative enthalpies (in italics) at 298 K in kJ mol^{-1}.

The global minimum, **cS1**, corresponds to an S-platinated complex. The carboxylic group in anti conformation is involved in two hydrogen bonds, as donor to the alpha amino nitrogen and as acceptor for a hydrogen atom from a neighbouring ammonia ligand, respectively. Isomer **cS2** is only slightly higher in energy although the syn conformation of the carboxylic group impairs the hydrogen bond to the alpha amino nitrogen. However, the syn conformation is thermodynamically favoured. For example, it is reported to be more stable than the anti by 21-29 kJ mol^{-1} in gaseous acetic acid.[57] The balance between loss of a hydrogen bond interaction and gain in stability due to the syn –C(O)OH conformation accounts for the similar energy of the two conformers, of otherwise comparable structure. The third isomer, **cN1**, is an example of amino platinated methionine. The conformation of **cN1** presents a hydrogen bond between the carbonyl oxygen of the syn carboxylic group and a hydrogen atom of the neighboring ammonia ligand. Other conformers for both S- and N-ligated complexes are displayed in figure S4.9. In order to gain a general view of the potential isomeric complexes, also an oxygen ligated species has been considered. However, the energy of this complex is significantly high (127 and 137 kJ mol^{-1} above the **cS1** global minimum in free energy and enthalpy at 298 K, respectively). Complete thermodynamic data on the calculated structures are given in table S4.5.

Square planar platinum(II) complexes lend themselves to display the operation of trans influence, related to the elongation of the metal ligand bond.[58] In fact, the higher trans influence of S-ligated methionine with respect to N-ligated methionine can be appreciated in the examined geometries of *cis*-[PtCl(NH$_3$)$_2$Met]$^+$ complexes by observing that the distance between Pt and NH$_3$ in trans position with respect to methionine is 2.11 Å in S-platinated complexes, whereas it declines to 2.08 Å in N-platinated ones.

The *trans*-[PtCl(NH$_3$)$_2$Met]$^+$ complexes provide a somewhat different pattern. Representative structures are shown in figure 4.15. Thermodynamic data show that S-ligated and N-ligated species are now closer in energy and N-coordination is favored in the displayed geometries. Conformers **tN1** and **tN2** present common structural motifs including a syn configuration of the carboxylic group that is

involved as hydrogen bond acceptor towards an ammonia ligand and a hydrogen bonding interaction linking the sulfur atom with a hydrogen atom of the second ammonia.

tN1 (0.0, *2.2*)   **tS1** (1.2, *0.0*)

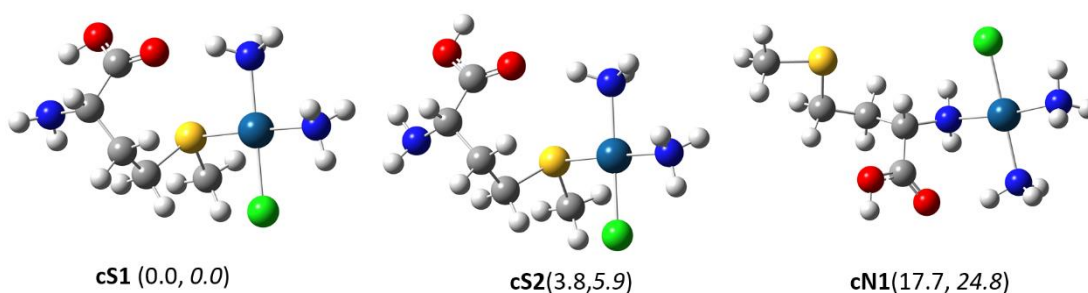**tN2** (5.9, *6.3*)   **tS2** (13.5, *19.5*)
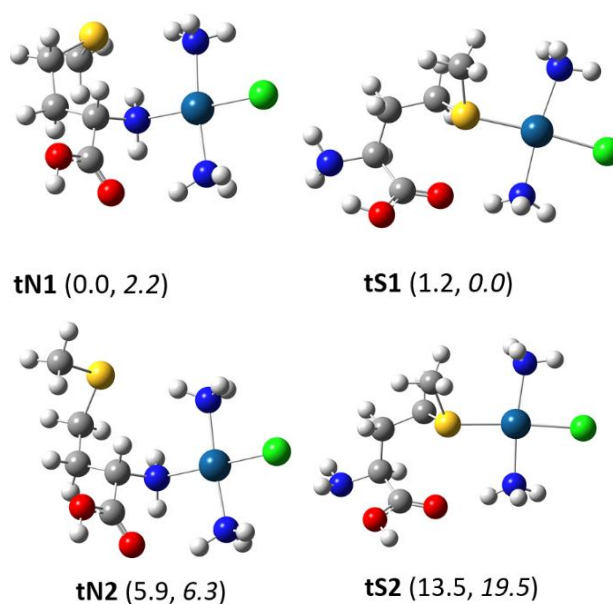
Figure 4.15 Optimized geometries for selected isomers of *trans*-[PtCl(NH$_3$)$_2$Met]$^+$. Numbers in brackets report relative free energies and relative enthalpies (in italics) at 298 K in kJ mol^{-1}.

4.4.3 Gas-phase structural and vibrational features of *cis*-[PtCl(NH$_3$)$_2$Met]$^+$

The experimental IRMPD spectra providing a signature of the structural motifs that are present in the sampled species are interpreted with the aid of computed IR spectra obtained by the vibrational analysis.

Figure 4.16 Calculated IR spectra for *cis*-[PtCl(NH$_3$)$_2$Met]$^+$ isomers. The experimental IRMPD spectrum is plotted in the background (in pale magenta).

167

In view of the extended network of hydrogen bonding interactions characterizing the $[PtCl(NH_3)_2Met]^+$ complexes, anharmonic frequency calculations have been performed aiming to verify closer correspondence with the experiment, as compared with the output of the more usual harmonic approximation. Indeed, no ad-hoc scale factor has been introduced in the computed spectra, so that the assignment of the experimental bands to the corresponding vibrational modes is very much reliable. As shown in the following, the agreement between the calculated and experimental peaks in the fingerprint region is very accurate, whereas the frequencies in the OPO part of the spectrum are slightly shifted to the red, showing that the VPT2 method probably overcorrects frequencies in that region. The so-obtained IR spectra of the representative isomers **cS1**, **cS2**, and **cN1** are shown in figure 4.16. The IR spectra computed for other optimized isomers are provided in figure S4.10.

Examining the fingerprint range, it is clear that the IRMPD spectrum is not justified by the presence of a single isomer, rather pointing to multiple species. However, the combined contribution of **cS1** and **cS2** accounts for the major vibrational features reasonably well. The X-H stretching range is also compatible with the joint presence of **cS1** and **cS2**. In particular, **cS2**, endowed with a 'free' OH in the syn configuration of the carboxylic group, accounts for the OH stretching band at 3564 cm^{-1}, in fair agreement with the calculated frequency of 3540 cm^{-1}. The broad band with a maximum at ca. 3178 may be assigned to the N-H stretch involved in hydrogen bonding calculated at 3154 and at 3042 cm^{-1} for conformer **cS2** and **cS1**, respectively, also including the O-H stretch at 3083 cm^{-1} due to conformer **cS1**. It is often found in IRMPD spectra that the X-H (X=O, N) stretching mode appears as a wide band, sometimes hardly emerging from background, when the sampled X-H is involved in hydrogen bonding. Significant redshift and considerable anharmonicity are known to affect these modes.[39,59-66] The non-linear character of IRMPD spectroscopy is an additional factor responsible for the poor matching of calculated IR resonances with the corresponding experimental features. In fact, the assumption that the amount of ion fragmentation is proportional to the IR absorbance is not always justified due to the multiphotonic nature of

IRMPD.[24,39,40,67-70] These three latter bands are calculated at lower frequency with respect to the experiment, an already reported bias of calculations regarding H-bonded X-H.[47,48] All of them are likely contributing to the experimental IRMPD feature at 3148-3184 cm^{-1} characterized by a large bandwidth. An additional feature characterizing the carboxylic OH involved in hydrogen bonding in conformer **cS1** is the notably active in plane COH bend that is blue shifted to 1380 cm^{-1} when compared with the 1295 cm^{-1} for the same mode by the 'free' OH in conformer **cS2**. As shown in figure 4.16 and table S4.3, the computed IR spectra of the representative isomers **cS1**, **cS2**, and **cN1** display several comparable absorptions, at least in terms of frequency. Notably, however, the experimental band at 3443 cm^{-1} is matched by a corresponding resonance that appears only in the IR spectra of **cS** isomers. The relevant vibrational mode is the asymmetric stretching of the α-amino group. The amino group is bonded to the metal in **cN1** (as in all N-platinated complexes) and the asymmetric NH$_2$ stretching is red-shifted to 3318 cm^{-1}, an effect that has also been recently noted for a NH$_2$ group bound to platinum.[71]

4.4.4 Gas phase structural and vibrational features of *trans*-[PtCl(NH$_3$)$_2$Met]$^+$

Figure 4.17 and table S4.4 present the calculated IR spectra for representative *trans*-[PtCl(NH$_3$)$_2$Met]$^+$ isomers, displaying unscaled anharmonic frequencies, to be compared with the experimental IRMPD spectrum. The harmonic IR spectra computed for other optimized isomers are provided in figure S4.10. One finds a generally satisfactory matching with the IR spectra of the **tN1**, **tN2**, and **tS2** representative isomers in the fingerprint range. Thus, one is not allowed to discard the contribution of any of them. In particular, one may observe the pronounced IRMPD band with a maximum at 1130 cm^{-1} that is well interpreted by the intense in plane COH bending, a common feature at ca 1141-1152 cm^{-1} in the IR spectra of all representative isomers. As stated in the previous paragraph, this frequency is typical of a carboxylic COH that is not partaking in any H bond other than the interaction with the syn carbonyl. The presence of multiple isomers is also consistent with the relatively large bandwidth of the C=O stretching mode at 1745 cm^{-1} which amounts to 52 cm^{-1}, to be compared with the 36 cm^{-1} width (fwhm) for the corresponding band at 1754 cm^{-1} in the IRMPD spectrum of the cis-complex.
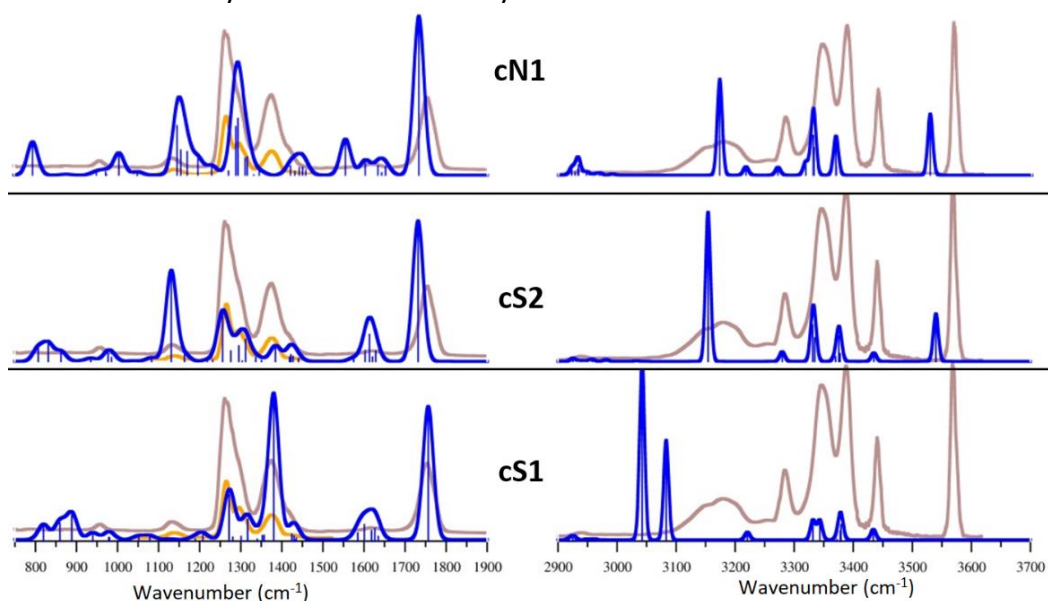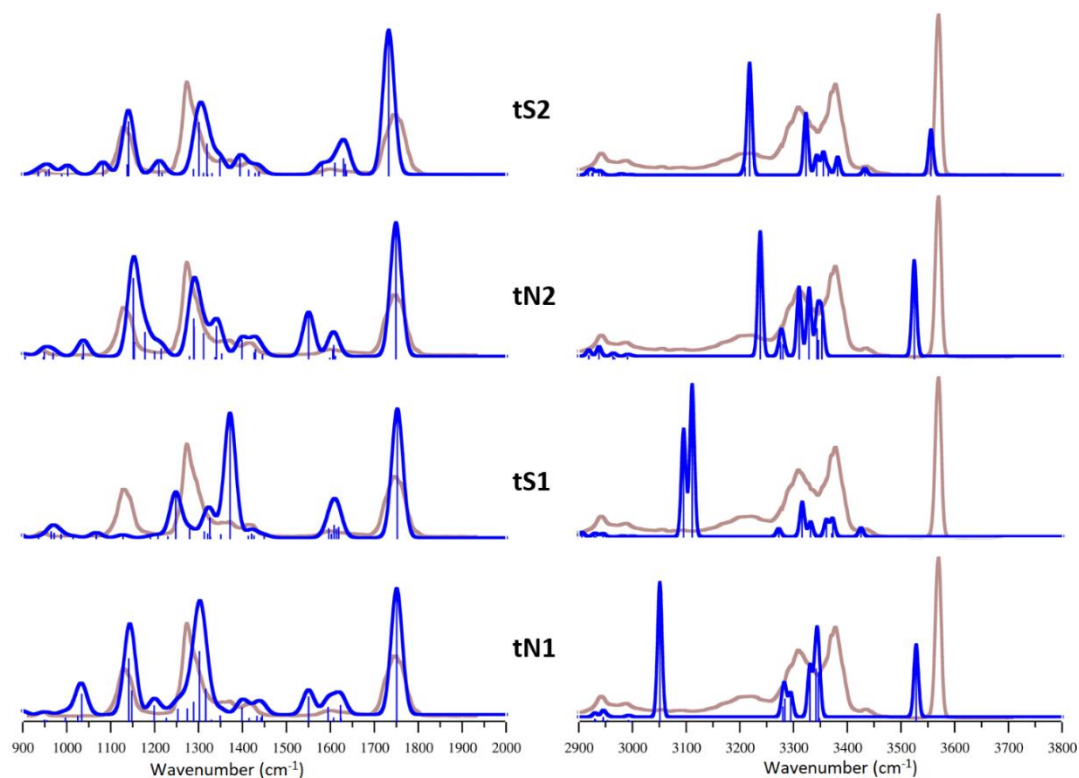
Figure 4.17 Calculated IR spectra for *trans*-[PtCl(NH$_3$)$_2$Met]$^+$ isomers. The experimental IRMPD spectrum is plotted in the background (in pale magenta).

Because the conformation and local environment of the carboxylic group is similar in the three isomers, it is not surprising that the frequency of the OH stretch is comparable for the three species tN1, tN2 and tS2, namely at 3528, 3525, and 3556 cm^{-1}, accounting for the distinct IRMPD band at 3570 cm^{-1}, that is comparatively more intense than in the IRMPD spectrum of the *cis*-[PtCl(NH$_3$)$_2$Met]$^+$ isomer. The matching between the calculated IR spectra and the experimental IRMPD features is thus fair also in the X-H (X = C, N, O) stretching range. One may note, though, a tendency of calculated anharmonic frequencies to lie at typically lower values in comparison with the experimental wavenumbers in the X-H stretching region. This observation applies for example to both the OH stretch and asymmetric NH$_3$ stretches calculated at 3525-3528 cm^{-1} and 3330-3346 cm^{-1}, respectively, for **tN1** and **tN2** conformers. Also for the *trans*-[PtCl(NH$_3$)$_2$Met]$^+$ isomer, particular interest is attached to what is now a weak IRMPD band at 3434 cm^{-1}. As already noted for *cis*-[PtCl(NH$_3$)$_2$Met]$^+$, this band is associated to the asymmetric NH$_2$ stretching of S-ligated complexes. In fact, it finds a counterpart in the IR resonance at 3426 cm^{-1} for

tS1 and at 3433 cm^{-1} for **tS2**, while in **tN1** and **tN2** isomers the asymmetric NH2 stretching appears at 3295 and 3329 cm^{-1}, respectively.

4.4.5 IRMPD kinetics to probe N- or S-platination in [PtCl(NH$_3$)$_2$Met]$^+$ complexes

As underlined in the previous paragraphs, both *cis-* and *trans-*[PtCl(NH$_3$)$_2$Met]$^+$ isomers present a diagnostic band at ca. 3440 cm^{-1} that is characteristic of S-ligated isomers, being associated to the asymmetric NH$_2$ stretch of the α-amino group when not involved in coordination to the metal. This resonance may therefore be exploited to gain a qualitative measure of the relative amount of S- and N-ligated complexes in the sampled ion population. To this end, one may rely on the extent of photogragmentation observed at this characteristic frequency, measuring the amplitude of the photofragmentation kinetics recorded upon increasing irradiation time, as described by Williams in his seminal papers.[49,52,53] It is preliminarily worth mentioning that any interconversion between S- and N-ligated complexes, once these species are isolated in the gas phase, is highly unlikely being hindered by a high energy barrier for the breakage of a coordination bond prior to rearrangement and bonding to the other methionine active site. An estimate for the barrier involved in such kind of rearrangement has been provided for the interconversion between N$_\pi$- and N$_\tau$-ligated cisplatin complexes with histidine where metal binding could involve either tautomeric form of the imidazole side group of the amino acid, as reported in section 4.3.

Figure 4.18 illustrates the depletion of the parent ion abundance as a function of irradiation time. For both *cis-* and *trans-*[PtCl(NH$_3$)$_2$Met]$^+$ isomers the decay responds to a monoexponential function suggesting that at the tested frequencies, 3443 and 3434 cm^{-1}, respectively, the assayed ion population conforms to a uniform photofragmentation behavior. This issue is further confirmed by the comparable kinetic rate constant, 0.067 and 0.11 s^{-1}, found for the two species. However, as shown in figure 4.18, the amplitude of the photofragmentation process is quite different. For the *trans*-isomer the parent ion abundance levels off at an unreactive fraction of ca. 64% while for the *cis*-isomer the depletion is nearly complete with a residual 6% of the sampled ions that is resistant to photofragmentation. Because the sampled mode is characteristic of S-platination of methionine, it may be

inferred that the vast majority of *cis*-[PtCl(NH₃)₂Met]⁺ is represented by S-ligated complexes, such as **cS1**, **cS2**, whereas the sampled *trans*-[PtCl(NH₃)₂Met]⁺ ions are in fact a more balanced mixture of S- and N-ligated complexes, such as **tN1/tN2** and **tS1/tS2**.
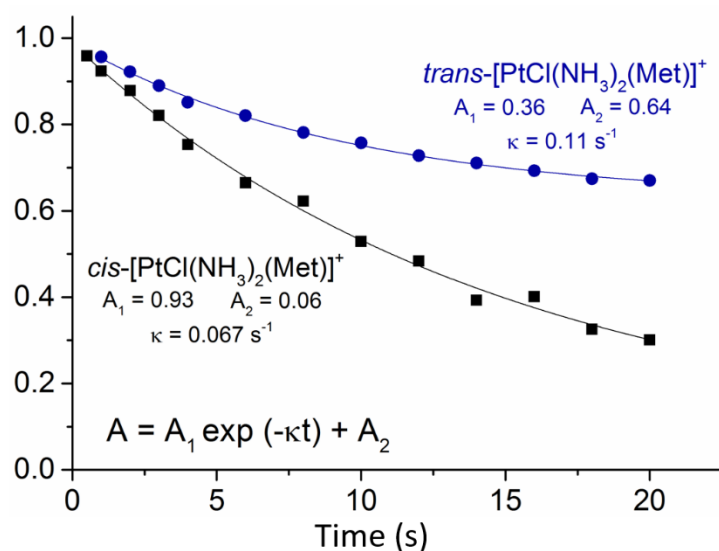
Figure 4.18 Plot of the relative abundance of the sampled ion, [PtCl(NH₃)₂Met]⁺ *cis* and *trans* isomers, as a function of the irradiation time. Fitting exponential functions are reported.

It is worth noting that the relative population of S- and N-ligated complexes obtained by photofragmentation experiments is very close to the one calculated by applying Boltzmann distribution with the computed free energy differences. In the latter case, a fraction of 62% is obtained for the N-ligated species.
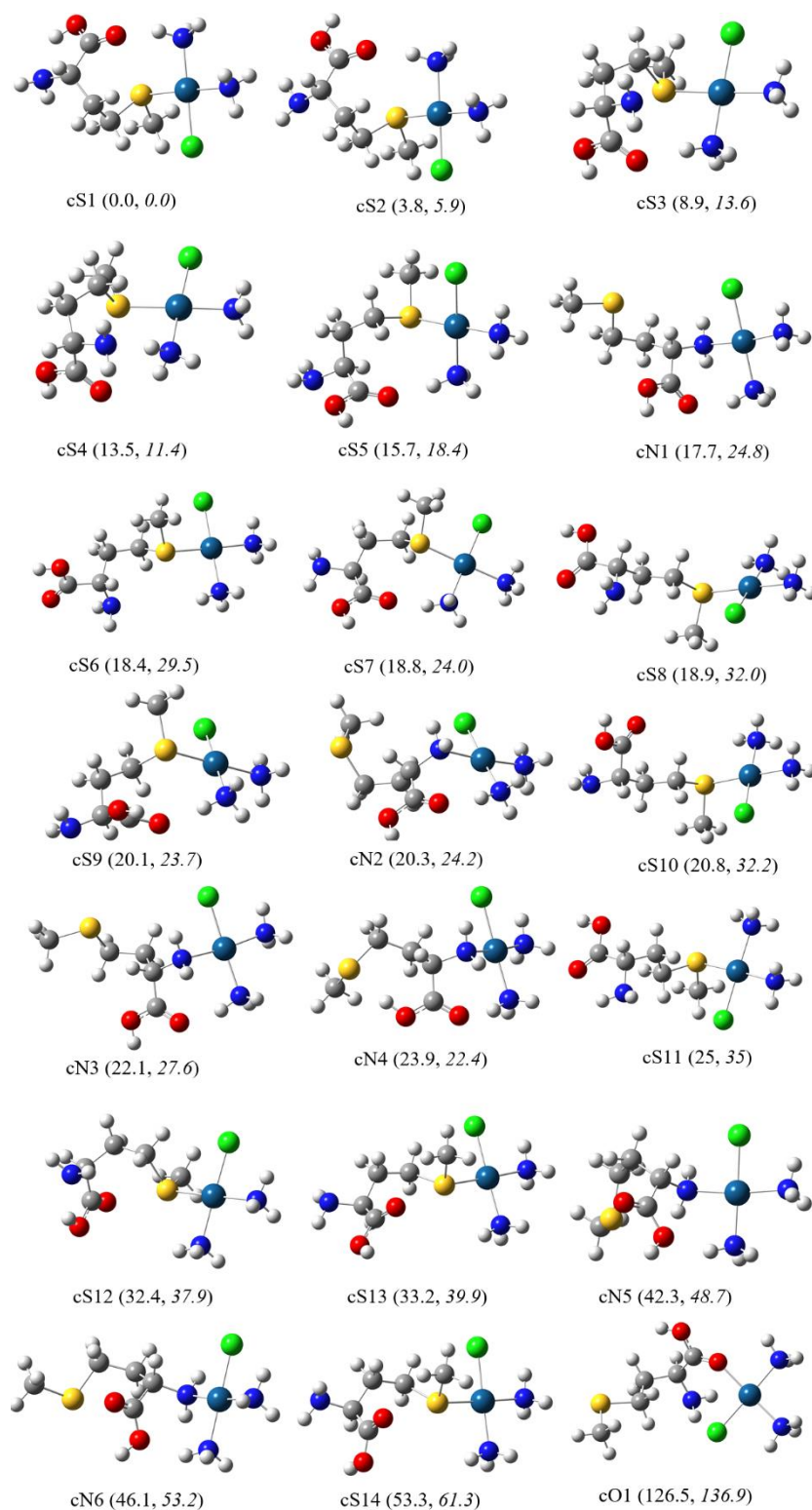
Figure S4.9 Optimized geometries for the most stable conformers of *cis*-[PtCl(NH₃)₂Met]⁺ involving platination of the amino acid at either thioether sulfur or amino nitrogen or (one example) carbonyl oxygen.

tN1 (0.0, *2.2*) tS1 (1.2, *0.0*) tN2 (5.9, *6.3*)

tN3 (11.9, *15.0*) tS2 (13.5, *19.5*) tS3 (20.7, *25.2*)

tN4 (25.3, *25.6*) tS4 (30.0, *33.6*) tS5 (41.5, *44.7*)

tN5 (55.8, *61.1*)
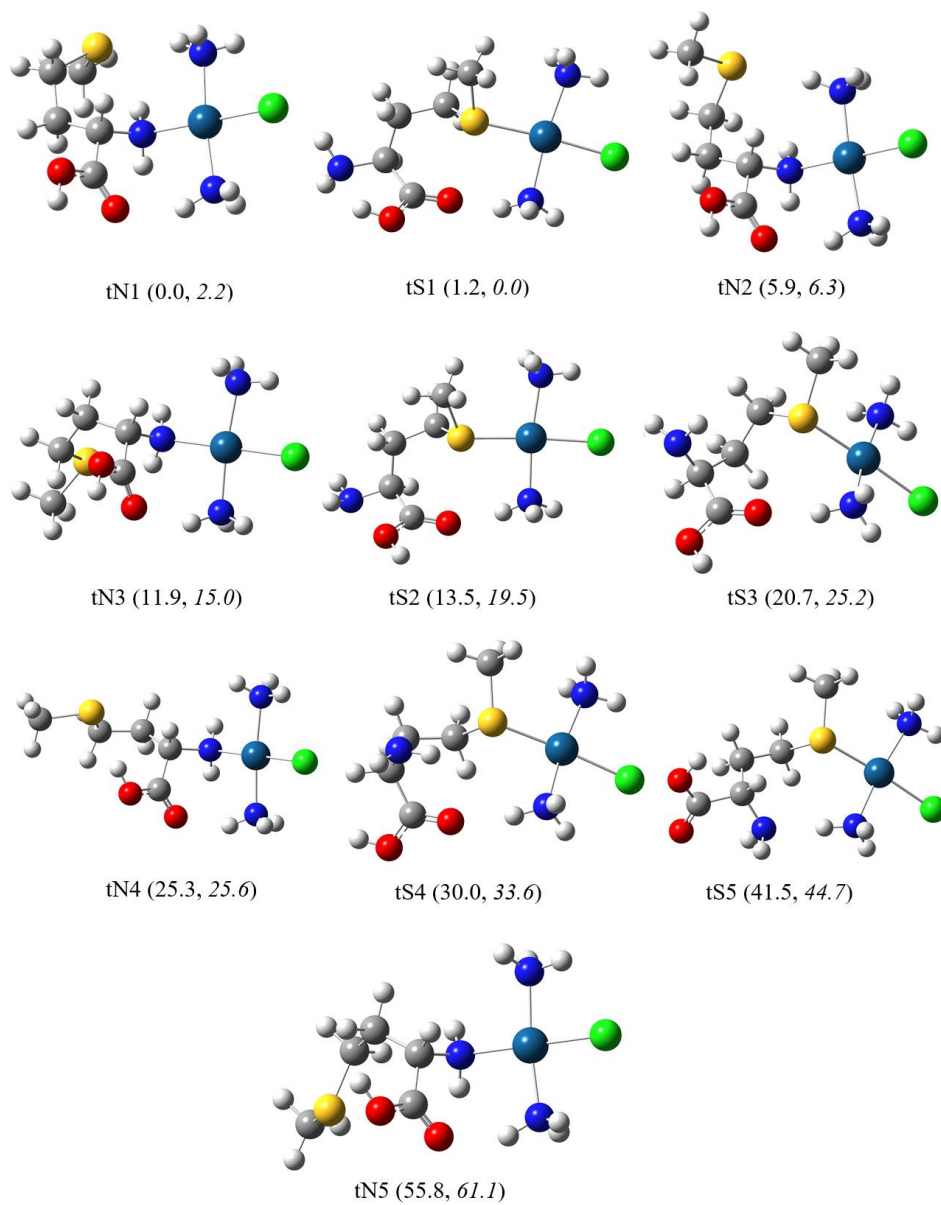
Figure S4.10 Optimized geometries for the most stable conformers of *trans*-[PtCl(NH$_3$)$_2$Met]$^+$ involving platination of the amino acid at either thioether sulfur or amino nitrogen.
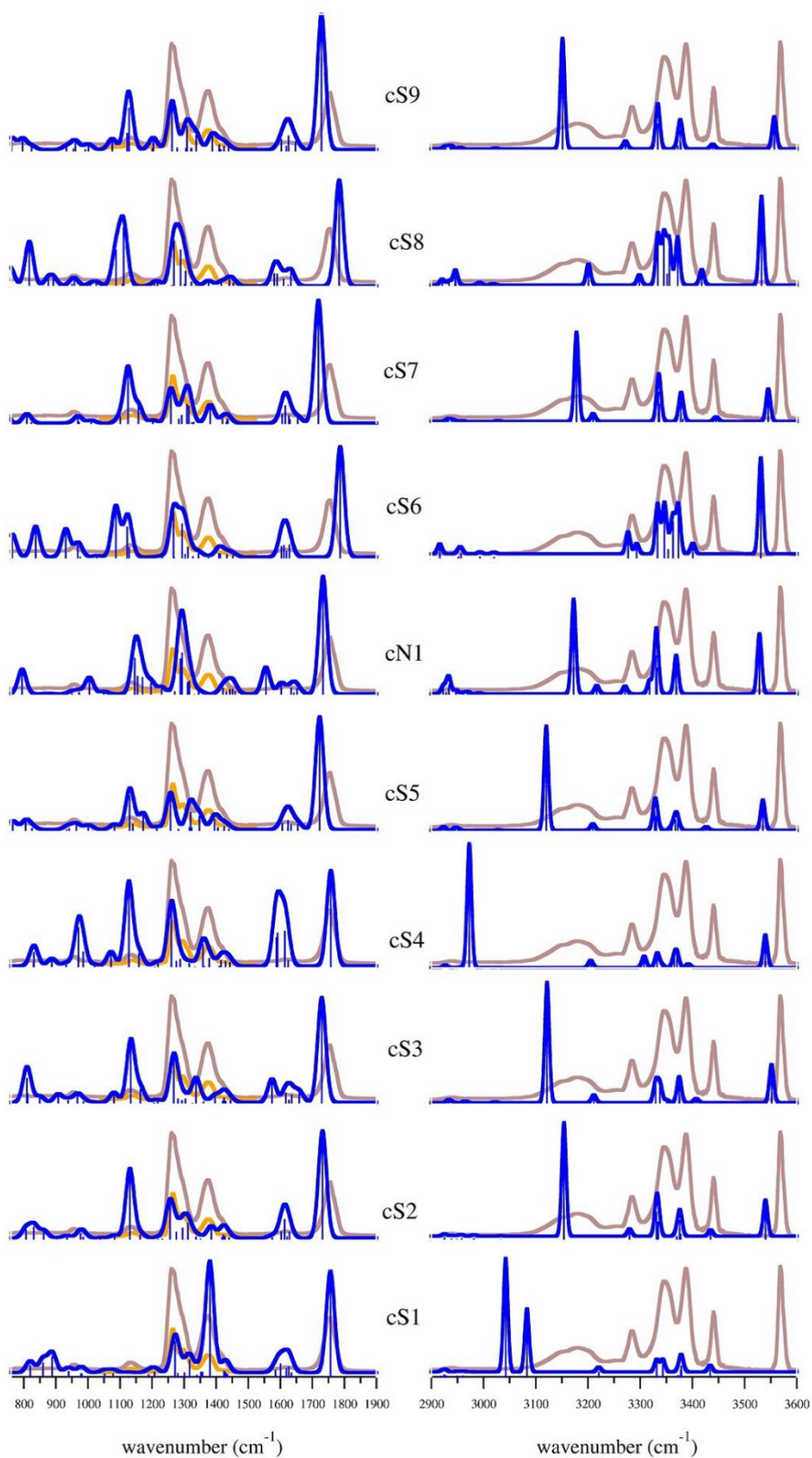
Figure S4.11 Calculated IR spectra for *cis*-[PtCl(NH₃)₂Met]⁺ isomers. The experimental IRMPD spectrum is plotted in the background (in pale magenta).
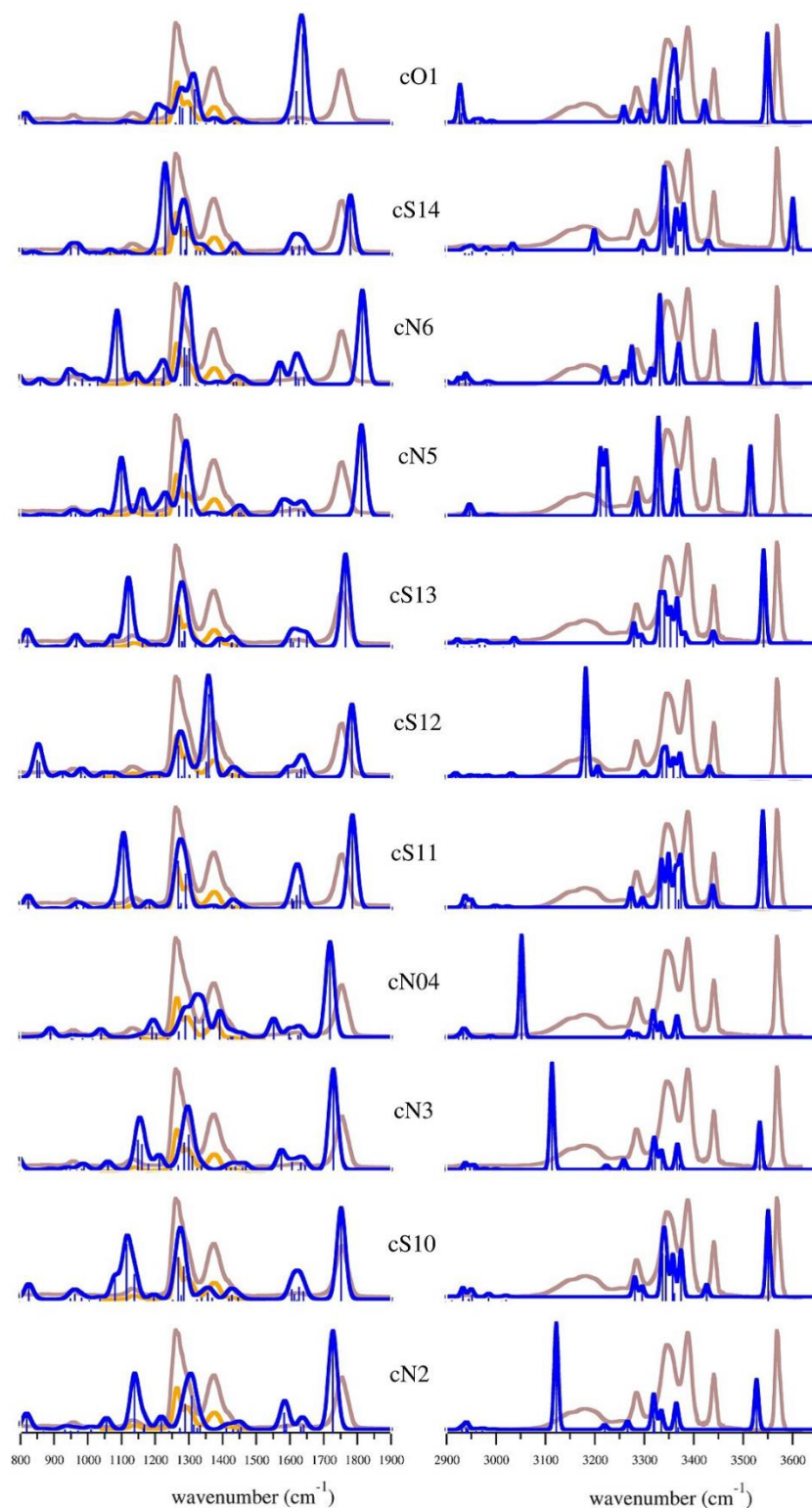
Figure S4.11 (continuation) Calculated IR spectra for *cis*-[PtCl(NH$_3$)$_2$Met]$^+$ isomers. The experimental IRMPD spectrum is plotted in the background (in pale magenta).
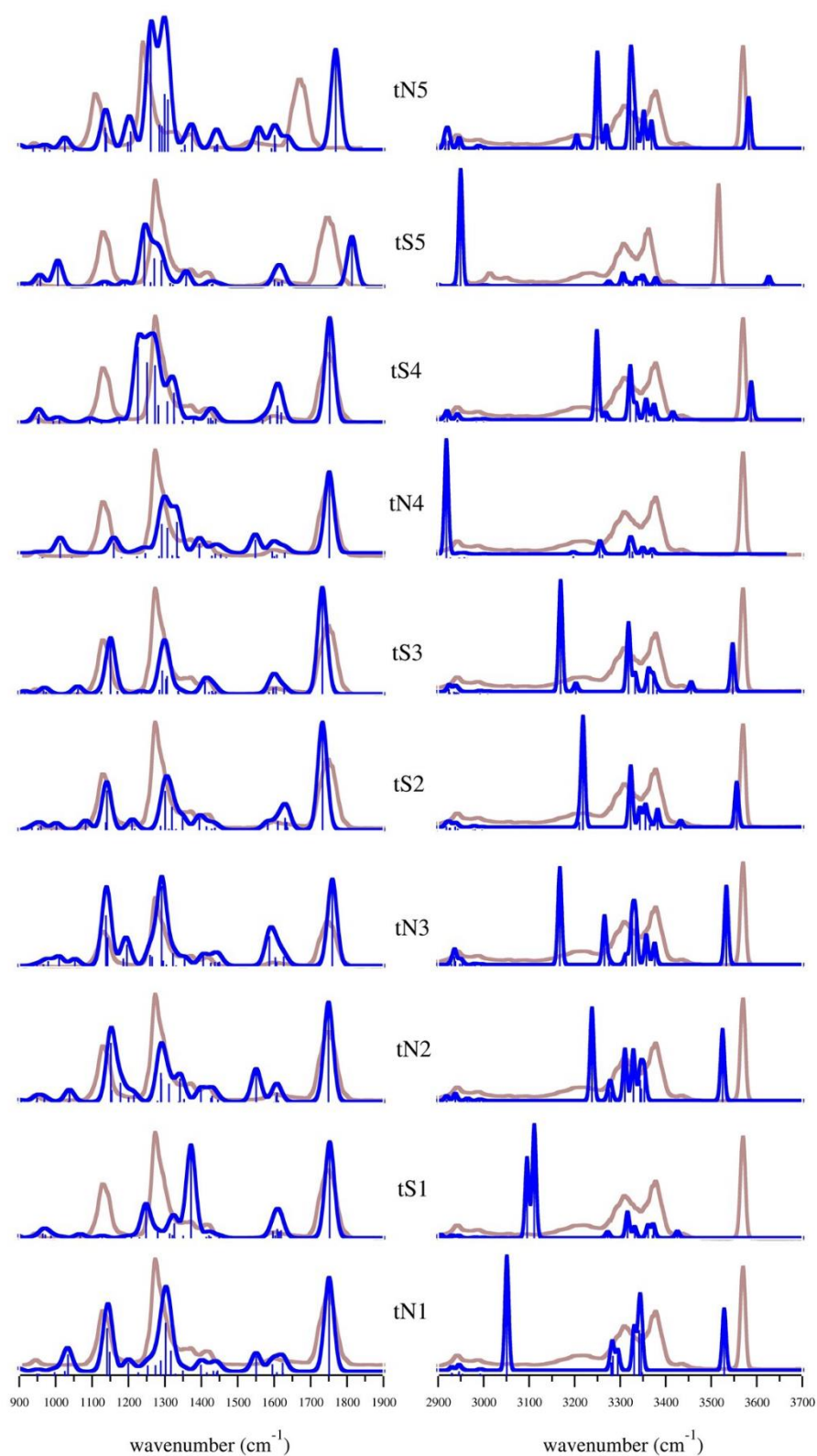
Figure S4.12 Calculated IR spectra for *trans*-[PtCl(NH$_3$)$_2$Met]$^+$ isomers. The experimental IRMPD spectrum is plotted in the background (in pale magenta).

Table S4.3 Selected vibrational transitions observed for *cis*-[PtCl(NH$_3$)$_2$(Met)]$^+$ in the IRMPD spectra compared with anharmonic frequencies calculated for representative isomers at the B3LYP/BS1 (BS1: 6311+G(2df,pd) for H, N, C and O; 6311+G(3df) for S; Pt:LANL2TZ-f) level, along with mode assignments.

v_{exp}[a]	v_{calc}(**cS1**)[a,b]	v_{calc}(**cS2**)[a,b]	v_{calc}(**cN1**)[a,b]	Mode assignment[d]
-	820 (42)	807 (37)	-	-NH$_3$ β$_t$
-	860 (51)	862 (28)	-	NH$_2$ β$_w$, CH$_2$-CH$_2$ σ
-	888 (73)	-	-	O-H β$_w$
955	-	977 (22)	-	CH$_3$ β$_t$
-	-	-	1004 (48)	NH$_2$-C$_\alpha$ σ, molecular deformation
1133	-	1131 (253)	-	O-H β$_s$, NH$_2$ β$_t$
-	-	-	1146 (108)	O-H β$_s$, C(=O)-OH σ, CH$_2$ β$_w$
-	-	-	1155 (55)	O-H β$_s$, C(=O)-OH σ, CH$_2$ β$_w$
-	-	-	1170 (52)	NH$_2$ β$_w$, CH$_2$ β$_w$
-	-	-	1196 (36)	NH$_2$ β$_t$, O-H β$_s$
1260	1272 (130)	1256 (133)	1288 (106)	-NH$_3$ β$_u$
-	-	1276 (30)	-	C$_\alpha$-H β
1294 (s)[c]	-	1295 (44)	-	O-H β$_s$
	1317 (62)	1312 (62)	1294 (123)	NH$_3$ β$_u$
-	-	-	1311 (37)	CH$_3$ β$_u$
-	-	-	1316 (41)	NH$_2$ β$_t$, O-H β$_s$
1376	1380 (404)	-	-	O-H β$_s$, C(=O)-OH σ
-	-	1384 (44)	-	C-OH σ, NH$_2$ β$_t$, molecular deformation
1426 (s)[c]	1424 (20)	-	-	C$_\beta$H$_2$ β$_s$
-	-	-	1555 (78)	NH$_2$ β$_s$
1616	1585 (24)	1603 (30)	1603 (32)	NH$_3$ β$_s$
	1601 (47)	1614 (76)	-	NH$_2$ β$_s$
	1626 (36)	1628 (29)	1634 (20)	NH$_3$ β$_s$
1754	1756 (372)	1732 (393)	1733 (345)	C=O σ
2942	-	-	2934 (23)	CH$_3$ σ$_s$
3148-3184 (3113-3225)	3042 (500)	3154 (333)	-	NH$_3$ σ$_s$
	3083 (278)	-	-	O-H σ
	3221 (21)	-	3173 (208)	NH$_3$ σ$_s$
3255	-	-	-	
3284	-	3280 (21)	-	NH$_3$ σ$_s$
-	-	-	3318 (29)	NH$_2$ σ$_a$
3347	-	3331 (82)	3330 (87)	NH$_3$ σ$_a$
	3332 (55)	-	-	NH$_3$ σ$_s$
	3343 (55)	3335 (55)	3332 (60)	NH$_3$ σ$_a$
3386	3378 (29)	3376 (58)	3369 (65)	NH$_3$ σ$_a$
	3379 (47)	-	-	NH$_3$ σ$_a$
	-	3280 (21)	-	NH$_3$ σ$_s$
3443	3434 (29)	3435 (19)	-	NH$_2$ σ$_a$
3564	-	3540 (106)	3528 (132)	O-H σ

[a] Wavenumbers in cm^{-1}.

[b] Calculated harmonic IR intensities are given in parentheses (km mol^{-1}). Transitions with intensity lower than 20 km mol^{-1} are (usually) not reported. Frequencies (anharmonic) are not scaled.

[c] s, shoulder.

[d] σ = stretching mode; σ$_a$ = asymmetric stretching; σ$_s$ = symmetric stretching; β= bending mode; β$_s$= scissoring (symmetric bending in plane); β$_w$ = wagging (symmetric bending out of plane), β$_t$ = twisting (asymmetric bending out of plane).

Table S4.4 Selected vibrational transitions observed for *trans*-[PtCl(NH$_3$)$_2$(Met)]$^+$ in the IRMPD spectra compared with anharmonic frequencies calculated for representative isomers at the B3LYP/BS1 (BS1: 6311+G(2df,pd) for H, N, C and O; 6311+G(3df) for S; Pt:LANL2TZ-f) level, along with mode assignments.

ν_{exp}[a]	ν_{calc}(**tN1**)[a,b]	ν_{calc}(**tS1**)[a,b]	ν_{calc}(**tN2**)[a,b]	ν_{calc}(**tS2**)[a,b]	Mode assignment[d]
-	842 (55)	830 (76),	844 (49)	-	NH$_3$ β_w
		863 (83)			O-H β_w
		878 (34)			NH$_3$ β_w
944	-	965 (22)	-	-	CH$_3$ β_w
-	1034 (60)		1038 (32)	-	NH$_2$-C σ, C$_\alpha$-C(=O) σ
-	-		-	1082 (34)	C$_\alpha$-NH$_2$ σ , NH$_2$ β_t , C$_\alpha$-H
1130	1141 (137)		1152 (175)	1141 (146)	O-H β_s , C(=O)-OH σ
	1148 (67)		1154 (36)	1138 (29)	NH$_2$ β_w , C$_\beta$H$_2$ β_t , C$_\gamma$H$_2$ β_t
-	1199 (35)		1178 (57)	1210 (32)	NH$_2$ β_t , O-H β_s , C$_\beta$H$_2$ β_t , C$_\gamma$H$_2$ β_t
1275	1253 (27)	1280 (30)	-	-	NH$_2$ β_t , CH$_2$ β
	1274 (28)		-	-	NH$_2$ β_t , CH$_2$ β
	1289 (42)	1248 (147)	1312 (55)	1301 (144)	NH$_3$ β_u
	1302 (153)	1326 (67)	1290 (69)	1319 (86)	NH$_3$ β_u
-	1316 (71)	1313 (22)	-	-	N-H β, C-H β, O-H β_s
1356-1372	-	1372 (405)	1341 (70)	1394 (48)	O-H β_s , C(=O)-OH σ, C$_\alpha$-H β
1416	1399 (30)		-	-	O-H β_s , NH$_2$ β_t, C$_\beta$H$_2$ β_t
	-		1399 (40)	-	C$_\alpha$-COOH σ , C$_\alpha$-H β , NH$_2$ β_t
-	1550 (54)	1609 (42)	1551 (96)	1630 (45)	NH$_2$ β_s
1600	1595 (31)	1596 (32)	-	1610 (34) /1634 (30)	NH$_3$ β_s
	1623 (35)	1614 (30)/1619 (36)	1608 (29)	1582 (29)	NH$_3$ β_s
1745	1751 (275)	1752 (414)	1749 (292)	1733 (394)	C=O σ
2942	-		-	-	C-H σ_s
2988	-		-	-	C-H σ_a
3055	3051 (294)	-	-	-	N(H$_2$)-H σ
-	-	3095 (293)	-	-	O-H σ
3202-3226 (3155-3250)	-	3111 (414)	-	3218 (242)	NH$_3$ σ_s
3308	3280 (32)	3272 (21)	3238 (204)	-	NH$_3$ σ_s
	3284 (49)		3276 (28)	-	NH$_3$ σ_s
	3295 (51)		-	-	NH$_2$ σ_a
	-	3316 (94)	-	3323 (135)	NH$_3$ σ_a
3378	-		3310 (113)	-	NH$_3$ σ_s
	-		3329 (112)	-	NH$_2$ σ_a
	3330 (111)	3332 (40)	3353 (65)	-	NH$_3$ σ_a
	3342 (115)		3344 (49)	3343 (43)	NH$_3$ σ_a
	3346 (106)	3361 (46)	-	3356 (49)	NH$_3$ σ_a
	-		3346 (30)	-	NH$_2$ σ_a
	-	3373 (38)	-	3382 (39)	NH$_3$ σ_a

3434	-	3426 (24)	-	3433 (14)	NH$_2$ σ$_a$
3570	3528 (157)	-	3525 (156)	3556 (99)	O-H σ

[a] Wavenumbers in cm^{-1}. [b] Calculated harmonic IR intensities are given in parentheses (km mol^{-1}). Transitions with intensity lower than 20 km mol^{-1} are (usually) not reported. Frequencies (anharmonic) are not scaled. [c] s, shoulder. [d] σ = stretching mode; σ$_a$ = asymmetric stretching; σ$_s$ = symmetric stretching; β= bending mode; β$_s$= scissoring (symmetric bending in plane); β$_w$ = wagging (symmetric bending out of plane), β$_t$ = twisting (asymmetric bending out of plane).

Table S4.5 Theoretically calculated thermodynamic parameters for the most stable structures of sampled [PtCl(NH$_3$)$_2$Met]$^+$ complexes.

cis-[PtCl(NH$_3$)$_2$Met]$^+$

conformer	ΔG(KJ/mol)	ΔH(KJ/mol)
cS1	0.0	0.0
cS2	3.8	5.9
cS3	8.9	13.6
cS4	13.5	11.4
cS5	15.7	18.4
cN1	17.7	24.8
cS6	18.4	29.5
cS7	18.8	24.0
cS8	18.9	32.0
cS9	20.1	23.7
cN2	20.3	24.2
cS10	20.8	32.2
cN3	22.1	27.6
cN4	23.9	22.4
cS11	24.8	35.2
cS12	32.4	37.9
cS13	33.2	39.9
cN5	42.3	48.7
cN6	46.1	53.2
cS14	53.3	61.3
cO1	126.5	136.9

trans-[PtCl(NH$_3$)$_2$Met]$^+$

conformer	ΔG(KJ/mol)	ΔH(KJ/mol)
tN1	0.0	2.0
tS1	1.2	0.0
tN2	5.9	6.3
tN3	11.9	15.0
tS2	13.5	19.5
tS3	20.7	25.2
tN4	25.3	25.6
tS4	30.0	33.6
tS5	41.5	44.7
tN5	55.8	61.1

4.5 Summary

In conclusion, ESI has allowed us to reveal the primary complex involving cisplatin coordination to histidine, and both cisplatin and its isomer transplatin with methionine, delivering it to the gas-phase for analysis by mass spectrometry and IR spectroscopy.

The *cis*-[PtCl(NH$_3$)$_2$(His)]$^+$ complex has shown metal coordination engaging the N$_\pi$ and N$_\tau$ imino nitrogens of the imidazole group. The so-formed **N$_\pi$** and **N$_\tau$** isomers result from cisplatin attack to either one of the same aza functional group of the imidazole ring, differing for the position relative to the amino acid side chain, existing in the two tautomers of histidine. Both sites are expected to bind the metal, as reported for similar platinum(II) complexes.[14] Moreover, we were able to give an estimate of the individual contributions of **N$_\pi$** and **N$_\tau$** isomers and conformers relying on IRMPD kinetic measurements. Ultimately, one may assign approximate fractions for the species partaking in the sampled population, namely 45% for **N$_\pi$_1**, 30% for **N$_\pi$_2**, and 12.5% for both **N$_\tau$_1** and **N$_\tau$_2**. The latter assignment is obtained from the 25% fraction that is not IRMPD active in the XH stretching range and assigned to **N$_\tau$_1** and **N$_\tau$_2** isomers, on account of their nearly equal free energy at room temperature (see table 4.1 at pag. 137). Notably, the relative fraction of **N$_\pi$** and **N$_\tau$** isomers sampled in the gas-phase does not respond to the respective gas-phase stabilities. It rather reveals the outcome of the cisplatin reaction in solution, reflecting the kinetically trapped **N$_\pi$** and **N$_\tau$** ratio. Indeed, several authors have reported that in a variety of instances the ion population sampled by ESI reflects kinetic trapping rather than being governed by the gas phase.[72-74] The comparable stability of **N$_\pi$** and **N$_\tau$** isomers when solvation is accounted for lends further support to this line of reasoning, although thermodynamic considerations alone do not provide a uniform rationale to the reactivity patterns observed in the solution chemistry of platinum(II) complexes.[14]

Regarding the isomeric [PtCl(NH$_3$)$_2$Met]$^+$ complexes obtained from cis- and transplatin, two major binding motifs of the platinated methionine complexes have

been identified analyzing the matching between the IR spectra for the computed geometries and the respective experimental IRMPD spectra, in particular the S atom of the thioether function and the nitrogen of the amino group. In this process, a diagnostic vibrational feature has been identified in the asymmetric NH_2 stretch of a 'free' α-amino group at ca. 3440 cm^{-1} that is characteristic of S-ligated complexes. Thus, besides viewing a comparative analysis of experimental vibrational spectra and computed IR spectra for representative isomers one can rely also on the relative amplitude of the photofragmentation process at the frequency of the characteristic asymmetric stretch of free NH_2 to obtain an estimate of S- and N-methionine platination. These criteria concur to the conclusion that both *cis*- and *trans*-[PtCl(NH$_3$)$_2$Met]$^+$ are represented by a mixture of isomers/conformers involving either S- or N-coordination. However, while *cis*-[PtCl(NH$_3$)$_2$Met]$^+$ is largely S-ligated, in the case of *trans*-[PtCl(NH$_3$)$_2$Met]$^+$ S- and N-coordination appear in approximate 1:2 ratio, respectively. Because substantial activation barriers are expected for any rearrangement process involving interconversion between S- and N-ligated complexes in the gas phase, the conclusion may be drawn that while cisplatin is highly selective in attacking the thioether function of methionine, transplatin does not appreciably discriminate between the S atom and the amino nitrogen. Whether this finding reflects the operation of kinetic barriers or conforms to a partition determined by equilibrium thermodynamics cannot be presently stated on the basis of exclusively experimental data. Thermodynamic and kinetic properties of cisplatin interactions have been addressed in a conspicuous number of theoretical papers, reflecting the complex nature of these interactions and their dependence on several factors. Ab initio calculations have been used to derive the second order rate constant for the associative ligand exchange mechanism according to transition state theory.[21] Agreement with the experimental rate constant was obtained using the supermolecular approach for S-binding of methionine.[21] In the kinetic competition of simple nitrogen and sulfur ligands quantum chemical calculations revealed a faster reaction of cisplatin derivatives with the N-nucleophile, affected, however, by significant substituent and solvent effects.[75] Using the supermolecular approach, the thermodynamic aspects for the

ligand substitution of cisplatin aqua complexes by Met have revealed that the formation of monodentate complexes involves similar free energy release for either S- or N-ligation. However, the effect of the environment is important and in water solution S-ligation is thermodynamically preferred in a broad range of pH.[19-21] The computational results that are presently reported confirm cisplatin derived complexes with Met to be preferentially S-bound, as isolated species, whereas in the transplatin complexes N-ligation is comparatively more favored. The different stabilities of N- and S-platinated isomers in *cis*-[PtCl(NH$_3$)$_2$Met]$^+$ and *trans*-[PtCl(NH$_3$)$_2$Met]$^+$ can be related to the thermodynamic trans influence. Although the affinity of platinum(II) for the sulfur atom is stronger than for nitrogen, the S-ligated trans isomer, which presents two ligands with a relatively marked trans influence in trans position, becomes less stable, so that a mixture of similarly populated S-platinated and N-platinated trans isomers is obtained as the product of the substitution reaction. Finally, the recorded IRMPD spectra and photofragmentation kinetics have provided valuable structural signatures for the sampled isomeric [PtCl(NH$_3$)$_2$Met]$^+$ complexes.

References

[1] Lippert, B. *Cisplatin: Chemistry and Biochemistry of a Leading Anticancer Drug* (1999) Wiley-VCH, Zurich.

[2] Jamieson, E.R., Lippard, S.J. **Structure, recognition, and processing of cisplatin–dna adducts** *Chem. Rev.* 99 (1999) 2467-2498.

[3] Wong, E., Giandomenico, C.M. **Current status of platinum-based antitumor drugs** *Chem. Rev.* 99 (1999) 2451–2466.

[4] Fuertes, M.A., Alonso, C., Pérez, J.M. **Biochemical modulation of cisplatin mechanisms of action: enhancement of antitumor activity and circumvention of drug resistance** *Chem. Rev.* 103 (2003) 645-662.

[5] Klein, A.V., Hambley, T.W. **Platinum drug distribution in cancer cells and tumors** *Chem. Rev.* 109 (2009) 4911-4920.

[6] Dasari, S., Tchounwou, P.B., **Cisplatin in cancer therapy: Molecular mechanisms of action** *Eur. J. Pharmacol.*, 740 (2014) 364-378.

[7] Wirth, R., White, J.D., Moghaddam, A.D., Ginzburg, A.L., Zakharov, L.N., Haley, M.M., Derose, V.J. **Azide vs Alkyne Functionalization in Pt(II) complexes for post-treatment click modification: solid-state structure, fluorescent labeling and cellular fate** *J. Am. Chem. Soc.* 137 (2015) 15169-15175.

[8] Sava, G., Jaouen, G., Hillard, E.A., Bergamo, A. **Targeted therapy vs. DNA-adduct formation-guided design: Thoughts about the future of metal-based anticancer drugs** *Dalton Trans.* 41 (2012) 8226-8234.

[9] Casini, A., Reedijk, J. **Interactions of anticancer Pt compounds with proteins: an overlooked topic in medicinal inorganic chemistry?** *Chem. Sci.* 3 (2012) 3135-3144.

[10] Calderone, V., Casini, A., Mangani, S., Messori, L., Orioli, P.L. **Structural investigation of cisplatin-protein interactions: Selective platination of His19 in a cuprozinc superoxide dismutase** *Angew. Chemie - Int. Ed.* 45 (2006) 1267-1269.

[11] Li, H., Zhao, Y., Phillips, H.I., Qi, Y., Lin, T.Y., Sadler, P.J., O'Connor, P.B. **Mass spectrometry evidence for cisplatin as a protein cross-linking reagent** *Anal. Chem.* 83 (2011) 5369-5376.

[12] Messori, L., Merlino, A. **Cisplatin binding to proteins: molecular structure of the ribonuclease A adduct** *Inorg. Chem.* 53 (2014) 3929–3931.

[13] Saudek, V., Pivcova, H., Noskova, D., Drobnik, J. **The reaction of Pt-antitumor Drugs with selected nucleophiles. II. Preparation and Characterization of Coordination Compounds of Pt(II) and L-Histidine** *J. Inorg. Biochem.* 23 (1985) 55-72.

[14] Appleton T.G. **Donor atom preferences in complexes of platinum and palladium with amino acids and related molecules** *Coord. Chem. Rev.* 166 (1997) 313-359.

[15] Norman, R.E., Ranford, J.D., Sadler, P.J. **Studies of platinum(II) methionine complexes: metabolites of cisplatin** *Inorg. Chem.* 31 (1992) 877-888.

[16] Appleton, T.G., Connor, J.W., Hall, J.R. **S,O- versus S,N-chelation in the reactions of the cis-diamminediaquaplatinum(II) cation with methionine and S-methylcysteine** *Inorg. Chem.* 27 (1988) 130-137.

[17] El-Khateeb, M., Appleton, T.G., Gahan, L.R., Charles, B.G., Berners-Price, S.J., Bolton, A.-M. **Reactions of cisplatin hydrolytes with methionine, cysteine, and plasma ultrafiltrate studied by a combination of HPLC and NMR techniques** *J. Inorg. Biochem.* 77 (1999) 13-21.

[18] Heudi, O., Cailleux, A., Allain, P.J. **Kinetic studies of the reactivity between cisplatin and its monoaquo species with L-methionine** *J. Inorg. Biochem.* 71 (1998) 61-69.

[19] Zimmermann, T., Chval, Z., Burda, J.V. **Cisplatin interaction with cysteine and methionine in aqueous solution: Computational DFT/PCM study** *J. Phys. Chem. B* 113 (2009) 3139-3150.

[20] Zimmermann, T., Burda, J.V. **Reactions of cisplatin with cysteine and methionine at constant pH; a computational study** *Dalton Trans.* 39 (2010) 1295-1301.

[21] Silva, V.J.D., Costa, L.A.S., Dos Santos, H.F. **Ab initio reaction path for cisplatin interaction with L-cysteine and L-methionine** *Int. J. Quantum Chem.* 108 (2008) 401-414.

[22] Zimmermann, T., Zeizinger, M., Burda, J.V. **Cisplatin interaction with cysteine and methionine, a theoretical DFT study** *J. Inorg. Biochem.* 99 (2005) 2184-2196.

[23] De Petris, A., Crestoni, M.E., Pirolli, A., Rovira, C., Iglesias-Fernández, J., Chiavarino, B., Ragno, R., Fornarini, S. **Binding of azole drugs to heme: A combined MS/MS and computational approach** *Polyhedron* 90 (2015) 245-251.

[24] MacAleese, L., Maitre, P. **Infrared spectroscopy of organometallic ions in the gas phase: from model to real world complexes** *Mass Spectrom. Rev.*26 (2007) 583-605.

[25] Bakker, J.M., Besson, T., Lemaire, J., Scuderi, D., Maître, P. **Gas-phase structure of a -allyl-palladium complex: efficient infrared spectroscopy in a 7 T Fourier transform mass spectrometer** *J. Phys. Chem. A* 111 (2007) 13415-13424.

[26] Sinha, R. K., Maitre, P., Piccirillo, S., Chiavarino, B., Crestoni, M. E., Fornarini, S. **Cysteine radical cation: a distonic structure probed by gas phase ir spectroscopy** *Phys. Chem. Chem. Phys.* 12 (2010) 9794-9800.

[27] Stewart, J. J. P. **Optimization of parameters for semiempirical methods V: Modification of NDDO approximations and application to 70 elements** *J. Mol. Model.* 13 (2007) 1173-1213.

[28] Frisch, M. J.; Trucks, G. W.; Schlegel, H. B.; Scuseria, G. E.; Robb, M. A.; Cheeseman, J. R.; Montgomery, J. A., Jr.; Vreven, T.; Kudin, K. N.; Burant, J. C.; Millam, J. M.; Iyengar, S. S.; Tomasi, J.; Barone, V.; Mennucci, B.; Cossi, M.; Scalmani, G.; Rega, N.; Petersson, G. A.; Nakatsuji, H.; Hada, M.; Ehara, M.; Toyota, K.; Fukuda, R.; Hasegawa, J.; Ishida, M.; Nakajima, T.; Honda, Y.; Kitao, O.; Nakai, H.; Klene, M.; Li, X.; Knox, J. E.; Hratchian, H. P.; Cross, J. B.; Bakken, V.; Adamo, C.; Jaramillo, J.; Gomperts, R.; Stratmann, R. E.; Yazyev, O.; Austin, A. J.; Cammi, R.; Pomelli, C.; Ochterski, J. W.; Ayala, P. Y.; Morokuma, K.; Voth, G. A.; Salvador, P.; Dannenberg, J. J.; Zakrzewski, V. G.; Dapprich, S.; Daniels, A. D.; Strain, M. C.; Farkas, O.; Malick, D. K.; Rabuck, A. D.; Raghavachari, K.;

Foresman, J. B.; Ortiz, J. V.; Cui, Q.; Baboul, A. G.; Clifford, S.; Cioslowski, J.; Stefanov, B. B.; Liu, G.; Liashenko, A.; Piskorz, P.; Komaromi, I.; Martin, R. L.; Fox, D. J.; Keith, T.; Al-Laham, M. A.; Peng, C. Y.; Nanayakkara, A.; Challacombe, M.; Gill, P. M. W.; Johnson, B.; Chen, W.; Wong, M. W.; Gonzalez, C.; Pople, J. A. *Gaussian 03, revision D.01* (2004) Gaussian, Inc.: Wallingford, CT.

[29] Lee, C. T., Yang, W. T., Parr, R. G. **Development of the Colle-Salvetti correlation-energy formula into a functional of the electron-density** *Phys. Rev. B* 37 (1988) 785-789.

[30] Becke, A.D. **Density-functional thermochemistry. III. The role of exact exchange** *J. Chem. Phys.* 98 (1993) 5648.

[31] Hay, P. J., Wadt, W. R. **Abinitio effective core potentials for molecular calculations - potentials for K to Au including the outermost core orbitals** *J. Chem. Phys.* 82 (1985) 299-310.

[32] Barone, V. **Anharmonic vibrational properties by a fully automated second-order perturbative approach** *J. Chem. Phys.* 122 (2005) 014108.

[33] Minenkov, Y., Singstad, A., Occhipinti, G., Jensen, V.R. **The accuracy of DFT-optimized geometries of functional transition metal compounds: a validation study of catalysts for olefin metathesis and other reactions in the homogeneous phase** *Dalton Trans.* 41 (2012) 5526-5541.

[34] *MACROMODEL, Version 9.6* (2008) Schrödinger, LLC, New York, NY.

[35] Barran, P., Ruotolo, B. **Ion mobility mass spectrometry** *Analyst* 140 (2015) 6772-6774.

[36] Bowers, M.T., Kemper, P.R., Von Helden, G., Van Koppen, P.A.M. **Gas-phase ion chromatography: Transition metal state selection and carbon cluster formation** *Science* 260 (1993) 1446-1451.

[37] Lanucara, F., Holman, S.W., Gray, C.J., Eyers, C.E. **The power of ion mobility-mass spectrometry for structural characterization and the study of conformational dynamics** *Nat. Chem.* 6 (2014) 281-294.

[38] Duncan, M.A. **Infrared laser spectroscopy of mass-selected carbocations** *J. Phys. Chem. A* 116 (2012) 11477-11491.

[39] Roithova, J. **Characterization of reaction intermediates by ion spectroscopy** *Chem. Soc. Rev.* 41 (2012) 547–559.

[40] Eyler, J.R. **Infrared multiple photon dissociation spectroscopy of ions in penning traps** *Mass Spectrom. Rev.* 28 (2009) 448–467.

[41] Sinha, R.K., Scuderi, D., Maitre, P., Chiavarino, B., Crestoni, M.E., Fornarini, S. **Elusive sulfurous acid: gas-phase basicity and IR signature of the protonated species** *J. Phys. Chem. Lett.* 6 (2015) 1605-1610.

[42] Filippi, A., Fraschetti, C., Piccirillo, S., Rondino, F., Botta, B., D'Acquarica, I., Calcaterra, A., Speranza, M. **Chirality effects on the IRMPD spectra of basket resorcinarene/nucleoside complexes** *Chem. Eur. J.* 18 (2012) 8320-8328.

[43] IUPAC, *Compendium of Chemical Terminology*, 2nd ed. (the "Gold Book") (Eds.: A. D. McNaught, A. Wilkinson) (1997) Blackwell Scientific Publications, Oxford.

[44] Chai, J.-D., Head-Gordon, M. **Long-range corrected hybrid density functionals with damped atom–atom dispersion corrections** *Phys. Chem. Chem. Phys.* 10 (2008) 6615-6620.

[45] Oomens, J., Steill, J.D., Redlich, B. **Gas-phase IR spectroscopy of deprotonated amino acids** *J. Am. Chem. Soc.* 131 (2009) 4310-4319.

[46] R Paciotti, R., Coletti, C., Re, N., Scuderi, D., Chiavarino, B., Fornarini, S., Crestoni, M. E. **Serine O-sulfation probed by IRMPD spectroscopy** *Phys. Chem. Chem. Phys.* 17 (2015) 25891-25904.

[47] Broquier, M., Lahmani, F., Zehnacker-Rentien, A., Brenner, V., Millier, P., Peremans, A. **Hydrogen-bonded bridges in complexes of o-cyanophenol: laser-induced fluorescence and IR/UV double-resonance studies** *J. Phys. Chem. A* 105 (2001) 6841-6850.

[48] Mackeprang, K., Kjaergaard, H.G., Salmi, T., Hänninen, V., Halonen L. **The effect of large amplitude motions on the transition frequency redshift in hydrogen bonded complexes: A physical picture** *J. Chem. Phys.* 140 (2014) 184309-1/9.

[49] Prell, J.S., Chang, T.M., Biles, J.A., Berden, G., Oomens, J., Williams, E.R. **Isomer Population Analysis of Gaseous Ions from Infrared Multiple Photon Dissociation Kinetics** *J. Phys. Chem. A* 115 (2011) 2745-2751.

[50] Prell, J.S., Chang, T.M., O'Brien, J. T., Williams, E.R. **Hydration isomers of protonated phenylalanine and derivatives: relative stabilities from infrared photodissociation** *J. Am. Chem. Soc.* 132 (2010) 7811-7819.

[51] Prell, J. S., O'Brien, J. T., Williams, E. R. **IRPD spectroscopy and ensemble measurements: Effects of different data acquisition and analysis methods** *J. Am. Soc. Mass Spectrom.* 21 (2010) 800–809.

[52] Hernandez, O., Paizs, B., Maitre, P. **Rearrangement chemistry of an ions probed by IR spectroscopy** *Int. J. Mass Spectrom.* 377 (2015) 172-178.

[53] Schmidt, J., Kass, S.R. **Zwitterion vs neutral structures of amino acids stabilized by a negatively charged site: infrared photodissociation and computations of proline–chloride anion** *J. Phys. Chem. A* 117 (2013) 4863-4869.

[54] M Citir, M., Hinton, C.S., Oomens, J., Steill, J.D., Armentrout, P.B. **Infrared multiple photon dissociation spectroscopy of protonated histidine and 4-phenyl imidazole** *Int. J. Mass Spectrom.* 330 (2012) 6-15.

[55] Riffet, V., Bouchoux, G. **Gas-phase structures and thermochemistry of neutral histidine and its conjugated acid and base** *Phys. Chem. Chem. Phys.* 15 (2013) 6097-6106.

[56] Wee, S., O'Hair, R.A.J., McFadyen, W.D. **Gas-phase ligand loss and ligand substitution reactions of platinum(II) complexes of tridentate nitrogen donor ligands** Rapid Comm. Mass Spectrom., 2004, 18, 1221-1226.

[57] Peter I.N. **The syn–anti equilibrium for the ACOOH group reinvestigated.Theoretical conformation analysis for acetic acid in the gas phase and in solution** *Comp. Theor. Chem.* 1022 (2013) 59–69.

[58] Pinter, B., Van Speybroeck, V., Waroquier, M., Geerlings P., De Proft, F. **Trans effect and trans influence: importance of metal mediated ligand–ligand repulsion** *Phys. Chem. Chem. Phys.* 15 (2013) 17354-17365.

[59] Turecek, F., Moss, C. L., Pikalov, I., Pepin, R., Gulyuz, K., Polfer, N.C., Bush, M.F., Brown, J., Williams, J., Richardson, K. **Gas-phase structures of phosphopeptide ions: a difficult case** *Int. J. Mass Spectrom.* 354 (2013) 249-256.

[60] Wang, D., Gulyuz, K., Stedwell, C.N., Yu, L., Polfer, N.C. **Effect of phenol and acidic side chains on the protonation sites of b2 ions confirmed by IRMPD spectroscopy** *Int. J. Mass spectrom.* 330 (2012) 144-151.

[61] Heine, N., Yacovitch, T.I., Schubert, F., Brieger, C., Neumark, D.M., Asmis, K.R. **Infrared photodissociation spectroscopy of microhydrated nitrate–nitric acid clusters NO_3^- $(HNO_3)_m(H_2O)_n$** Phys. Chem. A, 2014, 118, 7613–7622.

[62] Chiavarino, B., Crestoni, M.E., Schütz, M., Bouchet, A., Piccirillo, S., Steinmetz, V., Dopfer, O., Fornarini, S. **Cation-π interactions in protonated phenylalkylamines** *J. Phys. Chem. A* 118 (2014) 7130–7138.

[63] Roscioli, J. R., McCunn, L. R., Johnson, M. A. **Quantum structure of the intermolecular proton bond** *Science* 316 (2007) 249–254.

[64] Durand, S., Rossa, M., Hernandez, O., Paizs, B., Maitre, P. **IR Spectroscopy of B4 Fragment Ions of Protonated Pentapeptides in the X–H (X = C, N, O) Region** *J. Phys. Chem. A* 117 (2013) 2508–2516.

[65] De Petris, A., Chiavarino, B., Crestoni, M.E., Coletti, C., Re, N., Fornarini S. **Exploring the Conformational Variability in the Heme b Propionic Acid Side Chains through the Effect of a Biological Probe: A Study on the Isolated Ions** *J. Phys. Chem. B* 119 (2015) 1919-1929.

[66] Ung, H.U., Moehlig, A.R., Khodagholian, S., Berden, G., Oomens, J., Morton, T.H. **Proton-bridge motions in amine conjugate acid ions having intramolecular hydrogen bonds to hydroxyl and amine groups** *J. Phys. Chem. A* 117 (2013) 1360–1369.

[67] Zehnacker, A. **Optical spectroscopy coupled with mass spectrometry methods** *Phys. Chem. Chem. Phys.* 17 (2015) 25672-25675.

[68] Fridgen, T.D. **Infrared consequence spectroscopy of gaseous protonated and metal ion cationized complexes** *Mass Spectrom. Rev.* 28 (2009) 586-607.

[69] Polfer, N.C., Oomens, J. **Vibrational spectroscopy of bare and solvated ionic complexes of biological relevance** *Mass Spectrom. Rev.* 28 (2009) 468-494.

[70] Oomens, J., Sartakov, B. G., Meijer, G., von Helden, G. **Gas-phase infrared multiple photon dissociation spectroscopy of mass-selected molecular ions** *Int. J. Mass Spectrom.* 254 (2006) 1-19.

[71] Tai, T.B., Nhat, P.V. **A DFT investigation on interactions between asymmetric derivatives of cisplatin and nucleobase guanine** *Chem. Phys. Lett.* 680 (2017) 44-50.

[72] Zehnacker, A. **Chirality effects in gas-phase spectroscopy and photophysics of molecular and ionic complexes: contribution of low and room temperature studies** *Int. Rev. Phys. Chem.* 33 (2014) 151-207.

[73] Voronina, L., Rizzo, T.R. **Spectroscopic studies of kinetically trapped conformations in the gas phase: the case of triply protonated bradykinin** *Phys. Chem. Chem. Phys.* 17 (2015) 25828-25836.

[74] Hopkins, S.W., Marta, R.A., Steinmetz, V., McMahon, T.B. **Mode-specific fragmentation of amino acid-containing clusters** *Phys. Chem. Chem. Phys.* 17 (2015) 28548-28555.

[75] Deubel, D.V. **Factors governing the kinetic competition of nitrogen and sulfur ligands in cisplatin binding to biological targets** *J. Am. Chem. Soc.* 126 (2004) 5999-6004.

Moving to higher oxidation numbers: MS-based tecniques for the study of properties of Pt^{IV}-containing antineoplastic active complexes

5.1 Introduction

The redox behavior of transition metal complexes has represented an important topic since the dawn of coordination chemistry.[1] In particular, the mechanism of reduction of the six-coordinate octahedral d^6 Pt^{IV} complexes to the corresponding four-coordinated square planar d^8 Pt^{II} congeners was intensely studied by Basolo and coworkers.[2]

This process has raised high current interest because evidence indicates that Pt^{IV} anticancer prodrugs are reduced in the hypoxic tumor cells to the pharmacologically active Pt^{II} counterparts (scheme 5.1).[3-5] The interpretation of the experimental data concerning such process is not conclusive at all.
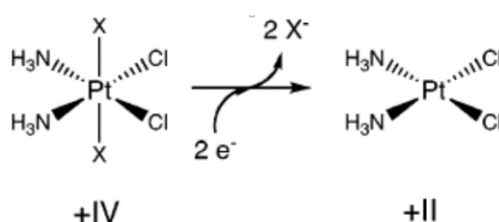
Scheme 5.1 A cisplatin-based Pt(IV) derivative bearing two axial ligands X. The 2e- reduction produces the active cisplatin metabolite with loss of two X$^-$ anions.

The electrochemical investigations (mainly by means of cyclic voltammetry, CV) were hampered by the chemically irreversible (non-Nernstian) character of such a reduction (EECC or ECEC process) that impedes the evaluation of a meaningful thermodynamic potential,[6] as well by the quick poisoning of the working electrode surface.[7] A number of computational studies at density functional theory (DFT) level has been recently carried out in order to estimate the electrochemical potentials and to suggest a reliable pathway of reduction.[8-10] Interestingly, most of these studies suggested a metastable six-coordinated Pt^{III} intermediate. A Pt^{III} containing polymeric material was indeed described as 'platinblau' (platinum blue) because of its characteristic dark blue color, thus Pt^{III} does exist at least in solid state.[11]

From another point of view, a number of kinetic experiments on the reduction of Pt^{IV} derivatives were carried out using biological reductants such as ascorbic acid H$_2$Asc (or more properly at physiologic pH its mono-anion HAsc$^-$), glutathione, cysteine or methionine.[12] Depending on the kind of the six ligands around the Pt^{IV} core and by the nature of the reducing agent, "inner-sphere" (attack of the reductant especially on hydroxo or chloro ligands) or "out-sphere" redox processes have been suggested. An alternative inner-sphere mechanism was suggested implying the role of a Pt^{II} "catalyst", but the concentrations of platinum under pharmacological conditions are very low (from µM to nM), thus such a pathway is unlikely in the context of inorganic medicinal chemistry.[13] Unfortunately, Gibson et al.[14] showed that the reduction of Pt^{IV} derivatives by extracts of cancer cells is mainly carried out by high MW cellular components, and Arnesano et al.[15] proved that cytochrome c is indeed able to promote such an activation by reduction. Although this mechanism is not fully elucidated in its intimate details, QSAR studies[16] indicated that appropriate reduction potential and lipophilicity are the key factors for design efficient Pt^{IV} anticancer prodrugs. Thus, any clue on such a mechanism and on the role of the ligands around the Pt^{IV} core will be very useful to design new prodrugs with better pharmacokinetics performances.

In section 5.3 the gas-phase behavior of sampled protonated Pt^{IV}-containing complexes is explored by means of tandem mass spectrometry and IRMPD spectroscopy. While the development of new anticancer drugs has involved the design and synthesis of numerous Pt^{IV} compounds, the present study is focused on a set of compounds characterized by two NH$_3$ molecules in cis position in the equatorial plane. Pt^{IV} complexes typically have octahedral coordination and react slowly in ligand substitution reactions. The remaining positions in the equatorial plane bear either two chloro ligands or 1,1-cyclobutanedicarboxylato ligands and the sampled compounds are shown in scheme 5.2 They can be reduced readily to their Pt^{II} counterparts, thus behaving as prodrugs, and reactivity can be tuned by the nature of the axial ligands.
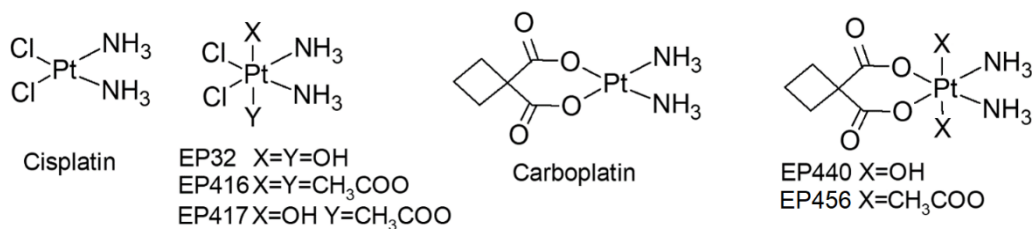
Scheme 5.2 Schematic representation of the sampled Pt^{IV} compounds either cisplatin- (EP32, EP416, EP417) or carboplatin-based (EP440, EP456). The structures of the related Pt^{II} drugs are also reported.

In the following section 5.4, indications on possible pathways of transformation from six-coordinated Pt(IV) to four-coordinated Pt(II) complexes have been sought from the evolution of ions sampled from the corresponding ESI-MS patterns in negative (deprotonated species) mode. In particular, in the fragmentation scheme of negative ions (electron rich species, potentially prone to undergo reduction) evidence for intermediates (in particular species formally containing Pt(III) ions) elusive in condensed phase[8,17-20] is specifically searched, also taking advantage of the long lived conditions that may be attained by a naked ion in the gas phase.[21,22] High resolution mass spectrometry (based on the use of a 7T Fourier Transform Ion Cyclotron Resonance, FT-ICR, mass spectrometer in France) and infrared multiple photon dissociation (IRMPD) spectroscopy are exploited to gain precise detail on the ion compositions and indication on their structures. All the proposed pathways and intermediates are corroborated by means of theoretical calculations at DFT level.

It should be noted though that protonation/deprotonation processes generate "even electron" species, potentially different from the "odd electron" species produced in electrochemical experiments and that the loss of ligands occurs as stable neutral molecules in the gas phase (H_2O, acetic acid, etc.) rather than in the form of solvated anions, as involved in solution.

5.2 Experimental details

5.2.1 Sample preparation

The samples were prepared solubilizing the complexes *cis,cis,trans*-diamminedichlorodihydroxoplatinum(IV) EP32 (*cis,trans,cis*-$PtCl_2(OH)_2(NH_3)_2$), *trans,cis,cis*-bis(acetate)diamminedichloroplatinum(IV) EP416 (*cis,trans,cis*-$PtCl_2(CH_3COO)_2(NH_3)_2$), *trans,cis,cis*-acetatohydroxodiamminedichloroplatinum(IV) EP417 (*cis,trans,cis*-$PtCl_2(CH_3COO)(OH)(NH_3)_2$), *cis,cis,trans*-diammine(1,1-ciclobutanedicarboxilato)dihydroxoplatinum(IV) EP440 (*cis,trans,cis*-$Pt(C_6H_6O_4)(OH)_2(NH_3)_2$) and *trans,cis,cis*-bid(acetate)diammine(1,1-ciclobutanedicarboxilato)platinum(IV) EP456 (*cis,trans,cis*-$Pt(C_6H_6O_4)(CH_3COO)_2(NH_3)_2$) in water, reaching a concentration of 10^{-3} M. The four stock solutions were subsequently diluted in $MeOH/H_2O$ 1:1 to obtain solutions $5 \cdot 10^{-5}$ M which have been directly infused in the electrospray ionization (ESI) source of the mass-spectrometry (MS) platforms described in the following paragraph. In order to enhance the intensity of the deprotonated species ammonia was added to a final concentrations of 0.1 M.

5.2.2 Mass analysis

Three different instruments were employed in the analysis of both protonated and deprotonated EP32, EP416, EP417, EP440 and EP456 ions .

Preliminary mass spectrometry analyses were conduced in a Paul ion-trap (Esquire 6000, Bruker) through direct infusion of the solutions prepared as stated above in the electrospray ionization (ESI) source of the instrument at a flow rate of 180 µL h^{-1}. Typical parameters used for the analyses include capillary voltage set at 3.8 kV and dry gas (N_2) fluxed with a pressure of 7 l/ min^{-1} at 300°C. Soft conditions were needed to avoid unwanted dissociation of the complexes in the ESI source. Therefore, low voltages were used for the capillary exit and the skimmer, respectively 60 V and 45 V (negative values were used to analyze anions). Collision induced dissociation (CID) experiments were performed on the mass selected ions with an activation amplitude comprises between 0.20 V and 0.35 V and an activation time of 0.50 ms.

The high-resolution mass spectra were recorded in a hybrid FT-ICR tandem MS (APEX-Qe Bruker Daltonics) sited in the Centre Laser Infrarouge d'Orsay (CLIO). The samples were directly infused in the ESI source of the mass spectrometer whose capillary voltage was set to ca. 4 kV. The instrument includes a quadrupole-hexapole interface that allows to mass select and accumulate the ions before the FT-ICR analyzer, equipped with a 7.0 T actively shielded cryomagnet. In particular, the Pt^{IV} complexes were mass selected in the quadrupole and subsequently accumulated for 1 sec in the hexapole pressurized with argon. Finally, the ions were mass analyzed in broadband mode using a 2 M data set. The final mass spectra result from the accumulation of 30 scans. The elemental composition of the parent ions was determined comparing the experimentally obtained accurate masses with the exact ones calculated from the list of isotopes of the National Institute of Standards and Tecnology (NIST https://physics.nist.gov/cgi-bin/Compositions/stand_alone.pl). The ions were assigned to their chemical formula with a tolerance below 3 ppm. Accurate masses of the fragments generated by CID of the deprotonated anions of EP32, EP416 and EP417 were also recorded after mass selection in the quadrupole and activation in the hexapole sector. The accurate masses were compared with the calculated ones as previously described in order to assess the chemical composition of the product ions of interest.

CID experiments varying the collision energy (CE) were performed using a hybrid triple quadrupole linear ion trap (Q1q2Q$_{LIT}$) instrument (Applied Biosystems API 2000 Q-Trap).[23] The presence of a LIT in the third sector of the instrument permits to accumulate the fragments obtained by the CID of the parent ions in the second sector (q2) in order to increase the sensitivity and resolution. The MS parameters used for the experiments were: curtain gas at 50.0 psi, ion source gas at 20.0 psi, declustering potential at 30 V and entrance potential at 5 V. Nitrogen was used as collision gas at a nominal pressure of 2.7 10^{-5} mbar. The fragmentation behavior was not affected by changes in the collisional gas pressure.

5.2.3 IRMPD experiments

The IR multiple photon dissociation (IRMPD) spectra were obtained in the X-H (X=C, N, O) stretching range (3000-3700 cm^{-1}) employing an optical parametric oscillator/amplifier (OPO/OPA) (LaserVision) laser system pumped by a 10 Hz Nd:YAG laser coupled with a Paul ion-trap (Bruker Esquire 6000) MS. The apparatus has been previously described in detail.[24] The mass selected ions were trapped for 10-40 ms depending on their intensity and irradiated for 1 s or 2 s based of the ease they undergo fragmentation. The typical output energy from the OPO/OPA laser was ca. 15 mJ pulse^{-1} with a spectral width of 5 cm^{-1}. Eventually a train of CO_2 pulses at 25 Hz was employed to enhance the fragmentation yield. The CO_2 laser pulse was synchronized to interact with the ion cloud after the OPO/OPA light and its length was adjusted and probed to avoid IRMPD by the CO_2 laser radiation alone. The IR action spectra are obtained by plotting the photofragmentation yield R = $-\ln I_p/(I_p + \Sigma I_f)$, where I_p and ΣI_f are the parent and sum of the fragment ion intensities, respectively, as a function of the radiation wavenumber.[25]

5.2.4 Computational details

Calculations were performed employing the Gaussian 09 rev. D01 package.[26] Two different methods were used for either the simulation of IR spectra or the computation of the free energy surfaces (FESs) of gas-phase reactions.

Regarding the calculation of vibrational features, a first optimization step was run at the B3LYP/6-31+G* level of theory and subsequently the 6-311+G** basis set was used to refine geometries and electronic energies. In order to consider in our calculations the relativistic effects involved in the behavior of heavy atoms like platinum,[27] the LanL2TZ effective core potential (ECP) was used.[28] The optimized structures were submitted to harmonic vibrational frequency analysis at the same level of theory to both calculate thermodynamic corrections and IR spectra and to identify all stationary points as minima (zero imaginary frequencies) or transition states (one imaginary fre- quency). Harmonic frequencies were scaled by a factor of 0.957. In addition, the same level was employed to calculate the FESs presented in section 5.3.

Calculations about the FESs presented in section 5.4 are run using the B3LYP functional, including dispersion corrections through the Grimme approach.[29] To properly treat the platinum atom, the relativistic compact Stuttgart/Dresden effective core potential[30] together with the split valence basis set has been used. Standard 6-311+G** Pople basis sets have been used to describe the rest of the atoms. Transition states identified by vibrational analysis at the same level of theory have been carefully checked to be properly connected to the corresponding minima by IRC (intrinsic reaction coordinate) analysis[31,32] and to confirm that the vibrational mode associated with the imaginary frequency corresponds to the correct movement of the involved atoms.

5.3 Investigation of the vibrational and structural features of protonated Pt^{IV} complexes

The data presented in this section are part of a still unpublished work and were collected and discussed by myself under the supervision of Prof. Simonetta Fornarini.

The Pt^{IV}-containing complexes have been synthetized and purified by the group of Prof. Domenico Osella in Università del Piemonte Orientale. I have performed the high-resolution analysis at the Centre Laser Infrarouge d'Orsay and the CID and IRMPD spectroscopy experiments in our laboratories in Rome. Calculations of both free energy surfaces and IR spectra were also done by myself.

5.3.1 Collision-induced dissociation experiments

The protonated complexes [EP32+H]⁺, [EP416+H]⁺, [EP417+H]⁺ and [EP440+H]⁺ were mass selected and activated towards CID in the cell of a quadrupole ion-trap (Esquire 6000 plus, Bruker). The MS^2 spectra are reported in figure 5.1.
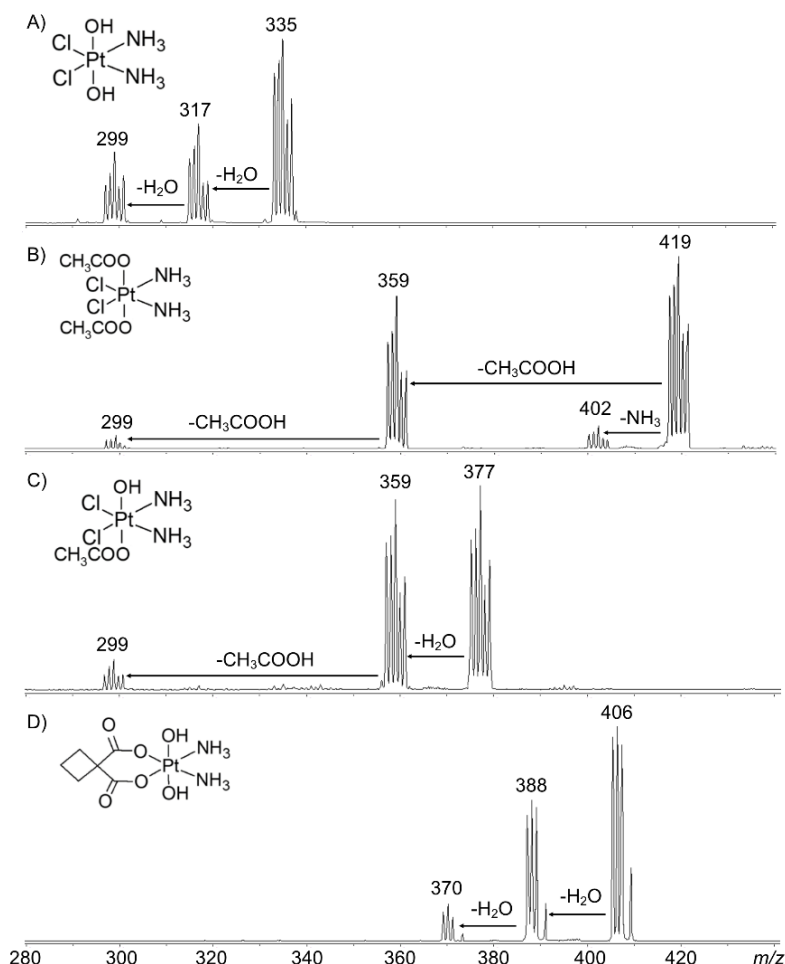
Figure 5.1 Mass spectra obtained upon mass selection and collisional activation of A) [EP32+H]⁺, B) [EP416+H]⁺, C) [EP417+H]⁺ and D) [EP440+H]⁺. Formal neutral losses are reported.

As shown in figure 5.1, the main primary fragmentation products are generated from the formal neutral loss of one of the axial ligands. In the cases of [EP32+H]⁺, [EP416+H]⁺ and [EP440+H]⁺, the fragments are formed by cleavage of H_2O (*m/z* 313-317), acetic acid (*m/z* 357-361) and again water (*m/z* 387-390), respectively. However, regarding [EP416+H]⁺ the prominent acetic acid dissociation channel is accompanied by ammonia loss (*m/z* 400-404), although showing minor intensity. Therefore, from the CID of the symmetric species, [EP32+H]⁺, [EP416+H]⁺ and

[EP440+H]⁺ possessing two identical axial ligands, no evident structural information can be obtained, beyond highlighting that the presence in the [EP416+H]⁺ fragmentation pattern of ammonia loss in competition with acetic acid suggests the acetate group to be in general more difficult to dissociate from platinum compared to the water molecule. This line of reasoning is confirmed looking at the dissociation of the complex [EP417+H]⁺, which presents a mixed situation where the axial positions are occupied by either acetato or hydroxo ligands, as reported in scheme 5.2. The CID spectrum of [EP417+H]⁺ (figure 5.1 C) shows an initial water loss (*m/z* 357-361) followed by the cleavage of acetic acid at *m/z* 297-301. We could not find any evidence of a competing channel involving acetic acid loss directly from the parent ion in agreement with our data about [EP32+H]⁺ and [EP416+H]⁺ suggesting that higher energy is needed to dissociate acetic acid from the platinum coordination sphere with respect to water.

Calculations at the B3LYP/6-311+G(d,p) level were employed to evaluate the thermodynamic features of the competing observed processes. Scheme 5.3 reports the calculated free energies at 298K for the direct cleavage of either water (A) or acetic acid (B) starting from the isomer of the [EP417+H]⁺ complex that is protonated on the axial ligand involved in the neutral loss upon CID.
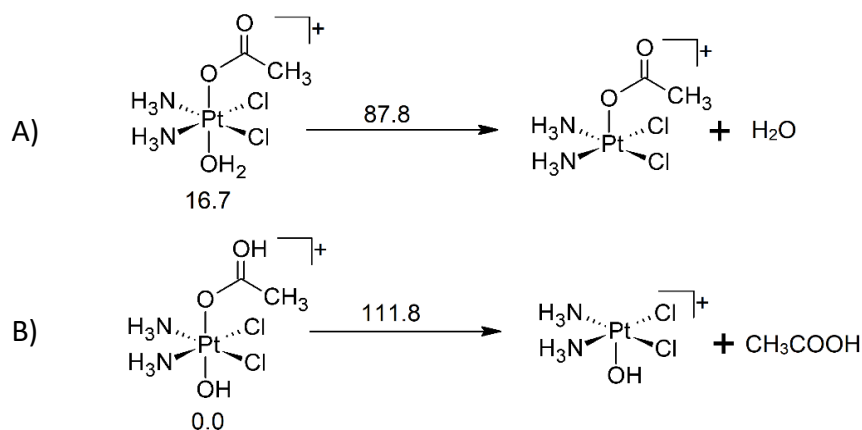
Scheme 5.3 Schematic representation of the direct cleavage of A) water and B) acetic acid from the two possible isomers of [EP417+H]⁺. The relative free energies of the isomers are reported below the structures, while on top of the arrows the dissociation energy for each process is reported All Gibbs free energies at 298K are in kJ mol⁻¹.

The calculated energies are in agreement with the experimental evidence. In fact water loss from [EP417+H]$^+$ is 24 kJ mol^{-1} less endoergonic than acetic acid loss. The energies are calculated from the lowest lying conformer of the isomeric families presenting protonation either on the hydroxo or acetato ligand. The relative free-energies show a preferential protonation on the acetato which should lead to the direct cleavage of acetic acid. The underlying notion is that either the interconversion between the two isomers or proton transfer from the ammine to the axial hydroxo ligand requires less energy than the direct cleavage of acetic acid from the most stable isomer (111.8 kJ mol^{-1}, path B scheme 5.3). Alternatively, it is conceivable that the protomer of path A is preferentially formed in solution and brought intact to the gas phase. It is thus necessary to resort to spectroscopic means to discriminate between the two possible isomers. In the forthcoming section the vibrational features of [EP32+H]$^+$, [EP417+H]$^+$ and [EP440+H]$^+$, recorded using IRMPD spectroscopy, are discussed in comparison with theoretically calculated IR spectra in order to unveil their main structural characteristics.

5.3.2. Vibrational and structural features of [EP32+H]$^+$

In figure 5.2 the IRMPD spectrum of [EP32+H]$^+$ is reported and compared with the calculated IR spectrum of the **EP32H_1**, **EP32H_2** and **EP32H_3** in the A, B and C panels, respectively.

Three isomers have been found in the exploration of the possible structures of [EP32+H]$^+$, whose structures are reported in figure 5.2. **EP32H_1** is the global minimum showing protonation on the axial OH group. In **EP32H_2** we have considered the possibility for one of the ammine ligand to release a proton to the second hydroxo ligand. However, the resulting isomer lays 100 kJ mol^{-1} higher in relative free energy. **EP32H_3** is protonated on the chloro ligand and even higher in energy at 141 kJ mol^{-1}. The calculated difference in energy between **EP32H_1** and **EP32H_3** is not surprising, though, considering the proton affinities of water and HCl (691.0, and 556.9 kJ mol^{-1}, respectively)[33], which are in line with the preference for the proton to reside on the hydroxo ligand with respect to the chloro one.

The comparison between the experimental vibrational features and the calculated IR spectra of the sampled isomers, suggests that the **EP32H_2** and **EP32H_3** isomers

are in low percentages in the sampled gas-phase population, in agreement with their higher relative energy compared to **EP32H_1**. Indeed, the experimental IRMPD signals of [EP32+H]$^+$ show consistency with the calculated vibrations of **EP32H_1**. In particular, the OH stretching region presents a broad absorption between 3450 and 3600 cm^{-1}, which can be attributed to a convolution of the OH stretching mode at 3620 cm^{-1}, and of the asymmetric and symmetric stretchings of the water molecule at 3578 and 3510 cm^{-1}, respectively.
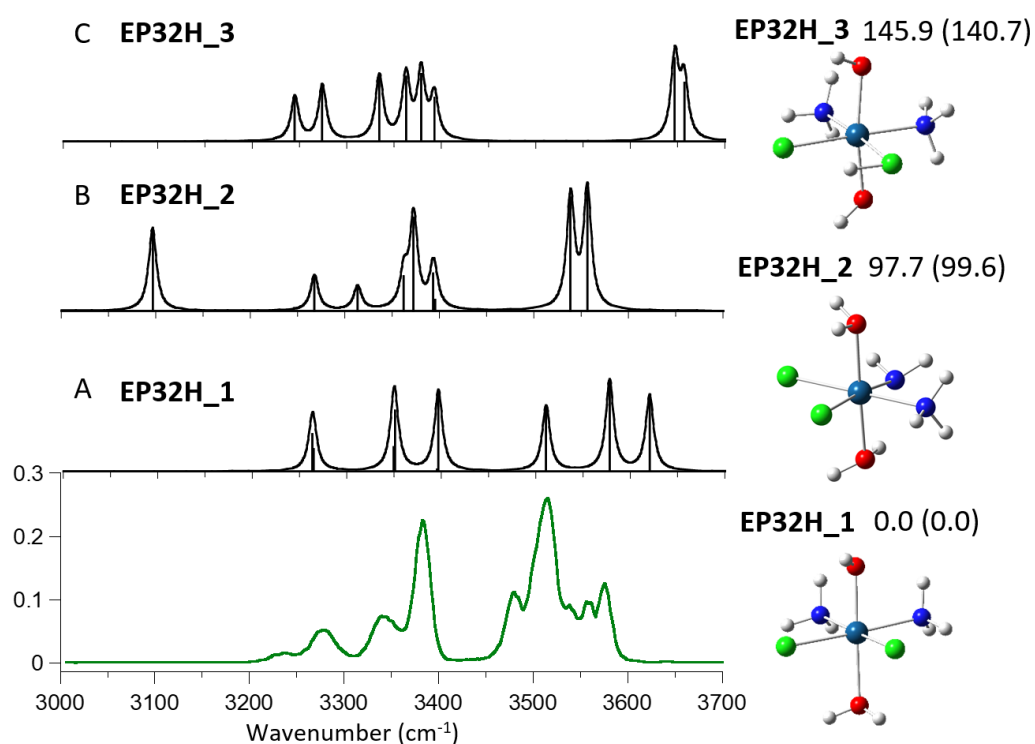
Figure 5.2 IRMDP spectrum of [EP32+H]$^+$ (green profile) compared to to the theoretical calculated spectra of (A) **EP32H_1**, (B) **EP32H_2** and (C) **EP32H_3**. Geometries are reported on the right side together with relative enthalpies and free-energies (in brackets) at 298K in kJ mol^{-1}.

The three absorption below this region experimentally recorded at 3383, 3340 and 3278 cm^{-1} are instead interpreted by the asymmetric and symmetric stretchings of the ammonia molecules, calculated at 3396,3350,3264 and 3263 cm^{-1}, respectively. The experimental IRMPD bands compared with the calculated vibrational modes of **EP32H_1** are reported in table 5.1.

Table 5.1 Experimental IRMPD signals of [EP32+H]$^+$ and calculated vibrational modes of **EP32H_1**.

	[EP32+H]$^+$	
Exp IRMPD[a]	Calculated IR [a,b]	Vibrational mode assignment
	EP32H_1	
3574	3620 (115)	OH stretching
3515	3578 (137)	H_2O asymm stretching
3478	3510 (98)	H_2O symm stretching
3383	3396 (119)	NH_3 asymm stretching
3340	3350 (92)	NH_3 asymm stretching
3278	3264 (34)	NH_3 symm stretching
	3263 (57)	NH_3 symm stretching

[a] in cm^{-1}. [b] Intensities are reported in brackets in km mol^{-1}.

5.3.3. IRMPD spectroscopy of [EP417+H]$^+$

In figure 5.3 the IRMPD spectrum of [EP417+H]$^+$ is reported and compared with calculated isomers and conformers presenting protonation on different sites of the complex. In particular, we were able to optimize local minima in which protonation occurs either on the OH axial group or on the acetato ligand. In this latter case we could ascertain the presence of at least three conformers, the lowest lying one (**EP417H_1**) presents a H-bond between the OH of the protonated acetate ligand and the chloro one. Regarding the other acetato-protonated species, the structure **EP417H_3**, lying at 19.1 kJ mol^{-1}, shows some interaction of the methyl hydrogen with a chloro ligand, and the carboxylic acid moiety is in cis conformation, while at 31.4 kJ mol^{-1} the **EP417H_4** conformer presents the carboxylic function in trans conformation with the oxygen oriented toward a hydrogen atom of the ammine ligand. The structure **EP417H_2**, second in energy at 16.7 kJ mol^{-1}, is instead protonated on the hydroxo ligand and shows the CO of the acetato directed towards the ammine ligands. The whole set of calculated spectra is reported in figure 5.3 together with relative free energies and enthalpies and optimized geometries at the B3LYP/6-311+G**(LanL2TZ) level of theory.
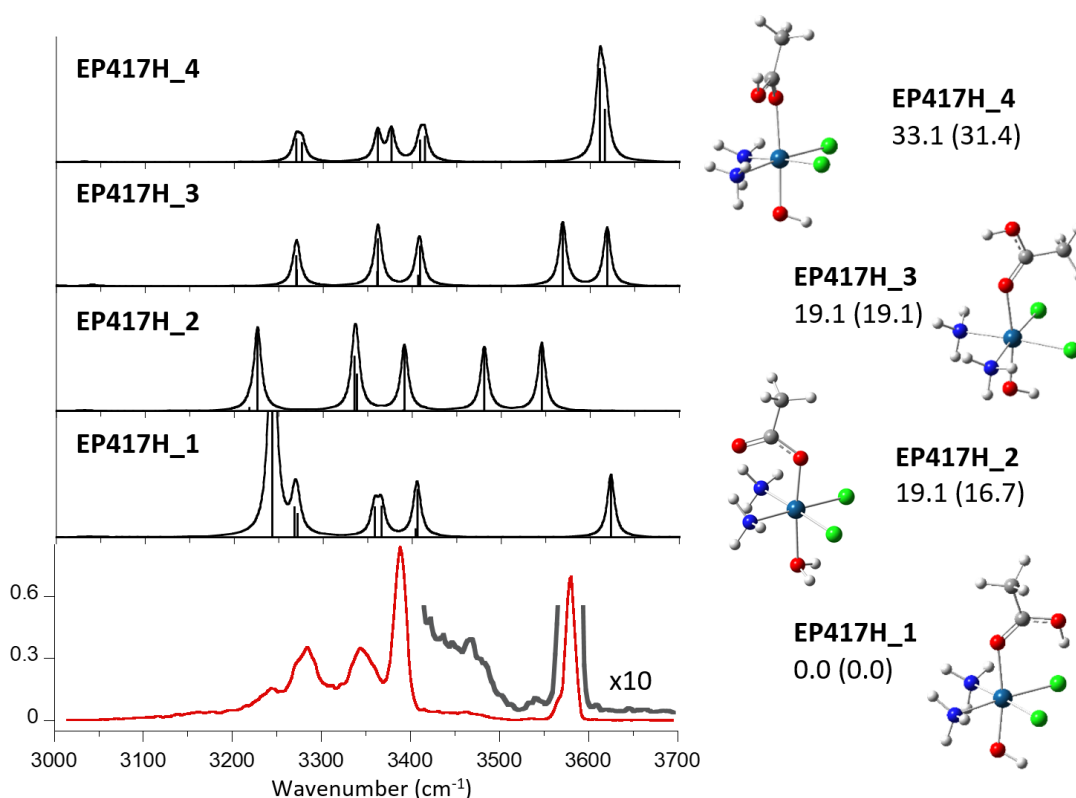
Figure 5.3 IRMDP spectrum of [EP417+H]$^+$ (red and grey profiles) compared to to the theoretical calculated spectra of the structures **EP417H_1**, **EP417H_2**, **EP417H_3** and **EP417H_4** at B3LYP/6-311+G**(LanL2TZ). Geometries are reported on the right together with relative enthalpies and free-energies (in brackets) at 298K in kJ mol^{-1}.

The IR spectrum of **EP417H_1** in figure 5.3 accounts for every major absorption, in particular it is the only structure that presents a single vibration in the high frequency region of the spectrum, the OH stretching at 3623 cm^{-1}, in fair agreement with the experimental band at 3579 cm^{-1}. However, considering the two small signals at 3537 and 3463 cm^{-1}, visible in the zoomed profile in grey in figure 5.3, we can hypothesize the presence of a small percentage of the isomer protonated on the OH, **EP417H_2** in the sampled gas-phase population**.** In fact, the mentioned experimental bands are compatible with the asymmetric and symmetric stretching modes of water, which are calculated for **EP417H_2** at 3542 and 3480 cm^{-1}, respectively. In the region below 3450 cm^{-1}, which is characterized by NH and CH stretchings, it is possible to highlight three major bands, at 3387, 3346 and 3286 cm^{-1}, in agreement with the ammonia asymmetric and symmetric stretchings calculated at 3405, 3365, 3357 and 3271, 3267 cm^{-1}, respectively for **EP417H_1**, together with

a broad absorption with maximum at 3239 cm^{-1} consistent with the OH stretching of the carboxilic acid at 3242 cm^{-1}, that is red-shifted due to its involvement in a H-bond with the chloro ligand. The experimental bands and calculated vibrational modes for the two lowest laying isomers are reported in table 5.2.

Table 5.2. Experimental IRMPD signals of [EP417+H]$^+$ and calculated vibrational modes of **EP417H_1** and **EP417H_2**.

	[EP417+H]$^+$		
Experimental IRMPD[a]	Calculated IR frequencies[a,b]		Vibrational mode assignment
	EP417H_1	**EP417H_2**	
3579	3623 (126)		OH stretching
3537 (low intensity)		3542 (137)	H$_2$O asymm stretching
3463 (small shoulder)		3480 (127)	H$_2$O symm stretching
3387	3405 (96)	3391 (131)	NH$_3$ asymm stretching
3346	3365 (62)	3337 (73)	NH$_3$ asymm stretching
	3357 (61)	3335 (109)	NH$_3$ asymm stretching
3286	3271 (47)		NH$_3$ symm stretching
	3267 (61)		NH$_3$ symm stretching
3239	3242 (522)		CO-H stretching
		3226 (167)	NH$_3$ symm stretching

[a] in cm^{-1}. [b] Intensities are reported in brackets in km mol^{-1}.

5.3.4 IRMPD spectroscopy of [EP440+H]$^+$

EP440 presents two axial hydroxo groups and a 1,1-ciclobutyldicarboxylato chelating ligand in equatorial position that replaces the two chloro ones in the coordination sphere of both EP32 and EP417. Therefore, two main possible protonation sites can be hypothesized, namely the hydroxo axial ligand or the carboxylato moiety of the chelating molecule. In figure 4 the optimized geometries of the calculated isomers are reported together with the experimental IRMPD spectrum and theoretical IR spectra. The most stable structure (**EP440H_1**) is protonated on the free CO of the carboxylate and the hydrogen is oriented toward the oxygen bound to platinum in a cis-like configuration. A structure in which this latter CO is protonated was also calculated resulting in an isomer, **EP440H_4**, 62.4

kJ mol^{-1} higher in energy relative to **EP440H_1**. The structures **EP440H_2** and **EP440H_3** both present protonation on the axial OH, but differ for the spatial position of the cyclobutyl group compared to the protonation site. In particular, **EP440H_2** has the protonated hydroxo ligand and the cyclobutyl grup in opposite regions relative to the plane defined by the equatorial square planar coordination around platinum. In contrast, **EP440H_3** shows both groups leaning towards each other, leading to an increase in relative energy from 5.0 to 17.7 kJ mol^{-1}, probably due to steric hindrance between the hydrogen atoms belonging to the methylene group and to the aqua ligand (figure 4).
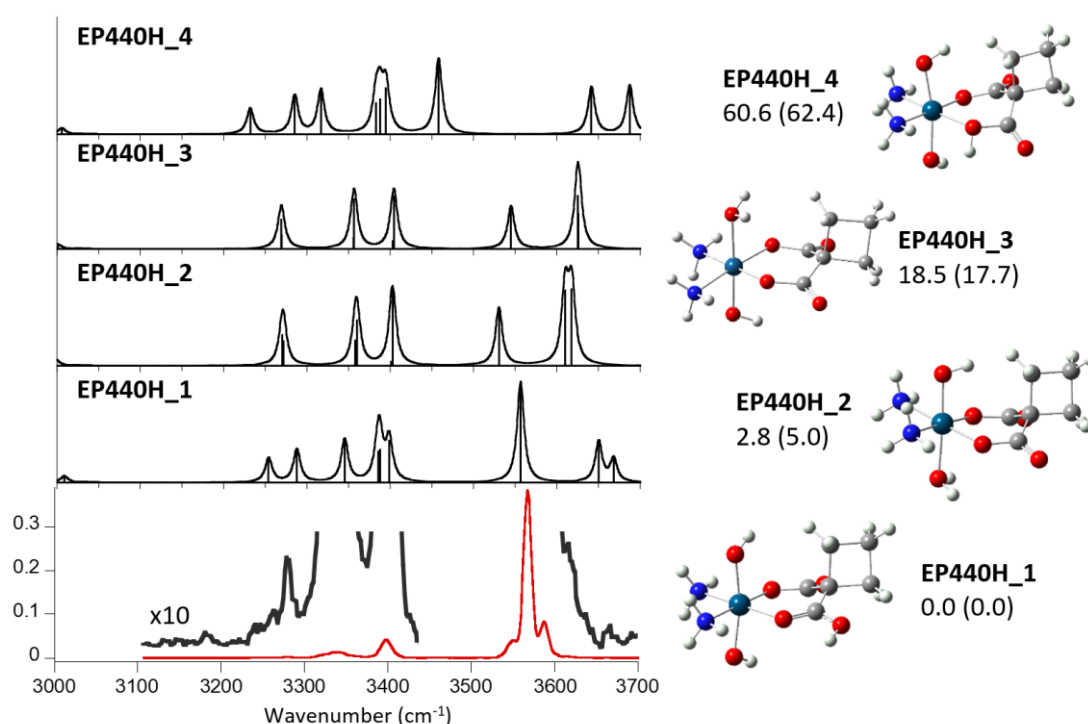
Figure 5.4 IRMDP spectrum of [EP440+H]$^+$ (red and grey profiles) compared to to the theoretical calculated spectrum of the structures **EP440H_1**, **EP440H_2**, **EP440H_3** and **EP440H_4** at B3LYP/6-311+G**(LanL2TZ). Geometries are reported on the right together with relative enthalpies and free-energies (in brackets) at 298K in kJ mol^{-1}.

The spectroscopic evidences are consistent with the computed relative energies, showing a fair agreement between the IRMPD spectrum and the calculated ones of both **EP440H_1** and **EP440H_2**. In particular the intense IRMPD band at 3569 cm^{-1} is well simulated by the stretching mode of the carboxylic OH calculated for **EP440H_1**

at 3556 cm^{-1}. However the two axial OH stretching modes of **EP440H_1** calculated at 3668 and 3650 cm^{-1} are hardly visible in the experimental spectrum at 3636 and 3618 cm^{-1}. In addition, it is possible to highlight some vibrational features that may be attributed to the isomer **EP440H_2** presenting protonation on the hydroxo group. In particular, the IRMPD band at 3586 cm^{-1} is in fair agreement with the OH stretching and H$_2$O asymmetric stretching of **EP440H_2** calculated at 3617 and 3610 cm^{-1}, respectively. Also the shoulder at 3553 cm^{-1} on the main band at 3569 cm^{-1} in the experimental spectrum is fairly well matched by the H$_2$O symmetric stretching of **EP440H_2** at 3530 cm^{-1}. Less information can be gathered from the spectral region below 3400 cm^{-1}. It presents three absorptions at 3397, 3339 and 3281 cm^{-1}, which can be attributed to a combination of the several asymmetric and symettric NH stretchings of the ammonia molecules, calculated in the same region for both **EP440H_1** and **EP440H_2**. The experimental vibrations together with the calculated ones for the lowest lying structures are reported in table 5.3.

Table 5.3 Experimental IRMPD signals of [EP417+H]$^+$ and calculated vibrational modes of **EP440H_1** and **EP440H_2**.

	[EP440+H]$^+$		
Experimental IRMPD[a]	Calculated IR frequencies[a,b]		Vibrational mode assignment
	EP440H_1	**EP440H_2**	
3636 (small shoulder)	3668 (40)		OH stretching
3618 (small shoulder)	3650 (70)		OH stretching
3586		3617 (128)	OH stretching
		3610 (126)	H$_2$O asymm stretching
3569	3556 (173)		CO-H stretching
3553 (shoulder)		3530 (96)	H$_2$O symm stretching
3397	3398 (72)	3402 (125)	NH$_3$ asymm stretching
	3387 (56)	3360 (75)	NH$_3$ asymm stretching
	3385 (54)	3357 (44)	NH$_3$ asymm stretching
3339	3345 (74)		NH$_3$ asymm stretching
3281	3287 (57)	3271 (43)	NH$_3$ symm stretching
	3254 (42)	3270 (53)	NH$_3$ symm stretching

[a] in cm^{-1}. [b] Intensities are reported in brackets in km mol^{-1}.

5.3.5 Discussion

IRMPD spectroscopy has allowed to characterize the protonated complexes of EP32, EP417 and EP440, species formed in solution and brought to the gas-phase using an ESI source. [EP32+H]$^+$ showed protonation on the hydroxo axial ligand, in agreement with its fragmentation behavior which involves a facile cleavage of water. On the contrary, the spectroscopic characterization of [EP417+H]$^+$ and [EP440+H]$^+$ unveiled a diverse isomeric landscape with the participation of different protomers to the sampled gas-phase population. Regarding [EP417+H]$^+$, the lowest lying calculated structure (**EP417H_1**) presents protonation on the acetate ligand, and its theoretical spectrum interprets the IRMPD one faily well. However, a few minor experimental vibrational features suggest the presence of a small percentage of the isomer protonated on the hydroxo axial ligand (**EP417H_2**). Interestingly, IR signals pertaining to both protomers present the same dissociation pattern involving only water loss, as also evidenced by CID experiments (figure 5.1). This evidence suggests that, regarding the isomer protonated on the acetato, one of the two processes already mentioned in section 1 is energetically favored with respect to the direct cleavage of acetic acid, which is calculated to require 111.8 kJ mol^{-1}. In particular, we have hypothesized either an isomerization reaction (e. g. **EP417H_1** $\rightarrow$ **EP417H_2**) or a proton transfer from the ammonia to the hydroxo ligand which may be occurring along the reaction coordinate for water loss. Employing DFT calculations the energy involved in the two mechanisms has been evaluated. The blue profile in figure 5.5 shows the free-energy surface (FES) for the dissociation reaction of water from **EP417H_1** that involves a preliminary proton transfer from the ammine ligand. The activation threshold is given by the energy of the transition state involved in the transfer of the proton from ammonia (**EP417H_TS**) lying at 94.8 kJ mol^{-1} with respect to **EP417H_1**. The reaction proceeds via a stable intermediate in which the hydrogen finally resides on the hydroxo group (**EP417H_int**, 81.43 kJ mol^{-1}) followed by a direct cleavage of water from this species accompanied by a change in the overall geometry of complex **EP417-H2O_1** as shown in figure 5.5.
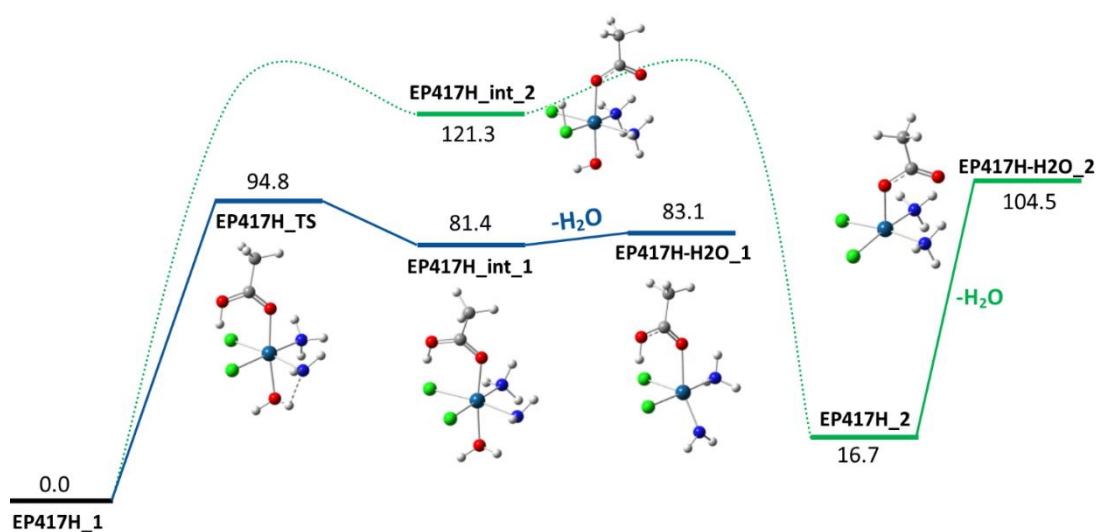
Figure 5.5 FESs for the water dissociation reaction from **EP417H_1**. The blue profile regards the reaction involving proton tranfer from ammonia, while the green profile the isomerization reaction in which the proton is transferred from the carboxilate to the hydroxo group through the chloro one. Optimized structures at the B3LYP/6-311+G** level are reported together with free energies at 298 K in kJ mol^{-1}.

Regarding the isomerization reaction, whose profile is reported in green in figure 4, we could not locate the transition states involved in the proton transfer from the acetate ligand to the chloro one and from the chloro to the hydroxo. However, the former step eventually leads to the intermediate structure reported in figure 5.5 as **EP417H_int_2**, lying at 121.3 kJ mol^{-1}, a value way higher than the activation energy simulated for the proton transfer reaction involving the ammine ligand (94.8 kJ mol^{-1}), suggesting this mechanism not to have an important role in the unimolecular water dissociation reaction. Indeed, it is interesting to note that the product from direct cleavage of water from **EP417H_2**, presented in figure 5.5 as **EP417H-H2O_2** and presenting a square-based pyramidal geometry, is higher in energy with respect to its protomer **EP417H-H2O_1** in which the position of the NH$_2$ group is off the equatorial plane. Finally, the activation energy for the proton transfer leading to water dissociation has been compared to the one needed for the direct cleavage of acetic acid from **EP417H_1**, in particular 94.8 with respect to 111.8 kJ mol^{-1}, respectively. The absence in the fragmentation pattern of [EP417+H]$^+$, under either

CID or IRMPD conditions, of the CH_3COOH neutral loss is therefore well simulated by our calculations showing loss of water to be energetically favored.

The same line of reasoning applies to $[EP440+H]^+$, where two protomers presenting the additional hydrogen either on a carbonyl oxygen of the 1,1-cyclobutyldicarboxilate (**EP440H_1**), or on the hydroxo axial ligand (**EP440H_2**) may have a role. In this case the relative energy of the higher energy isomer (**EP440H_2**) is closer to the global minimum, being just 5 kJ mol^{-1} in contrast to the 16.7 kJ mol^{-1} difference between **EP417H_1** and **EP417H_2**. This smaller energy difference is consistent with the higher relative intensity of IRMPD signals which can be related to the contribution of **EP440H_2**, compared to the minor role of **EP417H_2**, suggesting a major participation of the hydroxo-protonated isomer in the sampled population of $[EP440+H]^+$ with respect to $[EP417+H]^+$.

5.4　Gas-phase dissociation patterns of deprotonated platinum(IV) complexes

The following discussion is adapted from a manuscript in preparation written by myself and revised by Prof. Simonetta Fornarini:

D. Corinti, F. Ponte, E. Sicilia, B. Chiavarino, M. Elisa Crestoni, N. Russo, D. Osella, S. Fornarini

Breakdown reactivity patterns of prodrug platinum(IV) complexes

Manuscript in preparation

The Pt^{IV}-containing complexes have been synthetized and purified by the group of Prof. Domenico Osella　(Università del Piemonte Orientale). My contribution regarded performing the high-resolution analysis at the Centre Laser Infrarouge d'Orsay and the CID and IRMPD spectroscopy experiments in our laboratories in Rome. The group of Prof. Nino Russo (Università della Calabria) was involved in the calculation of the free energy surfaces while theoretical IR spectra were calculated by myself.

5.4.1 Mass spectrometric analysis of pro-drug Pt[IV] complexes

The mass spectra of the selected set of compounds, recorded by ESI in negative ion mode present common patterns as well as distinctive trends depending on their individual structural features. The mass spectrum of the prototypical complex in the series, namely EP32, is reported in figure 5.6. The major ion cluster in the spectrum corresponds to the deprotonated species [EP32-H]⁻, confirming the stability of the complex and its resistance to hydrolysis. The isotopic pattern reflects the natural abundances of Pt and Cl isotopes giving rise to the pattern well identified in high resolution FT-ICR mass spectrometry. The insert in figure 5.6 shows the isotopic cluster while the exact mass measurements on the individual peaks confirm the expected elemental composition. Henceforth, anionic complexes will be associated to and named after the *m/z* value of the first significant ion in the isotopic cluster.
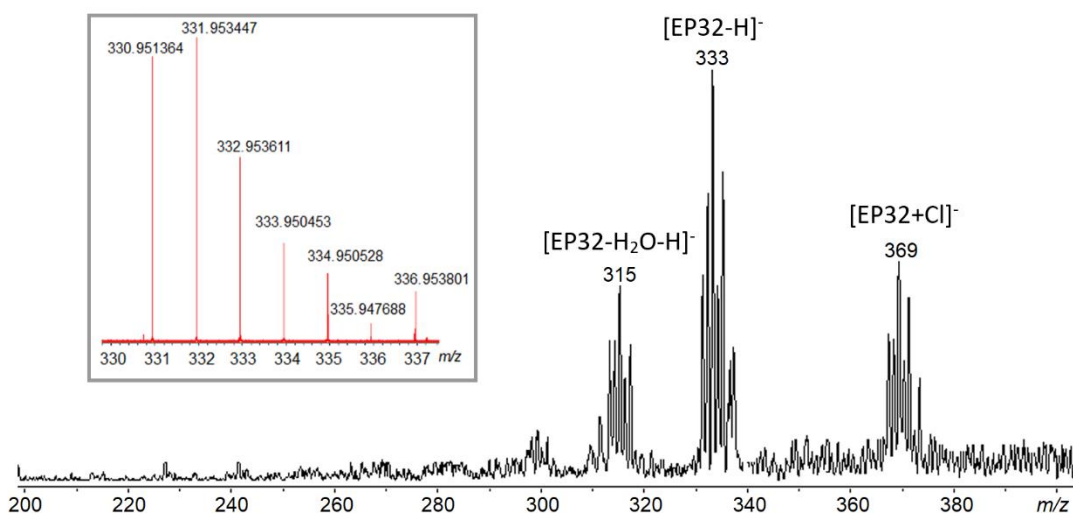
Figure 5.6 Negative ion ESI mass spectrum of EP32 in basic methanol/water solution. The inset shows an enlargement of the isotopic cluster for the [EP32-H]⁻ complex, recorded in high resolution FT-ICR mass spectrometry. The attribution of the molecular formula was confirmed comparing the measured mass of the signal containing ^{194}Pt and two ^{35}Cl (330.951364 Da) with the corresponding exact mass (330.951135 Da, error<0.7 ppm).

For example, [EP32-H]⁻ is represented by *m/z* 331, corresponding to the [{^{194}Pt(^{35}Cl)$_2$(NH$_3$)$_2$(OH)$_2$}-H]⁻ isotopic composition. Other ions appearing in the mass spectrum are related to [EP32-H$_2$O-H]⁻ and [EP32+Cl]⁻, the former due to H$_2$O loss and the second one to attachment of chloride, a ubiquitous ion in solution. The

mass spectra of the other compounds in the series conform to a similar pattern and are displayed in figures S5.1-S5.4 in the Supporting Material (SM). The minor presence of an ion due to water loss is observed also in the mass spectra of EP417 and EP440 while only negligible loss of acetic acid is found in the mass spectra of EP416, EP417 and EP456.

5.4.2 Breakdown behavior of pro-drug Pt^{IV} complexes

The naked negatively charged complexes [EPX-H]$^-$ (X = 32, 416, 417, 440, and 456) have been submitted to collision induced dissociation (CID) aiming to relate an observed array of fragmentation products to the tendency towards reduction in oxidation state and ligation number. In these experiments, the energy released on the activated ion may be varied to provide a relative trend of energy thresholds in dissociation processes. When submitted to CID, [EPX-H]$^-$ ions display a complex scheme of parallel and consecutive fragmentation paths. The first step, common to all species, involves loss of an axial ligand and is typically followed by either a direct cleavage of one of the equatorial ligands or a fragmentation process involving reduction of the remaining ionic species. In the following paragraph the fragmentation of [EP32-H]$^-$ is described in detail and used as reference for the behavior of other sampled Pt^{IV} complexes.

Figure 5.7 shows the CID mass spectra of selected [EP32-H]$^-$ ions recorded at high resolution in FT-ICR mass spectrometry. The analogous CID experiments performed on [EPX-H]$^-$ (X = 416, 417 and 440) are illustrated in figures S5.5-S5.7 in the SI. Mass spectra are collected in the FT-ICR cell after CID in the hexapole sector of the instrument run at two different values of collision energy (CE, in the laboratory frame). The main fragment formed from [EP32-H]$^-$ at low CE (4V) is the product ion at *m/z* 313 due to loss of water. Increasing the collision energy at 8V the abundance of the precursor ion [EP32-H]$^-$ at *m/z* 331 becomes negligible and also the relative fraction of [EP32-H-H$_2$O]$^-$ at *m/z* 313 decreases in favor of lower mass ions. A complete fragmentation scheme linking all the observed species is obtained by MS^n experiments, in which each individual product ion from [EP32-H]$^-$ is submitted to activation and subsequent mass analysis.
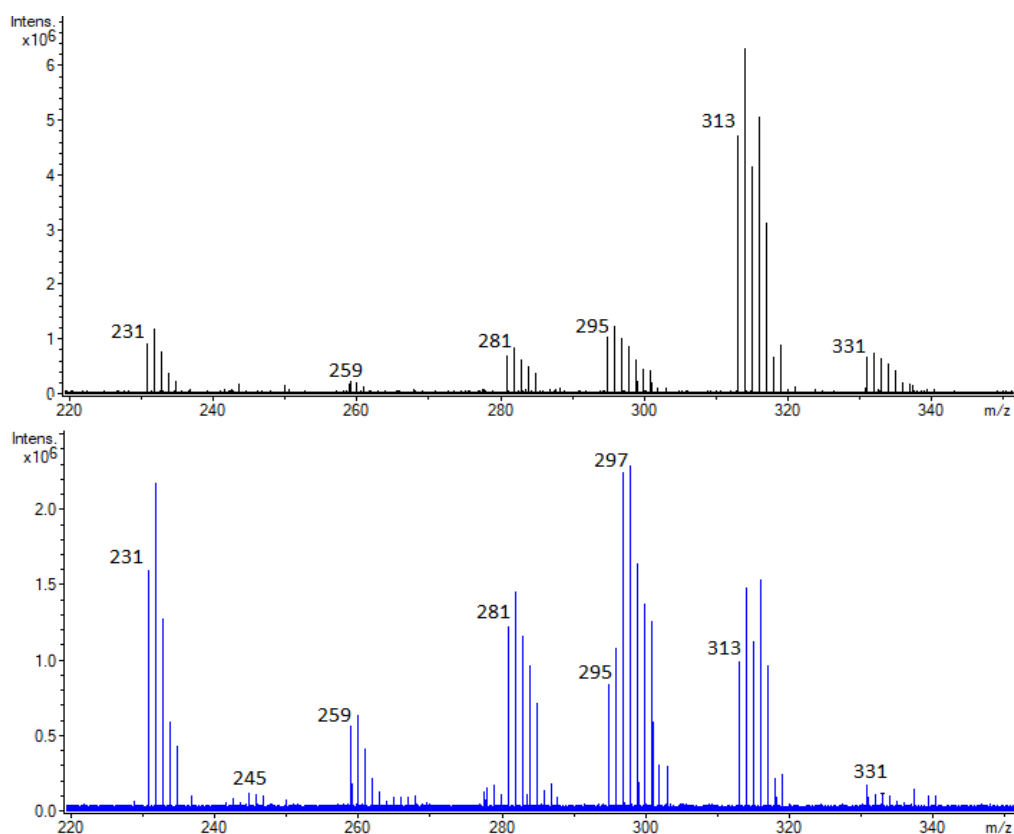
Figure 5.7 CID mass spectrum of [EP32-H]$^-$ (*m/z* 331-337) recorded with collision energy of 4 V (panel (a), black profile) and 8V (panel (b), blue profile). Relative abundances (RA) are in arbitrary units.

The complete frame linking the observed fragments is summarized in scheme 5.4, showing that all lower mass fragments are generated from the ion *m/z* 313. As also shown by the CID mass spectrum of [EP32-H]$^-$ at 4 V (Figure 2), two main product ions are formed by the subsequent fragmentation of [EP32-H-H$_2$O]$^-$ at *m/z* 313, namely an ion at *m/z* 295 corresponding to loss of a second water molecule and an ion at *m/z* 281 involving a neutral loss of 32 Da, possibly accounted for by either NHOH or N$_2$H$_4$ as neutral fragment. The former possibility involves a single-electron reduction, leading to a formal Pt^{III}-containing species, while in the second one a 2-electron redox process yields a Pt^{II} complex [PtCl$_2$(OH)]$^-$. Other fragments also observed in figure 5.7 pertain to dissociation paths from the ion at *m/z* 295. In particular, the species at *m/z* 259 derives from HCl loss yielding in turn the ion at *m/z* 231 by loss of N$_2$. Moving to higher CE (figure 5.7 b), a novel feature regards the formation of an ion at *m/z* 297 with an isotopic cluster overlaying the ion at *m/z*

295. This dissociation channel involves a 16 Da loss that can be ascribed to either NH$_2$ loss, concomitant with a one electron reduction of the complex, or an O atom loss implying a two electron reduction.
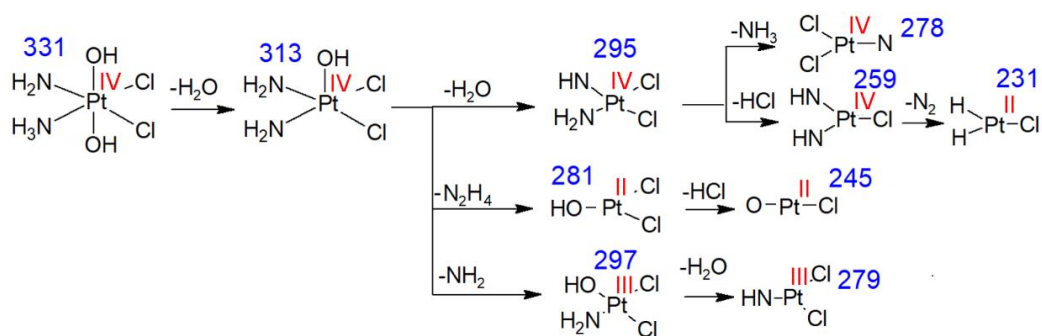
Scheme 5.4 Schematic representation of the dissociation pattern generated by CID of [EP32-H]$^-$. In blue is reported the *m/z* ratio of the species and in red the formal oxidation state of platinum. Every complex is negatively charged, charges are not made explicit.

In order to solve the ambiguities regarding fragments at *m/z* 297 and 281, their accurate mass obtained by high resolution (HR) FT-ICR mass spectrometry has been compared with the calculated exact mass for potential candidates. Figure 5.8 is an enlargement of the HR mass spectrum of figure 5.7 b showing that 4 elemental compositions are contributing to *m/z* 297. The most abundant at *m/z* 296.922099 is attributed to [^{194}Pt^{35}Cl$_2$(NH$_2$)(OH)]$^-$ with a confidence of 0.8 ppm, thus confirming the presence of a formal Pt^{III}-containing complex generated by a neutral NH$_2$ loss from the *m/z* 313 ion. No signal complying with the elemental composition of the Pt^{II} complex [Pt Cl$_2$(NH$_2$)(NH$_3$)]$^-$ was found, while the *m/z* signals at 296.927957 and 296.932279 are consistent with the presence of the ions [^{194}Pt^{35}Cl^{37}Cl(NH$_2$)(NH)]$^-$ and [^{196}Pt^{35}Cl$_2$(NH$_2$)(NH)]$^-$, respectively, which are part of the isotopic cluster of the fragment generated by water loss from the complex at *m/z* 313. Finally the ion *m/z* 296.916133 conforms to the formula [^{195}Pt^{35}Cl$_2$(NH)(OH)]$^-$ arguably obtained from a tiny fraction of secondary NH$_3$ loss (not reported in scheme 5.4 due to negligible intensity).

The whole set of fragments reported in scheme 5.4 has been confirmed comparing the high resolution experimental mass with the calculated exact mass (table S5.1), also assessing the nature of the ion at *m/z* 281, which has been attributed to a

formal Pt^{II}-containing complex, [PtCl$_2$(OH)]$^-$, generated by N$_2$H$_4$ loss from [PtCl$_2$(NH$_2$)$_2$(OH]$^-$.
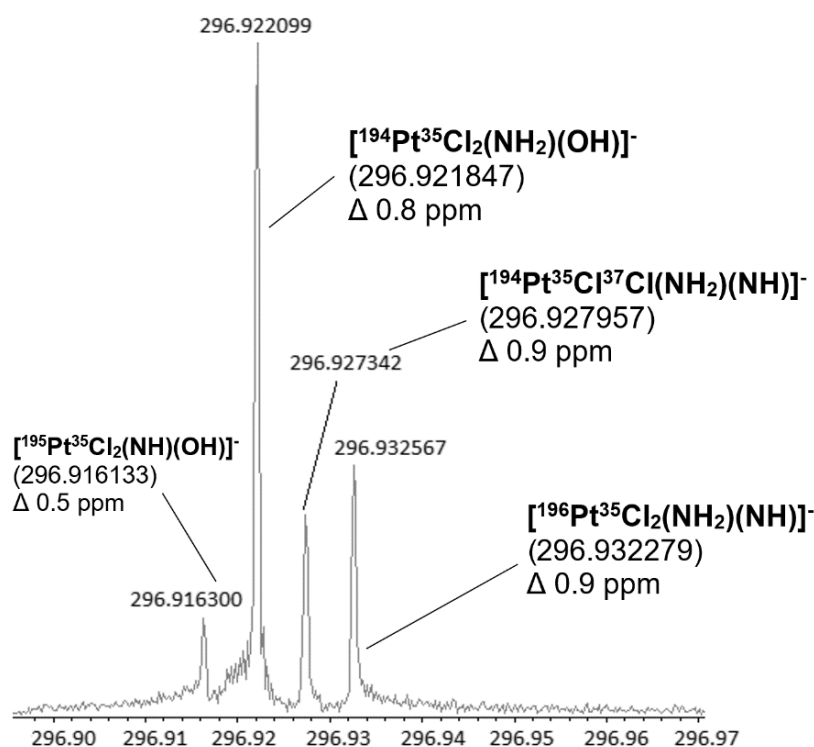
Figure 5.8 Excerpt of the CID mass spectrum of [EP32-H]$^-$. The elemental composition of the ions attributed to the signals is reported in figure together with the corresponding calculated exact mass in Da (brackets) and the error between the experiment and the theoretical mass in ppm.

The same procedure was employed to establish breakdown schemes for [EP416-H]$^-$, [EP417-H]$^-$, [EP440-H]$^-$, and [EP456-H]$^-$ (Schemes S5.1-S5.4 and Tables S5.2-S5.4 in the SI). The schemes display increasing complexity. For example the dissociation pattern of [EP416-H]$^-$ (Scheme S5.1) entails the presence of more than 25 different product ions. For the sake of simplicity we will refer to the primary channels generated from the precursor ion, noting two dissociation paths related to the axial ligands, acetic acid loss and CH$_2$COO loss, and two fragmentations involving the equatorial ligands, loss of ammonia and NH$_2$Cl loss. Intriguingly, the CH$_2$COO loss channel leads to the formation of a Pt^{II} complex, [PtCl$_2$(NH$_3$)$_2$(CH$_3$CO$_2$)]$^-$, presenting the base structure of cisplatin with an additional acetate ligand, arguably in an external coordination sphere. It represents the only dissociation channel involving a redox reaction ascribed to an axial ligand in the whole set of examined Pt^{IV} species.

215

The dissociation path involving NH_2Cl loss also requires a redox step generating a Pt^{II} complex in which the two axial ligands are still bound to platinum. Intriguingly, the redox process in water is considered to involve mainly the axial ligands,[8,13,34-37] while leaving the equatorial ones untouched, even if there are few evidences reporting a possible participation of the equatorial ligands in some redox process.[13,34] In contrast, the gas-phase reaction shows the equatorial ligands to be acting in the reduction reaction of platinum(IV). Figure 5.9 summarizes the normalized intensities of the major dissociation channels of [EPX-H]$^-$ (X = 32, 416, 417, 440, 456) at the same CE value.
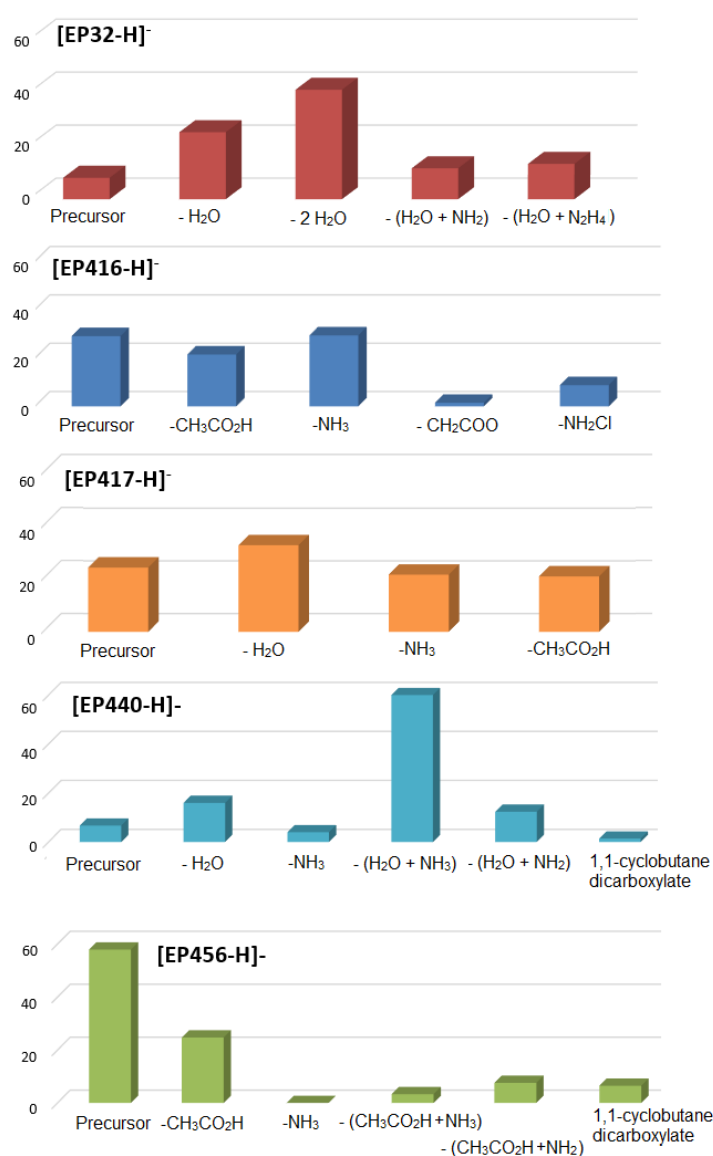
Figure 5.9 Major breakdown channels from the deprotonated ions of EPX (X = 32, 416, 417, 440, 456) and their normalized ratio in the CID mass spectrum at CE = 5V.

216

The behavior of [EP416-H]⁻, compared with that of [EP32-H]⁻, shows less extensive dissociation and the contribution of an important ammonia loss. Moving to [EP417-H]⁻, possessing different axial ligands, the behavior under CID condition reflects its mixed nature showing an intermediate percentage of precursor ion fragmentation and fragments pertaining to both [EP32-H]⁻ and [EP416-H]⁻, as reported in scheme 5.5 and in thoroughly in Scheme S5.2 of the SI. However, the primary water loss is the most prominent channel (Figure 5.9), confirming it to be the easiest dissociation path.
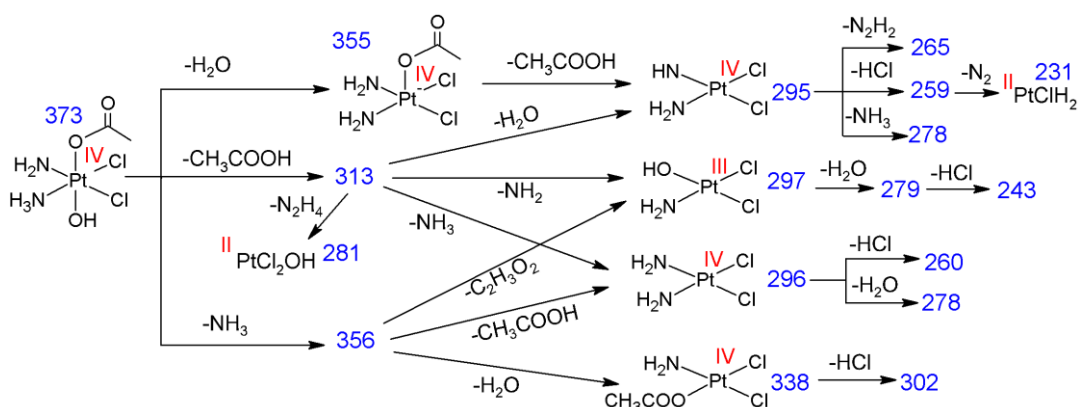
Scheme 5.5 Schematic representation of the dissociation pattern generated by CID of [EP417-H]⁻. In blue is reported the *m/z* ratio of the species and in red the formal oxidation state of platinum. Every complex is negatively charged, charges are not made explicit.

Concerning [EP440-H]⁻, it presents the same hydroxo axial ligands as EP32 but differs for the equatorial ligands, where the two chlorides are substituted by a chelating 1,1-cyclobutanedicarboxylato ligand. The low percentage of resistant precursor ion make it similar to [EP32-H]⁻ suggesting the crucial factor that ease the water loss path to be the presence of two hydroxo ligands in axial positions. In addition, it is interesting to note the presence of a small fraction of deprotonated ligand dissociating from the complex. Scheme S5.3 in the SI displays the complete fragmentation pattern of [EP440-H]⁻ showing the presence of the channel producing a formal Pt^{III}-containing complex by loss of NH$_2$ following the primary dissociation of water. This channel is instead missing in the CID of [EP416-H]⁻ suggesting the hydroxo ligand to have a major role in the reaction mechanism along the

EP32/EP416/EP417 series. The process is conceivably bound to the possibility for the OH to swap from axial to equatorial position thus replacing the NH_2 group in the pentacoordinated complexes formed by the primary water loss, as further illustrated in the following section. This evidence is limited to the cisplatin prodrugs EP32/EP416/EP417 though. In fact, in the case of the EP456, the fragmentation pattern of the deprotonated species, reported in scheme 5.6 and, more comprehensively, in scheme S5.4, shows the formation of an ion corresponding to [Pt(1,1-cyclobutanedicarboxylate)(CH_3COO)(NH_2)]$^-$ formally containing Pt^{III} despite the absence of any OH ligand. Interestingly, it is also the major secondary channel as shown in figure 5.9.
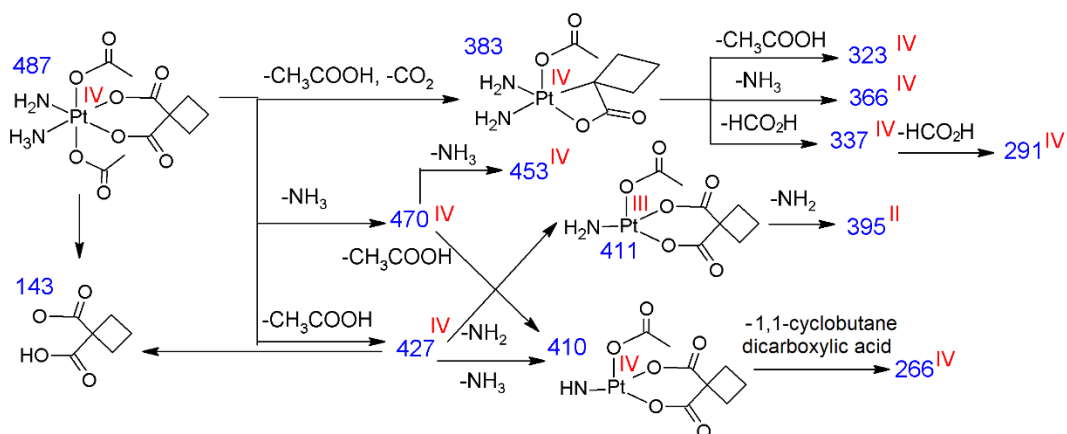
Scheme 5.6 Schematic representation of the dissociation pattern generated by CID of [EP456-H]$^-$. In blue is reported the *m/z* ratio of the species and in red the formal oxidation state of platinum. Every complex is negatively charged, charges are not made explicit.

The [Pt(1,1-cyclobutanedicarboxylate)(CH_3COO)(NH_2)]$^-$ complex fragments once again by loss of NH_2 forming a Pt^{II}-complex. This two step sequence, corresponding to stepwise reduction from Pt^{IV} to Pt^{II} is characteristic of EP456 and unusual with respect to the otherwise prevailing direct dissociation of N_2H_4. The [EP456-H]$^-$ complex is also the most resistant towards fragmentation, as demonstrated by the high percentage of undissociated parent ion reported in figure 5.9. In this respect EP456 conforms to the already mentioned lower ease to undergo dissociation shown by a complex presenting two acetate ligands in axial positions.

5.4.3 Computed paths for the gas-phase breakdown pattern

DFT calculations have allowed to outline the free energy profile for the gas-phase fragmentation pattern of two sampled Pt^{IV} complexes. Figure 5.10 presents the free energy surface (FES) for the [EP32-H]$^-$ complex, showing water loss as the common first event, prior to subsequent dissociation steps as depicted in scheme 5.4.
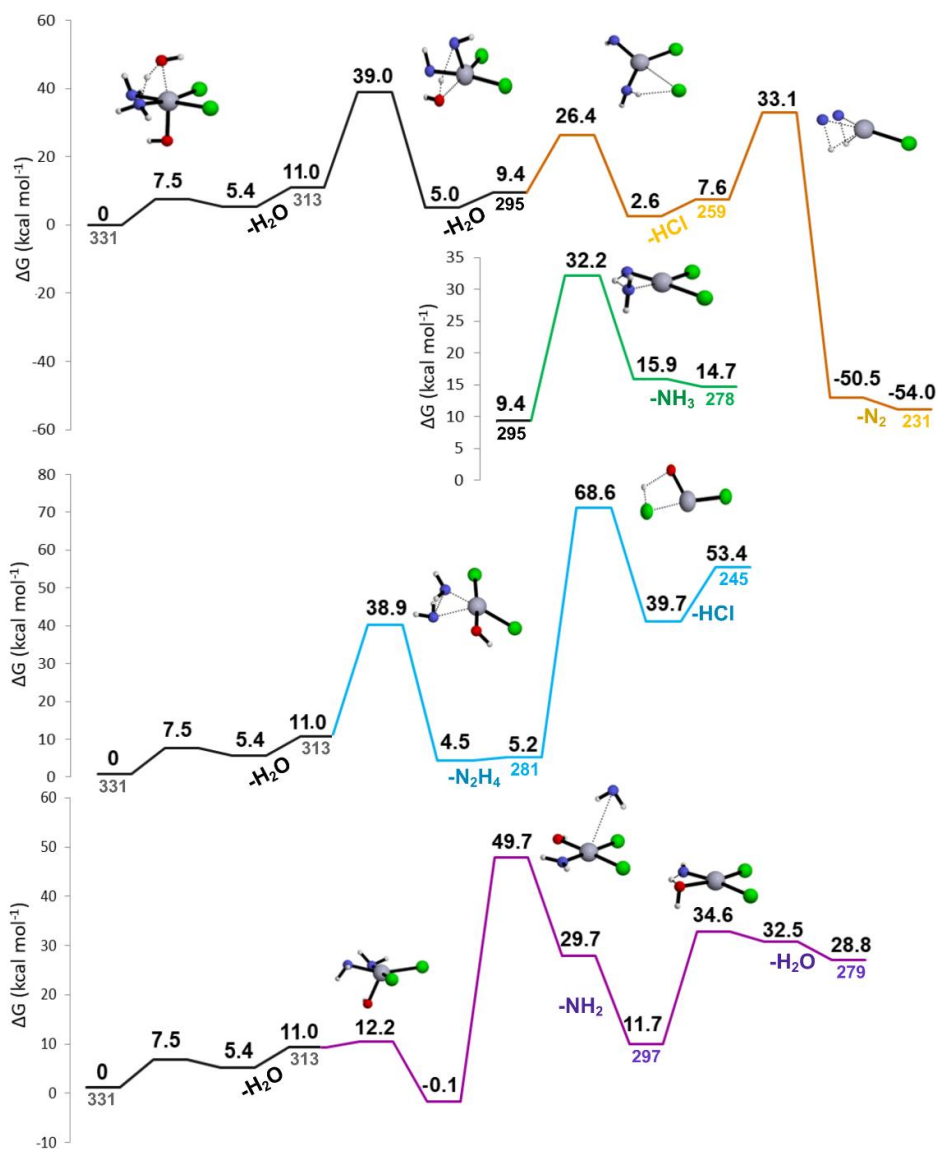
Figure 5.10 FES for the breakdown pattern of [EP32-H]$^-$. The black trace common to all profiles regards the common water loss step. The neutral losses for all dissociation events are indicated below the colored lines. Relative free energies at 298 K in kcal mol^{-1} are reported in black. The *m/z* value for each species is reported in color.

The first event of water loss in the dissociation pathway of [EP32-H]$^-$ involves a ΔG equal to 11.0 kcal mol^{-1}. This relatively low value is in agreement with the observed

ease for fragmentation even at low CE (figure 5.7 a and figure 5.9). Subsequent dissociation paths involve competing loss of a second H_2O molecule, loss of N_2H_4 and NH_2 loss, characterized by transition states lying at 39.0 (black profile figure 5.10), 38.9 (blue profile figure 5.10) and 49.7 (purple profile figure 5.10) kcal mol^{-1}, respectively. The data are consistent with the behavior of [EP32-H]$^-$ which shows a preferential second-step fragmentation involving water loss (*m/z* 295) and loss of N_2H_4 (*m/z* 281) at 4V CE (figure 5.7 a). At this CE value, hardly any product involving NH_2 loss is formed while it becomes a prevailing species at 8V CE (figure 5.7 b). At this same CE the product at *m/z* 295 undergoes subsequent dissociation yielding ions at *m/z* 259, *m/z* 231 and *m/z* 278. The last one is the least abundant (figure 5.7 b) in agreement with the higher activation free energy (32.2 kcal mol^{-1}, green profile of figure 5.10) compared to the 26.4 kcal mol^{-1} needed to activate the loss of HCl from *m/z* 295 (orange profile, figure 5.10). Finally, the ion *m/z* 259 generates the fragment at *m/z* 231 in a process involving of neutral N_2 as shown in scheme 5.4. This latter dissociation channel presents a calculated transition state energy 16.6 kcal mol^{-1} lower than the one involved in the secondary channel involving loss of NH_2, as shown in the orange and purple profiles of figure 5.10, respectively.

Overall, the computational survey offers a reliable description and interpretation of the experimentally observed phenomena. A few details regarding the reactions mechanism can be underlined, focusing in particular on the processes generating the reduced platinum species. There are three paths leading to either Pt^{II} (*m/z* 231 and 281) or Pt^{III} (*m/z* 297) species that are formed via a redox process involving ammonia molecules bound to the metal. Indeed, it is a different landscape when compared with the reactivity pattern in solution where reduction of platinum(IV) is suggested to be mainly accompanied by oxidation and dissociation of the axial ligands.[8,13,34-37] However, in the naked gaseous platinum(IV) complex water molecules are largely lost by direct cleavage concomitant with proton transfer from the ammonia ligand, whose acidity is enhanced by ligation to the metal. The so-formed cis NH_2 groups react upon CID by donating two electrons to the electron-poor Pt^{IV} atom to generate a N-N bond and dissociate from the complex (blue profile in figure 5.10). In contrast, the reaction producing the Pt^{III} complex proceeds

by a direct cleavage of NH_2 with a preliminary swapping of the hydroxo axial group to the equatorial position leading to a complex in which the NH_2 group is in axial position. The so-formed Pt^{III} complex $[PtCl_2(OH)(NH_2)]^-$ is fairly stable and can be isolated and subsequently assayed in the gas-phase in spite of there being no clearcut evidence for the formation of Pt^{III} species in the reaction paths of Pt^{IV} complexes in solution. [8,17-20]

The second Pt^{IV} complex sampled by DFT calculations is $[EP417-H]^-$, where the different ligands in axial position open a larger variety of breakdown paths as reported in scheme 5.5 and scheme S5.2. The calculated FES for the early dissociation paths is depicted in figure 5.11 and shows the first competing processes involving loss of either water (orange profile), acetic acid (green profile) or ammonia (blue profile).
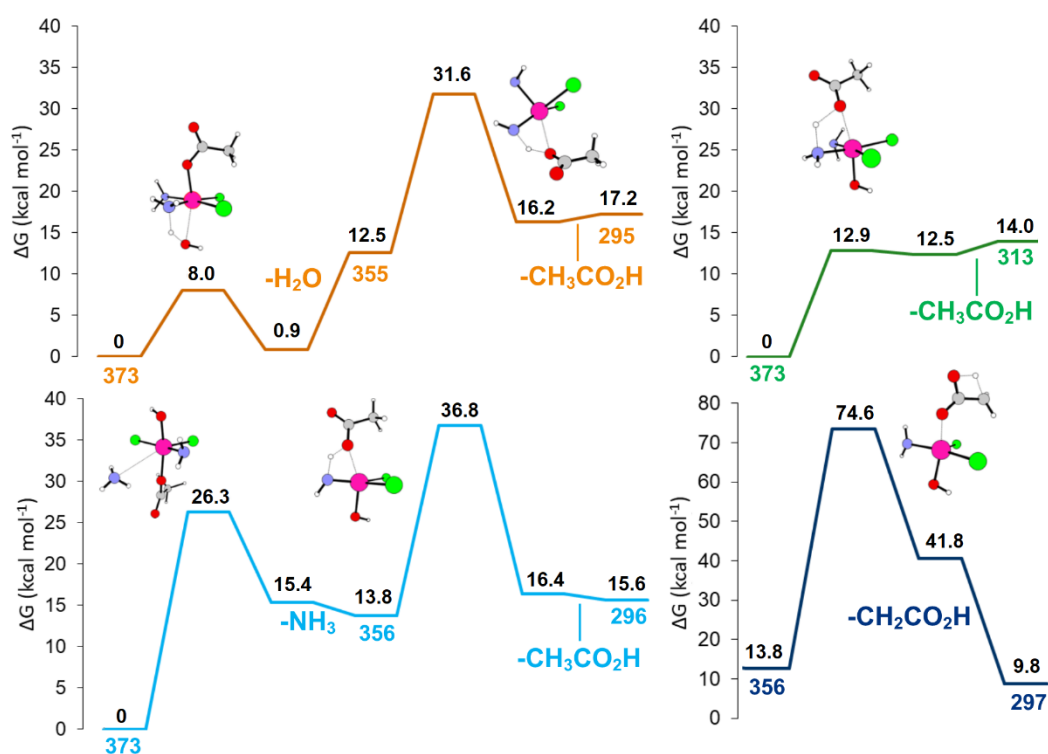
Figure 5.11 FES for the breakdown pattern of $[EP417-H]^-$. The neutral losses for all dissociation events are indicated below the colored lines. Relative free energies at 298 K in kcal mol^{-1} are reported in black. The *m/z* value for each species is reported in color.

The threshold energy is 12.5, 14.0, and 26.3 for dissociation of water, acetic acid, and ammonia, respectively. Even the less demanding process, loss of water, is more

endoergonic than loss of water from [EP32-H]⁻, which may account for the higher resistance to dissociation displayed by [EP417-H]⁻ (figure 5.9). Both paths for dissociation of either water or acetic acid are characterized by a transition state involving proton transfer from the ammine to the axial ligand, lying relatively close to the intermediate product anion-neutral complex, then evolving by departure of neutral water or acetic acid. In contrast, the NH_3 cleavage path, though not requiring any proton transfer event, presents a transition state relatively high in energy, not quite compatible with the rather extensive process nearly as efficient as loss of acetic acid. The lowest energy requirement for water loss is also consistent with this one being the only fragmentation path displayed by [EP32-H]⁻ under CID conditions.

5.4.4 A structural assay of the sampled deprotonated complexes by IRMPD spectroscopy

Two items among the set of deprotonated complexes have been assayed by vibrational spectroscopy in the X-H (X = C, N, O) stretching range, namely [EP32-H]⁻ and [EP417-H]⁻, in order to gain independent, experimental evidence for the computed structures of the sampled species.

The experimental spectrum of [EP32-H]⁻ in the 3000-3700 cm⁻¹ region is reported in red in figure 5.12 together with the calculated IR spectra for two isomers **EP32-H-_1** and **EP32-H-_2**. The first species is obtained from the EP32 neutral complex by abstraction of a proton from one of the ammine ligands. This isomer is lowest in energy. The search for a local minimum corresponding to deprotonation from the OH group has failed in spite of sustained effort. In the second isomer, **EP32-H-_2**, a proton has moved from NH_3 to one of the hydroxo ligands. The ensuing species is higher in free energy by 10.4 kcal mol⁻¹. It is thus not surprising that the comparison between experimental and theoretical spectra points to the **EP32-H-_1** as the major species representing the gas-phase population. The IRMPD spectrum is dominated by a broad and asymmetric feature around 3400 cm⁻¹ comprising two signals at 3410 and 3332 cm⁻¹, in fair agreement with the presence of the asymmetric stretching modes of the intact ammine ligand at 3439 and 3392 cm⁻¹. The sharp feature at 3625 cm⁻¹ can be assigned to the OH stretching mode that is however

calculated at 3672 cm^{-1} for **EP32-H-_1**. The observed higher frequency for an OH stretching mode in the calculated IR spectrum compared with the experimental one finds precedent in previous work dealing with similar Pt-containing complexes (see section 3.4 and reference 38). Interestingly, the IRMPD spectrum presents also a small band around 3247 cm^{-1} ascribed to the N-H symmetric stretching at 3622 cm^{-1} for Pt-bound NH$_3$ in **EP32-H-_1**. A minor contribution of **EP32-H-_2** cannot be discarded, though, in view of the broad absorbance around 3400 cm^{-1} on the red side. This isomer is likely to play a role as intermediate in the water loss path, the largely prevailing dissociation process in the breakdown chemistry of [EP32-H]$^-$.
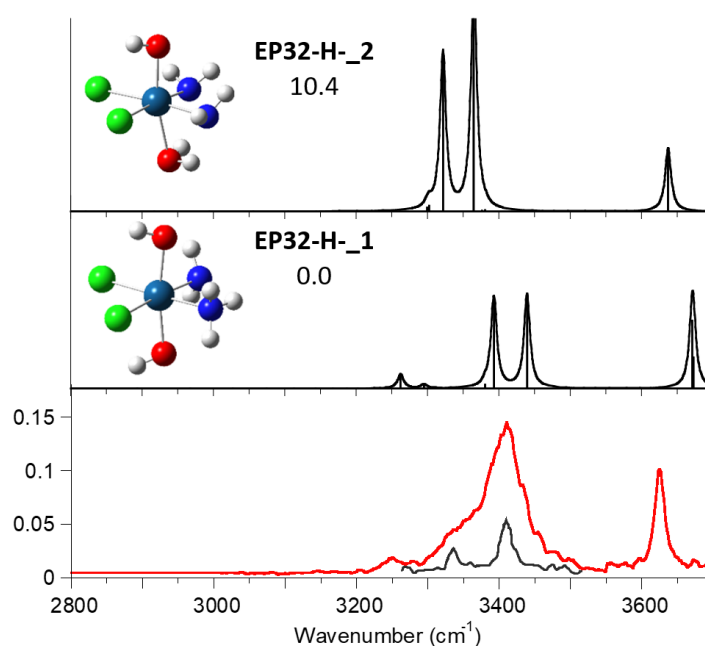
Figure 5.12 IRMPD spectrum of [EP32-H]$^-$ (red profile and gray profile recorded at lower laser power) compared to the theoretical calculated IR spectra at the B3LYP/6-311+G** (Pt = LanL2TZ) level for **EP32-H-_1** and **EP32-H-_2**. Optimized geometries at the same level of theory are reported together with relative free energies at 298K in kcal mol^{-1}. A factor of 0.957 is used to scale the calculated harmonic frequencies.

Figure 5.13 shows the IRMPD spectrum of [EP417-H]$^-$ (red profile) compared with the theoretical spectrum of the calculated geometry **EP417-H-_1** showing once again deprotonation from the ammonia molecule. No other isomeric complexes were found exploring possible prototropic rearrangements. The experimental spectrum shows a signal at 3600 cm^{-1}, in agreement with the OH stretching frequency calculated at 3605 cm^{-1}, followed by two broad absorption at 3395 and

3332 cm^{-1} that can be arguably attributed to the convolution of the NH stretching modes, in particular the NH$_3$ asymmetric and symmetric ones at 3403, 3358 and 3265 cm^{-1}, respectively, and the NH$_2$ asymmetric and symmetric stretchings at 3345 and 3246 cm^{-1}. Finally, the IRMPD signal at 2917 cm^{-1} is matched by the CH$_3$ symmetric stretching at 2912 cm^{-1}.
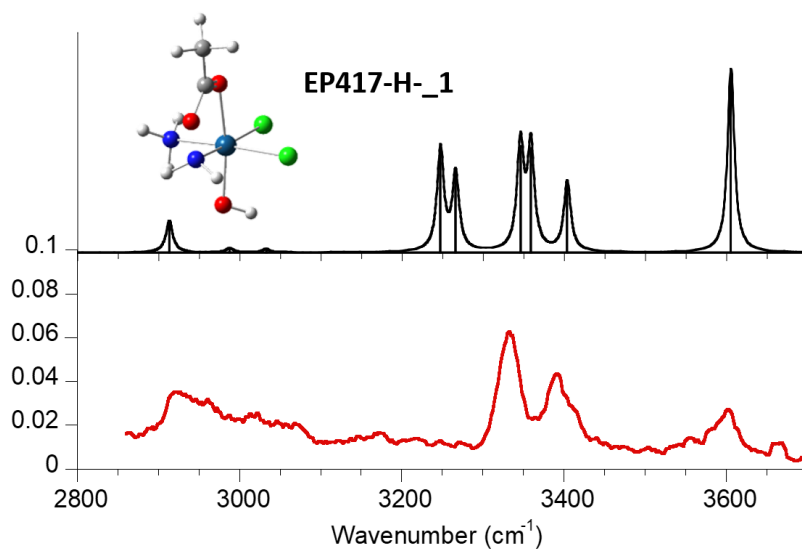
Figure 5.13 IRMPD spectrum of [EP417-H]$^-$ (red profile) compared to the theoretical calculated IR spectrum at the B3LYP/6-311+G** (Pt = LanL2TZ) level for **EP417-H-_1**. The optimized geometry is obtained at the same level of theory. A factor of 0.957 is used to scale the calculated harmonic frequencies.
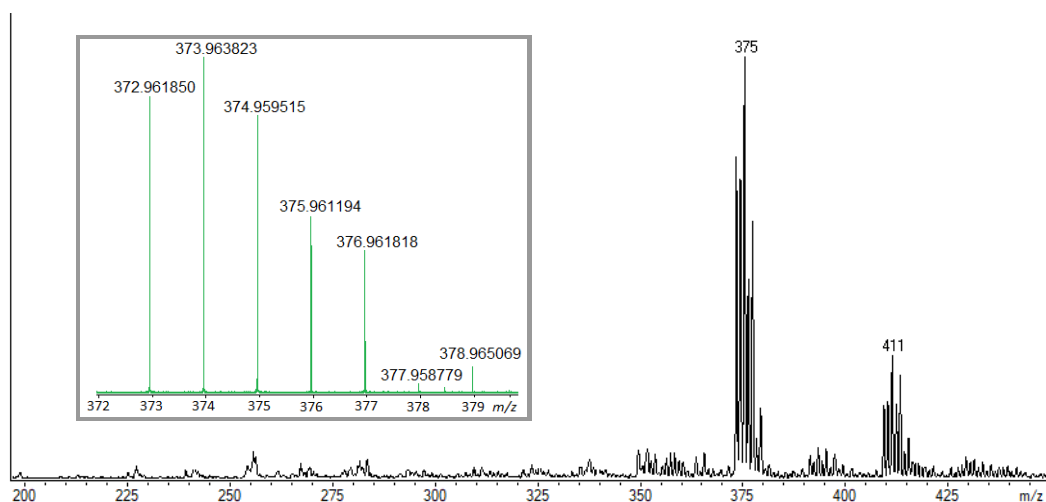
Figure S5.1 Negative ion ESI mass spectrum of an EP417 solution water/methanol 1:1. The ion [EP417-H]$^-$ is present at *m/z* 373-379. At *m/z* 409-415 is also present the chloride adduct [EP417+Cl]$^-$. In the inset is reported the high resolution mass spectrum of the isotopic cluster corresponding to [PtCl$_2$(CH$_3$COO)(OH)(NH$_3$)(NH$_2$)]$^-$. The attribution of the molecular formula was confirmed comparing the measured mass of the signal containing ^{194}Pt and two ^{35}Cl (372.961850 Da) with the corresponding exact mass (372.961699 Da). The error found is 0.4 ppm.
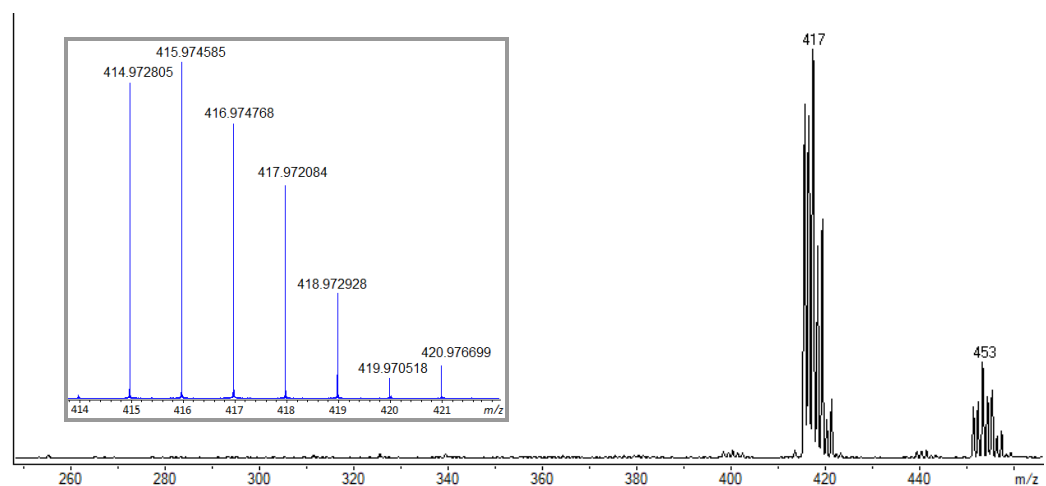
Figure S5.2 Negative ion ESI mass spectrum of an EP416 solution water/methanol 1:1. The ion [EP416-H]$^-$ is present at *m/z* 415-421. A chloride adduct with the platinum complex is also present at *m/z* 451-457. In the inset is reported the high resolution mass spectrum of the isotopic cluster corresponding to [PtCl$_2$(CH$_3$COO)$_2$(NH$_3$)(NH$_2$)]$^-$. The attribution of the molecular formula was confirmed comparing the measured mass of the signal containing ^{194}Pt and two ^{35}Cl (414.972805 Da) with the corresponding exact mass (414.972263 Da), showing a 1.3 ppm error.
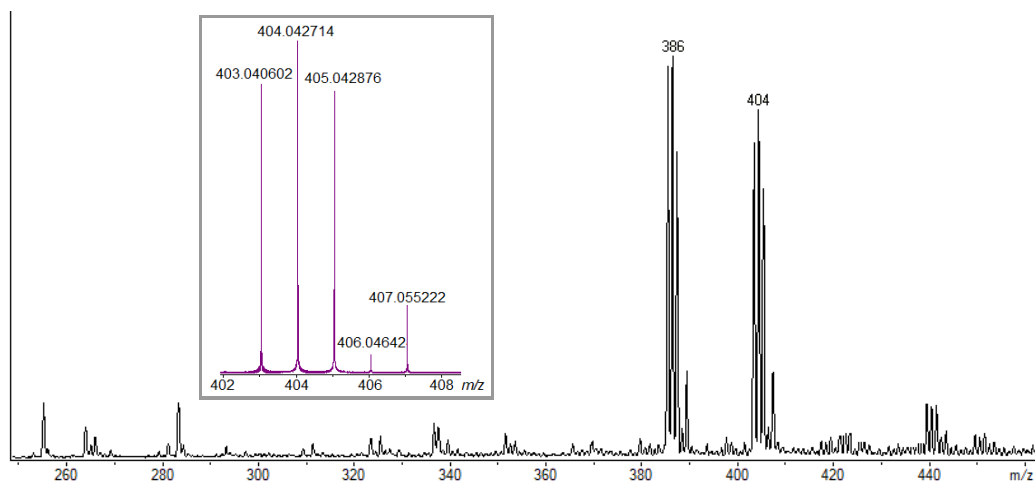
Figure S5.3 Negative ion ESI mass spectrum of an EP440 solution water/methanol 1:1. The ion [EP440-H]⁻ is present at *m/z* 403-407. Eventually, an important fragmentation is obtained even with soft ionization condition as shown by the presence of the fragment [EP440-H₂O-H]⁻ at *m/z* 385-389. In the inset is reported the high resolution mass spectrum of the isotopic cluster corresponding to [Pt(C₆H₆O₄)(OH)₂(NH₃)(NH₂)]⁻. The attribution of the molecular formula was confirmed comparing the measured mass of the signal containing ^{194}Pt (403.040602 Da) with the corresponding exact mass (403.040758 Da), showing a 0.4 ppm error.
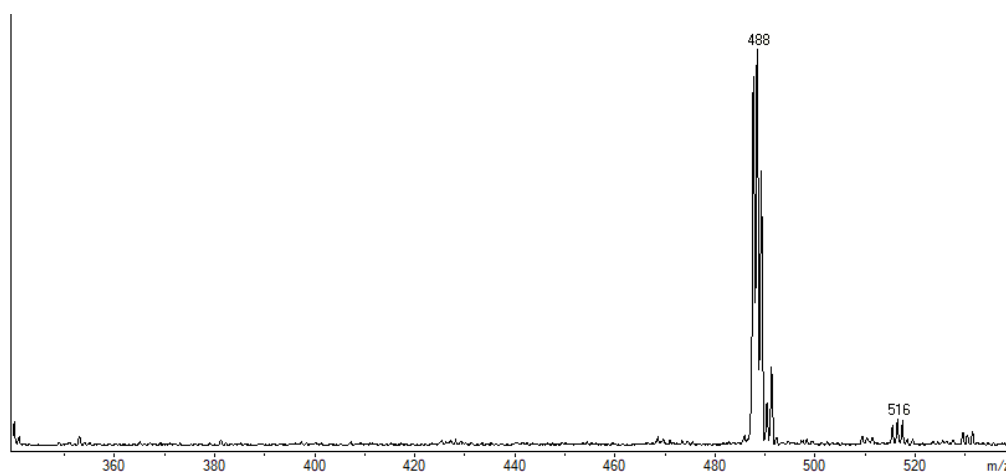
Figure S5.4 Negative ion ESI mass spectrum of an EP456 solution water/methanol 1:1. The ion [EP456-H]⁻ is present at *m/z* 487-491 having the molecular formula [Pt(C₆H₆O₄)(CH₃COO)₂(NH₃)(NH₂)]⁻.
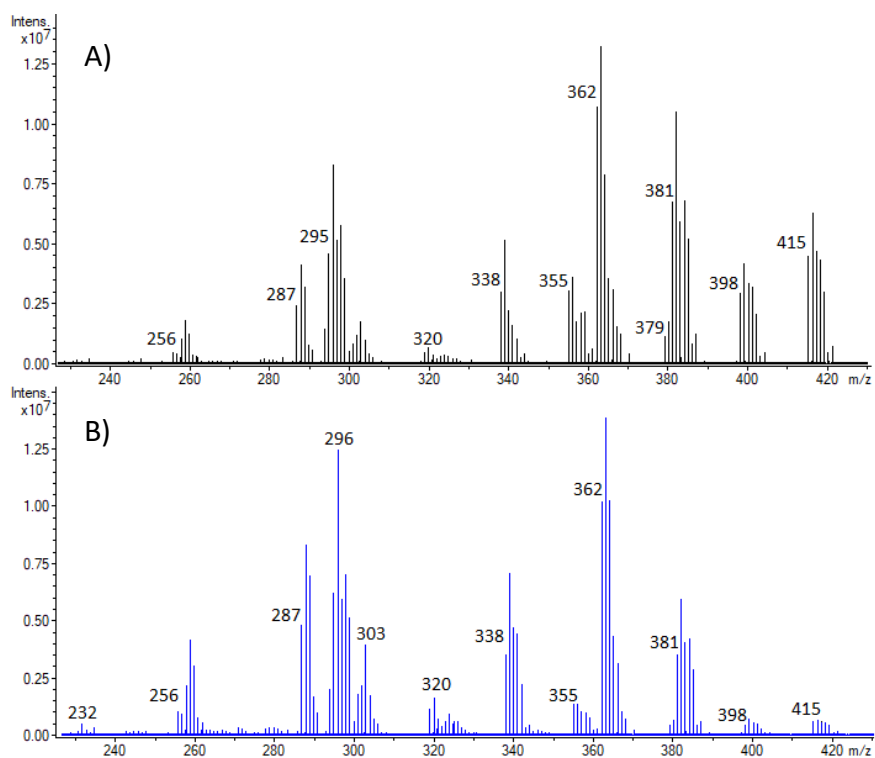
Figure S5.5 CID mass spectrum of [EP416-H]⁻ (*m/z* 415-421) recorded with a CE of A) 4 V (black profile) and B) 8V (blue profile).
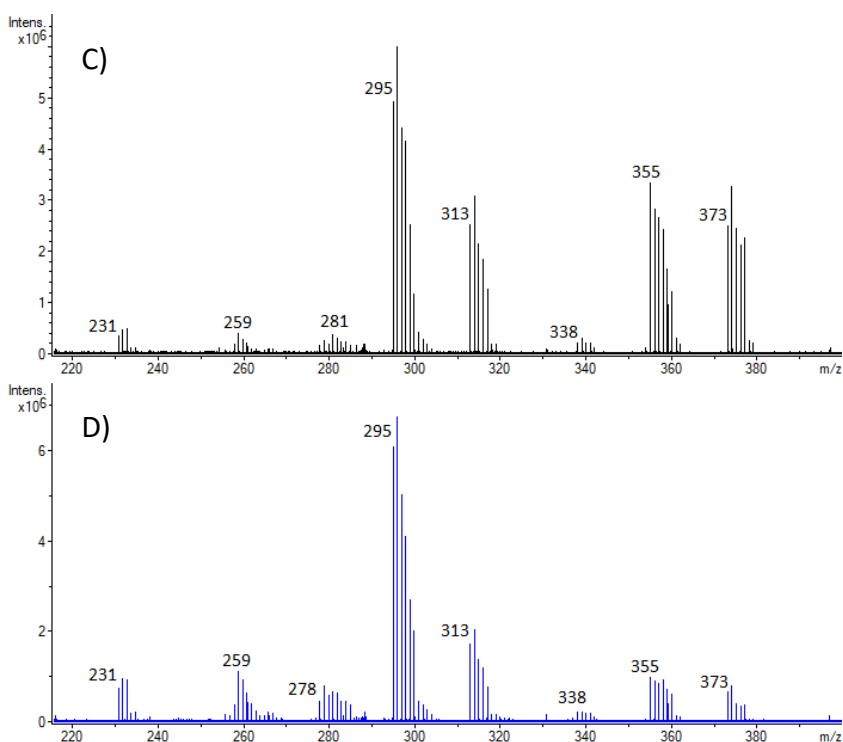
Figure S5.6. CID mass spectrum of [EP417-H]⁻ (*m/z* 373-377) recorded with a CE of C) 4 V (black profile) and D) 8V (blue profile).
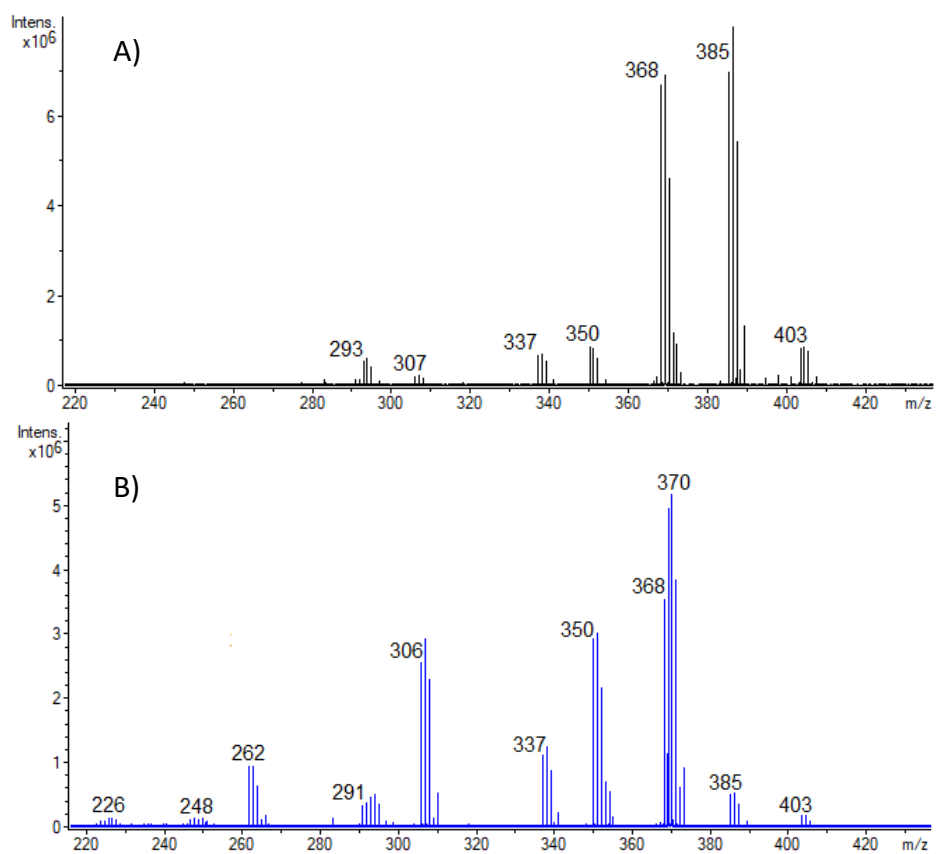
Figure S7. CID mass spectrum of [EP440-H]⁻ (*m/z* 403-407) recorded with a CE of A) 4 V (black profile) and B) 8V (blue profile).

Scheme S5.1 Schematic representation of the dissociation pattern generated by CID of [EP416-H]$^-$. In purple is reported the *m/z* ratio of the species and in blue the formal oxidation state of platinum. Every complex is negatively charged, charges are not made explicit.

Scheme S5.2 Schematic representation of the dissociation pattern generated by CID of [EP417-H]⁻. In purple is reported the *m/z* ratio of the species and in blue the formal oxidation state of platinum. Every complex is negatively charged, charges are not made explicit.

Scheme S5.3 Schematic representation of the dissociation pattern generated by CID of [EP440-H]⁻. In purple is reported the *m/z* ratio of the species and in blue the formal oxidation state of platinum. Every complex is negatively charged, charges are not made explicit.
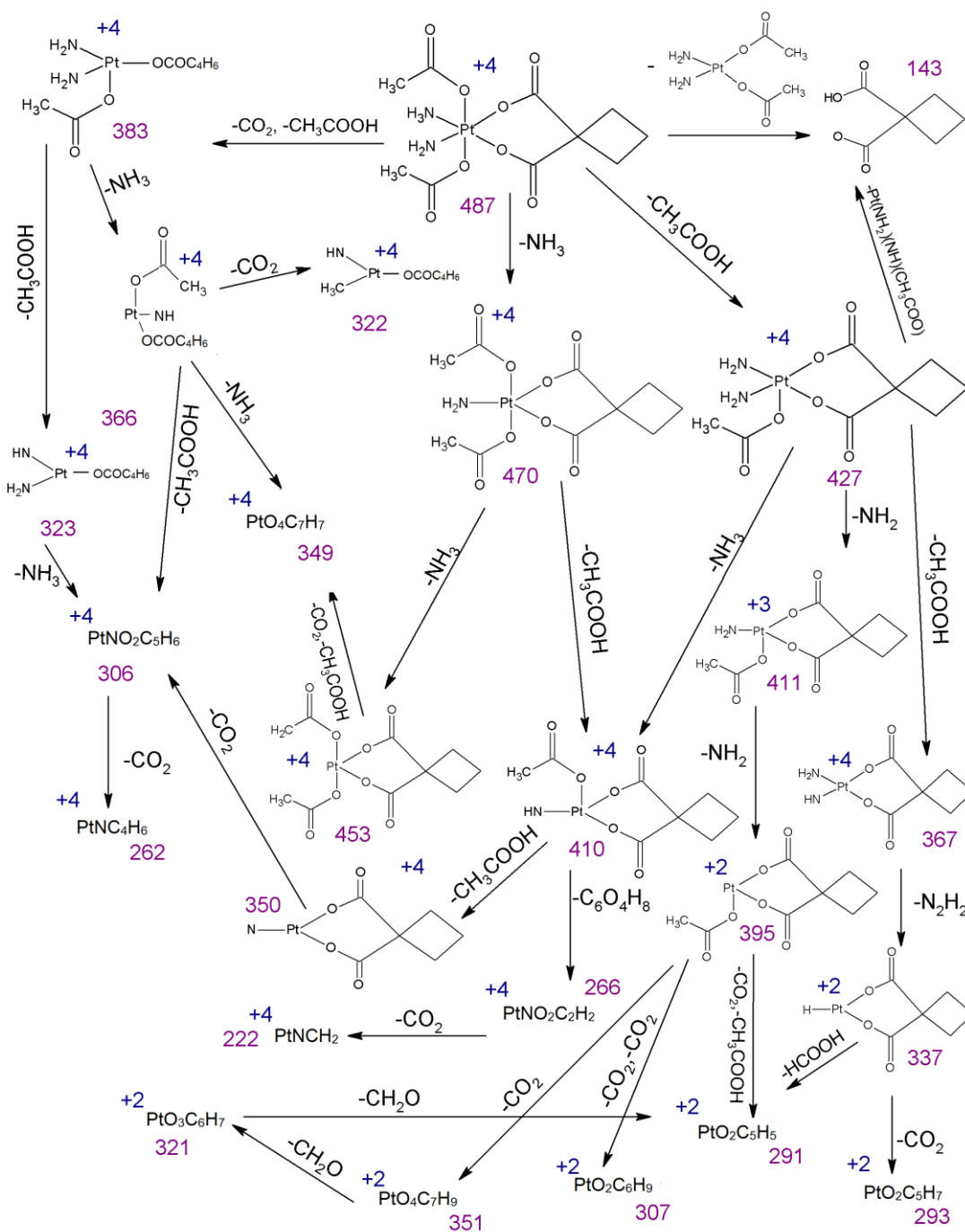
Scheme S5.4 Schematic representation of the dissociation pattern generated by CID of [EP456-H]⁻. In purple is reported the *m/z* ratio of the species and in blue the formal oxidation state of platinum. Every complex is negatively charged, charges are not made explicit.

Table S5.1 Experimentally obtained high-resolution *m/z* values for the fragments obtained by CID of [EP32-H]⁻ compared with the calculated exact masses of the correspondent attributed molecular formula. The relative error is reported in ppm.

Formal *m/z*	Experimental *m/z*	Theoretical exact mass	Molecular formula	Δ*m/m*
331	330.951539	330.951135	$[^{194}Pt^{35}Cl_2(OH)_2(NH_3)(NH_2)]^-$	1.2
313	312.940753	312.940571	$[^{194}Pt^{35}Cl_2(OH)(NH_2)_2]^-$	0.6
297	296.922099	296.921847	$[^{194}Pt^{35}Cl_2(OH)(NH_2)]^-$	0.8
296	295.914272	295.914022	$[^{194}Pt^{35}Cl_2(OH)(NH)]^-$	0.8
295	294.930281	294.930007	$[^{194}Pt^{35}Cl_2(NH_2)(NH)]^-$	0.9
281	280.903376	280.903123	$[^{194}Pt^{35}Cl_2(OH)]^-$	0.9
279	278.911552	278.911283	$[^{194}Pt^{35}Cl_2(NH)]^-$	1.0
278	277.903701	277.903458	$[^{194}Pt^{35}Cl_2N]^-$	0.9
265	264.908368	264.908209	$[^{194}Pt^{35}Cl_2H]^-$	0.6
260	259.937546	259.937345	$[^{194}Pt^{35}Cl(NH)(O)]^-$	0.7
259	258.953504	258.953330	$[^{194}Pt^{35}Cl(NH)_2]^-$	0.7
245	244.926652	244.926446	$[^{194}Pt^{35}ClO]^-$	0.8
231	230.947342	230.947182	$[^{194}Pt^{35}ClH_2]^-$	0.7

Table S5.2 Experimentally obtained high-resolution *m/z* values for the fragments obtained by CID of [EP416-H]$^-$ compared with the calculated exact masses of the corresponding attributed molecular formula. The relative error is reported in ppm.

Formal *m/z*	Experimental *m/z*	Theoretical exact mass	Molecular formula	Δ*m/m*
415	414.972805	414.972263	[^{194}Pt^{35}Cl$_2$(OCOCH$_3$)$_2$(NH$_3$)(NH$_2$)]$^-$	1.3
398	397.946654	397.945714	[^{194}Pt^{35}Cl$_2$(OCOCH$_3$)(NH$_2$)]$^-$	2.3
381	380.919916	380.919165	[^{194}Pt^{35}Cl$_2$(OCOCH$_3$)(OCOCH$_2$)]$^-$	1.9
364	363.985538	363.984687	[^{194}Pt^{35}Cl(NH$_3$)(OCOCH$_3$)$_2$]$^-$	2.3
362	361.969656	361.969037	[^{194}Pt^{35}Cl(NH$_2$)(OCOCH$_3$)(OCOCH$_2$)]$^-$	1.7
357	356.967870	356.966785	[^{194}Pt^{35}Cl$_2$(OCOCH$_3$)(NH$_2$)(NH$_2$)H]$^-$	3.0
355	354.951865	354.951135	[^{194}Pt^{35}Cl$_2$(NH$_2$)$_2$(OCOCH$_3$)]$^-$	2.0
338	337.925186	337.924586	[^{194}Pt^{35}Cl$_2$(OCOCH$_3$)(NH)]$^-$	1.7
323	322.914312	322.913687	[^{194}Pt^{35}Cl$_2$(OCOCH$_2$)H]$^-$	1.9
321	320.898670	320.898037	[^{194}Pt^{35}Cl$_2$(OCOCH)]$^-$	2.0
302	301.948419	301.947909	[^{194}Pt^{35}Cl(NH)(OCOCH$_2$)]$^-$	1.7
301	300.953190	300.952660	[^{194}Pt^{35}Cl(CH$_2$)(OCOCH$_2$)]$^-$	1.8
295	294.930479	294.930007	[^{194}Pt^{35}Cl$_2$(NH$_2$)(NH)]$^-$	1.6
294	293.935260	293.934758	[^{194}Pt^{35}Cl$_2$(NH)(CH$_3$)]$^-$	1.7
287	286.937373	286.937010	[^{194}Pt^{35}Cl(OCOCH$_2$)]$^-$	1.3
259	258.953624	258.953330	[^{194}Pt^{35}Cl(NH)$_2$]$^-$	1.1
258	257.958452	257.958081	[^{194}Pt^{35}Cl(NH)(CH$_2$)]$^-$	1.4
256	255.942772	255.942431	[^{194}Pt^{35}ClNCH]$^-$	1.3

Table S5.3 Experimentally obtained high-resolution *m/z* values for the fragments obtained by CID of [EP417-H]⁻ compared with the calculated exact masses of the corresponding attributed molecular formula. The relative error is reported in ppm.

Formal *m/z*	Experimental *m/z*	Theoretical exact mass	Molecular formula	Δ*m/m*
373	372.962505	372.961699	[$^{194}Pt^{35}Cl_2(OH)(OCOCH_3)(NH_3)(NH_2)$]⁻	2.2
356	355.935674	355.935150	[$^{194}Pt^{35}Cl_2(OH)(OCOCH_3)(NH_2)$]⁻	1.5
355	354.951937	354.951135	[$^{194}Pt^{35}Cl_2(OCOCH_3)(NH_2)_2$]⁻	2.3
338	337.925214	337.924586	[$^{194}Pt^{35}Cl_2(OCOCH_3)(NH)$]⁻	1.9
313	312.941081	312.940571	[$^{194}Pt^{35}Cl_2(NH_2)_2(OH)$]⁻	1.6
302	301.948897	301.947909	[$^{194}Pt^{35}Cl(NH)(OCOCH_3)$]⁻	3.3
297	296.922249	296.921847	[$^{194}Pt^{35}Cl_2(NH_2)(OH)$]⁻	1.4
296	295.914317	295.914022	[$^{194}Pt^{35}Cl_2(NH)(OH)$]⁻	1.0
295	294.930287	294.930007	[$^{194}Pt^{35}Cl_2(NH_2)(NH)$]⁻	1.0
281	280.903540	280.903123	[$^{194}Pt^{35}Cl_2(OH)$]⁻	1.5
279	278.911635	278.911283	[$^{194}Pt^{35}Cl_2(NH)$]⁻	1.3
278	277.903778	277.903458	[$^{194}Pt^{35}Cl_2N$]⁻	1.2
265	264.908531	264.908209	[$^{194}Pt^{35}Cl_2H$]⁻	1.2
260	259.937696	259.937345	[$^{194}Pt^{35}Cl(OH)N$]⁻	1.4
259	258.953629	258.953330	[$^{194}Pt^{35}Cl(NH)_2$]⁻	1.2
258	257.958401	257.958081	[$^{194}Pt^{35}Cl(NH)(CH_2)$]⁻	1.2
256	255.942743	255.942431	[$^{194}Pt^{35}ClN(CH)$]⁻	1.2
245	244.926743	244.926446	[$^{194}Pt^{35}ClO$]⁻	1.2
231	230.947402	230.947182	[$^{194}Pt^{35}Cl(H_2)$]⁻	1.0

Table S5.4 Experimentally obtained high-resolution *m/z* values for the fragments obtained by CID of [EP440-H]$^-$ compared with the calculated exact masses of the corresponding attributed molecular formula. The relative error is reported in ppm.

Formal *m/z*	Experimental *m/z*	Theoretical exact mass	Molecular formula	Δ*m/m*
403	403.040037	403.040758	[^{194}Pt(OH)$_2$(NH$_3$)(NH$_2$)(O$_4$C$_6$H$_6$)]$^-$	1.8
385	385.029473	385.030110	[^{194}Pt(NH$_2$)$_2$(OH)(O$_4$C$_6$H$_6$)]$^-$	1.7
369	369.010749	369.011390	[^{194}Pt(NH$_2$)(OH)(O$_4$C$_6$H$_6$)]$^-$	1.7
368	368.002924	368.003097	[^{194}Pt(NH)(OH)(O$_4$C$_6$H$_6$)]$^-$	0.5
351	351.000185	351.000677	[^{194}Pt(NH)(O$_4$C$_6$H$_6$)]$^-$	1.4
350	349.992360	349.992677	[^{194}Pt(N)(O$_4$C$_6$H$_6$)]$^-$	0.9
337	336.997111	336.997292	[^{194}Pt(H)(O$_4$C$_6$H$_6$)]$^-$	0.5
306	306.002532	306.002742	[^{194}Pt(N)(O$_2$C$_5$H$_6$)]$^-$	0.2
293	293.007283	293.007526	[^{194}Pt(H)(O$_2$C$_5$H$_6$)]$^-$	0.8
291	290.991633	290.991817	[^{194}Pt(H)(O$_2$C$_5$H$_4$)]$^-$	0.6
263	263.020529	263.020932	[^{194}Pt(NH)(C$_4$H$_6$)]$^-$	1.5
262	262.012704	262.012920	[^{194}Pt(N)(C$_4$H$_6$)]$^-$	0.8
245	244.986155	244.986215	[^{194}PtC$_4$H$_3$]$^-$	0.2
247	247.001805	247.002003	[^{194}Pt(H)(C$_4$H$_4$)]$^-$	0.8

5.5 Summary

In conclusion, we were able to isolate and characterize protonated and deprotonated Pt^{IV} complexes with different axial and equatorial ligands with the aim to gain new insights about their gas-phase behavior after activation. Moreover, IRMPD spectroscopy allowed us to obtain infrared spectra of selected protonated and deprotonated complexes ([EP32+H]$^+$, [EP417+H]$^+$, [EP440+H]$^+$, [EP32-H]$^-$ and [EP417-H]$^-$). The experimental vibrational features were interpreted with the aid of DFT calculations allowing to unveil protonation and deprotonation sites in the sampled complexes.

When the protonated Pt^{IV} complexes are assayed by CID the prevalent dissociation path involves the cleavage of the axial ligand as a neutral molecule. In this regard, it is possible to recognize a preference for the loss of the hydroxo ligand as water compared to the acetato as acetic acid. In agreement with the experimental results, calculations showed that the cleavage of water, calculated for the asymmetric complex [EP417+H]$^+$, was energetically less demanding than loss of acetic acid . In particular the threshold energy values were found to be 88 kJ mol^{-1} and 112 kJ mol^{-1}, respectively. IRMPD spectroscopy provided clear vibrational signatures showing exclusive protonation on the hydroxo ligand in the case of [EP32+H]$^+$, while regarding the [EP417+H]$^+$ complex presenting both acetato and hydroxo ligands the former was the favored protonation site. Calculations at the DFT level of the FES for the reaction of proton transfer from the ammine ligand to the hydroxo one showed that the reaction is energetically favored with respect to the direct acetic acid cleavage. A rationale is thus obtained for the observed CID reactivity of [EP417+H]$^+$,showing exclusive water loss. Our finding about the different free energy barriers involved in the cleavage of the axial ligands may also have an implication for the understanding of the redox behavior of Pt^{IV} complexes. Indeed, there are several cases in which the electrochemical reduction potential does not correlate with the rate of reduction of Pt^{IV} complexes.[39,40] For example, Dan Gibson et al.[39] reported the reduction rate and electrochemical potential of Pt^{IV} derivatives of oxaliplatin with either two hydroxo ligands, one acetato and one hydroxo ligands

or two acetato ligands. Their data show an increasingly positive potential moving from the hydroxo to the acetato ligands, but a decreasing reduction rate. The authors hypothesized this effect to be correlated to the inefficient electron transfer generated by the carboxylate compared to the OH. In this regard, our investigation suggests that the ease of fragmentation of the hydroxo axial ligands compared to the acetate one can also influence the reduction rate, considering that the cleavage of the axial ligands is commonly associated with the reduction reaction.[3,8]

The investigation of deprotonated Pt[IV] complexes permitted to obtain a different, but complementary range of information. IRMPD spectroscopy allowed to characterize the ammine ligand as the preferred deprotonation site. When interrogated by CID, the deprotonated species show a surprisingly complex dissociation pattern, involving ammonia loss and dissociation channels eventually leading to reduction of the platinum atom in addition to the direct cleavage of the axial ligands. The presence of reduced species after CID activation was reported in few papers about deprotonated U-containing complexes,[41-43] and, in a similar fashion as reported in our exploration, the corresponding protonated species showed no reduction reactions.[42] Intriguingly, the reduction processes we observed after gas-phase activation were always accompanied by equatorial ligand loss, either ammine or chloro. On the contrary, condensed-phase reduction reactions are considered to be concomitant with axial ligands loss.[8,13,34-37] Indeed some authors suggested the equatorial ligands to have a role in the reduction,[13,34] however the nature of the relative products is unclear. In this regard, the reduced species we have characterized using ESI and high-resolution mass spectrometry can pave the way to a better understanding of the reduction mechanism of platinum(IV) prodrugs. In addition, gas-phase activation of [EP32-H][-], [EP-417][-], [EP440-H][-] and [EP456-H][-] permitted to isolate and characterize complexes in which platinum showed a formal oxidation state of +3. Intriguingly, platinum(III) containing species have been seldom observed in solution, [8,17-20] and have been only theoretically postulated in the reaction mechanism of Pt[IV] prodrugs.[8,10] However, as shown in the present work, the mononuclear Pt[III] complexes generated by dissociation in the gas phase were found to be stable enough to be isolated and further activated. A

reported previous example has regarded a formal Pt[III] dinuclear cluster obtained in the gas phase by degradation of a tetrameric compound in the ESI source.[44] Finally, DFT calculations of the free energy surfaces for fragmentation reactions allowed to clarify the CID dissociation pattern in view of mechanistic and thermodynamic reasons.

References

[1] Taube, H. *Electron Transfer Reactions of Complex Ions in Solution* (1970) Academic Press: New York, 1970.

[2] Basolo, F., Morris, M.L., Pearson R.G. **Bridged mechanism for the platinum(II) catalysis of chloride exchange in chloroammine-platinum(IV) complexes** *Disc. Faraday Soc.* 29 (1960) 80-91.

[3] Hall, M.D., Hambley, T.W. **Platinum(IV) antitumor compounds: their bioinorganic chemistry** *Coord. Chem. Rev* 232 (2002) 49-67.

[4] Hall, M.D., Amjadi, S., Zhang, M., Beale, P.J., Hambley, T.W. **The mechanism of action of platinum(IV) complexes in ovarian cancer cell lines** *J. Inorg. Biochem.* 98 (2004) 1614–1624.

[5] Hall, M.D., Mellor, H.R., Callaghan, R., Hambley T.W. **Basis for Design and Development of Platinum(IV) Anticancer Complexes** *J. Med. Chem.* 50 (2007) 3403-3411.

[6] Platts, J.A., Ermondi, G., Caron, G., Ravera, M., Gabano, E., Gaviglio, L., Pelosi, G., Osella, D. **Molecular and statistical modeling of reduction peak potential and lipophilicity of platinum(IV) complexes** *J. Biol. Inorg. Chem.* 16 (2011) 361–372.

[7] McCormick, M.C., Schultz, F.A., Baik, M.-H. **Glassy carbon electrodes deliver unpredictable reduction potentials for platinum(IV) antitumor prodrugs** *Polyhedron* 103 (2016) 28-34.

[8] McCormick, M.C., Keijzer, K., Polavarapu, A., Schultz, F.A., Baik, M.-H., **Understanding Intrinsically Irreversible, Non-Nernstian, Two-Electron Redox Processes: A Combined Experimental and Computational Study of the Electrochemical Activation of Platinum(IV) Antitumor Prodrugs** *J. Am. Chem. Soc.* 136 (2014) 8992–9000.

[9] Šebesta, F., Baxová, K., Burda, J.V. **Redox Potentials for Tetraplatin, Satraplatin, Its Derivatives, and Ascorbic Acid: A Computational Study** *Inorg. Chem.* 57 (2018) 951–962.

[10] Tolbatov, I., Coletti, C., Marrone, A., Re, N. **Insight into the Electrochemical Reduction Mechanism of Pt(IV) Anticancer Complexes** *Inorg. Chem.* 57 (2018) 3411–3419.

[11] Gillard, R.D., Wilkinson, G. **Platinum blue and related compounds** *J. Chem. Soc.* (1964) 2835–2837.

[12] Jovanović, S., Petrović, B., Bugarčić, Z.D., van Eldik, R. **Reduction of some Pt(IV) complexes with biologically important sulfur-donor ligands** *DaltonTrans.* 42 (2013) 8890-8896, and references therein.

[13] Sinisi, M., Intini, F.P., Natile, G. **Dependence of the reduction products of platinum(IV) prodrugs upon the configuration of the substrate, bulk of the carrier ligands, and nature of the reducing agent** *Inorg. Chem.* 51 (2012) 9694–9704.

[14] Nemirovski, A., Kasherman, Y., Tzaraf, Y., Gibson, D. **Reduction of *cis,trans,cis*-[PtCl$_2$(OCOCH$_3$)$_2$(NH$_3$)$_2$] by Aqueous Extracts of Cancer Cells** *J. Med. Chem.* 50 (2007) 5554–5556.

[15] Lasorsa, A., Stuchlíková, O., Brabec, V., Natile, G., Arnesano, F. **Activation of platinum(IV) prodrugs by cytochrome c and characterization of the protein binding sites** *Mol. Pharmaceutics* 13 (2016) 3216–32.

[16] Gramatica, P., Papa, E., Luini, M., Monti, E., Gariboldi, M.B., Ravera, M., Gabano, E., Gaviglio, L., Osella, D. **Antiproliferative Pt(IV) complexes: synthesis, biological activity, and quantitative structure–activity relationship modeling** *J. Biol. Inorg. Chem.* 15 (2010) 1157–1169.

[17] Uson, R., Fonies, J., Tomas, M., Menjon, B., Suenkel, K., Bau, R. **The first mononuclear Pt^{III} complex. Molecular structures of (imbu$_4$)[Pt^{III}(C$_6$Cl$_5$)$_4$] and of its parent compound (NBu$_4$)$_2$[Pt^{II}(C$_6$Cl$_5$)$_4$]-2CH$_2$Cl$_2$** *J. Chem. Sot. Chem. Commun.* (1984) 751.

[18] Bontchev, P.R., Metewa, M., Gentcheva, G. **New platinum(II) and platinum(III) complexes of creatinine** *Pure Appl. Chem.* 61 (1989) 897.

[19] Waltz, W.L., Lilie, J., Goursot, A., Chermette H. **Photolytic and radiolytic study of platinum(III) complex ions containing aquo and chloro ligands** *Inorg. Chem.* 28 (1989) 2247.

[20] Rivada-Wheelaghan, O., Ortuño, M.A., García-Garrido, S.E., Alonso, P.J., Lledos, A., Conejero, S. **A stable, mononuclear, cationic Pt(III) complex stabilised by bulky N-heterocyclic carbenes** *Chem Commun.* 50 (2014) 1299-1301.

[21] Leonardo S. Santos, *Reactive intermediates: MS Investigations in Solution*. Ed. Leonardo S. Santos (2010) WILEY-VCH Verlag GmbH & Co. KGaA, Weinheim.

[22] Aliprantis, A.O., Canary, J.W. **Observation of Catalytic Intermediates in the Suzuki Reaction by Electrospray Mass Spectrometry** *J. Am. Chem. Soc.* 116 (1994) 6985-6986.

[23] De Petris, A., Crestoni, M.E., Pirolli, A., Rovira, C., Iglesias-Fernández, J., Chiavarino, B., Ragno, R., Fornarini, S. **Binding of azole drugs to heme: A combined MS/MS and computational approach** *Polyhedron* 90 (2015) 245-251.

[24] Sinha, R. K., Maitre, P., Piccirillo, S., Chiavarino, B., Crestoni, M. E., Fornarini, S. **Cysteine radical cation: a distonic structure probed by gas phase ir spectroscopy** *Phys. Chem. Chem. Phys.* 12 (2010) 9794-9800.

[25] Prell, J. S., O'Brien, J. T., Williams, E. R. **IRPD spectroscopy and ensemble measurements: Effects of different data acquisition and analysis methods** *J. Am. Soc. Mass Spectrom.* 21 (2010) 800–809.

[26] Frisch, M. J.; Trucks, G. W.; Schlegel, H. B.; Scuseria, G. E.; Robb, M. A.; Cheeseman, J. R.; Montgomery, J. A., Jr.; Vreven, T.; Kudin, K. N.; Burant, J. C.; Millam, J. M.; Iyengar, S. S.; Tomasi, J.; Barone, V.; Mennucci, B.; Cossi, M.; Scalmani, G.; Rega, N.; Petersson, G. A.; Nakatsuji, H.; Hada, M.; Ehara, M.; Toyota, K.; Fukuda, R.; Hasegawa, J.; Ishida, M.; Nakajima, T.; Honda, Y.; Kitao, O.; Nakai, H.; Klene, M.; Li, X.; Knox, J. E.; Hratchian, H. P.; Cross, J. B.; Bakken, V.; Adamo, C.; Jaramillo, J.; Gomperts, R.; Stratmann, R. E.;

Yazyev, O.; Austin, A. J.; Cammi, R.; Pomelli, C.; Ochterski, J. W.; Ayala, P. Y.; Morokuma, K.; Voth, G. A.; Salvador, P.; Dannenberg, J. J.; Zakrzewski, V. G.; Dapprich, S.; Daniels, A. D.; Strain, M. C.; Farkas, O.; Malick, D. K.; Rabuck, A. D.; Raghavachari, K.; Foresman, J. B.; Ortiz, J. V.; Cui, Q.; Baboul, A. G.; Clifford, S.; Cioslowski, J.; Stefanov, B. B.; Liu, G.; Liashenko, A.; Piskorz, P.; Komaromi, I.; Martin, R. L.; Fox, D. J.; Keith, T.; Al-Laham, M. A.; Peng, C. Y.; Nanayakkara, A.; Challacombe, M.; Gill, P. M. W.; Johnson, B.; Chen, W.; Wong, M. W.; Gonzalez, C.; Pople, J. A. *Gaussian 03, revision D.01* (2004) Gaussian, Inc.: Wallingford, CT.

[27] Hay, P. J., Wadt, W. R. **Abinitio effective core potentials for molecular calculations - potentials for K to Au including the outermost core orbitals** *J. Chem. Phys.* 82 (1985) 299-310.

[28] Schwarz, H. **Relativistic effects in gas-phase ion chemistry: An experimentalist's view** *Angew. Chemie – Int. Ed.* 42 (2003) 4442-4454.

[29] Grimme, S., Antony, J., Ehrlich, S., Krieg, H. **A consistent and accurate ab initio parametrization of density functional dispersion correction (DFT-D) for the 94 elements H-Pu** *J. Chem. Phys.* 132 (2010) 154104.

[30] Andrae, D., Häußermann, U., Dolg, M., Stoll, H., Preuß, H. **Energy-adjusted ab initio pseudopotentials for the second and third row transition elements** *Theor. Chim. Acta* 77 (1990) 123–141.

[31] Fukui, K. **Formulation of the reaction coordinate** *J. Phys. Chem.* 74 (1970) 4161–4163.

[32] Gonzalez, C., Schlegel, H.B. **An improved algorithm for reaction path following** *J. Chem. Phys.* 90 (1989) 2154–2161.

[33] Hunter, E.P., Lias, S.G. **Evaluated Gas Phase Basicities and Proton Affinities of Molecules: An Update**. *J. Phys. Chem. Ref. Data* 27 (1998) 413-656.

[34] Gibson, D. **The mechanism of action of platinum anticancer agents—what do we really know about it?** *Dalton Trans.* 48 (2009) 10681.

[35] Hall, M.D., Hambley, T.W. **Platinum (IV) antitumour compounds: their bioinorganic chemistry** *Coord. Chem. Rev.* 232 (2002) 49–67.

[36] Wexselblatt, E., Gibson, D. **What do we know about the reduction of Pt(IV) pro-drugs?** *J. Inorg. Biochem.* 117 (2012) 220-229.

[37] Choi, S., Filotto, C., Bisanzo, M. et al. **Reduction and Anticancer Activity of Platinum(IV) Complexes** *Inorg. Chem.* 37 (1998) 2500-2504.

[38] De Petris, A., Ciavardini, A., Coletti, C., Re, N., Chiavarino, B., Crestoni, M.E., Fornarini, S. **Vibrational signatures of the naked aqua complexes from platinum(II) anticancer drugs** *J. Phys. Chem. Lett.* 4 (2013) 3631-3635.

[39] Zhang, J.Z., Wexselblatt, E., Hambley, T.W., Gibson, D. **Pt(IV) analogs of oxaliplatin that do not follow the expected correlation between electrochemical reduction potential and rate of reduction by ascorbate** *Chem. Comm.* 48 (2012) 847–849.

[40] Gibson, D. **Platinum(IV) anticancer prodrugs – hypotheses and facts** *Dalton Trans.* 45 (2016) 12983–12991.

[41] Dau, P.D., Gibson, J.K., **Halide abstraction from halogenated acetate ligands by actinyls: a competition between bond breaking and bond making** *J. Phys. Chem. A* 119 (2015) 3218–3224.

[42] Van Stipdonk, M.J., Chien, W., Anbalagan, V., Bulleigh, K., Hanna, D., Groenewold, G.S. **Gas-phase complexes containing the uranyl ion and acetone** *J. Phys. Chem. A* 108 (2004) 10448–10457.

[43] Van Stipdonk, M.J., Bubas, A., Tatosian, I., Perez, E., Polonsky, N., Metzler, L., Somogyi, A. **Formation of [UVOF$_4$]$^-$ by collision-induced dissociation of a [UVIO$_2$(O$_2$)(O$_2$C-CF$_3$)$_2$]$^-$ precursor** *Int. J. Mass Spectrom.* 424 (2018) 58–64.

[44] Butschke, B., Schwarz, H. **The "missing link": The gas-phase generation of platinum-methylidyne clusters Pt$_n$CH$^+$ (n=1, 2) and their reactions with hydrocarbons and ammonia** *Chem. A Eur. J.*17 (2011) 11761-11772.

Appendix A: further joint publications

In this section is reported the research work done during the period of my Ph. D. that is not strictly relevant to the main project. It is collected in two already published papers:

- D. Corinti, D. Catone, S. Turchini, F. Rondino, M.E. Crestoni, S. Fornarini
  Photoionization mass spectrometry of ω -phenylalkylamines: Role of radical cation- π interaction
  J. Chem. Phys. 148 (2018). doi:10.1063/1.5027786.

  My personal contribution to the manuscript regarded performing the mass spectrometry and VUV photoionization experiments at the ELETTRA synchrotron with the help of Dr. Daniele Catone and Dr. Flaminia Rondino, as well as performing the IE calculations. I have also prepared the first draft, which was revised by Prof. Simonetta Fornarini.

- D. Corinti, B. Gregori, L. Guidoni, D. Scuderi, T.B. McMahon, B. Chiavarino, S. Fornarini, M.E. Crestoni
  Complexation of halide ions to tyrosine: role of non-covalent interactions evidenced by IRMPD spectroscopy
  Phys. Chem. Chem. Phys. (2018). doi:10.1039/C7CP06657K.

  I have contributed to the research work performing the calculations of minima structures and IR spectra. I was also involved in the OPO/OPA experiments, in the interpretation of the experimental data and in the revision of the draft prepared by Prof. Maria E. Crestoni.

A.1 Photoionization mass spectrometry of ω -phenylalkylamines: Role of radical cation- π interaction

Abstract. Linear ω-phenylalkylamines of increasing alkyl chain length have been investigated employing synchrotron radiation in the photon energy range from 7 to 15 eV. These molecules have received considerable interest because they bear the skeleton of biologically relevant compounds including neurotransmitters and because of the possible interaction between the amino moiety and the phenyl ring. Recently, the contribution of this interaction has been assayed in both neutral and protonated species, pointing to a role of the polymethylene chain length. In this work, the ionization energy (IE) values of benzylamine (BA), 2-phenylethylamine (2-PEA), 3-phenylpropylamine (3-PPA), and 4-phenylbutylamine (4-PBA) were investigated in order to ascertain the impact of the different alkyl chain length and to verify an amino radical cation – π interaction. The IEs obtained experimentally, 8.54, 8.37, 8.29, and 8.31 eV for BA, 2-PEA, 3-PPA and 4-PBA, respectively, show a decreasing trend that is discussed employing calculations at the CBS-QB3 level. Moreover, the appearance energy values for major fragments produced by the photofragmentation process are reported.

A.1.1 Introduction

Phenylalkylamines (PAAs) bearing a phenyl and an amino group on the terminal carbon atoms of a linear (poly)methylene chain ($C_6H_5(CH_2)_nNH_2$, ω-phenylalkylamines) include parent molecules of important families of compounds such as the ethylamino neurotransmitters.[1] Depending on the number of methylene units (n), the end functional groups may be allowed to interact, taking advantage of the flexible character of the linker. The ensuing structural and dynamical properties represent simplified models of interactions occurring in more complex biomolecular systems. In particular, isolated molecular constituents in the gas phase lend themselves to reveal intrinsic factors that affect functionality in biological networks. In this view, several spectroscopic studies have addressed the conformational landscape of gaseous 2-phenylethylamine ($C_6H_5(CH_2)_2NH_2$), the simplest member of aromatic neurotransmitter molecules which include dopamine and amphetamine[2].

2-Phenylethylamine (2-PEA) conformers present either an extended arrangement of the ethylamino ($H_2N(CH_2)_2$-) side chain with the NH_2 group pointing away (*anti*) from the phenyl group or a folded conformation where NH_2 is in a *gauche*-type relation relative to the phenyl ring. The ensuing structures are grouped in Figure 1 including the relative zero point corrected electronic energies as reported at MP2/6-311++G(d,p) level.[3] The two most stable gauche conformers G1 and G2 are stabilized by a NH$\cdots\pi$ interaction which is missing in G3 due to the orientation of the NH bonds away from the phenyl ring. Conformers G1 and G2 have been detected and their shape determined by microwave spectroscopy.[4]

G1 (0)   G2 (1.54)   G3 (7.43)

A1 (4.53)   A2 (4.83)
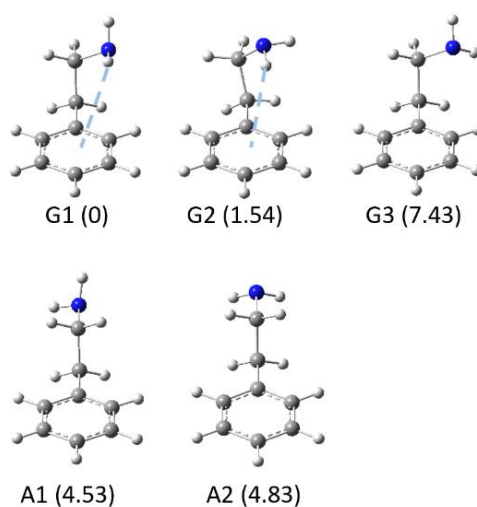
Figure 1. Gauche (G1-G3) and anti (A1, A2) conformers of 2-phenylethylamine (2-PEA).[3] Relative energies (in kJ mol^{-1}) are calculated at MP2/6-311++G(d,p) level and include zero point correction.[3]

The rotational spectra of both G1/G2 and A1/A2 have been recorded using molecular beam Fourier transform microwave spectroscopy while G3 is not sampled in the supersonic expansion, likely due to selective collisional relaxation of this species to G1.[3] Previous studies on the conformation and electronic spectroscopy of PEA and more recent work using ab initio calculations, fluorescence spectroscopy and mass spectrometry are consistent with these results.[5-9] Also ionization loss Raman spectra combined with quantum chemical calculations have confirmed the presence of four conformers.[10,11]

When the basic amino group of 2-PEA is protonated, the interaction between the so-formed alkylammonium ion and the phenyl ring becomes a significant

contribution to the relative stability of the possible conformational structures. The folded conformer allowing the $NH^+\cdots\pi$ interaction is found to be ca. 20 kJ mol^{-1} lower in energy relative to the extended anti conformation, according to ab initio calculations at the ωB97X-D/6-311++G(d,p) level.[12] The theoretical results are consistent with a thorough assay of protonated PEA ions as isolated gaseous species, based on IR multiple photon dissociation (IRMPD) spectroscopy. In particular, a distinct vibrational signature at 3143 cm^{-1} is reported to characterize the stretching mode of the NH bond involved in the π interaction, significantly red-shifted with respect to the 'free' NH stretching modes at 3307 and 3351 cm^{-1}.[12] IRPD spectroscopy and rare gas tagging of cold ions have also been exploited to reveal geometric and vibrational properties of protonated 2-PEA and related neurotransmitters.[1,13,14] The amino acid phenylalanine is a molecule closely related to 2-PEA, bearing an additional carboxylic group ($-CO_2H$) on the amino-substituted carbon. Not surprisingly, protonated phenylalanine shows clear evidence of cation-π interaction between the protonated amino group and the aromatic ring as shown by the vibrational signatures of the naked species.[15-17]

Whereas cation-π interactions are widely documented non-covalent forces, the open shell version, namely radical cation-π ($RC^{\bullet+}$-π) interactions, has received much less consideration.[18-20] Energetic and geometric characteristics of $C^{\bullet+}$-π interactions have been described using computational tools. The $RC^{\bullet+}$-π interaction has resulted to be energetically more favorable than the cation-π interaction and the spin density found to reside basically on the aromatic ring. The interaction energy of the benzene·$NH_3^{\bullet+}$ complex is calculated at 85 kJ mol^{-1}, corresponding to a structure where the N atom is centered above the aromatic ring and the three hydrogen atoms point away from the ring. In this geometry a significant extent of electron transfer has taken place as shown by orbitalic and spin density analyses.[18]

In this contribution photoionization mass spectrometry in the VUV region is performed on ω-phenylalkylamines, $C_6H_5(CH_2)_nNH_2$ with n varying from one to four (Scheme 1). The interest placed in this family of molecules resides in their differing flexibility and in the potential approach of the phenyl and amino group which may be expected to affect their properties. Previous studies combining an experimental

and theoretical survey of appearance energies have provided valuable information on specific effects due to varying structures.[21] A similar approach, based on a VUV synchrotron beamline, is pursued in the present contribution.

	n	Species
NH$_2$	1	benzylamine
(CH$_2$)$_n$	2	2-phenylethylamine
	3	3-phenylpropylamine
	4	4-phenylbutylamine
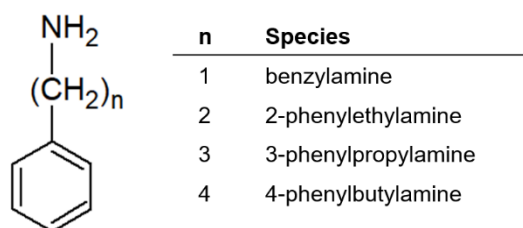
Scheme 1. Schematic representation of the sampled ω-phenylalkylamines.

A.1.2 Methods

VUV photodissociation experiments

Benzylamine (BA), 2-phenylethylamine (2-PEA), 3-phenylpropylamine (3-PPA), and 4-phenylbutylamine (4-PBA), collectively shown in Scheme 1, are commercial products. The pure substances are liquid at room temperature and were purified by repeated evaporation/condensation cycles. They were placed in a test tube connected to the gas line of the vacuum chamber and admitted in the chamber in vapor phase through a needle. The experiments were performed at the "Circular Polarization" (CiPo) beamline 4.2 at the Elettra synchrotron facility (Trieste, Italy).[22] The energy of the synchrotron radiation was selected by an aluminium normal incidence monochromator (NIM) that covers the photon energy range 5–17 eV with a resolving power of about 1000. The setup of the chamber consists of five electrostatic lenses that focus and accelerate the ions from the region of interaction to the quadrupole mass spectrometer (10-4000 u, Extrel 150-QC 0.88 MHz), mounted perpendicular to the photon beam and to the effusive gas beam. A detailed overview of the instrumental apparatus is reported in previous works.[21,23] Photoionization efficiency curves (PECs) for the selected ions were obtained from 7 to 15 eV of photon energy scanned in steps of 20 meV with an acquisition time of about 1 to 5 s/point, depending on the intensity of the assayed ion. Photon fluency was measured during each run employing a photo-diode in order to normalize the PECs. To inspect the region up to 11.7 eV a lithium fluoride filter was used, thus

removing the second order contribution of NIM. Above this threshold, the influence of second order radiation was evaluated through the analysis of the argon atom photoionization efficiency curve. Being the ionization energy of Ar 15.76 eV,[24] in fact, we can directly obtain the trend of second order radiation generated from the first order in the 11.7 – 15.6 eV range monitoring the intensity of the generated Ar^+ ions. Subsequently, these data have been used to correct the PEC of the fragment ions in order to obtain their appearance energy (AE) values. In addition, mass spectra of the selected species were recorded at 15 eV of photon energy.

Computational methods

The set of neutral ω-phenylalkylamines conformers presented in the forthcoming sections was chosen following a computational procedure which involves progressive steps of optimization, and subsequent selection of the lowest lying conformers while increasing the accuracy of the computational method. A preliminary exploration of the ω-phenylalkylamines conformer population was performed using the conformer distribution tool as implemented in the Spartan'16 suite, employing molecular mechanics as computational method.[25]

With regard to 2-PEA we also relied for the selection of the guess geometries on the work by Alonso et al. in which the authors analyze the 2-PEA conformers by theoretical calculations and microwave spectroscopy.[3] Subsequently, the selected geometries were optimized at the B3LYP/6-31+G* level of theory using Gaussian09 Rev. D01.[26] Vibrational modes were computed at the same level of theory to confirm the stationary states found as local minima. The lowest lying conformers of neutral ω-phenylalkylamines together with structures at higher energy, but representative of peculiar structural motifs, were treated with the CBS-QB3 composite method.[27] It includes a preliminary optimization at the B3LYP/6-311G(2d,d,p) level followed by a series of single point calculations involving post-Hartree-Fock methods. Furthermore, the neutral geometries were used as starting point to obtain the corresponding radical cations of BA, 2-PEA, 3-PPA and 4-PBA. The restricted open-shell version of CBS-QB3 (ROCBS-QB3) was used for the radical cations in order to avoid the influence of spin-contamination.[28] Finally to obtain the vertical IEs of the neutral conformers previously sampled, the ROCBS-QB3 method

was employed without geometry optimization of the neutral geometries, imposing positive charge and doublet electronic state. From now on, for the sake of simplicity, we will uniformly use the denomination CBS-QB3 for both the restricted and restricted open versions of the method.

A.1.3 Results and discussion

VUV photodissociation of ω-phenylalkylamines

The selected ω-phenylalkylamines were ionized by VUV radiation with an energy ranging from 7 to 15 eV, leading to the respective radical cations and fragment ions. Figure 2 shows the PEC for the ionization of 2-PEA, (2-PEA$^{+\bullet}$), as a function of the photon energy, together with zoomed data in semilogarithmic scale reported in the inset.
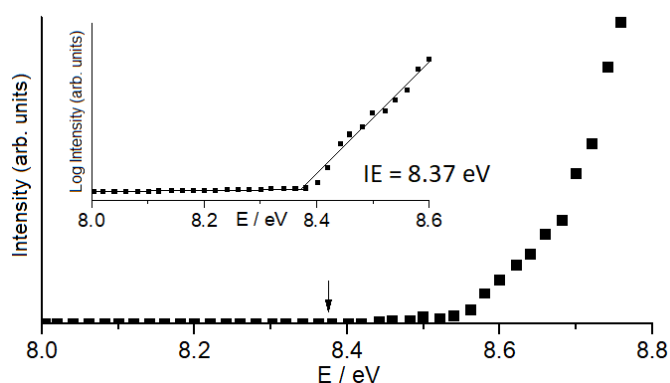
Figure 2. PEC of 2-PEA$^{+\bullet}$ at *m/z* 121. The inset reports an expansion of the threshold region in semi-logarithmic scale. The IE value is determined by the intersection between the lines fitting the background and the rising ion signal in the threshold region. The measured IE value is indicated by an arrow.

The IE value is obtained from the intersection point of the linear fitting of the PEC in the threshold region with the background signal, as reported in previous papers.[22,29] A conservative estimate of ± 0.05 eV error range is associated to the experimental determinations, mainly reflecting the bandwidth of the monochromator and the uncertainty of the ionization threshold as determined from the PEC. Thus, the IE of 2-PEA is obtained as 8.37 ± 0.05 eV. The same procedure was employed to evaluate the IEs of the other ω-phenylalkylamines, yielding values of 8.54 ± 0.05 eV, 8.29 ± 0.05 eV and 8.31 ± 0.05 eV for BA, 3-PPA, and 4-PBA, respectively. The

corresponding PECs are reported in Figure S1 in the Supporting Material (SM). The consistency of the employed procedure is validated by the good agreement of the IE of BA obtained in this work with the value of 8.58 eV obtained by Xie et al.[29] using similar experimental conditions.

Increasing the photon energy above the IE, the formation of the radical cation is accompanied by extensive fragmentation. Figure 3 shows the mass spectra of BA, 2-PEA, 3-PPA and 4-PBA acquired at 15 eV and Figure S2 displays the PECs of the most abundant fragments. A more detailed discussion of the observed fragmentation paths is reported in the following paragraphs.
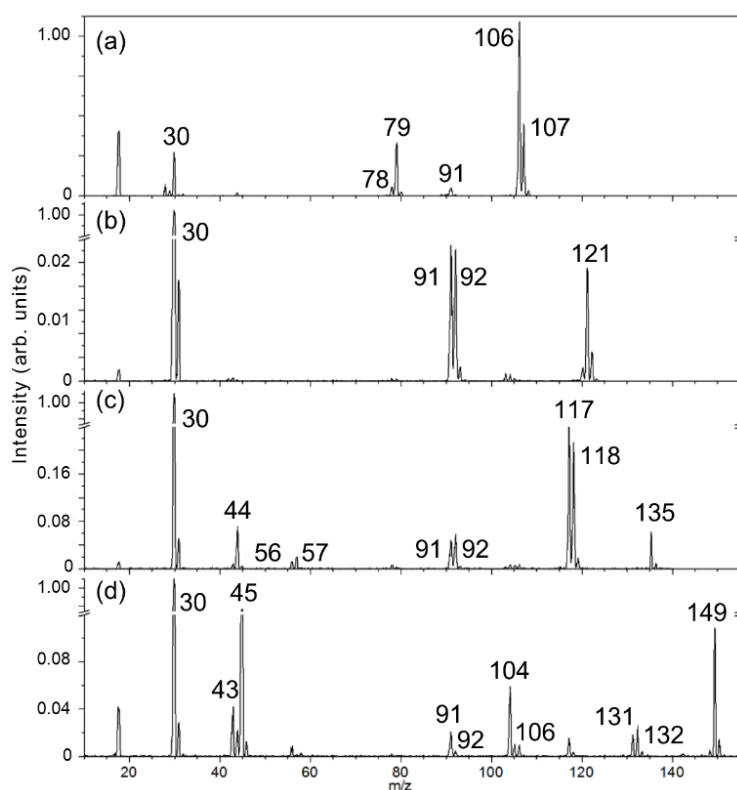
Figure 3. Mass spectra of (a) BA (molecular ion at *m/z* 107), (b) 2-PEA (*m/z* 121), (c) 3-PPA (*m/z* 135) and (d) 4-PBA (*m/z* 149) acquired at 15 eV photon energy. The break in the y-axis is meant to emphasize the lesser intense signals.

Benzylamine

In panel a) of Figure 3 the mass spectrum of BA acquired at 15 eV of photon energy is reported. The most abundant fragment is the ion at *m/z* 106, formed by loss of a hydrogen atom from the molecular radical cation. Other important fragmentation products are the ions at *m/z* 91, *m/z* 79, *m/z* 78 and *m/z* 30. The signal at *m/z* 17

corresponds to the radical cation of ammonia that is present as a contaminant in the sample, as confirmed comparing the AE of the ion with the IE of ammonia reported in the literature (10.07 ± 0.01 eV).[30] The fragmentation pattern of BA was previously described by Witting et al. using a variety of ionization/activation techniques, including electron ionization (EI), IR multiple photon absorption and UV multiphoton absorption.[31] Intriguingly, significant alterations in the fragmentation pattern of the ions generated by the three different techniques are reported. These dissimilarities are suggested to arise from the different kinetics of the three heating processes. A major difference lies in the absence of the fragment at m/z 30 in the mass spectrum obtained by IR multiple photon absorption, which is instead present in the EI spectrum at 23 and 50 eV. The observation of a significant abundance of the fragment at m/z 30 in the mass spectrum reported in Figure 3a, suggests that the photo-absorption process in the present experimental setup is comparable with EI, as far as the pattern of fragment ions is concerned. This behavior has been explained by the different activation regime. IRMPD, a 'slow' activation process, leads selectively to the lowest energy fragmentation products. In contrast, UV multiphoton absorption drives higher energy paths such as hydrogen atom loss, whose occurrence precludes the formation of the m/z 30 ion. The AEs of the assayed fragments together with the formal attribution and the corresponding neutral loss are reported in Table 1. The AE of the m/z 106 fragment observed at 9.05 ± 0.05 eV is in fair agreement with the value of 9.14 eV reported in literature.[29]

2-Phenylethylamine

The mass spectrum of 2-PEA, reported in Figure 3b, shows relatively few fragments and is dominated by the ion at m/z 30 that has by far the highest intensity. The AE of the ion at m/z 30 (8.63 eV ± 0.05 eV), formally $CH_2=NH_2^+$, is also remarkable, being the lowest among all the fragments and just 0.26 eV higher than the IE of 2-PEA. The other two signals at m/z 92 ($C_7H_8^{+\bullet}$) and m/z 91 ($C_7H_7^+$) present AEs at 9.58 ± 0.05 eV and 11.77 ± 0.05 eV, respectively. The fragment at m/z 91 is likely to arise from hydrogen atom loss from the ion at m/z 92 rather than ensue by a direct C-C bond cleavage. In fact, in the latter case the formation of the $CH_2NH_2^+$ cation is

expected to be highly favored, on considering that the relative IEs of the $C_6H_5CH_2^{\cdot}$ and $NH_2CH_2^{\cdot}$ radicals are 7.24 eV and 6.29 eV, respectively.[32,33]

Table 1. Appearance energies of BA, 2-PEA, 3-PPA and 4-PBA product ions. Ion and neutral formulas are reported.

Benzylamine (*m/z* 107)

m/z	AE (eV)[a]	Neutral loss	Product ion composition
106	9.05	H	C_7H_8N
91	11.28	NH_2	C_7H_7
79	11.66	CH_2N	C_6H_7
78	10.58	CH_3N	C_6H_6
30	10.22	C_6H_5	CH_4N

2-Phenylethylamine (*m/z* 121)

m/z	AE (eV)	Neutral loss	Product ion composition
92	9.58	CH_3N	C_7H_8
91	11.77	CH_4N	C_7H_7
30	8.63	C_7H_7	CH_4N

3-Phenylpropylamine (*m/z* 135)

m/z	AE (eV)	Neutral loss	Product ion composition
118	8.63	NH_3	C_9H_{10}
117	10.62	NH_4	C_9H_9
92	10.59	C_2H_5N	C_7H_8
91	11.78	C_2H_6N	C_7H_7
57	9.34	C_6H_6	C_3H_7N
56	11.17	C_6H_7	C_3H_6N
44	8.85	C_7H_7	C_2H_6N
30	8.91	C_8H_9	CH_4N

4-Phenylbuthylamine (*m/z* 149)

m/z	AE (eV)	Neutral loss	Product ion composition
132	8.64	NH_3	$C_{10}H_{12}$
131	10.73	NH_4	$C_{10}H_{11}$
106	8.67	C_2H_5N	C_8H_{10}
104	9.11	C_2H_7N	C_8H_8
92	10.75	C_3H_7N	C_7H_8
91	10.92	C_3H_8N	C_7H_7
45	8.83	C_8H_8	C_2H_7N
43	9.38	C_8H_{10}	C_2H_5N
30	9.00	C_9H_{11}	CH_4N

[a] A conservative estimate of ± 0.05 eV error range is associated to the experimental determinations.

3-Phenyl-propylamine

The mass spectrum of 3-PPA reported in Figure 3c presents a rich fragmentation pattern when compared to the mass spectra of the lighter ω-phenylalkylamines, though sharing some features in common. In particular, the presence of the most abundant fragment at *m/z* 30 has to be highlighted. Also fragment ions at *m/z* 91

and 92 are observed. Compared to the AE of $CH_2NH_2^+$ from 2-PEA, 3-PPA presents a higher AE for the same ion, namely at 8.91 ± 0.05 eV, as reported in Table 1. The fragment ions at *m/z* 92 and 91 present AEs of 10.59 ± 0.05 eV and 11.78 ± 0.05 eV, respectively. Once again, the lower AE of the *m/z* 92 ion with respect to the one at *m/z* 91 is confirmed, which may be compatible with a consecutive dissociation linking the two species. As a novel feature, it is now observed a fragment ion arising from the loss of ammonia at *m/z* 118, characterized by an AE value of 8.63 ± 0.05 eV. This dissociation channel is followed by the loss of a hydrogen atom generating the fragment at *m/z* 117 with an AE of 10.52 ± 0.05 eV. There are also lighter fragmentation products, in particular the ions at *m/z* 44, 56 and 57 presenting an AE of 8.85 ± 0.05 eV, 11.17 ± 0.05 eV and 9.34 ± 0.05 eV, respectively. These species arise from C-C bond cleavages occurring at different sections in the alkyl chain with the charge retained by the amino containing moiety ($C_2H_6N^+$, $C_3H_6N^+$ and $C_3H_7N^{+\bullet}$, respectively).

4-phenyl-butylamine

The dissociation pattern of 4-PBA at 15 eV presents similarities with 3-PPA as reported in Figure 3d and Table 1. The predominance of the fragment at *m/z* 30 is confirmed. The reported AE of 9.00 eV for the ion at *m/z* 30 suggests a fragmentation process of similar energy requirements as the one occurring from the 3-PPA radical cation. In fact, the excess energy required to form $CH_2NH_2^+$ from the molecular ion of 3-PPA and 4-PBA is almost the same, being 0.62 eV and 0.69 eV (namely the difference between IE and AE values reported in Table 1), respectively. The fragmentation products related to $C_7H_8^{+\bullet}$ (*m/z* 92) and $C_7H_7^+$ (*m/z* 91) are also present and are characterized by AEs of 10.75 ± 0.05 eV and 10.92 ± 0.05 eV, respectively.

As discussed in the previous paragraph, it is interesting to note that the loss of ammonia is the dissociation channel presenting the lowest AE, i.e. 8.66 ± 0.05 eV. It generates the fragment at *m/z* 132 and, as observed in the 3-PPA sample, the ion at *m/z* 132 loses a hydrogen atom yielding an ion at *m/z* 131 with an AE of 10.73 ± 0.05 eV. The mass spectrum of 4-PBA also includes fragment ions at *m/z* 45, 43, 106 and 104. Among these ones, the ion at *m/z* 45, formally $C_2H_7N^{+\bullet}$, is the second most

intense signal of the spectrum and presents an AE of 8.83 ± 0.05 eV. A subsequent loss of H_2 could be related to the signal at *m/z* 43 in agreement with the slightly higher AE of this ion (9.38 ± 0.05 eV). The same process seems to govern the behavior of the ion at *m/z* 106, formally $C_8H_{10}^{+\bullet}$, presenting an AE of 8.66 ± 0.05 eV. In fact, the related species at *m/z* 104 is consistent with H_2 loss from $C_8H_{10}^{+\bullet}$, linked to the higher AE of 9.11 ± 0.05 eV. This interpretation is supported comparing the difference between the AEs of the ions at *m/z* 45 and *m/z* 106, and the ones of the dehydrogenated species at *m/z* 43 and *m/z* 104, that are 0.55 eV and 0.45 eV, respectively.

Theoretical investigation of neutral and cationic species

The observed IEs show a decreasing trend ranging from 8.54 ± 0.05 eV for BA to 8.29 ± 0.05 eV for 3-PPA. This last value is just about equal to the IE of 4-PBA at 8.31 ± 0.05 eV while the IE of 2-PEA is placed in between, at 8.37 ± 0.05 eV. The reported differences are not negligible considering the similar structure of the ω-phenylalkylamines examined. Therefore, theoretical calculations were performed at the CBS-QB3 level to aid in the interpretation of the experimental data. The sampled ω-phenylalkylamines may present several rotational conformers that can be gathered in two main groups. As already described in the introduction with regard to 2-PEA,[3] the conformation of the alkyl chain allows to discriminate between two families. In fact, the dihedral angle linking the amino nitrogen, the two methylene carbon atoms and the ipso carbon of the phenyl group permits to distinguish between a *gauche*-conformation, allowing NH_2 to lean towards the aromatic ring, and an *anti*-conformation, where the amino group is far from the phenyl group.[3] The same argument can be applied to 3-PPA and 4-PBA. In these cases, the longer alkyl chain does not allow to select a single dihedral angle distinguishing two families, but one may still compare either elongated or compact conformers, where the amino-phenyl proximity is verified only in the latter ones. In the cited work[3] the four experimentally observed conformers of 2-PEA lie within an energy range of 4.9 kJ mol^{-1} and the most stable species is the *gauche* one with the amino hydrogen directed towards the phenyl group (namely G1 in Figure 1), as also

confirmed by the presently adopted computational method. Calculations run on the other neutral species (BA, 3-PPA and 4-PBA) confirm that the conformational changes have a relatively small impact on the relative energies, leading to an utmost span of 5.2 kJ mol^{-1}. Optimized geometries of representative conformers for the sampled ω-phenylalkylamines are displayed in Figure 4. Geometries depicting the same compound are grouped together and ordered according to their increasing ZPE corrected electronic energy. Thus, for example, G1 and A1 conformers of 2-PEA (Figure 1)[3] are named here **PEA1** and **PEA2**, respectively. Concerning 3-PPA and 4-PBA, it is interesting to note that the lowest lying conformers do not present the amino group oriented towards the ring. Apparently, the small energetic profit gained from the amino hydrogen-π interaction is not enough to outweigh the destabilization due to the associated unfavourable arrangement (tending to eclipsed configurations) of the methylene units. Thermodynamic data for the whole set of optimized structures shown in Figure 4 are summarized in Table 2.

A set of representative structures for the radical cations of the selected PPAs is reported in Figure 4. In order to directly relate each neutral conformer with the radical cation presumably formed in the photoionization transition, ionized species are optimized from the starting neutral geometry once an electron has been removed and the so-obtained structures are presented one below the other, so maintaining their linked origin. The progressive numbering of radical cation structures once again reflects an increasing energy ordering. The conformers of PAA radical cations displayed in Figure 4 comprise geometries presenting an either elongated or compact structure. Here, the energy spread is distinctly wider within each conformational landscape. In fact, there are large differences in energy between the two families of conformers described above, particularly evident in the cases of 3-PPA and 4-PBA.
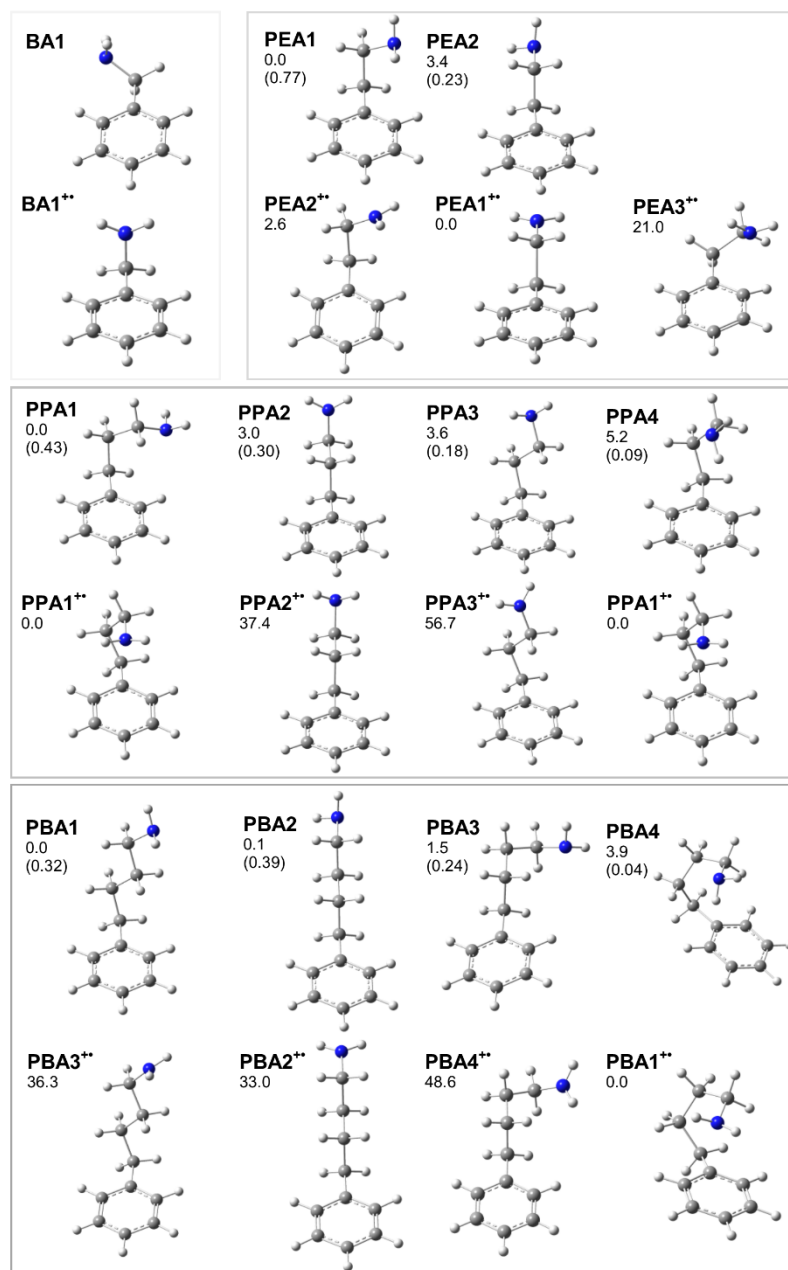
Figure 4. Geometries of the representative species calculated at the CBS-QB3 level of theory. Relative ZPE corrected electronic energies for neutral and cationic species are reported in kJ mol^{-1} and are referred to the most stable conformer within each set. Progressive numbering within each set goes in parallel with increasing energy. In parentheses are reported the Boltzmann population fractions of the neutral species, calculated from relative free energies at 298K, expected for thermal equilibration of the conformers at the temperature of the experiment.

Table 2. Thermodynamic data calculated at the CBS-QB3 level for neutral and ionized PAA conformers.

	EE[a]	EE$_{rel}$[b]	H$_{rel}$(298K)[b]	G$_{rel}$(298K)[b]
BA1	-326.278871	0.0	0.0	0.0
BA1$^+$	-325.966463	819.6	820.2	818.1
PEA1	-365.514541	0.0	0.0	0.0
PEA2	-365.513231	3.4	3.7	3.1
PEA1$^{+\bullet}$	-365.206997	807.5	808.5	805.6
PEA2$^{+\bullet}$	-365.206005	810.1	811.2	808.2
PEA3$^{+\bullet}$	-365.198984	828.5	828.3	828.8
PPA1	-404.739967	0.0	0.0	0.0
PPA2	-404.738827	3.0	3.6	1.1
PPA3	-404.738602	3.6	3.9	2.6
PPA4	-404.737994	5.2	5.4	4.6
PPA1$^{+\bullet}$	-404.446121	771.5	771.2	772.6
PPA2$^{+\bullet}$	-404.431858	808.9	810.5	805.9
PPA3$^{+\bullet}$	-404.424505	828.2	829.9	824.6
PBA1	-443.964955	0.0	0.0	0.0
PBA2	-443.964921	0.1	0.5	-0.6
PBA3	-443.964384	1.5	1.4	0.9
PBA4	-443.963452	3.9	3.4	6.5
PBA1$^{+\bullet}$	-443.666573	783.4	782.3	788.0
PBA2$^{+\bullet}$	-443.653994	816.4	817.9	814.1
PBA3$^{+\bullet}$	-443.652737	819.7	821.0	817.7
PBA4$^{+\bullet}$	-443.648046	832.0	833.8	827.7

[a] Electronic energies (in Hartree) are ZPE corrected. [b] In kJ mol^{-1}.

Moving from the neutral species to the radical cation, calculations show a distinct geometry change involving the NH_2 group. As already reported in the literature, when the amino group is devoid of an electron, it switches from tetrahedral to trigonal planar geometry.[8,34] This change clearly exhibits the site of the charge in the radical cations, mainly localized on the amino moiety in about any conformer. The calculated thermodynamic data clearly show that the presence of the amino group-π interaction in the case of radical cations strongly stabilizes the more folded

258

structures of **PPA2$^{+\bullet}$** and **PBA2$^{+\bullet}$** with respect to **PPA1$^{+\bullet}$** and **PBA1$^{+\bullet}$**, by ca. 35 kJ mol^{-1}, according to the adopted computational method. The interaction involves the nitrogen atom of the amino group and the phenyl ring in a quite similar fashion as reported by the theoretical work by Deyà et al.[18] concerning the interaction between ionized ammonia and benzene. No effect is instead observed in the case of 2-PEA. In fact, the *gauche* structure **PEA2$^{+\bullet}$** is slightly less stable than the *anti* one (**PEA1$^{+\bullet}$**), as already described by Metsala et al.[8] Any interaction between the ionized amino group and the ring is missing here, probably due to the geometric constraint imposed by the shorter length of the alkyl chain, which prevents an appropriate relationship between the two groups. A third optimized structure, **PEA3$^{+\bullet}$**, where the amino group is directed towards the ring, presents peculiar structural features when compared to **PEA1$^{+\bullet}$** and **PEA2$^{+\bullet}$**. The NH$_2$ group is, in fact, almost tetrahedral suggesting an important charge transfer from the amino to the phenyl group. This species is 21 kJ mol^{-1} less stable than **PEA1$^{+\bullet}$** at CBS-QB3 level. The tetrahedral geometry at the alkylamino nitrogen placed 2.58 Å above an ortho ring carbon is rather reminiscent of the NH$_3$ − ionized benzene adduct, rather complying to covalent bond formation as evidenced by an analysis of vibrational features.[35-36] It is worthwhile noting that the difference in energy between conformers **PEA1$^{+\bullet}$** and **PEA3$^{+\bullet}$** cannot be explained solely by the stabilization given by the methylene units in the *anti*-conformation. In fact, the *gauche* conformer **PEA2$^{+\bullet}$**, where the amino group is not interacting with the ring, is just 2.6 kJ mol^{-1} higher in energy. The extensive computational exploration of radical cations interacting with aromatic rings by Deyà et al.[18] has shown an important electron transfer from the amino group to the π-system when radical cations interact with benzene. This phenomenon is likely playing a role also in the present systems. We analyzed the singly occupied molecular orbital (SOMO) and the spin density of the PAA radical cations in order to ascertain the extent of electron transfer to the amino group from the ring. The SOMO and spin density isosurfaces are reported respectively in Figure 5 and Figure S3 of the SM, the second one being in perfect agreement with the former. From the orbitalic point of view, the interaction of the amino radical cation with the aryl group results in a significant electron transfer,

particularly in the compact conformers of ionized 3-PPA and 4-PBA. When the amino group is far from the aryl, instead, different behaviors are found depending on the number of methylene units in the selected PPA. Specifically, in the radical cations of 2-PEA and 3-PPA a certain delocalization of the SOMO on the aryl group is evidenced, even when the methylene groups are in all *anti*-arrangement. This effect stabilizes **PEA1**$^{+\bullet}$, **PEA2**$^{+\bullet}$ and **PPA2**$^{+\bullet}$ conformers and can partly contribute to the peculiar behavior of 2-PEA. In fact, while conformer **PEA1**$^{+\bullet}$ presents the methylene units in the favored *anti*-conformation and the SOMO somewhat delocalized on the aryl group, **PEA3**$^{+\bullet}$ shows eclipsed CH$_2$ groups and electron transfer to the amino radical cation from the benzene orbital, underlying the peculiar interaction between the amino nitrogen and the ortho ring carbon holding a major fraction of spin density. Comparing **PPA2**$^{+\bullet}$ and **PPA3**$^{+\bullet}$ is also interesting. The former conformer is, in fact, more stable by ca. 20 kJ mol^{-1} probably due to the contribution of the delocalized SOMO.[18] In the species with the longest alkyl chain (4-PBA), instead, there is almost no contribution to the stabilization of the molecular radical cation due to spin delocalization. In fact, the difference in energy between **PBA2**$^{+\bullet}$ and **PBA3**$^{+\bullet}$ is only 3 kJ mol^{-1}.
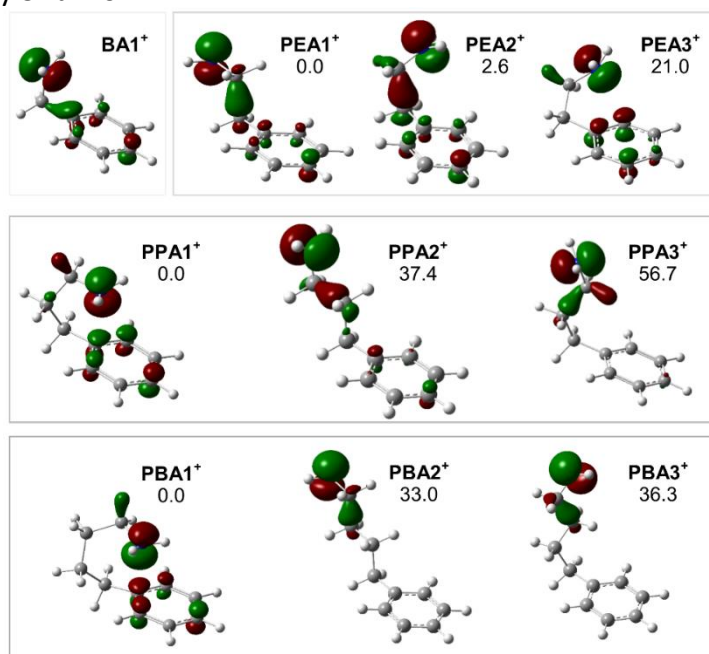

Figure 5. Singly occupied molecular orbitals computed for representative radical cations of the assayed PAAs are plotted using an isovalue of 0.08. Relative ZPE corrected electronic energies calculated at the CBS-QB3 level are reported in kJ mol^{-1}.

Computed versus experimental ionization energies

Insight into the information attached to the experimental IE values should rely on a survey of the photoionization transitions at play. We calculated for each conformer (their Boltzmann weighted fractions are reported in Figure 4 in parentheses) the corresponding vertical ionization energy, assuming the Frank Condon approximation.[37-40] The energy of the radical cation was then calculated at the neutral geometry. These vertical IEs are reported in Table 3. The agreement with the experimental IEs is meager though. The values are in fact leveled around an average value of ca. 8.90 eV, hardly displaying any trend with respect to variation in structure along the PPA series. Moreover the values of vertical IE are always higher with respect to the experimental data. This difference is absolutely reasonable since we expect that the experimental IEs will be closer to the theoretical adiabatic values than to the vertical ones.[21] Table 3 reports the adiabatic IEs representing the energy difference between each neutral conformer and the corresponding optimized radical cation, whose geometries are depicted in Figure 4. The adiabatic IEs afford, as reported in previous works,[41-43] a more consistent matching with the experimental IEs, also reported in Table 3. Thus, the experimental value of 8.54 ± 0.05 eV for BA is well accounted for by the theoretical IE of 8.50 eV for the **BA1 → BA1$^{+\bullet}$** transition. In the case of 2-PEA the experimental IE of 8.37 ± 0.05 eV is in good agreement with the calculated values of 8.39 and 8.33 eV for the **PEA1 → PEA2$^{+\bullet}$** and for the **PEA2 → PEA1$^{+\bullet}$** transition, respectively. Both **PEA1** and **PEA2** are well represented conformers and the corresponding optimized radical cation structures involve relatively minor structural adjustments. For 3-PPA, the ionization of the most stable conformer, **PPA1 → PPA1$^{+\bullet}$**, at 8.00 eV does not appear to contribute appreciably to the experimental value of 8.29 ± 0.05 eV. The reason is likely due to the considerable structural reorganization which accompanies leaning of the NH$_2$ group over the π-system, thus hampering the transition probability. Similarly, the **PPA4 → PPA1$^{+\bullet}$** transition at 7.94 eV suffers from a relatively minor frequency of the neutral conformer in the thermal population. The experimental value is instead rather well matched by the **PPA2 → PPA2$^{+\bullet}$** and **PPA3 → PPA3$^{+\bullet}$** transitions at 8.35 and 8.55 eV, respectively, both of them involving well

represented conformers in the thermal population and requiring very minor structural rearrangement. In particular, the **PPA2** → **PPA2$^{+\bullet}$** transition, delivering a radical cation with a largely delocalized SOMO embracing the π system, nicely accounts for the experimental value.

The 4-PBA case is another example where the lowest energy transition **PBA4** → **PBA1$^{+\bullet}$** at 8.08 eV does not agree with the experimental IE of 8.31 ± 0.05 eV. This finding may be justified by the low abundance of **PBA4** in the conformer mixture. However, none of the alternative transitions presented in Table 3, namely **PBA2** → **PBA2$^{+\cdot}$** at 8.46 eV, **PBA1** → **PBA3$^{+\cdot}$** at 8.50 eV, and **PBA3** → **PBA4$^{+\cdot}$** at 8.61 eV, can be reasonably discarded, all neutral conformers being well populated and turning into radical cations with only minor structural adjustments.

Table 3. Calculated zero point corrected IEs at the CBS-QB3 level of selected conformers of ω-phenylalkylamines, obtained comparing the energies of the neutral and radical cationic species. Experimentally determined IEs are also reported. All the energies are in eV.

Species	Experimental IE	Neutral	Radical	Vertical IE	Adiabatic IE
BA	8.54±0.05[a]	**BA1**	**BA1$^{+\bullet}$**	8.95	8.50
2-PEA	8.37±0.05[b]	**PEA1**	**PEA2$^{+\bullet}$**	8.98	8.39
		PEA2	**PEA1$^{+\bullet}$**	8.99	8.33
3-PPA	8.29±0.05[c]	**PPA1**	**PPA1$^{+\bullet}$**	8.80	8.00
		PPA2	**PPA2$^{+\bullet}$**	8.92	8.35
		PPA3	**PPA3$^{+\bullet}$**	8.95	8.55
		PPA4	**PPA1$^{+\bullet}$**	8.94	7.94
4-PBA	8.31±0.05	**PBA1**	**PBA3$^{+\bullet}$**	8.85	8.50
		PBA2	**PBA2$^{+\bullet}$**	8.93	8.46
		PBA3	**PBA4$^{+\bullet}$**	8.75	8.61
		PBA4	**PBA1$^{+\bullet}$**	8.95	8.08

[a] IE values previously reported in literature include 8.49±0.06 eV using EI[44] and 8.8 eV by photo-electron spectroscopy (PE)[45]. [b] An IE value of 8.5 eV is reported employing PE[46]. [c] An IE value of 8.89±0.12 eV is reported from PE measurement[46].

A.1.4 Conclusions

Photoionization and photofragmentation energies of four linear ω-phenylalkylamines of increasing alkyl chain length were explored in the VUV region. The resulting IE values are 8.54 eV, 8.37 eV, 8.29 eV and 8.31 eV for BA, 2-PEA, 3-PPA and 4-PBA, respectively. Theoretical calculations run at the CBS-QB3 level allowed to gain insight into the progressive reduction of IE values moving from BA to 3-PPA and 4-PBA. In particular, the computational survey has provided a detailed description on both orbitalic aspects and geometric features regarding the radical cation conformers with the most appropriate geometry revealing radical cation – π interaction. The higher members of the PPA series, 3-PPA and 4-PBA, display a significant role of the radical cation-π interaction in affecting the stability of the folded conformers **PPA1$^{+\bullet}$** and **PBA1$^{+\bullet}$**. However, this interaction, lowering the relative energy of the radical cation, requires a significant extent of structural rearrangement when the starting geometry corresponds to the thermally populated precursor neutral conformer, hampering both **PPA1$^{+\bullet}$** and **PBA1$^{+\bullet}$** to be in fact sampled with the adopted VUV photoionization mass spectrometry experiment.

The mass spectra of the selected phenylalkylamines were also acquired at a photon energy of 15 eV and the AEs of the most important fragments obtained from the PECs are reported. The dissociation channel that leads to the formation of the $CH_2=NH_2^+$ fragment is by far the dominant path for all PAAs with the exception of BA for which hydrogen atom loss is largely prevailing.

Given the ubiquitous presence of the PAA scaffold in a variety of biomolecules, notably in the arylethylamino neurotransmitters, the present results may be relevant in understanding and predicting properties of these units in biological environments.

Figure S1. Photoionization efficiency curve (PEC) of A) $BA^{+\cdot}$, B) $3\text{-}PPA^{+\cdot}$ and C) $4\text{-}PBA^{+\cdot}$.

Figure S2. Photoionization efficiency curves for the parent ion and most intense fragments of a) benzylamine, b) 2-phenylethylamine, c) 3-phenylpropylamine, d) 4-phenylbuthylamine.

Figure S3. Spin density computed for representative radical cations of the assayed PAAs is plotted using an isovalue of 0.007. Relative ZPE corrected electronic energies calculated at the CBS-QB3 level are reported in kJ mol^{-1}.
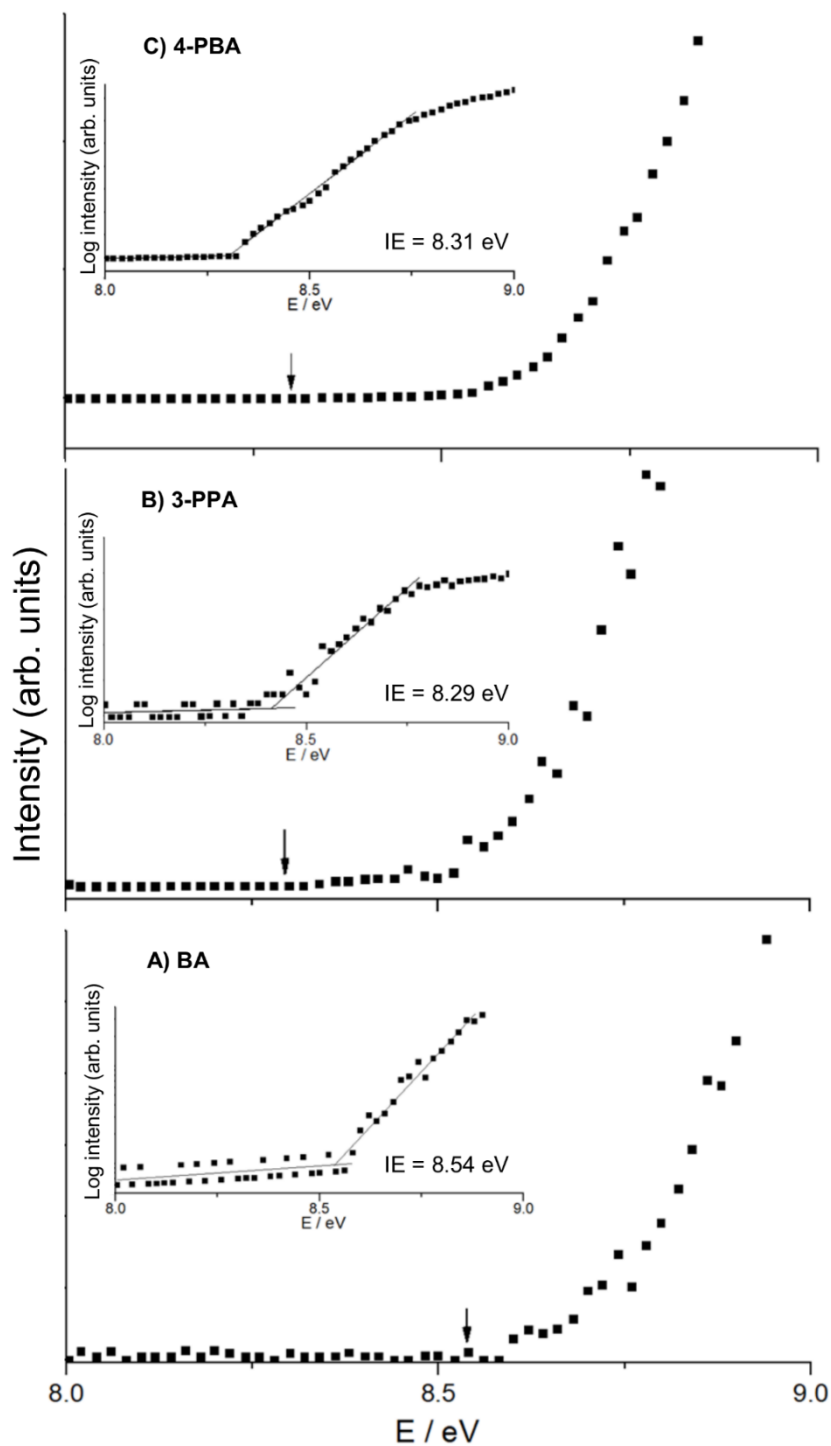
Figure S1. Photoionization efficiency curves (PECs) of A) BA[+.], B) 3-PPA[+.] and C) 4-PBA[+.]. The inset present in each panel reports the corresponding data in semi-logarithmic scale. The IE value is determined by the linear plots fitting the background and the rising ion signal in the threshold region.

Figure S2. Photoionization efficiency curves for the parent ion and most intense fragments of a) benzylamine, b) 2-phenylethylamine, c) 3-phenylpropylamine, d) 4-phenylbuthylamine.

Figure S3. Spin density computed for representative radical cations of the assayed PAAs is plotted using an isovalue of 0.007. Relative ZPE corrected electronic energies calculated at the CBS-QB3 level are reported in kJ mol⁻¹.
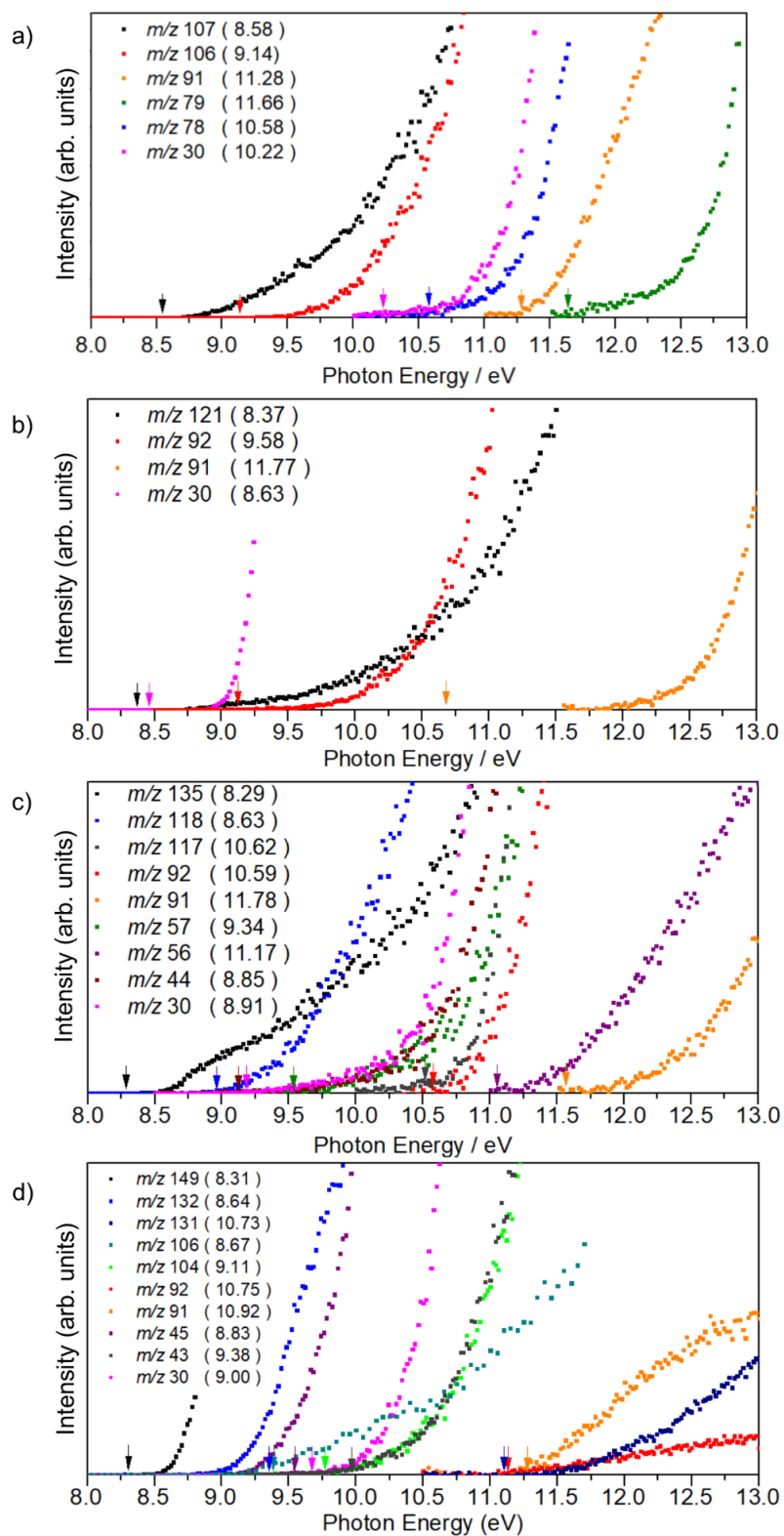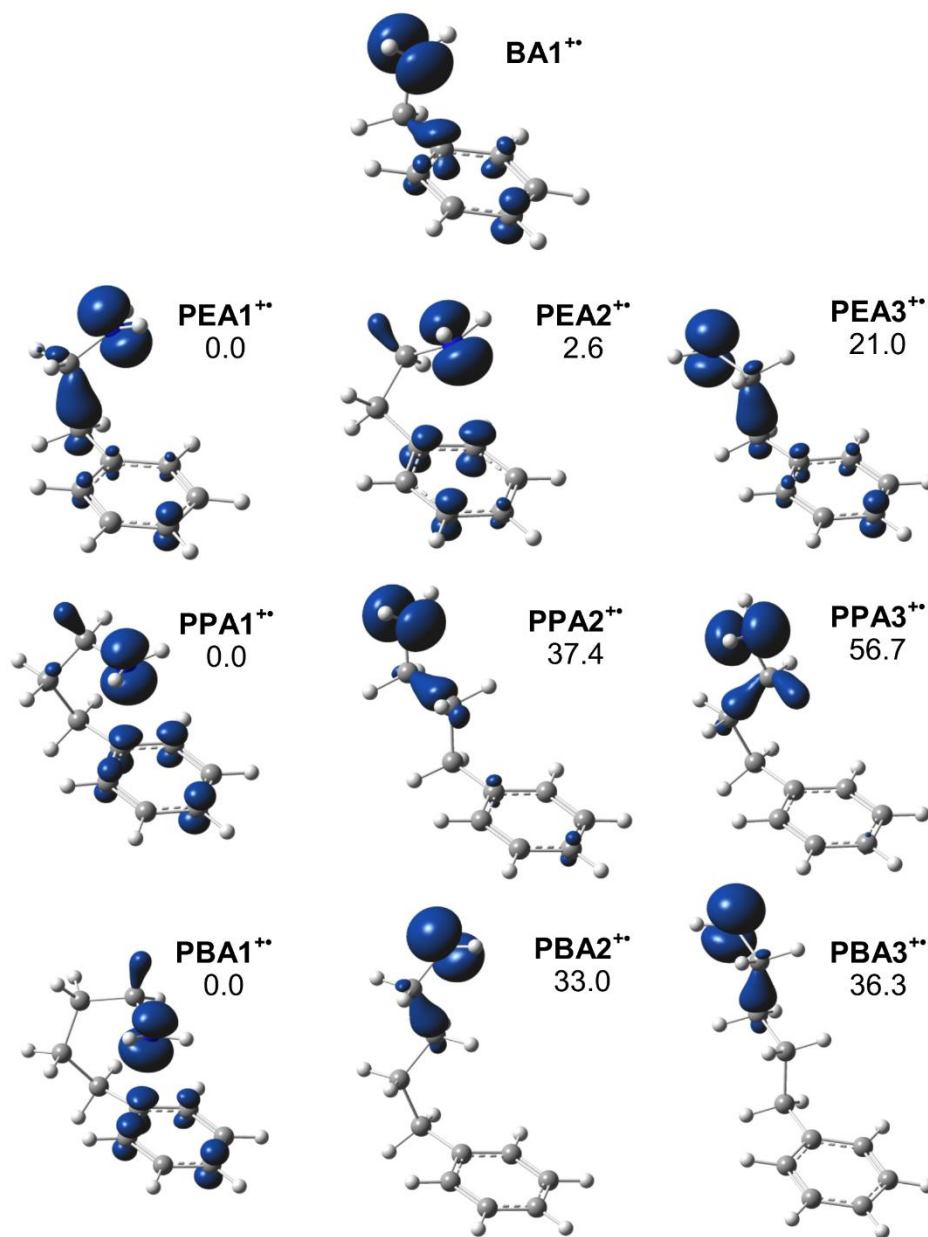
References

1. A. Bouchet, M. Schütz, B. Chiavarino, M. E. Crestoni, S. Fornarini and O. Dopfer, Phys. Chem. Chem. Phys. 17, 25742 (2015).
2. S. Shaik, Chemistry as A Game of Molecular Construction: The Bond Click Way, eds. Wiley, New Jersey, (2016).
3. J. C. Lopez, V. Cortijo, S. Blanco and J. L. Alonso, Phys. Chem. Chem. Phys. 9, 4521 (2007).
4. P. D. Godfrey, L. D. Hatherley and R. D. Brown, J. Am. Chem. Soc. 117, 8204 (1995).
5. S. J. Martinez, J. C. Alfano, D. H. Levy, J. Mol. Spectrosc. 158, 82 (1993).
6. J. A. Dickinson, M. R. Hockridge, R. T. Kroemer, E. G. Robertson, J. P. Simons, J. McCombie and M. Walker, J. Am. Chem. Soc. 120, 2622 (1998).
7. J. Yao, H. S. Im, M. Foltin and E. R. Bernstein, J. Phys. Chem. A 104, 6197 (2000).
8. R. Weinkauf, F. Lehrer, E. W. Schlag and A. Metsala, Faraday Discuss. 115, 363 (2000).
9. P. R. Richardson , S. P. Bates and A. C. Jones, J. Phys. Chem. A 108, 1233 (2004).
10. A. Golan, N. Mayorkas, S. Rosenwaks and I. Bar, J. Chem. Phys. 131, 024305 (2009).
11. N. Mayorkas, S. Cohen, H. Sachs and I. Bar, RSC Adv. 4, 58752 (2014).
12. B. Chiavarino, M. E. Crestoni, M. Schütz, A. Bouchet, S. Piccirillo, V. Steinmetz, O. Dopfer and S. Fornarini, J. Phys. Chem. A 118, 7130 (2014).
13. M. Schütz, A. Bouchet, B. Chiavarino, M. E. Crestoni, S. Fornarini and O. Dopfer, Chem. Eur. J. 22, 8124 (2016).
14. M. Schütz, A. Bouchet, O. Dopfer, Phys.Chem.Chem.Phys. 18, 26980 (2016).
15. R. Wu and T. B. McMahon, ChemPhysChem 9, 2826 (2008).
16. J. A. Stearns, S. Mercier, C. Seaiby, M. Guidi, O. V. Boyarkin and T. R. Rizzo, J. Am. Chem. Soc. 129, 11814 (2007).
17. W. Fu, P. J. J. Carr, M. J. Lecours, M. Burt, R. A. Marta, V. Steinmetz, E. Fillion, T. B. McMahon and W. S. Hopkins, Phys. Chem. Chem. Phys. 19, 729 (2017).
18. C. Estarellas, A. Frontera, D. Quiñonero and P. M. Deyà, Phys. Chem. Chem. Phys. 13, 16698 (2011).
19. N. P.-A. Monney, T. Bally, G. S. Bhagavathy and R. S. Glass, Org. Letters 15, 4932 (2013).
20. D. W. Werst, J. Am. Chem. Soc. 113, 4345 (1991).
21. M. C. Castrovilli, P. Bolognesi, A. Cartoni, D. Catone, P. O'Keeffe, A. R. Casavola, S. Turchini, N. Zema and L. Avaldi, J. Am. Soc. Mass Spectrom. 25, 351 (2014).
22. A. Derossi, F. Lama, M. Piacentini, T. Prosperi and N. Zema, Rev. Sci. Instrum. 66, 1718 (1995).
23. M. C. Castrovilli, P. Bolognesi, A. Casavola, A. Cartoni, D. Catone, P. O'Keeffe and L. Avaldi, Eur. Phys. J. D 68, 2 (2014).
24. K.-M. Weitzel, J. Mahnert and M. Penno, Chem. Phys. Lett. 224, 371, (1994).
25. Spartan 10, Program for Calculation of Molecular Properties; Wavefunction Inc.: Irvine, CA, USA.
26. M. J. Frisch, G. W. Trucks, H. B. Schlegel, G. E. Scuseria, M. A. Robb, J. R. Cheeseman, G. Scalmani, V. Barone, B. Mennucci, G. A. Petersson, H. Nakatsuji, M. Caricato, X. Li, H. P. Hratchian, A. F. Izmaylov, J. Bloino, G. Zheng, J. L. Sonnenberg, M. Hada, M. Ehara, K. Toyota, R. Fukuda, J. Hasegawa, M. Ishida, T. Nakajima, Y. Honda, O. Kitao, H. Nakai, T. Vreven, J. A. Montgomery, Jr., J. E. Peralta, F. Ogliaro, M. Bearpark, J. J. Heyd, E. Brothers, K. N. Kudin, V. N. Staroverov, R. Kobayashi, J. Normand, K. Raghavachari, A. Rendell, J. C. Burant, S. S. Iyengar, J. Tomasi, M. Cossi, N. Rega, J. M. Millam, M. Klene, J. E. Knox, J. B. Cross, V. Bakken, C. Adamo, J. Jaramillo, R. Gomperts, R. E. Stratmann, O. Yazyev, A. J. Austin, R. Cammi, C. Pomelli, J. W. Ochterski, R. L. Martin, K. Morokuma, V. G. Zakrzewski, G. A. Voth, P. Salvador, J. J. Dannenberg, S. Dapprich, A. D. Daniels, Ö. Farkas, J. B. Foresman, J. V. Ortiz, J. Cioslowski and D. J. Fox, Gaussian 09, Revision D.01, Gaussian, Inc., Wallingford CT (2009).
27. J. A. Montgomery Jr., M. J. Frisch, J.W. Ochterski, and G. A. Petersson, J. Chem. Phys. 112, 6532 (2000).
28. G. P. F. Wood, L. Radom, G. A. Petersson, E. C. Barnes, M. J. Frisch and J. A. Montgomery Jr., J. Chem. Phys. 125, 094106 (2006).
29. M. Xie, Z. Zhou, Z. Wang, D. Chen and F. Qi, Int. J. of Mass Spectrom. 303, 137 (2011).
30. R. Ruede, H. Troxler, C. Beglinger and M. Jungen, Chem. Phys. Lett. 203, 477 (1993).
31. J. H. Catanzarite, Y. Haas, H. Reisler and C. Wittig, J. Chem. Phys. 78, 5506 (1983).

32. S.G. Lias "Ionization Energy Evaluation" in NIST Chemistry WebBook, NIST Standard Reference Database Number 69, Eds. P.J. Linstrom and W.G. Mallard, National Institute of Standards and Technology, Gaithersburg MD, 20899.

33. J. M. Dyke, E. P. F. Lee and M. H. Z. Niavaran, Int. J. Mass Spectrom. Ion Phys., 94, 221 (1989).

34. M. N. R. Ashford, R. N. Dixon, R. J. Stickland and C. M. Western, Chem. Phys. Lett. 138, 201 (1987).

35. K. Mizuse, A. Fujii and N. Mikami, J. Phys. Chem A 110, 6387 (2006).

36. K. Mizuse, H. Hasegawa, N. Mikami and A. Fujii, J. Phys. Chem. A 114, 11060 (2010).

37. J. H. Gross, Mass Spectrometry, 2nd ed., ed. Springer-Verlag Berlin Heidelberg, chap. 2, 21 (2011).

38. R. Seiler, Int. J. Quantum Chem. 3, 25 (1969).

39. R. H. Lipson, Ultraviolet and Visible Absorption Spectroscopy, in Encyclopedia of Applied Spectroscopy, D. L. Andrews, ed. Wiley-VCH Berlin, chap. 11, 353 (2009).

40. J. Franck, Trans. Faraday Soc. 21, 536 (1925).

41. L. Wei, B. Yang, J. Wang, C. Huang, L. Sheng, Y. Zhang, F. Qi, C.-S. Lam and W.-K. Li, J. Phys. Chem. A 110, 9089 (2006).

42. R. Sun, Q. Meng, M. Wang, W. Fei, Y. Zhang, J. Chen, W. Fang, X. Shan, F. Liu and L. Sheng, J. Phys. B: At. Mol. Opt. Phys. 50, 235101 (2017).

43. C. Joblin, L. Dontot, G. A. Garcia, F. Spiegelman, M. Rapacioli, L. Nahon, P. Parneix, T. Pino and P. Bréchignac, J. Phys. Chem. Lett. 8, 3697 (2017).

44. E. T. Selim, M. A. Rabbih and M. A. Fahmey, Org. Mass Spectrom. 22, 381 (1987).

45. D. H. and M. T. Bowers, "Chapter 9. Stabilities of positive ions from equilibrium gas phase basicity measurements" in Ions Chemistry, ed. M.T. Bowers, 1979.

46. L. N. Domelsmith, L. L. and K. N. Houk, J. Am. Chem. Soc. 99, 4311 (1977).

A.2 Complexation of halide ions to tyrosine: role of non-covalent interactions evidenced by IRMPD spectroscopy

Abstract. The binding motifs in the halide adducts with tyrosine ([Tyr+X]$^-$, X = Cl, Br, I) have been investigated and compared with the analogues with 3-nitrotyrosine (nitroTyr), a biomarker of protein nitration, in a solvent-free environment by mass-selected infrared multiple photon dissociation (IRMPD) spectroscopy over two IR frequency ranges, namely 950-1950 and 2800-3700 cm^{-1}. Extensive quantum chemical calculations at B3LYP, B3LYP–D3 and MP2 levels of theory have been performed using the 6-311++G(d,p) basis set to determine the geometry, relative energy and vibrational properties of likely isomers and interpret the measured spectra. A diagnostic carbonyl stretching band at ~1720 cm^{-1} from the intact carboxylic group characterizes the IRMPD spectra of both [Tyr+X]$^-$ and [nitroTyr+X]$^-$, revealing that the canonical isomers (maintaining intact amino and carboxylic functions) are the prevalent structures.

The spectroscopic evidence reveals the presence of multiple non-covalent forms. The halide complexes of tyrosine conform to a mixture of plane and phenol isomers. The contribution of phenol-bound isomers is sensitive to anion size, increasing from chloride to iodide, consistent with the decreasing basicity of the halide, with relative amounts depending on the relative energies of the respective structures. The stability of the most favorable phenol isomer with respect to the reference plane geometry is in fact 1.3, -2.1, -6.8 kJ mol^{-1}, for X = Cl, Br, I, respectively. The change in π-acidity by ring nitration also stabilizes anion-π interactions yielding ring isomers for [nitroTyr+X]$^-$, where the anion is placed above the face of the aromatic ring.

A.2.1 Introduction

The importance of anion-amino acid interactions is well documented in biology playing a role in relevant functions such as neuron signaling, ion transport, drug-receptor recognition.[1,2] Although many proteins are commonly negatively charged, anionic amino acid clusters are much less studied than metal cation adducts. However, anion complexation also relies on hydrogen bonding, ion-dipole

interactions, and hydrophobic effects which in principle may also preferentially stabilize zwitterionic forms relative to their neutral, canonical counterparts.[3] In addition, other non-covalent contacts, including anion-π effects favored between π-acidic arenes and charge-diffuse anions, may contribute in stabilizing negatively charged adducts of (aromatic) amino acids.

Recently, Infrared Multiple Photon Dissociation (IRMPD) spectroscopy,[4-7] a powerful tool to identify the structural and electronic features of various ionic species in the gas phase,[8-14] including mono-[15-16] and divalent-[17] metal-bound amino acids, has revealed canonical structures for halide adducts of glutamic acid, histidine, and phenylalanine.[18] In contrast arginine is rather in the zwitterionic form[19], and canonical and zwitterionic isomers are both significantly populated in the proline-chloride complex.[20] Different binding motifs have been also highlighted by IRMPD assay of halide adducts of 1,3,5-trinitrobenzene, a representative π–acidic arene, showing that: i) the fluoride adduct [TNB + F]$^-$ conforms to a strongly covalent σ-complex (Meisenhemer complex); ii) the chloride complex [TNB + Cl]$^-$ places the anion on the periphery of the aromatic ring;[21] the bromide [TNB + Br]$^-$ and iodide [TNB + I]$^-$ adducts display weakly covalent structures.[22,23]

The present study is focused on the bonding motifs of halide ions (Cl$^-$, Br$^-$, and I$^-$) with L-tyrosine (Tyr) and 3-nitro-tyrosine (nitroTyr), where phenolic ring nitration is a post-translational modification effected by reactive nitrogen species. The structure of deprotonated tyrosine, [Tyr-H]$^-$, interrogated by IRMPD spectroscopy has shown clear evidence of a carboxylate structure. This result is consistent with the fact that the phenoxide anion isomer is higher in energy by ca. 10 kJ mol^{-1} in the gas phase.[24] However, the gas phase structure of [Tyr-H]$^-$ is reported to depend on the (a)protic nature of the solvent used in the electrospray ionization.[25-27]

In addition, the protonated forms of tyrosine and of 3-NO$_2$-tyrosine have been assayed by IRMPD spectroscopy in two complementary IR frequency ranges showing unambiguous evidence of amino group protonation and characteristic absorptions associated to nitration.[28]

Herein, [Tyr + X]$^-$ and [nitroTyr + X]$^-$ (X = Cl, Br, I) complexes have been investigated to broaden the little-existing documentation about anion/amino acid interactions.

The intrinsic properties of [Tyr + X]⁻ ions have been inspected by IRMPD spectroscopy in the 950-1950 cm^{-1} range, exploiting the bright and tunable radiation from the free electron laser beamline at the CLIO (Centre Laser Infrarouge d'Orsay) facility, along with quantum chemical calculations to aid in the interpretation of the observed spectra. Additional spectroscopic information has been obtained in the 2800-3700 cm^{-1} range that is especially revealing of non-covalent interactions involving NH/OH bonds. Diagnostic vibrational features of tyrosine nitration are expected to be useful to reveal direct structural clues related to biological activity, including whether the (modified) amino acid adopts either a canonical, charge solvated or a zwitterionic, form in these complexes, whether anion-π interactions may contribute to stabilize the gas-phase population, and to what extent the ground state geometries are sensitive to the halide anion identity.

A.2.2 Methods

IRMPD spectroscopy

IRMPD spectra of halide adducts of (3-NO₂-)tyrosine were acquired employing two different experimental setups: i) a modified Paul ion-trap mass spectrometer (Bruker Esquire 3000+) equipped with an electrospray ionization ESI source and coupled to the IR radiation of a tunable (5-25 μm) free electron laser (FEL) at CLIO[29]; ii) a tabletop KTP/KTA optical parametric oscillator/amplifier system (OPO/OPA, Laser Vision) whose radiation output is admitted into a modified Paul ion-trap mass spectrometer (Esquire 6000+, Bruker Daltonics), assembled at the Università di Roma "La Sapienza". Details on these integrated setups have been previously described.[30-32]

Solutions were prepared 30 μM NH₄X (X= Cl, Br, I) and 20 μM of either Tyr or nitroTyr in water: methanol (1:1), with 2% ammonia to assist deprotonation. All reagents were commercial products (Sigma-Aldrich srl Milan, Italy), used as received. A dilute solution 5 μM in each analyte was continuously infused into the ESI source at a flow rate of 2.5 μL min⁻¹ to generate the halide clusters. In either ion trap, precursor ions were accumulated for 5-10 ms and mass-selected by resonance ejection prior to IR irradiation for: i) 0.2-0.5 s by the CLIO-FEL over the mid-IR range

(950-1950 cm^{-1}); ii) 2 s by the OPO/OPA laser covering the NH/OH stretching region (2800-3700 cm^{-1}). The irradiation time is controlled by an electromechanical shutter synchronized with the mass spectrometer.

The FEL radiation is generated by a 10-50 MeV electron linear accelerator and delivered in 9 µs macropulses (25 Hz), each containing 600 micropulses (0.5–3 ps long). Typical macropulse energies are 40 mJ. For the present study, the electron energy was set to 44 MeV with a fairly stable laser power ranging from 1.1 to 0.8 W upon increasing frequency. The IR-FEL spectral width (fwhm) was less than 0.5% of the central wavelength.

The parametric converter is pumped using a Nd:YAG laser (Continuum Surelite II) running at 10 Hz and delivering 600 mJ per pulse (4‑6 ns long). The typical output energy from the OPO/OPA laser was 18-20 mJ/pulse in the investigated spectral range with 3-4 cm^{-1} bandwidth.

A stepwise process based on the absorption of multiple resonant photons, associated with intramolecular vibrational energy redistribution, can heat the ions to a threshold energy for fragmentation, typically proceeding along the lowest energy pathway.[4]

By recording the abundances of the precursor ion (I_P) and of all fragment ions (I_F) as a function of the photon wavenumber, the IRMPD spectrum is collected as the photodissociation yield R, defined as $-\ln[I_P/(I_P + \Sigma I_F)]$.[33] Mass spectra were obtained by accumulation of five sequences and averaged over four at each photon energy, which was increased in steps of 4–5 cm^{-1}. In all the acquired spectra, a quantitative accord is verified between the reduction of the precursor ion signal and the increase of the product ion signals. A good overlap of the laser beam with the ion cloud has been observed.

Computational details

A preliminary conformational search to identify candidate low-energy isomers and conformers of [Tyr+X]$^-$ and [nitroTyr+X]$^-$ (X = Cl, Br, I) was carried out by performing 300 cycles of simulated annealing using tools of Amber8, Sander[34] with the GAFF (General Amber Force Field) force field.[35] For higher level optimization, low-energy

geometries were sorted into families with similar non-covalent interactions, and those within 50 kJ mol^{-1} from the global minimum structure were fully optimized by means of density functional theory calculations at the B3LYP/6-311++G(d,p) level. Harmonic vibrational frequency analysis was carried out on all optimized structures to characterize the stationary points as local minima, and to obtain linear IR spectra. In addition, zero-point energy (ZPE) and thermal corrections were also obtained at the same level of theory. In order to improve the agreement between experimental and calculated spectra, harmonic frequencies were uniformly scaled by using a factor of 0.978 (0.955) in the 950-1950 cm^{-1} (2800-3700 cm^{-1}) frequency region.[18] For the sake of comparison, calculated resonances were convoluted by assuming a Lorentzian profile with 20 cm^{-1} (5 cm^{-1}) full width at half-maximum (FWHM)) in the 950-1950 cm^{-1} (2800-3700 cm^{-1}) spectral range. Calculations on the complete set of conformers have been also performed at B3LYP-D3/6-311++G(d,p) level as employed into the Spartan 16 suite of programs (Wavefunction, Inc., Irvine, CA). The Grimme dispersion correction was employed in order to account more accurately for non-covalent interactions, which may play a major role in the adducts subject of this work.

As the geometric and vibrational properties of the low-energy isomers and conformers of [Tyr+X]$^-$ and [nitroTyr+X]$^-$ do not present substantial changes using either B3LYP or B3LYP-D3, henceforth we will uniformly refer to the geometries and IR spectra obtained at the B3LYP/6-311++G(d,p) level.

In order to more accurately evaluate relative electronic energies, single-point energy calculations were also performed on the optimized B3LYP geometries at the MP2/6-311++G(d,p) level. We employed the ORCA 3.0.1 software package with a SCF convergence set as TightSCF (energy change 1e−08; max-density change 1e−07; rms-density change 5e−09; DIIS error 5e−07) and a high precision for the integration grids.[36-37]

An effective core potential (def2-TZVP) is employed in the MP2 calculations for the iodine atom.[38]

MP2 refined relative enthalpies (or Gibbs free energies) were obtained by adding B3LYP thermal (298 K) and ZPE corrections to MP2 electronic energies and are denoted as MP2(full)//6-311++G(d,p)//B3LYP/6-311++G(d,p).

A.2.3 Results and discussion

Photodissociation mass spectra

Electrosprayed halide-bound complexes of L-tyrosine, and 3-NO$_2$-L-tyrosine have been mass-selected, trapped and studied by IRMPD spectroscopy, taking advantage of its potential to provide diagnostic clues that could integrate poorly informative collision induced dissociation (CID) assays. Upon absorption of resonant IR photons, the internal energy of the sampled species slowly increases, ultimately promoting a wavelength-dependent dissociation process along the lowest energy fragmentation route.[4, 39-40]

The photofragmentation of chloride adducts [Tyr+Cl]$^-$ (*m/z* 216/218) and [nitroTyr+Cl]$^-$ (*m/z* 261/263) in both the explored fingerprint and NH/OH stretching ranges involves the loss of HCl, which leads to deprotonated tyrosine, [Tyr-H]$^-$ (*m/z* 180), and 3-NO$_2$-tyrosine, [nitroTyr-H]$^-$ (*m/z* 225), as displayed in the mass spectra obtained when [Tyr+Cl]$^-$ and [nitroTyr+Cl]$^-$ are irradiated at the IR-active frequency of 1505 and 1477 cm^{-1}, respectively (Fig. S1(a) and S2(a)). However, the relatively low mass cut off of the ion trap mass spectrometer used precluded the possibility to reveal the product ion at m/z 35/37 [Cl]$^-$. As a matter of fact, the evidence that the signal depletion detected in the parent ion channel, [Tyr+Cl]$^-$, largely exceeds the ion abundance change in the fragment ion channel, [Tyr-H]$^-$, is indicative that the photofragmentation also proceeds by the blind fragment channel [Cl]$^-$ involving loss of neutral tyrosine (Fig. S3).

Despite this blind dissociation channel, the neat correspondence in the position of the features in both the parent ion depletion and the fragment ion profile confirms that the [Cl]$^-$ dissociation path presents the same vibrational features as the [Tyr-H]$^-$ fragmentation channel. This evidence has enabled us to present the IRMPD spectra of [Tyr+Cl]$^-$ and [nitroTyr+Cl]$^-$ by recording the photofragmentation yield R as a

function of the photon energy (see below) relying on the abundance of the [Tyr-H]$^-$ as only fragment.

In contrast, the assayed bromide, [Tyr+Br]$^-$ (*m/z* 260/262) and [nitroTyr+Br]$^-$ (*m/z* 305/307), and iodide, [Tyr+I]$^-$ (*m/z* 308) and [nitroTyr+I]$^-$ (*m/z* 353), complexes fragment by loss of intact amino acid and release of halide anions, Br$^-$ and I$^-$, as photofragments.

The exemplary mass spectra collected after exposure of tyrosine, [Tyr+Br]$^-$ and [Tyr+I]$^-$, and 3-nitrotyrosine, [nitroTyr+Br]$^-$ and [nitroTyr+I]$^-$, adducts to IR photons tuned at 1297 and 1177 cm^{-1}, and to 1325 and 1737 cm^{-1} are presented in Fig. S1(b-c) and Fig. S2(b-c), respectively. The same fragmentation pattern is found when [Tyr+X]$^-$ and [nitroTyr+X]$^-$ (X = Cl, Br, I) are assayed by low-energy CID.

This behavior conforms to the lower binding energy with increasing anion size from Cl$^-$ to I$^-$, according to the calculated halide-ion dissociation energies reported in Table S1, combined with the stronger gas-phase acidity of HX ($\Delta G°_{acid}$) of HBr (1332 kJ/mol)[41] and HI (1294 kJ/mol)[42] as compared to HCl (1372 kJ/mol).[43] Notably, the same fragmentation channels have been recently observed upon IRMPD assay of halide-bound histidine, [His+X]$^-$ (X= Cl, Br, I),[19] and phenylalanine, [Phe+Cl]$^-$,[18] adducts.

IRMPD spectroscopy

A structural characterization of [Tyr+X]$^-$ (X = Cl, Br, I) complexes as naked species was sought by IRMPD spectroscopy performed in the fingerprint region (950–1950 cm^{-1}), a range which encompasses highly informative modes, including COH and NH bending vibrations along with carbonyl C=O and carboxylate OCO stretches.

As illustrated in Fig. 1, the IRMPD spectra of [Tyr+Cl]$^-$, [Tyr+Br]$^-$ and [Tyr+I]$^-$ exhibit similar profiles with several common features, including the pronounced bands around 1178, 1250, 1507, and 1608 cm^{-1}. However, some notable systematic shifting in the band positions and relative intensities appear with increasing anion size from Cl$^-$ to I$^-$, overall allowing a distinction of these complexes. In the low wavenumber region, the strong, poorly resolved absorbances centred at 1312 and 1376 cm$^-$ for [Tyr+Cl]$^-$ become even broader with increasing anion size (from ~90 to

~170 cm^{-1} fwhm), up to progressively encompass the weak band at ca. 1250 cm^{-1} in the case of [Tyr+I]$^-$.
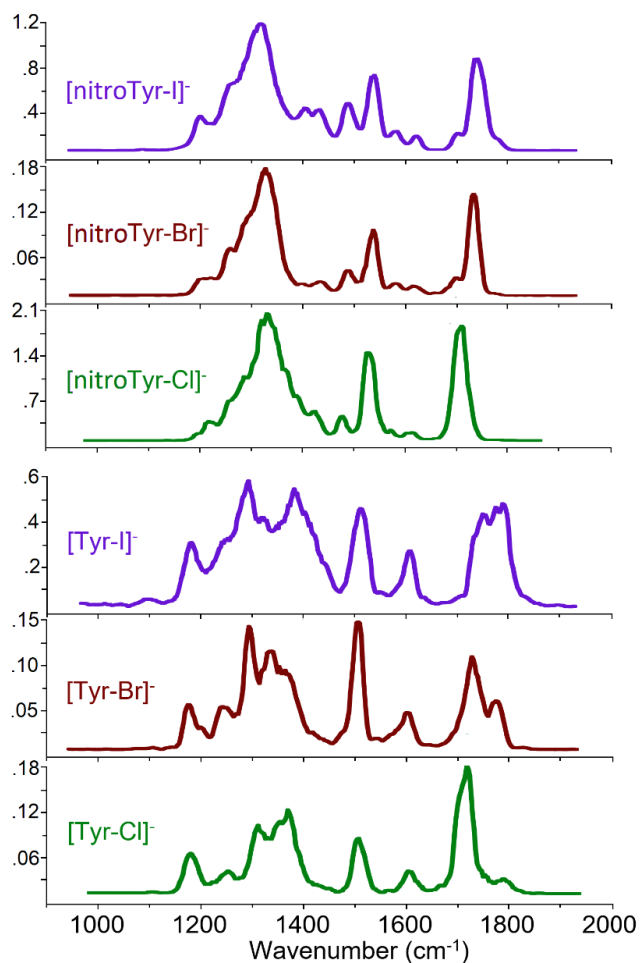
Fig. 1 Experimental IRMPD spectra of [Tyr+X]$^-$ and [nitroTyr+X]$^-$ (X= Cl, Br, I) complexes in the 950-1950 cm^{-1} range.

In the higher frequency side, the peak at 1720 cm^{-1} for [Tyr+Cl]$^-$ steadily shifts to 1730 for [Tyr+Br]$^-$ and 1750 cm^{-1} [Tyr+I]$^-$, whereas the small shoulder observed as a separate band at 1790 cm^{-1} for [Tyr+Cl]$^-$, progressively magnifies, appearing as a still distinct band at 1775 cm^{-1} for [Tyr+Br]$^-$, and as a strong, almost merged feature at 1785 cm^{-1} in the case of [Tyr+I]$^-$. These bands, definitely outside the range for antisymmetric carboxylate stretching mode, expected near 1635 cm^{-1} for deprotonated tyrosine,[26] rather correspond to the CO stretching mode of a carboxylic group, and closely approach v(CO) of chloride-bound phenylalanine (1710 cm^{-1}),[18] thus implying that also tyrosine is predominantly non-zwitterionic in these halide complexes. This motif is also supported by the lack in [Tyr+X]$^-$ of a

signature for protonation at the amino group, namely the NH_3^+ umbrella mode observed at 1420 cm^{-1} in protonated tyrosine,[28] and by the position of the COH in-plane bending mode of the carboxylic group at ca. 1358-1375 cm^{-1}. The latter frequencies are in very good agreement with a related absorption observed at 1360 cm^{-1} for chloride-bound phenylalanine, previously interpreted as a diagnostic feature of halide-carboxylic hydrogen interaction.[18] Interestingly, a charge solvated (CS) canonical structure with a tridentate N/O/ring structure as the preferred binding geometry for K$^+$-tagged tyrosine was also unveiled by IRMPD spectroscopy, with υ(CO) at 1744 cm^{-1}.[44] The lower υ(CO) frequency of [Tyr+Cl]$^-$ relative to the value found for [Tyr+K]$^+$ entails significantly different modes of interaction between the amino acid and the monoatomic ions, as already observed in analogous phenylalanine adducts.

Herein, the effect of a change in π-acidity on halide-tyrosine recognition has been also investigated by recording the IRMPD spectra of [nitroTyr+X]$^-$ (X= Cl, Br, I) adducts (Fig. 1). The spectra exhibit common features, including the prominent, broad peak (~100 cm^{-1} fwhm) at 1316/1330 cm^{-1}, the intense, sharp absorption at 1528/1540 cm^{-1}, and the strong band at 1710 cm^{-1} for [nitroTyr+Cl]$^-$, which progressively shifts to 1733 cm^{-1} for [nitroTyr+Br]$^-$, and to 1743 cm^{-1} for [nitroTyr+I]$^-$. In addition, the weaker resonances of [nitroTyr+Cl]$^-$ observed at 1220, 1474, 1572, and 1610 cm^{-1} are almost the same for the three complexes, with frequency variations of less than 15 cm^{-1}, whereas an additional peak around 1700 cm^{-1} appears only in the case of [nitroTyr+X]$^-$ (X= Br$^-$, I$^-$). A few notable differences with the native [Tyr+X]$^-$ adducts, likely associated to the nitration modification, are: i) the absence of any detectable features at 1180 cm^{-1} and 1774-1790 cm^{-1}; ii) the presence of a broad intense band at 1316-1330 cm^{-1} instead of the two partially resolved features at 1312 and 1375 cm^{-1}.

Spectroscopic information in the NH/OH range (2800–3700 cm^{-1}) has also been obtained for two examples of tyrosine adducts, [Tyr+X]$^-$ (X = Cl, Br), as illustrated in Fig. S4 and S5, respectively, in the Supporting Material (SM). In this region, the two sampled adducts share very similar features, with a sharp (fwhm = 10 cm^{-1}), intense

peak at 3663 cm^{-1}, a signature of the free OH of the phenol group, together with broad resonance structures at ca. 3200 and 3000 cm^{-1}, more conspicuous for X = Br. For each sampled halide adduct, the IRMPD process can be very efficient in both the explored regions, leading to considerable signal depletion of the precursor ion population, whose trend neatly follows the appearance of the detected fragments.

Calculated structures

[Tyr+X]$^-$ (X = Cl, Br, I)

An extensive conformational search aimed at collecting the low-energy structures for [Tyr+X]$^-$ complexes has led to identify families of isomers arising from charge solvated (CS) or salt bridge (SB) structures, where X$^-$ may interact with either the phenolic or carboxylic hydroxyl group, the amino hydrogens, the phenyl ring, or the ammonium ion. In addition to the different binding sites, one needs to consider two variants, differing in the orientation of the phenolic hydroxyl group which may lean either towards (*right*) or away from (*left*) the side of the amino group. However, as previously observed, the ensuing rotamers lie within 1 kJ mol^{-1},[45-46] and henceforth we will preferentially refer to the usually lowest energy *left* variant.

The optimized geometries of the lowest energy canonical and zwitterion structures for [Tyr+Cl]$^-$ obtained at the B3LYP/6-311++G(d,p) level of theory are shown in Fig. 2, along with their relative enthalpy ($\Delta H°_{rel}$) and free energy ($\Delta G°_{rel}$) values at 298 K calculated at the same level. In addition, further check at B3LYP-D3/6-311++G(d,p) level and single point energy calculations at MP2//B3LYP/6-311++G(d,p) have been carried out in order to account for dispersive interactions and to clarify the importance of the exact exchange energy in the interpretation of the system.[47-48] Fig. S6 and Table S2 provide comprehensive geometric and thermodynamic information on these and other conformational variants, deriving from systematic stepwise rotation of each torsional angle in the flexible skeleton of [Tyr+Cl]$^-$. There is an overall reasonable agreement among all levels of theory in predicting as most favorable the canonical structures, with either a phenol, plane or terminal halide binding site. However, while the same trend in relative energy is envisioned by the two DFT levels of theory, MP2 data favor the bidentate plane relative to mono

dentate phenol arrangements. This finding reflects the delicate energetic balance between these structures.[18, 49]

Although the averaged population at 298 K is very sensitive to the theoretical description, however the close energy spacing predicted at any level implies that more than a single structure would contribute to the thermal ion population at 298 K.

Henceforth, we will uniformly refer to Gibbs free energy values at 298 K at MP2 level, due to the comparatively improved accuracy in the treatment of non-covalent interactions.
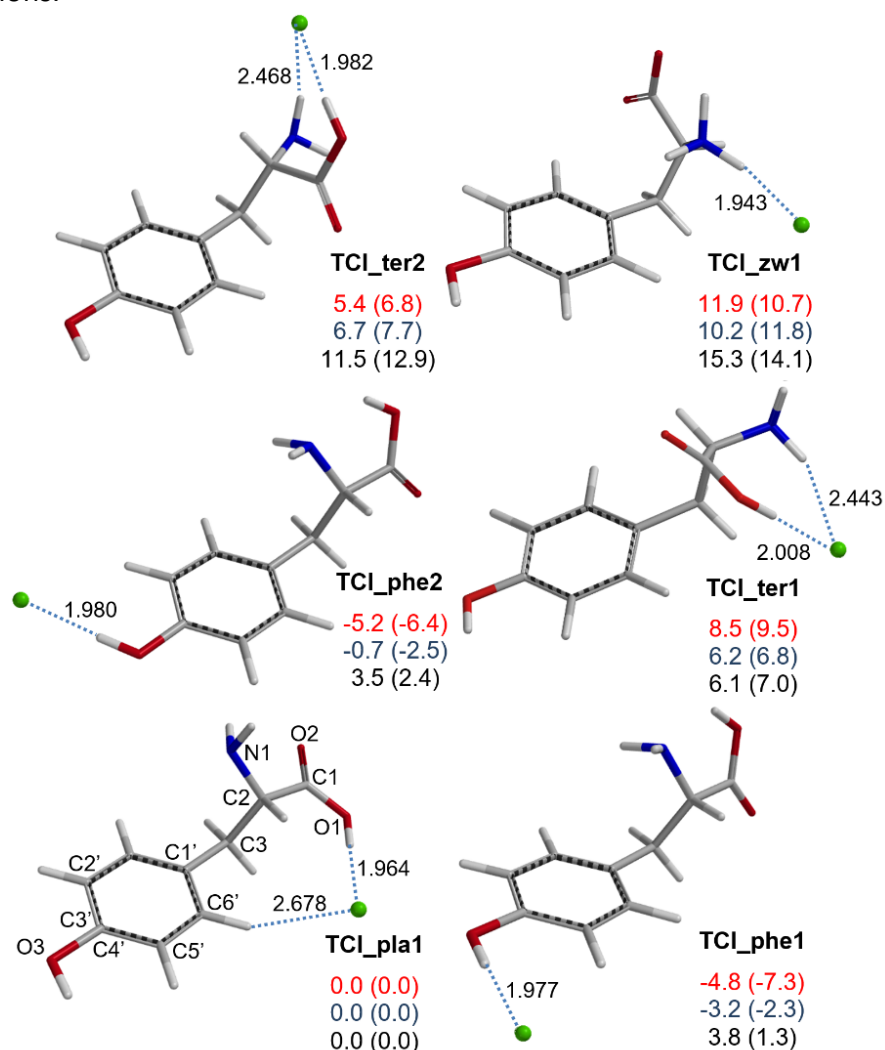

Fig. 2 Optimized geometries for selected isomers of [Tyr+Cl]⁻. Relative enthalpies and relative free energies (bracketed) at the B3LYP/6-311++G(d,p) (in red), B3LYP-D3/6-311++G(d,p) (in blue) and MP2//B3LYP/6-311++G(d,p) (in black) levels are provided at 298 K in kJ mol⁻¹. Interatomic bond distances, marked by dashed lines, are reported in Å.

In the lowest energy structure (**TCl_pla1**), the ∠O1C1C2N and ∠NC2C3C1' dihedral angles, equal to 157.1° and -67.3° (Table S3), respectively, allow a *gauche* conformation (meaning the relationship between NH_2 and the aromatic ring along the C2-C3 bond) with the phenol OH turned *left* with respect to the amino group, and the anion bound in a bidentate CH···Cl⁻···HOC(O) arrangement to both an aromatic hydrogen ($r_{Cl···HC}$ = 2.68 Å) and the carboxylic OH group in *trans* configuration ($r_{Cl···HOC(O)}$ = 1.96 Å). The amino unit, flipping apart from the ring toward the carbonyl oxygen, is engaged in a hydrogen bond interaction ($r_{CO···HN}$ = 2.31 Å).

The *gauche* monodentate species (**TCl_phe1**), located 1.3 kJ mol⁻¹ above **TCl_pla1**, is endowed with a Cl⁻···HO motif, where chloride is bound to a *left* phenol OH ($r_{Cl···HOC}$ =1.98 Å), and the carboxylic OH in a *trans* configuration is hydrogen bonded with the N terminus ($r_{N···OHC(O)}$ = 1.86 Å). This arrangement brings the ∠O1C1C2N dihedral angle to 10.2°, leaving the ∠ NC2C3C1' almost unperturbed (-56.5°).

A decrease of the relative stability of only 1.1 kJ mol⁻¹ is found by reversing the orientation of the phenol group so as to provide a *right* conformer (**TCl_phe2**). Notably, both these structures are stabilized by a weak N−H···π interaction due to the amino hydrogens pointing towards the aromatic ring. In the neutral amino acid, similar favourable O-H···N and NH···π contacts were already predicted,[50-51] and identified in laser ablated jet cooled amino acid by microwave,[52] and electronic[53-55] spectroscopy.

The lowest energy terminal isomer (**TCl_ter1**), placed 7.0 kJ mol⁻¹ higher in free energy than the global minimum, presents an *anti* NH···Cl⁻···HOC(O) arrangement, which modifies both the ∠O1C1C2N and ∠NC2C3C1' dihedral angles to -57.6° and -176.7° , respectively, enabling chloride binding to the aminoacid terminal sites, i.e. the carboxylic acid ($r_{Cl···HOC(O)}$ = 2.01 Å) in *trans* and the amino ($r_{Cl···HN}$ = 2.44 Å) group, without any contact with the aromatic side chain. Similar hydrogen bonding motifs are shared by the *anti* terminal rotamer **TCl_ter2** (where the *anti* notation refers to the relationship between the aryl and amino groups along the C2-C3 bond), characterized by a ∠O1C1C2N dihedral angle equal to 74.4° and relative stability of 12.9 kJ mol⁻¹ with respect to **TCl_pla1**.

Several other low-lying species have been identified (Table S2 and Fig. S6), including the left phenol conformer (**TCl_phe3**), which lies 12.4 kJ mol^{-1} higher in free energy than the lowest energy phenol structure **TCl_phe1**, although bearing a *cis* geometry of the carboxylic OH group, the commonly preferred configuration in several amino acids.[56] The most representative of them are briefly described in the Supporting Material.

The lowest energy SB structure (**TCl_zw1**), bearing an ammonium and a carboxylate group, lies 14.1 kJ mol^{-1} above **TCl_pla1**. In **TCl_zw1** the flexible chain takes on a favorable *gauche* conformation and the ammonium hydrogens establish comparatively short and strong contacts with both chloride ($r_{Cl\cdots+HN}$ = 1.94 Å) and carboxylate ($r_{OCO\cdots+HN}$ = 1.93 Å). A long-range NH$^+\cdots\pi$ interaction with the aromatic ring may be noted, characterized by a distance between the NH$^+$ proton donor and the center of the aryl ring equal to 3.12 Å.

Recently, a related, strongly stabilizing NH$_3^+\cdots\pi$ interaction has been found to operate in protonated 2-phenylethylamine and related neurotransmitters, including dopamine.[12, 57-59] Moreover, in analogy with the chloride-phenylalanine complex, where the anion was found to favor the formation of the zwitterion by ca. ~80 kJ mol^{-1}, a similar stabilization of the SB form of tyrosine is likewise expected here for the [Tyr+Cl]$^-$ adduct, due to the close similarity of the examined chloride complexes.[18, 60]

Interestingly, deprotonation at the phenol site is much more energy demanding as evident in the SB structure **TCl_O1**, which places the chloride anion in a terminal configuration, between the ammonium group ($r_{Cl\cdots HN}$ = 1.93 Å) and the carboxylic acid ($r_{Cl\cdots HOC(O)}$ = 2.01 Å). This isomer lies 85.0 kJ mol^{-1} above **TCl_pla1**, thus discarding a significant contribution of this species to the sampled ion population.

From a comparative inspection of Fig. 2, the steady decrease of relative free energy in the couple **TCl_phe1/TCl_pla1**, being 7.3, 2.3, and -1.3 kJ mol^{-1} at B3LYP, B3LYP-D3 and MP2(full), respectively, may be ascribed to the comparatively improved accuracy in the treatment of non-covalent interactions, particularly crucial in the bidentate binding motif of the **TCl_pla1** structure, which presents a long-range C-

H⋯Cl⁻ interaction. Anyway, the close energy spacing predicted at any level underlines the presence of multiple species in the averaged ion population at 298 K. For [Tyr+Br]⁻ and [Tyr+I]⁻, a survey of conformational landscape has been independently carried out, in order to obtain a reliable pattern of low energy species. Indeed, theory predicts the same binding motifs as described in [Tyr+Cl]⁻, though a reverse energy ordering for the lowest lying structures **TCl_pla1** and **TCl_phe1**, along with somewhat broader energy gaps with increasing anion size (Table S2-3 and Fig. S7 and S8). Accordingly, the lowest energy structures of [Tyr+Br]⁻ and [Tyr+I]⁻ adducts correspond to a phenol-bound isomer (**TBr_phe1** and **TI_phe1**). At the different levels of theory (namely B3LYP, B3LYP-D3 and MP2(full)), the free energy bias for phenol (**TBr_phe1**) as compared to plane (**TBr_pla1**) isomers is reduced from 9.1 to 4.7 and 2.1 kJ mol⁻¹ for [Tyr+Br]⁻, and from 14.3 to 5.8 and 6.8 kJ mol⁻¹, for [Tyr+I]⁻, respectively. This finding confirms the trend already observed for the [Tyr+Cl]⁻ complex.

All **TCl_phe1**, **TBr_phe1**, and **TI_phe1** present strictly similar values of dihedral angles irrespective of the halide, while the anion–phenol (X⁻⋯HOC$_{aryl}$) bond distances increase by 0.195 Å (X = Br) and 0.513 Å (X = I) as compared to [Tyr+Cl]⁻.

Also in the bidentate plane arrangement (**TBr_pla1** and **TI_pla1**), both the anion-ring hydrogen (X⁻⋯HC) and the anion-carboxyl (X⁻⋯HOC) distances increase by 0.217 and 0.196 Å (X = Br), and by 0.470 and 0.528 Å (X = I), respectively, as compared to [Tyr+Cl]⁻. These species are only 2.1 kJ mol⁻¹ (X = Br) and 6.8 kJ mol⁻¹ (X = I) higher in energy relative to their respective global minima (**TBr_phe1** and **TI_phe1**), 5.6 and 5.3 kJ mol⁻¹ more favourable than their respective terminal isomers (**TBr_ter1** and **TI_ter1**), and 13.2 and 11.6 kJ mol⁻¹ lower in energy than the lowest energy SB isomers (**TBr_zw1** and **TI_zw1**).

In spite of a careful search, any attempt to localize the halide anion atop the aromatic ring in [Tyr+X]⁻ failed, likely owing to repulsion with the π cloud.

[nitroTyr+X]⁻ (X= Cl, Br, I)

A similar computational analysis has been performed on [nitroTyr+X]⁻ complexes, so attaining the optimized structures depicted in Fig. 3 and Fig. S9 and S10 (X = Cl), Fig. S11 (X = Br) and Fig. S12 (X = I). Here, the presence of the nitro moiety engaged in a

strong hydrogen bond with the ortho hydroxyl group changes the structural landscape, strongly stabilizing anions in plane and terminal configuration with respect to the phenol site (Table S4). Halide binding to the phenolic hydrogen hampers in fact the hydrogen bond with the nitro group.
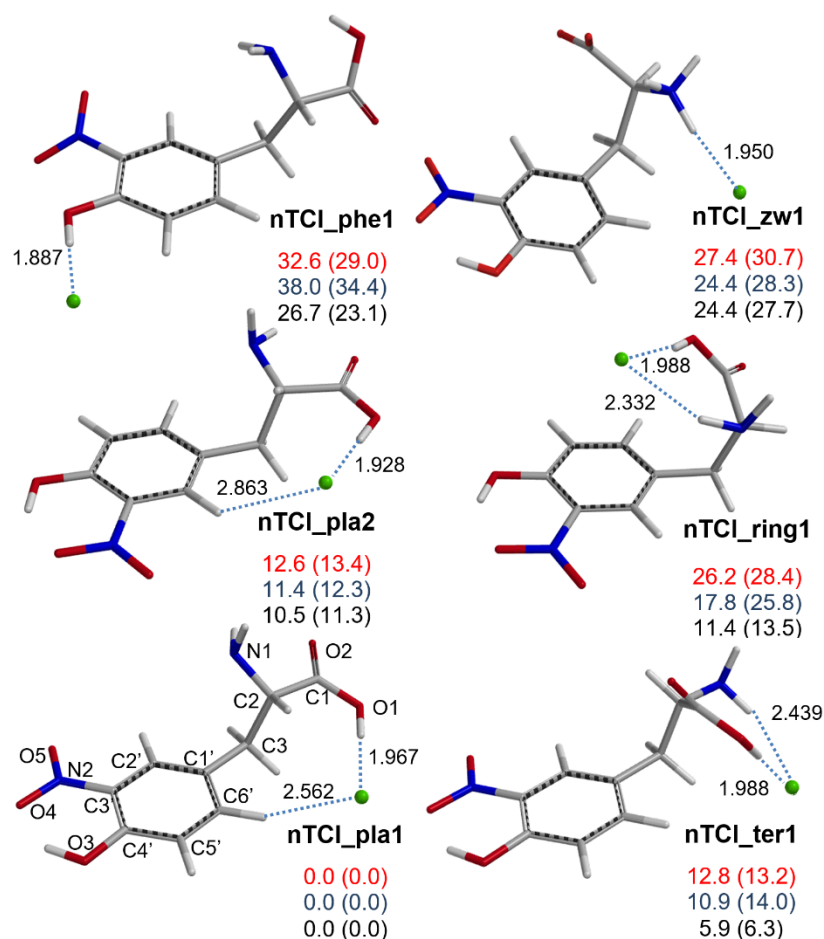
Fig. 3 Optimized geometries for selected isomers of [nitroTyr+Cl]⁻. Relative enthalpies and relative free energies (bracketed) at the B3LYP/6-311++G(d,p) (in red), B3LYP-D3/6-311++G(d,p) (in blue) and MP2//B3LYP/6-311++G(d,p) (in black) levels are provided at 298 K in kJ mol^{-1}. Interatomic bond distances, marked by dashed lines, are reported in Å.

Analogously to [Tyr+Cl]⁻, the global minimum of [nitroTyr+Cl]⁻ is the canonical, *gauche* isomer **nTCl_pla1**, which benefits from a bifurcated C$_{aryl}$H···Cl⁻···HOC(O) hydrogen bonding motif and a NH···O=C interaction, in an arrangement characterized by ∠O1C1C2N, ∠NC2C3C1' and ∠C2C3C1'C2' dihedral angles of 159.1°, -66.0° and 101.2°, respectively (Table S5). The rotation of 180° around the

C$_{aryl}$-C bond weakens this arrangement by 11.3 kJ mol^{-1} likely due to the coordination of chloride to an aromatic hydrogen made less acid by interaction with the vicinal nitro moiety (**nTCl_pla2**). The lowest energy terminal structures **nTCl_ter1** and **nTCl_ter3** (shown in Fig. 3 and S9, respectively), which feature a bidentate interaction of chloride with the carboxylic acid and the amine group, lie 6.3, and 16.8 kJ mol^{-1} above **nTCl_pla1**, respectively. Their *anti* arrangement modifies the ∠O1C1C2N, ∠NC2C3C1' dihedral angles to -56.3°, -178.3° (**nTCl_ter1**), and -55.2°, -175.8° (in **nTCl_ter3**), respectively. Interestingly, the position of the ring substituents relative to the side chain is almost irrelevant, as evident in the couple **nTCl_ter3** / **nTCl_ter4** (Fig. S9).Other terminal conformers adopt a *gauche* arrangement. Among these, **nTCl_ring1** and **nTCl_ring2** (Fig. 3 and S9, respectively), represent the first examples of ring-terminal structures identified herein, where the anion is placed above the center of the ring, showing an anion-π interaction (Fig. 3). Likely, the addition of the electron-withdrawing nitro substituent to the aryl ring yields a π-acidic unit that enables chloride to interact with the π-system besides the amino and carboxylic groups (**nTCl_ring1**) or only with the amino site interacting in turn with the carboxylic hydroxyl group (**nTCl_ring2**). However, the two structures result 7.2 and 26.0 kJ mol^{-1} respectively less favourable than **nTCl_ter1** and should thus be minor contributor to the spectra of [nitroTyr+Cl]$^-$ adduct. Conversely, similar binding motifs have already been found to contribute to the IRMPD spectra of halide-bound ring-fluorinated phenylalanine anions.[18]

Conversely, coordination at the phenol site, which prevents the formation of the strong intramolecular OH···ONO hydrogen bond, significantly reduces the stability, as observed for isomer **nTCl_phe1**, lying 23.1 kJ mol^{-1} above **nTCl_pla1**. This observation is in marked contrast with halide-tyrosine complexes, where binding at the phenol site is expected to contribute significantly to the ion population.

SB structures of [nitroTyr+Cl]$^-$ have been also identified, the lowest energy one among them (**nTCl_zw1**) is 27.7 kJ mol^{-1} higher in energy than the global minimum **nTCl_pla1**, a comparatively much larger energy difference than the 14.1 kJ mol^{-1} value found for the corresponding couple **TCl_pla1**/ **TCl_zw1** of [Tyr+Cl]$^-$ adduct/ in the tyrosine complex.

Deprotonation at the phenol function has been also explored and found much less favorable, with **nTCl_O1** predicted to be 81.8 kJ mol^{-1} above the global minimum **nTCl_pla1**, which does not support its contribution to any significant extent in the probed ion population.

Due to the relatively close gas-phase acidities of 2-nitrophenol, tyrosine and HCl, all within 4 kJ mol^{-1} of each other,[61] we have hypothesized a structure where the phenolic hydrogen has moved to the chloride anion so that the ensuing HCl is now involved in a hydrogen bridging interaction with both the oxygen atoms of the nitro and the phenoxide groups. However, a local minimum could not be found by geometry optimization using either the B3LYP or B3LYP-D3 functionals. Eventually, the structure ended in the transition state (**ST-1**) located along the coordinates of the proton translational reaction from an initial geometry showing a bisected hydrogen bond to the one observed in **nTCl_phe1** (Fig. S10). The imaginary frequency shows in fact displacement of H towards the phenoxide oxygen leading to a structure resembling **nTCl_phe1**.

Overall, the same trend holds for [nitroTyr+X]$^-$ (X= Br, I) with plane and terminal structures as the lowest energy isomers, ring configurations identified as local minima stabilized by anion-π effects, and phenol functionality as the least favorable binding site (Table S4-5; Fig. S11 and S12). Interestingly, it emerges that the more charge diffuse iodide significantly narrows the energy gaps inside the whole set of [nitroTyr+I]$^-$ species, with the lowest energy zwitterion isomer (**nTI_zw1**) only 2.4 kJ mol^{-1} above the phenol structure (**nTI_phe1**).

Spectral assignment

[Tyr+X]$^-$ (X = Cl, Br, I)

In order to ascertain the structural features of the sampled ion population, experimental IRMPD spectra, which mainly reflect the absorption of the first resonant IR photon, have been recorded and compared with the theoretical IR spectra for the lowest energy representative geometries of [Tyr+Cl]$^-$. The comparison covers both the IR fingerprint (Fig. 4) and OH/NH stretching (Fig. S13) ranges. A comprehensive presentation of the IR spectra of the other identified [Tyr+Cl]$^-$ structures (Fig. S6) is provided in Fig. S14. For a more quantitative

evaluation, the positions and intensities of the major IRMPD features are presented in Table S6, along with the computed IR transitions for the lowest energy structures, **TCl_pla1**, **TCl_phe1**, **TCl_ter1**, and **TCl_ter2**, and a brief mode description.
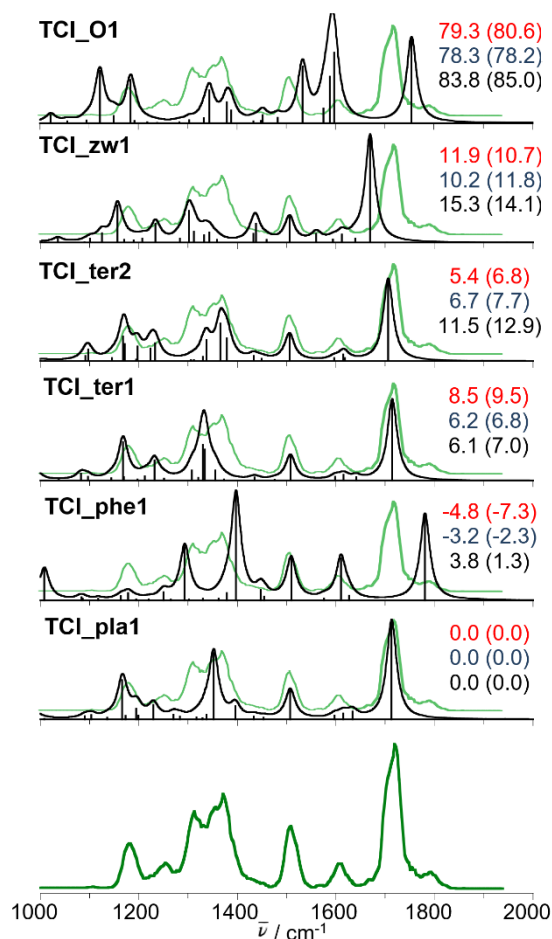
Fig. 4 Experimental IRMPD spectrum (green profile) of chloride-bound tyrosine adduct, [Tyr+Cl]⁻, compared with IR spectra for **TCl_pla1**, **TCl_phe1**, **TCl_ter1**, **TCl_ter2**, **TCl_zw1** and **TCl_O1** structures obtained at the B3LYP/6-311++G(d,p) level of theory and scaled by a factor of 0.978. The y-axis is the same for all theoretical IR spectra. The pale green profile reports the experimental [Tyr+Cl]⁻ spectrum. Relative enthalpies and relative free energies (bracketed) at the B3LYP/6-311++G(d,p) (in red), B3LYP-D3/6-311++G(d,p) (in blue) and MP2//B3LYP/6-311++G(d,p) (in black) levels are provided at 298 K in kJ mol⁻¹.

From the comparative inspection of Fig. 4, it emerges clearly that [Tyr+Cl]⁻ does not conform to a single structure, but rather exists as a mixture of at least two low-lying canonical structures. All the main IRMPD absorptions in the mid-IR region find a counterpart in the features of the lowest energy plane and phenol isomers (Table

S6), in agreement with their relative Gibbs energies (Table S2). The prominent, structured absorption observed at 1720 cm^{-1}, may be assigned to the υ(C=O) stretching mode of **TCl_pla1**, calculated at 1713 cm^{-1}, but also compatible with the analogous absorptions of the terminal structures **TCl_ter1** and **TCl_ter2** predicted at 1714 and 1706 cm^{-1}, respectively. The carbonyl stretching mode of either plane or terminal species is significantly redshifted when compared to protonated or potassiated tyrosine, presenting a feature at 1757 and 1744 cm^{-1}, respectively.[28, 45] Conversely, the shoulder at 1790 cm^{-1} agrees with only the υ(CO) predicted at 1781 cm^{-1} for **TCl_phe1**, a structure bearing an almost unperturbed C=O group. In addition, the IR spectra of SB structures present strong discrepancy, being characterized by the intense antisymmetric carboxylate stretch of **TCl_zw1**, expected at 1669 cm^{-1}, signature of deprotonation at the carboxylic moiety, and the υ(CO) of **TCl_O1**, blue-shifted at 1754 cm^{-1}, both inconsistent with experimental evidence. Although the zwitterionic **TCl_O1** structure is high in energy, it is interesting to note that its participation to the sampled ion population can be ruled out, based on the IRMPD spectra. In fact, ESI may deliver in the gas phase so-called kinetically trapped species, endowed with significant stability in solution, like zwitterionic structures.

The band observed at 1178 cm^{-1} arises from the phenolic OH bend, expected for **TCl_pla1** at 1166 cm^{-1}, and for **TCl_ter2** at 1171 cm^{-1}, besides the carboxylic COH bending mode coupled with NH$_2$ wagging, contributed by the **TCl_pla1** and **TCl_phe1** modes predicted at 1194 and at 1178 cm^{-1}, respectively, and compatible with the **TCl_ter2** band at 1197 cm^{-1}. The IRMPD absorption at 1250 cm^{-1} is consistent with the phenolic OH bend of **TCl_phe1**, and **TCl_ter2**, calculated at 1250 and 1223 cm^{-1}, respectively, and ring deformation of **TCl_pla1** and **TCl_ter2**, expected at 1230-1233 cm^{-1}. The envelope of intense bands between 1300 and 1400 cm^{-1} mainly comprises the ring deformation of **TCl_phe1**, predicted at 1293 cm^{-1}, the COH bending of **TCl_pla1, TCl_phe1** and **TCl_ter2**, calculated at 1352, 1397, and 1337 cm^{-1}, respectively, the COH bending mode coupled with NH$_2$ twisting of **TCl_ter2**, expected at 1365 cm^{-1}, and the CH bend of **TCl_pla1** and **TCl_ter2**, calculated at 1395 and 1379 cm^{-1}, respectively. At higher frequencies, the

feature at 1503 cm^{-1} represents the CH bending of **TCl_phe1**, and **TCl_pla1**, and **TCl_ter2**, predicted at 1506-1509 cm^{-1}, while the band at 1608 cm^{-1} is mostly due to ring deformation of **TCl_phe1**, expected at 1615 cm^{-1}. Noteworthy is the absence in the IRMPD spectrum of detectable peaks for: i) the NH$_3$ umbrella mode, expected at 1438 cm^{-1} for **TCl_zw1**, and at 1594 cm^{-1} for **TCl_O1**; ii) the phenoxide C-O stretching coupled to ring CC stretching for **TCl_O1**, signature of deprotonation at the phenol functionality, predicted at 1533 and 1580 cm^{-1}; iii) the coupled CH and NH$_3$ bending modes calculated at 1121 cm^{-1} for **TCl_zw1**.[27]

Table 1 Experimental IRMPD resonances and calculated (at B3LYP/6-311++G(d,p) level of theory) vibrational frequencies for the low-lying isomers **TCl_pla1**, **TCl_phe1**, **TCl_ter1** and **TCl_ter2** of [Tyr+Cl]$^-$ adduct.

[Tyr+Cl]$^-$					
IRMPD[a]	Calculated[a,b]				Vibrational mode
	TCl_pla1	TCl_phe1	TCl_ter1	TCl_ter2	
1105 (low)	1104 (20)		1083 (32)	1097 (53)	NH$_2$ wagging
1178				1168 (112)	CH in plane bend
	1166 (176)		1168 (172)	1171 (77)	OH phenol bend
	1194 (47)	1178 (33)		1197 (66)	OH carboxyl bend + NH$_2$ wagging
1250		1250 (37)		1223 (57)	OH phenol bend
	1230 (64)		1232 (90)	1233 (80)	ring def
	1270 (21)				NH$_2$ twist
1312		1293 (238)	1307 (45)		ring def
1358	1336 (22)				CH in plane bend
	1352 (293)		1329 (159)	1337 (96)	OH carboxyl bend
			1334 (138)		OH carboxyl bend+OH phenol bend
				1365 (168)	COO-H bend + NH$_2$ twisting
1376		1378 (32)			OH phenol bend
	1395 (60)		1355 (46)	1379 (102)	CH bend
		1397 (474)			OH carboxyl bend
1451		1447 (46)			OH phenol bend
1507	1507 (132)	1509 (185)	1507 (113)	1506 (120)	CH in plane bend
1608	1615 (26)	1610 (190)	1626 (26)	1615 (29)	ring def
	1633 (35)	1627 (22)			NH$_2$ scissor
1720	1713 (442)		1714 (364)	1706 (368)	C=O stretch
1790		1781 (389)			C=O stretch
	2710 (1871)		2850 (1705)	2759 (1879)	OH carboxyl stretch
		2751 (2962)			OH phenol stretch
			2918 (38)		

					CH stretch
	2898 (32)	2884 (29)			CH$_2$ symm stretch
	2994 (44)	2998 (21)		2994 (32)	CH asymm stretch
3008	3004 (42)		3005 (29)		CH symm stretch
3060	3046 (21)	3037 (32)			CH symm stretch
3200		3242 (343)			OH carboxyl stretch
3272			3239 (218)	3242 (209)	NH$_2$ symm stretch
3330			3381 (20)	3368 (25)	NH$_2$ asymm stretch
3663	3676 (45)		3680 (48)	3671 (47)	OH phenol stretch

^{a} In cm^{-1}. ^{b} The reported intensities given in parentheses are in km mol^{-1}. Bands with an intensity lower than 20 km mol^{-1} are not included. Frequencies are scaled by a factor of 0.978.

In the high-energy portion of the spectrum (2800-3800 cm^{-1}), a prominent and sharp peak centered at 3663 cm^{-1} faithfully reproduces the phenol OH stretch not engaged in hydrogen bonding and theoretically predicted at 3676 cm^{-1} for the lowest energy isomer **TCl_pla1** (Fig. S13). This band may also include contributions from the terminal species **TCl_ter1** and **TCl_ter2**, calculated at 3680 and 3671 cm^{-1}, respectively. At lower frequency, the spectrum appears rather flat, with few weak and broad resonances around 3000 cm^{-1} and 3200 cm^{-1}, where the peaks for ring CH stretches (for both **TCl_pla1** and **TCl_phe1**) and carboxylic OH stretch involved in hydrogen bonding with the amino group (for **TCl_phe1**) are expected. However, the integrated area under these wide features is not negligible, and seems to confirm a substantial contribution from the plane (major) and phenol and/or terminal (minor) structures to the sampled ion population. In all cases the NH$_2$ (a)symmetric stretches hardly emerge from the background due to their low intensity (Table 1). Both the carboxylic (**TCl_pla1**) and phenolic (**TCl_phe1**) OH stretches coordinated to the anion are expected to display a marked redshift (below 2800 cm^{-1}), thus falling out of the accessible range (Table S6). Also very similar is the IR spectrum of the lowest energy SB species (**TCl_zw1**), which however should not be populated, according to theoretical predictions. Overall, although this region is not very sensitive to the structural features, and may suffer from red-shift and broadening owing to anharmonicity and nonlinear effects. However, it provides evidence for a free phenolic OH, fully consistent with an important contribution of a plane structure to the [Tyr+Cl]$^-$ spectrum.

All these results taken together indicate **TCl_pla1** and **TCl_phe1** as the most probable chloride-bound tyrosine isomers. However, the terminal isomers **TCl_ter1** and **TCl_ter2**, whose IR spectra fit large energy regions, cannot be excluded spectroscopically nor distinguished from the **TCl_pla1** isomer. However, based on relative energies, **TCl_ter1** and **TCl_ter2** should not represent a significant part of the ion population sampled at 298 K. Accordingly, the thermally averaged spectrum of [Tyr+Cl]⁻ adduct, obtained by considering contributions from all thermally accessible structures according to their relative free energy values, is also presented for comparison in Fig. S15.
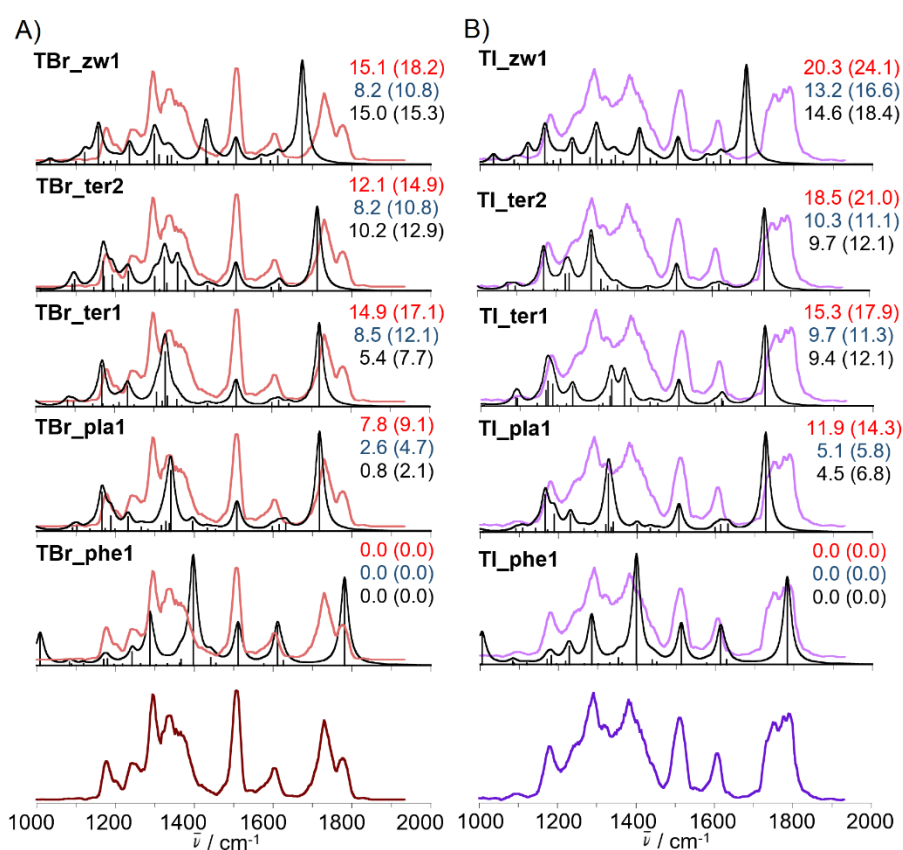
Fig. 5 Experimental IRMPD spectrum of: [Tyr+Br]⁻ (brown profile, panel A) compared with IR spectra [km mol⁻¹] for **TBr_phe1**, **TBr_pla1**, **TBr_ter1**, **TBr_ter2**, and **TBr_zw1** structures; [Tyr+I]⁻ (purple profile, panel B) compared with IR spectra [km mol⁻¹] for **TI_phe1**, **TI_pla1**, **TI_ter1**, **TI_ter2**, and **TI_zw1** structures. Theoretical vibrational modes were obtained at the B3LYP/6-311++G(d,p) level of theory and scaled by a factor of 0.978. The y-axis is the same for all theoretical IR spectra. Relative enthalpies and relative free energies (bracketed) at the B3LYP/6-311++G(d,p) (in red), B3LYP-D3/6-311++G(d,p) (in blue) and MP2//B3LYP/6-311++G(d,p) (in black) levels are provided at 298 K in kJ mol⁻¹.

The mid-IR spectra of [Tyr+Br]⁻ and [Tyr+I]⁻, which present many resemblances with [Tyr+Cl]⁻, are compared with the calculated spectra of their lowest energy representative structures in Fig. 5. The major IRMPD bands are given in Table S6 along with the calculated frequencies of the low-lying phenol (**TCl_phe1**), plane (**TCl_pla1**), and terminal (**TCl_ter1** and **TCl_ter2)** structures, which allow the assignment of vibrational modes. As in the case of [Tyr+Cl]⁻, it turns out that an admixture of the lower energy **TCl_phe1** and **TCl_pla1** isomers dominate the IRMPD spectra of both [Tyr+Br]⁻ and [Tyr+I]⁻. However, the significantly stronger intensity of the υ(CO) at ca. 1790 cm^{-1} that emerges with increasing halide ion size reflects the progressive depletion of **TCl_pla1** relative to **TCl_phe1** in the isomeric population (Table S2) corroborated in the best way by the computational results at MP2 level.In agreement with the different relative energies of the [Tyr+X]⁻ (X = Cl, Br, I) complexes, the fingerprint IRMPD spectra reflect their anion-dependent structures. Any relevant contribution of the higher energy [Tyr+X]⁻ isomers can be spectroscopically ruled out (Fig. S14).

In the NH/OH stretch spectral region (Fig. S13), the sharp feature at 3664 cm^{-1} in the spectrum of [Tyr+Br]⁻ is associated to the free ring hydroxyl group of plane (**TBr_pla1**), but it is also compatible, as for [Tyr+Cl]⁻, with a terminal arrangement (**TBr_ter1** and **TBr_ter2**) and a SB species (**TBr_zw1**), which should be ruled out on energetic grounds. Interestingly, the higher contribution of the phenol structures in [Tyr+Br]⁻ vs [Tyr+Cl]⁻ ion populations, as deduced from relative energy and mid-infrared spectroscopic evidence, may be responsible for the larger integrated area of the broad feature detected below 3300 cm^{-1} for [Tyr+Br]⁻.

In order to provide a deeper understanding of the solvation processes, the bonding features in complexes between neutral hydrogen donors (HR) and halide anions, [X⁻+HR], have been largely investigated in the gas phase.[62] It was thus assessed that the binding energy depends on the Brønsted acidity of HR. In particular, the binding energy was found to decrease from the smaller and more basic fluoride ion[63] to the larger and less basic chloride and iodide anions,[64-65] in parallel with the decreasing extent of covalent vs increasing fraction of electrostatic character of the bonding interaction. Accordingly, in the present study Cl⁻, prone to engage in a stronger

hydrogen bond, shows a clear bias toward the carboxylic site of tyrosine, which is relatively more acid than the phenol group, so favouring **TCl_pla1** vs **TCl_phe1**. In contrast, the less energetic interaction of I⁻, due to the larger size, makes the coordination at the two acid functionalities of tyrosine comparably favored.[66]

Interestingly, an evident correlation between the vibrational red-shift of the CH, NH, and OH stretching mode in substituted benzenes (SB), the acidity of the aromatic molecule and the elongation of the H-bonded group has been also reported for Cl⁻-SB complexes studied by vibrational predissociation spectroscopy.[67] An additional signature of the different strength of the halide-carboxyl contact within [Tyr+X]⁻ is the anion size-dependent red-shift of the carbonyl stretching mode. This evidence, already pointed out in other halide-bound as well as metallated amino acids,[19,68,69] has been related to the positive interaction of the carbonyl dipole moment with the ion's electric field (Stark effect), in addition to the increase in partial carboxylate character when raising the basicity from I⁻ to Br⁻ up to Cl⁻ anion.

[nitroTyr+X]⁻ (X = Cl, Br, I)

In Fig. 6, the experimental IRMPD spectrum of [nitroTyr+Cl]⁻ in the explored mid-IR range is presented along with the linear IR spectra of the low-lying canonical species, gauche plane (**nTCl_pla1**); terminal-*left* (**nTCl_ter1**); gauche, ring-terminal (**nTCl_ring1**); gauche phenol (**nTCl_phe1**); and the SB structure deprotonated at the carboxylic site (**nTCl_zw1**). A direct comparison reveals that above 1400 cm⁻¹ there is a rather good agreement between the main experimental absorptions and the computed spectra of both lowest energy isomers **nTCl_pla1** and **nTCl_ter1**, whose features are instead quite complementary in the 1000-1400 cm⁻¹ range. Vibrational assignments of low-lying **nTCl_pla1**, **nTCl_ter1** and **nTCl_ring1** are reported in Table S7.
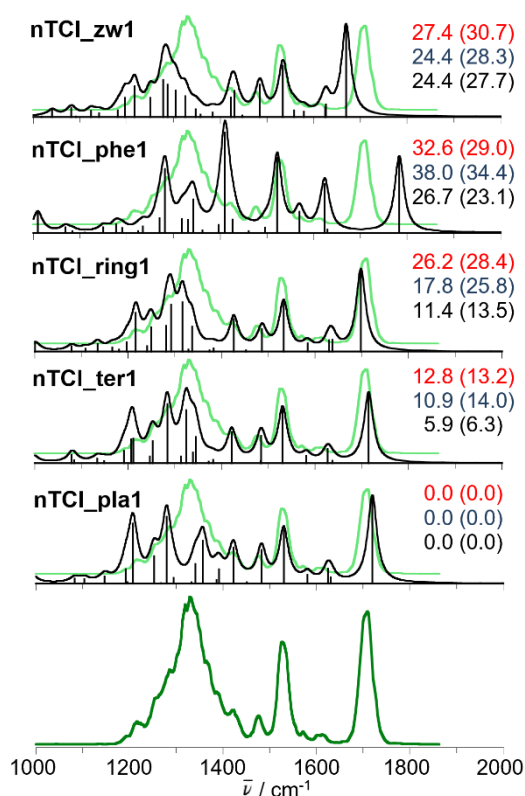
Fig. 6 Experimental IRMPD spectrum (green profile) of chloride-bound 3-NO$_2$-tyrosine adduct, [nitroTyr+Cl]$^-$, compared with IR spectra [km mol^{-1}] for **nTCl_pla1**, **nTCl_ter1**, **nTCl_ring1**, **nTCl_phe1** and **nTCl_zw1** structures obtained at the B3LYP/6-311++G(d,p) level of theory and scaled by a factor of 0.978. The y-axis is the same for all theoretical IR spectra. The pale green profile reports the experimental [nitroTyr+Cl]$^-$ spectrum. Relative enthalpies and relative free energies (bracketed) at the B3LYP/6-311++G(d,p) (in red), B3LYP-D3/6-311++G(d,p) (in blue) and MP2//B3LYP/6-311++G(d,p) (in black) levels are provided at 298 K in kJ mol^{-1}.

The band appearing at 1710 cm^{-1} is a clear signature of a carbonyl stretch predicted at 1720 cm^{-1} for **nTCl_pla1** and at 1715 cm^{-1} for **nTCl_ter1**, although its moderate width (Fwhm=40 cm^{-1}) suggests that **nTCl_ring1**, whose CO group is expected as low as 1698 cm^{-1}, might be also populated under our experimental conditions. The observed redshift of the carbonyl stretching mode by ca. 50 cm^{-1} relative to protonated 3-NO$_2$-Tyrosine[28] is well matched by the difference observed in the spectra of [Tyr+Cl]$^-$ and protonated native Tyrosine. In the range between 1400-1650 cm^{-1}, the **nTCl_pla1**, **nTCl_ter1** and **nTCl_ring1** isomers have very similar IR absorption spectra which fully fit with the experiment. According to Table S7, the

294

strong absorbance at 1528 cm^{-1} is due to asymmetric NO$_2$ stretch, the features at 1423 and 1475 cm^{-1} are attributed to NO stretch combined with in plane bending of the ring OH group and CH bending, respectively, and the weak peak at 1610 cm^{-1} corresponds to ring deformation.

At lower frequency, an envelope of unresolved absorbances is responsible for the strong, broad band centered at 1330 cm^{-1}, whose resolution was not improved by the use of attenuators. This complex feature includes the intense CN stretch coupled with in plane CH bending, the phenol OH bending combined with in plane CH bending, the strongly active phenol OH bending, the ring deformation, and the OH carboxylic bending, besides the NH$_2$ twisting. For **nTCl_pla1**, these modes are predicted at 1207, 1252, 1280, 1341, 1357, and 1392 cm^{-1}, respectively. However, the centroid of the envelope cannot be accounted for, based only on this isomer, but likely arises from **nTCl_ter1** as well, where the OH carboxylic bending redshifted at 1324 cm^{-1} and the CH$_2$ wagging predicted at 1344 cm^{-1} nicely complement the previous assignment in interpreting the experimental band. In addition, although energetically less favorable, the presence of **nTCl_ring1** cannot be discarded due to resemblance with large portion of the IRMPD spectrum.

Clear marks that coordination has not occurred at the phenol site (**nTCl_phe1**) nor that SB isomers (**nTCl_zw1**, **nTCl_zw1**, and **nTCl_O1**) can appreciably contribute to the ion population derive from the evidence that none of these structures have calculated spectra that match the experimental spectrum (Fig. 6). Comparison with other computed structures shown in Fig. S16 suggests that they do not appreciably contribute to the sampled ion population.

The IRMPD spectra of [nitroTyr+Br]$^-$ and [nitroTyr+I]$^-$ are presented against the IR spectra of the lowest energy species, the canonical isomers **nTBr_pla1**, **nTBr_ter1**, **nTBr_ring1**, **nTBr_ter2** and **nTI_pla1**, **nTI_ter1**, **nTI_ring1**, **nTI_ter2**, respectively (Fig. S17). In both cases, and similarly to [nitroTyr+Cl]$^-$, it turns out that a mixture of **nTBr_pla1** (**nTI_pla1**) and **nTBr_ter1** (**nTI_ter1)** are likely present in the ESI sampled ion population. Interestingly, the strong absorbance due the carbonyl stretch at 1733 cm^{-1} (X = Br) and 1743 cm^{-1} (X = I) is structured with a weak peak on the red side at 1698 and 1705 cm^{-1}, respectively, that may be related to the contribution of

nTBr_ring1 (**nTI_ring1**), expected at relatively lower concentration. According to the IR spectra presented in Fig. S18, any appreciable contribution of other higher energy structures can be safely ruled out.

Overall, although the anion size shows little consequence on the adopted arrangement of [nitroTyr+X]$^-$ (X = Cl, Br, I), the observed blue shift of the carbonyl stretching mode with increasing anion size confirms that the strength of the contact between the carboxylic hydrogen and the halide decreases, namely with decreasing gas phase basicity of X$^-$.

A.2.4 Conclusions

The halide complexes of both Tyr and nitroTyr reveal a variety of bonding motifs thoroughly explored by computations at three different levels, B3LYP/6-311++G(d,p), B3LYP-D3/6-311++G(d,p), and MP2(full)//6-311++G(d,p)//B3LYP/6-311++G(d,p). The experimental tool to assay the six distinct families of clusters, [Tyr+X]$^-$ and [nitroTyr+X]$^-$ (where X = Cl, Br, I), has relied on vibrational spectroscopy of the mass selected ions obtained by ESI. The IRMPD spectra were analyzed by comparison with the calculated IR spectra for the array of plausible geometries. In the general pattern of various binding motifs the lowest energy and represented structures correspond to 'plane' and 'phenol' geometries. The first class is characterized by the halide engaged in a CH···X$^-$···HOC(O) interaction with both a ring hydrogen and a carboxyl group. In the second coordination mode the halide is simply bound to the hydroxyl function on the aromatic ring. As another possible contribution one should take into account a 'terminal' structure involving only the amino acidic end in the general NH···X$^-$···HOC(O) arrangement. It is interesting to note that the lowest energy geometries, 'plane' and 'phenol', both involve the aromatic ring that is the side chain substituent that remains exposed also when tyrosine is part of a peptide or protein. The PTM yielding nitroTyr strongly affects the properties of the ring, in the first place by competing for hydrogen bonding to the ring OH group. Overall the following major points may be evinced: (i) 'plane' and 'phenol' structures are major contributors to the [Tyr+X]$^-$ ion population; (ii) the relative weight of 'plane' and 'phenol' structures is sensitive to the nature of X, favoring the 'phenol' species with increasing size of X; (iii) the presence of the 3-

296

nitro substituent has a dramatic effect in inhibiting X$^-$ association to the ring OH while also directing the interaction with a ring hydrogen in preferential para position with respect to the electron withdrawing group; (iv) only in the presence of the nitro group, depleting π-electron density, do anion-π interactions play a role as additional binding motif.

Hopefully, an insight is provided into the intrinsic nature of non covalent interactions involving ubiquitous halide ions and Tyr/nitroTyr. Tyrosine residues may line the cavity within biological and synthetic ion channels and the present data show that a variety of binding motifs may be at play and be tuned to achieve specific functioning.
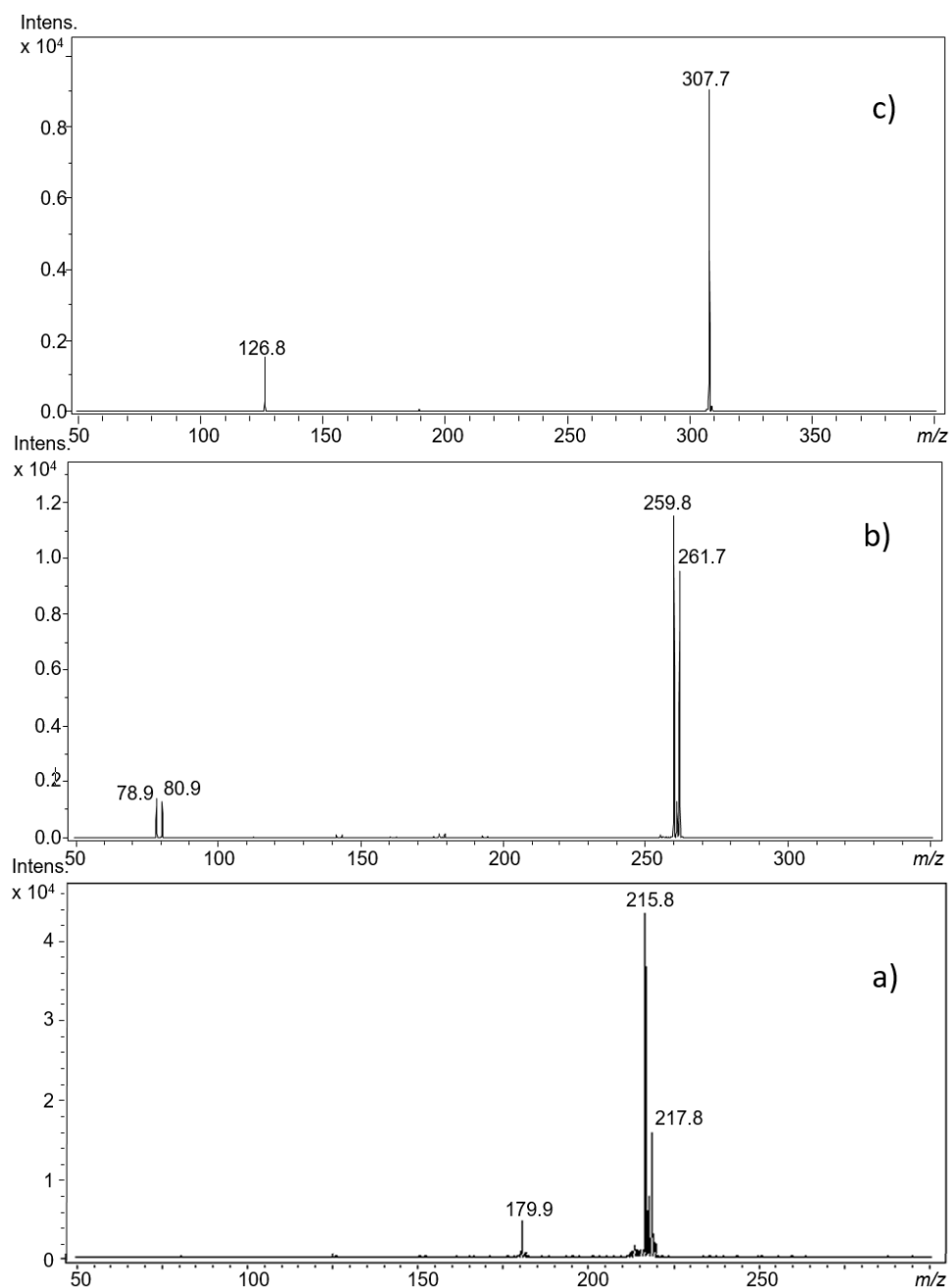
Fig. S1 Negative ESI mass spectra recorded upon selection of halide L-tyrosine adducts, a) [Tyr+Cl]⁻ (*m/z* 216/218); b) [Tyr+Br]⁻ (*m/z* 260/262); and c) [Tyr+I]⁻ (*m/z* 308), upon irradiation with CLIO FEL light on resonance at 1505, 1297, 1177 cm⁻¹, respectively. Spectra recorded in a Bruker Esquire Paul ion trap mass spectrometer (Bruker, Esquire 3000+).
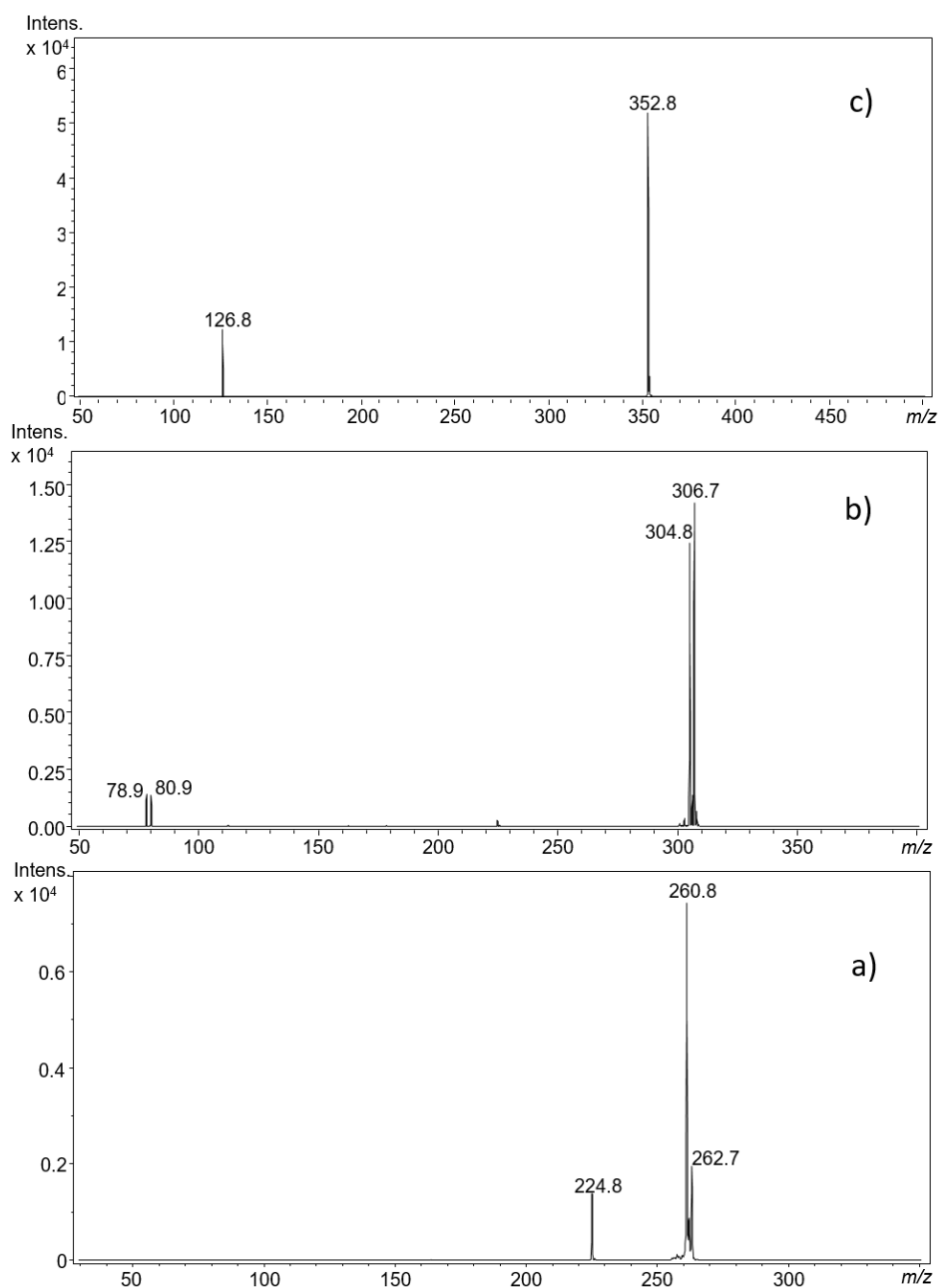
Fig. S2 Negative ESI mass spectra recorded upon selection of halide 3-NO$_2$-L-tyrosine adducts, a) [nitroTyr+Cl]$^-$ (*m/z* 261/263); b) [nitroTyr+Br]$^-$ (*m/z* 305/307); and c) [nitroTyr+I]$^-$ (*m/z* 353), upon irradiation with CLIO FEL light on resonance at 1477, 1325, 1737 cm^{-1}, respectively. Spectra recorded in a Bruker Esquire Paul ion trap mass spectrometer (Bruker, Esquire 3000+).
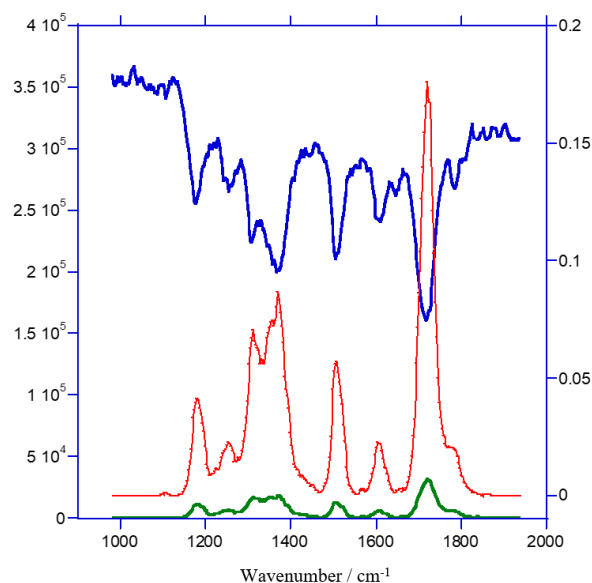
Fig. S3 Experimental IRMPD signals of [Tyr+Cl]⁻ recorded in the parent ion channel depletion ([Tyr+Cl]⁻, blue profile), the fragment ion channel ([Tyr-H]⁻, green profile), and the IRMPD efficiency (*R*, red profile) in the 950-1950 cm⁻¹ range. R scale is on the right vertical axis and ion abundances (in arbitrary units) are on the left vertical axis.
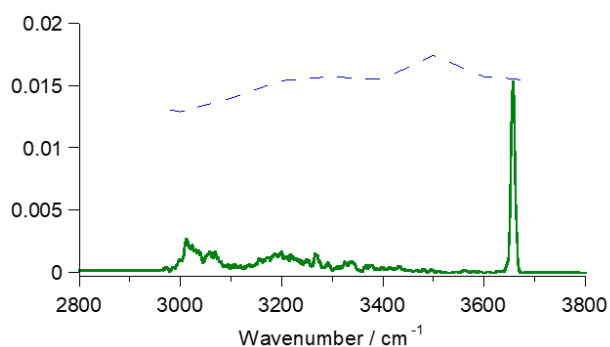
Fig. S4 Experimental IRMPD spectrum of [Tyr+Cl]⁻ (green profile) in the 2800-3800 cm⁻¹ range. The blue dashed profile shows the laser power as a function of the IR wavenumber.
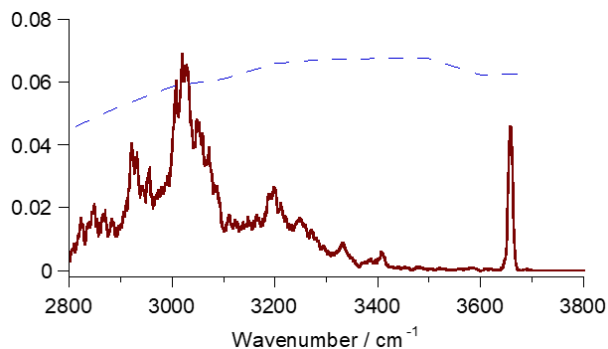
Fig. S5 Experimental IRMPD spectrum of [Tyr+Br]⁻ (brown profile) in the 2800-3800 cm⁻¹ range. The blue dashed profile shows the laser power as a function of the IR wavenumber.
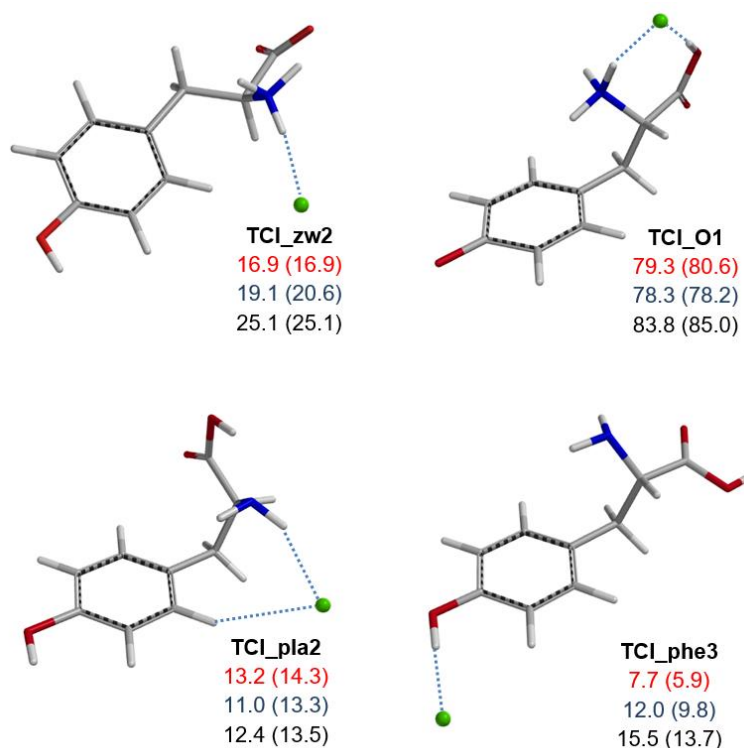
Fig. S6 Optimized minimum energy structures for selected isomers (**TCl_pla2**, **TCl_phe3**, **TCl_zw2**, and **TCl_O1**) of [Tyr+Cl]⁻. Relative enthalpies and relative free energies (bracketed) at the B3LYP/6-311++G(d,p) (in red), B3LYP-D3/6-311++G(d,p) (in blue) and MP2//B3LYP/6-311++G(d,p) (in black) levels are provided at 298 K in kJ mol⁻¹. Thermodynamic data are relative to the calculated energies of the most stable isomer presented in Fig. 2 (**TCl_pla1**). The monodentate **TCl_phe3**, 13.7 5 kJ mol⁻¹ above the global minimum, features chloride coordinated to the phenol site, and a *right*, *gauche* structure, which arises from the rotation about the C1-C2 and O1-C1 bonds of **TCl_phe1**. These changes modify the ∠O1C1C2N dihedral angle to 150.7° for **TCl_phe3** and allows the amino hydrogen to interact with the carbonyl oxygen ($r_{\text{CO...HN}}$ = 2.48 Å) of the carboxylic acid in a *cis* arrangement. The bidentate **TCl_pla2** structure, 13.5 kJ mol⁻¹ above the global minimum is endowed with a *left*, *gauche* geometry, obtained by rotation of C1C2, C2C3, and C2N bonds of **TCl_pla1**, and binds chloride between amine ($r_{\text{Cl...HN}}$ = 2.28 Å) and aromatic ($r_{\text{Cl...HC}}$ = 2.89 Å) hydrogens, while the carboxylic acid in *trans* interacts as a H-bond donor with the N-terminus ($r_{\text{N...HOC}}$ = 1.81 Å). Not unexpectedly, from the above comparison it turns out that the dual CH···Cl···HOC(O) hydrogen-bonding interactions (in **TCl_pla1**) are more beneficial than CH···Cl···HN (in **TCl_pla2**) in stabilizing chloride-bound tyrosine adduct. The **TCl_zw2** conformer, with a more extended conformation than **TCl_zw1** results 25.1 kJ mol⁻¹ less favorable than **TCl_pla1**.
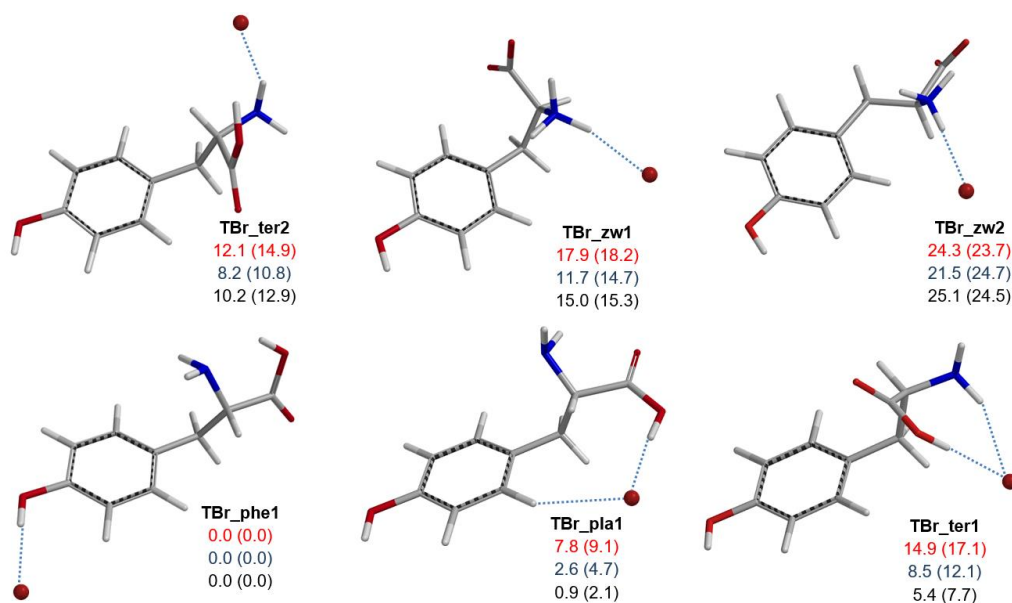
Fig. S7 Optimized minimum energy structures for selected isomers (**TBr_phe1**, **TBr_pla1**, **TBr_ter1, TBr_ter2**, **TBr_zw1**, and **TBr_zw2**) of [Tyr+Br]⁻. Relative enthalpies and relative free energies (bracketed) at the B3LYP/6-311++G(d,p) (in red), B3LYP-D3/6-311++G(d,p) (in blue) and MP2//B3LYP/6-311++G(d,p) (in black) levels are provided at 298 K in kJ mol⁻¹.
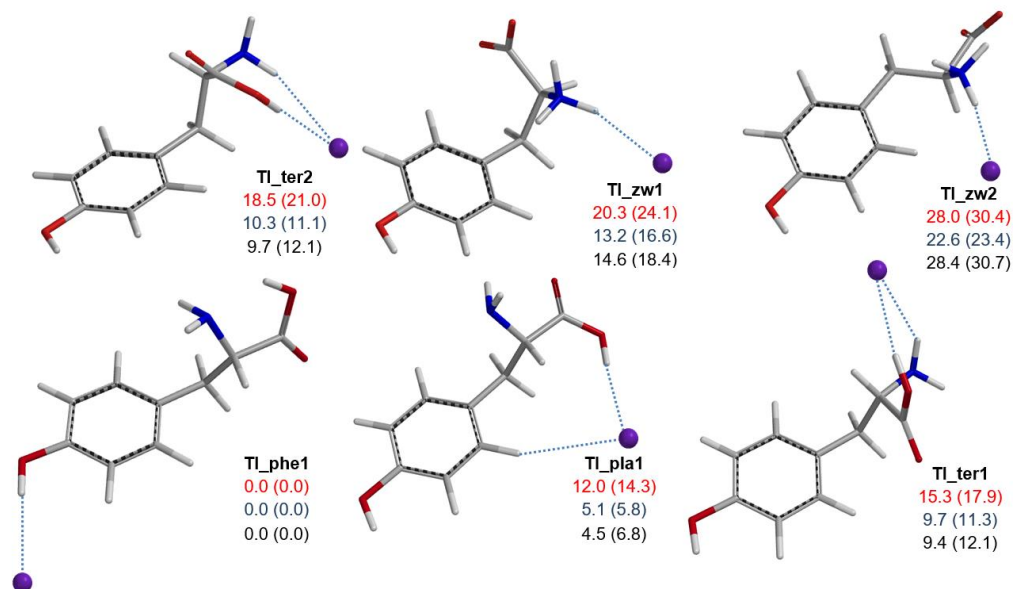
Fig. S8 Optimized minimum energy structures for selected isomers (**TI_phe1**, **TI_pla1**, **TI_ter1**, **TI_ter2**, **TI_zw1**, and **TI_zw2**) of [Tyr+I]⁻. Relative enthalpies and relative free energies (bracketed) at the B3LYP/6-311++G(d,p) (in red), B3LYP-D3/6-311++G(d,p) (in blue) and MP2//B3LYP/6-311++G(d,p) (in black) levels are provided at 298 K in kJ mol⁻¹.
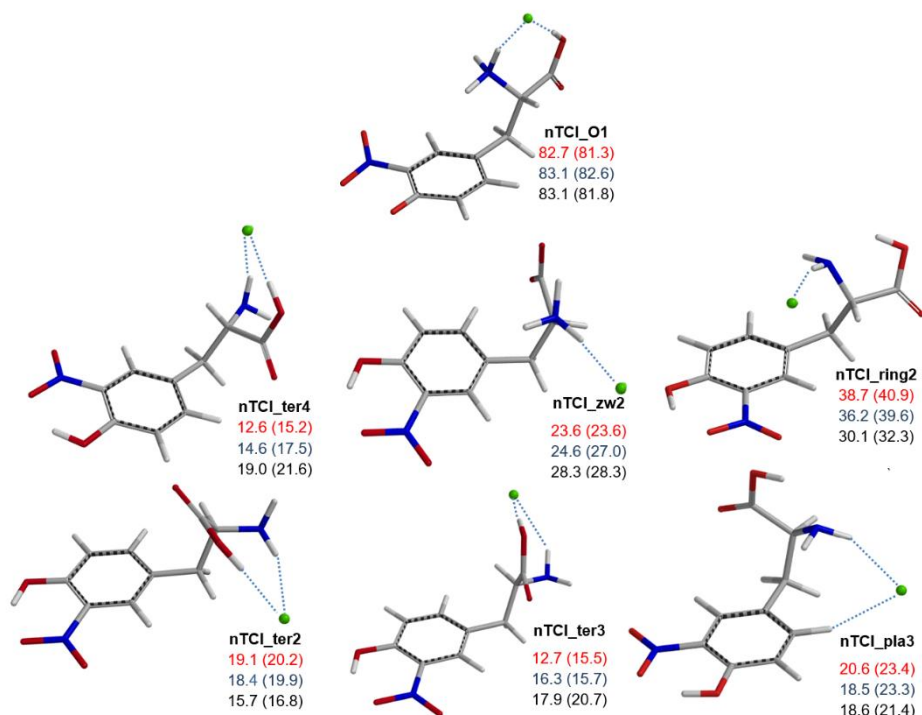
Fig. S9 Optimized minimum energy structures for selected isomers (**nTCl_ter2**, **nTCl_ter3**, **nTCl_pla3**, **nTCl_ter4**, **nTCl_zw2**, **nTCl_ring2**, **nTCl_O1**) of [nitroTyr+Cl]⁻. Relative enthalpies and relative free energies (bracketed) at the B3LYP/6-311++G(d,p) (in red), B3LYP-D3/6-311++G(d,p) (in blue) and MP2//B3LYP/6-311++G(d,p) (in black) levels are provided at 298 K in kJ mol⁻¹. Thermodynamic data are relative to the calculated energies of the most stable isomer presented in Fig. 3 (**nTCl_pla1**).
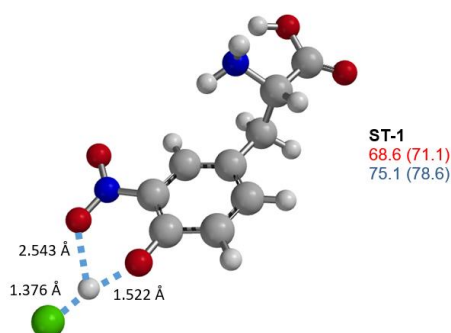
Fig. S10 Optimized geometry deriving from an initial structure whereby HCl is acting as hydrogen bond donor towards both phenoxide oxygen and an oxygen atom of the nitro group. This species (**ST-1**) is not a minimum being characterized by an imaginary frequency. Relative enthalpies and relative free energies (bracketed) at the B3LYP/6-311++G(d,p) (in red), and B3LYP-D3/6-311++G(d,p) (in blue) levels are provided at 298 K in kJ mol⁻¹. Interatomic bond distances, marked by dashed lines, are reported in Å.
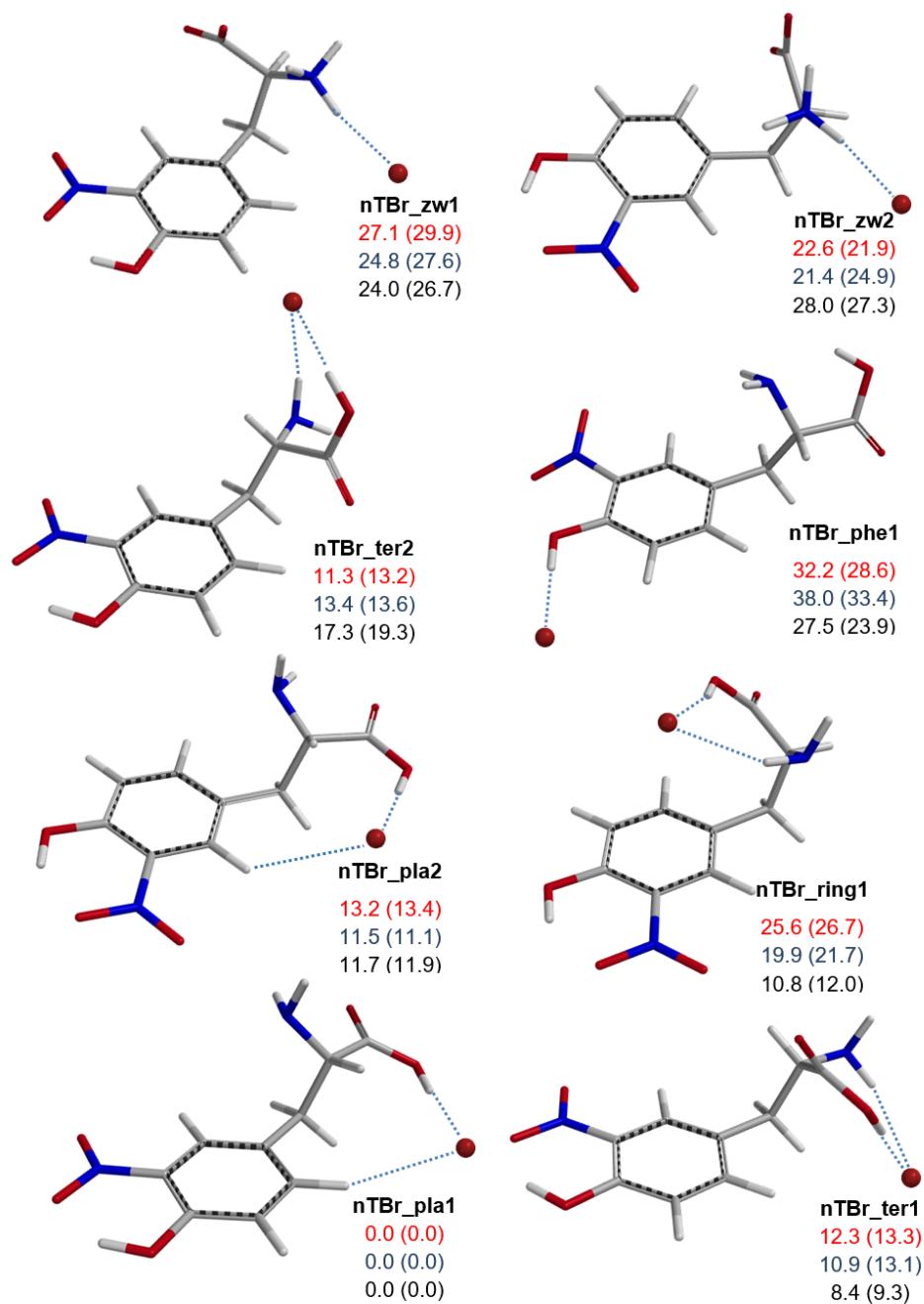
Fig. S11 Optimized minimum energy structures for selected isomers (**nTBr_pla1**, **nTBr_ter1**, **nTBr_pla2**, **nTBr_ring1**, **nTBr_ter2**, **nTBr_phe1**, **nTBr_zw1**, **nTBr_zw2**) of [nitroTyr+Br]$^-$. Relative enthalpies and relative free energies (bracketed) at the B3LYP/6-311++G(d,p) (in red), B3LYP-D3/6-311++G(d,p) (in blue) and MP2//B3LYP/6-311++G(d,p) (in black) levels are provided at 298 K in kJ mol^{-1}.
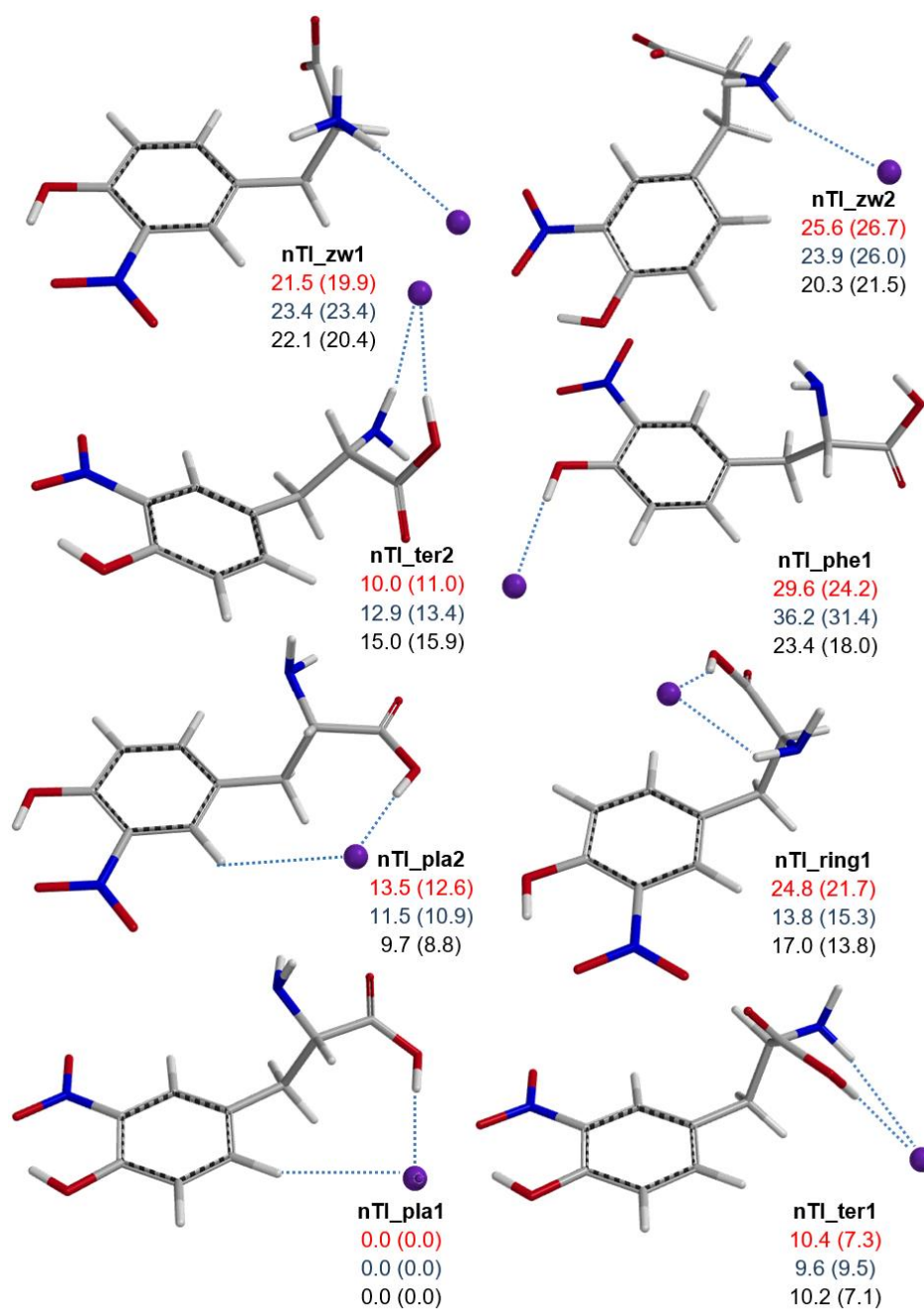
Fig. S12 Optimized minimum energy structures for selected isomers (**nTI_pla1**, **nTI_ter1**, **nTI_pla2**, **nTI_ring1**, **nTI_ter2**, **nTI_phe1**, **nTI_zw1**, **nTI_zw2**) of [nitroTyr+I]$^-$. Relative enthalpies and relative free energies (bracketed) at the B3LYP/6-311++G(d,p) (in red), B3LYP-D3/6-311++G(d,p) (in blue) and MP2//B3LYP/6-311++G(d,p) (in black) levels are provided at 298 K in kJ mol^{-1}.
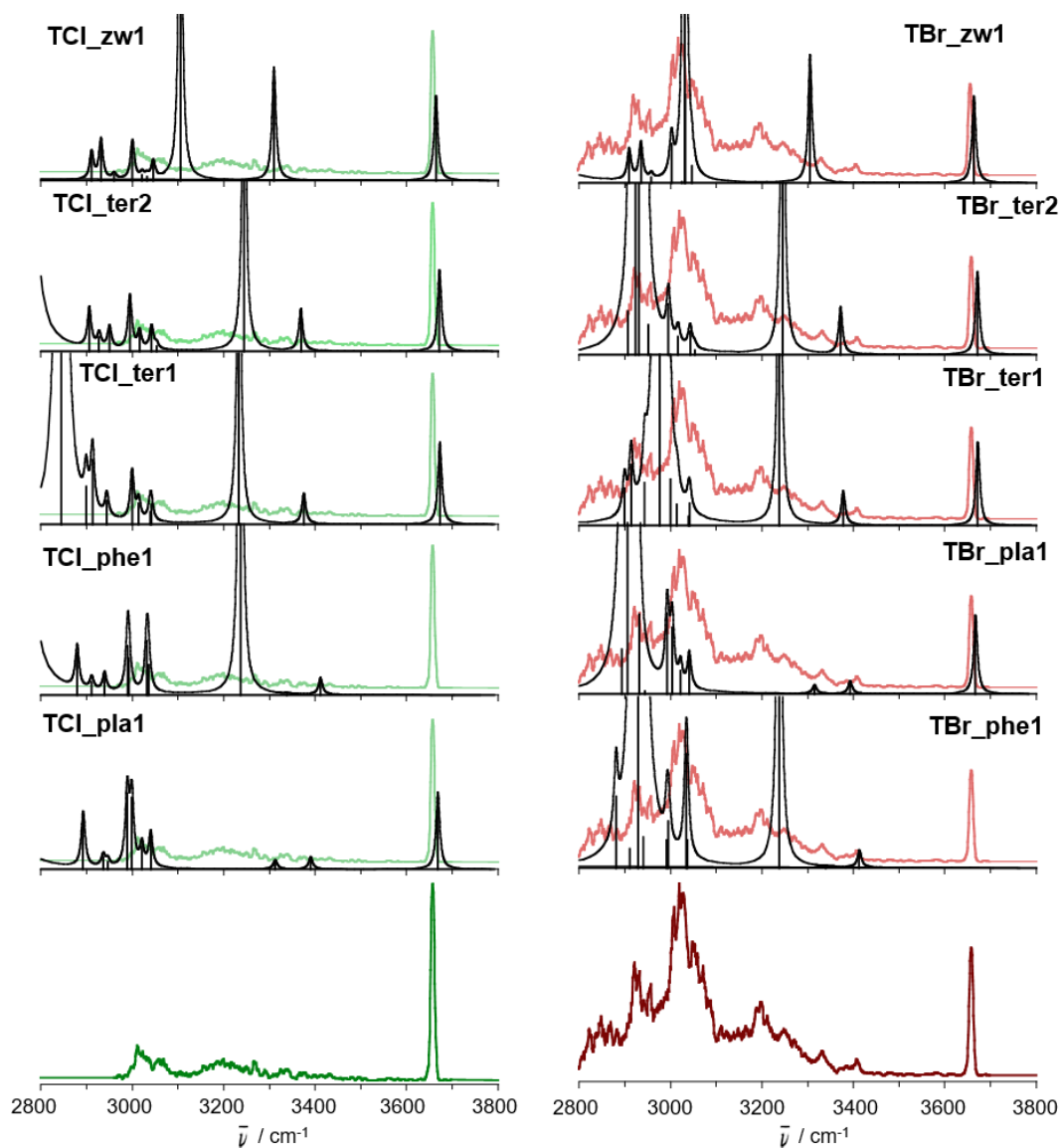
Fig. S13 Experimental IRMPD spectra of [Tyr+Cl]⁻ (green profile) and [Tyr+Br]⁻ (brown profile) in the NH/OH stretch range compared with IR spectra [km mol⁻¹] for **TCl_pla1**, **TCl_phe1**, **TCl_ter1**, **TCl_ter2**, **TCl_zw1** and **TBr_phe1**, **TBr_pla1**, **TBr_ter1**, **TBr_ter2**, **TBr_zw1** structures obtained at the B3LYP/6-311++G(d,p) level of theory and scaled by a factor of 0.955. The pale profiles report the experimental [Tyr+Cl]⁻ (pale green) and [Tyr+Br]⁻ (pale brown) spectra.
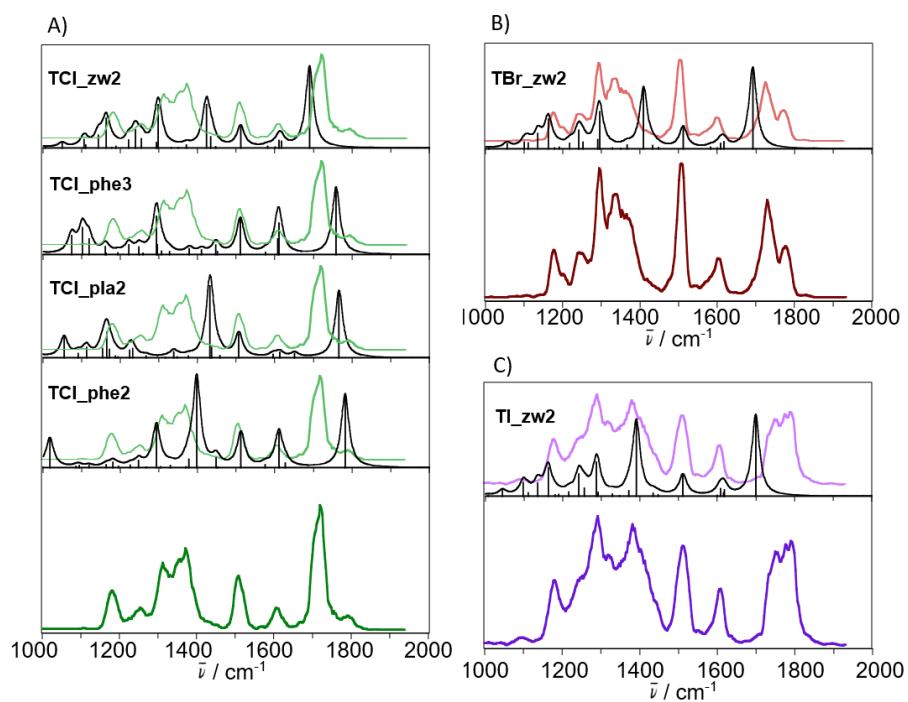
Fig. S14 Experimental IRMPD spectra of: [Tyr+Cl]⁻ (green profile, panel A) compared with IR spectra [km mol⁻¹] for **TCl_phe2**, **TCl_pla2**, **TCl_phe3**, **TCl_zw2** structures; [Tyr+Br]⁻ (brown profile, panel B) compared with IR spectra [km mol⁻¹] for **TBr_zw2**; [Tyr+I]⁻ (purple profile, panel C) compared with IR spectra [km mol⁻¹] for **TI_zw2**. Theoretical vibrational modes were obtained at the B3LYP/6-311++G(d,p) level of theory and scaled by a factor of 0.978.
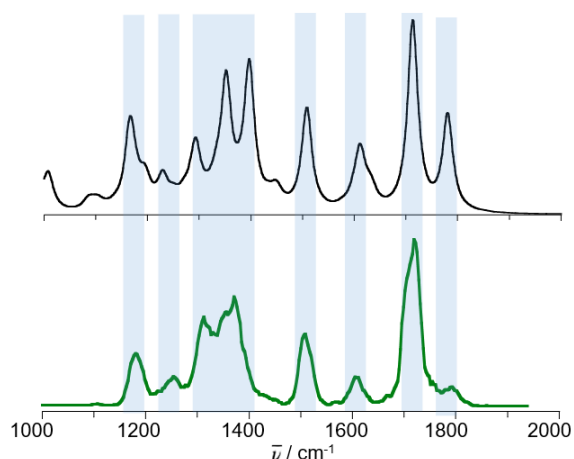
Fig. S15 Averaged spectrum of [Tyr+Cl]⁻ computed from the calculated Boltzmann populations of **TCl_pla1**, **TCl_phe1** and **TCl_ter1** obtained from single-point free energy calculations at MP2//B3LYP/6-311++G(d,p) level. The experimental spectrum (green profile) is also shown to enable comparison.
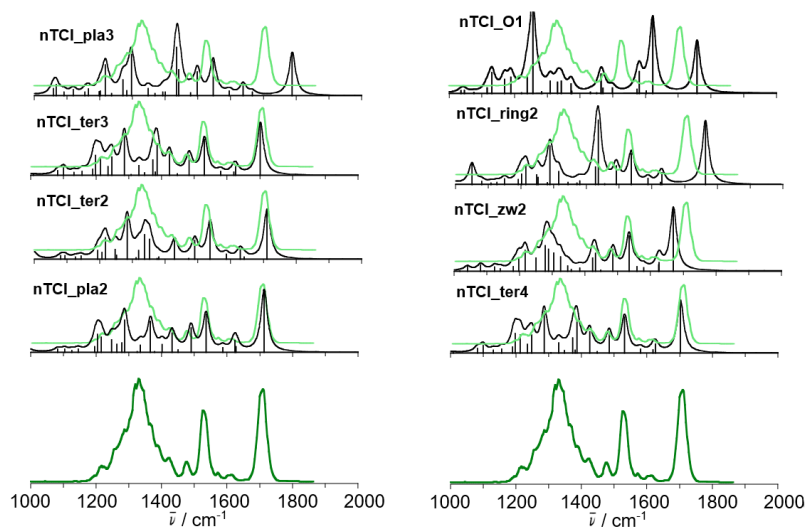
Fig. S16 Experimental IRMPD spectrum (green profile) of chloride-bound 3-NO$_2$-tyrosine adduct, [nitroTyr+Cl]$^-$, compared with IR spectra [km mol^{-1}] for **nTCl_pla2**, **nTCl_ter2**, **nTCl_ter3**, **nTCl_pla3**, **nTCl_ter4**, **nTCl_zw2**, **nTCl_ring2**, **nTCl_O1** structures obtained at the B3LYP/6-311++G(d,p) level of theory and scaled by a factor of 0.978.
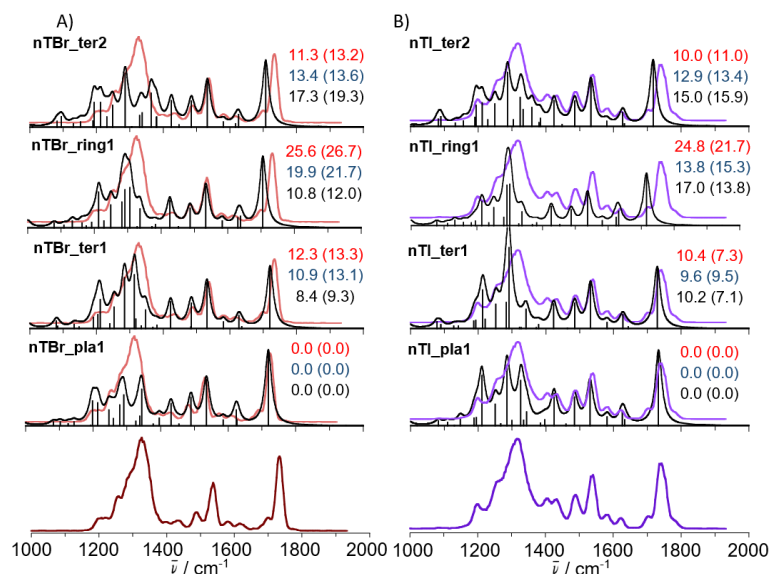
Fig. S17 Experimental IRMPD spectra of: [nitroTyr+Br]$^-$ (brown profile, panel A) compared with IR spectra [km mol^{-1}] for **nTBr_pla1**, **nTBr_ter1**, **nTBr_ring1** and **nTBr_ter2** structures; [nitroTyr+I]$^-$ (purple profile, panel B) compared with IR spectra [km mol^{-1}] for **nTI_pla1**, **nTI_ter1**, **nTI_ring1** and **nTI_ter2** structures. Theoretical vibrational modes were obtained at the B3LYP/6-311++G(d,p) level of theory and scaled by a factor of 0.978. Relative enthalpies and relative free energies (bracketed) at the B3LYP/6-311++G(d,p) (in red), B3LYP-D3/6-311++G(d,p) (in blue) and MP2//B3LYP/6-311++G(d,p) (in black) levels are provided at 298 K in kJ mol^{-1}.
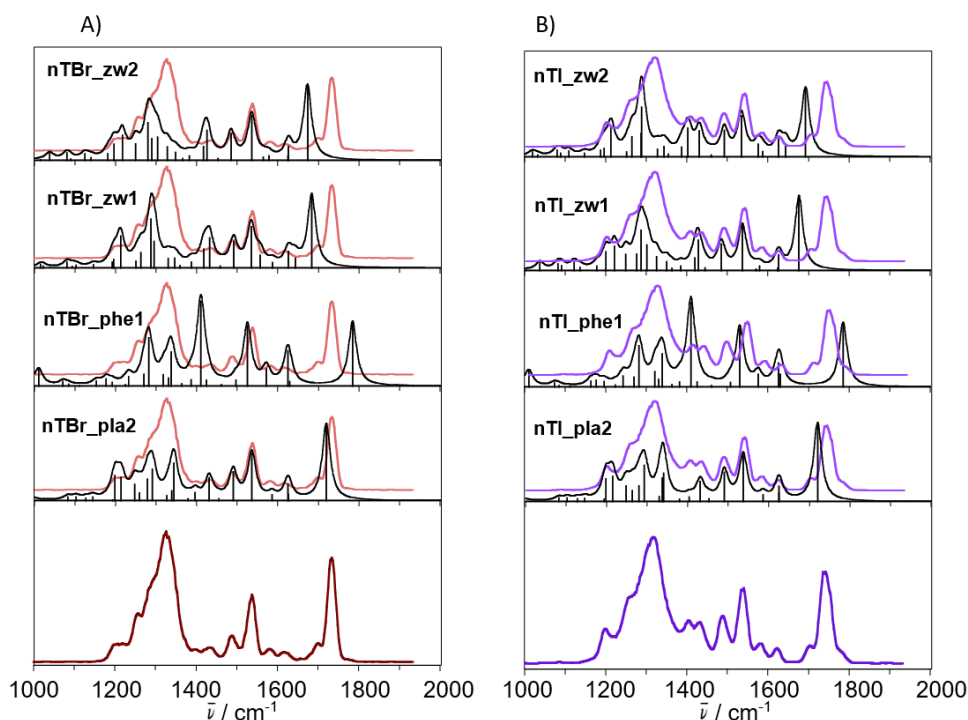
Fig. S18 Experimental IRMPD spectra of: [nitroTyr+Br]⁻ (brown profile, panel A) compared with IR spectra [km mol⁻¹] for **nTBr_pla2**, **nTBr_phe1**, **nTBr_zw1** and **nTBr_zw2** structures; [nitroTyr+I]⁻ (purple profile, panel B) compared with IR spectra [km mol⁻¹] for **nTI_pla2**, **nTI_phe1**, **nTI_zw1** and **nTI_zw2** structures. Theoretical vibrational modes were obtained at the B3LYP/6-311++G(d,p) level of theory and scaled by a factor of 0.978.

Table S1 Calculated energies (kJ mol⁻¹) at the B3LYP/6-311++G** level for the reaction: [(nitro)Tyr+X]⁻ → (nitro)Tyr + X⁻ (X = Cl, Br, I).

	[Tyr+X]⁻		[nitroTyr+X]⁻	
	ΔH_{298}	ΔG_{298}	ΔH_{298}	ΔG_{298}
X = Cl	121.21	96.01	153.01	124.08
X = Br	108.26	81.05	136.01	106.71
X = I	97.83	69.10	118.82	84.43

Table S2 Thermodynamic data (kJ mol^{-1}) for the most stable structures of [Tyr+X]$^-$ (X = Cl, Br, I) adducts calculated at different levels of theory.

	B3LYP[a]		B3LYP-D3[a]		MP2//B3LYP[b]	
	H_{rel}	G_{rel}	H_{rel}	G_{rel}	H_{rel}	G_{rel}
[Tyr+Cl]$^-$						
TCl_pla1	0.0	0.0	0.0	0.0	0.0	0.0
TCl_phe1	-4.8	-7.3	-3.2	-2.3	3.8	1.3
TCl_phe2	-5.3	-6.4	-0.7	-2.5	3.5	2.4
TCl_ter1	8.5	9.5	6.2	6.8	6.1	7.0
TCl_ter2	5.4	6.8	6.7	7.7	11.5	12.9
TCl_pla2	13.2	14.3	11.0	13.3	12.4	13.5
TCl_phe3	7.7	5.9	12.0	9.8	15.5	13.7
TCl_zw1	11.9	10.7	10.2	11.8	15.3	14.1
TCl_zw2	16.9	16.9	19.1	20.6	25.1	25.1
TCl_O1	79.3	80.6	78.3	78.2	83.8	85.0
[Tyr+Br]$^-$						
TBr_phe1	0.0	0.0	0.0	0.0	0.0	0.0
TBr_pla1	7.8	9.1	2.6	4.7	0.9	2.1
TBr_ter1	14.9	17.1	8.5	12.1	5.4	7.7
TBr_ter2	12.1	14.9	8.2	10.8	10.2	12.9
TBr_zw1	17.9	18.2	11.7	14.7	15.0	15.3
TBr_zw2	24.3	23.7	21.5	24.7	25.1	24.5
[Ty+-I]$^-$						
TI_phe1	0.0	0.0	0.0	0.0	0.0	0.0
TI_pla1	12.0	14.3	5.1	5.8	4.5	6.8
TI_ter1	15.3	17.9	9.7	11.3	9.4	12.1
TI_ter2	18.5	21.0	10.3	11.1	9.7	12.1
TI_zw1	20.3	24.1	13.2	16.6	14.6	18.4
TI_zw2	28.0	30.4	22.6	23.4	28.4	30.7

[a]The 6-311++G(d,p) basis set was employed. [b]Thermal and zero-point energy corrections obtained from B3LYP calculations. The Def2-TZVP ECP was used for iodine while keeping the 6-311++G(d,p) basis set for lighter atoms.

TABLE S3 Selected dihedral angles (in Degrees) of the lowest energy structures of [Tyr+X]⁻ (X = Cl, Br, I) adducts, calculated at the B3LYP/6-311++G(d,p) level of theory.

Species	O1C1C2N ϕ_1 [a]	NC2C3C1' ϕ_2 [b]	C2C3C1'C2' ϕ_3 [c]	
[Tyr+Cl]⁻				
TCl_pla1	157.1	-67.3	102.4	gauche
TCl_phe1	10.2	-56.5	106.8	gauche
TCl_phe2	11.8	-59.5	98.0	gauche
TCl_ter1	-57.6	-176.7	82.3	anti
TCl_ter2	74.4	-163.8	93.9	anti
TCl_pla2	17.4	50.5	88.4	gauche
TCl_phe3	150.7	-58.7	97.8	gauche
TCl_zw1	19.4	51.2	79.8	gauche
TCl_zw2	1.4	-65.2	175.5	gauche
TCl_O1	54.8	-41.5	102.6	gauche
[Tyr+Br]⁻				
TBr_phe1	10.4	-57.2	107.2	gauche
TBr_pla1	155.3	-66.0	101.8	gauche
TBr_ter1	-57.3	-177.6	86.0	anti
TBr_ter2	74.6	-163.3	94.5	anti
TBr_zw1	17.6	50.9	77.5	gauche
TBr_zw2	0.1	-60.6	165.2	gauche
[Tyr+I]⁻				
TI_phe1	10.3	-55.9	109.2	gauche
TI_pla1	156.3	-60.8	103.5	gauche
TI_ter1	82.8	-168.7	86.1	anti
TI_ter2	-59.7	-175.2	87.3	anti
TI_zw1	15.6	53.1	76.6	gauche
TI_zw2	1.0	-67.0	-180.0	gauche

[a] ϕ_1 = O1C1C2N dihedral angle.

[b] ϕ_2 = NC2C3C1' dihedral angle.

[c] ϕ_3 = C2C3C1'C2' dihedral angle.

Table S4 Thermodynamic data (kJ mol^{-1}) for the most stable structures of [nitroTyr+X]$^-$ (X = Cl, Br, I) adducts calculated at different levels of theory.

	B3LYP[a]		B3LYP-D3[a]		MP2//B3LYP[b]	
	H_{rel}	G_{rel}	H_{rel}	G_{rel}	H_{rel}	G_{rel}
[nitroTyr+Cl]$^-$						
nTCl_pla1	0.0	0.0	0.0	0.0	0.0	0.0
nTCl_ter1	12.8	13.2	10.9	14.0	5.9	6.3
nTCl_pla2	12.6	13.4	11.4	12.3	10.5	11.3
nTCl_ring1	26.2	28.4	17.8	25.8	11.4	13.5
nTCl_ter2	19.1	20.2	18.4	19.9	15.7	16.8
nTCl_ter3	12.7	15.5	16.3	15.7	17.9	20.7
nTCl_pla3	20.6	23.4	18.5	23.3	18.6	21.4
nTCl_ter4	12.6	15.2	14.6	17.5	19.0	21.6
nTCl_phe1	32.6	29.0	38.0	34.4	26.7	23.1
nTCl_zw1	27.4	30.7	24.4	28.3	24.4	27.7
nTCl_zw2	23.6	23.6	24.6	27.0	28.3	28.3
nTCl_ring2	38.7	40.9	36.2	39.6	30.1	32.3
nTCl_O1	82.7	81.3	83.1	82.6	83.1	81.8
[nitroTyr+Br]$^-$						
nTBr_pla1	0.0	0.0	0.0	0.0	0.0	0.0
nTBr_ter1	12.3	13.3	10.9	13.1	8.4	9.3
nTBr_pla2	13.2	13.4	11.5	11.1	11.7	11.9
nTBr_ring1	25.6	26.7	19.9	21.7	10.8	12.0
nTBr_ter2	11.3	13.2	13.4	13.6	17.3	19.3
nTBr_phe1	32.2	28.6	38.0	33.4	27.5	23.9
nTBr_zw1	27.1	29.9	24.8	27.6	24.0	26.7
nTBr_zw2	22.6	21.9	21.4	24.9	28.0	27.3
[nitroTyr+I]$^-$						
nTI_pla1	0.0	0.0	0.0	0.0	0.0	0.0
nTI_ter1	10.4	7.3	9.6	9.5	10.2	7.1
nTI_pla2	13.5	12.6	11.5	10.9	9.7	8.8
nTI_ring1	24.8	21.7	13.8	15.3	17.0	13.8
nTI_ter2	10.0	11.0	12.9	13.4	15.0	15.9
nTI_phe1	29.6	24.2	36.2	31.4	23.4	18.0
nTI_zw1	21.5	19.9	23.4	23.4	22.1	20.4
nTI_zw2	25.6	26.7	23.9	26.0	20.3	21.5

[a]The basis set 6-311++G(d,p) was employed. [b]Thermal and zero-point energy corrections obtained from B3LYP calculations. The Def2-TZVP ECP was used for the iodine atom together with the 6-311++G(d,p) basis set for lighter atoms.

TABLE S5 Selected dihedral angles (in Degrees) of the lowest energy structures of [nitroTyr+X]⁻ (X = Cl, Br, I) adducts, calculated at the B3LYP/6-311++G(d,p) level of theory.

Species	O1C1C2N ϕ_1 [a]	NC2C3C1' ϕ_2 [b]	C2C3C1'C2' ϕ_3 [c]	
[nitroTyr+Cl]⁻				
nTCl_pla1	159.1	-66.0	101.2	gauche
nTCl_ter1	-56.3	-178.3	96.6	anti
nTCl_pla2	162.5	-62.9	81.5	gauche
nTCl_ring1	-25.3	62.6	84.6	gauche
nTCl_ter2	-55.2	-175.8	69.8	anti
nTCl_ter3	74.9	-166.8	67.4	anti
nTCl_pla3	9.9	-59.5	109.7	gauche
nTCl_ter4	73.4	-163.5	99.4	anti
nTCl_phe1	9.4	-60.0	104.8	gauche
nTCl_zw1	18.7	48.9	92.5	gauche
nTCl_zw2	15.0	61.1	70.1	gauche
nTCl_ring2	9.9	-59.5	109.7	gauche
nTCl_O1	52.5	-50.1	99.0	gauche
[nitroTyr+Br]⁻				
nTBr_pla1	157.9	-63.7	102.4	gauche
nTBr_ter1	-55.6	-179.7	94.7	anti
nTBr_pla2	161.2	-61.2	79.7	gauche
nTBr_ring1	106.1	62.4	83.1	gauche
nTBr_ter2	74.6	-165.0	98.2	anti
nTBr_phe1	9.6	-60.2	105.1	gauche
nTBr_zw1	-10.4	65.6	86.3	gauche
nTBr_zw2	14.2	59.8	71.3	gauche
[nitroTyr+I]⁻				
nTI_pla1	158.1	-59.9	103.0	gauche
nTI_ter1	-54.0	-177.8	84.1	anti
nTI_pla2	159.3	-60.6	77.5	gauche
nTI_ring1	-13.6	61.9	81.5	gauche
nTI_ter2	77.6	-164.2	102.7	anti
nTI_phe1	14.1	59.4	72.3	gauche
nTI_zw1	10.1	-60.1	106.2	gauche
nTI_zw2	-8.6	65.6	85.69	gauche

[a] ϕ_1 = ∠O1C1C2N dihedral angle.
[b] ϕ_2 = ∠NC2C3C1' dihedral angle.
[c] ϕ_3 = ∠C2C3C1'C2' dihedral angle.

Table S6 Experimental IRMPD resonances and calculated (at B3LYP/6-311++G(d,p) level of theory) vibrational frequencies for the low-lying isomers of [Tyr+X]⁻ (X = Cl, Br, I) adducts.

[Tyr+Cl]⁻

IRMPD[a]	Calculated[a,b]				Vibrational mode
	TCl_pla1	TCl_phe1	TCl_ter1	TCl_ter2	
1105 (low)	1104 (20)		1083 (32)	1097 (53)	NH2 wagging
1178				1168 (112)	CH in plane bend
	1166 (176)		1168 (172)	1171 (77)	OH phenol bend
	1194 (47)	1178 (33)		1197 (66)	OH carboxyl bend + NH2 wagging
1250		1250 (37)		1223 (57)	OH phenol bend
	1230 (64)		1232 (90)	1233 (80)	ring def
	1270 (21)				NH2 twist
1312		1293 (238)	1307 (45)		ring def
1358	1336 (22)				CH in plane bend
	1352 (293)		1329 (159)	1337 (96)	OH carboxyl bend
			1334 (138)		OH carboxyl bend+OH phenol bend
				1365 (168)	COO-H bend + NH2 twisting
1376		1378 (32)			OH phenol bend
	1395 (60)		1355 (46)	1379 (102)	CH bend
		1397 (474)			OH carboxyl bend
1451 (shoulder)		1447 (46)			OH phenol bend
1507	1507 (132)	1509 (185)	1507 (113)	1506 (120)	CH in plane bend
1608	1615 (26)	1610 (190)	1626 (26)	1615 (29)	ring def
	1633 (35)	1627 (22)			NH2 scissor
1720	1713 (442)		1714 (364)	1706 (368)	C=O stretch
1790		1781 (389)			C=O stretch
	2710 (1871)		2850 (1705)	2759 (1879)	OH carboxyl stretch
		2751 (2962)			OH phenol stretch
			2918 (38)		CH stretch
	2898 (32)	2884 (29)			CH2 symm stretch
	2994 (44)	2998 (21)		2994 (32)	CH asymm stretch
3008	3004 (42)		3005 (29)		CH symm stretch
3060	3046 (21)	3037 (32)			CH symm stretch
3200 (broad)		3242 (343)			OH carboxyl stretch
3272			3239 (218)	3242 (209)	NH2 symm stretch
3330			3381 (20)	3368 (25)	NH2 asymm stretch
3663	3676 (45)		3680 (48)	3671 (47)	OH phenol stretch

[Tyr+Br]⁻

IRMPD[a]	Calculated[a,b]				Vibrational mode
	TBr_phe1	TBr_pla1	TBr_ter1	TBr_ter2	
1104 (low)		1103 (20)	1081 (29)	1096 (50)	NH2 wag
1177		1166 (173)	1168 (183)	1168 (192)	OH phenol bend
	1170 (26)				CH in plane bend
	1179 (28)				OH carboxyl bend + NH2 wagging
1204		1189 (66)		1191 (70)	CH bend
1242	1243 (60)				OH phenol bend
		1232 (63)	1233 (91)	1233 (85)	ring def
1295	1287 (224)				ring def
1333		1328 (42)	1307 (63)	1299 (62)	OH carboxyl bend + CH2 wagging
		1337 (33)		1331 (34)	OH phenol bend + CH in plane bend
		1341 (268)	1328 (243)	1324 (148)	OH carboxyl bend
			1333 (45)		OH phenol bend + CH in plane bend
1375 (shoulder)				1357 (127)	OH carboxyl bend + CH bend
	1367 (26)				OH phenol bend + CH in plane bend
		1396 (41)	1358 (32)	1378 (46)	CH bend
	1397 (476)				OH carboxyl bend
1447 (low)	1442 (33)				OH phenol bend + ring def
1508	1511 (180)	1508 (127)	1507 (116)	1506 (120)	CH in plane bend
1602	1611 (178)	1615 (28)	1616 (27)	1615 (30)	ring def
1729		1718 (439)	1719 (371)	1712 (372)	C=O stretch
1775	1781 (388)				C=O stretch
2841	2880 (42)	2892 (26)	2898 (22)	2906 (25)	CH2 symm stretch
2921	2929 (2685)				OH phenol stretch
			2913 (36)	2922 (352)	CH stretch
			2942 (25)		CH2 asymm stretch
		2904 (1784)	2976 (1663)	2930 (1538)	OH carboxyl stretch
		2931 (47)			CH stretch
3022 (broad)	2994 (27)	2992 (47)	3000 (27)	2994 (30)	CH asymm stretch
	3033 (67)	3002 (39)			CH symm stretch
		3040 (21)			CH symm stretch
3251 (broad)	3236 (345)				OH carboxyl stretch
			3238 (240)	3245 (242)	NH2 symm stretch
3331		3314 (5)			NH2 symm stretch
3400	3412 (10)	3392 (7)	3378 (20)	3371 (27)	NH2 asymm stretch
3664		3667 (46)	3672 (48)	3670 (48)	OH phenol stretch

[Tyr+I]⁻

IRMPD[a]	Calculated[a,b]				Vibrational mode
	TI_phe1	TI_pla1	TI_ter1	TI_ter2	

1090 (low)		1092 (20)	1078 (26)	1089 (38)	NH2 wag + CH in plane bend
1177	1171 (24)			1166 (71)	CH in plane bend
		1166 (164)	1168 (189)	1170 (114)	OH bend
	1181 (38)				OH carboxyl bend + NH2 wagging
		1189 (78)		1183 (101)	CH bend
1239 (shoulder)			1223 (77)		OH carboxyl bend + NH2 wagging
	1228 (80)				OH phenol bend
		1231 (79)	1234 (79)	1234 (91)	ring def
1288			1289 (256)		OH carboxyl bend + CH in plane bend
	1284 (210)				ring def
1323	1353 (29)				OH phenol bend + CH in plane bend
		1320 (34)	1314 (51)	1329 (45)	OH carboxyl bend + CH in plane bend
		1328 (257)		1333 (120)	OH carboxyl bend
		1339 (44)			CH2 wag
			1356 (26)	1365 (141)	CH bend
1382	1399 (479)				OH carboxyl bend
		1400 (33)		1381 (35)	NH2 twist
1517	1513 (175)	1507 (120)	1508 (119)	1504 (116)	CH in plane bend
1608	1613 (160)	1614 (33)	1616 (28)	1614 (33)	ring def
		1632 (35)			NH2 scissor
1750		1728 (440)	1731 (375)	1724 (368)	C=O stretch
1785	1783 (386)				C=O stretch

[a] In cm^{-1}. [b] The reported intensities given in parentheses are in $km\ mol^{-1}$. Bands with an intensity lower than 20 $km\ mol^{-1}$ are usually not included. Frequencies are scaled by a factor of 0.978 in the 1000-2000 cm^{-1} region and 0.955 in the 2800-3800 cm^{-1} region.

Table S7 Experimental IRMPD resonances and calculated (at B3LYP/6-311++G(d,p) level of theory) vibrational frequencies for the low-lying isomers of [nitroTyr+X]$^-$ (X = Cl, Br, I) adducts.

[nitroTyr+Cl]$^-$

IRMPD[a]	Calculated[a,b]			Vibrational mode
	nTCl_pla1	**nTCl_ter1**	**nTCl_ring1**	
			1001 (43)	NH2 wag
	1083 (25)	1079 (42)	1079 (28)	ring def + NO2 symm stretch
	1147 (37)	1133 (24)	1134 (40)	CH in plane bend + NH2 twist
1220	1191 (73)	1191 (64)	1197 (47)	CH in plane bend + OH phenol bend
	1207 (305)	1211 (247)	1216 (197)	C-N stretch + CH in plane bend
1330		1247 (33)	1241 (27)	OH carboxyl bend
	1252 (140)	1253 (113)	1249 (125)	OH phenol bend + CH in plane bend + NO2 symm stretch
			1281 (132)	CH bend
	1280 (341)	1284 (302)	1291 (237)	OH phenol bend
	1294 (29)	1313 (33)		CH2 twist
	1341 (100)			ring def
	1357 (218)	1324 (271)	1316 (250)	OH carboxyl bend
		1339 (55)	1337 (128)	OH carboxyl bend + CH2 twist
		1344 (135)		CH2 wag
	1392 (73)			NH2 twist
1423	1422 (184)	1422 (159)	1426 (165)	NO2 asymm stretch + OH phenol bend
1474	1482 (172)	1485 (140)	1487 (116)	NO2 asymm stretch + CH in plane bend
1528	1530 (271)	1531 (273)	1533 (245)	NO2 asymm stretch + ring def
1572			1584 (41)	ring def
1610	1625 (76)	1627 (74)	1630 (59)	ring def
1710	1720 (448)	1715 (360)	1698 (415)	C=O stretch

[nitroTyr+Br]$^-$

IRMPD[a]	Calculated[a,b]			Vibrational mode
	nTBr_pla1	**nTBr_ter1**	**nTBr_ring1**	
	1083 (26)	1079 (43)	1079 (28)	ring def + NO2 sym stretch
	1147 (40)	1133 (24)	1134 (41)	CH in plane bend + NH2 twist
1197	1188 (31)		1163 (29)	CH bend

				CH in plane bend + OH phenol bend
	1193 (55)	1191 (65)	1192 (31)	CH in plane bend + OH phenol bend
		1204 (82)		CH2 wag + NH2 twist
1214	1208 (293)	1211 (169)	1213 (210)	C-N stretch + CH in plane bend
1257		1240 (27)	1228 (39)	OH carboxyl bend
	1252 (120)	1253 (126)	1250 (133)	OH phenol bend + CH in plane bend + NO2 symm stretch
			1282 (151)	CH bend + CH2 twist
	1279 (295)	1284 (297)		OH phenol bend
	1292 (72)		1292 (223)	CH2 twist
1323	1326 (47)			CH2 wag
	1337 (107)	1314 (315)	1307 (237)	OH carboxyl bend
		1318 (55)		OH carboxyl bend + CH2 wag
	1340 (214)	1347 (109)	1337 (110)	OH carboxyl bend + CH2 twist
	1394 (46)			NH2 twist
1437	1422 (180)	1422 (156)	1426 (159)	NO2 asym stretch + OH phenol bend
1487	1484 (166)	1484 (147)	1487 (115)	NO2 asym stretch + CH in plane bend
1538	1531 (267)	1531 (270)	1534 (242)	NO2 asym stretch + ring def
1579	1581 (44)	1581 (38)	1583 (39)	ring def
1618	1625 (83)	1627 (76)	1630 (58)	ring def
	1630 (31)		1638 (66)	NH2 scissor
1698			1705 (414)	C=O stretch
1733	1726 (450)	1720 (365)		C=O stretch

[nitroTyr+I]⁻

IRMPD[a]	Calculated[a,b]			Vibrational mode
	nTI_pla1	nTI_ter1	nTI_ring1	
	1083 (27)	1078 (39)	1077 (29)	ring def + NO2 symm stretch
			1133 (38)	CH in plane bend
	1147 (43)		1159 (23)	CH in plane bend + NH2 twist
1198	1187 (45)			CH bend
		1187 (45)	1195 (33)	OH carboxyl bend
	1195 (46)	1193 (49)		CH in plane bend + OH phenol bend
	1211 (294)	1213 (229)	1215 (179)	C-N stretch + CH in plane bend
1253		1221 (54)		OH carboxyl bend + NH2 twist
	1251 (124)	1252 (145)	1251 (133)	OH phenol bend + CH in plane bend +

318

				NO2 symm stretch
			1281 (64)	CH bend + CH2 twist
	1285 (345)	1283 (155)	1291 (300)	OH phenol bend
1316	1300 (30)			CH2 twist
		1291 (480)	1300 (308)	OH carboxyl bend
	1326 (265)			OH carboxyl bend + CH2 wag
	1335 (30)		1337 (103)	OH carboxyl bend + CH2 twist
	1343 (80)	1341 (114)		CH2 wag
			1381 (22)	OH phenol bend + ring def
1403	1397 (33)			NH2 twist
1431	1424 (187)	1423 (146)	1426 (144)	NO2 asymm stretch + OH phenol bend
1488	1484 (167)	1485 (151)	1487 (117)	NO2 asymm stretch + CH in plane bend
1540	1530 (254)	1532 (264)	1536 (241)	NO2 asymm stretch + ring def
1580	1581 (50)	1581 (37)	1581 (36)	ring def
1621	1626 (88)	1628 (83)	1631 (108)	ring def
	1633 (33)		1624 (62)	NH2 scissor
1705			1716 (383)	C=O stretch
1743	1733 (439)	1729 (364)		C=O stretch

[a] In cm-1. [b] The reported intensities given in parentheses are in km mol^{-1}. Bands with an intensity lower than 20 km mol^{-1} are not included. Frequencies are scaled by a factor of 0.978.

References

1 P.A. Gale, *Acc. Chem. Res.,* 2011, 44, 216–226

2 H. T. Chifotides and K. R. Dunbar, *Acc. Chem. Res.*, 2013, 46, 894–906.

3 E. M. Milner, M. G. D. Nix and C. E. H. Dessent, *J. Phys. Chem. A*, 2012, 116, 801-809.

4 J. Oomens, B.G. Sartakov, G. Meijer and G. Von Helden, *Int. J. Mass Spectrom.,* 2006, 254, 1-19.

5 L. MacAleese and P. Maitre, *Mass Spectrom. Rev.,* 2007, 26, 583–605.

6 N.C. Polfer, *Chem. Soc. Rev.,* 2011, 40, 2211–2221.

7 J. Roithova, *Chem. Soc. Rev*., 2012, 41, 547–559.

8 B. Chiavarino, M. E. Crestoni, O. Dopfer, P. Maitre and S. Fornarini, *Angew. Chem., Int. Ed.* 2012, 51, 4947 –4949.

9 B. Chiavarino, M. E. Crestoni, S. Fornarini, S. Taioli, I. Mancini and P. Tosi, *J. Chem. Phys.,* 2012, 137, 024307.

10 F. Lanucara, B. Chiavarino, D. Scuderi, P. Maitre, S. Fornarini and M. E. Crestoni, *Chem. Commun.,* 2014, 50, 3845-3848.

11 D. Corinti, C. Coletti, N Re, B. Chiavarino, M. E. Crestoni and S. Fornarini, *Chem. Eur. J.,* 2016, 22, 3794 – 3803.

12 B. Chiavarino, M. E. Crestoni, M. Schütz, A. Bouchet, S. Piccirillo, V. Steinmetz, O. Dopfer and S. Fornarini, *J. Phys. Chem. A,* 2014, 118, 7130−7138.

13 D. Scuderi, E. Bodo, B. Chiavarino, S. Fornarini and M. E. Crestoni, *Chem. Eur. J.,* 2016, 22, 17239-17250.

14 B. Chiavarino, M. E. Crestoni, S. Fornarini, D. Scuderi and J.-Y. Salpin, *Inorg. Chem.*, 2015, 54, 3513–3522.

15 M. F. Bush, J. Oomens and E. R. Williams, *J. Phys. Chem. A,* 2009, 113, 431-438.

16 C. Kapota, J. Lemaire, P. Maitre and G. Ohanessian, *J. Am. Chem. Soc.*, 2004, 126, 1836-1842.

17 R. C. Dunbar, A. C. Hopkinson, J. Oomens, C. K. Siu, K. W. M. Siu, J. D. Steill, U. H. Vertek and J. F. Zhao, *J. Phys. Chem. B,* 2009, 113, 10403-10408.

18 M. Burt, K. Wilson, R. Marta, M. Hasan, W. S. Hopkins and T. McMahon, *Phys. Chem. Chem. Phys.,* 2014, 16, 24223-24234.

19 J. T. O'Brien, J. S. Prell, G. Berden, J. Oomens and E. R. Williams, *Int. J. Mass Spectrom*., 2010, 297, 116-123.

20 J. Schmidt and S. R. Kass, *J. Phys. Chem A,* 2013, 117, 4863-4869.

21 B. Chiavarino, M. E. Crestoni, P. Maitre and S. Fornarini, *Int. J. Mass Spectrom.,* 2013, 354-355, 62-69.

22 M. E. Crestoni, B. Chiavarino, S. Fornarini, *Pure Appl. Chem*., 2015, 87, 379-390.

23 B. Chiavarino, M.E. Crestoni, S. Fornarini, F. Lanucara, J. Lemaire, P. Maitre and D. Scuderi, *Chem. Eur. J.,* 2009, 15, 8185–8195.

24 M. L. Stover, V. E. Jackson, M. H. Matus, M. A. Adams, C. J. Cassady and D. A. Dixon, *J. Phys. Chem. B,* 2012, 116, 2905−2916.

25 Z. Tian and S. R. Kass, *J. Am. Chem. Soc.,* 2008, 130, 10842–10843.

26 J. Oomens, J. D. Steill and B. Redlich, *J. Am. Chem. Soc.,* 2009, 131, 4310-4319.

27 J. D. Steill and J. Oomens, *J. Am. Chem. Soc.,* 2009, 131, 13570-13571.

28 R. K. Sinha, B. Chiavarino, M. Elisa Crestoni, D. Scuderi and S. Fornarini, *Int. J. Mass Spectrom.,* 2011, 308, 209-216.

29 J. Lemaire, P. Boissel, M. Heninger, G. Mauclaire, G. Bellec, H. Mestdagh, A. Simon, S. Le Caer, J. M. Ortega, F. Glotin and P. Maitre, *Phys. Rev. Lett.,* 2002, 89, 273002.

30 L. Mac Aleese, A. Simon, T. B. McMahon, J.-M. Ortega, D. Scuderi, J. Lemaire and P. Maitre, *Int. J. Mass Spectrom.* 2006, 249/250, 14-20.

31 P. Maitre, J. Lemaire and D. Scuderi, *Physica Scripta,* 2008, 78, 058111/1-058111/6.

32 R. K. Sinha, P. Maitre, S. Piccirillo, B. Chiavarino, M. E. Crestoni and S. Fornarini, *Phys. Chem. Chem. Phys.,* 2010, 12, 9794-9800.

33 J. S. Prell, J. T. O'Brien and E. R. Williams, *J. Am. Soc. Mass Spectrom.,* 2010, 21, 800-809.

34 D. A. Case, T. Darden, T. E. Cheatham, C. Simmerling, J. Wang, R. E. Duke, R. Luo, K. M. Merz, B. Wang, D. A.Pearlman, et al. *Amber 8 User's Manual*; University of California: San Francisco, CA, 2004.

35 J. Wang, R. M. Wolf, J. W. Caldwell, P. A. Kollman and D. A. Case, *J. Comput. Chem.,* 2004, 25, 1157–1174.

36 F. Neese, *"ORCA," an ab initio, Density Functional and Semiempirical Program Package* (v. 2.6-35) Universitat Bonn: Bonn, Germany, 2007.

37 F. Neese, *WIREs Comput. Mol. Sci.,* 2012, 2, 73–78.

38 F. Weigend and R. Ahlrichs, *Phys. Chem. Chem. Phys.*, 2005, 7 , 3297–3305.

39 O. Dopfer, N. Solca, J. Lemaire, P. Maitre, M. E. Crestoni and S. Fornarini, *J. Phys. Chem. A,* 2005, 109, 7881–7887.

40 B. Gregori, L. Guidoni, B. Chiavarino, D. Scuderi, E. Nicol, G. Frison, S. Fornarini and M. E. Crestoni, *J. Phys. Chem. B,* 2014, 118, 12371-12382.

41 C. Blondel, P. Cacciani, C. Delsart and R.Trainham, *Phys. Rev. A*, 1989, 40, 3698.

42 R. J. Pelez, C. Blondel, C. Delsart and C. Drag, *J. Phys. B: Atom. Mol. Opt. Phys*., 2009, 42, 125001.

43 J.D.D. Martin and J.W. Hepburn, *J. Chem. Phys.,* 1998, 109, 8139-8142.

44 N. C. Polfer, B. Paizs, L. C. Snoek, I. Compagnon, S. Suhai, G. Meijer, G. von Helden and J. Oomens, *J. Am. Chem. Soc.,* 2005, 127, 8571 −8579.

45 R. C.Dunbar, *J. Phys. Chem. A,* 2000, 104, 8067 −8074.

46 P. B. Armentrout, Bo Yang and M. T. Rodgers, *J. Phys. Chem. B,* 2013, 117, 3771−3781.

47 J. D. Chai and M. Head-Gordon, *Phys. Chem. Chem. Phys.,* 2008, 10, 6615-6620.

48 M. Head-Gordon, J. A. Pople and M. J. Frisch, *Chem. Phys. Lett.,* 1988, 153, 503-506.

49 M. Walker, A. Sen, A. J. A. Harvey and C. E. H. Dessent, *Chem. Phys. Lett.,* 2013, 588, 43-46.

50 C. Ruan and M. T. Rodgers, *J. Am. Chem. Soc.,* 2004, 126, 14600-14610.

51 G. Bouchoux, *Mass Spectrom. Rev.,* 2012, 31, 391–435.

52 C. Perez, S. Mata, C. Cabezas, J. C. Lopez and J. L. Alonso, *J. Phys. Chem. A,* 2015, 119, 3731-3735.

53 Y. Inokuchi, Y. Kobayashi, T. Ito and T. Ebata, *J. Phys. Chem. A,* 2007, 111, 3209-3215.

54 A Abo-Riziq, L. Grace, B. Crews†, M. P. Callahan, T. Mourik and M. S. de Vries, *J. Phys. Chem. A,* 2011, 115, 6077–6087.

55 Y. Shimozono, K. Yamada, S.-i. Ishiuchi, K. Tsukiyama and M. Fujii, *Phys. Chem. Chem. Phys.,* 2013, 15, 5163-5175.

56 F. Gabas, R. Conte and M. Ceotto, *J. Chem. Theory Comput.* 2017, 13, 2378-2388.

57 A. Bouchet, M. Schutz, B. Chiavarino, M. E. Crestoni, S. Fornarini and O. Dopfer, *Phys. Chem. Chem. Phys.*, 2015, 17, 25742-25754.

58 M. Schütz, A. Bouchet, B. Chiavarino, M. E. Crestoni, S. Fornarini and O. Dopfer, *Chem. Eur. J.,* 2016, 22, 8124-8136.

59 A. Lagutschenkov, J. Langer, G. Berden, J. Oomens and O. Dopfer, *Phys. Chem. Chem. Phys.,* 2011, 13, 2815-2823.

60 L. C. Snoek, E. G. Robertson, R. T. Kroemer and J. P. Simons, *Chem Phys Lett.,* 2000, 321, 49-56.

61 NIST Chemistry WebBook, NIST Standard Reference Database, Number 69 (Eds.: P. J. Linstrom, W. G. Mallard) National Institute of Standards and Technology, Gaithersburg MD, 20899, http://webbook.nist.gov.

62 S. Tshepelevitsh, A. Trummal, K. Haav, K. Martin and I. Leito, *J. Phys. Chem. A,* 2017, 121, 357−369.

63 J. W. Larson and T. B. McMahon, *J. Am. Chem. Soc.,* 1983, 105, 2944-2950.

64 J. W. Larson and T. B. McMahon, *J. Am. Chem. Soc.,* 1984, 106, 517-521.

65 G. Caldwell and P. Kebarle *J. Am. Chem. Soc*., 1984, 106, 961-969.

66 J. W. Larson and T. B. McMahon, *J. Am. Chem. Soc.,* 1987, 109, 6230-6236.

67 C. Emmeluth, B. L. J. Poad, C. D. Thompson and E. J. Bieske, *J. Phys. Chem. A*, 2007, 111, 7322-7328.

68 M. F. Bush, J. Oomens, R. J. Saykally and E. R. Williams, *J. Phys. Chem. A,* 2008, 112, 8578-8584.

69 M. T. Rodgers, P. B. Armentrout, J. Oomens and J. D. Steill, *J. Phys. Chem. A,* 2008, 112, 2258-2267.

Appendix B: List of Publications

1. D. Corinti, L. Mannina, B. Chiavarino, V. Steinmetz, S. Fornarini, M.E. Crestoni
   IRMPD signature of protonated pantothenic acid, an ubiquitous nutrient
   Chem. Phys. Lett. 646 (2016) 162–167
   http://dx.doi.org/10.1016/j.cplett.2016.01.032

2. D. Corinti, C. Coletti, N. Re, B. Chiavarino, M.E. Crestoni, S. Fornarini
   Cisplatin Binding to Biological Ligands Revealed at the Encounter Complex Level by IR Action Spectroscopy
   Chem. - A Eur. J. 22 (2016) 3794–3803
   http://dx.doi.org/10.1002/chem.201504521

3. D. Corinti, A. De Petris, C. Coletti, N. Re, B. Chiavarino, M.E. Crestoni, S. Fornarini
   Cisplatin Primary Complex with l-HistidineT arget Revealed by IR Multiple Photon Dissociation (IRMPD) Spectroscopy
   ChemPhysChem. 18 (2017) 318–325
   http://dx.doi.org/10.1002/cphc.201601172

4. D. Corinti, C. Coletti, N. Re, S. Piccirillo, M. Giampà, M.E. Crestoni, S. Fornarini
   Hydrolysis of cis- and transplatin: structure and reactivity of the aqua complexes in a solvent free environment
   RSC Adv. 7 (2017) 15877–15884
   http://dx.doi.org/10.1039/C7RA01182B

5. R. Paciotti, D. Corinti, A. De Petris, A. Ciavardini, S. Piccirillo, C. Coletti, N. Re, P. Maitre, B. Bellina, P. Barran, B. Chiavarino, M. Elisa Crestoni, S. Fornarini
   Cisplatin and transplatin interaction with methionine: bonding motifs assayed by vibrational spectroscopy in the isolated ionic complexes
   Phys. Chem. Chem. Phys. 117 (2017) 4863–4869
   http://dx.doi.org/10.1039/C7CP05203K

6. C. Coletti, D. Corinti, R. Paciotti, N. Re, M.E. Crestoni, S. Fornarini
   Structure and dynamics of gas phase ions: Interplay between experiments and computations in IRMPD spectroscopy
   AIP Conference Proceedings (2017) 1906:1
   http://dx.doi.org/10.1063/1.5012290

7. D. Corinti, D. Catone, S. Turchini, F. Rondino, M.E. Crestoni, S. Fornarini

Photoionization mass spectrometry of ω -phenylalkylamines: Role of radical cation-π interaction
J. Chem. Phys. 148 (2018)
http://dx.doi.org/10.1063/1.5027786

8. D. Corinti, B. Gregori, L. Guidoni, D. Scuderi, T.B. McMahon, B. Chiavarino, S. Fornarini, M.E. Crestoni
    Complexation of halide ions to tyrosine: role of non-covalent interactions evidenced by IRMPD spectroscopy
    Phys. Chem. Chem. Phys. (2018)
    http://dx.doi.org/10.1039/C7CP06657K

9. A. Theisen, R. Black, D. Corinti, J.M. Brown, B. Bellina, P.E. Barran
    Initial Protein Unfolding Events in Ubiquitin, Cytochrome c and Myoglobin Are Revealed with the Use of 213 nm UVPD Coupled to IM-MS
    J. Am. Soc. Mass Spectrom. (2018)
    http://dx.doi.org/10.1007/s13361-018-1992-0.

10. D. Corinti, C. Coletti, N. Re, R. Paciotti, P. Maître, B. Chiavarino, M.E. Crestoni, S. Fornarini
    Short-lived intermediates (encounter complexes) in cisplatin ligand exchange elucidated by infrared ion spectroscopy
    Int. J. Mass Spectrom. 435 (2019) 7–17
    http://dx.doi.org/10.1016/j.ijms.2018.10.012

11. D. Corinti, M. E. Crestoni, M. Pieper, K. Niehaus, M. Giampà, S. Fornarini
    An integrated approach to study novel properties of a MALDI matrix (4-maleicanhydridoprotonsponge) for MS imaging analyses
    Manuscript submitted

Appendix C: Contribution to conferences, schools and awards

C.1 Oral presentations

<u>D. Corinti</u>, C. Coletti, N. Re, B. Chiavarino, M. E. Crestoni and S. Fornarini
Ion chemistry of cisplatin with biological ligands at the encounter complex level
XV Sigma-Aldrich Young Chemists Symposium in Rimini (RN), Italy October 27-29, 2015

<u>D. Corinti</u>, C. Coletti, N. Re, B. Chiavarino, M. E. Crestoni and S. Fornarini
Exploring ligand substitution mechanisms at the molecular level with IRMPD/MS: the case of cisplatin
XX Italian Congress of Mass Spectrometry in Rome (RM), Italy September 6-8, 2016

<u>D. Corinti</u>, B. Chiavarino, M. E. Crestoni and S. Fornarini
MS coupled with IRMPD spectroscopy and fixed-wavelength kinetics to disclose isomeric mixtures of antitumor Pt^{II}-complexes with amino acids
XXX Annual Tandem Mass Spectrometry workshop in Lake Louise, Alberta, Canada, November 29 – December 2, 2017

<u>D. Corinti</u>, B. Chiavarino, M. E. Crestoni, S. Fornarini
Gas-phase kinetics and IRMPD spectroscopy towards a better understanding of cisplatin reactivity
EU FT-ICR MS 1st End User School in Joensuu Finland August, 19-23, 2018

C.2 Poster presentations

<u>D. Corinti</u>, C. Coletti, N. Re, B. Chiavarino, M. E. Crestoni and S. Fornarini
Cisplatin reactions with model biological ligands monitored by IR multiphoton dissociation spectroscopy
XLIII Italian Congress of Inorganic Chemistry held in Camerino (MC), Italy, September 9-12, 2015

<u>D. Corinti</u>, B. Chiavarino, M. E. Crestoni and S. Fornarini
Probing Biomolecules of Nutritional Interest: IRMPD Spectroscopy of Bare Protonated Pantothenic Acid
1st NatMedDay workshop at Aboca, SanSepolcro (AR), Italy September 22-23, 2015

<u>D. Corinti</u>, B. Chiavarino, M. E. Crestoni and S. Fornarini
Distinction between Cyanidin 3-O-glucoside and Cyanidin 3-O-galactoside by mass spectrometry combined with IRMPD spectroscopy
XX Italian Congress of Mass Spectrometry in Rome (RM), Italy, September 6-8, 2016

<u>D. Corinti</u>, C. Coletti, N. Re, S. Piccirillo, M. Giampà, M. E. Crestoni and S. Fornarini
Structural characterization and reactivity of bare cis- and transplatin hydrolysis products
XXVI Congress of the Italian Chemistry Society in Paestum (SA), Italy, September 10-14, 2017

<u>D. Corinti</u>, B. Gregori, L. Guidoni, D. Scuderi, T. B. McMahon, B. Chiavarino, S. Fornarini and M. E. Crestoni

Structural insights into non-covalent halide adducts with tyrosine and 3-nitrotyrosine using ion-spectroscopy

XXIV IUPAC Conference on Physical Organic Chemistry (ICPOC24) in Faro, Portugal, July 1-6 2018

<u>D. Corinti</u>, R. Paciotti, C. Coletti, N. Re, S. Piccirillo, P. Maitre, B. Bellina, P. Barran, B. Chiavarino, M. E. Crestoni and S. Fornarini

Elusive monofunctional adducts of cisplatin with natural aminoacids revealed by IRMPD spectroscopy and photofragmentation kinetics

XXII International Mass Spectrometry Conference in Florence (FI), Italy, August 26-31, 2018

C.3 Schools

20th Mass Spectrometry School
Certosa di Pontignano (SI), Italy, March 12-18, 2016

CECAM Summer School on Atomistic Simulation Techniques
Trieste (TS), Italy, June 14-30, 2017

EU FT-ICR MS 1st End User School
Joensuu Finland August, 19-23, 2018

C.4 Awards

Best Poster Prize granted by the division of Inorganic Chemistry of the Italian Chemical Society for the contribution:
Cisplatin reactions with model biological ligands monitored by IR multiphoton dissociation spectroscopy
XLIII Italian Congress of Inorganic Chemistry held in Camerino (MC), Italy, September 9-12, 2015

Best Poster Prize granted by the division of Mass Spectrometry of the Italian Chemical Society for the contribution:
Distinction between Cyanidin 3-O-glucoside and Cyanidin 3-O-galactoside by mass spectrometry combined with IRMPD spectroscopy
XX Italian Congress of Mass Spectrometry in Rome (RM), Italy, September 6-8, 2016

Lake Louise Student Travel Award granted by the Lake Louise Tandem-MS Workshop Scientific Committee for the contribution:
MS coupled with IRMPD spectroscopy and fixed-wavelength kinetics to disclose isomeric mixtures of antitumor Pt^{II}-complexes with amino acids
XXX Annual Tandem Mass Spectrometry workshop in Lake Louise, Alberta, Canada, November 29 – December 2, 2017

Acknowledgments

This thesis would not have seen the light of day without the help and support of Prof. Simonetta Fornarini who has been my supervisor and mentor for the past years and has helped me to grow as a resercher but also as a person.
Thanks for everything.

A special thanks go to Prof. Maria Elisa Crestoni for her invaluable help, she has followed every step of my scientific and personal development with dedication and kindness.

I would like to thank Prof. Perdita Barran that has been my local supervisor during my abroad research period at the University of Manchester and welcomed me in her group like a family member.

Thanks go to all of the people who work and have worked in our lab in Rome and helped me throughout my PhD. In particular Dr. Barbara Chiavarino, Dr. Annito di Marzio and Valentina Lilla.

A very special thank goes to Alessandro Maccelli, colleague and primarly friend of mine, who has aglow the period of my PhD with insightful discussions, neverthless with smiles and jokes.

I would also like to thank my family, my mother and my brother. They have supported me and loved me every second of my life, I could never thank them enough.

Last but not least I thank my girlfriend Valeria, she has walked with me all along this journey, celebrating with me the the joys and enduring the troubles. Thank you for not letting me down and holding me every time I needed you.